

Pertanika Journal of
**SCIENCE &
TECHNOLOGY**

JST

VOL. 31 (5) AUG. 2023



PERTANIKA
JOURNALS

A scientific journal published by Universiti Putra Malaysia Press

PERTANIKA JOURNAL OF SCIENCE & TECHNOLOGY

About the Journal

Overview

Pertanika Journal of Science & Technology is an official journal of Universiti Putra Malaysia. It is an open-access online scientific journal. It publishes original scientific outputs. It neither accepts nor commissions third party content.

Recognised internationally as the leading peer-reviewed interdisciplinary journal devoted to the publication of original papers, it serves as a forum for practical approaches to improve quality on issues pertaining to science and engineering and its related fields.

Pertanika Journal of Science & Technology currently publishes 6 issues a year (*January, March, April, July, August, and October*). It is considered for publication of original articles as per its scope. The journal publishes in **English** and it is open for submission by authors from all over the world.

The journal is available world-wide.

Aims and scope

Pertanika Journal of Science & Technology aims to provide a forum for high quality research related to science and engineering research. Areas relevant to the scope of the journal include: bioinformatics, bioscience, biotechnology and bio-molecular sciences, chemistry, computer science, ecology, engineering, engineering design, environmental control and management, mathematics and statistics, medicine and health sciences, nanotechnology, physics, safety and emergency management, and related fields of study.

History

Pertanika Journal of Science & Technology was founded in 1993 and focuses on research in science and engineering and its related fields.

Vision

To publish a journal of international repute.

Mission

Our goal is to bring the highest quality research to the widest possible audience.

Quality

We aim for excellence, sustained by a responsible and professional approach to journal publishing. Submissions can expect to receive a decision within 90 days. The elapsed time from submission to publication for the articles averages 180 days. We are working towards decreasing the processing time with the help of our editors and the reviewers.

Abstracting and indexing of Pertanika

Pertanika Journal of Science & Technology is now over 27 years old; this accumulated knowledge and experience has resulted the journal being abstracted and indexed in SCOPUS (Elsevier), Clarivate Web of Science (ESCI), EBSCO, ASEAN CITATION INDEX, Microsoft Academic, Google Scholar, and MyCite.

Citing journal articles

The abbreviation for Pertanika Journal of Science & Technology is *Pertanika J. Sci. & Technol.*

Publication policy

Pertanika policy prohibits an author from submitting the same manuscript for concurrent consideration by two or more publications. It prohibits as well publication of any manuscript that has already been published either in whole or substantial part elsewhere. It also does not permit publication of manuscript that has been published in full in proceedings.

Code of Ethics

The *Pertanika* journals and Universiti Putra Malaysia take seriously the responsibility of all of its journal publications to reflect the highest in publication ethics. Thus, all journals and journal editors are expected to abide by the journal's codes of ethics. Refer to *Pertanika's Code of Ethics* for full details, or visit the journal's web link at http://www.pertanika.upm.edu.my/code_of_ethics.php

Originality

The author must ensure that when a manuscript is submitted to *Pertanika*, the manuscript must be an original work. The author should check the manuscript for any possible plagiarism using any program such as Turn-It-In or any other software before submitting the manuscripts to the *Pertanika* Editorial Office, Journal Division.

All submitted manuscripts must be in the journal's acceptable similarity index range:
≤ 20% – PASS; > 20% – REJECT.

International Standard Serial Number (ISSN)

An ISSN is an 8-digit code used to identify periodicals such as journals of all kinds and on all media—print and electronic.

Pertanika Journal of Science & Technology: e-ISSN 2231-8526 (Online).

Lag time

A decision on acceptance or rejection of a manuscript is reached in 90 days (average). The elapsed time from submission to publication for the articles averages 180 days.

Authorship

Authors are not permitted to add or remove any names from the authorship provided at the time of initial submission without the consent of the journal's Chief Executive Editor.

Manuscript preparation

For manuscript preparation, authors may refer to *Pertanika*'s **INSTRUCTION TO AUTHORS**, available on the official website of *Pertanika*.

Editorial process

Authors who complete any submission are notified with an acknowledgement containing a manuscript ID on receipt of a manuscript, and upon the editorial decision regarding publication.

Pertanika follows a **double-blind peer-review** process. Manuscripts deemed suitable for publication are sent to reviewers. Authors are encouraged to suggest names of at least 3 potential reviewers at the time of submission of their manuscripts to *Pertanika*, but the editors will make the final selection and are not, however, bound by these suggestions.

Notification of the editorial decision is usually provided within 90 days from the receipt of manuscript. Publication of solicited manuscripts is not guaranteed. In most cases, manuscripts are accepted conditionally, pending an author's revision of the material.

The journal's peer review

In the peer-review process, 2 to 3 referees independently evaluate the scientific quality of the submitted manuscripts. At least 2 referee reports are required to help make a decision.

Peer reviewers are experts chosen by journal editors to provide written assessment of the **strengths** and **weaknesses** of written research, with the aim of improving the reporting of research and identifying the most appropriate and highest quality material for the journal.

Operating and review process

What happens to a manuscript once it is submitted to *Pertanika*? Typically, there are 7 steps to the editorial review process:

1. The journal's Chief Executive Editor and the Editor-in-Chief examine the paper to determine whether it is relevance to journal needs in terms of novelty, impact, design, procedure, language as well as presentation and allow it to proceed to the reviewing process. If not appropriate, the manuscript is rejected outright and the author is informed.
2. The Chief Executive Editor sends the article-identifying information having been removed, to 2 to 3 reviewers. They are specialists in the subject matter of the article. The Chief Executive Editor requests that they complete the review within 3 weeks.

Comments to authors are about the appropriateness and adequacy of the theoretical or conceptual framework, literature review, method, results and discussion, and conclusions. Reviewers often include suggestions for strengthening of the manuscript. Comments to the editor are in the nature of the significance of the work and its potential contribution to the research field.

3. The Editor-in-Chief examines the review reports and decides whether to accept or reject the manuscript, invite the authors to revise and resubmit the manuscript, or seek additional review reports. In rare instances, the manuscript is accepted with almost no revision. Almost without exception, reviewers' comments (to the authors) are forwarded to the authors. If a revision is indicated, the editor provides guidelines for attending to the reviewers' suggestions and perhaps additional advice about revising the manuscript.
4. The authors decide whether and how to address the reviewers' comments and criticisms and the editor's concerns. The authors return a revised version of the paper to the Chief Executive Editor along with specific information describing how they have addressed the concerns of the reviewers and the editor, usually in a tabular form. The authors may also submit a rebuttal if there is a need especially when the authors disagree with certain comments provided by reviewers.
5. The Chief Executive Editor sends the revised manuscript out for re-review. Typically, at least 1 of the original reviewers will be asked to examine the article.
6. When the reviewers have completed their work, the Editor-in-Chief examines their comments and decides whether the manuscript is ready to be published, needs another round of revisions, or should be rejected. If the decision is to accept, the Chief Executive Editor is notified.
7. The Chief Executive Editor reserves the final right to accept or reject any material for publication, if the processing of a particular manuscript is deemed not to be in compliance with the S.O.P. of *Pertanika*. An acceptance letter is sent to all the authors.

The editorial office ensures that the manuscript adheres to the correct style (in-text citations, the reference list, and tables are typical areas of concern, clarity, and grammar). The authors are asked to respond to any minor queries by the editorial office. Following these corrections, page proofs are mailed to the corresponding authors for their final approval. At this point, **only essential changes are accepted**. Finally, the manuscript appears in the pages of the journal and is posted on-line.

Pertanika Journal of

**SCIENCE
& TECHNOLOGY**

Vol. 31 (5) Aug. 2023



A scientific journal published by Universiti Putra Malaysia Press



EDITOR-IN-CHIEF

Luqman Chuah Abdullah
Chemical Engineering

CHIEF EXECUTIVE EDITOR

Mohd Sapuan Salit

UNIVERSITY PUBLICATIONS COMMITTEE

CHAIRMAN

Nazamid Saari

EDITORIAL STAFF

Journal Officers:

Ellyianur Puteri Zainal
Kanagamalar Silvarajoo
Muhammad Shafique Ardi Abdul Rahman
Siti Zuhaila Abd Wahid
Tee Syin Ying

Editorial Assistants:

Ku Ida Mastura Ku Baharom
Siti Juridah Mat Arip
Zulinaardawati Kamarudin

English Editor:

Norhanizah Ismail

PRODUCTION STAFF

Pre-press Officers:

Nur Farrah Dila Ismail
Wong Lih Jiun

WEBMASTER

IT Officer:

Illi Najwa Mohamad Sakri

EDITORIAL OFFICE

JOURNAL DIVISION

Putra Science Park
1st Floor, IDEA Tower II
UPM-MTDC Technology Centre
Universiti Putra Malaysia
43400 Serdang, Selangor Malaysia.

General Enquiry

Tel. No: +603 9769 1622 | 1616

E-mail:

executive_editor.pertanika@upm.edu.my

URL: www.journals-jd.upm.edu.my

PUBLISHER

UPM Press

Universiti Putra Malaysia
43400 UPM, Serdang, Selangor, Malaysia.
Tel: +603 9769 8851
E-mail: penerbit@putra.upm.edu.my
URL: <http://penerbit.upm.edu.my>



ASSOCIATE EDITOR

2021-2023

Adem Kilicman
Mathematical Sciences
Universiti Putra Malaysia, Malaysia

Miss Laiha Mat Kiah
Security Services Sn: Digital Forensic, Steganography, Network Security, Information Security, Communication Protocols, Security Protocols
Universiti Malaya, Malaysia

Saidur Rahman
Renewable Energy, Nanofluids, Energy Efficiency, Heat Transfer, Energy Policy
Sunway University, Malaysia

EDITORIAL BOARD

2022-2024

Abdul Latif Ahmad
Chemical Engineering
Universiti Sains Malaysia, Malaysia

Ho Yuh-Shan
Water research, Chemical Engineering and Environmental Studies
Asia University, Taiwan

Mohd Zulkifly Abdullah
Fluid Mechanics, Heat Transfer, Computational Fluid Dynamics (CFD)
Universiti Sains Malaysia, Malaysia

Ahmad Zaharin Aris
Hydrochemistry, Environmental Chemistry, Environmental Forensics, Heavy Metals
Universiti Putra Malaysia, Malaysia

Hsiu-Po Kuo
Chemical Engineering
National Taiwan University, Taiwan

Mohd. Ali Hassan
Bioprocess Engineering, Environmental Biotechnology
Universiti Putra Malaysia, Malaysia

Azlina Harun@Kamaruddin
Enzyme Technology, Fermentation Technology
Universiti Sains Malaysia, Malaysia

Ivan D. Rukhlenko
Nonlinear Optics, Silicon Photonics, Plasmonics and Nanotechnology
The University of Sydney, Australia

Nor Azah Yusof
Biosensors, Chemical Sensor, Functional Material
Universiti Putra Malaysia, Malaysia

Bassim H. Hameed
Chemical Engineering: Reaction Engineering, Environmental Catalysis & Adsorption
Qatar University, Qatar

Lee Keat Teong
Energy Environment, Reaction Engineering, Waste Utilization, Renewable Energy
Universiti Sains Malaysia, Malaysia

Norbahiah Misran
Communication Engineering
Universiti Kebangsaan Malaysia, Malaysia

Biswajeet Pradhan
Digital image processing, Geographical Information System (GIS), Remote Sensing
University of Technology Sydney, Australia

Mohamed Othman
Communication Technology and Network, Scientific Computing
Universiti Putra Malaysia, Malaysia

Roslan Abd-Shukur
Physics & Materials Physics, Superconducting Materials
Universiti Kebangsaan Malaysia, Malaysia

Daud Ahmad Israf Ali
Cell Biology, Biochemical, Pharmacology
Universiti Putra Malaysia, Malaysia

Mohd Shukry Abdul Majid
Polymer Composites, Composite Pipes, Natural Fibre Composites, Biodegradable Composites, Bio-Composites
Universiti Malaysia Perlis, Malaysia

Wing Keong Ng
Aquaculture, Aquatic Animal Nutrition, Aqua Feed Technology
Universiti Sains Malaysia, Malaysia

Hari M. Srivastava
Mathematics and Statistics
University of Victoria, Canada

INTERNATIONAL ADVISORY BOARD

2021-2024

CHUNG, Neal Tai-Shung
Polymer Science, Composite and Materials Science
National University of Singapore, Singapore

Mohamed Pourkashanian
Mechanical Engineering, Energy, CFD and Combustion Processes
Sheffield University, United Kingdom

Yulong Ding
Particle Science & Thermal Engineering
University of Birmingham, United Kingdom

Hiroshi Uyama
Polymer Chemistry, Organic Compounds, Coating, Chemical Engineering
Osaka University, Japan

Mohini Sain
Material Science, Biocomposites, Biomaterials
University of Toronto, Canada

ABSTRACTING AND INDEXING OF PERTANIKA JOURNALS

The journal is indexed in SCOPUS (Elsevier), Clarivate-Emerging Sources Citation Index (ESCI), BIOSIS, National Agricultural Science (NAL), Google Scholar, MyCite, ISC. In addition, Pertanika JSSH is recipient of "CREAM" Award conferred by Ministry of Higher Education (MoHE), Malaysia.

The publisher of Pertanika will not be responsible for the statements made by the authors in any articles published in the journal. Under no circumstances will the publisher of this publication be liable for any loss or damage caused by your reliance on the advice, opinion or information obtained either explicitly or implied through the contents of this publication. All rights of reproduction are reserved in respect of all papers, articles, illustrations, etc., published in Pertanika. Pertanika provides free access to the full text of research articles for anyone, web-wide. It does not charge either its authors or author-institution for refereeing/publishing outgoing articles or user-institution for accessing incoming articles. No material published in Pertanika may be reproduced or stored on microfilm or in electronic, optical or magnetic form without the written authorization of the Publisher.
Copyright ©2021 Universiti Putra Malaysia Press. All Rights Reserved.



Pertanika Journal of Science & Technology
Vol. 31 (5) Aug. 2023

Contents

Foreword <i>Mohd Sapuan Salit</i>	i
<i>In Silico</i> Screening of Breadfruit (<i>Artocarpus altilis</i>) Prenylated Flavonoids Identify Potential SARS-CoV Inhibitors <i>Nisha Govender; Siti Nur Athirah Mohd Kaspi, Thennavan Krishnan and Zeti-Azura Mohamed-Hussein</i>	2145
Super-Resolution Approach to Enhance Bone Marrow Trephine Image in the Classification of Classical Myeloproliferative Neoplasms <i>Umi Kalsom Mohamad Yusof, Syamsiah Mashohor, Marsyita Hanafi, Sabariah Md Noor and Norsafina Zainal</i>	2161
Weight Development of Captive Malayan Sun Bears (<i>Helarctos malayanus</i>) in the Malaysian Wildlife Rehabilitation Centre <i>Muhammad Izzat-Husna, Noor Nabilah Nazri, Kamaruddin Zainul Abidin, Mohammad Saiful Mansor, Zubaidah Kamarudin, Rahmat Topani and Shukor Md Nor</i>	2177
<i>Review Article</i> Salmonella Biofilm on Food Contact Surfaces and the Efficacy of Chemical Disinfectants: A Systematic Review <i>Xue Wei Tee and Noor Azira Abdul-Mutalib</i>	2187
Chest Computed Tomography (CT) and Clinical Findings Among COVID-19 Patients of Tertiary Hospital in Bangladesh <i>Tarek Shams, Jamil Haider Chowdhury, Hasna Hena Chowdhury, Qumrul Ahsan, Hrionmoy Dutta, Mohammad Ali Tareq, Lubna Shirin, Sanjida Akhter and Tania Islam</i>	2203
Image Retrieval Using Fusion of Sauvola and Thepade's Sorted Block Truncation Coding-Based Color Features <i>Jaya H. Dewan and Sudeep D. Thepade</i>	2217
On Estimating the Parameters of the Generalised Gamma Distribution based on the Modified Internal Rate of Return for Long-Term Investment Strategy <i>Amani Idris Ahmed Sayed and Shamsul Rijal Muhammad Sabri</i>	2241
Underdetermined Blind Source Separation of Bioacoustic Signals <i>Norsalina Hassan and Dzati Athiar Ramli</i>	2257

Correlation Studies and Kinetic Modelling of Electrocoagulation Treatment of Pepper Wastewater <i>Puteri Nurain Megat Ahmad Azman, Rosnah Shamsudin, Hasfalina Che Man and Mohammad Effendy Ya'acob</i>	2273
<i>Short Communication</i>	
The Digestibility and Bacterial Growth Rates of Microwave Treated Sago (<i>Metroxylon sagu</i>) Starch <i>Mohd Alhafizh Zailani, Hanisah Kamilah, Ahmad Husaini, Awang Zulfikar Rizal Awang Seruji and Shahrul Razid Sarbini</i>	2283
Effects of Microwave Power and Carrier Materials on Anthocyanins, Antioxidants, and Total Phenolic Content of Encapsulated <i>Clitoria ternatea</i> Flower Extract <i>Nurul Asyikin Md Zaki, Junaidah Jai, Mohd Hakim Syuwari Hasan, Nur Qistina Mohamad Kamarul Azman, Syafiza Abd Hashib, Nozieana Khairuddin, Norashikin Mat Zain and Nurul Hidayah Samsulrizal</i>	2291
Utilization of Water Hyacinth and Spent Coffee Ground as Raw Materials to Produce Bio-Compost <i>Thanakorn Saengsanga and Napat Noinumsai</i>	2303
Effect of Pre-Treatment Methods on the Extractability of <i>Christia vespertilionis</i> by Supercritical Carbon Dioxide <i>Izni Atikah Abd Hamid, Najla Laazizi, Ana Najwa Mustapa and Norazah Abd Rahman</i>	2311
Spatial Distribution of Malaysian Storks Determined Based on Citizen Science (eBird) Data <i>Ain Afifah Tolohah, Fatimah Najihah Arazmi, Shukor Md. Nor and Mohammad Saiful Mansor</i>	2329
<i>Review Article</i>	
Analysis of Environmental Stresses on the Mechanical Properties of Laminated Glass Composites: A Review of Experimental Results and Outlook <i>Ufuoma Joseph Udi, Mustafasanie M. Yussof Felix Nkapheeyan Isa and Luqman Chuah Abdullah</i>	2339
Thermal Properties of Kenaf Fiber Reinforced Polyamide 6 Composites by Melt Processing <i>Norihan Abdullah, Khalina Abdan, Mohd Huzaifah Mohd Roslim, Mohd Nazren Radzuan, Lee Ching Hao and Ayu Rafiqah Shafi</i>	2361
Innovative Formulation and Characterisation of Grease Made from Waste Engine Oil <i>Muhammad Auni Hairunnaja, Mohd Aizudin Abd Aziz, Nurul Waheeda Abdu Rahman, Mohd Azmir Arifin, Khairuddin Md Isa and Umi Fazara Md Ali</i>	2375

A Study on Bio-Stabilisation of Sub-Standard Soil by Indigenous Soil Urease-Producing Bacteria <i>Abdulaziz Dardau Aliyu, Muskhazli Mustafa, Nor Azwady Abd Aziz and Najaatu Shehu Hadi</i>	2389
Occupational Formaldehyde Exposure and the Health Symptoms Among Histopathology Laboratory Workers in North Borneo <i>Alif Ramli, Shamsul Bahari Shamsudin, Jac Fang Lim and Mei Ching Lim</i>	2413
Estimating Disability-Free Life Expectancy of Malaysian Population Using the Sullivan's Approach <i>Khairunnisa Mokhtar, Syazreen Niza Shair and Norazliani Md Lazam</i>	2427
Effects of UV Irradation on Electrospun PLLA and PAN in the Production of Short Electropun Fibres Using Ultrasonication Method <i>Marini Sawawi, Cheryl Rinnai Raja, Shirley Jonathan Tanjung, Sinin Hamdan, Siti Kudnie Sahari, Rohana Sapawi, Ervina Junaidi, Mahshuri Yusof and Noor Hisyam Noor Mohamed</i>	2441
A Comparison of the Performance of MAPbI ₃ and MASnI ₃ as an Inverted Perovskite Structure Using NiO as HTL Through Numerical GPVDM Simulation <i>Subathra Muniandy, Muhammad Idzdihar Idris, Zul Atfyi Fauzan Mohammed Napiah, Zarina Baharudin Zamani, Marzaini Rashid and Luke Bradley</i>	2453
Fabrication of PES MMMs with Improved Separation Performances Using Two-Dimensional rGO/ZIF-8 and MoS ₂ /ZIF-8 Nanofillers <i>Noor Fauziyah Ishak, Nur Hidayati Othman, Najihah Jamil, Nur Hashimah Alias, Fauziah Marpani, Munawar Zaman Shahrudin, Lau Woei Jye and Ahmad Fauzi Ismail</i>	2473
The Influence of Abiotic Factors on the Occurrence of Jackfruit Dieback Disease <i>Nurul Hawani Idris, Erneeza Mohd Hata, Norliza Adnan, Sazlieya Saupi Teri, Mohamad Jahidi Osman, Ami Hassan Md Din and Mohamad Hafis Izran Ishak</i>	2487
<i>Review Article</i> The Grease Formulation Using Waste Substances from Palm Oil Refinery and Other Industrial Wastes: A Review <i>Muhammad Auni Hairunnaja, Mohd Aizudin Abd Aziz, Nur Amira Fatihah Bashari, Mohd Azmir Arifin, Navinash Nedumaran, Khairuddin Md Isa and Umi Fazara Md Ali</i>	2505

<i>Review Article</i>	
The Unified Model of Electronic Government Adoption (UMEGA): A Systematic Literature Review with Meta-Analysis <i>Rakib Ahmed Saleh, Rozi Nor Haizan Nor, Md. Tariqul Islam, Yusmadi Yah Jusoh and Salfarina Abdullah</i>	2531
Workload Characterization and Classification: A Step Towards Better Resource Utilization in a Cloud Data Center <i>Avita Katal, Susheela Dahiya and Tanupriya Choudhury</i>	2559
Reactivity Enhancement of Lignin Extracted from Preconditioning Refiner Chemical-Recycle Bleached Mechanized Pulp (PRC-RBMP) Black Liquor by Phenolation <i>Lim Kah Yen, Tengku Arisyah Tengku Yasim-Anuar, Farhana Aziz Ujang, Hazwani Husin, Hidayah Ariffin, Paridah Md Tahir, Li Xin Ping and Mohd Termizi Yusof</i>	2577
<i>Fusarium solani</i> Species Complex (FSSC) in Nests of Hawksbill Turtles (<i>Eretmochelys imbricata</i>) with High Hatching Success in Melaka, Malaysia <i>Khai Wei See and Nurul Salmi Abdul Latip</i>	2601
<i>Review Article</i>	
Progress, Trends and Development of Drying Studies on Coconut Kernel Products: A Review <i>Yahya Sahari, Mohd Shamsul Anuar, Mohd Zuhair Mohd Nor, Nur Hamizah Abdul Ghani and Suraya Mohd Tahir</i>	2621

Foreword

Welcome to the fifth issue of 2023 for the *Pertanika Journal of Science and Technology (PJST)*!

PJST is an open-access journal for studies in Science and Technology published by Universiti Putra Malaysia Press. It is independently owned and managed by the university for the benefit of the world-wide science community.

This issue contains 30 articles; five review articles, one short communication and the rest are regular articles. The authors of these articles come from different countries namely Bangladesh, China, England, India, Malaysia, Nigeria and Thailand.

A regular article titled “Super-resolution approach to enhance bone marrow trephine image in the classification of Classical Myeloproliferative Neoplasms” was presented by Umi Kalsom Mohamad Yusof and co-researchers from Universiti Putra Malaysia & Hospital Serdang, Malaysia. This study has developed a classification system for classical MPN subtypes: polycythemia vera, essential thrombocythemia, and primary myelofibrosis. It was done by reconstructing low-resolution images of bone marrow trephine using a super-resolution approach to address the issue. Identified low-resolution images from calculating Laplacian variance were reconstructed using a super-resolution convolution neural network (SRCNN) to transform into rich information of high-resolution images. Based on the result, the dataset of SRCNN images produced higher results, with an accuracy of 92% compared to the control images (88%). In conclusion, image reconstruction using SRCNN has proven to effectively improve the quality of BMT images in the pre-processing stage and enhance the performance in the development of the prediction model. Detailed information on this study is available on page 2161.

The next article discussed image retrieval using a fusion of Sauvola and Thepade’s sorted block truncation coding-based color features. The proposed technique is tested using two standard datasets with mean square error (MSE) as a distance measure and average retrieval accuracy (ARA) as a performance metric. The technique has contributed to the enhancement of ARA with the small and fixed-size image feature vector. The feature vector generated is much smaller than the image dimension and is used as a feature vector to represent the image for retrieval. Results prove that the proposed technique of SBTC 8-ary with 0.1 weight and SLT with 0.9 weight feature fusion gives better ARA than other techniques studied. Details of this study are available on page 2217.

An investigation on *Fusarium solani* species complex (FSSC) in nests of hawksbill turtles (*Eretmochelys imbricata*) with high hatching success in Melaka, Malaysia, was conducted by Khai Wei See and Nurul Salmi Abdul Latip from Universiti Sains Malaysia. Samples of cloacal mucus, nest sand, eggshells, and eggs were collected from seven hawksbill turtles and their corresponding

nests at Melaka's nesting beaches and hatchery site. FSSC was prevalent in the unhatched eggs (n = 32) from the seven study nests, colonizing 96.9%. The remaining eggs from the study nests were found to have high hatching success, with a mean of $85.8 \pm 10.5\%$ (n = 7). It is unknown if the presence of FSSC contributed directly to embryonic mortality in this study. Further details of the investigation can be found on page 2601.

We anticipate that you will find the evidence presented in this issue to be intriguing, thought-provoking and useful in reaching new milestones in your own research. Please recommend the journal to your colleagues and students to make this endeavour meaningful.

All the papers published in this edition underwent Pertanika's stringent peer-review process involving a minimum of two reviewers comprising internal as well as external referees. This was to ensure that the quality of the papers justified the high ranking of the journal, which is renowned as a heavily-cited journal not only by authors and researchers in Malaysia but by those in other countries around the world as well.

We would also like to express our gratitude to all the contributors, namely the authors, reviewers, Editor-in-Chief and Editorial Board Members of PJST, who have made this issue possible.

PJST is currently accepting manuscripts for upcoming issues based on original qualitative or quantitative research that opens new areas of inquiry and investigation.

Chief Executive Editor

Mohd Sapuan Salit

executive_editor.pertanika@upm.edu.my

***In Silico* Screening of Breadfruit (*Artocarpus altilis*) Prenylated Flavonoids Identify Potential SARS-CoV Inhibitors**

Nisha Govender^{1*}, Siti Nur Athirah Mohd Kaspi^{1,2}, Thennavan Krishnan^{1,3} and Zeti-Azura Mohamed-Hussein^{1,2}

¹*Institute of Systems Biology (INBIOSIS), Universiti Kebangsaan Malaysia, 43600 UKM, Bangi, Selangor, Malaysia*

²*Department of Applied Physics, Faculty of Science and Technology, Universiti Kebangsaan Malaysia, 43600 UKM, Bangi, Selangor, Malaysia*

³*Infrastructure University Kuala Lumpur (IUKL), Unipark Suria 43000, Jalan Ikram-Uniten, Kajang, Selangor, Malaysia*

ABSTRACT

Coronavirus Disease 2019 (COVID-19) caused by severe acute respiratory syndrome coronavirus 2 (SARS-CoV-2) is a global health threat. Traditional herbals and dietary plants with medicinal values have a long antiviral history and, thus, are extensively studied in COVID-19 therapeutics development. Breadfruit (*Artocarpus altilis*) is a food crop with rich nutrient composition. This study screened selected breadfruit prenylated flavonoids for their potential inhibitory activities against the SARS-CoV family receptors using molecular docking and molecular dynamics (MD) simulation. The *A. altilis* prenylated flavonoids were selected as target ligands (artocarpin, artoindonesianin V, artonin M, cudraflavone A and cycloartobiloxanthone) and molecular targets from the SARS-CoV family were designated as receptors. Molecular docking was applied with the Lamarckian Genetic algorithm to measure the receptor-ligand orientation using AutoDock Vina software. The structural interactions of the receptor-ligand complexes were visualised using the Biovia Discovery Studio 4.5. Under all possible receptor-ligand combinations, the complexes'

minimum binding affinities (MBA) ranged from -5.5 to -9.1 kcal/mol and held by hydrophobic interactions, hydrogen bonds and electrostatic attractions. Receptor-ligand complexes with the least MBA (<-6.0 kcal/mol) along with strong structural interactions were validated by MD simulation using the GROMACS software. The 5RE4-artocarpin and 5RE4-artoindonesianin V showed the

ARTICLE INFO

Article history:

Received: 01 April 2022

Accepted: 16 August 2022

Published: 13 July 2023

DOI: <https://doi.org/10.47836/pjst.31.5.01>

E-mail addresses:

nishag@ukm.edu.my (Nisha Govender)

a164782@siswa.ukm.edu.my (Siti Nur Athirah Mohd Kaspi)

tenakrish92@yahoo.com (Thennavan Krishnan)

zeti.hussein@ukm.edu.my (Zeti-Azura Mohamed-Hussein)

* Corresponding author

highest hydrophobic interactions at $MBA = -6.6$ kcal/mol and -6.4 kcal/mol, respectively. The trajectory analysis of 5RE4-artocarpin and 5RE4-artoindonesianin V complexes was fairly stable throughout a 50 ns MD simulation run. The findings conclude that artocarpin and artoindonesianin V are good potential SARS-CoV family receptor inhibitors.

Keywords: *Artocarpus altilis*, COVID-19, dietary plant, herbal medicine, molecular docking, prenylated flavonoids, SARS-CoV-2, traditional medicine

INTRODUCTION

Breadfruit (*Artocarpus altilis*), commonly known as 'sukun' in Malaysia and Indonesia, is a multi-purpose tree. The fruit tree is native to New Guinea, Moluccas (Indonesia) and the Philippines (Sikarwar et al., 2018) and was first cultivated in the western Pacific. In tropical regions, the different tree parts are utilised as food (fruit), medicine (fruit, leaves and bark), building material (trunk) and feed (leaves) (Ragone, 2018). The evergreen tree belongs to the Moraceae family and bears large starchy, carbohydrate-rich seeded or seedless fruits. The tree starts to fruit within 3 to 5 years of establishment, thriving well in adverse conditions (Sofoini et al., 2018). Fruits are either oval or oblong, with an average weight of 1.5-2.0 kg (Figure 1). The monoecious tree has been an important staple food in the South-Pacific region for decades (Jamil et al., 2018).

Malaysia is a tropical country with great species diversity. An extensive range of fruit plants, from exotic (minor) to common (major) ones, are included in dietary consumption. Apart from their unique and desirable mouthfeel, taste, and flavour, these fruits are rich in nutraceutical values (Daley et al., 2020; Baba et al., 2016). As such, breadfruit is a well-known edible food often consumed as chips or incorporated in curries among rural Malaysians. It is also used in traditional folk medicine to combat inflammation and

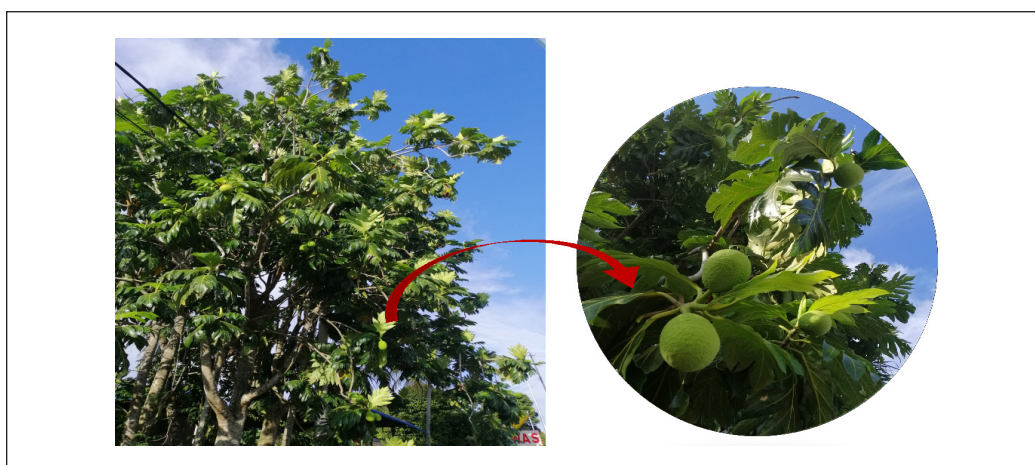


Figure 1. Breadfruit (*Artocarpus altilis*) tree along the roadside at Sungai Merab, Selangor. The image in circle is the zoom view of the unripe fruits

inflammation-associated diseases (Page, 2021; Lin et al., 2012; Fang et al., 2008; Wei et al., 2005). Breadfruit leaves hold pharmacological potential in treating liver cirrhosis, hypertension, renal function and diabetes (Jamil et al., 2018; Baba et al., 2016; Adewole & Oiewole, 2007). The leaves contain bioactive compounds with potent anti-allergenic, anti-inflammatory, anti-microbial and antioxidant activities (Leng et al., 2018). Latex and bark can be used to treat sprains, sciatica, and skin diseases, and the fruit extract has shown cytotoxic effects against human cancer cell lines (Jamil et al., 2018). In Indonesia, *Artocarpus* is used to treat inflammation and malaria fever (Hano et al., 1990).

Phytochemical analyses of various *Artocarpus* species have shown the occurrence of various bioactive compounds, particularly flavonoids, in different plant parts (Jalal et al., 2015): flavonoids, stilbenes, and 4-substituted resorcinols in *A. altilis* heartwood (Shimizu et al., 1998), cyclogeracommunin and artoflavone A in *A. communis* cortex (Lin et al., 2012), prenylflavonoids (Cidade et al., 2001), artomunioisoxanthone, artocommunol C, artochamin D, artochamin B, dihydroartomunoxanthonein in *A. communis* (Weng et al., 2006), cycloartelastoxanthone, artelastoheterol, cycloartobiloxanthone and arthonol A in *A. elasticus* (Ko et al., 2005), artocarpin, artoindonesianin, artonin M, cudraflavone and cycloartobiloxanthone in *A. altilis* heartwood and cortex (Hari et al., 2014; Lan et al., 2013; Amarasinghe et al., 2008; Hakim et al., 2006).

Flavonoids are polyphenols of naturally occurring antioxidants present in higher plants. They display free-radical scavenging, immunomodulating and antiviral properties implicated in pathological disorders such as carcinogenesis, ageing and inflammation (Shah et al., 2016; Lin et al., 2012). The general class of flavonoids have shown antiviral activities against influenza A virus (H1N1), hepatitis B and C virus (HBV/HVC), herpes simplex virus 1 (HSV-1), human immunodeficiency virus (HIV) and Epstein-Barr (Sofoini et al., 2018). No studies have reported on the potential inhibitory activities of breadfruit prenylated flavonoids against the coronavirus family.

Coronavirus disease-2019 (COVID-19) is an unprecedented health crisis of recent times. The disease sparks an inflammatory immune response with the burst of inflammatory cytokines leading to acute respiratory distress syndrome and multi-organ dysfunctionality (Tang et al., 2020). Herbal medicines are claimed to ease disease severity, improve clinical symptoms and reduce mortality. In previous studies, many plant extracts have demonstrated a broad range of immunomodulatory effects on the human immune system (Jantan et al., 2015). Further, plant-based medicines and supplements (traditional Chinese medicine, Ayurveda medicine) are reported to function effectively by minimising the burst of pro-inflammatory cytokine TNF, IL-6 and IL-8, among which are involved in the human immune response against SARS-CoV-2 infection (Rehman et al., 2021; Aucoin et al., 2021; Demeke et al., 2021; Paraiso et al., 2020; Liu et al., 2010).

Due to their potency and safety, natural products are at a better edge than cytotoxic drugs (Ali-Reza et al., 2021). Under this context, screening the breadfruit phytochemicals

against SARS-CoV family receptors to shed information on their antiviral potentials is important to leverage the exploration of plant medicinal properties against infectious disease. In this study, the physical interaction of selected breadfruit prenylated flavonoid-bound SARS-CoV receptor complexes was evaluated via molecular docking and the most stable receptor-ligand complexes was validated by molecular dynamics simulation.

MATERIALS AND METHODS

Protein Files and Pre-Processing

The 3-dimensional structures of SARS-CoV family receptors were retrieved from the Protein Data Bank (PDB) (www.rcsb.org): membrane protein (PDB ID: 3I6G), main protease (PDB ID: 5RE4) and spike glycoproteins (PDB ID: 6VXX and 6VYB). A detailed structural view of each receptor is presented in Figure 2. The receptor files were pre-processed using AutoDock Tools 1.5.6 (Trott & Olson, 2010): remove water molecules, polar hydrogen atoms, and Kollman charges. The pre-processed receptor files were saved in PDBQT format.

Ligand Files and Pre-Processing

A sub-structure search was performed for the following breadfruit flavonoids using PubChem database (<https://pubchem.ncbi.nlm.nih.gov>): artocarpin (CID: 24850643), artoindonesianin V (CID: 10053761), artonin M (CID: 44258661), cudraflavone A (CID: 5316261) and cycloartobiloxanthone (CID: 10342859) (Figure 2). The ligand files obtained

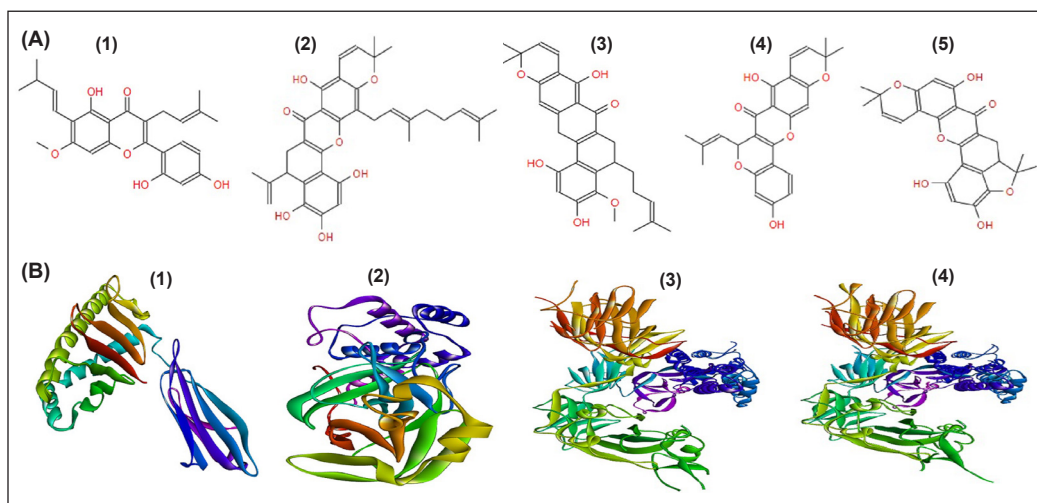


Figure 2. Ligand and receptor structure view. (A) *Artocarpus altilis* prenylated flavonoid 2D structures obtained from PubChem (<https://pubchem.ncbi.nlm.nih.gov>): (1) artocarpin (CID: 24850643), (2) artoindonesianin V (CID: 10053761), (3) artonin M (CID: 44258661), (4) cudraflavone A (CID: 5316261) and (5) cycloartobiloxanthone (CID: 10342859). (B) The 3D structures of SARS-CoV family receptors retrieved from Protein Data Bank (www.rcsb.org): (1) membrane protein: 3I6G, (2) main protease: 5RE4, (3) spike glycoprotein: 6VXX; and (4) spike glycoprotein: 6VYB.

in SDF format were converted into PDB format using Open Babel (www.cheminfo.org), a chemical toolbox for chemical structure inter-conversions (O'Boyle et al., 2011). These structures were then pre-processed using AutoDock Tools 1.5.6 (Trott & Olson, 2010), removing heteroatom, assigning torsion and adding Gasteiger charges. All ligand files were saved in PDBQT format.

Molecular Docking and Visualisation

Four different SARS-CoV family receptors were docked with breadfruit prenylated flavonoids (ligands) under all receptor-ligand, pair-wise combinations. All pre-processed structure files (PDBQT format) were docked using AutoDock Vina 1.1.2 (Trott & Olson, 2010). A grid box of 40x40x40 encompassing the active residues of the receptor was set based on the x, y and z coordinates of the receptor binding pocket region. The Lamarckian Genetic algorithm was applied using its default settings. For each receptor-ligand complex, the docking procedure was repeated thrice. The best conformation for each complex was determined by the minimum binding affinity (MBA) expressed in kcal/mol, root-mean-square-deviation (RMSD) and the extent of favourable interactions between the receptor residues (RR) and ligand atoms. All receptor-ligand complexes were visualised using the Biovia Discovery Studio 4.5 (Dhurga et al., 2016).

Molecular Dynamics Simulation

Based on the molecular docking output, the best receptor-ligand complex with the least minimum binding affinity and fairly high number of interactions was selected and validated by molecular dynamics (MD) simulation using GROMACS version 5.1.4 (<http://gromacs.org>) and CHARMM General Force Field (cGENFF) program (Vanommeslaeghe et al., 2010). The CHARMM36 all-atom force field (Feb 2021) was retrieved from the MacKerell lab website (<http://mackerell.umaryland.edu>). The ligand-receptor complex was solvated in a dodecahedron box (edge box set at 10 Å) using the TIP3P water model. The system was neutralised with Na⁺/Cl⁻ ion addition. The energy minimisation steps were set as follows: the maximum number of steps set= 50 000, and the energy step size=0.01. The 'nsteps' set for NVT and NPT equilibration was fixed at 50 000 ns. Molecular dynamic simulation of the ligand-receptor complex was performed under a 50 ns run (Lemkul, 2018; Pronk et al., 2013). The following parameters evaluated the trajectory analysis of the MD run: (1) root-mean-square-deviation (RMSD), (2) root-mean-square-fluctuation (RMSF), (3) radius of gyration (Rog), and (4) the number of hydrogen bonds.

RESULTS AND DISCUSSION

Although COVID-19 has shifted from pandemic to endemic status, ongoing control measures are cautiously deliberated as the viral-specific medication is yet to be discovered.

The most common control measures exercised routinely include regular hand washing, social distancing at crowded places, masking, isolation of infected persons and self-care or immune system enhancement via dietary consumption of nutritious food (Das et al., 2021). The likelihood of being infected with COVID-19 is directly correlated with personal health practices and compliance with general measures (WHO, 2020). Numerous studies on identifying COVID-19 inhibitors have indicated that phytochemicals are an excellent source of therapeutic ingredients.

In this regard, plant-based food (fruits and vegetables) enriched with potent phytochemicals could be exploited for immune system protection and preparation against invading viral infections. No previous research had reported on the breadfruit phytochemicals' inhibitory potential against SARS-CoV family receptors of COVID-19. Scientific information enables prediction, informs, and prepares effective, innovative solutions and holistic management strategies against COVID-19 (Skariyachan et al., 2020). In this study, the breadfruit phytochemicals from the prenylated flavonoid class were screened and evaluated via computational structure-based design (CSD) to understand and shed meaningful insights on breadfruit therapeutics' role against COVID-19 molecular targets.

In recent times, especially considering the COVID-19 pandemic, computational approaches have been rapidly deployed for phytochemical screening, antiviral agent identification, and drug discovery and development (Jorgensen, 2004). With the advent of high-throughput computational architectures coupled with algorithms dedicated to high-level computations, the implementation of CSD, which includes molecular docking and MD simulation, has been accelerated significantly. In a protein-ligand (pharmacophores) docking, the analysis calculates and evaluates the free natural affinity of the ligand to the protein active site. It infers the potential occurrence of interactions between pharmacophores. The protein-ligand conformations are ranked using a scoring function. On the other hand, the MD simulation evaluates the protein-ligand conformations' strength of interactions according to Newton's law of motion (De Vivo et al. 2016).

The molecular docking analysis predicted the interaction between the receptor residues (RRs) and ligand atoms under the lowest energy conformation at root-mean-square deviation (RMSD) =0. The prenylated breadfruit ligands (artocarpin, artoindonesianin V, artonin M, cudraflavone A and cycloartobioxanthone) were docked with SARS-CoV family receptors, and the minimum binding affinity (MBA) for all the pair-wise receptor-ligand complexes ranged at -5.5 to -9.1 kcal/mol (Table 1). These values were comparable to numerous previous studies reported on SARS-CoV-2 molecular targets and phytochemical computational docking analyses (Kaspi et al., 2022; Khaerunnisa et al., 2020). The SARS-CoV-2 spike protein (PDB ID: 6LU7) bound with gingerol (ginger), allicin (garlic), curcumin, demethoxycurcumin (turmeric), catechin, epicatechin-gallate (tea), nelfinavir,

lopinavir, kaempferol, quercetin, luteolin-7-glucoside and naringenin (phytochemicals) complexes showed MBA= -4.03 to -7.6 kcal/mol (Khaerunnisa et al., 2020). In another study, a total of 18 different compounds isolated from honey and propolis (Dawood, 2020) and java tea (Mohd Kaspi et al., 2022) showed MBA= -5.6 to -7.8 kcal/mol through an *in silico* docking against SARS-CoV-2 molecular targets.

Table 1

The ligand-receptor minimum binding affinity is expressed as energy in kcal/mol

Ligand	Receptors (Protein Data Bank ID)			
	3I6G	5RE4	6VXX	6VYB
artocarpin	-7.2	-6.6	-5.5	-5.5
artoindonesianin V	-8.4	-6.4	-6.1	-5.4
artonin M	-8.5	-7.1	-6.3	-6.5
cudraflavone A	-8.0	-6.8	-5.8	-6.1
cycloartobiloxanthone	-9.1	-7.7	-6.3	-6.0

Note. The first row represents the SARS-CoV receptors, while the first column represents the breadfruit prenylated flavonoids. All numerical values denote the minimum binding affinities expressed in kcal/mol

The receptors selected in this study represented the structural components of SARS-CoV: i) spike protein (6VXX and 6VYB), ii) main protease (5RE4) and iii) membrane protein (3I6G). The first represents the viral envelope type 1 transmembrane S glycoprotein, largely distributed protruding on the surface of mature SARS-CoV-2. The spike protein is the cognate receptor facilitating the viral entry into host cells (ACE2) and then initiates infection. Initial infection is mediated through the fusion of the viral spike protein into the host cell membrane. The main protease (M^{pro}) controls the proteolysis of large polyproteins and papain-like protease (PL^{pro}). Upon SARS-CoV-2, the positive-stranded genomic RNA attaches to the host ribosome for translation into polyproteins. With proteolysis, these polyproteins are orderly packaged into new virions. The membrane and envelope proteins modulate the maturation and retention processes for successful virion assembly (Boson et al., 2021).

The MBA for all the prenylated breadfruit ligand-bound complexes ranged from -6.3 to -5.5 kcal/mol for spike protein receptors. Slightly in a much smaller range, the MBA of main protease-bound ligand complexes ranged between -7.7 to -6.4 kcal/mol. The membrane protein-bound ligand complexes showed the least MBA range at -7.2 to -9.1 kcal/mol. The cycloartobiloxanthone-bound complexes showed the least MBA range at -9.1 to -6.0 kcal/mol, followed by artonin M-bound complexes at -8.5 to -6.5 kcal/mol (Table 1). All the receptor-ligand complexes were held by hydrogen bond, hydrophobic interaction and/or electrostatic interaction except 6VXX-artocarpin and 6VYB-cudraflavone A complexes. In most receptor-ligand complexes, at least two interactions (hydrogen bond and hydrophobic interactions) were present except 6VXX-cycloartobiloxanthone (Table 2).

Table 2

Interactions between the receptor residues and ligand atoms of the ligand-receptor complexes

Receptor-ligand complex	Hydrogen bond	Hydrophobic interaction	Electrostatic interaction	Total number of interactions
3I6G-artocarpin	ARG97, TRP147, GLN155	TYR99, LEU156, VAL152, HIS114, TRP147, TYR159, VAL152	-	10
3I6G-artoindonesianin V	THR73	TYR99, TYR159, ALA69, LYS66,	ARG97	6
3I6G-artonin M	ARG97, LYS146,	TYR159, TRP147, VAL76, HIS70, TYR99, ALA150, VAL152	ARG97	10
3I6G-cudraflavone A	TYR7, ARG97, GLU63, GLU63, LYS66	LEU156, LYS66	LYS66	8
3I6G-cycloartobioxanthone	ARG97, LYS146, TRP147	TRP147, ALA150, VAL152	-	6
5RE4-artocarpin	VAL77	GLN74, VAL73, ARG76, ARG76, VAL77	ARG76	7
5RE4-artoindonesianin V	GLN74, PHE66	ARG76, ILE78, VAL77	ARG76	6
5RE4-artonin M	ASP92	VAL73, ARG76	ARG76	4
5RE4-cudraflavone A	ARG76	ARG76, VAL73	ARG76	4
5RE4-cycloartobioxanthone	GLN74, LEU75, LEU67	VAL77	ARG76	5
6VXX-artocarpin	-	-	-	-
6VXX-artoindonesianin V	ASN87	THR236	-	2
6VXX-artonin M	PHE86, ASN87	THR236, PRO85	-	4
6VXX-cudraflavone A	ASN196	THR236	-	2
6VXX-cycloartobioxanthone	GLN115, ASN234	-	-	2
6VYB-artocarpin	ASN87, ASN196	THR236, LEU54, ILE197	-	5
6VYB-artoindonesianin V	ASN87, ASN196, ASP88	THR236	-	4
6VYB-artonin M	ASN87, THR236	THR236, PRO85	-	4
6VYB-cudraflavone A	-	-	-	-
6VYB-cycloartobioxanthone	ASN234, ASN196, ASN87	THR236	-	4

Based on the MBA values and the extent of structural interactions characterisation, the 5RE4-artocarpin and 5RE4-artoindonesianin V complexes were selected for further validation by MD simulation. The root-mean-square-fluctuation (RMSF) of 5RE4-artocarpin and 5RE4-artoindonesianin V ranged from 0.08-0.4 and 0.1-0.5, respectively (Figure 3A). A high RMSF suggests the occurrence of the flexible region within the structure complex, whereas a much lower value may implicate the presence of a secondary structure

(O'Boyle et al., 2011). The results may also suggest the stabilising effect of artocarpin and artoindonesianin V on the structure complex. The root-mean-square-deviation (RMSD), which corresponds to the conformational stability and dynamics of the complexes, was calculated for all the backbone residues. In general, the receptor-ligand complex structure remained stable for 50 ns at the following range: 5RE4-artocarpin; 0.18-0.32 ns and 5RE4-artoindonesianin V; 0.2-0.5 ns (Figure 3B). The RMSD values indicate fairly strong complex structural stability at adhering the ligand molecule at the binding site throughout the simulation run. The radius of gyration of the 5RE4-artocarpin complex was slightly higher than the 5RE4-artoindonesianin V complex (Figure 3C). Likewise, the number of hydrogen bonds formed within the 5RE4-artocarpin complex was greater than 5RE4-artoindonesianin V. At least three hydrogen bonds were consistently present throughout the 50 ns MD simulation in both the 5RE4-artocarpin and 5RE4-artoindonesianin V complexes (Figure 3D).

Prenylated flavonoids have wide pharmacological properties, highly beneficial to human health; they are anti-inflammation, anti-Alzheimer, antioxidant, anti-diabetes, vasorelaxant and cytotoxic (Shi et al., 2021). Artocarpin is abundantly distributed in the genus of *Artocarpus* (*Artocarpus communis*, *Artocarpus integrifolia*, *A. lakoocha*).

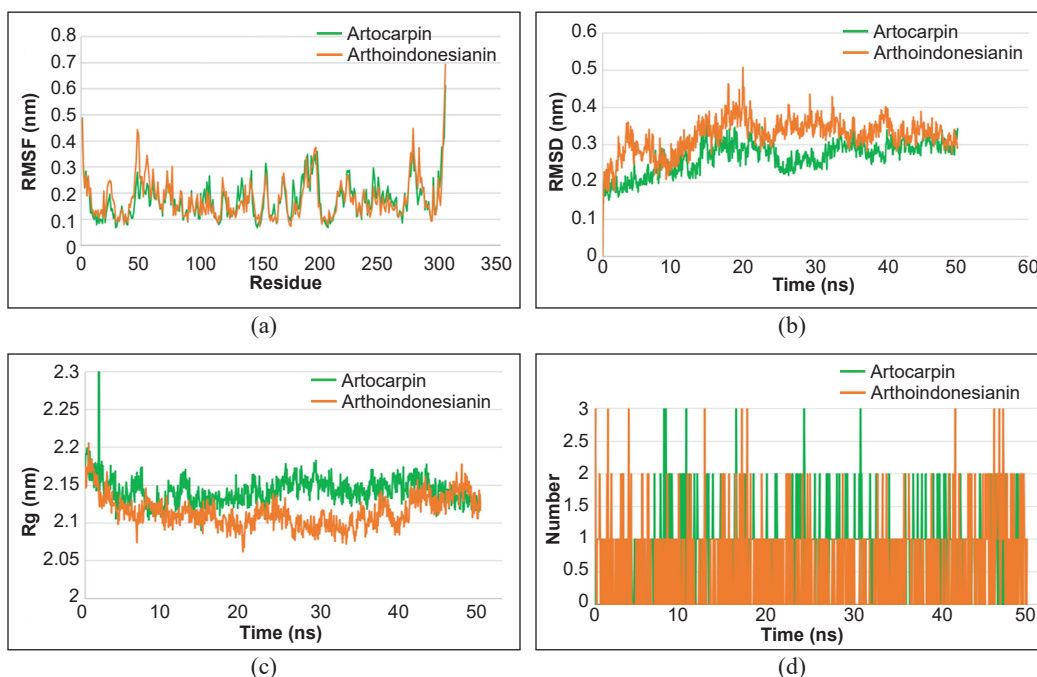


Figure 3. Trajectory analysis of 5RE4-artocarpin and 5RE4-artoindonesianin V, receptor-ligand complexes under a 50 ns molecular dynamics (MD) simulation run at 300 K (temperature) and 1 bar pressure. The green and orange lines represent 5RE4-artocarpin and 5RE4-artoindonesianin V, respectively. (a) Root-mean-square-deviation (RMSD), (b) Root-mean-square-fluctuation (RMSF), (c) Radius of gyration (Rg) and (d) The number of hydrogen bonds

Previous reports have demonstrated interesting biological activities of artocarpin, such as inhibitory effects on melanin biosynthesis, antibacterial activities, and cytotoxicity. On the other hand, the artoindonesianin V is not only found in stem bark extracts of *A. altilis* (Shamaun et al., 2010) but is also present in the heartwood of *A. champeden*, locally known as chempedak in Malaysia. Artoindonesianin V has shown cytotoxic effects against murine leukaemia P38 cells (Hakim et al., 2006). The artonin (art) M has been reported to be present in *A. altilis* (Hano et al., 1990) and *A. rotunda* (Suhartati et al., 2008). No studies have recorded specific medicinal effects/actions against human cell lines (Bailly, 2021). Similarly, cudraflavone A and cycloartobiloxanthone medicinal properties are least reported compared to other prenylated flavonoids identified in the genus *Artocarpus*. Cudraflavone A is reportedly present in *A. communis* root bark (Shieh & Lin, 1992) and *A. altilis*. In a study by Septama et al. 2018, artocarpanone and artocarpin compounds were shown to suppress the phagocytosis of phagocyte cells.

Considering the new norm of living with COVID-19, there is an ever-growing awareness among the public for better health management. The demand for dietary supplements, herbal products, and fortified diets is soaring. Phytochemicals are excellent sources for pharmacological applications often integrated as immune health boosters (Chang et al., 2021). Non-pharmaceutical interventions in infectious disease management are gaining momentum with the inclusion of dietary bioactive compounds, which are good nutraceuticals. Under this context, breadfruit prenylated flavonoids from a readily available fruit crop within the tropical region can be integrated into the human diet, enhancing the immune health system with better protection against the SARS-CoV-2 of COVID-19 (Bhat & Paliyath, 2016; Shi et al., 2021).

CONCLUSION

Breadfruit prenylated flavonoids hold good therapeutic potential in COVID-19 prevention and management. The current findings predicted a good minimum binding affinity between artocarpin, artoindonesianin V, artonin M, cudraflavone A and cycloartobiloxanthone and SARS-CoV family receptors. The MD simulation analysis of artocarpin and artoindonesianin V compounds provides valuable insights into developing new breadfruit-based therapeutic agents for COVID-19 treatment and management. However, complementary laboratory scale experiments are required prior to upstream application strategies.

ACKNOWLEDGEMENT

The second and third authors thank the Institute of Systems Biology (INBIOSIS), Universiti Kebangsaan Malaysia, for the internship training provided. The authors acknowledge the tutorial lessons available at www.mdtutorials.com/gmx/.

REFERENCES

- Adewole, S. O., & Oiewole, J. O. (2007). Hyperglycaemic effect of *Artocarpus communis* Forst (Moraceae) root bark aqueous extract in Wistar rats: Cardiovascular topic. *Cardiovascular Journal of Africa*, 18(4), 221-227.
- Ali-Reza, A. S. M., Nasrin, M. S., Hossen, M. A., Rahman, M. A., Jantan, I., Haque, M. A., & Sobarzo-Sanchez, E. (2021). Mechanistic insight into immunomodulatory effects of food-functioned plant secondary metabolites. *Critical Reviews in Food Science and Nutrition*, 1-31. <https://doi.org/10.1080/10408398.2021.2021138>
- Amarasinghe, N. R., Jayasinghe, L., Hara, N., & Fujimoto, Y. Chemical constituents of the fruits of *Artocarpus altilis*. *Biochemical Systematics and Ecology*, 36(4), 323-325. <https://doi.org/10.1016/j.bse.2007.09.007>
- Aucoin, M., Cardozo, V., McLaren, M. D., Garber, A., Remy, D., Baker, J., Gratton, A., Kala, M. A., Monteiro, S., Warder, C., Perciballi, A., & Cooley, K. (2021). A systematic review on the effects of Echinacea supplementation on cytokine levels: Is there a role in COVID-19? *Metabolism Open*, 11, Article 100115. <https://doi.org/10.1016/j.metop.2021.100115>
- Baba, S., Chan, H. T., Kezuka, M., Inoue, T., & Chan, E. W. C. (2016). *Artocarpus altilis* and *Pandanus tectorius*: Two important fruits of Oceania with medicinal values. *Emirates Journal of Food and Agriculture*, 28(8), 531-539. <https://doi.org/10.9755/ejfa.2016-02-207>
- Bailly, C. (2021). Anticancer mechanism of artonin E and related prenylated flavonoids from the medicinal plant *Artocarpus elasticus*. *Asian Journal of Natural Product Biochemistry*, 19(2), 45-47. <https://doi.org/10.13057/biofar/f190202>
- Bhat, R., & Paliyath, G. (2016). Fruits of tropical climates: Biodiversity and dietary importance. In B. Caballero, P. M. Finglas & F. Toldrá (Eds.), *Encyclopedia of Food and Health* (pp. 138-143). Academic Press. <https://doi.org/10.1016/B978-0-12-384947-2.00337-8>
- Boson, B., Legros, V., Zhou, B., Siret, E., Mathieu, C., Cosset, F.-L., Lavillette, D. & Denolly, S. (2021). The SARS-CoV-2 envelope and membrane proteins modulate maturation and retention of the spike protein, allowing assembly of virus-like particles. *Journal of Biological Chemistry*, 296, Article 100111. <https://doi.org/10.1074/jbc.RA120.016175>
- Chang, S. K., Jiang, Y., & Yang, B. (2021). An update of prenylated phenolics: Food sources, chemistry and health benefits. *Trends in Food Science & Technology*, 108, 197-213. <https://doi.org/10.1016/j.tifs.2020.12.022>
- Cidade, H. M., Nascimento, M. S. J., Pinto, M. M. M., Kijjoa, A., Silva, A. M. S., & Herz, W. (2001). Artelastocarpin and carpelastofuran, two new flavones and cytotoxicities of prenyl flavonoids from *Artocarpus elasticus* against three cancer cell lines. *Planta Medica*, 67(9), 867-870. <https://doi.org/10.1055/s-2001-18845>
- Daley, O. O., Roberts-Nkrumah, L. B., & Alleyne, A. T. (2020). Morphological diversity of breadfruit [*Artocarpus altilis* (Parkinson) Fosberg] in the Caribbean. *Scientia Horticulturae*, 266, Article 109278. <https://doi.org/10.1016/j.scienta.2020.109278>
- Das, A., Ahmed, R., Akhtar, S., Begum, K., & Banu, S. (2021). An overview of basic molecular biology of SARS-CoV-2 and current COVID-19 prevention strategies. *Gene Reports*, 23, Article 101122. <https://doi.org/10.1016/j.genrep.2021.101122>

- Dawood, A. A. (2020). Mutated COVID-19 may foretell a great risk for mankind in the future. *New Microbes and New Infections*, 35, Article 100673. <https://doi.org/10.1016/j.nmni.2020.100673>
- De Vivo, M., Masetti, M., Bottegoni, G., & Cavalli, A. (2016). Role of molecular dynamics and related methods in drug discovery. *Journal of Medicinal Chemistry*, 59(9), 4035-4061. <https://doi.org/10.1021/acs.jmedchem.5b01684>.
- Demeke, C. A., Woldeyohanins, A. E., & Kifle, Z. D. (2021). Herbal medicine use for the management of COVID-19: A review article. *Metabolism Open*, 12, Article 100141. <https://doi.org/10.1016/j.metop.2021.100141>
- Dhurga, K., Gunasekaran, G., Senthilraja, P., Manivel, G., & Stalin, A. (2016). Molecular modeling and docking analysis of *Pseudomonas* bacterial proteins with *Eugenol* and its derivatives. *Research Journal of Life Sciences, Bioinformatics, Pharmaceutical and Chemical Sciences*, 2(1), 40-50.
- Fang, S. C., Hsu, C. L., Yu, Y. S., & Yen, G. C. (2008). Cytotoxic effects of new geranyl chalcone derivatives isolated from the leaves of *Artocarpus communis* in SW 872 human liposarcoma cells. *Journal of Agricultural and Food Chemistry*, 56(19), 8859-8868. <https://doi.org/10.1021/jf8017436>
- Hakim, E. H., Achmad, S. A., Juliawaty, L. D., Makmur, L., Syah, Y. M., Aimi, N., Kitajima, M., Takayaman, H., & Ghisalberti, E. L. (2006). Prenylated flavonoids and related compounds of the Indonesian *Artocarpus* (Moraceae). *Journal of Natural Medicines*, 60, 161-184. <https://doi.org/10.1007/s11418-006-0048-0>
- Hano, Y., Yamagami, Y., Kobayashi, M., Isohata, R., & Nomura, T. (1990). Artonins E and F, two new prenylflavones from the bark of *Artocarpus communis* Forst. *Heterocycles*, 31(5), 877-882. <https://doi.org/10.3987/COM-90-5350>
- Hari, A., Revikumar, K. G., & Divya, D. (2014). *Artocarpus*: A review of its phytochemistry and pharmacology. *Journal of Pharma Search*, 9(1), 7-12.
- Jalal, T. L., Ahmed, I. A., Mikail, M., Momand, L., Draman, S., Md Isa, M. L., Abdul Rasad, M. S. B., Omar, M. N., Ibrahim, M., & Wahab, R. A. (2015). Evaluation of antioxidant, total phenol and flavonoid content and antimicrobial activities of *Artocarpus altilis* (Breadfruit) of underutilised tropical fruit extracts. *Applied Biochemistry and Biotechnology*, 175(7), 3231-3243. <https://doi.org/10.1007/s12010-015-1499-0>
- Jamil, M. M. A., Ganeson, S., Mammam, H. B., & Wahab, R. A. (2018). *Artocarpus altilis* extract effect on cervical cancer cells. *Materials Today: Proceedings*, 5(7), 15559-15566. <https://doi.org/10.1016/j.matpr.2018.04.163>
- Jantan, I., Ahmad, W., & Bukhari, S. N. A. (2015). Plant-derived immunomodulators: An insight on their preclinical evaluation and clinical trials. *Frontiers in Plant Science*, 6, Article 655. <https://doi.org/10.3389/fpls.2015.00655>
- Jorgensen, W. L. (2004). The many roles of computation in drug discovery. *Science*, 303(5665), 1813-1818. <https://doi.org/10.1126/science.1096361>
- Kaspi, S. N. A. M., Govender, N., & Mohamed-Hussein, Z. A. (2022). Brief communication: Caffeic acid derivatives and polymethoxylated flavonoids from cat's whiskers (*Orthosiphon stamineus*) form stable complexes with SARS-CoV molecular targets: An *In silico* analysis. *Pertanika Journal of Tropical Agricultural Science*, 45(1), 235-244. <https://doi.org/10.47836/pjtas.45.1.13>

- Khaerunnisa, S., Kurniawan, H., Awaluddin, R., Suhartati, S., & Soetjipto, S. (2020). Potential inhibitor of COVID-19 main protease (Mpro) from several medicinal plant compounds by molecular docking study. *Preprints, 2020*, Article 2020030226. <https://doi.org/10.20944/preprints202003.0226.v1>
- Ko, H. H., Lu, Y. H., Yang, S. Z., Won, S. J., & Lin, C. N. (2005). Cytotoxic prenylflavonoids from *Artocarpus elasticus*. *Journal of Natural Products, 68*(11), 1692-1695. <https://doi.org/10.1021/np050287j>
- Lan, W. C., Tzeng, C. W., Lin, C. C., Yen, F. L., & Ko, H. H. (2013). Prenylated flavonoids from *Artocarpus altilis*: Antioxidant activities and inhibitory effects on melanin production. *Phytochemistry, 89*, 78-88.
- Lemkul, J. A. (2018). From proteins to perturbed Hamiltonians: A suite of tutorials for the GROMACS-2018 Molecular Simulation Package [Article v1.0]. *Living Journal of Computational Molecular Science, 1*(1), Article 5068. <https://doi.org/10.33011/livecoms.1.1.5068>
- Leng, L. Y., Nadzri, N. B., Yee, K. C., Razak, N. B. A., & Shaari, A. R. (2018). Antioxidant and total phenolic content of breadfruit (*Artocarpus altilis*) leaves. In *MATEC Web of Conferences* (Vol. 150, p. 06007).. EDP Sciences.
- Lin, J. A., Wu, C. H., Fang, S. C. & Yen, G. C. (2012). Combining the observation of cell morphology with the evaluation of key inflammatory mediators to assess the anti-inflammatory effects of geranyl flavonoid derivatives in breadfruit. *Food Chemistry, 132*(4), 2118-2125. <https://doi.org/10.1016/j.foodchem.2011.12.070>
- Liu, J., Sun, Y., Qi, J., Chu, F., Wu, H., Gao, F., Li, T., Yan, J., & Gao, G. F. (2010). The membrane protein of severe acute respiratory syndrome coronavirus acts as a dominant immunogen revealed by a clustering region of novel functionally and structurally defined cytotoxic T-lymphocyte epitopes. *The Journal of Infectious Diseases, 202*(8), 1171-1180. <https://doi.org/10.1086/656315>
- O'Boyle, N. M., Banck, M., James, C. A., Morley, C., Vandermeersch, T., & Hutchison, G. R. (2011). Open babel: An open chemical toolbox. *Journal of Cheminformatics, 3*, Article 33. <https://doi.org/10.1186/1758-2946-3-33>
- Page, M. L. (2021). Climate change: Breadfruit could be food of future as planet warms. *New Scientist, 251*(3356), 11. [https://doi.org/10.1016/S0262-4079\(21\)01817-0](https://doi.org/10.1016/S0262-4079(21)01817-0)
- Paraiso, I. L., Revel, J. S., & Stevens, J. F. (2020). Potential use of polyphenols in the battle against COVID-19. *Current Opinion in Food Science, 32*, 149-155. <https://doi.org/10.1016/j.cofs.2020.08.004>
- Pronk, S., Páll, S., Schulz, R., Larsson, P., Bjelkmar, P., Apostolov, R., Shirts, M. R., Smith, J. C., Kasson, P. M., van der Spoel, D., Hess, B., & Lindahl, E. (2013). GROMACS 4.5: A high-throughput and highly parallel open source molecular simulation toolkit. *Bioinformatics, 29*(7), 845-854. <https://doi.org/10.1093/bioinformatics/btt055>
- Ragone, D. (2018). Breadfruit-*Artocarpus altilis* (Parkinson) Fosberg. In S. Rodrigues, O., E. de Oliveira Silva & E. S. de Brito (Eds.), *Exotic Fruits* (pp. 53-60). Academic Press. <https://doi.org/10.1016/B978-0-12-803138-4.00009-5>
- Rehman, S. U., Rehman, S. U., & Yoo, H. H. (2021). COVID-19 challenges and its therapeutics. *Biomedicine & Pharmacotherapy, 142*, Article 112015. <https://doi.org/10.1016/j.biopha.2021.112015>

- Septama, A. W., Jantan, I., & Panichayupakaranant, P. (2018). Flavonoids of *Artocarpus heterophyllus* Lam. heartwood inhibit the innate immune responses of human phagocytes. *Journal of Pharmacy and Pharmacology*, 70(9), 1242-1252. <https://doi.org/10.1111/jphp.12952>
- Shah, M. K. K., Sirat, H. M., Jamil, S., & Jalil, J. (2016). Flavonoids from the bark of *Artocarpus integer* var. *silvestris* and their anti-inflammatory properties. *Natural Product Communications*, 11(9), 1275-1278. <https://doi.org/10.1177/1934578X1601100921>
- Shamaun, S. S., Rahmani, M., Hashim, N. M., Ismail, H. B. M., Sukari, M. A., Lian, G. E. C., & Go, R. (2010). Prenylated flavones from *Artocarpus altilis*. *Journal of Natural Medicines*, 64, 478-481. <https://doi.org/10.1007/s11418-010-0427-4>
- Shi, S., Li, J., Zhao, X., Liu, Q., & Song, S. J. (2021). A comprehensive review: Biological activity, modification and synthetic methodologies of prenylated flavonoids. *Phytochemistry*, 191, Article 112895. <https://doi.org/10.1016/j.phytochem.2021.112895>
- Shieh, W. L., & Lin, C. N. (1992). A quinonoid pyranobenzoxanthone and pyranodihydrobenzoxanthone from *Artocarpus communis*. *Phytochemistry*, 31(1), 364-367. [https://doi.org/10.1016/0031-9422\(91\)83081-U](https://doi.org/10.1016/0031-9422(91)83081-U)
- Shimizu, K., Kondo, R., Sakai, K., Lee, S. H., & Sato, H. (1998). The Inhibitory Components from *Artocarpus incisus* on Melanin Biosynthesis. *Planta Medica*, 64(5), 408-412. <https://doi.org/10.1055/s-2006-957470>
- Sikarwar, M. S., Hui, B. J., Subramaniam, K., Valeisamy, B. D., Yean, L. K., & Balaji, K. (2014). A review on *Artocarpus altilis* (Parkinson) Fosberg (breadfruit). *Journal of Applied Pharmaceutical Science*, 4(08), 091-097.
- Skariyachan, S., Gopal, D., Chakrabarti, S., Kempanna, P., Uttarkar, A., Muddebhalkar, A. G., & Niranjan, V. (2020). Structural and molecular basis of the interaction mechanism of selected drugs towards multiple targets of SARS-CoV-2 by molecular docking and dynamic simulation studies-deciphering the scope of repurposed drugs. *Computational Biology Medicine*, 126, Article 104054.
- Sofoini, T., Donno, D., Jeannoda, V., Rakotoniaina, E., Hamidou, S., Achmet, S. M., Solo, N. R., Afraitane, K., Giacomina, C., & Beccaro, G. L. (2018). Bioactive compounds, nutritional traits, and antioxidant properties of *Artocarpus altilis* (Parkinson) fruits: Exploiting potential functional food for food security on the Comoros Islands. *Journal of Food Quality*, 2018, Article 5697928. <https://doi.org/10.1155/2018/5697928>
- Suhartati, T., Yandri, Y., & Hadi, S. (2008). The bioactivity test of Artonin E from the bark of *Artocarpus rigida* Blume. *European Journal of Scientific Research*, 23(2), 330-337.
- Tang, Y., Liu, J., Zhang, D., Xu, Z., Ji, J., & Wen, C. (2020). Cytokine storm in COVID-19 : The current evidence and treatment strategies. *Frontiers in Immunology*, 11, Article 1708. <https://doi.org/10.3389/fimmu.2020.01708>
- Trott, O., & Olson, A. J. (2010). AutoDock Vina: Improving the speed and accuracy of docking with a new scoring function, efficient optimization and multithreading. *Journal of Computational Chemistry*, 31(2), 455-461. <https://doi.org/10.1002/jcc.21334>
- Vanommeslaeghe, K., Hatcher, E., Acharya, C., Kundu, S., Zhong, S., Shim, J., Darian, E., Guvench, O., Lopes, P., Vorobyov, I., & Mackerell Jr, A. D. (2009). CHARMM general force field: A force field for drug-like molecules compatible with the CHARMM all-atom additive biological force fields. *Journal of Computational Chemistry*, 31(4), 671-690. <https://doi.org/10.1002/jcc.21367>

- Wei, B. L., Weng, J. R., Chiu, P. H., Hung, C. F., Wang, J. P. & Lin, C. N. (2005). Anti-inflammatory flavonoids from *Artocarpus heterophyllus* and *Artocarpus communis*. *Journal of Agricultural and Food Chemistry*, 53, 3867-3871. <https://doi.org/10.1021/jf047873n>
- Weng, J. R., Chan, S. C., Lu, Y. H., Lin, H. C., Ko, H. H., & Lin, C. N. (2006). Antiplatelet prenylflavonoids from *Artocarpus communis*. *Phytochemistry*, 67(8), 824-829. <https://doi.org/10.1016/j.phytochem.2006.01.030>



Super-Resolution Approach to Enhance Bone Marrow Trepine Image in the Classification of Classical Myeloproliferative Neoplasms

Umi Kalsom Mohamad Yusof¹, Syamsiah Mashohor^{1*}, Marsyita Hanafi¹, Sabariah Md Noor² and Norsafina Zainal³

¹Department of Computer and Communication Systems Engineering, Faculty of Engineering Universiti Putra Malaysia, 43400 UPM, Serdang, Selangor, Malaysia

²Department of Pathology, Faculty of Medicine and Health Sciences, Universiti Putra Malaysia, 43400 UPM, Serdang, Selangor, Malaysia

³Pathology Department, Hospital Serdang, Jalan Puchong, 43000 Kajang, Selangor, Malaysia

ABSTRACT

Many diseases require histopathology images to characterise biological components or study cell and tissue architectures. The histopathology images are also essential in supporting disease classification, including myeloproliferative neoplasms (MPN). Despite significant developments to improve the diagnostic tools, morphological assessment from histopathology images obtained by bone marrow trephine (BMT) remains crucial to confirm MPN subtypes. However, the assessment outcome is challenging due to subjective characteristics that are hard to replicate due to its inter-observer variability. Apart from that, image processing may reduce the quality of the BMT images and affect the diagnosis result. This study has developed a classification system for classical MPN subtypes: polycythemia vera (PV), essential thrombocythemia (ET), and primary myelofibrosis (MF). It was done by reconstructing low-resolution images of BMT using a super-resolution approach to address the issue. Identified low-resolution images from calculating Laplacian variance

were reconstructed using a super-resolution convolution neural network (SRCNN) to transform into rich information of high-resolution images. Original BMT images and reconstructed BMT images using the SRCNN dataset were fed into a CNN classifier, and the classifier's output for both datasets was compared accordingly. Based on the result, the dataset consisting of the reconstructed images showed better output

ARTICLE INFO

Article history:

Received: 28 April 2022

Accepted: 07 September 2022

Published: 13 July 2023

DOI: <https://doi.org/10.47836/pjst.31.5.02>

E-mail addresses:

ukalsomyusof@gmail.com (Umi Kalsom Mohamad Yusof)

syamsiah@upm.edu.my (Syamsiah Mashohor)

marsyita@upm.edu.my (Marsyita Hanafi)

md_sabariah@upm.edu.my (Sabariah Md Noor)

finazz8081@yahoo.com.my (Norsafina Zainal)

* Corresponding author

with 92% accuracy, while the control images gave 88% accuracy. In conclusion, the high quality of histopathology images substantially impacts disease process classification, and the reconstruction of low-resolution images has improved the classification output.

Keywords: Artificial intelligence, histopathology images, image reconstruction, myeloproliferative neoplasm, super-resolution

INTRODUCTION

Hematopoietic cells are developing blood cells in the bone marrow and are divided into three categories, each producing a different type of blood cell. Cells from all three lineages, namely erythroid, granulocytic, and megakaryocytic, are found in normal bone marrow, as shown in Figure 1, which refers to the normal production of certain white blood cells (WBC), red blood cells (RBC), and platelets.

Myeloproliferative neoplasms (MPN) are a group of diseases that perform clonal proliferation of bone marrow stem cells, which causes the increased production of platelets, WBC, or RBC in the circulation and sometimes causes marrow fibrosis with consequent of extramedullary haematopoiesis (cell production outside the marrow).

The concept of MPN was founded by William Dameshek in 1951 (Dameshek, 1951). However, critical advances in its proper understanding and approach have been happening in the recent 20 years (Arber et al., 2016; Tavares et al., 2019; Vannucchi & Harrison, 2017) with significant scientific advances have been attained with higher accuracy in diagnosis, new risk classifications, and therapeutic approach updates. Essential improvements were described in a document ‘WHO Classification of Hematopoietic and Lymphoid Tissue Tumors’ by the World Health Organization (WHO), including bone marrow histology, which advocates from a minor to a major diagnostic criterion (Barbui et al., 2018). Following the guidelines, the MPN entities were grouped into seven subtypes (Hasserjian, 2018), as shown in Table 1.

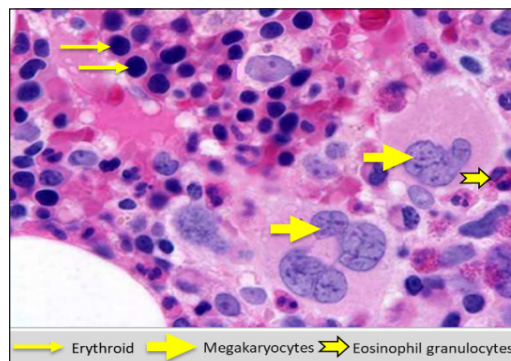


Figure 1. Elements of all three major cell lines are seen in an image of normal bone marrow

Table 1
MPN subtypes

No	Diseases
1.	Chronic myeloid leukaemia (CML), BCR-ABL1-positive
2.	Chronic neutrophilic leukaemia (CNL)
3.	Polycythemia vera (PV)
4.	Primary myelofibrosis (MF)
5.	Essential thrombocythemia (ET)
6.	Chronic eosinophilic leukaemia (CEL), not otherwise specified (NOS)
7.	Myeloproliferative neoplasm, unclassifiable (MPN-U)

A genetic abnormality in the chromosome contains a fusion gene called BCR-ABL1, identified by a translocation (9;22) known as the Philadelphia chromosome (Ph). For example, a diagnosis with BCR-ABL1 positive indicates a CML type. On the other hand, BCR-ABL1-negative MPNs (also referred to as the classical MPNs) are PV, ET, and MF (Sirinukunwattana et al., 2019), and these three subtypes of MPN are encountered as the main scope in this study.

Quality of Data and Image Reconstruction

Image quality is often neglected in the design of machine vision systems (Dodge & Karam, 2016). Usually, machine vision systems are trained and tested on high-quality image datasets, yet in practice, the input images are exposed to numerous factors that cause quality distortions. Blur images, for example, are among the undesirable effects that lead to the loss of necessary details. Automatic detection of blurred and sharp pixels in an image and their classification into respective regions are vital for different image processing and computer vision applications (Ali & Mahmood, 2018), including in medical applications. Medical image reconstruction has become one of the most fundamental and necessary medical imaging components in recent years, with the primary goal of obtaining high-quality medical images for clinical use at the lowest cost and risk to patients (Zhang & Dong, 2020). Leena and Sreenath's (2019) study applied blur detection in pre-processing stage by determining the score of blurriness using the Laplacian operator. The image is classified as blurred or non-blurred when the calculated score is less than the measured threshold. The major advantage of the technique is that it is less time-consuming because the output is yielded immediately within five to seven microseconds (Leena & Sreenath, 2019). Another approach is shown by Huang et al. (2018) using discriminative blur features via deep convolutional neural networks (DCNN). Six layers of the CNN model were developed with five layers for feature extraction for binary classification, which can faithfully produce patch-level blur likelihood. Multiscale image patches are extracted for each pixel by sliding window manner to detect an image. The final blur detection result is obtained by fusing multiscale blur probability maps (Huang et al., 2018). Despite the high performance at blur detection for single and multiple scales, this method consumes many training data and causes a real-time problem.

Generating a high-resolution image with the most commonly used and straightforward approach is by applying linear interpolation methods such as the nearest neighbour, bilinear, and bicubic interpolations (Parsania & Virparia, 2016). However, these approaches frequently result in over-smoothed images with artefacts like aliasing, blur, and halo around the edges (Umehara et al., 2018). Inspired by the success of deep learning in computer vision problems and medical image analysis, researchers have recently investigated deep learning approaches, including Super-resolution Convolutional Neural Network (SRCNN) and

Very Deep Convolutional Network (VDSR) for various biomedical image reconstruction problems (Chen et al., 2019; Cheng et al., 2018; Hou et al., 2020; Zhang et al., 2020). VDSR was developed based on the popular VGG network for image classification, where the VDSR consists of many convolutional layers with ReLU activation.

Hwang et al.'s (2018) study involved the application of VDSR to restore compressed images of cone beam computed tomography (CBCT) in the dental field. The output of the image shows more delicate details and a sharper edge. However, deeper networks in VDSR can bring drawbacks to overfitting and produce a vast model that needs high computational processing power (Hayat, 2017). Another SRCNN approach was applied in image enhancement, for instance, in computed tomography (CT) images. The outcome of an Umahera et al. (2018) experiment to enhance image resolution in the chest CT images demonstrated that the SRCNN significantly outperformed conventional linear interpolation methods. In the pandemic of COVID-19, predicting patients that have coronavirus was done via X-rays and CT-scans (Alzubaidi et al., 2021; Jain & Kosamkar, 2022). However, these images sometimes suffer blurriness or low visibility. Jain & Kosamkar (2022) transformed these low-visibility images into high-visibility images by applying super-resolution using SRCNN. As a result, the classification of COVID-19 attained an accuracy of 95.31%, which is higher than those without image super-resolution (ISR) (Jain & Kosamkar, 2022). Another study was shown by Taş and Yılmaz (2021) on automatic colonoscopy-based diagnosis and polyp detection and localisation. SRCNN pre-processing approach was used to increase the resolution of the training colonoscopy images. This method provides better results and reached an F2 score of 0.945 for the correct localisation of colon polyps compared to the low-resolution cases (Taş & Yılmaz, 2021).

METHODOLOGY

This study consisted of a few stages, as shown in Figure 2. Data collection was prepared from online resources labelled 'validated by hematologist' followed by a data cleaning process. Then, data augmentation was implemented to increase the variety of images and expand the number of images in the dataset. Later, data quality was performed to check the blurry level, and the blurred images were reconstructed using SRCNN. The learning-based classification was performed to evaluate the efficiency of the SRCNN reconstruction method. Finally, the classification output between the control and reconstructed images was compared to observe the model performance.

Data Preparation

In the advancement of the digitisation era nowadays (Mariam et al., 2022; Vasudevan et al., 2022), researchers can share datasets that are foreseen to benefit the academic community virtually. Every discovery and new finding can be shared globally, and anyone interested in

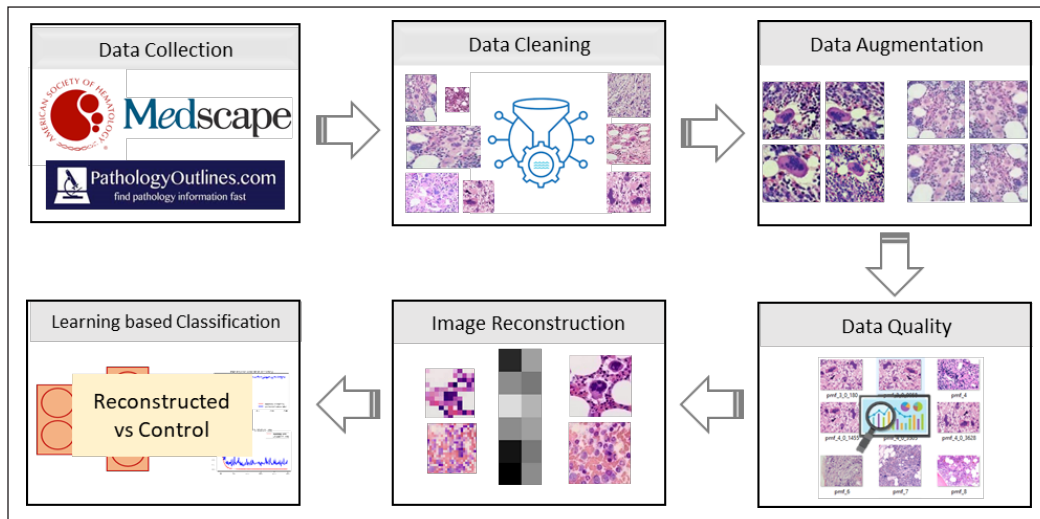


Figure 2. The flow of the study

the subject domain can access the information and contribute back through digital platforms. Similar circumstances were observed in the medical field, including haematology. Three platforms that provide shared information and free downloadable image dataset with expert peer review were chosen as data sources for data collection: The American Society of Haematology Image Bank (AHS), PathologyOutlines.com (Path.com), and Medscape. In total, 268 BMT images were collected, with 161 images from AHS, 67 from Path.com, and 40 from Medscape. The dataset was reviewed thoroughly, and similar images were filtered. A high possibility of duplicate images can occur for a similar disease type due to the open-sharing dataset's data sources. The image description from the data sources was also rechecked to confirm the inclusion and exclusion criteria. The selected BMT images were also observed to discriminate features based on the standardised morphological criteria in bone marrow specimens provided by WHO, such as bone marrow cellularity, formation of fibrosis, and megakaryopoiesis, including the size of cells, cluster formation, and nuclear features. These data cleaning and data checking processes were conducted with the guidance of a 10-year experienced haematologist.

Bone Marrow Image Augmentation and Image Quality Checking

Some research has demonstrated the efficiency of deep learning in classifying images (Loey et al., 2020; Rahaman et al., 2021; Talo, 2019). However, these networks rely heavily on big-quality data to predict well. On the other hand, data augmentation is a critical strategy for enhancing generalisation ability when deep learning models are furnished with the original images and numerous image variants. This approach also has proven to prevent the memorisation of deep learning models efficiently and hence becomes a helpful

technique in improving the model's performance to predict real data. Therefore, data augmentation was applied to the dataset to expand the training dataset's size and enhance the images' variability. Transformations include a range of operations from the field of image manipulation, such as shifting (0.1 to 0.2), zooming (0.3 to 0.5), rotating (10 to 30 degrees), and flipping (horizontal and vertical), as presented in Figure 3.

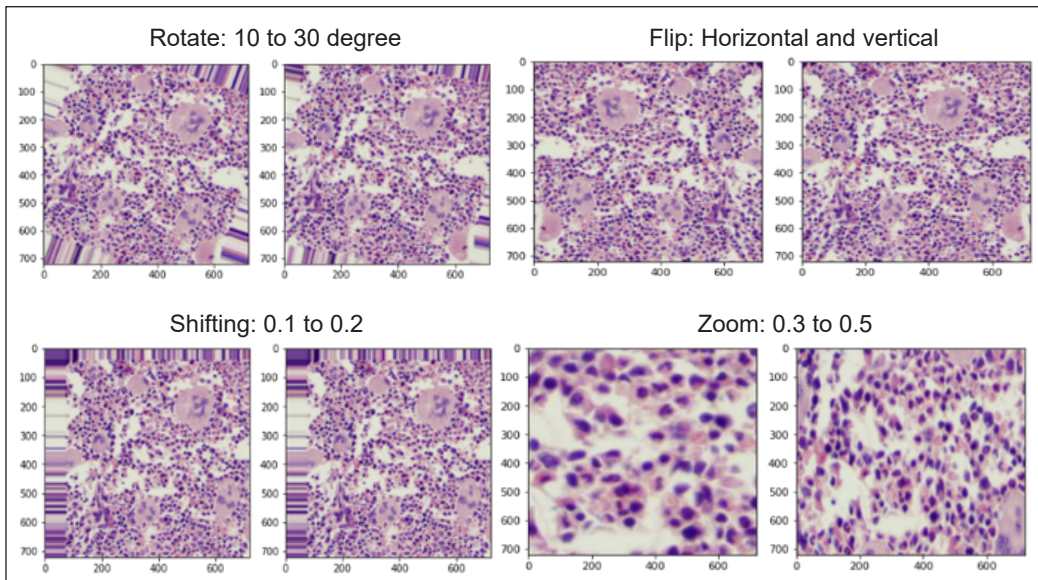


Figure 3. Augmentation output of samples of BMT image using rotating, flipping, shifting, and zooming manipulations

The augmentation applied to the images has successfully increased the dataset size, but it needed to be re-reviewed to observe the effect of the augmentation. The occurrence of low-quality images, such as blurry images with poor surrounding features and black padding with duplicated pixel values, was expected even after applying the preferred setting values. The expectation is that the augmentation happened randomly within the range setting, and the variety of positions of the features in the images may cause defects in the augmentation. From the observation, the undesirable images were removed. Moreover, with a suitable image frame, the images were cropped to the region of interest (ROI). Removing generated images with poor surrounding features and black padding with duplicated pixel values was unavoidable because it could cause the training process to feed unclean input and give wrong output predictions. Meanwhile, the blurry images underwent reconstruction to be transformed into high-quality images. The input was also carefully cropped to square as the deep learning model only receives square images as input.

Following the augmentation process, the quality checking of the bone marrow images in the dataset was done to identify low-resolution images. The working process for blur identification is presented in Figure 4.

The image source in RGB containing three channels of images was converted to grayscale images as a single-channel image. The purpose of the conversion was to simplify the calculation of Laplacian variance to calculate only a single channel of the image. Immediately after the conversion, the value of the Laplacian variance was computed using the Laplacian operator. The Laplacian operator is the second-order differential operator in n -dimensional Euclidean space. It is expressed as the divergence (∇) of the gradient (∇f). The Laplacian of f is the sum of the second partial derivatives in the Cartesian coordinates, x_i . The Laplacian variance was calculated for each image by applying Equation 1 to emphasise regions with rapid intensity changes. Lesser edges with a lower value of Laplacian variance were assumed to be blurred images. In contrast, high variance disclosed that there were more edge-like to imply a sharper type of image.

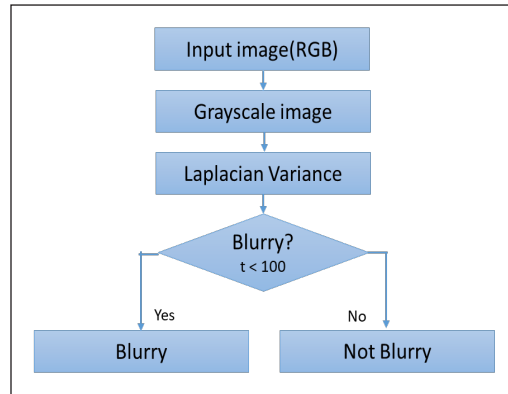


Figure 4. Blur detection flow in images dataset

$$\nabla^2 f = \sum_{i=1}^n \frac{\delta^2 f}{\delta x_i^2} \quad [1]$$

The default threshold value, $t = 100$, was set as a discriminant value to classify the image quality category. From the output, an image with a variance of less than 100 was categorised as ‘Blurry’; meanwhile, output for more or equal to 100 was identified as ‘Not Blurry’. The threshold value selection was referred to based on a previous study (Leena & Sreenath, 2019) and was observed in the data collection for suitability for implementation.

Application of SRCNN to Blur Images

In implementing the image reconstruction, hardware and software parts were vigilantly prepared since the architecture is well known for high computational power. The program was run in a Colab notebook provided by Google Colaboratory (Colab). The model was scripted in Python (version Python 3) using the backend framework of TensorFlow and Keras. Colab is a jupyter notebook environment that provides a runtime that fully configures for deep learning and has free-of-charge access to a robust virtual GPU. A 12GB RAM is available, with the types of GPU vary over time. Often available GPU includes NVIDIA K80, T4, P4, and P100.

The SRCNN is a pioneering work in applying CNN to ISR reconstruction. It mainly implements end-to-end LR and HR image mapping, as shown in Figure 5 (Umehara et al., 2018).

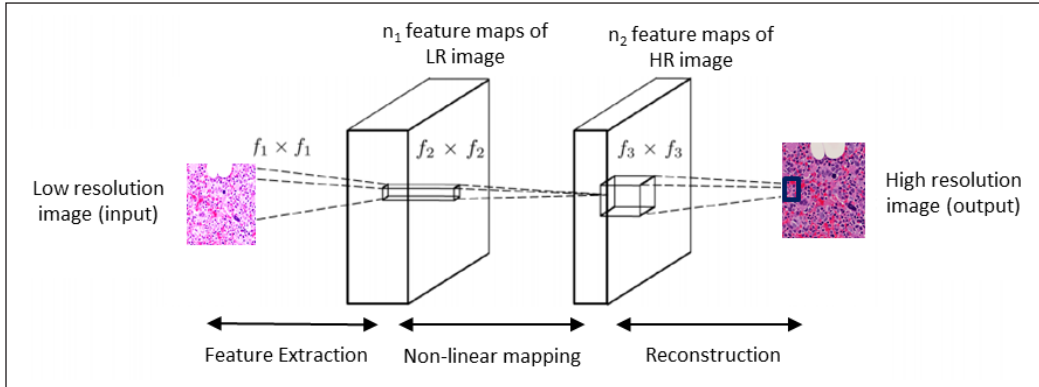


Figure 5. The architecture of SRCNN in BMT image reconstruction

The implementation of SRCNN consists of three processes. The low-resolution BMT images were fed as input to begin the image reconstruction as the first convolution with feature extraction to extract the image blocks, while the dimensions of feature vectors were still in low-dimensional space and expressed in Equation 2:

$$F_1(Y) = \max(0, W_1 * Y + B_1) \quad [2]$$

where F = mapping function, Y = bicubic interpolated low-resolution image, W_i = filters, and B_i = biases.

Followed by non-linear mapping in the second convolution, low-dimensional features were mapped to high-dimensional features. The second layer maps n_1 – dimensional, the representations (feature vectors) of several patches, into n_2 – dimensional, resulting in a non-linear mapping. The number of patches for each mapping operation depends on the kernel size of the second convolution layer, and the operation for this stage is stated as in Equation 3:

$$F_2(Y) = \max(0, W_2 * F_1(Y) + B_2) \quad [3]$$

where W_2 with the size of $n_1 \times f_2 \times f_2$ corresponds to n_2 filters and B_2 as n_2 -dimensional vector.

Subsequently, the image reconstruction where the process was equivalent to the convolution used the mean convolution kernel with the final operation as in Equation 4:

$$F_3(Y) = W_3 * F_2(Y) + B_3 \quad [4]$$

where W_3 with the size of $n_2 \times f_3 \times f_3$ corresponds to c filters and B_3 , as c -dimensional vector.

Then, the image reconstruction output produced better quality images with rich information of high-resolution input for the learning algorithm model.

Classification of BMT Images

Two datasets were prepared, with one consisting of a control dataset (original images without image reconstruction) and another (reconstructed images by SRCNN). Both datasets contained 600 images, with 200 images for each class split by a ratio of 70% (training): 20% (validation): and 10% (testing) and were fed into the CNN classifier. Cross-validation was applied in parallel with hyperparameter tuning. Subsequently, the average of the test result was taken into consideration. The importance of cross-validation in the model development was to avoid bias in the dataset, whereby the dataset was split randomly and swapped between training, validation, and testing. This strategy allowed the model to learn better of the whole dataset. Consequently, every observation in the dataset appeared in training, thus enabling the model to discover the underlying data distribution. The classifier's output for both datasets was then compared to observe the efficiency of SRCNN.

RESULTS AND DISCUSSION

Image Quality Checking

The greyscale images in Figure 6 show the output, which was categorised as 'Blurry', with faded segmentation of blood cells in the bone marrow images. Based on the example shown in the ET class, the output of the Laplacian variance was 28.65. From the greyscale image, the cell separation was seen as unclear. The feature of the megakaryocyte that carried important ET class morphology could not be observed accurately. This low-quality image could disrupt the learning process in developing the classification model as the features could not be differentiated from the background and neighbour cells. Thus, the morphology of the bone marrow that should represent a subtype of MPN could not be identified and may feed inaccurate information to the model. A similar observation was found in the MF class image, where the value of Laplacian variance was 68.32. The fibrosis could be seen roughly, and another detailed feature, such as the presence of megakaryopoiesis for maturation defect in nuclear components, was unclear. Despite being categorised as a blurred image, the value of Laplacian variance was high, approaching 100, which means that more apparent segmentation of the bone marrow image could be observed.

Meanwhile, the PV class has the highest Laplacian variance; more features can be seen in the bone marrow greyscale images. However, the value was still lower than the threshold, and the image was blurry. Details such as erythroid were probably missed, and the dense cellularity can cause the image to be classified as MF class. Therefore, the identified blur images needed to undergo image reconstruction using SRCNN to observe the important morphological features further.

On the other hand, the 'Not Blurry' category is presented in Figure 7, whereby the greyscale image shows clear separability between the cells and their background. The segmentation of the features was identifiable, and the morphology of the MPN subtype

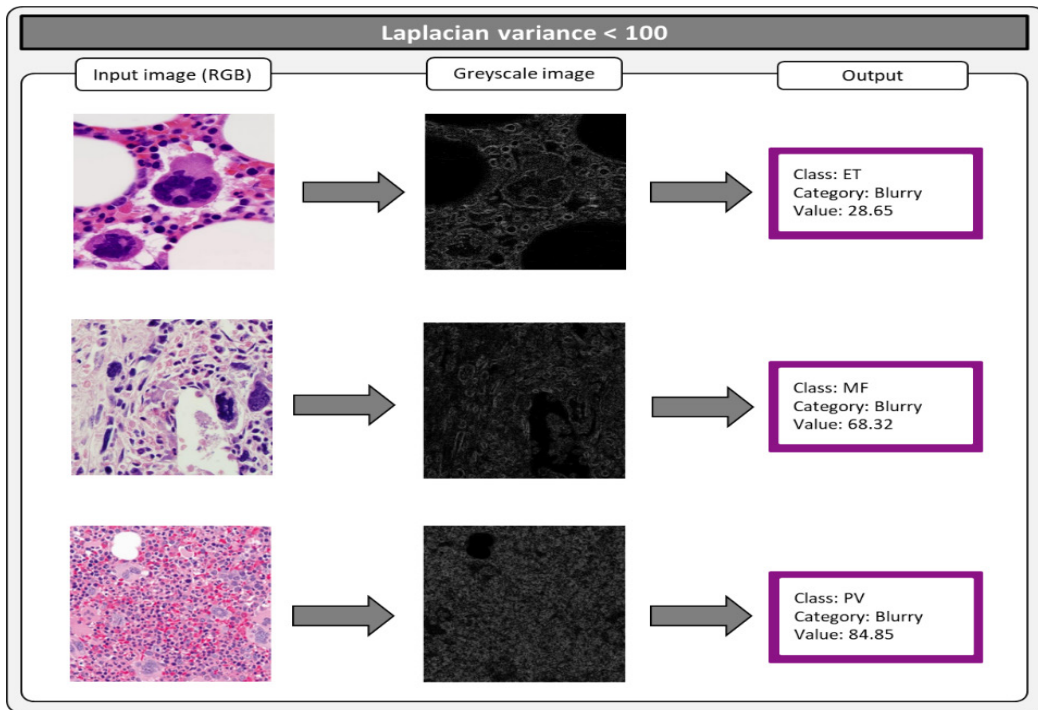


Figure 6. RGB and greyscale image for Laplacian variance <100

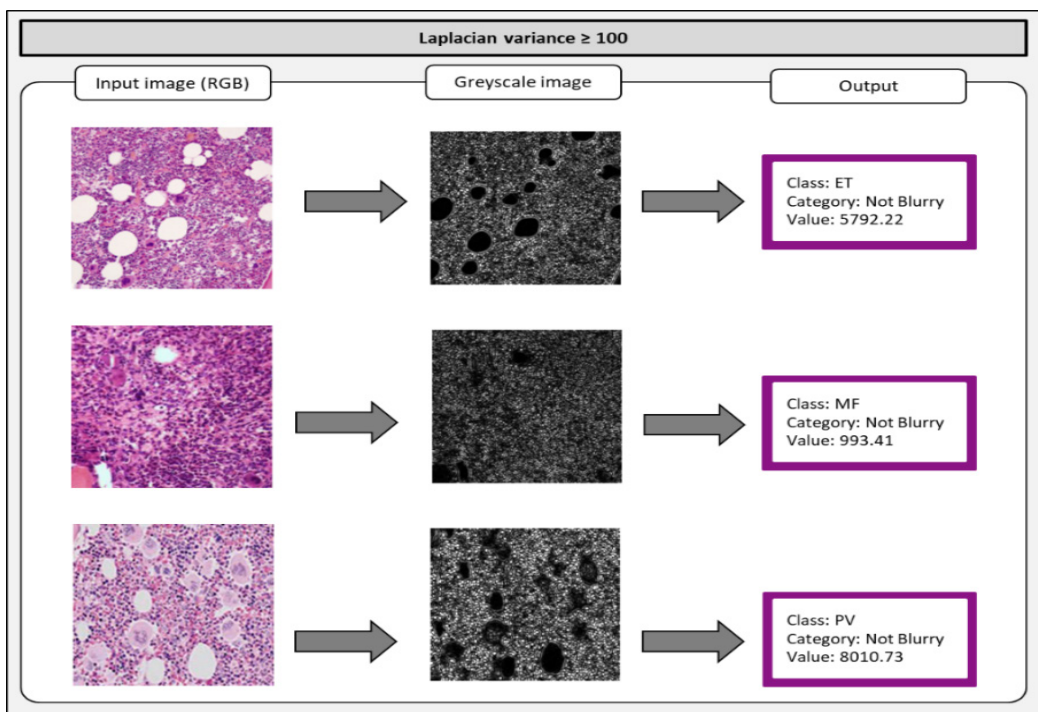


Figure 7. RGB and greyscale images for Laplacian variance ≥ 100

in the bone marrow image was well-detected. For example, for the ET class output, the Laplacian variance output was 5,792.22, and the features of the megakaryocytes could be assessed and differentiated from the fat cells in the image effortlessly. More dense cellularity could be seen for both MF and PV classes, with the Laplacian variance output were 993.41 and 8,010.73, respectively. Furthermore, the hyperlobulation nuclear features of the megakaryocytes could be seen clearly, which provided more dominant features of the bone marrow to be identified as PV class. Certainly, good image quality boosts the performance of the classification model in the learning process and produces better results in predicting the output.

Application of SRCNN to Blur Images

An example of bone marrow images for the MF class classified as a blur with a Laplacian variance of less than 100 is shown in Figure 8. For the ET class, the value of the Laplacian variance of 28.65 was recorded before the image reconstruction. After the image reconstruction, the Laplacian variance was increased to 331.65. The segmentation of features or cells in the bone marrow image was hard to be seen as separable in the greyscale image. After the image reconstruction, the segmentation could be observed clearly. Staghorn-like shape to indicate hyperlobulation in nuclear features of megakaryocytes was seen clearer. Another example is that the original Laplacian variance for the MF class was 68.32 and improved to 804.72 after the image reconstruction. Also, the high cellularity of the bone marrow image and a small cluster of megakaryocytes could be observed better after the reconstruction. Similarly, for the image of the PV class, a low value of Laplacian variance (84.85) before the reconstruction increased to 1,010.37 after the reconstruction, which provides a better image in identifying the features of the bone marrow. The hypercellular features, too, could be observed better, and the megakaryocytes that were seen increased in quantity.

Based on the findings, the original low-resolution images with faded and unclear segmentation were transformed into high-resolution images that provided better morphological information to the learning algorithm. The observation from the greyscale images and the output of the Laplacian variance proved the effectiveness of image reconstruction in improving the image quality in the dataset.

Classification Performance

The classification performance was observed using the test dataset and is presented in Table 2. The classification report found that the precision output for the ET class by the control dataset is higher than the SRCNN dataset. A similar result was observed for both SRCNN and control datasets for the MF class, and higher precision output by SRCNN was reported for the PV class. The SRCNN showed better recall or sensitivity for the ET

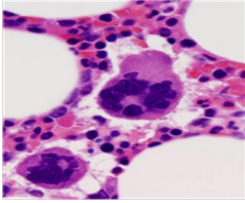
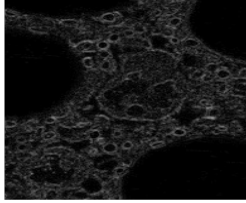
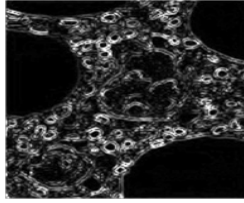
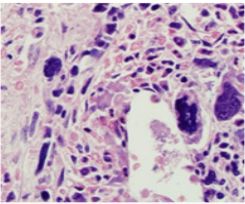
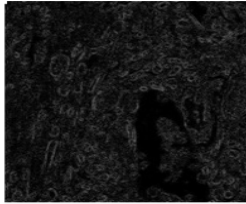
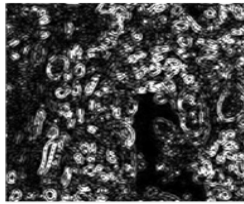
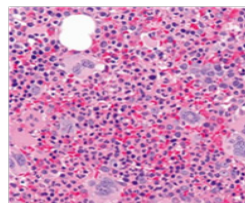
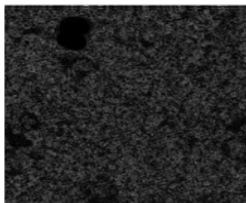
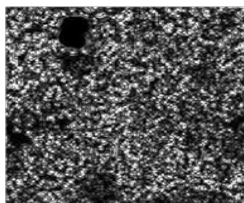
Image Reconstruction		
Class	Before	After
<p>ET</p> 	<p>Value: 28.65</p> 	<p>Value: 331.65</p> 
<p>MF</p> 	<p>Value: 68.32</p> 	<p>Value: 804.72</p> 
<p>PV</p> 	<p>Value: 84.85</p> 	<p>Value: 1010.37</p> 

Figure 8. The output of image reconstruction using SRCNN

Table 2
Classification report for SRCNN and control dataset

Type of Dataset	Precision			Recall			F1-Score			Accuracy
	ET	MF	PV	ET	MF	PV	ET	MF	PV	
SRCNN	0.89	0.95	0.90	0.85	1.00	0.90	0.87	0.98	0.90	0.92
Control	1.00	0.95	0.77	0.75	0.90	1.00	0.86	0.92	0.87	0.88

and MF classes, but the control dataset provided a better output for the PV class. In the F1-score result, the best outcome was given by the SRCNN dataset for all three classes. Overall, higher accuracy was shown in the SRCNN dataset, with 92% accuracy, compared to the control dataset, with 88% accuracy in classifying the MPN subtypes.

A further observation from the confusion matrix as presented in Figure 9, the SRCNN dataset predicted 17 images of the ET class accurately compared to the control dataset (15 images). The best performance shown by the SRCNN was in the MF class, with all images correctly predicted to true label. Meanwhile, 18 images were classified correctly for the MF

class by the control dataset. However, the control dataset gave the best output to classify 20 images correctly for the PV class, while the SRCNN dataset predicted 18 images correctly. This outcome suggests that the edges of features in the blurry images were softened (Figure 8) before the image reconstruction. It may change the morphology features in the PV class, where the hypercellularity becomes less visible and more generalised. Due to that, the control dataset has a simpler image to classify and produces better output. Overall, the SRCNN dataset shows better output to classify two classes (ET and MF classes) than only one class (PV class) for the control dataset.

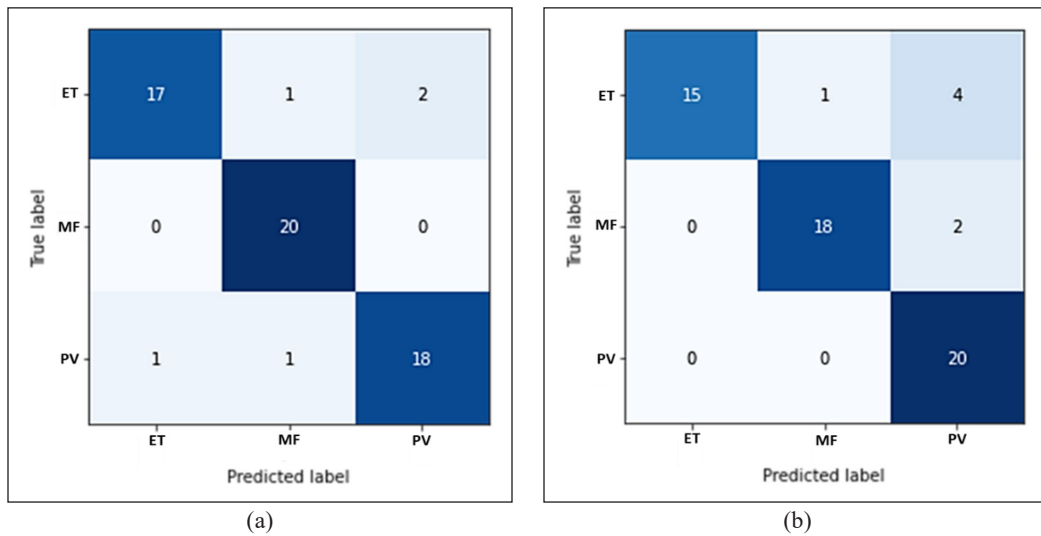


Figure 9. Confusion matrix for: (a) SRCNN; and (b) control

CONCLUSION

Image quality is a significant practice frequently disregarded in developing a classification model (Dodge & Karam, 2016). Low-quality input images can reduce the ability of the learning algorithm to produce a robust model. Therefore, enhancing blur images from low-quality images is highly significant to be implemented at the early stage of the model development. For instance, a low value of Laplacian variance that indicates blur images can cause difficulties in observing the morphological cells in BMT images that carry major criteria to differentiate MPNs. This situation may reduce information to the learning algorithm in identifying important features from the images. Subsequently, the enhancement of image quality for BMT image from the SRCNN image reconstruction indicated by the improvement of the calculated value of Laplacian variance can produce good quality input data. Hence better accuracy from the output of the prediction model can be observed. Based on the result, the dataset of SRCNN images produced higher results, with an accuracy of 92% compared to the control images (88%). In conclusion, image reconstruction using

SRCNN has proven to effectively improve the quality of BMT images in the pre-processing stage and enhance the performance in the development of the prediction model.

ACKNOWLEDGEMENT

Umi Kalsom Mohamad Yusof is a PhD student who performed this research. The supervisory committees are Syamsiah Mashohor, Marsyita Hanafi, and Sabariah Md Noor. Nusafina Zainal is a pathologist and prepares clinical data from Hospital Serdang. Clinical data used in this research was approved by the Medical Research and Ethics Committee, Ministry of Health Malaysia (NMRR-18-4023-42507 (IIR)). This research publication is supported by the UPM-Kyutech International Symposium on Applied Engineering and Sciences 2021 (SAES2021) and Universiti Putra Malaysia.

REFERENCES

- Ali, U., & Mahmood, M. T. (2018). Analysis of blur measure operators for single image blur segmentation. *Applied Sciences*, 8(5), Article 807. <https://doi.org/10.3390/app8050807>
- Alzubaidi, L., Zhang, J., Humaidi, A. J., Al-Dujaili, A., Duan, Y., Al-Shamma, O., Santamaria, J., Fadhel, M. A., Al-Amidie, M., & Farhan, L. (2021). Review of deep learning: concepts, CNN architectures, challenges, applications, future directions. *Journal of Big Data*, 8, Article 53. <https://doi.org/10.1186/s40537-021-00444-8>
- Arber, D. A., Orazi, A., Hasserjian, R., Thiele, J., Borowitz, M. J., Le Beau, M. M., Bloomfield, C. D., Cazzola, M., & Vardiman, J. W. (2016). The 2016 revision to the World Health Organization classification of myeloid neoplasms and acute leukemia. *Blood*, 127(20), 2391-2405. <https://doi.org/10.1182/blood-2016-03-643544>
- Barbui, T., Thiele, J., Gisslinger, H., Kvasnicka, H. M., Vannucchi, A. M., Guglielmelli, P., Orazi, A., & Tefferi, A. (2018). The 2016 WHO classification and diagnostic criteria for myeloproliferative neoplasms: document summary and in-depth discussion. *Blood Cancer Journal*, 8, Article 15. <https://doi.org/10.1038/s41408-018-0054-y>
- Chen, Y., Wang, J., Chen, X., Sangaiah, A. K., Yang, K., & Cao, Z. (2019). Image super-resolution algorithm based on dual-channel convolutional neural networks. *Applied Sciences*, 9(11), Article 2316. <https://doi.org/10.3390/app9112316> (Retraction published 2021, *Applied Sciences*, 11(20), Article 9442)
- Cheng, Z., Sun, H., Takeuchi, M., & Katto, J. (2018). Performance comparison of convolutional autoencoders, generative adversarial networks and super-resolution for image compression. In *Proceedings of the IEEE Conference on Computer Vision and Pattern Recognition Workshops* (pp. 2613-2616). Computer Vision Foundation. <https://doi.org/10.48550/arXiv.1807.00270>
- Dameshek, W. (1951). Some speculations on the myeloproliferative syndromes. *Blood*, 6(4), 372-375. <https://doi.org/10.2307/j.ctvczzbq.35>
- Dodge, S., & Karam, L. (2016). Understanding how image quality affects deep neural networks. In *2016 Eighth International Conference on Quality of Multimedia Experience (QoMEX)* (pp. 1-6). IEEE Publishing. <https://doi.org/10.1109/QoMEX.2016.7498955>

- Hasserjian, R. P. (2018). Changes in the World Health Organization 2016 classification of myeloid neoplasms everyone should know. *Current Opinion in Hematology*, 25(2), 120-128. <https://doi.org/10.1097/MOH.0000000000000404>
- Hayat, K. (2018). Multimedia super-resolution via deep learning: A survey. *Digital Signal Processing*, 81, 198-217. <https://doi.org/10.1016/j.dsp.2018.07.005>
- Hou, J., Si, Y., & Yu, X. (2020). A novel and effective image super-resolution reconstruction technique via fast global and local residual learning model. *Applied Sciences*, 10(5), Article 1856. <https://doi.org/10.3390/app10051856>
- Huang, R., Feng, W., Fan, M., Wan, L., & Sun, J. (2018). Multiscale blur detection by learning discriminative deep features. *Neurocomputing*, 285, 154-166. <https://doi.org/10.1016/j.neucom.2018.01.041>
- Jain, P. A., & Kosamkar, P. K. (2022). Analysis and prediction of COVID-19 with image super-resolution using CNN and SRCNN-Based approach. In T. Senjyu, P. N. Mahalle, T. Perumal & A. Joshi (Eds.), *Smart Innovation, Systems and Technologies: Vol. 248. ICT with Intelligent Applications* (pp. 33-40). Springer. https://doi.org/10.1007/978-981-16-4177-0_5
- Leena, M. F., & Sreenath, N. (2019). Pre-processing techniques for detection of blurred images. In N. Chaki, N. Devarakonda, A. Sarkar & N. Debnath (Eds.), *Lecture Notes on Data Engineering and Communications Technologies: Vol. 28. Proceedings of International Conference on Computational Intelligence and Data Engineering* (pp. 59-66). Springer. https://doi.org/10.1007/978-981-13-6459-4_7
- Loey, M., Naman, M., & Zayed, H. (2020). Deep transfer learning in diagnosing leukemia in blood cells. *Computers*, 9(2), Article 29. <https://doi.org/10.3390/computers9020029>
- Mariam, K., Afzal, O. M., Hussain, W., Javed, M. U., Kiyani, A., Rajpoot, N., Khurram, S. A., & Khan, H. A. (2022). On smart gaze based annotation of histopathology images for training of deep convolutional neural networks. *IEEE Journal of Biomedical and Health Informatics*, 26(7), 3025-3036. <https://doi.org/10.1109/JBHI.2022.3148944>
- Parsania, P. S., & Virparia, P. V. (2016). A comparative analysis of image interpolation algorithms. *International Journal of Advanced Research in Computer and Communication Engineering*, 5(1), 29-34. <https://doi.org/10.17148/ijarcc.2016.5107>
- Rahaman, M. A., Chen, J., Fu, Z., Lewis, N., Iraj, A., & Calhoun, V. D. (2021). Multi-modal deep learning of functional and structural neuroimaging and genomic data to predict mental illness. In *2021 43rd Annual International Conference of the IEEE Engineering in Medicine and Biology Society (EMBC)* (pp. 3267-3272). IEEE Publishing. <https://doi.org/10.1109/EMBC46164.2021.9630693>
- Sirinukunwattana, K., Aberdeen, A., Theissen, H., Sousos, N., Psaila, B., Mead, A. J., Turner, G. D. H., Rees, G., Rittscher, J., & Royston, D. (2019). *Improving the diagnosis and classification of ph-negative myeloproliferative neoplasms through deep phenotyping*. BioRxiv. <https://doi.org/10.1101/762013>
- Talo, M. (2019). Automated classification of histopathology images using transfer learning. *Artificial Intelligence in Medicine*, 101, Article 101743. <https://doi.org/10.1016/j.artmed.2019.101743>
- Taş, M., & Yılmaz, B. (2021). Super resolution convolutional neural network based pre-processing for automatic polyp detection in colonoscopy images. *Computers and Electrical Engineering*, 90, Article 106969. <https://doi.org/10.1016/j.compeleceng.2020.106959>

- Tavares, R. S., Nonino, A., Pagnano, K. B. B., Nascimento, A. C. K. V. d. Conchon, M., Fogliatto, L. M., Funke, V. A. M., Bendit, I., Clementino, N. C. D., Chauffaille, M. d. L. L. F., Bernardo, W. M., & de Souza Santos, F. P. (2019). Guideline on myeloproliferative neoplasms: Associação Brasileira de Hematologia, Hemoterapia e Terapia Celular: Project guidelines: Associação Médica Brasileira - 2019. *Hematology, Transfusion and Cell Therapy*, 41(Supplement 1), 1-73. <https://doi.org/10.1016/j.htct.2019.03.001>
- Umehara, K., Ota, J., & Ishida, T. (2018). Application of super-resolution convolutional neural network for enhancing image resolution in chest CT. *Journal of Digital Imaging*, 31, 441-450. <https://doi.org/10.1007/s10278-017-0033-z>
- Vannucchi, A. M., & Harrison, C. N. (2017). Emerging treatments for classical myeloproliferative neoplasms. *Blood*, 129(6), 693-703. <https://doi.org/10.1182/blood-2016-10-695965>
- Vasudevan, S., Saha, A., Tarver, M. E., & Patel, B. (2022). Digital biomarkers: Convergence of digital health technologies and biomarkers. *Npj Digital Medicine*, 5, Article 36. <https://doi.org/10.1038/s41746-022-00583-z>
- Zhang, H. M., & Dong, B. (2020). A review on deep learning in medical image reconstruction. *Journal of the Operations Research Society of China*, 8, 311-340. <https://doi.org/10.1007/s40305-019-00287-4>
- Zhang, J., Shao, M., Yu, L., & Li, Y. (2020). Image super-resolution reconstruction based on sparse representation and deep learning. *Signal Processing: Image Communication*, 87, Article 115925. <https://doi.org/10.1016/j.image.2020.115925>

Weight Development of Captive Malayan Sun Bears (*Helarctos malayanus*) in the Malaysian Wildlife Rehabilitation Centre

Muhammad Izzat-Husna¹, Noor Nabilah Nazri¹, Kamaruddin Zainul Abidin², Mohammad Saiful Mansor^{1*}, Zubaidah Kamarudin³, Rahmat Topani³ and Shukor Md Nor¹

¹Department of Biological Sciences and Biotechnology, Faculty of Science and Technology, Universiti Kebangsaan Malaysia, 43600 UKM, Bangi, Selangor, Malaysia

²School of Biology, Faculty of Applied Science, Universiti Teknologi MARA Campus Pahang, 26400 UiTM, Jengka, Pahang, Malaysia

³Ex-Situ Conservation Division, Department of Wildlife and National Parks (DWNP), KM 10 Jalan Cheras, 56100 Kuala Lumpur, Malaysia

ABSTRACT

This study documents a cost-effective strategy for managing Malayan sun bears (*Helarctos malayanus*) in the captive, focusing on their weight at the National Wildlife Rescue Centre (NWRC), Perak, Malaysia. The weight and development of captive bears' average aged of two months were assessed using data collected over 18 months. Asymptotic bear weight was estimated using the von Bertalanffy equation. The growth curves significantly differed between male and female bears, with males growing much larger than females from early to later growth stages. This study has determined three types of age classes of bears, where the age of adult Malayan sun bears are fully grown at 11 years and six months for males and eight years and nine months for females. Sub-adult bears ranged between one and six years old for males and one and four years for females, while cubs ranged from zero to one year old. Furthermore, the ideal weight for captive Malayan sun bears by age was also

successfully determined. Such information is important for the management of this species in captivity. Ensuring the correct weight and age stage, among other criteria, could be useful for successfully releasing rehabilitated sun bears into their natural habitats.

Keywords: Captivity, ideal weight, National Wildlife Rescue Centre (NWRC), von Bertalanffy equation, weight estimation

ARTICLE INFO

Article history:

Received: 16 May 2022

Accepted: 02 November 2022

Published: 13 July 2023

DOI: <https://doi.org/10.47836/pjst.31.5.03>

E-mail addresses:

izzathusnamih90@gmail.com (Muhammad Izzat-Husna)

noornabilahnazri@gmail.com (Noor Nabilah Nazri)

kamaruddinzainul@gmail.com (Kamaruddin Zainul Abidin)

msaifulmansor@gmail.com (Mohammad Saiful Mansor)

zubaidah@wildlife.gov.my (Zubaidah Kamarudin)

rahmat@wildlife.gov.my (Rahmat Topani)

shukormn63@gmail.com (Shukor Md Nor)

* Corresponding author

INTRODUCTION

The National Wildlife Rescue Centre (NWRC) is part of the central government agency of the Department of Wildlife and National Parks (DWNP). As a government agency, the DWNP was entrusted to handle human-wildlife conflict in Peninsular Malaysia. This agency operates based on the 3R approach: rescue, rehabilitation, and release. In particular, this refers to rescuing wildlife and providing shelter, treatment, and rehabilitation before being released into their natural habitat. The NWRC has kept many wildlife species (i.e., birds and large mammals), including the Malayan sun bear (*Helarctos malayanus*).

Malayan sun bears are the smallest species of bear on earth and the only bear inhabiting the lowland forests of Peninsular Malaysia. Malayan sun bears are threatened by ongoing habitat destruction, degradation, and forest fragmentation, leading to human-bear conflicts (Sethy & Chauhan, 2012). According to the Department of Wildlife and National Park Malaysia (2014), <1% of wildlife conflicts reported were from human-bear conflicts throughout Peninsular Malaysia. However, this figure does not entirely represent the actual human-bear conflict occurring in Peninsular Malaysia since such cases are rarely reported (Department of Wildlife and National Parks, 2017) and can be considered “silent wildlife conflict”. Moreover, increased poaching and illegal trade (domestic and international) in sun bears have become potential threats to their populations in Peninsular Malaysia (Shepherd & Shepherd, 2010). These issues must be considered in the sun bear conservation strategies; otherwise, the Malayan sun bear may shift from a vulnerable to an endangered species.

In managing and conserving wildlife in captivity, animal welfare is compulsory and must be prioritised (Bousfield & Brown, 2010). Apart from providing adequate treatment to injured animals, assessing their physical features and body weight provides extra information regarding their health and helps avoid the possibility of obesity among wildlife in captivity (Brook et al., 2014). At the NWRC, three tracks based on the 3R framework (rescue, rehabilitation, and release) are used for sun bear rehabilitation. All rescued sun bears are assigned to one of the following tracks: (1) immediately released after rescue (Track 1), (2) released after undergoing treatment and a short quarantine period (45 days) (Track 2), or (3) released after undergoing a long (18 months) rehabilitation process (Track 3) (Nabilah et al., 2018).

Weight and age data are often used to examine the growth patterns of captive animals, particularly in the Ursidae family (bears) (Kingsley et al., 1983; Kingsley et al., 1988; McDonough & Christ, 2012). However, information on the weight growth curve of the Malayan sun bear remains scarce, especially in the context of rehabilitation centres. Moreover, captive Malayan sun bears ideal and mature weights are also scarce, and these factors are evolving into a commonly debated issue related to release criteria. Therefore, to inform the management and successful release of captive Malayan sun bears, this study

examined the growth patterns of male and female bears to determine their ideal weight in captivity according to age.

METHODS

Data Collection

Weight data for eight sun bears (four males and four females) were collected under anaesthesia to ensure data accuracy and avoid bias. The age of each sun bear was estimated based on their physical appearance and previous history. Also, it was confirmed by a cross-section of the tooth root by trained veterinarians from DWNP (for certain individuals). Sun bears with an average age of two months were assessed using data collected over 18 months. Throughout the assessment, every individual was weight once every month. Most sun bears in this study had a conflicting background (Table 1).

Table 1
The backgrounds of individual sun bears received by the NWRC

Individual name	Sex	Background conflict
Ibam	Female	Previously kept by indigenous people from Kg. Ibam (Pahang). Experienced hydrocephalus that affected her balance, movement, and vision.
Rina	Female	Previously kept by local people from Pahang.
Tebang	Female	Previously kept by local people and surrendered to NWRC at the age of 2 months.
Muaz	Female	Previously kept by local people from Pahang.
Ampang	Male	Previously surrendered to the Society for the Prevention of Cruelty to Animals in Ampang. One of the legs was amputated due to a serious injury from a snare.
Bani	Male	Previously kept by illegal traders before being confiscated by PERHILITAN.
Bukit Mertajam	Male	Previously kept by local people from Bukit Mertajam, Pulau Pinang.
Damak	Male	Previously kept by indigenous people from Perlok, Pahang.

All study individuals were fed up with 10% of their body weight per day. Diets for cubs, sub-adults, and adults in captivity were based on NWRC guidelines (Nabilah et al., 2018). Sub-adults and adults were fed various foods, including commercial fruit, wild fruit, fresh meat (chicken, beef and fish), honey, and eggs. Cubs were fed 15% of their total body weight in reconstituted milk daily, which did not exceed 5% per feed. Cubs were fed milk every 2–3 hours, and the feeding frequency was reduced until cubs reached a total weight of 20 kg. It is the standard feeding procedure for both genders of Malayan sun bear at NWRC (Nabilah et al., 2018). The body weight of bears was maintained at the optimum body condition score (body score 3), in which the body appears to be corpulent, with an obvious layer of fat covering the pelvis and shoulder region and a sunken area between the ribs and rump being absent (Beecham et al., 2016).

Data Analysis

We used the von Bertalanffy method to determine the growth rate of Malayan sun bears. This method is widely used to measure the growth of many animal groups, particularly among the Ursidae family (Kingsley, 1979; Kingsley et al., 1983; Swenson et al., 2007; McDonough & Christ, 2012). This method estimates the length or weight of wild and captive animals (de Lima Amancio et al., 2014). As such, the von Bertalanffy method is useful for estimating bears' maximum growth (mature growth). Furthermore, the calculated parameter equation can determine other parameters, such as the rate parameter, k , and the weight or length at early ages ($t = 0$).

Thus, in the present study, we used the von Bertalanffy equation for best fit to determine the weight-age relationship pattern of sun bears in captivity.

The weight-age equation is:

$$W_t = W_\infty [1 - \exp(-k(t - t_0))]^3$$

where W_t is the weight at age t ; W_∞ is the limiting or final weight; k is the rate parameter; and t_0 is the weight at $t = 0$.

Moreover, the standard error and confidence interval were calculated for both male and female sun bears. All analyses were conducted using the statistical program R (v 3.4.3) using the FSA and nlstools packages.

The ideal weights of Malayan sun bear according to age were grouped based on the age percentile growth of the population. This method was adapted based on the classification of age percentile growth patterns of human children and teens in the United States (CDC, 2000), which includes the following categories: underweight (5% confidence interval), overweight (85% confidence interval), and obese (95% confidence interval) while the mean curve represents the optimum weight for the population.

A comparison of weight growth between male and female Malayan sun bears was performed based on information produced by the von Bertalanffy models. In order to compare weight growth between sexes, extrapolation growth curves were plotted for both sexes, and comparisons were based on the confidence intervals of both growth curves (McDonough & Christ, 2012).

RESULTS

The parameters based on the von Bertalanffy equation are provided in Table 2, while the extrapolation of fitted curves is presented in Figure 1. The estimated final weight of male Malayan sun bears is significantly greater compared to females, as male weight ranged from 59.16–71.54 kg, and female weight ranged from 59.10–53.74 kg. Although the average male weight is greater than the female's, all parameters showed no significant sex-based differences.

Table 2

Estimated male and female sun bear parameters were calculated using the von Bertalanffy method, with the standard error and upper/lower confidence intervals

	Final Estimation	Std. Error	5% LCI (kg)	95% UCI (kg)
W_{∞} (male)	65.35	6.185	58.03	83.65
W_{∞} (female)	51.92	1.824	49.71	55.31
K (male)	0.067	0.018	0.035	0.102
K (female)	0.094	0.009	0.076	0.111
t_0 (male)	-11.626	4.276	-24.315	-6.51
t_0 (female)	-5.943	1.017	-8.387	-4.375

Note. W_{∞} :limiting or final weight; k: rate parameter; t_0 : weight at t = 0

Growth curves for both males and females increased greatly during the initial year of growth, and the growth rate gradually began to decrease in the second year and then became much slower until reaching an asymptote. However, males reached an asymptote of the estimated mature adult weight slightly later (11 years and 6 months) than females (eight years and nine months). Comparing growth curves based on the confidence intervals between male and female bears indicated that males differed significantly from females, growing much larger than females from early until final growth stages (Figure 1).

The findings suggest that bears aged zero to one year can be considered juveniles, a stage with a higher growth rate. After one year, both male and female bears tend to exhibit the sub-adult growth pattern, where weight growth begins to develop slowly. For male

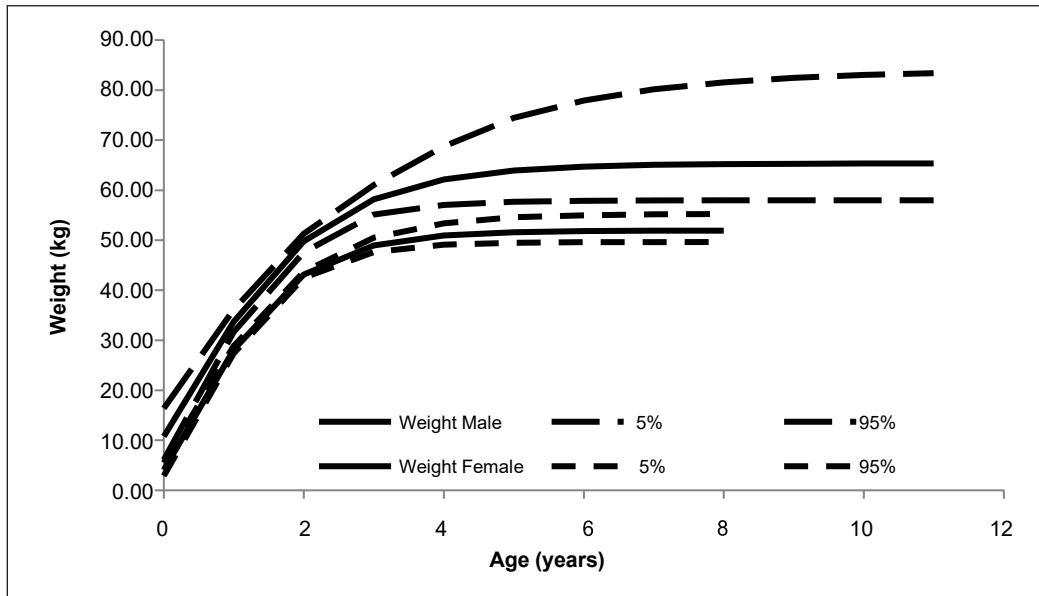


Figure 1. Growth weight curve for male and female Malayan sun bears at the NWRC

bears, the sub-adult growth pattern occurs from one to six years of age, with males reaching the adult stage at six years of age or more. However, males were estimated to reach the mature adult stage at 11 years and six months, where growth reaches an asymptote. The sub-adult growth pattern was evident for females between one and four years of age. After that, females reach the adult stage at four years old and then the mature adult stage at eight and nine months.

The ideal weight of Malayan sun bears in captivity was determined based on the von Bertalanffy model, with confidence intervals of 5%, 85%, and 95% (Table 3). Five per cent of the confidence interval will represent underweight, an 85% confidence interval will represent overweight, and a 95% confidence interval will represent obese. The mean middle curve indicates the optimum weight for the population.

DISCUSSION

The weight development patterns between male and female sun bears were similar to that of polar bears (*U. maritimus*) (Kingsley, 1979), grizzly bears (*U. arctos horribilis*) (Kingsley et al., 1983), Asiatic black bears (*U. thibetanus*) (Skripova, 2007), and brown bear (*U. arctos*) (Swenson et al., 2007), where males are heavier than females. Such findings correspond with the higher aggressiveness of males compared to females. It could be due to sexual dimorphism in ursids, where males are commonly larger, heavier, and more aggressive and competitive for food and territory. For example, due to competition over mates, evolutionary effects on the weaponry and body size of males have made them more aggressive, larger, and heavier than females (Lindenfors & Tullberg, 2011). Therefore, this finding supports the obvious sexual dimorphism observed in Malayan sun bears.

Based on the growth curves in this study, growth rates are highest between 0–1 year for both genders, then become slower between years 1–6, and are slowest at six years and above before reaching an asymptote for male, while females become slower between years 1–4, and are slowest at four years and above before reaching an asymptote. This study recognised three growth stages: juvenile, sub-adult, and adult. These three growth stages were based on growth rates, with juvenile stages characterised by the highest growth rates and adults being the slowest than sub-adults (Begall et al., 1999).

This information is important for ex-situ conservation programmes and wildlife management, where more intensive care is needed at the present stage. At 12 months of age, we determined that Malayan sun bears can be considered in a transition stage from juvenile to sub-adult, with the transition from milk to fully solid food being recognised as the end of the weaning stage (Hayseen & Orr, 2017). However, weaning in captivity could be different from wild conditions since it involves the introduction of solid foods. Lintzenich et al. (2006) reported that juvenile sun bears consuming a solid food mix with reconstituted milk could begin as early as two months old, while the process can last until

they are 11 months old. This observation is congruent with our findings, in which the end of the weaning stage occurs at less than 12 months of age and involves these individuals being considered sub-adults. At this stage, solid foods of high nutrient content are important for maintaining the health and growth development of Malayan sun bears, as the growing juvenile-sub-adult stage (increasing in size) has greater caloric requirements compared to the adult stage.

Males reach the adult stage at six years old, while females reach it at four years old. The adult stage is characterised by the slowest growth rates or a lack of growth, following Begall et al. (1999). This result could provide useful information for sun bear management in both wild and captive conditions and inform the optimal timing for the release of rehabilitated individuals back into the wild. Releasing wildlife following rehabilitation has become a hot topic among conservation and rehabilitation centres, with the success of conservation or rehabilitation programmes being measured on the survivability of released wildlife (Grogan & Kelly, 2013). Thus, the timing of releasing sub-adult and adult bears has become an issue of concern currently being debated among conservation practitioners.

The present study provides important information for wildlife management programmes, such as the Malayan sun bear release programme practised by the NWRC. Choosing suitable individuals with accurate age stages for release is critical for ensuring the survivability of Malayan sun bears in the wild. Previous studies have indicated that young bears or cubs rarely survive after being released (Beecham et al., 2016) due to being prone to predation by large carnivores and relatively defenceless against human threats such as poachers. Furthermore, young bears' lack of survival skills also contributes to their low survival in natural habitats (Fagen & Fagen, 2004). Therefore, it is crucial to ensure that they develop appropriate skills for foraging for food, climbing, and nesting in rehabilitation centres so that they possess the capacity to explore their surroundings and adapt to a new habitat. Thus, releasing juveniles into the wild is not the best option for release programmes. However, releasing adults is also not the best option, as the more time bears are kept captive, the more habituated they become towards keepers, thereby decreasing their possibility of survival in the wild (Beecham et al., 2015). Thus, the present study suggests that the optimal time for releasing sun bears is at the sub-adult stage (one to six years for males; one to four years for females). In addition, individuals' physical characteristics and behaviour are also important factors to consider (Beecham et al., 2016).

Furthermore, the ideal weight of a captive Malayan sun bear was established according to sex (Tables 3 and 4). Food and weight management are crucial to successfully managing wildlife in captivity. Notably, the establishment of an optimal weight is very important in managing captive bear health and monitoring food requirements since too much food causes obesity and an increased risk of health problems such as coronary heart disease and diabetes (Goodchild & Schwitzer, 2008), while the presence of underweight individuals

potentially indicates a diet of poor nutritional value, underfeeding, parasites, diseases, or dental issues. Thus, the guidelines provided in the present study can increase the efficiency of managing the welfare and health of captive Malayan sun bears, particularly at the National Wildlife Rescue Centre (NWRC).

Table 3
The ideal weight of male Malayan sun bears from early to late growth stages

Age/year	Weight (kg)	Underweight 5%	Overweight 85%	Obese 95%
0	10.85	6.16	14.49	16.43
1	33.75	31.7	35.44	36.16
2	49.78	47.62	50.69	51.31
3	58.17	55.19	60.24	61.06
4	62.13	57.09	66.19	68.82
5	63.92	57.73	69.49	74.47
6	64.72	57.94	71.37	77.94
7	65.08	58	72.4	80.2
8	65.23	58.03	72.98	81.61
9	65.30	58.03	73.3	82.5
10	65.33	58.03	73.48	83.07
11	65.34	58.03	73.57	83.42
11.5	65.35	58.03	73.62	83.65

Note. Weight stage indicators: underweight (5% confidence interval), overweight (85% confidence interval), and obese (95% confidence interval)

Table 4
The ideal weight of female Malayan sun bears from early to late growth stages

Age/year	Weight (kg)	Underweight 5%	Overweight 85%	Obese 95%
0	4.07	2.92	3.04	5.55
1	28.09	27.44	27.59	28.86
2	43.13	42.55	42.65	43.73
3	48.96	47.66	47.82	50.59
4	50.95	49.16	49.29	53.44
5	51.6	49.56	49.72	54.63
6	51.82	49.67	49.86	55.06
7	51.89	49.7	49.91	55.23
8	51.91	49.71	49.92	55.29
8.75	51.92	49.71	49.92	55.31

Note. Weight stage indicators: underweight (5% confidence interval), overweight (85% confidence interval), and obese (95% confidence interval)

CONCLUSION

The present study supports that weight data cannot be neglected in managing captive wildlife. A reliable model to determine the sub-adult stage is important for release. This model is important for creating work plans to handle wildlife, prioritising animal welfare until their release into natural habitats. We propose that the present findings can be used to inform captive wildlife management, rehabilitation, and release programmes.

ACKNOWLEDGEMENTS

We thank FGV Holdings Berhad for funding the Malayan Sun Bear Conservation Program under the grant project of ST-2016-007. All experimental procedures were approved by the Department of Wildlife and National Park of Peninsular Malaysia (ref. no KATS 600-2/2/21 JLD.9(7)). We also thank the Department of Wildlife and National Park (DWNP) and National Wildlife Rescue Centre for their help throughout this project, especially the previous and current heads of the National Wildlife Rescue Centre (NWRC), Mr Ahmad Azhar bin Mohammmad and Mr Hasdi bin Hassan @ Asang, also bear keepers of NWRC, Mr Rahmat bin Rohani, Mr Nor Faizal bin Sulong and Khairul Anuar bin Abd Latif for their guidance and idea in make it this research possible.

REFERENCES

- Beecham, J. J., Hernando, M. D. G., Karamanlidis, A. A., Beausoleil, R. A., Burguess, K., Jeong, D. H., Binks, M., Berezky, L., Ashraf, N. V. K., Skripova, K., Rhodin, L., Auger, J., & Lee, B. K. (2015). Management implications for releasing orphaned, captive-reared bears back to the wild. *The Journal of Wildlife Management*, 79(8), 1327-1336. <https://doi.org/10.1002/jwmg.941>
- Beecham, J. J., Loeffler, I. K., & Beausoleil, R. A. (2016). Strategies for captive rearing and reintroduction of orphaned bears. *Journal of Wildlife Rehabilitation*, 36(1), 7-16.
- Begall, S., Burda, H., & Gallardo, M. H. (1999). Reproduction, postnatal development, and growth of social Coruros, *Spalacopus cyanus* (Rodentia: Octodontidae), from Chile. *Journal of Mammalogy*, 80(1), 210-217. <https://doi.org/10.2307/1383221>
- Bousfield, B., & Brown, R. (2010). Animal welfare. *Veterinary Bulletin-Agriculture, Fish and Conservation Department Newsletter*, 1(4), 1-12.
- Brooks, D., Churchill, J., Fein, K., Linder, D., Michel, K. E., Tudor, K., Ward, E., & Witze, A. (2014). Veterinary practice guidelines: 2014 AAHA weight management guidelines for dogs and cats. *Journal of the American Animal Hospital Association*, 50(1), 1-11. <http://doi.org/10.5326/JAAHA-MS-6331>
- de Lima Amancio, A. L., da Silva, J. H. V., Fernandes, J. B. K., Sakomura, N. K., & da Cruz G. R. B. (2014). Use of mathematical models in the study bodily growth in gift strain nile tilapia. *Revista Ciencia Agronomica*, 45(2), 257-266. <https://doi.org/10.1590/S1806-66902014000200005>
- Department of Wildlife and National Park. (2014). *2013 Annual report*. https://www.wildlife.gov.my/images/stories/penerbitan/laporan_tahunan/LAPORAN%20TAHUNAN%20PERHILITAN%2013.pdf

- Department of Wildlife and National Park. (2017). *2016 Annual report*. <https://www.wildlife.gov.my/images/document/penerbitan/laporantahunan/LP2016%20-%2020022018.pdf>
- Fagen, R., & Fagen, J. (2004). Juvenile survival and benefits of play behaviour in brown bears, *Ursus arctos*. *Evolutionary Ecology Research*, 6, 89-102.
- Goodchild, S., & Schwitzer, C. (2008). The problem of obesity in captive lemurs. *International Zoo News*, 55(6), 353-357.
- Grogan, A., & Kelly, A. (2013). A review of RSPCA research into wildlife rehabilitation. *Veterinary Record*, 172(8), 211-211. <https://doi.org/10.1136/vr.101139>
- Hayssen, V., & Orr, T. (2017). *Reproduction in Mammals: The Female Perspective*. John Hopkins University Press.
- Kingsley, M. C. S. (1979). Fitting the von Bertalanffy growth equation to polar bear age- weight data. *Canadian Journal of Zoology*, 57, 1020-1025.
- Kingsley, M. C. S., Nagy, J. A., & Reynolds, H. V. (1988). Growth in length and weight of northern brown bears: Differences between sexes and populations. *Canadian Journal of Zoology*, 66, 981-986.
- Kingsley, M. C. S., Nagy, J. A., & Russell, R. H. (1983). Patterns of weight and loss for grizzly bears in Northern Canada. *Ursus*, 5, 174-178.
- Lindfors, P., & Tullberg, B. S. (2011). Evolutionary aspects of aggression: The importance of sexual selection. *Advances in Genetics*, 75, 7-21.
- Lintzenich, B. A., Edwards, M. S., Griffin, M. E., & Robbins, C. T. (2006). *Polar Bear Nutrition Guidelines*. The Association of American Feed Control Officials.
- McDonough, T. J., & Christ, A. M. (2012). Geographic variation in size, growth, and sexual dimorphism of Alaska brown bears, *Ursus arctos*. *Journal of Mammalogy*, 93(3), 686- 697.
- Nabilah, N., Kamarudin, Z. A., Izzat-Husna, M., Mansor, M. S., Rahmat, T., & Shukor, M. N. (2018). *Pengurusan beruang matahari di Pusat Menyelamat Hidupan Liar Kebangsaan* [Sun Bear Management at the National Wildlife Refuge]. Felda Global Ventures Holdings Berhad (FGV).
- Sethy, J., & Chauhan, N. P. S. (2012). Conservation status of Sun bear (*Helarctos malayanus*) in Nagaland State, North-East India. *Asian Journal of Conservation Biology*, 1(2), 103-109.
- Shepherd, C. R., & Shepherd, L. A. (2010). The poaching and trade of Malayan sun bears in Peninsular Malaysia. *TRAFFIC Bulletin*, 23, 49-52.
- Skripova, K. V. (2007). Rearing of orphan Asiatic Black Bear cubs (*Ursus thibetanus*) for released back to the wild. In J. J. Beecham & A. Ramanathan (Eds.), *Proceeding of International Workshops on the Rehabilitation, Release, and Monitoring of Orphan Bear Cubs 2007* (pp. 85-93). International Fund for Animal Welfare.
- Swenson, J. E., Adamić, M., Huber, D., & Stokke, S. (2007). Brown bear body mass and growth in northern and southern Europe. *Oecologia*, 153, 37-47.

Review Article

***Salmonella* Biofilm on Food Contact Surfaces and the Efficacy of Chemical Disinfectants: A Systematic Review**

Xue Wei Tee¹ and Noor Azira Abdul-Mutalib^{1,2*}

¹Department of Food Service and Management, Faculty of Food Science and Technology, Universiti Putra Malaysia, 43400 UPM, Serdang, Selangor, Malaysia

²Laboratory of Food Safety and Food Integrity, Institute of Tropical Agriculture and Food Security, Universiti Putra Malaysia, 43400 UPM, Serdang, Selangor, Malaysia

ABSTRACT

Foodborne illness has always been a major public health concern, usually caused by cross-contamination during food preparation. *Salmonella* is one of the most reported pathogens, which can attach to and survive on food contact surfaces by forming a biofilm. Biofilm formation enhances the persistence of food pathogens and protects them from external threats, and increases their resistance to chemical disinfectants. This systematic review aims to obtain an overview of the *Salmonella* biofilm formation on food contact surfaces and the efficacy of chemical disinfectants based on the latest scientific data. Preferred Reporting Items for Systematic Reviews and Meta-analyses (PRISMA) guidelines were used to carry out the study. From the review, plastic (91%), stainless steel (64%), and sodium hypochlorite (86%) were most commonly tested. Most chemical disinfectants used in the reported studies were sodium hypochlorite (NaOCl, 100–500 mg/L), hydrogen peroxide (H₂O₂, 0.56%), and benzalkonium chloride (BAC, 100–400 µg/ml). The result showed that *Salmonella* contamination was more common on hydrophobic food contact surfaces like wood and concrete than on hydrophilic surfaces like glass. In addition, the previous studies also revealed that biofilm formation on stainless steel, plastic, and silicone rubber surfaces was not significantly different. Plus, most chemical disinfectants showed

inefficacy in eliminating *Salmonella* biofilm at regular concentrations (<0.05%). It shows that frequent cleaning is important to avoid biofilm formation and ensure the maximum efficacy of the sanitisers.

Keywords: Biofilm, disinfectant, efficacy, food contact surface, *Salmonella*

ARTICLE INFO

Article history:

Received: 19 May 2022

Accepted: 05 October 2022

Published: 13 July 2023

DOI: <https://doi.org/10.47836/pjst.31.5.04>

E-mail addresses:

snoweit107@gmail.com (Tee Xue Wei)

n_azira@upm.edu.my (Noor Azira Abdul-Mutalib)

* Corresponding author

INTRODUCTION

Foodborne illness or food poisoning is any disease caused by consuming contaminated food or food containing toxins. Foodborne illness is a serious global public health issue. According to the World Health Organization (WHO, 2020), around 600 million people are affected by foodborne illness, and 420,000 deaths are reported yearly. One of the most prevalent bacteria that can cause foodborne disease is *Salmonella* spp. They are rod-shaped, Gram-negative, and non-spore-forming foodborne pathogens (Abeyundara et al., 2018). Food contaminated with *Salmonella* can pose health issues and lead to diarrhoeal diseases. Contaminated eggs and poultry also cause most *Salmonella*-related foodborne outbreaks, and many cases related to fresh produce like tomatoes and leafy vegetables were also reported (Anderson et al., 2011; Painter et al., 2013). *Salmonella* is ubiquitous bacteria that can survive in a dry environment for several weeks and months in water. The cell diameter can range from 0.7 to 1.5 μm and 2 to 5 μm in length (Fábregaa & Vila, 2013). *Salmonella* grows between 5°C to 45°C, with an optimum growth temperature of 35°C to 37°C.

Salmonella is classified into 2 major serovars: Typhoidal and Non-Typhoidal *Salmonella* (NTS). *Salmonella enterica* serotype Enteritidis (*S. Enteritidis*) and *Salmonella enterica* serotype Typhimurium (*S. Typhimurium*) are the two major NTS that cause salmonellosis. *Salmonella* Enteritidis and *S. Typhimurium* are also classified as broad-host-range serovars that seldom trigger systemic infection; however, they can inhabit the alimentary tract of a wide range of animals (Graziani et al., 2017). Salmonellosis can cause infection in most people, but certain groups are more vulnerable, like youngsters, the elderly, and those with chronic diseases and weakened immune systems. Thoroughly cooking the food can effectively destroy most cells, and freezing may cause damage to *Salmonella*, but it does not guarantee destruction to these microbes as it can survive prolonged storage under freezing conditions (Jay et al., 2003). *Salmonella* cross-contamination can happen during the whole food supply chain: harvesting, processing, transportation, storage, and distribution. Therefore, proper food handling measures are important in every stage of the food supply chain. The cleanliness of food contact surfaces is vital, especially during food preparation. It is where the application of disinfectants and sanitisers is crucial.

Disinfection of food contact surfaces is crucial in maintaining the safety and quality of food products and reducing contamination by foodborne pathogens (Zhang et al., 2021). Most commonly, the disinfectants would have active ingredients such as chlorine, quaternary ammonium compounds, peroxides, peracids, acid anionics, and alcohol that have an antimicrobial effect (Fraser et al., 2021). The general protocol for using chemical disinfectants is to clean the surface, rinse with potable water, apply the disinfectant, rinse again using potable water, and finally apply a food-grade sanitiser. However, the effectiveness of sanitisers and disinfectants may be affected by multiple factors such as temperature, the presence of organic matter, its concentration, and the type of surfaces (Møretro et al., 2009).

Salmonella biofilm can also affect the efficacy of disinfectants. Once *Salmonella* biofilm is formed, its survival ability and persistence will be enhanced and made very difficult to kill by normal sanitation compared to planktonic cells (Giaouris et al., 2012).

Biofilm is responsible for most food poisoning outbreaks related to food contact surfaces (Chen & Wang, 2020; Shao et al., 2020). Unlike planktonic cells, it is hard to eliminate biofilm as it has higher persistence to sanitiser and disinfectant. In addition, *Salmonella* spp. has been linked as the causative agent for foodborne illness in many cases in recent years (Akinola et al., 2020), and the formation of biofilm on food contact surfaces certainly contributes to cross-contamination and increases the risk of a foodborne outbreak (Lee et al., 2020). Therefore, many studies were conducted to identify the characteristics of biofilm and the effectiveness of disinfectants on it. Therefore, this research aims to obtain an overview of the *Salmonella* biofilm formation on food contact surfaces and the efficacy of chemical disinfectants based on the latest scientific data systematically extracted from authoritative publications databases.

METHODS

Data Sources and Search Strategy

The preferred Reporting Items for Systematic Reviews and Meta-analyses (PRISMA) guideline was used for the study. The literature search was conducted on ScienceDirect, PubMed, and Scopus using specific search terms (Table 1). Keywords used were *Salmonella*, biofilm, disinfectants, and food contact surface.

Table 1
The search string used for the systematic review process

Databases	Keywords used
ScienceDirect	Title, abstract, keywords: (" <i>Salmonella</i> ") AND ("biofilm") AND ("food contact surface*") AND ("disinfect*" OR "clean*") AND ("resist*" OR "surviv*" OR "inactiv*")
Scopus	OR "infectioncontrol" OR "cross infection") AND ("resist*" OR "surviv*" OR "inactiv*"))
PubMed	(<i>Salmonella</i>) AND (biofilm) AND (food contact surface*) AND (disinfect* OR clean* OR decontamina* OR sanitiz*) AND (resist* OR surviv* OR inactiv*)

Inclusion and Exclusion Criteria

Studies were included if they focused on *Salmonella* biofilm on food contact surfaces; the prevalence of *Salmonella* biofilm can be calculated; are written in English; focusing on the *Salmonella* biofilm sensitivity to chemical disinfectants; and were published between 2010 to 2021.

Studies were excluded if the articles were unrelated to *Salmonella* contamination; samples were collected from other resources instead of food contact surfaces; specific

pathogenic bacteria and the sample sources were not reported; focusing on physical disinfectants; and published in non-English language journals.

Data Extraction

In this review, the data extraction focused on relevant descriptive and quantitative variables from the selected manuscripts. The variables include the *Salmonella* strains, food contact surface types, total samples collected, disinfectant types and concentrations, and the bacterial count of the *Salmonella* strains. The extracted data analysis was conducted by reading the full articles and then narrowing them with specific search terms. Only relevant information was synthesised and summarised in the result of this study.

RESULTS AND DISCUSSION

General Finding and Results of Search

The online database search on ScienceDirect, Scopus, and PubMed was completed in September 2021, limiting studies from 2010 to 2021. After a proper screening process, only 11 articles were included in the review (Figure 1).

Among 11 articles included in the literature review, only 1 article did not mention the specific serotype of *Salmonella*, while the numbers of articles focused on *S. Enteritidis*, *S. Agona*, *S. Typhimurium*, and *S. Hadar* were 6, 2, 5, and 1, respectively. Four out of

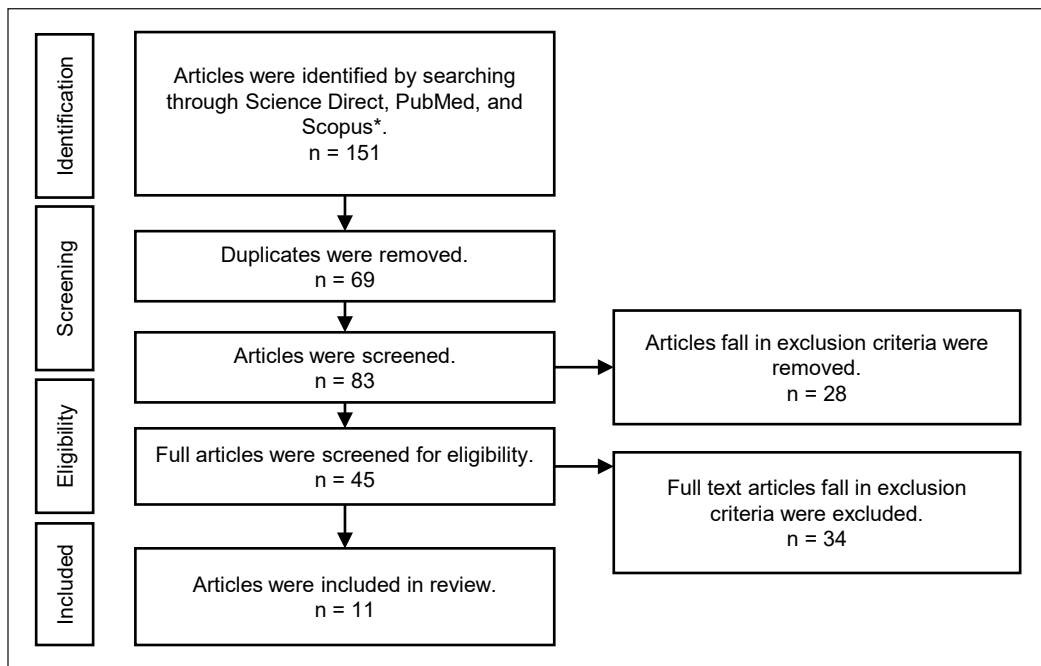


Figure 1. PRISMA flowchart—Selection process of eligible articles
 Note. *One additional article was retrieved from Wiley Online Library

11 articles focus mainly on *Salmonella* biofilm formation on food contact surfaces, 2 articles focus on chemical disinfectant efficacy on *Salmonella* biofilms only, and 5 articles focus on *Salmonella* biofilm formation and chemical disinfectant efficacy on *Salmonella* biofilms.

A total of 9 types of surfaces were tested in the studies. Plastic is the most studied food surface area (10/11), followed by stainless steel (7/11), glass (4/11), silicon rubber (2/11), concrete (2/11), and tile (2/11) (Table 2). Several types of plastic were used as the surface for the biofilm formation: polycarbonate, polystyrene, polyvinyl chloride, polyethylene, and polypropylene. Most authors did not specify the constituents of surface materials used in their study. Only Corcoran et al. (2013a; 2013b) mention borosilicate glass and glazed tile.

As for the articles that evaluate the efficacy of chemical disinfectants, sodium hypochlorite (NaOCl) was most commonly used (6/7), followed by benzalkonium chloride (BAC) (2/7) and hydrogen peroxide (H₂O₂) (2/7) (Table 2). In addition, Singla et al. (2014) studied the effective concentrations of ozonated water and organic acids against the growth of bacterial pathogens.

Biofilm Formation on Food Contact Surfaces

The outcome of *Salmonella* biofilm adherence on food contact surfaces is presented in Table 3. Corcoran et al. (2013b) reported that all tested strains of *S. Agona*, *S. Typhimurium*, and *S. Enteritidis* formed denser biofilm on tile and concrete (hydrophobic) and formed less dense biofilm on steel (hydrophilic). In general, *S. Agona* biofilms are denser than *S. Enteritidis* on all five surfaces (glass, stainless steel, polycarbonate, concrete, and tile). *S. Typhimurium* also formed a denser biofilm than *S. Enteritidis*. However, the comparison of *S. Typhimurium* and *S. Agona* biofilm shows a less consistent pattern and overall insignificant differences.

Moreover, Dantas et al. (2018) found that the glass surface is better at preventing *Salmonella* biofilm formation (P<0.05) as compared to wood and plastic. After being

Table 2
Food contact surfaces and types of chemical disinfectants extracted from the articles

Types of surfaces	Article numbers
1. Plastic	10/11
2. Stainless steel	7/11
3. Glass	4/11
4. Silicone rubber	2/11
5. Concrete	2/11
6. Tiles	2/11
7. Wood	1/11
8. Granite	1/11
9. Formica laminate	1/11
Types of chemical disinfectants	
1. Sodium hypochlorite (NaOCl)	6/7
2. Benzalkonium chloride (BAC)	2/7
3. Chlorine oxide (Cl ₂)	2/7
4. Sodium hydroxide (NaOH)	1/7
5. Triclosan	1/7
6. Peracetic acid	1/7
7. Ammonium quaternary compound (QUAT)	1/7
8. Chlorine (Cl ₂)	1/7

Table 3
The selected outcome of Salmonella biofilm adhesion on food contact surfaces

Test Organism	Surface	Study	Adhesion time (hour)	Bacterial count (log CFU/cm ²)
<i>Salmonella</i> spp. (without specifying serovars)	Stainless steel	Ashrafudoulla et al. (2021)	24	6.17±0.04
	Silicon rubber	Ashrafudoulla et al. (2021)	24	6.30±0.08
	Plastic	Ashrafudoulla et al. (2021)	24	6.28±0.05
<i>S. Enteritidis</i>	Stainless steel	Corcoran et al. (2013b)	24	4.73–5.71
		Corcoran et al. (2013a)	48	4.73
		Corcoran et al. (2013a)	168	6.87
		Silva et al. (2010)	12	5.26
	Plastic	Corcoran et al. (2013b)	24	5.20–5.72
		Corcoran et al. (2013a)	48	5.20
		Corcoran et al. (2013a)	168	6.80
	Glass	Corcoran et al. (2013b)	24	4.85–5.61
		Corcoran et al. (2013a)	48	4.85
		Corcoran et al. (2013a)	168	6.73
	Concrete	Corcoran et al. (2013b)	24	6.43–6.74
		Corcoran et al. (2013a)	48	6.43
		Corcoran et al. (2013a)	168	7.65
	tile	Corcoran et al. (2013b)	24	7.02
		Corcoran et al. (2013a)	48	7.02
Corcoran et al. (2013a)		168	8.04	
Granite	Silva et al. (2010)	12	6.00	
<i>S. Agona</i>	Stainless steel	Corcoran et al. (2013b)	24	5.38–6.12
		Corcoran et al. (2013a)	48	5.80–6.12
		Corcoran et al. (2013a)	168	5.29–6.92
	Plastic	Corcoran et al. (2013b)	24	6.03–6.81
		Corcoran et al. (2013a)	48	5.59–6.33
		Corcoran et al. (2013a)	168	5.46–6.67
	Glass	Corcoran et al. (2013b)	24	5.41–6.16
		Corcoran et al. (2013a)	48	5.41–5.81
		Corcoran et al. (2013a)	168	5.91–7.26
	Concrete	Corcoran et al. (2013b)	24	6.08–7.47
		Corcoran et al. (2013a)	48	6.75–7.08
		Corcoran et al. (2013a)	168	7.08–7.59
	tile	Corcoran et al. (2013b)	24	6.94–7.59
		Corcoran et al. (2013a)	48	6.94–7.56
		Corcoran et al. (2013a)	168	7.52–7.87
<i>S. Typhimurium</i>	Stainless steel	Corcoran et al. (2013b)	24	5.46–6.28
		Corcoran et al. (2013a)	48	5.71–6.28
		Corcoran et al. (2013a)	168	6.00–6.59
		Bayoumi et al. (2012)	72	1.63–1.96

Table 3 (continue)

Test Organism	Surface	Study	Adhesion time (hour)	Bacterial count (log CFU/cm ²)
	Plastic	Corcoran et al. (2013b)	24	5.92–6.10
		Corcoran et al. (2013a)	48	6.10–6.53
		Corcoran et al. (2013a)	168	6.25–6.30
		Singla et al. (2014)	72	4.20±0.07–6.20±0.05
	Glass	Bayoumi et al. (2012)	72	1.74–2.03
		Corcoran et al. (2013b)	24	5.15–5.41
		Corcoran et al. (2013a)	48	5.15–5.41
	Concrete	Corcoran et al. (2013a)	168	5.97–6.30
		Corcoran et al. (2013b)	24	6.70–7.00
		Corcoran et al. (2013a)	48	6.78–7.00
	tile	Corcoran et al. (2013a)	168	6.93–7.47
		Corcoran et al. (2013b)	24	7.01–7.23
Corcoran et al. (2013a)		48	7.17–7.23	
		Corcoran et al. (2013a)	168	7.62–7.73

washed with disinfectant and hot water, the highest percentage of recovery was seen on wood (60%) and plastic (40%), whereas glass (10%) showed the lowest percentage of recovery of *S. Enteritidis*. The result also suggested that the cleaning procedure did not remove the *Salmonella* biofilm completely. Similarly, Djebbi-Simmons et al. (2019) reported that *S. Typhimurium* survived better on plastic and Formica laminate (hydrophobic surface) than on stainless steel (hydrophilic surface) at drying time of 24 h at medium and high (4 log CFU/cm² and 6 log CFU/cm², respectively) microbial loads. Furthermore, Silva et al. (2010) noted that the number of *S. Enteritidis* adhered to granite (hydrophobic) was greater than stainless steel (hydrophilic) (P<0.05), which were 6.00 and 5.26 log CFU/cm² respectively. Besides, in between the two types of plastic tested, Singla et al. (2014) recovered more counts of *S. Typhimurium* biofilm from PVC (ranged from 4.5±0.07 to 6.2±0.05 log CFU/g) than from polyethene bag (ranged from 4.2±0.07 to 5.8±0.08 log CFU/g).

In studies by Corcoran et al. (2013a), even though limitation existed as there was incomplete removal of 168h biofilm from coupons by sonication, 168 h biofilm were overall denser than 48 h biofilm on all surfaces (glass, stainless steel, polycarbonate, concrete, and tile) for all *S. Agona*, *S. Typhimurium*, and *S. Enteritidis* tested. Moreover, tile recorded the highest number of pathogens recovered (7.56 and 8.04 log CFU/cm² for 48 h and 168 h, respectively). In comparison, stainless steel recorded the least (4.73 and 5.29 log CFU/cm² for 48 h and 168 h, respectively) among 5 tested surfaces. Besides, the *S. Enteritidis* strain also formed denser biofilm on 4 (stainless steel, plastics, glass, and concrete) out of

5 surface areas (stainless steel, plastics, glass, concrete, and tile) tested as compared to *S. Agona* and *S. Typhimurium* strains.

In contrast, Rodríguez-Melcón et al. (2018) observed higher *S. Hadar* biofilm formation on a hydrophilic surface (glass) than on a hydrophobic surface (polystyrene) with regards to the biovolume and percentage of coverage. However, other tested microorganisms like *Listeria monocytogenes*, methicillin-resistant *Staphylococcus aureus*, and vancomycin-resistant *Enterococcus faecium* showed no difference in biofilm formation on both surfaces. Further analysis revealed that the percentage of surface coverage, biovolume, and thickness of the *S. Hadar* increased when the incubation time increased.

On the other hand, Ashrafudoulla et al. (2021) reported there is no significant difference among the *S. Enteritidis* biofilm formation on plastic, stainless steel, and silicon rubber ($P > 0.05$) at 24 h adherence times, ranging from 6.17 ± 0.04 log CFU/cm² (stainless steel) to 6.30 ± 0.08 log CFU/cm² (silicon rubber). In another study, Bayoumi et al. (2012) tested the adherence of *S. Typhimurium* isolated from raw milk and dairy product to stainless steel and polypropylene and found that the type of surface used does not significantly influence the adherence of the pathogen. Although all strains tested were able to adhere to both surfaces, no significant difference was observed between tested surfaces for *S. Typhimurium* (polypropylene and stainless steel). This study also found that the *S. Typhimurium* strain had the highest recovered count (7.34 log CFU/cm² on polypropylene and 7.27 log CFU/cm² on stainless steel) as compared to *Staphylococcus aureus* and *Cronobacter sakazakii* after 72 h incubation (*S. aureus* and *C. sakazakii* were 5.7 and 5.48 log CFU/cm², respectively on polypropylene and 5.23 and 5.44 log CFU/cm², respectively on stainless steel).

Biofilm formation often depends on three factors: bacteria cells, type of surfaces, and environmental factors. This review highlights the role of food contact surfaces in *Salmonella* biofilm formation and adherence and the effect of chemical disinfectants on the *Salmonella* biofilm. Surface roughness, texture, porosity, and wettability often affect the hydrophobicity of a surface. Generally, a surface will be classified as hydrophobic if its droplet contact angle is higher than 90 degrees; however, hydrophilic surfaces have less than 90 degrees of droplet contact angle measurement (Chieng et al., 2019). Six out of nine articles agreed that hydrophobic surfaces are more susceptible to biofilm formation (Silva et al., 2010; Corcoran et al., 2013a; 2013b; Singla et al., 2014; Dantas et al., 2018; Djebbi-Simmons et al., 2019); however, the opposite was observed in Rodríguez-Melcón et al. (2018) while Bayoumi et al. (2012) and Ashrafudoulla et al. (2021) found no significant difference in biofilm formation on hydrophobic and hydrophilic surfaces.

The result showed there is a trend that biofilms are more likely to form on hydrophobic surfaces than on hydrophilic surfaces, which is under numerous studies (Cerca et al., 2005; Di Ciccio et al., 2015; Delaviz et al., 2015). It is because most bacterial cell wall proteins adhere easily to a hydrophobic surface, which results in a strong binding force, thus,

allowing the formation of more abundant and profuse biofilms (De-la-Pinta et al., 2019). Nevertheless, the variability of the results may be due to several reasons, including high variability in testing procedure, types of tested *Salmonella* strains, and physiochemical properties of the microbes. Besides, most studies did not report information regarding the degree of surface hydrophobicity, which significantly impacts biofilm adherence. A general name such as plastic was used in some studies despite there being at least 7 types of plastic available, and each has its distinct characteristics (Dantas et al., 2018; Djebbi-Simmons et al., 2019; Byun et al., 2021).

Chemical Disinfectants' Efficacy

Selected chemical disinfection efficacy against *Salmonella* biofilm on food contact surfaces is summarised in Table 4. Bayoumi et al. (2012) noted that applying 250 mg/L of NaOCl for 30 s disinfected all *S. Typhimurium* planktonic cells on stainless steel and polypropylene. Although the same amount of NaOH cannot completely remove *S. Typhimurium* biofilm on both surfaces, it showed more than 6 log CFU/cm² reduction, which was significant (P<0.05).

Byun et al. (2021) studied the efficacy of chlorine-based disinfectants against *S. Enteritidis* biofilm formed on stainless steel, silicone rubber, and plastic and found that the average population of *S. Enteritidis* biofilm decreased significantly (P<0.05) on all tested surfaces as the disinfectant concentration increased from 10 to 100 µg/mL and reaction time increased from 1 to 5 min. On stainless steel, a minimum 3.77 log CFU/cm² reduction was shown by NaOCl and not detected by ClO₂. On plastic, a minimum 3.50 log CFU/cm² reduction was shown by NaOCl and 5.49 log CFU/cm² by ClO₂. Silicon rubber showed the least minimum reduction among tested surfaces: 3.21 log CFU/cm² by NaOCl and 5.20 log CFU/cm² by ClO₂. The results indicated that ClO₂ is more effective than NaOCl at removing *S. Enteritidis* biofilm from stainless steel, followed by plastic and silicon rubber.

Corcoran et al. (2013a) reported a reduction in cell counts increased as exposure time (up to 90 minutes) to disinfectant increased for 48h biofilm. Nevertheless, NaOCl (500 mg/L) and BAC (0.02%) were not effective in eliminating 48h *Salmonella* biofilm as only sodium hydroxide (1 M) demonstrates complete elimination. No disinfectants fully eradicate 168h biofilm or achieve a ≥4 log reduction.

Silva et al. (2010) observed greater efficacy (P<0.05) of NaOCl (100 mg/L of total available chlorine, pH=10) and peracetic acid (60 mg/L, pH=3) than the QUAT (200 mg/L, pH=9). In addition, no significant difference in disinfectant efficacy against *S. Enteritidis* that adhered to granite and stainless-steel surfaces was observed.

The study by Djebbi-Simmons (2019) showed that H₂O₂ (0.88%, 10 min) was able to eradicate *S. Typhimurium* biofilm on all tested surfaces completely, whereas NaOCl (0.0095%, 2 min) achieved 31–32% and 34–35% disinfection efficacy against long-term

Table 4
Selected chemical disinfection efficacy against *Salmonella* biofilm on food contact surfaces

Test Organism	Surface	Study	Disinfectant	Concentration	Exposure time	*LRV (log CFU/cm ²)
S. Enteritidis	Stainless steel	Byun et al. (2021)	NaOCl	10–100 mg/L	1–5min	0.96–4.91
		Byun et al. (2021)	ClO ₂	10–100 mg/L	1–5min	1.38–>6.00
	Plastic	Byun et al. (2021)	NaOCl	10–100 mg/L	1–5min	0.97–4.20
		Byun et al. (2021)	ClO ₂	10–100 mg/L	1–5min	1.14–>6.00
	Concrete	Rodrigues et al. (2011)	NaOCl	6.3–12.5 µg/ml	-	>6.00
		Rodrigues et al. (2011)	BAC	100.0–400.0 µg/ml	-	>6.00
		Rodrigues et al. (2011)	H ₂ O ₂	5.6–90.0 mg/ml	-	>6.00
		Rodrigues et al. (2011)	Triclosan	>4000 µg/ml	-	<6.00
		Corcoran et al. (2013a)	NaOCl	500 mg/L	10–90min	0.35–0.79
		Corcoran et al. (2013a)	NaOH	1 M	10–90min	0.79–0.84
Corcoran et al. (2013a)		BAC	0.02%	10–90min	0.10–0.19	
Corcoran et al. (2013a)		NaOCl	500 mg/L	10–90min	0.13–0.97	
S. Agona	Concrete	Corcoran et al. (2013a)	NaOH	1 M	10–90min	1.66–7.66
		Corcoran et al. (2013a)	BAC	0.02%	10–90min	0.03–0.97
	Stainless steel	Bayoumi et al. (2012)	NaOCl	250 mg/L	30s	>6.00
		Djebbi-Simmons	NaOCl	0.0095%	2min	0.68–3.85
S. Typhimurium	Plastic	Djebbi-Simmons	H ₂ O ₂	0.88%	10min	>6.00
		Bayoumi et al. (2012)	NaOCl	250 mg/L	30s	>6.00
	Concrete	Djebbi-Simmons	NaOCl	0.0095%	2min	0.73–3.79
		Djebbi-Simmons	H ₂ O ₂	0.88%	10min	>6.00
		Singla et al. (2014)	Malic acid	4.1–4.3%	-	>6.00
		Singla et al. (2014)	Acetic acid	4.7–4.9%	-	>6.00
		Singla et al. (2014)	Citric acid	4.1–4.3%	-	>6.00
		Singla et al. (2014)	Lactic acid	5.2–5.3%	-	>6.00
		Singla et al. (2014)	Ozonated water	2.0–2.2 ppm	-	>6.00
		Corcoran et al. (2013a)	NaOCl	500 mg/L	10–90min	0.15–1.11
Formica laminate	Corcoran et al. (2013a)	NaOH	1 M	10–90min	1.50–7.63	
Formica laminate	Corcoran et al. (2013a)	BAC	0.02%	10–90min	0.06–0.83	
	Djebbi-Simmons	NaOCl	0.0095%	2min	0.63–2.74	
		Djebbi-Simmons	H ₂ O ₂	0.88%	10min	>6.00

Note. *Log reduction value

stationery (14 days) cell at 2 and 24 h, on plastic and stainless-steel surfaces respectively, but only 26% on Formica laminate surface when the initial microbial load was high. The log-phase cell (6 h) showed the least resistance to NaOCl disinfection among the 3 growth-phase cells.

In a study by Rodrigues et al. (2011) comparing the minimum biofilm eradication concentration (MBEC) of 4 disinfectants, NaOCl showed the lowest MBEC for all *S. Enteritidis* strains tested, ranging from 6.3 to 12.5 µg/ml, followed by BAC (100 to 400 µg/ml) and H₂O₂ (5.6-90 mg/ml). On the other hand, disinfection by triclosan showed lower susceptibility since it failed to eliminate any *S. Enteritidis* biofilm even at the maximum concentration (4,000 µg/ml).

Another study by Singla et al. (2014) was conducted to determine the efficacy of disinfectants in reducing biofilm on food contact surfaces such as PVC pipes, polyethene bags, plastic surfaces, and fresh produce. The research discovered that 2 ppm of ozonated water was most effective in inhibiting *S. Typhimurium* biofilm growth, and 2% organic acid is needed to inhibit *S. Typhimurium* biofilm growth. Results also showed that the sensitivity of the tested strain against disinfectant decreased biofilm formation. Interestingly, the study discovered that with a combination of 2% malic acid and 2 ppm of ozonated water, biofilm formation was significantly reduced ($p < 0.05$) after 20 h and 40 h exposure.

As for the efficacy of chemical disinfectants, NaOCl has been widely applied in disinfection for its low cost, ease of use, and effectiveness (CDC, 2014). In the present review, despite showing higher efficacy among tested chemical disinfectants, four out of six studies found that NaOCl was less effective in eradicating *Salmonella* biofilm (Silva et al., 2010; Bayoumi et al., 2012; Corcoran et al., 2013a; Djebbi-Simmons et al., 2019). The concentration of NaOCl used ranged from 100 mg/L to 500 mg/L. Although significant reductions were observed, none of the NaOCl used in these studies could fully eliminate *Salmonella* biofilm, even at high concentrations. These results also suggested that NaOCl is less effective in removing *Salmonella* biofilm at regulatory concentration. However, using a high concentration of chlorine-based disinfectant may produce by-products that are potentially harmful to public health, such as chloroform which is probable carcinogenic (CDC, 2014). Plus, sodium hypochlorite is reported to cause inflammation and skin irritation (Chia et al., 2016).

On the other hand, Rodrigues et al. (2011) and Byun et al. (2021) reported that NaOCl was effective against *Salmonella* biofilm. Rodrigues et al. (2011) found that the MBEC of tested NaOCl were lower than recommended concentration, and BAC. In contrast with Djebbi-Simmons et al. (2019), NaOCl in this study also proved to have higher efficacy than H₂O₂. Again, the inconsistency may be due to the high variation of the testing procedure, types of tested *Salmonella* strains, and physiochemical properties of the microbes. Exposure time may act as a factor that affects the efficacy of disinfectants; as shown in the studies

by Corcoran et al. (2013a), disinfectant efficacy increases as the contact time increases (up to 90 min). However, it is less applicable in the real-life setting as high costs may be induced and result in inconvenience.

Moreover, Singla et al. (2014) were the only article that studied the disinfectant efficacy of ozonated water on *Salmonella* biofilm and acid. Hence, insufficient data were available to compare disinfectant efficacies between ozonated water and acid and other disinfectants.

Plastic and stainless steel are often used in surface disinfectant efficacy research due to their wide application in household kitchen and food premises, and chemical disinfectant, especially chlorine-based, is readily available and have been used for over a century. Therefore, it is unsurprising that most studies in this review focus on plastic, stainless steel, and chlorine-based disinfectant. However, the efficacy of similar disinfectants is inconsistent in *Salmonella* biofilm-forming ability on similar food contact surfaces. As a result, it is difficult to formulate a statistically valid conclusion regarding the research objective. Nevertheless, the chemical disinfectant included in this review showed less effectiveness in regular concentration. High concentration may enhance the effectiveness, but harmful by-products could be formed; thus, it is not recommended. In short, most food industries use NaOCl as a chemical disinfectant because it is cheap and is proven to reduce the planktonic bacterial number to a safe level. However, due to this disinfectant's low efficacy in eliminating biofilm, consistent cleaning is highly critical.

CONCLUSION

In conclusion, despite the variability that existed in reported *Salmonella* biofilm susceptibility on various food contact surfaces and the efficacy of chemical disinfectants, the result showed a trend that hydrophobic food contact surfaces such as wood and concrete are more susceptible to *Salmonella* contamination. Plus, *Salmonella* Enteritidis and *Salmonella* Typhimurium are used in most studies as they are the common outbreak serovars and can contaminate the surface easily. Furthermore, the result also suggested that regular concentrations of chemical disinfectants, like NaOCl, are less effective in *Salmonella* biofilm eradication. High concentration is not encouraged as it may form by-products that affect public health, such as chloroform. It shows that the cleanliness of the food contact surfaces is important, and cleaning should be done regularly to avoid the formation of biofilm.

ACKNOWLEDGEMENT

The publication fee is supported by UPM-Kyutech International Symposium on Applied Engineering and Sciences 2021 (SAES2021) and Universiti Putra Malaysia.

REFERENCES

- Abeyundara, P. D. A., Dhowlaghar, N., Nannapaneni, R., Schilling, M. W., Mahmoud, B., Sharma, C. S., & Ma, D. P. (2018). *Salmonella enterica* growth and biofilm formation in flesh and peel cantaloupe extracts on four food-contact surfaces. *International Journal of Food Microbiology*, 280, 17-26. <https://doi.org/10.1016/j.ijfoodmicro.2018.04.042>
- Akinola, A. A., Tshimpamba, M. E., Mwanza, M., & Ateba, A. N. (2020). Biofilm production potential of *Salmonella* serovars isolated from chickens in North West Province, South Africa. *Polish Journal of Microbiology*, 69(4), 427-439. <https://doi.org/10.33073/pjm-2020-046>
- Anderson, M., Jaykus, L. A., Beaulieu, S., & Dennis, S. (2011). Pathogen-produce pair attribution risk ranking tool to prioritize fresh produce commodity and pathogen combinations for further evaluation (P3ARRT). *Food Control*, 22(12), 1865-1872. <https://doi.org/10.1016/j.foodcont.2011.04.028>
- Ashrafudoulla, M., Na, K. W., Byun, K. H., Kim, D. H., Yoon, J. W., Mizan, M. F. R., Kang, I., & Ha, S. D. (2021). Isolation and characterization of *Salmonella* spp. from food and food contact surfaces in a chicken processing factory. *Poultry Science*, 100(8), Article 101234. <https://doi.org/10.1016/j.psj.2021.101234>
- Bayoumi, M. A., Kamal, R. M., El Aal, S. F. A., & Awad, E. I. (2012). Assessment of a regulatory sanitization process in Egyptian dairy plants in regard to the adherence of some food-borne pathogens and their biofilms. *International Journal of Food Microbiology*, 158(3), 225-231. <https://doi.org/10.1016/j.ijfoodmicro.2012.07.021>
- Byun, K. H., Han, S. H., Yoon, J., Park, S. H., & Ha, S. D. (2021). Efficacy of chlorine-based disinfectants (sodium hypochlorite and chlorine dioxide) on *Salmonella* Enteritidis planktonic cells, biofilms on food contact surfaces and chicken skin. *Food Control*, 123, Article 107838. <https://doi.org/10.1016/j.foodcont.2020.107838>
- Cerca, N., Pier, G. B., Vilanova, M., Oliveira, R., & Azeredo, J. (2005). Quantitative analysis of adhesion and biofilm formation on hydrophilic and hydrophobic surfaces of clinical isolates of *Staphylococcus epidermidis*. *Research in Microbiology*, 156(4), 506-514. <https://doi.org/10.1016/j.resmic.2005.01.007>
- Chen, J., & Wang, Y. (2020). Genetic determinants of *Salmonella enterica* critical for attachment and biofilm formation. *International Journal of Food Microbiology*, 320, Article 108524. <https://doi.org/10.1016/j.ijfoodmicro.2020.108524>
- Chia, G. S. Z., Green, A., Fong, Y. T., Lee, H. Y., & Ho, S. F. (2016). Rare case of type I hypersensitivity reaction to sodium hypochlorite solution in a healthcare setting. *BMJ*, 2016, 1-4. <https://doi.org/10.1136/bcr-2016-217228>
- Chieng, B. W., Ibrahim, N. A., Daud, N. A., & Talib, Z. A. (2019). Functionalization of graphene oxide via gamma-ray irradiation for hydrophobic materials. In S. A. Rashid, R. N. I. R. Othman & M. Z. Hussein (Eds.), *Synthesis, Technology and Applications of Carbon Nanomaterials* (pp. 177-203). Elsevier. <https://doi.org/10.1016/b978-0-12-815757-2.00008-5>
- Corcoran, M., Morris, D., de Lappe, N., O'Connor, J., Lalor, P., Dockery, P., & Cormican, M. (2013a). Commonly used disinfectants fail to eradicate *Salmonella enterica* biofilms from food contact surface materials. *Applied and Environmental Microbiology*, 80(4), 1507-1514. <https://doi.org/10.1128/aem.03109-13>

- Corcoran, M., Morris, D., de Lappe, N., O'Connor, J., Lalor, P., Dockery, P., & Cormican, M. (2013b). *Salmonella enterica* biofilm formation and density in the centers for disease control and prevention's biofilm reactor model is related to serovar and substratum. *Journal of Food Protection*, 76(4), 662-667. <https://doi.org/10.4315/0362-028X.JFP-12-303>
- Dantas, S. T. A., Rossi, B. F., Bonsaglia, E. C. R., Castilho, I. G., Hernandez, R. T., Fernandes, A., & Rall, V. L. M. (2018). Cross-contamination and biofilm formation by *Salmonella enterica* serovar Enteritidis on various cutting boards. *Foodborne Pathogens and Disease*, 15(2), 81-85. <https://doi.org/10.1089/fpd.2017.2341.44>
- Delaviz, Y., Santerre, J., & Cvitkovitch, D. (2015). Infection resistant biomaterials. In L. Barnes & I. R. Cooper (Eds.), *Biomaterials and Medical Device - Associated Infections* (pp. 223-254). Elsevier. <https://doi.org/10.1533/9780857097224.2.223>
- De-la-Pinta, I., Cobos, M., Ibarretxe, J. Montoya, E., Eraso, E., Guraya, T., & Quindós, G. (2019). Effect of biomaterials hydrophobicity and roughness on biofilm development. *Journal of Materials Science: Materials in Medicine*, 30, Article 77. <https://doi.org/10.1007/s10856-019-6281-3>
- Di Ciccio, P., Vergara, A., Festino, A., Paludi, D., Zanardi, E., Ghidini, S., & Ianieri, A. (2015). Biofilm formation by *Staphylococcus aureus* on food contact surfaces: Relationship with temperature and cell surface hydrophobicity. *Food Control*, 50, 930-936. <https://doi.org/10.1016/j.foodcont.2014.10.048>
- Djebbi-Simmons, D., Xu, W., Janes, M., & King, J. (2019). Survival and inactivation of *Salmonella enterica* serovar Typhimurium on food contact surfaces during log, stationary and long-term stationary phases. *Food Microbiology*, 84, Article 103272. <https://doi.org/10.1016/j.fm.2019.103272>
- Fàbrega, A., & Vila, J. (2013). *Salmonella enterica* serovar Typhimurium skills to succeed in the host: Virulence and regulation. *Clinical Microbiology Reviews*, 26(2), 308-341. <https://doi.org/10.1128/CMR.00066-12>
- Fraser, A. M., Anderson, J., Goncalves, J., Black, E., Starobin, A., Buckley, D., Grinstead, D., Manuel, C., & Hollingsworth, J. (2021). Sanitizers and disinfectants: A retail food and foodservice perspective. *Food Protection Trends*, 41(3), 358-367.
- Giaouris, E., Chorianopoulos, N., Skandamis, P., & Nychas, G. J. (2012). Attachment and biofilm formation by *Salmonella* in food processing environments. In B. S. M. Mahmoud (Ed.), *Salmonella - A Dangerous Foodborne Pathogen* (pp. 157-180). Intech Open. <https://doi.org/10.5772/1308>
- Graziani, C., Losasso, C., Luzzi, I., Ricci, A., Scavia, G., & Pasquali, P. (2017). *Salmonella*. In C. E. R. Dodd, T. Aldsworth, R. A. Stein, D. O. Cliver & H. P. Riemann (Eds.), *Foodborne Diseases* (3rd ed., pp. 133-169). Academic Press. <https://doi.org/10.1016/b978-0-12-385007-2.00005-x>
- Jay, L. S., Davos, D., Frankish, E., & Lightfoot, D. (2003). *Salmonella*. In A. D. Hocking (Ed.), *Foodborne Microorganisms of Public Health Significance* (6th ed., pp. 207-266). Australian Institute of Food Science and Technology (NSW Branch), Food Microbiology Group.
- Lee, K. H., Lee, J. Y., Roy, P. K., Mizan, M. F. R., Hossain, M. I., Park, S. H., & Ha, S. D. (2020). Viability of *Salmonella* Typhimurium biofilms on major food-contact surfaces and eggshell treated during 35 days with and without water storage at room temperature. *Poultry Science*, 99(9), 4558-4565. <https://doi.org/10.1016/j.psj.2020.05.055>

- Møretrø, T., Vestby, L., Nesse, L., Storheim, S., Kotlarz, K., & Langsrud, S. (2009). Evaluation of efficacy of disinfectants against *Salmonella* from the feed industry. *Journal of Applied Microbiology*, *106*(3), 1005-1012. <https://doi.org/10.1111/j.1365-2672.2008.04067.x>
- Painter, J. A., Hoekstra, R. M., Ayers, T., Tauxe, R. V., Braden, C. R., Angulo, F. J., & Griffin, P. M. (2013). Attribution of foodborne illnesses, hospitalizations, and deaths to food commodities by using outbreak data, United States, 1998-2008. *Emerging Infectious Diseases*, *19*(3), 407-415. <https://doi.org/10.3201/eid1903.111866>
- Rodrigues, D., Cerca, N., Teixeira, P., Oliveira, R., Ceri, H., & Azeredo, J. (2011). *Listeria monocytogenes* and *Salmonella enterica* enteritidis biofilms susceptibility to different disinfectants and stress-response and virulence gene expression of surviving cells. *Microbial Drug Resistance*, *17*(2), 181-189. <https://doi.org/10.1089/mdr.2010.0183>
- Rodríguez-Melcón, C., Riesco-Peláez, F., Carballo, J., García-Fernández, C., Capita, R., & Alonso-Calleja, C. (2018). Structure and viability of 24- and 72-h-old biofilms formed by four pathogenic bacteria on polystyrene and glass contact surfaces. *Food Microbiology*, *76*, 513-517. <https://doi.org/10.1016/j.fm.2018.06.016>
- Shao, L., Dong, Y., Chen, X., Xu, X., & Wang, H. (2020). Modeling the elimination of mature biofilms formed by *Staphylococcus aureus* and *Salmonella* spp. using combined ultrasound and disinfectants. *Ultrasonics Sonochemistry*, *69*, Article 105269. <https://doi.org/10.1016/j.ultsonch.2020.105269>
- Silva, I. D., Careli, R. T., Lima, J. C., & Andrade, N. J. (2010). Effectiveness of cleaning and sanitizing procedures in controlling the adherence of *Pseudomonas fluorescens*, *Salmonella* Enteritidis, and *Staphylococcus aureus* to domestic kitchen surfaces. *Food Science and Technology*, *30*(1), 231-236. <https://doi.org/10.1590/s0101-20612010005000015>
- Singla, R., Goel, H., & Ganguli, A. (2014). Novel synergistic approach to exploit the bactericidal efficacy of commercial disinfectants on the biofilms of *Salmonella enterica* serovar Typhimurium. *Journal of Bioscience and Bioengineering*, *118*(1), 34-40. <https://doi.org/10.1016/j.jbiosc.2013.12.025>
- WHO. (2020, April 30). *Food safety*. World Health Organization. [https://www.who.int/news-room/fact-sheets/detail/food-safety#:~:text=An%20estimated%20600%20million%20%E2%80%93%20almost,healthy%20life%20years%20\(DALYs\).&text=Children%20under%205%20years%20of,125%20000%20deaths%20every%20year](https://www.who.int/news-room/fact-sheets/detail/food-safety#:~:text=An%20estimated%20600%20million%20%E2%80%93%20almost,healthy%20life%20years%20(DALYs).&text=Children%20under%205%20years%20of,125%20000%20deaths%20every%20year)
- Zhang, J., Wang, J., Zhao, D., & Hao, J. (2021). Efficacy of the two-step disinfection with slightly acidic electrolyzed water for reduction of *Listeria monocytogenes* contamination on food raw materials. *LWT - Food Science and Technology*, *140*, Article 110699. <https://doi.org/10.1016/j.lwt.2020.110699>



Chest Computed Tomography (CT) and Clinical Findings Among COVID-19 Patients of Tertiary Hospital in Bangladesh

Tarek Shams¹, Jamil Haider Chowdhury², Hasna Hena Chowdhury³, Qumrul Ahsan², Hrionmoy Dutta¹, Mohammad Ali Tareq^{4,5}, Lubna Shirin^{6,7}, Sanjida Akhter⁸ and Tania Islam^{8,9*}

¹Department of Medicine, Chittagong Medical College, Chittagong, Bangladesh

²Department of Radiology, Ma O Shishu Hospital Medical College, Chittagong, Bangladesh

³Department of Clinical Pathology, Southern Medical College and Hospital, Chittagong, Bangladesh

⁴Malaysia Japan International Institute of Technology, Universiti Teknologi Malaysia (UTM), Kuala Lumpur, Malaysia

⁵Department of Finance, Faculty of Business and Economics, University of Malaya (UM), Malaysia

⁶Department of Anatomy, Faculty of Medicine, Malaysian Allied Health Sciences Academy University (MAHSA), Selangor, Malaysia

⁷Department of Anatomy, Faculty of Medicine, Universiti Teknologi Mara (UiTM), Malaysia

⁸Department of Surgery, Faculty of Medicine, University of Malaya (UM), Kuala Lumpur, Malaysia

⁹Centre for Population Health, Department of Social and Preventive Medicine, Faculty of Medicine, University of Malaya (UM), Malaysia

ABSTRACT

Bangladesh has experienced a sharp rise in cases during the third wave of the COVID-19 pandemic. This study investigates chest computed tomography (CT) and clinical findings of COVID-19 patients in Bangladesh. It is a single-centred cross-sectional study conducted at Chittagong Ma O Shishu Hospital. In total, 242 COVID-19 patients were recruited between June 2020 and July 2021 from a tertiary hospital in Chittagong, Bangladesh—most patients

had a fever (90%) and cough (74.7%). Only a few patients had dyspnoea (13.3%), body aches (3.6%), sore throat (0.4%), fatigue (0.8%), diarrhoea (1.2%), headache (2%), and anosmia (2%). Most (91.3%) patients had abnormal CT image findings. Findings revealed that 89.6% had bilateral lung patchy opacities, 84.3% had ground glass opacities and crazy paving appearance, 29.3% had consolidation, and 16.9% had traction bronchiectasis. Clinical features, i.e., fever (93.7%) and cough (78.3%), were

ARTICLE INFO

Article history:

Received: 20 May 2022

Accepted: 05 October 2022

Published: 13 July 2023

DOI: <https://doi.org/10.47836/pjst.31.5.05>

E-mail addresses:

drtarekshams@gmail.com (Tarek Shams)

chowdhuryjamil23@gmail.com (Jamil Haider Chowdhury)

hasnahena37@hotmail.com (Hasna Hena Chowdhury)

qumrulahsan@yahoo.com (Qumrul Ahsan)

hiranmoydutta50@gmail.com (Hrionmoy Dutta)

tareq.mjiit@gmail.com (Mohammad Ali Tareq)

lubnashirin2012@gmail.com (Lubna Shirin)

sanjida.akter.cmc@gmail.com (Sanjida Akhter)

tania.omee@gmail.com (Tania Islam)

* Corresponding author

significantly more common ($P<0.05$) among those with positive radiological findings compared to those with negative radiological findings. However, this found that patients with negative radiological findings were more likely to have body aches (4.8%) than those with positive radiological findings ($P=0.012$). Most patients had lung involvement. There was no statistically significant difference in the demographic and patient comorbidities between these two radiological groups. A Chest CT scan was the best radiological option for detecting the progression of COVID-19 in high-risk and low-risk groups to initiate early clinical management and prevent complications during the pandemic.

Keywords: COVID-19, CT scan, lung, radiological findings

INTRODUCTION

The novel severe acute respiratory syndrome coronavirus 2 (SARS-CoV-2) epidemic emerged in December 2019 from Wuhan, Hubei and is responsible for the coronavirus disease (COVID-19) (Huang et al., 2020). The incubation period of COVID-19 varies from 2 to 14 days, with a median of 5–6 days. Its infectivity is higher than in previous epidemics from other viruses (Kolifarhood et al., 2020). In March 2020, the World Health Organization (WHO) officially acknowledged that the outbreak of COVID-19 was a global pandemic (WHO, 2021). The symptoms of patients with COVID-19 include fever, fatigue, dry cough, anorexia, myalgias, dyspnoea, sputum production, chills, lethargy, arthralgias, headache, nausea, vomiting, and diarrhoea (Valencia, 2020). However, the symptoms can vary drastically, as some could be asymptomatic, while others could have severe symptoms of acute respiratory distress syndrome or even death. The diagnosis of COVID-19 is confirmed by real-time reverse transcription polymerase chain reaction on respiratory or blood samples. At the same time, computed tomography (CT) findings such as bilateral ground-glass opacities and peripheral posterior distribution can be suggestive findings of COVID-19. Although many patients had no abnormal radiologic findings, a CT scan may show a paving pattern of multifocal consolidations as the disease progresses and is used in monitoring disease progression (Bernheim et al., 2020; Guan et al., 2020; Sun et al., 2020; Valencia, 2020). Moreover, clinical features and chest imaging can indicate higher levels of medical care (Cocconcelli et al., 2020), while risk factors such as age, smoking and hypertension may increase the severity of COVID-19 (Jeong et al., 2020).

COVID-19 is highly infectious and can become fatal acute respiratory distress syndrome (ARDS). Its early detection is an important factor in controlling its spread. Proper monitoring and management can drastically reduce mortality and morbidity rates. The most reliable screening method for COVID-19 is reverse-transcription polymerase chain reaction (RT-PCR) testing. However, it is a laborious and time-consuming method, and some studies reported its low sensitivity during the early stages (Mamun et al., 2021). Even though the

diagnosis of being COVID-19 positive or negative is primarily based on RT-PCR, a chest scan, such as a chest X-ray (CXR) and CT, are routine diagnostic approaches to detect abnormal lung changes linked to COVID-19 (Dey et al., 2020; Sun et al., 2020). According to WHO guidelines in June 2020, chest CT has a relatively high sensitivity for COVID-19 compared to chest X-rays (WHO, 2020). It is because COVID-19 mainly causes respiratory tract infections but can affect any organ in the body (Amit et al., 2021; Dey et al., 2020; Islam et al., 2020). A chest CT scan was frequently used in the diagnosis and disease prognosis of COVID-19 (Ai et al., 2020; Dey et al., 2020; Islam et al., 2020). The COVID-19 diagnosis involves a combination of epidemiological history, clinical manifestations, early chest CT examinations, and RT-PCR, with a particular emphasis on definite epidemiological history and early chest CT findings when positive RT-PCR tests lag, or test results are negative but clinically positive signs are shown (Ai et al., 2020; Rong et al., 2021). Only a few studies were conducted on a limited number of chest CT image findings among Bangladeshi COVID-19 patients (Biswas et al., 2021; Clump et al., 2020). It is unclear whether CT should be used as a first-line imaging technique and can be used as a preliminary test to detect the diagnosis quickly and to determine lung condition simultaneously.

However, chest abnormalities associated with COVID-19 differ from those associated with SARS and MERS and are also related to the disease extent and clinical findings. Therefore, detecting common and uncommon imaging findings on chest CT examinations is clinically important (Sun et al., 2020). Moreover, different countries are affected by different strains, and immunity can be different, so the presentation of signs, symptoms and chest findings may vary. Since the onset of COVID-19 in December 2019, many studies have reported the clinical characteristics and chest imaging appearances of COVID-19, specifically describing a variety of abnormalities in the lungs (Sun et al., 2020).

Bangladesh is considered one of the 25 most vulnerable countries and possesses the potential risk for the virus's rapid spread (Mohiuddin, 2020). The country confirmed the first COVID-19 case in its territory on March 8, 2020 (Dey et al., 2020; Mamun et al., 2021). Currently, Bangladesh is facing widespread community transmission. It has experienced a sharp rise in positive cases with a relatively lower recovery rate than neighbouring countries (Dey et al., 2020; Islam et al., 2020). The outbreak is evolving very rapidly in Bangladesh. The country was experiencing an increase in cases during the third wave of the pandemic (Amit et al., 2021). Therefore, we aim to explore the clinical and chest image findings of COVID-19 patients in Bangladesh.

MATERIALS AND METHOD

This cross-sectional study was conducted at Chattogram Maa o Shishu Hospital (CMOSH). CMOSH is a tertiary hospital located in Chittagong Port City, Bangladesh. Purposive sampling was used to recruit the patients. Initially, 251 COVID-19 patients aged 18 years

and above who were diagnosed with COVID-19 for the first time were recruited from June 2020 to July 2021. Nine patients whose history of radiological information was unknown were excluded, leaving 242 cases eligible for further analysis. Patients with severe illnesses were excluded from this study. Face-to-face interviews were conducted to collect socio-demographic and comorbidity data, i.e., age, gender, education level, residence status, presence of comorbidities such as diabetes mellitus, hypertension, chronic obstructive pulmonary disease, chronic kidney disease, ischemic heart disease, chronic liver disease, malignancy and hypertension and immunocompromised status. A chest CT scan was done at admission with symptoms of fever/cough for 3 to 5 days or more. Clinical and imaging findings such as fever, body ache, dyspnoea, cough, sore throat, fatigue, diarrhoea, headache, anosmia, and CT images were extracted from the patient's medical records. All CT images were reviewed and inferred by well-trained radiologists at the hospital.

Age was classified into five categories: 18–40 years, 41–60, 61–80, >80 and unknown. Morbid obesity was classified as “yes” or “no” based on patients having a body mass index of 40 or more 40 (kg/m²).

For further analysis, COVID-19 patients were re-categorised into positive and negative radiological findings. Positive radiological findings were defined as any features in the CT scan, ground glass opacities (bilateral/subplural/peripheral), and/or crazy paving appearance, and/or consolidation, and/or traction bronchiectasis. Negative radiological findings were defined as the absence of chest CT findings, i.e., ground glass, crazy paving, consolidation and traction bronchiectasis.

This study was approved by the Ethical Review Committee of Chittagong Medical College, Chittagong, Bangladesh (CMC/PG/2021/174). Written informed consent was obtained from all the participants before taking part in this study.

Statistical Analysis

Descriptive statistics (frequencies and percentages) were used to present the socio-demographics, clinical features, and chest CT image findings among the COVID-19 patients. Differences in the categorised demographic, clinical features, and chronic illness variables between patients with positive and negative radiological findings were tested using the Chi-squared test. Values were considered statistically significant when $p < 0.05$. Data were analysed using the Statistical Package for Social Sciences (SPSS Inc, Chicago, IL) version 21.0.

Statistical Power

We estimated to recruit about 200 positive patients with CT reports during the 12 months of enrolment in CMOSH. A previous study recorded that among Covid-19 patients, about 53.3% of patients had positive radiological (CT) findings (Jeong et al., 2020). A sample of 148

COVID-19 patients with a 53.3 % frequency of radiological findings in the population can achieve 80% statistical power at a 5% significance level. Recruitment of even 208 patients achieved 99% statistical power at a 5% significance to detect a significant difference.

RESULTS

A total of 242 confirmed COVID-19 patients who had complete information were included in this study. The background characteristics of the participants are shown in Table 1. In total, 63.2% (n=153) of the patient were aged 60 years or below, and male 66.1% (n=160) and 61.2% resided in urban areas.

Table 2 shows that 66.1% of the patients had at least one comorbidity. Almost half of our patients had hypertension 49.2% (n=119), 46.3% (n=112) had diabetes mellitus, 8.7% (n=21) had obstructive pulmonary disease, 6.6% (n=16) patients had ischemic heart disease, 3.3% (n=8) patients had chronic kidney disease, 0.8% (n=2) had malignancy, and 0.4% (n=1) were immunocompromised.

Table 1
Sociodemographic characteristics of COVID-19 patients (n = 242)

Variables	n (%)
Age	
40 or less	46 (19.0%)
41–60	107 (44.2%)
61 and above	82 (33.9%)
Unknown	7 (2.9%)
Gender	
Male	160 (66.1%)
Female	82 (33.9%)
Residence	
Urban	148 (61.2%)
Rural	81 (33.5 %)
Unknown	13 (5.4 %)

Table 2
Comorbidities for patients with COVID-19 (n = 242)

Variables	n (%)
Comorbidity	
Yes	160 (66.1%)
No	74 (30.6%)
Unknown	8 (3.3%)
Hypertension	
Yes	119 (49.2%)
No	116 (47.9%)
Unknown	7 (2.9%)
Diabetes	
Yes	112 (46.3%)
No	123 (50.8%)
Unknown	7 (2.9%)
Chronic Obstructive Pulmonary Disease	
Yes	21 (8.7%)
No	214 (88.4%)
Unknown	7 (2.9%)
Chronic Kidney Disease	
Yes	8(3.3%)
No	227 (93.8)
Unknown	7 (2.9%)
Morbid obesity	
Yes	3(1.2%)
No	231 (95.5%)
Unknown	8 (3.3%)
Ischemic Heart Disease	
Yes	16 (6.6%)
No	219 (90.5%)
Unknown	7 (2.9%)
Malignancy	
Yes	2(0.8%)
No	231 (95.5%)
Unknown	9 (3.7%)
Immunocompromised State	
Yes	1 (0.4%)
No	232 (95.9%)
Unknown	9 (3.7%)

Most patients are with a fever of 91.3% (n=221) and a cough of 76.0% (n=184) (Table 3). Only a few patients had dyspnoea 15.7% (n=38), body ache (5.4%), sore throat (3.3%), fatigue (3.7%), diarrhoea (2.5%), headache (4.1%), and anosmia (4.5%).

Table 3
Clinical features (signs and symptoms) of COVID-19 patients (n= 242)

Variable name	Yes	No	Unknown
Fever	221 (91.3%)	14 (5.8%)	7 (2.9%)
Body ache	13 (5.4%)	222 (91.7%)	7 (2.9%)
Dyspnoea	38 (15.7%)	203 (83.9%)	1 (0.4%)
Cough	184 (76.0%)	48 (19.8%)	10 (4.1%)
Sore throat	8 (3.3%)	232 (95.9%)	2 (0.8%)
Fatigue	9 (3.7%)	227 (93.8%)	6 (2.5%)
Diarrhoea	6 (2.5%)	230 (95.0%)	6 (2.5%)
Headache	10 (4.1%)	224 (92.6%)	8 (3.3%)
Anosmia	11 (4.5%)	224 (92.6%)	7 (2.9%)

Table 4 shows the chest CT image findings for the 242 patients. The majority (91.3%; n=221) had abnormal CT image findings. Among all the COVID-19 patients (n=242), the majority (86.4%) had ground glass opacities (Bilateral and/or subpleural and/or peripheral); either or any combination of the bilateral, subpleural, peripheral involvements (Figures 1 & 2). 36.4% of patients had the crazy paving appearance, 30.2% had consolidation, and 17.4% of COVID-19 patients had traction bronchiectasis. Out of 221, only 0.8% (n=2) patients exhibited atypical unilateral lung involvement (Figure 3).

According to the radiological findings, patients having any kind of chest image findings in the CT scan were grouped into either the positive (n=221, 91.3%) or negative (n=21, 8.7%) radiological findings group (Table 5). These two groups' demographic characteristics and clinical features were analysed to explore the potential risk factors of COVID-19. No statistically significant difference existed between these two radiological groups in the socio-demographic and patient comorbidities or chronic illness factors. Clinical features, i.e., fever (93.7%) were significantly ($P<0.05$), and cough [$\chi^2(1) = 3.939, p= 0.04$] were also significantly more

Table 4
Lung involvement according to the CT scan image findings (n= 242)

Findings	n (%)
Normal chest imaging	21 (8.7%)
Abnormal Chest image findings	221 (91.3%)
Ground Glass opacities (GGO) (Bilateral and/or Subpleural and/ or peripheral)	209 (86.4%)
Crazy Paving Appearance	88 (36.4%)
Consolidation	73 (30.2%)
Traction bronchiectasis	42 (17.4%)
Lung involvement according to the site (in CT scan)	
Unilateral	2 (0.8%)
Bilateral	219 (90.5%)
Not applicable (normal lung)	21 (8.7%)

common (78.3%) among patients with positive radiological findings compared to those with negative radiological findings. The two groups had no significant difference in dyspnoea, body ache, sore throat, fatigue, diarrhoea, headache, and anosmia.

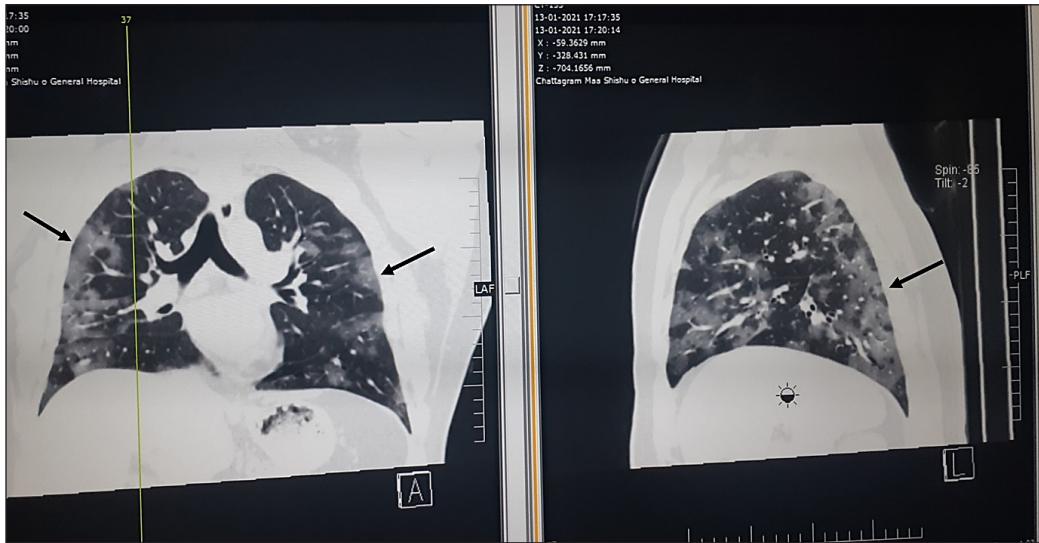


Figure 1. Bilateral multifocal subpleural peripheral ground glass opacities with a crazy paving appearance at all lobes of both lungs - typical COVID-19 CT findings

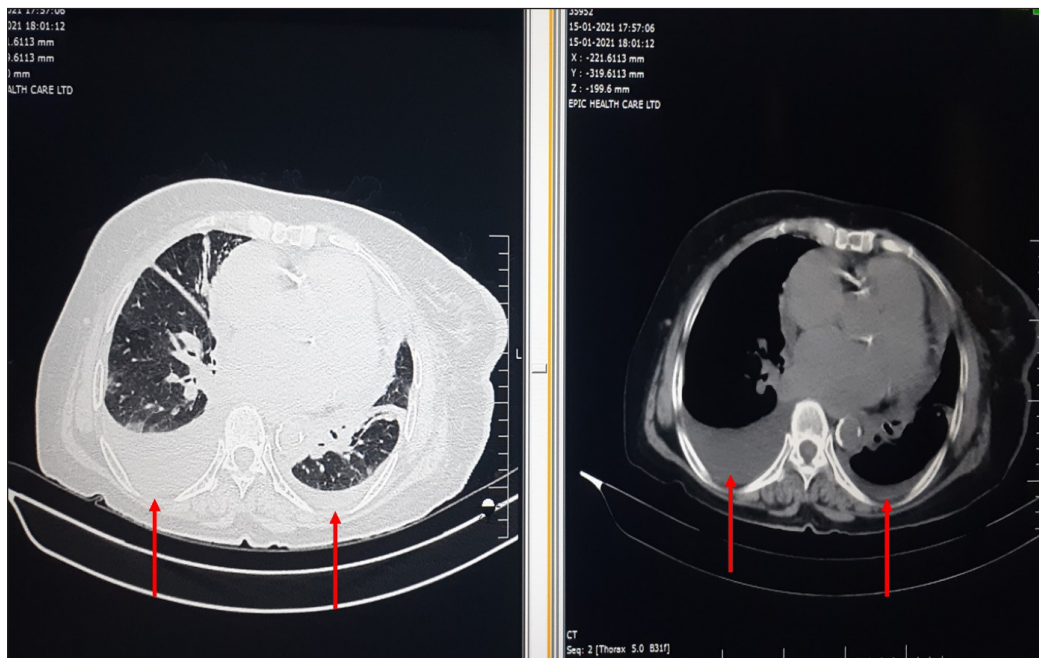


Figure 2. Bilateral ground glass opacities at basal segments of both lungs with bilateral pleural effusion, more on right COVID-19 with bilateral pleural effusion



Figure 3. Unilateral ground glass opacities, crazy paving appearance and consolidation at right lower lobe- atypical COVID-19 CT findings

Table 5

Relationship between socio-demographic characteristics, comorbidities, symptom variables, and radiological (CT scan) findings of COVID-19 patients (n= 242)

Variables	Negative Radiological Findings group (n =21)	Positive Radiological Findings group (n =221)	Chi-square value (df)	P value
Socio-demographic Variables				
*Age				
18 –≤40	6 (28.6%)	41 (19.2%)	1.775 (2)	0.412
41–60	7 (33.3%)	99 (46.3%)		
61 and above	8 (38.1%)	74 (34.6%)		
Unknown	0 (0.0%)	7 (3.2%)		
*Gender				
Male	12 (57.1%)	148 (67.0%)	0.826 (1)	0.36
Female	9 (42.9%)	73 (33.0%)		
*Residences				
Urban	14 (66.7%)	134 (60.61%)	1.493 (1)	0.47
Rural	5 (23.8%)	76 (34.4%)		
Unknown	2 (9.5%)	11 (5.0%)		
Comorbidity Variables				
*Comorbidity (1 or more)				
Yes	11 (52.4%)	149(67.4%)	2.73 (1)	0.098
No	10 (47.6%)	64 (29.0%)		

Table 5 (continue)

Variables	Negative Radiological Findings group (n =21)	Positive Radiological Findings group (n =221)	Chi-square value (df)	P value
Unknown	0 (0.0%)	8 (3.6%)		
^bIschemic Heart Disease				
Yes	1 (4.8%)	15 (6.8%)	-	1
No	20 (95.2%)	199 (90%)		
Unknown	0 (0.0%)	7 (3.2%)		
^aDiabetes				
Yes	7 (33.3%)	105 (47.5%)	1.897 (1)	0.168
No	14 (66.7%)	109 (49.3%)		
Unknown	0 (0.0%)	7 (3.2%)		
^aHypertension				
Yes	7 (33.3%)	112 (50.7%)	2.763 (1)	0.096
No	14 (66.7%)	102(46.2%)		
Unknown	0 (0.0%)	7 (3.2%)		
^bChronic Obstructive Pulmonary Disease				
Yes	2 (9.5%)	19 (8.6%)	-	1
No	19 (90.5%)	195 (88.2%)		
Unknown	0 (0.0%)	7 (3.2%)		
^bChronic Kidney Disease				
Yes	0 (0%)	8 (3.6%)	-	1
No	21 (100.0%)	206 (93.2%)		
Unknown	0 (0%)	7 (3.2%)		
^bMorbid obesity				
Yes	0 (0.0%)	3 (1.4%)	-	1
No	21 (100.0%)	210 (95.0%)		
Unknown	0 (0.0%)	8 (3.6%)		
Symptom Variables				
^bFever				
Yes	14 (66.7%)	207 (93.7%)	-	0.01*
No	4 (19.0%)	10 (4.5%)		
Unknown	3 (14.3%)	4 (1.8%)		
^bBody ache				
Yes	3 (14.3%)	10 (4.5%)	-	0.076*
No	16 (76.2%)	206 (93.6%)		
Unknown	2 (9.5%)	4 (1.8%)		
^bDyspnoea				
Yes	3 (14.3%)	35 (15.9%)	-	1
No	18 (85.7%)	185 (84.1%)		
^aCough				

Table 5 (continue)

Variables	Negative Radiological Findings group (n =21)	Positive Radiological Findings group (n =221)	Chi-square value (df)	P value
Yes	11 (52.4%)	173 (78.3%)	3.939 (1)	0.04*
No	7 (33.3%)	41 (18.6%)		
Unknown	3 (14.3%)	7 (3.2%)		
^bSore throat				
Yes	1 (4.8%)	7 (3.2%)	-	0.52
No	20 (95.2%)	212 (95.9%)		
Unknown	0 (0.0%)	2 (0.9%)		
^bFatigue				
Yes	1 (4.8%)	8 (3.6%)	-	0.51
No	17 (81.0%)	210 (95.5%)		
Unknown	3 (14.3%)	3 (1.4%)		
^bDiarrhoea				
Yes	1 (4.8%)	5 (2.3%)	-	0.39
No	18 (85.7%)	212 (95.9%)		
Unknown	2 (9.5%)	4 (1.8%)		
^bHeadache				
Yes	2 (9.5 %)	8 (3.6%)	-	0.17
No	16 (76.2%)	208 (94.1%)		
Unknown	3 (14.3%)	5 (2.3%)		
^bAnosmi				
Yes	1 (4.8%)	10 (4.5%)	-	0.59
No	17 (81.0%)	207 (93.7%)		
Unknown	3 (14.3%)	4 (1.8%)		

Note. Categorical data are expressed as a percentage

P values were calculated using the ^aChi-square and ^bFisher's exact test for the categorical variables. Df: degree of freedom.

*Significantly different at P <0.05.

DISCUSSION

Most patients have fever (91.3%) and cough (76%). Only a few patients had dyspnoea (15.7%), body aches (5.4%), sore throat (3.3%), fatigue (3.7%), diarrhoea (2.5%), headache (4.1%), and anosmia (4.5%). We found a significant prevalence of fever and cough symptoms among patients with positive radiological findings compared to those with negative radiological findings. Most patients (91.3%, n=221) had abnormal CT image findings, while 8.7 % (n=21) of the chest images were normal.

Among 242 patients, almost half (107, 44.2%) were in the 41–60 age group and predominantly male (66.1%). Similar findings were reported by another Bangladeshi study

where 43% were in the 40–60 age group, and 66.5% were male participants (Biswas et al., 2021), and by a study on the American population that the median age of the patients was 63 years old (Guan et al., 2020).

Most patients have a fever (91.3%) and cough (76%), similar to another study that reported that 93.3% of cases had a fever and 86.1% had a cough. Another study reported admission symptoms of mild-to-moderate cases which is in contrast to a Bangladesh study that included many non-critical patients who had a fever (79%), weakness (68%), cough (45%), altered sensation of taste or smell (35%), headache (32%) and body ache (32%) (Rong et al., 2021).

Among the abnormal chest image findings, out of 221 patients, the majority (86.4%) had ground glass opacities (Bilateral and/or subpleural and/or peripheral) and crazy paving appearance (36.4%). In total, 30.2% had consolidation, and 17.4% had traction bronchiectasis. Only 0.8% exhibited atypical unilateral lung involvement. Our findings align with previous studies (Biswas et al., 2021), which reported that 34.9% had patchy bilateral opacities and 32.1% had consolidation. Another study found that the hallmark of COVID-19 infection in high-resolution CT included ground glass opacities and consolidation, ground glass opacities and crazy paving, and consolidation with parenchymal bands (Clump et al., 2020)

No statistically significant difference existed between the positive and negative radiological groups in the socio-demographic and patient comorbidities or chronic illness factors. Clinical features, i.e., fever (93.7%) and cough (78.3%), were significantly more common ($P < 0.05$) among the patients with positive radiological findings compared to those with negative radiological findings, which indicates acute lung infection.

In this cross-sectional study, we included both RT-PCR positive and confirmed cases and those with clinical and radiologically (CT) COVID-19 cases. Prior studies stated that a CT scan was a more sensitive diagnostic tool than RT-PCR, which can detect 98% of asymptomatic patients (Coconcelli et al., 2020; Fang et al., 2020). During this study, there was a rapid surge of patients having typical COVID-19 symptoms. Nevertheless, these were difficult to diagnose due to the limited availability and time required to obtain results from the RT-PCR. So many hospitals use a CT scan as a tool for triage, especially in the emergency department. A CT scan was done for patients with typical symptoms and needing admission. It was also done for high-risk patients with typical symptoms to start treatment early and prevent complications.

There are several limitations and strengths in our study. One of the weaknesses might be selection bias. We selected those with CT scans and were more likely to include moderate to severe patients. A few repeat CTs were done but not included in this study. Comparison with follow-up scans was beyond the scope of this study. We could not obtain most patients' laboratory data (e.g., CRP & D-Dimer) and outcome information. Although the percentage of lung affected and CT severity score was not included, we included many COVID-19 patients with CT scans.

CONCLUSION

We found that the COVID-19 patients presented more with fever and cough in the hospital. Males and aged groups of more than 40 years were more affected. Most patients had lung involvement. A chest CT scan was one of the radiological options for screening when RT-PCR was lagging or when test results were negative but clinically showing positive signs. It was useful for detecting the progression of COVID-19 in high-risk and low-risk groups to initiate early clinical management and prevent any life-threatening complications during the early stages of the pandemic.

ACKNOWLEDGEMENTS

The authors thank the doctors, nurses, technical staff, hospital administration staff and COVID-19 patients of Chattogram Maa o Shishu Hospital, Bangladesh, who have contributed greatly to this project.

REFERENCES

- Ai, T., Yang, Z., Hou, H., Zhan, C., Chen, C., Lv, W., Tao, Q., Sun, Z., & Xia, L. (2020). Correlation of chest CT and RT-PCR testing for Coronavirus disease 2019 (COVID-19) in China: A report of 1014 cases. *Radiology*, 296(2), E32-E40. <https://doi.org/10.1148/radiol.2020200642>
- Amit, S., Barua, L., & Kafy, A. A. (2021). A perception-based study to explore COVID-19 pandemic stress and its factors in Bangladesh. *Diabetes and Metabolic Syndrome: Clinical Research and Reviews*, 15(4), Article 102129. <https://doi.org/10.1016/j.dsx.2021.05.002>
- Bernheim, A., Mei, X., Huang, M., Yang, Y., Fayad, Z. A., (2020). Chest CT findings in coronavirus disease-19 (COVID-19): Relationship to duration of infection. *Radiology*, 295(3), Article 200463. <https://doi.org/10.1148/radiol.2020200463>
- Biswas, R. S. R., Nath, J. D., Barua, P. K., Karim, M. R., Jahan, S., Islam, M. S., Ahmed, K. F., & Kanti, K. (2021). Clinicopathological features and outcome of COVID-19 - Early experiences from three COVID hospitals, Chittagong, Bangladesh. *Journal of the Scientific Society*, 48, 156-60.
- Clump, J., Rozario, D. T. D., Quadir, S., Uddin, K. M. M., Nahid, F., Islam, M. U., & Sarker, D. D. (2020). High resolution computed tomography (HRCT) chest findings in COVID-19 patients in relation to duration of infection in a tertiary care private hospital in Chittagong, Bangladesh. *European Journal of Pharmaceutical and Medical Research*, 7(8), 772-778.
- Cocconcelli, E., Biondini, D., Giraud, C., Lococo, S., Bernardinello, N., & Fichera, G. (2020). Clinical features and chest imaging as predictors of intensity of care in patients with COVID-19. *Journal of clinical medicine*, 9(9), Article 2990. <https://doi.org/10.3390/jcm9092990>
- Dey, S. K., Rahman, M. M., Siddiqi, U. R., & Howlader, A. (2020). Exploring epidemiological behavior of novel coronavirus (COVID-19) outbreak in Bangladesh. *SN Comprehensive Clinical Medicine*, 2, 1724-1732. <https://doi.org/10.1007/s42399-020-00477-9>

- Fang, Y., Zhang, H., Xie, J., Lin, M., Ying, L., Pang, P., & Ji, W. (2020). Sensitivity of chest CT for COVID-19: Comparison to RT-PCR. *Radiology*, *296*(2), E115-E117. <https://doi.org/10.1148/radiol.2020200432>
- Guan, W. J., Ni, Z. Y., Hu, Y., Liang, W. H., Ou, C. Q., He, J. X., Liu, L., Shan, H., Lei, C. L., Hui, D. S. C., Du, B., Li, L. J., Zeng, G., Yuen, K. Y., Chen, R. C., Tang, C. L., Wang, T., Chen, P. Y., Xiang, J., & Zhong, N. S. (2020). Clinical characteristics of coronavirus disease 2019 in China. *New England Journal of Medicine*, *382*(18), 1708-1720. <https://doi.org/10.1056/NEJMoa2002032>
- Huang, C., Wang, Y., Li, X., Ren, L., Zhao, J., & Hu, Y., (2020). Clinical features of patients infected with 2019 novel Coronavirus in Wuhan, China. *Lancet*, *395*(10223), 497-506. [https://doi.org/10.1016/S0140-6736\(20\)30183-5](https://doi.org/10.1016/S0140-6736(20)30183-5)
- Ieong, C. M., Xu, X., Kong, S. C., & Luo, L. (2020). Evaluation of chest CT and clinical features of COVID-19 patient in Macao. *European Journal of Radiology Open*, *7*, Article 100275. <https://doi.org/10.1016/j.ejro.2020.100275>
- Islam, M. T., Talukder, A. K., Siddiqui, M. N., & Islam, T. (2020). Tackling the COVID-19 pandemic: The Bangladesh perspective. *Journal of Public Health Research*, *9*, 389-397. <https://doi.org/10.4081/jphr.2020.1794>
- Kolifarhood, G., Aghaali, M., Saadati, H. M., Taherpour, N., Rahimi, S., & Izadi, N., (2020). Epidemiological and clinical aspects of COVID-19: A narrative review. *Archives of Academic Emergency Medicine*, *8*(1), Article e41.
- Mamun, M. A., Sakib, N., Gozal, D., Bhuiyan, A. I., & Hossain, S. (2021). The COVID-19 pandemic and serious psychological consequences in Bangladesh: A population-based nationwide study. *Journal of Affective Disorders*, *279*, 462-472. <https://doi.org/10.1016/j.jad.2020.10.036>
- Mohiuddin, A. K. (2020). A pandemic review of Covid-19 situation in Bangladesh. *The American Journal of Medical Sciences and Pharmaceutical Research*, *2*(05), 38-50.
- Rong, Y., Wang, F., Tian, J., Liang, X., & Wang, J. (2021). Clinical and CT features of mild-to-moderate COVID-19 cases after two sequential negative nucleic acid testing results: A retrospective analysis. *BMC Infectious Diseases*, *21*(1), Article 333. <https://doi.org/10.1186/s12879-021-06013-x>
- Sun, Z., Zhang, N., Li, Y., & Xu, X. (2020). A systematic review of chest imaging findings in COVID-19. *Quantitative Imaging in Medicine and Surgery*, *10*(5), 1058-1079. <https://doi.org/10.21037/qims-20-564>
- Valencia, D. N. (2020). Brief review on COVID-19: The 2020 pandemic caused by SARS-CoV-2. *Cureus*, *12*(3), Article e7386. <https://doi.org/10.7759/cureus.7386>
- WHO. (2021). Coronavirus disease (COVID-19) weekly epidemiological update and weekly operational update. World Health Organization. <https://www.who.int/emergencies/diseases/novel-coronavirus-2019/situation-reports>
- WHO. (2020). Global surveillance for COVID-19 caused by human infection with COVID-19 virus. World Health Organization. https://www.who.int/docs/default-source/coronaviruse/2020-03-20-surveillance.pdf?sfvrsn=e6be6ef1_2



Image Retrieval Using Fusion of Sauvola and Thepade's Sorted Block Truncation Coding-Based Color Features

Jaya H. Dewan¹ and Sudeep D. Thepade^{2*}

¹Department of Information Technology, Pimpri Chinchwad College of Engineering, Pune 411044, India

²Department of Computer Engineering, Pimpri Chinchwad College of Engineering, Pune 411044, India

ABSTRACT

Because of the tremendous growth in digital imaging, enhanced communication and storage technology, billions of images are captured, stored, and exchanged daily. Finding and searching for an image in a large collection is becoming challenging. The query by reference image retrieval (IR) technique aims to close the semantic gap between the query and retrieve images while improving performance. The primary goal of the work proposed here is to develop discriminative and descriptive features of the image with the minimum possible size. Here, the weighted feature fusion-based IR technique is proposed using Sauvola local thresholding (SLT) and Thepade's Sorted Block Truncation Coding (SBTC) methods. The proposed technique is tested using two standard datasets with mean square error (MSE) as a distance measure and average retrieval accuracy (ARA) as a performance metric. The technique has contributed to the enhancement of ARA with the small and fixed-size image feature vector. The feature vector generated is much smaller than the image dimension and is used as a feature vector to represent the image for retrieval. Results prove that the proposed technique of SBTC 8-ary with 0.1 weight and SLT with 0.9 weight feature fusion gives better ARA than other techniques studied.

Keywords: Color features, content-based image retrieval, Sauvola thresholding, Thepade's Sorted Block Truncation Coding (SBTC)

ARTICLE INFO

Article history:

Received: 27 May 2022

Accepted: 14 November 2022

Published: 13 July 2023

DOI: <https://doi.org/10.47836/pjst.31.5.06>

E-mail addresses:

jaya.h.dewan@gmail.com (Jaya H. Dewan)

sudeepthepade@gmail.com (Sudeep D. Thepade)

* Corresponding author

INTRODUCTION

People have been utilizing images to transmit thoughts and information to one another since prehistoric times using cave drawings. Images have long been regarded as necessary for communication, as images can easily catch attention, elicit emotions,

and transmit information quickly. Use of digital cameras, smartphones, and the Internet have increased due to technological imaging, networking, and storage advancements. The complexity and the amount of multimedia, especially image data generated, stored, transmitted, shared, analyzed, and accessed, is increasing enormously. However, this data is only useful if it can be accessed quickly. Finding a meaningful image from an archive is challenging research for the computer vision community (Latif et al., 2019).

Most search engines use traditional text-based algorithms that rely on captions and metadata to retrieve images. This technique can obtain images that are not relevant as there is a difference between human visual perception and manual categorization or tagging. IR based on image contents has become increasingly popular in recent decades and is regarded as one of the most effective methods of visual data access.

Content-based image retrieval (CBIR) is the visual content analysis of an image. The fundamental need for this IR method is to supply a query image as an input. The visual likeness in terms of image feature vector gives a basis for finding images with matching contents. Low-level visual features (like spatial layout, color, shape, and texture) are derived from the query in IR, and then these features are matched to rank the output.

Medical IR like skin cancer detection, microscopic pathology IR (Müller, 2020), trademark IR (Cao et al., 2021), fabric retrieval (Ji et al., 2020), and crime scene investigation using face retrieval (Tarawneh et al., 2018), tattoo retrieval (Lee et al., 2012), image searching in personal and public digital libraries and satellite IR, image analysis in traffic control (Tunio et al., 2020), image steganography (Shifa et al., 2018), and medical image diagnosis (Kayhan & Fekri-Ershad, 2021) are some of the applications of IR (Yang et al., 2021).

The effectiveness of feature extraction and description approaches determines the success of the IR method. The retrieved features convey the images' identities and aid retrieval. As a result, the researchers' attention has been drawn to the investigation for effective feature extraction and description approaches to investigate a higher success rate of IR based on image contents.

Image thresholding is an image segmentation method that uses pixel intensities to binarize the image pixels into the foreground or background. If the pixel's intensity exceeds the threshold, it is considered the foreground pixel; otherwise, it is considered a background pixel. The image thresholding techniques can be categorized as global or local. The global thresholding techniques use the same threshold for the whole image. In contrast, local thresholding techniques use different thresholds to separate the pixels into foreground or background in different parts of the image depending upon the local image regions. Here, feature fusion-based image retrieval is proposed using Sauvola local thresholding and SBTC techniques. The similarity is measured with the mean squared error (MSE) distance metric, and average retrieval accuracy is used as the performance metric. The key contributions of the work presented are as follows:

- Fusion of global and local features for improved image retrieval
- Consideration of Thepade's SBTC for extracting global features and Sauvola thresholding for local feature extraction.
- Exploration of weighted feature fusion of local and global features for image retrieval.
- Experimental validation of the proposed method on two benchmarked image datasets.

RELATED WORK

The image feature vector can be represented using global, local, and low-level features like texture, color, and shape. The feature vector based on color uses pixel intensities to represent the image. In comparison to other features, color features are consistent and robust. Most color attributes are unaffected by scale, translation, or rotation changes. The computational cost of simple color moment-based approaches is minimal, but the precision is low. Techniques based on histograms are more accurate, although they have a higher processing cost. Techniques based on BTC are more accurate and have a lower processing cost. "Color Coherence vector" (Pass et al., 1996), "Color Correlogram" (Huang et al., 1997), Block Truncation Coding(BTC) and its variants like "Optimized Dot Diffusion" (Guo & Liu, 2014), "error diffused BTC"(Guo et al., 2015), "half-toning based BTC" (Guo & Prasetyo, 2015), "Dot Diffused BTC (DDBTC)" (Guo et al., 2015), "ant colony optimization based BTC" (Chen et al., 2018), "Thepade's Sorted BTC(SBTC)," color moment-based techniques (Wang et al., 2018), histogram of colors-based techniques like "MPEG-7 Dominant Color Descriptor" (Shao et al., 2008) and "Fuzzy Histogram" (Han & Ma, 2002) are some of the color feature-based techniques.

Another important element in IR strategies is texture. An image's texture denotes the shift in illumination in a small area. An image's texture reflects the visual pattern by describing the spatial relationship of pixels. Statistical methods and structural approaches are the two types of texture-based algorithms. "Gray level histogram," "edge histogram," "local binary pattern(LBP)" (Ojala et al., 1996) and its variants like "Local Binary Extrema Pattern" (LBEP) (Murala et al., 2012b), "Local Tetra Pattern" (LTrP) (Murala et al., 2012a), "Local Derivative Pattern" (Zhang et al., 2010), "Utilizing multiscale LBP" (Srivastava & Khare, 2018), "gray level co-occurrence matrix(GLCM)"(Haralick et al., 1973), "wavelet coefficients" (Loupias et al., 2000), "ridgelets and curvelets" (Sumana et al., 2008), "Tamura features" (Tamura et al., 1978), and "Gabor wavelet filter" (Manjunath & Ma, 1996) are examples of texture-based feature techniques. Texture approaches based on structure are not effective for retrieving generic images. Statistical texture features are better than the other approaches because they are invariant to illumination, but the feature vector is larger.

In addition to texture and color features, shape features are explored in the literature to retrieve similar images since humans perceive objects based on their shape (Baji & Mocanu, 2018; Sun & Wu, 2006; Xiaoling & Kanglin, 2004). The use of shape-based features for IR is limited since these approaches require segmented object images, which are tough to obtain in datasets with non-homogeneous generic images.

Local features-based techniques locate prominent parts termed interest points and describe the image by expressing the surrounding region of these interest points. The detected interest points must be extremely repetitive to be identified with several distortions like rotation and light. Some of the most often used strategies for detecting local features are “Harris corner detector” (Harris & Stephens, 1988), “Fast Hessian” (Bay et al., 2006), “Hessian affine detector” (Mikolajczyk & Schmid, 2002), “Harris-Laplace” (Mikolajczyk & Schmid, 2001), “Shi and Tomasi corner detector” (Shi & Tomasi, 1994), “Difference of Gaussian” (Lowe, 2004), MSER, (Matas et al., 2004) SUSAN (Smith & Brady, 1997), FAST (Rosten & Drummond, 2006), SIFT and its variants like “PCA-SIFT” (Ke & Sukthankar, 2004), “N-SIFT” (Cheung & Hamarneh, 2007), “CSIFT” (Abdel-Hakim & Farag, 2006), “edge-SIFT” (Zhang et al., 2013), “Color-SIFT” (Van De Sande et al., 2010), “Affine-SIFT” (Yu & Morel, 2011), “root-SIFT” (Arandjelovic & Zisserman, 2012), BRISK (Leutenegger et al., 2011), ORB (Rublee et al., 2011), BRIEF (Calonder et al., 2010), SURF (Bay et al., 2006) and FREAK (Alahi et al., 2012). These techniques generate high-dimensional feature vectors and thus require more memory for storage and matching time during query execution.

Jabeen et al. (2018) combine a bag of visual words (BoVW) with FREAK and SURF local feature extraction algorithms. Dhotre and Bamnote (2017) integrate multilevel Haar wavelet features with a color histogram. Color and edge features are integrated into Hua et al. (2019) to create a resilient color volume histogram-based feature vector. The BoVW technique is paired with SURF and SIFT-based features in Alkhawlan et al. (2015). The features of chromaticity moments, co-occurrence, and color moments are combined to form a feature vector in Singh and Srivastava (2018). Local and global properties are fused in Mehmood et al. (2018) by considering the image’s Histogram of Gradient (HoG) and SURF features. In Alhassan and Alfaki (2017), HSV color moments and texture features based on the 2D Gabor filter are presented. In Mistry et al. (2016), the feature descriptor is generated using a fusion of DWT in YCbCr color space and LBP. In Du et al. (2019), a weighted fusion of HSV color space-based histogram, GLCM, LBP, and normalized moment of inertia (NMI) with particle swarm optimization-based pulse code neural network (PCNN) is proposed. Yu et al. (2013) present the fusion of SIFT and LBP features with the Kmeans clustering algorithm.

Also, in the literature, few IR methods use the weighted fusion of color and texture features (Kayhan & Fekri-Ershad, 2021). Few authors have proposed using quantized color bins with tetrolet transform for image retrieval (Varish et al., 2020).

Image datasets have images that are widely diversified and non-homogeneous. Using simple and individual low-level image features to retrieve the matching images is quite challenging. As a result, in the literature, integrating low-level features (color, shape, and texture), global features, and local features for encoding feature vectors has improved the performance of IR algorithms.

Here, the weighted feature fusion of the color-based Sauvola local thresholding technique with global SBTC to generate the feature vector of the image is presented.

THEPADE’S SORTED BLOCK TRUNCATION CODING (SBTC)

Let the image block be ‘B’ of size ‘a x b x 3’, with R, G, and B color planes. The SBTC n-ary can be represented as [FR₁, FR₂,..., FR_n, FG₁, FG₂,..., FG_n, FB₁, FB₂,..., FB_n]. Here the FR_p, FG_p, and FB_p indicate the pth cluster centroids of the red, green, and blue planes, respectively (Dewan & Thepade, 2021).

The feature extraction using SBTC is shown in Figure 1. Here, for the sample input image, the color planes are extracted, which are further converted to a 1D array for getting sorted. In the end, features are generated by clustering these sorted 1D arrays. In SBTC 4-ary, for image block B of size ‘a x b x 3’ pixels, the color planes R, G, and B are converted into a one-dimensional array and sorted as sR, sG, and sB. The sorted 1D arrays are divided into four equal-size clusters. The centroid of each cluster is computed as [FR₁, FR₂, FR₃, FR₄, FG₁, FG₂, FG₃, FG₄, FB₁, FB₂] as shown in Equations 1 to 4. Here, X= R, G, or B.

$$FX_1 = \frac{4}{a * b} \sum_{r=1}^{\frac{a*b}{4}} sX(r) \tag{1}$$

$$FX_2 = \frac{4}{a * b} \sum_{r=1+\frac{a*b}{4}}^{\frac{a*b}{2}} sX(r) \tag{2}$$

$$FX_3 = \frac{4}{a * b} \sum_{r=1+\frac{a*b}{2}}^{\frac{3*a*b}{4}} sX(r) \tag{3}$$

$$FX_4 = \frac{4}{a * b} \sum_{r=1+\frac{3*a*b}{4}}^{a*b} sX(r) \tag{4}$$

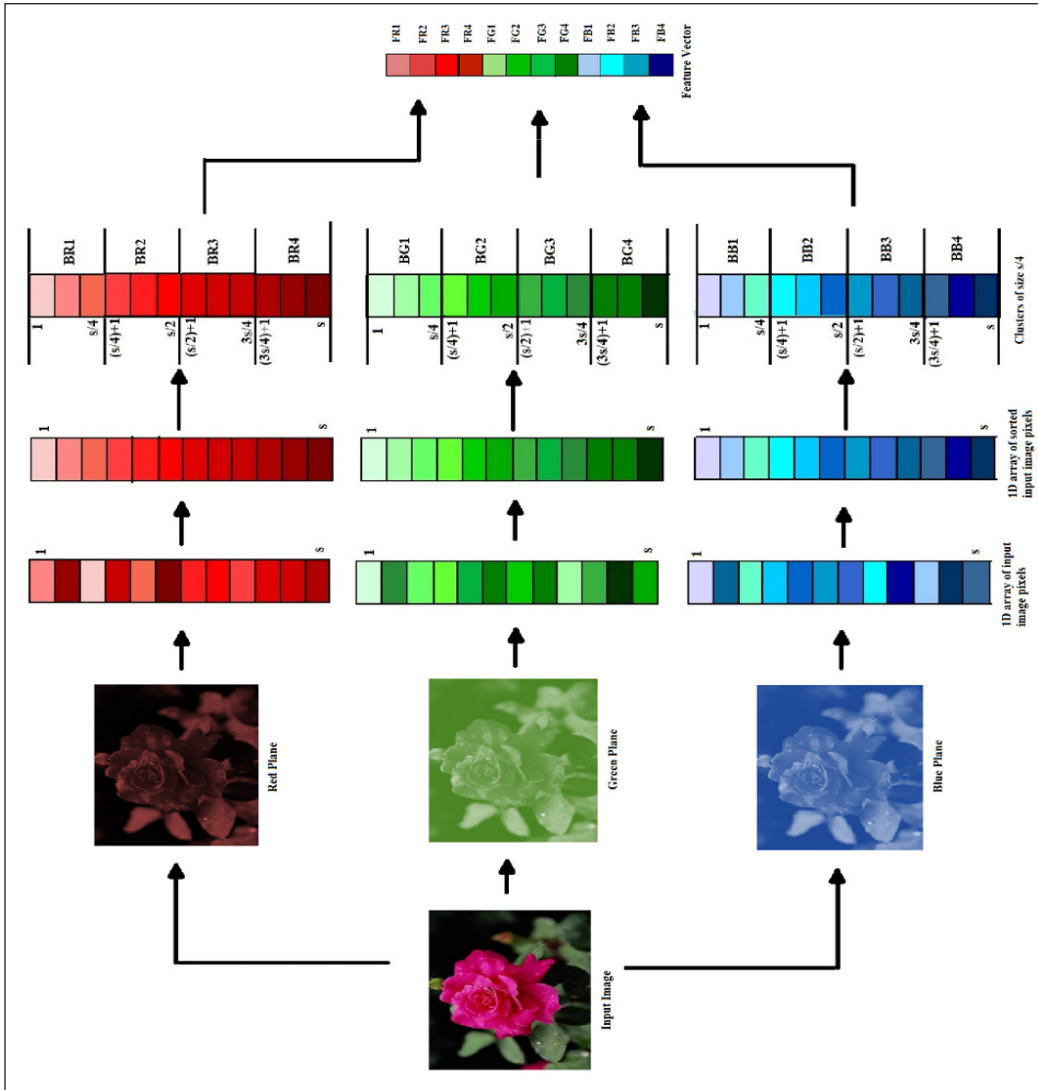


Figure 1. Feature vector generation using SBTC

SAUVOLA THRESHOLDING TECHNIQUE

It is a local thresholding method that determines the threshold for each pixel. The threshold is calculated using a local variance. The technique is effective when the image's brightness is not constant (Bataineh et al., 2011; Hadjadj et al., 2016; Lazzara & Géraud, 2014; Sauvola & Pietikäinen, 2000).

The threshold for each pixel is calculated using Equations 5, 6, and 7:

$$T_{(p,q)} = Mean_{(p,q)} * \left[1 + k * \left(\frac{dev_{(p,q)}}{D} - 1 \right) \right] \tag{5}$$

$$dev_{(p,q)} = \sqrt{\frac{1}{x * y} \sum_{x=1}^3 \sum_{y=1}^3 I(x,y)^2 - \left[\frac{1}{x * y} \sum_{x=1}^3 \sum_{y=1}^3 I(x,y) \right]^2} \tag{6}$$

$$D = \max(dev) \tag{7}$$

where,

$T(p,q)$ is the threshold for the pixel position in the image at (p,q) , where p is the row number, and q is the column number of the pixel.

$Mean(p,q)$ and $dev(p,q)$ are the average and standard deviation using the intensity values of the pixels present in the window centered at the (p,q) pixel in the image.

$I(x,y)$ represents the intensity of the neighborhood pixel located at the (x,y) position in the image.

k is the user-defined constant, and D is the dynamic range of standard deviation.

Figure 2 portrays the extraction of binary planes from red, green, and blue color components of the original sample image obtained using the Sauvola thresholding technique. As the Sauvola threshold values for respective color planes differ, the binary color planes also differ.

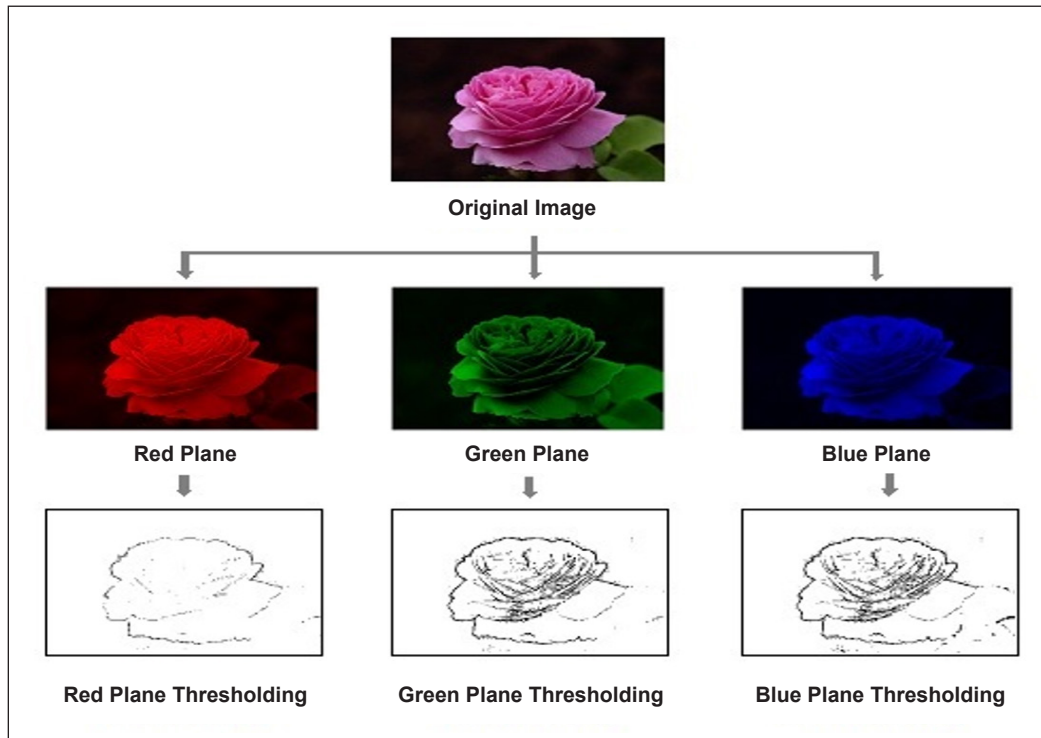


Figure 2. Sauvola local thresholding

PROPOSED IMAGE RETRIEVAL TECHNIQUE

The block diagram of the proposed weighted fusion-based IR system using SBTC and Sauvola Local Thresholding (SLT) features is shown in Figure 3. The steps for image feature vector detection and description are given in the algorithm.

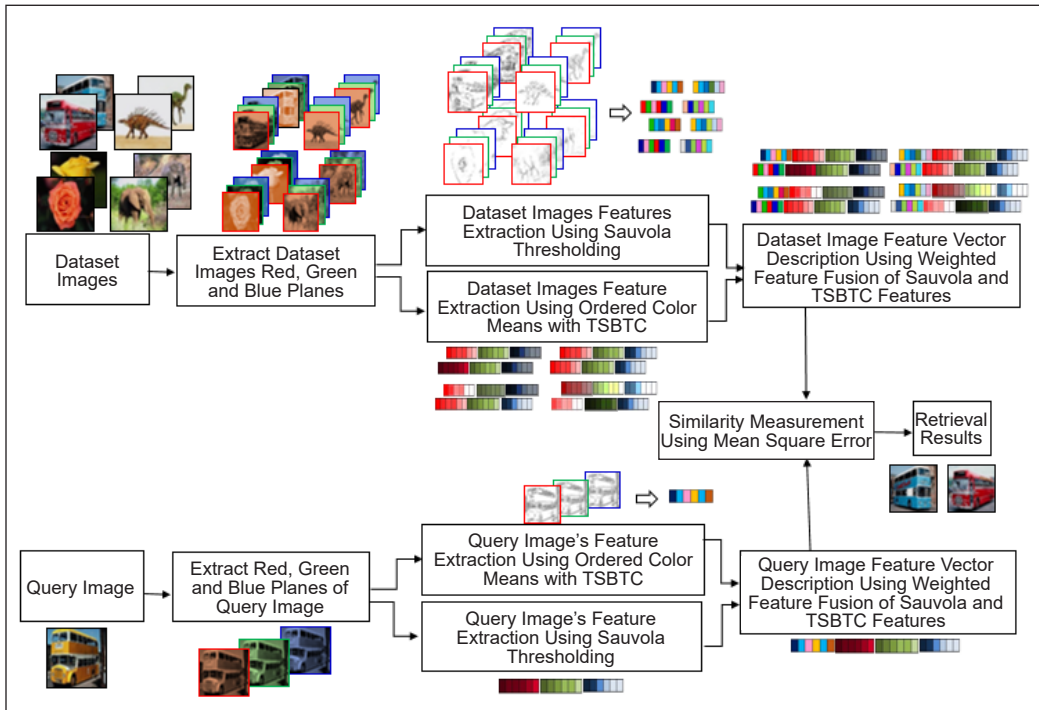


Figure 3. Block diagram of weighted feature fusion-Based IR using Sauvola and SBTC features

Algorithm

1. Input the image color image I of size $m \times n \times 3$ with red R_i , green G_i , and blue B_i planes.
2. Generate the SBTC color feature vector by applying steps 2.1 to 2.5.
 - 2.1 Convert the color plane of size $m \times n$ into $(m \times n) \times 1$ size one-dimensional array (SDA).
 - 2.2 Sort the pixel intensity values of the SDA array in ascending order.
 - 2.3 Divide the array SDA into N blocks where N is 2-ary, 4-ary, or 8-ary of SBTC selected.
 - 2.4 Find the mean of pixel values for each block. These mean values form the color feature vector of an image plane.
 - 2.5 Apply steps 2.1 to 2.4 on an image's red, green, and blue planes. An image's color-based feature vector F_c is formed by concatenating the features of all the planes.

3. Generate Sauvola thresholding-based feature vector by applying steps 3.1 to 3.5 (Figure 2).

3.1 The color image is separated into red, green, and blue planes.

3.2 Compute the threshold T_x for each image pixel red, green, and blue plane using Equations 5, 6, and 7.

3.3 Compute the bitmap of all the color planes of the image using Equation 8. Let I_j be the j th color plane of image I , T_j be the threshold of color plane I_j , and B_j be the binary plane of the I_j color plane. The pixel positions are represented as (p,q) .

$$B_j(p, q) = \begin{cases} 1, & \text{if } I_j(p, q) \geq T_j(p, q) \\ 0, & \text{if } I_j(p, q) < T_j(p, q) \end{cases} \quad (8)$$

3.4 Generate Sauvola features S_{j1} and S_{j2} of the given image for each color plane with size $m*n$ using Equations 9 and 10. Here (a,b) indicates the pixel position.

$$S_{j1} = \frac{1}{\sum_{a=1}^m \sum_{b=1}^n B_j(a, b)} \left\{ \sum_{a=1}^m \sum_{b=1}^n [I_j(a, b) * B_j(a, b)] \right\} \quad (9)$$

$$S_{j2} = \frac{1}{\sum_{a=1}^m \sum_{b=1}^n (1 - B_j(a, b))} \left\{ \sum_{a=1}^m \sum_{b=1}^n [I_j(a, b) * [1 - B_j(a, b)]] \right\} \quad (10)$$

3.5 Concatenate the Sauvola features F_s of all the color planes to generate the vector of the Sauvola local thresholding image features.

4. The fusion-based feature vector F_v is generated by concatenating the SBTC color-based feature vector F_c multiplied by weight w_1 and Sauvola thresholding-based feature vector F_s multiplied by weight w_2 .

5. Steps 1 to 4 are applied to all the images of the dataset.

6. During query execution, steps 1–4 are applied to the query image.

7. The query image’s feature vector is compared to the dataset image’s feature vectors using mean square error (MSE) as the distance measure. Images with the shortest distance are deemed more relevant and are retrieved from the dataset.

In the case of the Sauvola thresholding technique, the mean of image pixel intensities greater than the threshold and the mean of image pixel intensities less than the threshold are used to represent the feature vector for each image. It has generated a feature size of two for each image plane. SBTC 8-ary has generated the feature of size eight for each image plane. The feature vector size is independent of the image dimension and has a considerably smaller footprint. The similarity is measured with

the mean squared error (MSE) distance metric, and average retrieval accuracy is used as the performance metric.

Image Dataset Used for Experimentation

Various datasets are published in the literature. Images of artificial things like monuments, landscapes, creatures, and natural sceneries such as beaches, mountains, and water can be found in these datasets. The images were captured under various lighting, rotation, scale, and occlusion settings. The experimentation testbed is built using a modified COIL dataset and an augmented version of the standard image dataset generated by Wang.

There are 1100 images in the augmented Wang (AWang) dataset, divided into 11 categories. Figure 4 depicts sample images of the AWang dataset (J. Z. Wang et al., 2001; Li & Wang, 2003).

The modified COIL(MCOIL) dataset contains 1440 photos. The images depict a variety of products from several categories, such as toys, pharmaceutical boxes, and coffee mugs. The objects were placed on a turntable with a dark background to capture these images in PNG format. Figure 5 displays a sample of images from the MCOIL dataset (Nene et al., n.d.).












			
Tribes	Beach	Monuments	Fooditems
			
Buses	Dinasour	Elephant	Aeroplane
			
Roses	Horses	Mountains	

Figure 4. AWang dataset sample images



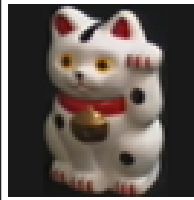

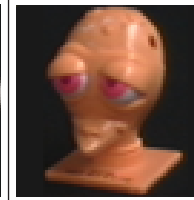



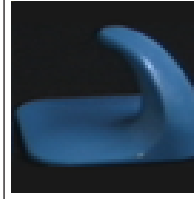


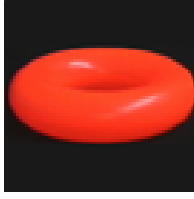



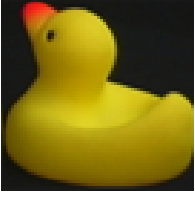
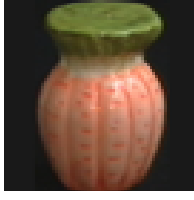



				
Category No. 1	Category No. 2	Category No. 3	Category No. 4	Category No. 5
				
Category No. 6	Category No. 7	Category No. 8	Category No. 9	Category No. 10
				
Category No. 11	Category No. 12	Category No. 13	Category No. 14	Category No. 15
				
Category No. 16	Category No. 17	Category No. 18	Category No. 19	Category No. 20

Figure 5. MCOIL dataset sample images

Performance Measurement Criteria

The retrieval accuracy is used to assess the quality of the IR system. Query images are fired on the image dataset. The query image feature vector is extracted and matched to the dataset image feature vectors, and the mean square error (MSE) is computed. The computed MSEs are sorted in ascending order to rank the dataset images to the query image. Relevant and irrelevant images are separated from the obtained images. The average retrieval accuracy is used for the performance measuring criterion. The definition of retrieval accuracy is given in Equation 11.

$$\text{Retrieval accuracy} = \frac{\text{significant images retrieved count}}{\text{total images retrieved count}} \quad (11)$$

The presented IR system is tested using MATLAB on an Intel Core i5 Processor computer with 1.7 GHz processing speed and 8 GB RAM.

RESULTS AND DISCUSSION

AWang and MCOIL datasets are used in the experimentation. The image feature vectors are generated from extracted features of the dataset images. In a feature table, these feature vectors are stored. During query execution, features from the query image are extracted, and a feature vector is created. This feature vector is compared to the dataset image feature vectors using MSE to extract matched photos from the dataset.

Tables 1 and 2 indicate the ARA of Sauvola Local Thresholding (SLT) and SBTC feature fusion techniques for AWang and MCOIL datasets with equal proportions, respectively. Results prove that the SLT and SBTC feature fusion-based technique results better ARA than the individual methods.

Table 1
IR using feature fusion of SLT and SBTC features for AWang dataset

Category	SLT	SBTC 2-ary	SLT + SBTC 2-ary	SBTC 4-ary	SLT + SBTC 4-ary	SBTC 8-ary	SLT + SBTC 8-ary
C1	39.56	30.65	35.58	32.51	35.27	33.36	34.78
C2	18.02	22.56	22.41	24.01	23.9	24.66	24.64
C3	20.63	18.74	20.5	18.69	19.56	18.97	19.43
C4	34.25	33.03	37.09	33.03	35.85	32.58	34.12
C5	97.4	95.68	96.29	95.58	96.07	95.28	95.66
C6	32.08	37.31	37.64	37.08	37.42	37.13	37.25
C7	54.13	43.11	48.2	41.89	44.97	42.77	44.38
C8	40.58	49.77	48.2	50.74	50	50.48	50.29
C9	18.6	22.7	21.14	21.82	21.04	21.67	21.38
C10	27.96	27.27	28.41	27.39	28.38	28	28.42
C11	67.04	71.26	72.45	74.07	74.55	74.12	74.68
ARA (%)	40.93	41.10	42.54	41.53	42.46	41.73	42.28

Table 2
IR using feature fusion of SLT and SBTC features for MCOIL dataset

Category	SLT	SBTC 2-ary	SLT + SBTC 2-ary	SBTC 4-ary	SLT + SBTC 4-ary	SBTC 8-ary	SLT + SBTC 8-ary
1	45.62	42.38	43.42	47.01	47.16	46.97	47.05
2	55.67	43.07	51.52	40.63	43.69	37.06	38.29
3	60.57	61.84	64.00	75.52	78.01	77.78	79.53
4	68.44	72.55	75.77	93.71	94.58	96.89	97.03
5	89.33	98.90	98.80	99.61	99.48	99.81	99.92
6	100.00	98.59	100.00	99.98	100.00	100.00	100.00

Table 2 (continue)

Category	SLT	SBTC 2-ary	SLT + SBTC 2-ary	SBTC 4-ary	SLT + SBTC 4-ary	SBTC 8-ary	SLT + SBTC 8-ary
7	83.06	80.73	84.66	82.74	85.07	83.16	84.49
8	55.11	47.55	53.13	54.07	56.33	54.46	55.59
9	97.55	99.92	99.71	100.00	100.00	100.00	100.00
10	51.25	42.26	46.20	47.80	48.92	48.11	48.96
11	100.00	100.00	100.00	100.00	100.00	100.00	100.00
12	98.92	100.00	100.00	100.00	100.00	100.00	100.00
13	39.85	34.39	38.37	31.58	33.89	30.48	31.50
14	93.36	85.90	90.78	89.22	90.68	89.85	90.59
15	51.52	45.54	48.73	47.70	49.59	46.53	47.92
16	78.07	82.21	80.50	79.57	79.34	79.05	78.92
17	95.60	96.49	99.42	100.00	100.00	100.00	100.00
18	57.16	43.25	50.14	48.90	51.76	50.91	52.47
19	69.68	61.79	64.47	62.73	63.70	61.92	62.58
20	54.24	46.59	50.83	50.81	52.28	51.99	52.64
ARA (%)	72.25	69.20	72.02	72.58	73.72	72.75	73.37

Table 3 indicates the ARA for weighted SLT and SBTC 2-ary feature fusion using the AWang dataset. The fusion of 0.7 for SLT and 0.3 for SBTC 2-ary features performs better than other proportions considered.

Table 3
IR using weighted SLT and SBTC 2-ary feature fusion for AWang dataset

Category	SLT	SBTC 2-ary	SLT: 0.9 SBTC: 0.1	SLT: 0.8 SBTC: 0.2	SLT: 0.7 SBTC: 0.3	SLT: 0.6 SBTC: 0.4	SLT: 0.5 SBTC: 0.5	SLT: 0.4 SBTC: 0.6	SLT: 0.3 SBTC: 0.7	SLT: 0.2 SBTC: 0.8	SLT: 0.1 SBTC: 0.9
C1	39.56	30.65	39.14	38.44	37.68	36.6	35.58	34.55	33.6	32.7	31.68
C2	18.02	22.56	19.77	20.9	21.74	22.06	22.41	22.77	22.83	22.84	22.82
C3	20.63	18.74	20.99	21.2	21.18	20.81	20.5	20.14	19.77	19.51	19.05
C4	34.25	33.03	36.57	37.7	37.88	37.76	37.09	36.58	35.74	34.79	33.9
C5	97.4	95.68	97.33	96.91	96.64	96.42	96.29	96.12	95.97	95.91	95.75
C6	32.08	37.31	34.01	35.65	36.73	37.31	37.64	37.81	37.67	37.59	37.46
C7	54.13	43.11	52.93	51.66	50.27	49.33	48.2	47.18	46.01	44.89	43.91
C8	40.58	49.77	43.23	45.13	46.52	47.49	48.2	48.72	49.14	49.3	49.59
C9	18.6	22.7	19.3	19.94	20.29	20.79	21.14	21.43	21.96	22.19	22.52
C10	27.96	27.27	28.38	28.72	28.66	28.54	28.41	28.22	28	27.81	27.52
C11	67.04	71.26	69.47	70.85	71.65	72.16	72.45	72.39	72.27	71.94	71.56
ARA(%)	40.93	41.10	41.92	42.46	42.66	42.66	42.54	42.36	42.09	41.77	41.43

Table 4 indicates the ARA for weighted SLT and SBTC 4-ary feature fusion using the AWang dataset. The fusion of 0.8 for SLT and 0.2 for SBTC 4-ary features performs better than other proportions considered.

Table 4
IR using weighted SLT and SBTC 4-ary feature fusion for AWang dataset

Category	SLT	SBTC 4-ary	SLT: 0.9 SBTC: 0.1	SLT: 0.8 SBTC: 0.2	SLT: 0.7 SBTC: 0.3	SLT: 0.6 SBTC: 0.4	SLT: 0.5 SBTC: 0.5	SLT: 0.4 SBTC: 0.6	SLT: 0.3 SBTC: 0.7	SLT: 0.2 SBTC: 0.8	SLT: 0.1 SBTC: 0.9
C1	39.56	32.51	39.15	37.92	36.94	36.11	35.27	34.59	33.84	33.18	32.87
C2	18.02	24.01	21.48	22.93	23.51	23.71	23.9	24.05	24.06	24.01	24.00
C3	20.63	18.69	20.86	20.7	20.36	20	19.56	19.39	19.06	18.92	18.77
C4	34.25	33.03	37.99	38.05	37.37	36.49	35.85	35.1	34.45	33.96	33.47
C5	97.4	95.58	96.86	96.45	96.29	96.21	96.07	95.94	95.87	95.78	95.68
C6	32.08	37.08	35.5	36.78	37.27	37.44	37.42	37.4	37.33	37.29	37.23
C7	54.13	41.89	51.17	49.17	47.36	45.94	44.97	44.12	43.45	42.87	42.35
C8	40.58	50.74	45.39	47.86	48.87	49.54	50	50.26	50.37	50.45	50.64
C9	18.6	21.82	19.8	20.1	20.49	20.83	21.04	21.34	21.36	21.45	21.68
C10	27.96	27.39	28.92	28.88	28.8	28.59	28.38	28.21	28.03	27.79	27.61
C11	67.04	74.07	71.73	73.5	74.14	74.62	74.55	74.48	74.35	74.25	74.19
ARA (%)	40.93	41.53	42.62	42.94	42.85	42.68	42.46	42.26	42.02	41.81	41.68

Table 5 indicates the ARA for weighted SLT and SBTC 8-ary feature fusion using the AWang dataset. The fusion of 0.9 for SLT and 0.1 for SBTC 8-ary features performs better than other proportions considered.

Table 5
IR using weighted SLT and SBTC 8-ary feature fusion for AWang dataset

Category	SLT	SBTC 8-ary	SLT: 0.9 SBTC: 0.1	SLT: 0.8 SBTC: 0.2	SLT: 0.7 SBTC: 0.3	SLT: 0.6 SBTC: 0.4	SLT: 0.5 SBTC: 0.5	SLT: 0.4 SBTC: 0.6	SLT: 0.3 SBTC: 0.7	SLT: 0.2 SBTC: 0.8	SLT: 0.1 SBTC: 0.9
C1	39.56	33.36	38.32	37.02	36.08	35.35	34.78	34.33	34.03	33.72	33.53
C2	18.02	24.66	23.11	23.93	24.46	24.6	24.64	24.68	24.69	24.72	24.74
C3	20.63	18.97	20.8	20.24	19.87	19.64	19.43	19.24	19.12	19.04	18.98
C4	34.25	32.58	37.89	36.64	35.49	34.74	34.12	33.6	33.27	32.99	32.76
C5	97.4	95.28	96.41	96.2	95.97	95.76	95.66	95.52	95.43	95.37	95.33
C6	32.08	37.13	36.87	37.31	37.52	37.41	37.25	37.25	37.24	37.25	37.19
C7	54.13	42.77	49.75	47.22	45.81	45.01	44.38	43.91	43.52	43.19	42.93
C8	40.58	50.48	47.68	49.19	49.76	50.07	50.29	50.46	50.46	50.44	50.46

Table 5 (continue)

Category	SLT	SBTC 8-ary	SLT: 0.9 SBTC: 0.1	SLT: 0.8 SBTC: 0.2	SLT: 0.7 SBTC: 0.3	SLT: 0.6 SBTC: 0.4	SLT: 0.5 SBTC: 0.5	SLT: 0.4 SBTC: 0.6	SLT: 0.3 SBTC: 0.7	SLT: 0.2 SBTC: 0.8	SLT: 0.1 SBTC: 0.9
C9	18.6	21.67	20.11	20.49	20.95	21.3	21.38	21.41	21.59	21.68	21.7
C10	27.96	28	29.18	29.09	28.8	28.65	28.42	28.27	28.22	28.18	28.1
C11	67.04	74.12	73.86	74.77	74.97	74.79	74.68	74.47	74.34	74.3	74.18
ARA (%)	40.93	41.73	43.09	42.92	42.70	42.48	42.28	42.10	41.99	41.90	41.81

Table 6 indicates the ARA for weighted SLT and SBTC 2-ary feature fusion using the MCOIL dataset. The fusion of 0.8 for SLT and 0.2 for SBTC 2-ary features performs better than other proportions considered.

Table 6
IR using weighted SLT and SBTC 2-ary feature fusion for MCOIL dataset

Category	SLT	SBTC 2-ary	SLT: 0.9 SBTC: 0.1	SLT: 0.8 SBTC: 0.2	SLT: 0.7 SBTC: 0.3	SLT: 0.6 SBTC: 0.4	SLT: 0.5 SBTC: 0.5	SLT: 0.4 SBTC: 0.6	SLT: 0.3 SBTC: 0.7	SLT: 0.2 SBTC: 0.8	SLT: 0.1 SBTC: 0.9
1	45.62	42.38	44.83	44.06	43.89	43.63	43.42	43.17	42.94	42.61	42.46
2	55.67	43.07	54.36	53.67	52.95	52.28	51.52	50.46	49.23	47.45	45.47
3	60.57	61.84	62.94	64.14	64.45	64.43	64.00	63.54	63.14	62.71	62.29
4	68.44	72.55	72.86	75.04	76.08	76.18	75.77	75.29	74.50	73.65	73.07
5	89.33	98.90	93.06	95.58	97.24	98.28	98.80	99.09	99.29	99.34	99.25
6	100.0	98.59	100.0	100.0	100.0	100.0	100.0	100.0	100.0	100.0	99.86
7	83.06	80.73	84.59	85.44	85.88	85.59	84.66	83.74	83.14	82.52	81.50
8	55.11	47.55	55.21	54.84	54.48	53.94	53.13	52.24	51.20	49.98	48.50
9	97.55	99.92	98.44	99.02	99.31	99.56	99.71	99.83	99.88	99.88	99.92
10	51.25	42.26	49.98	49.21	48.42	47.30	46.20	45.02	43.98	43.19	42.80
11	100.0	100.0	100.0	100.0	100.0	100.0	100.0	100.0	100.0	100.0	100.0
12	98.92	100.0	99.56	99.90	100.0	100.0	100.0	100.0	100.0	100.0	100.0
13	39.85	34.39	39.12	38.54	38.14	38.00	38.37	38.10	37.60	36.52	35.19
14	93.36	85.90	93.54	93.04	92.42	91.51	90.78	89.99	88.99	88.02	87.02
15	51.52	45.54	50.52	49.90	49.40	49.02	48.73	48.32	47.74	46.99	46.24
16	78.07	82.21	78.82	79.44	79.90	80.09	80.50	80.81	81.17	81.58	81.93
17	95.60	96.49	97.03	98.01	98.59	99.00	99.42	99.59	99.77	99.85	99.75
18	57.16	43.25	55.96	55.02	53.65	51.99	50.14	48.44	46.91	45.58	44.21
19	69.68	61.79	68.00	66.99	65.99	65.03	64.47	63.83	63.18	62.79	62.38
20	54.24	46.59	53.38	52.68	51.99	51.49	50.83	50.12	49.36	48.53	47.70
ARA (%)	72.25	69.20	72.61	72.73	72.64	72.36	72.02	71.58	71.10	70.56	69.98

Table 7 indicates the ARA for weighted SLT and SBTC 4-ary feature fusion using the MCOIL dataset. The fusion of 0.9 for SLT and 0.1 for SBTC 4-ary features performs better than other proportions considered.

Table 8 indicates the ARA for weighted SLT and SBTC 8-ary feature fusion using the MCOIL dataset. The fusion of 0.9 for SLT and 0.1 for SBTC 8-ary features performs better than other proportions considered.

Comparison with Existing Methods

Figures 6 and 7 show the performance of existing and proposed IR techniques in terms of ARA using Sauvola local thresholding, SBTC with 2, 4, and 8-arys, and weighted feature fusion of SLT and SBTC for AWang and MCOIL datasets, respectively. Weighted feature fusion of SLT and SBTC performs better for SBTC 2, 4, and 8-arys. Results show that the fusion of 0.9 for SLT and 0.1 for SBTC 8-ary features gives better results than all other methods considered.

Table 7
IR using weighted SLT and SBTC 4-ary feature fusion for MCOIL dataset

Category	SLT	SBTC 4-ary	SLT: 0.9 SBTC: 0.1	SLT: 0.8 SBTC: 0.2	SLT: 0.7 SBTC: 0.3	SLT: 0.6 SBTC: 0.4	SLT: 0.5 SBTC: 0.5	SLT: 0.4 SBTC: 0.6	SLT: 0.3 SBTC: 0.7	SLT: 0.2 SBTC: 0.8	SLT: 0.1 SBTC: 0.9
1	45.62	47.01	47.11	47.30	47.26	47.26	47.16	47.07	47.05	47.01	46.99
2	55.67	40.63	51.60	48.63	46.64	44.75	43.69	42.75	42.01	41.42	40.93
3	60.57	75.52	77.16	79.17	79.07	78.40	78.01	77.53	76.93	76.41	75.98
4	68.44	93.71	93.61	95.06	95.10	94.85	94.58	94.43	94.17	94.04	93.81
5	89.33	99.61	95.56	98.09	99.00	99.36	99.48	99.59	99.61	99.59	99.61
6	100.0	99.98	100.0	100.0	100.0	100.0	100.0	100.0	100.0	100.0	100.0
7	83.06	82.74	87.83	87.87	86.81	85.82	85.07	84.43	84.09	83.58	83.08
8	55.11	54.07	57.37	57.75	57.25	56.75	56.33	55.90	55.40	54.96	54.53
9	97.55	100.0	99.38	99.96	100.0	100.0	100.0	100.0	100.0	100.0	100.0
10	51.25	47.80	51.08	50.39	50.02	49.54	48.92	48.51	48.28	48.19	47.99
11	100.0	100.0	100.0	100.0	100.0	100.0	100.0	100.0	100.0	100.0	100.0
12	98.92	100.0	100.0	100.0	100.0	100.0	100.0	100.0	100.0	100.0	100.0
13	39.85	31.58	37.09	36.28	35.19	34.61	33.89	33.41	32.89	32.41	31.96
14	93.36	89.22	93.77	92.82	91.96	91.24	90.68	90.28	90.01	89.66	89.39
15	51.52	47.70	51.49	50.93	50.42	49.88	49.59	49.21	48.80	48.40	47.97
16	78.07	79.57	78.72	78.99	79.11	79.24	79.34	79.42	79.51	79.53	79.53
17	95.60	100.00	99.50	99.88	99.98	100.0	100.0	100.0	100.0	100.0	100.0
18	57.16	48.90	56.54	55.48	54.01	52.78	51.76	50.96	50.42	49.85	49.29
19	69.68	62.73	67.11	65.66	64.62	64.08	63.70	63.41	63.21	62.96	62.83
20	54.24	50.81	53.55	52.82	52.78	52.51	52.28	51.93	51.58	51.33	51.04
ARA (%)	72.25	72.58	74.92	74.85	74.46	74.05	73.72	73.44	73.20	72.97	72.75

Table 8
 IR using weighted SLT and SBTC 8-ary feature fusion for MCOIL dataset

Category	SLT	SBTC 8-ary	SLT: 0.9 SBTC: 0.1	SLT: 0.8 SBTC: 0.2	SLT: 0.7 SBTC: 0.3	SLT: 0.6 SBTC: 0.4	SLT: 0.5 SBTC: 0.5	SLT: 0.4 SBTC: 0.6	SLT: 0.3 SBTC: 0.7	SLT: 0.2 SBTC: 0.8	SLT: 0.1 SBTC: 0.9
1	45.62	46.97	47.38	47.18	47.18	47.09	47.05	47.03	47.01	47.01	46.97
2	55.67	37.06	45.29	41.67	39.87	38.91	38.29	37.83	37.64	37.42	37.23
3	60.57	77.78	81.33	80.92	80.50	79.92	79.53	79.13	78.53	78.24	78.03
4	68.44	96.89	96.66	97.18	97.13	97.11	97.03	96.93	96.82	96.88	96.88
5	89.33	99.81	98.77	99.71	99.85	99.88	99.92	99.92	99.86	99.86	99.85
6	100.00	100.00	100.00	100.00	100.00	100.00	100.00	100.00	100.00	100.00	100.00
7	83.06	83.16	88.10	86.65	85.53	84.80	84.49	84.09	83.89	83.66	83.37
8	55.11	54.46	58.45	57.52	56.64	55.90	55.59	55.23	54.94	54.76	54.57
9	97.55	100.00	100.00	100.00	100.00	100.00	100.00	100.00	100.00	100.00	100.00
10	51.25	48.11	51.23	50.35	49.75	49.36	48.96	48.71	48.55	48.32	48.19
11	100.00	100.00	100.00	100.00	100.00	100.00	100.00	100.00	100.00	100.00	100.00
12	98.92	100.00	100.00	100.00	100.00	100.00	100.00	100.00	100.00	100.00	100.00
13	39.85	30.48	35.24	33.28	32.27	31.87	31.50	31.33	31.00	30.92	30.65
14	93.36	89.85	93.09	91.90	91.24	90.76	90.59	90.41	90.18	90.03	89.97
15	51.52	46.53	50.42	49.46	48.84	48.30	47.92	47.51	47.18	46.91	46.70
16	78.07	79.05	78.61	78.72	78.88	78.84	78.92	78.95	78.95	78.99	79.01
17	95.60	100.00	100.00	100.00	100.00	100.00	100.00	100.00	100.00	100.00	100.00
18	57.16	50.91	57.06	54.76	53.65	53.09	52.47	52.01	51.54	51.23	51.06
19	69.68	61.92	65.14	63.91	63.16	62.83	62.58	62.42	62.31	62.17	62.06
20	54.24	51.99	53.88	53.36	53.16	52.91	52.64	52.53	52.33	52.16	52.08
ARA (%)	72.25	72.75	75.03	74.33	73.88	73.58	73.37	73.20	73.04	72.93	72.83

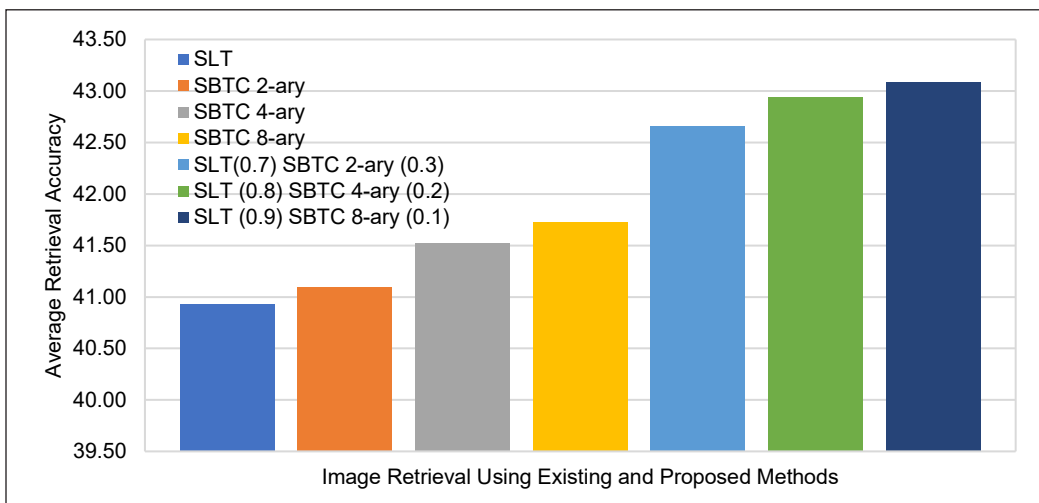


Figure 6. ARA using various existing and proposed IR methods (AWang dataset)

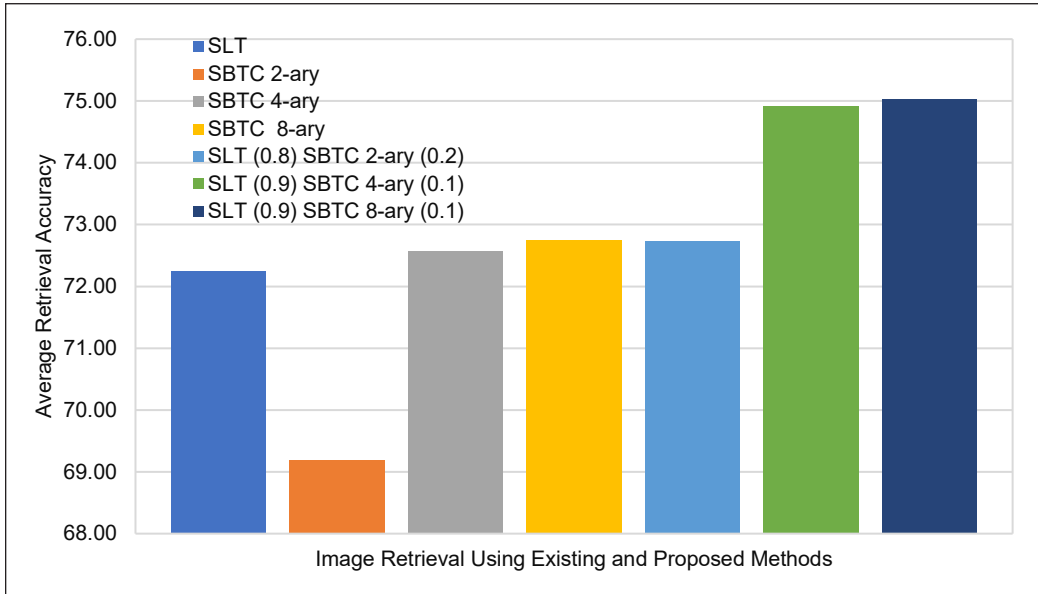


Figure 7. ARA using various existing and proposed IR methods (MCOIL dataset)

Statistical Significance

For statistical validation of obtained results, the proposed IR using weighted SLT and SBTC 8-ary feature fusion is compared with existing methods using a 2-variable t-Test, assuming equal variance is defined as:

H0: There is no significant difference between IR accuracy using weighted SLT and SBTC 8-ary and existing methods.

Ha: There is a significant difference between IR accuracy using weighted SLT and SBTC 8-ary and existing methods.

The obtained t-Stat, t-Critical, and P-value are given in Table 9. For the proposed method, when compared with the existing SLT method, the p-value for 2-tail is less than $\alpha(0.05)$, rejecting the null hypotheses (H0) and proving that the proposed weighted SLT (0.9 weight) and SBTC 8-ary (0.1 weight) method is statistically significant than the existing method.

Table 9
Statistical validation of proposed IR techniques

Parameters	SLT:	SLT:	SLT:	SLT:	SLT:	SLT:	SLT:	SLT:	SLT:
	0.9	0.8	0.7	0.6	0.5	0.4	0.3	0.2	0.1
	SBTC:	SBTC:	SBTC:	SBTC:	SBTC:	SBTC:	SBTC:	SBTC:	SBTC:
	0.1	0.2	0.3	0.4	0.5	0.6	0.7	0.8	0.9
Mean	63.70	63.18	62.82	62.54	62.34	62.17	62.02	61.92	61.82
t Stat	-2.01	-1.46	-1.15	-0.95	-0.80	-0.68	-0.58	-0.51	-0.45
P(T<=t) two-tail	0.05	0.15	0.26	0.35	0.43	0.50	0.57	0.61	0.66
t Critical two-tail	2.04	2.04	2.04	2.04	2.04	2.04	2.04	2.04	2.04

CONCLUSION

The research paper has presented the fusion-based IR technique using weighted features of Sauvola local thresholding and the SBTC technique. The proposed method is tested with two different standard datasets, viz. AWang and MCOIL. The introduced IR using feature fusion of SLT and SBTC techniques has surpassed the performance in terms of average retrieval accuracy of the existing methods. It has revealed the statistical significance of improved IR. Results show that the proposed technique with SBTC 8-ary with 0.1 weight and SLT with 0.9 weight feature fusion gives better ARA than all the studied methods across the datasets considered.

In the future, it will be interesting to explore using various color spaces for feature extraction using the proposed method in IR. Future work can use various similarity metrics in addition to the currently used mean square error like Euclidian distance, cosine distance, and city block distance can be explored.

ACKNOWLEDGEMENT

The authors appreciate the cooperation of the Pimpri Chinchwad College of Engineering, India, in completing this work.

REFERENCES

- Abdel-Hakim, A. E., & Farag, A. A. (2006, June 17-22). *CSIFT: A SIFT descriptor with color invariant characteristics*. [Paper presentation]. 2006 IEEE Computer Society Conference on Computer Vision and Pattern Recognition (CVPR'06), New York, USA. <https://doi.org/10.1109/CVPR.2006.95>
- Alahi, A., Ortiz, R., & Vandergheynst, P. (2012, June 16-21). *FREAK: Fast retina keypoint*. [Paper presentation]. 2012 IEEE Conference on Computer Vision and Pattern Recognition, Providence, USA. <https://doi.org/10.1109/CVPR.2012.6247715>
- Alhassan, A. K., & Alfaki, A. A. (2017, January 16-18). *Color and texture fusion-based method for content-based image retrieval*. [Paper presentation]. 2017 International Conference on Communication, Control, Computing and Electronics Engineering (ICCCCEE), Khartoum, Sudan. <https://doi.org/10.1109/ICCCCEE.2017.7867649>
- Alkhawani, M., Elmogy, M., & Elbakry, H. (2015). Content-based image retrieval using local features descriptors and bag-of-visual words. *International Journal of Advanced Computer Science and Applications*, 6(9), 212-219. <https://doi.org/10.14569/IJACSA.2015.060929>
- Arandjelovic, R., & Zisserman, A. (2012, June 16-21). *Three things everyone should know to improve object retrieval*. [Paper presentation]. 2012 IEEE Conference on Computer Vision and Pattern Recognition, Providence, USA. <https://doi.org/10.1109/CVPR.2012.6248018>
- Baji, F., & Mocanu, M. (2018). Chain code approach for shape based image retrieval. *Indian Journal of Science and Technology*, 11(3), 1-17. <https://doi.org/10.17485/ijst/2018/v11i3/119998>

- Bataineh, B., Abdullah, S. N. H. S., Omar, K., & Faizul, M. (2011). Adaptive thresholding methods for documents image binarization. In J. F. Martinez-Trinidad, J. A. Carrasco-Oschoa, C. B. Y. Brants & E. R. Hancock (Eds.), *Pattern recognition* (pp. 230-239). Springer. https://doi.org/10.1007/978-3-642-21587-2_25
- Bay, H., Tuytelaars, T., & Van Gool, L. (2006). SURF: Speeded up robust features. In A. Leonardis, H. Bischof & A. Pinz (Eds.), *Computer vision ECCV 2006* (pp. 404-417). Springer. https://doi.org/10.1007/11744023_32
- Calonder, M., Lepetit, V., Strecha, C., & Fua, P. (2010). BRIEF: Binary robust independent elementary features. In K. Daniilidis, P. Maragos & N. Paragios (Eds.), *Computer vision ECCV 2010* (pp. 778-792). Springer. https://doi.org/10.1007/978-3-642-15561-1_56
- Cao, J., Huang, Y., Dai, Q., & Ling, W. K. (2021). Unsupervised trademark retrieval method based on attention mechanism. *Sensors*, 21(5), Article 1894. <https://doi.org/10.3390/s21051894>
- Chen, Y. H., Chang, C. C., Lin, C. C., & Hsu, C. Y. (2018). Content-based color image retrieval using block truncation coding based on binary ant colony optimization. *Symmetry*, 11(1), Article 21. <https://doi.org/10.3390/sym11010021>
- Cheung, W., & Hamarneh, G. (2007, April 12-15). *N-SIFT: N-dimensional scale invariant feature transform for matching medical images*. [Paper presentation]. 2007 4th IEEE International Symposium on Biomedical Imaging: From Nano to Macro, Arlington, USA. <https://doi.org/10.1109/ISBI.2007.356953>
- Dewan, J. H., & Thepade, S. D. (2021, March 5-7). *Fusion based image retrieval using haralick moments and TSBTC features*. [Paper presentation]. 2021 International Conference on Emerging Smart Computing and Informatics (ESCI), Pune, India. <https://doi.org/10.1109/ESCI50559.2021.9396833>
- Dhotre, D. R., & Bamnote, G. R. (2017, September 22-24). Multilevel haar wavelet transform and histogram usage in content based image retrieval system. [Paper presentation]. 2017 International Conference on Vision, Image and Signal Processing (ICVISIP), Osaka, Japan. <https://doi.org/10.1109/ICVISIP.2017.34>
- Du, A., Wang, L., & Qin, J. (2019). Image retrieval based on colour and improved NMI texture features. *Automatika: Časopis Za Automatiku, Mjerenje, Elektroniku, Računarstvo I Komunikacije*, 60(4), 491-499. <https://doi.org/10.1080/00051144.2019.1645977>
- Guo, J. M., & Liu, Y. F. (2014). Improved block truncation coding using optimized dot diffusion. *IEEE Transactions on Image Processing*, 23(3), 1269-1275. <https://doi.org/10.1109/TIP.2013.2257812>
- Guo, J. M., & Prasetyo, H. (2015). Content-based image retrieval using features extracted from halftoning-based block truncation coding. *IEEE Transactions on Image Processing*, 24(3), 1010-1024. <https://doi.org/10.1109/TIP.2014.2372619>
- Guo, J. M., Prasetyo, H., & Chen, J. H. (2015). Content-based image retrieval using error diffusion block truncation coding features. *IEEE Transactions on Circuits and Systems for Video Technology*, 25(3), 466-481. <https://doi.org/10.1109/TCSVT.2014.2358011>
- Guo, J. M., Prasetyo, H., & Wang, N. J. (2015). Effective image retrieval system using dot-diffused block truncation coding features. *IEEE Transactions on Multimedia*, 17(9), 1576-1590. <https://doi.org/10.1109/TMM.2015.2449234>

- Hadjadj, Z., Meziane, A., Cherfa, Y., Cheriet, M., & Setitra, I. (2016). ISauvola: Improved sauvola's algorithm for document image binarization. In A. Campilho & F. Karray (Eds.), *Image Analysis and Recognition* (pp. 737-745). https://doi.org/10.1007/978-3-319-41501-7_82
- Han, J., & Ma, K. K. (2002). Fuzzy color histogram and its use in color image retrieval. *IEEE Transactions on Image Processing*, *11*(8), 944-952. <https://doi.org/10.1109/TIP.2002.801585>
- Haralick, R. M., Shanmugam, K., & Dinstein, I. (1973). Textural features for image classification. *IEEE Transactions on Systems, Man, and Cybernetics*, *6*(SMC-3), 610-621. <https://doi.org/10.1109/TSMC.1973.4309314>
- Harris, C., & Stephens, M. (1988). A combined corner and edge detector. *Alvey Vision Conference*, *15*(50), 147-151.
- Hua, J. Z., Liu, G. H., & Song, S. X. (2019). Content-based image retrieval using color volume histograms. *International Journal of Pattern Recognition and Artificial Intelligence*, *33*(11), Article 1940010. <https://doi.org/10.1142/S021800141940010X>
- Huang, J., Kumar, S. R., Mitra, M., Zhu, W. J., & Rabih, R. (1997, June 17-19). *Image indexing using color correlograms*. [Paper presentation]. Proceedings of IEEE Computer Society Conference on Computer Vision and Pattern Recognition, Puerto Rico, USA. <https://doi.org/10.1109/CVPR.1997.609412>
- Jabeen, S., Mehmood, Z., Mahmood, T., Saba, T., Rehman, A., & Mahmood, M. T. (2018). An effective content-based image retrieval technique for image visuals representation based on the bag-of-visual-words model. *PloS One*, *13*(4), Article e0194526. <https://doi.org/10.1371/journal.pone.0194526>
- Ji, Y., Wang, W., Lv, Y., & Zhou, W. (2020). Research on fabric image retrieval method based on multi-feature layered fusion. *Journal of Physics: Conference Series*, *1549*(5), Article 052038. <https://doi.org/10.1088/1742-6596/1549/5/052038>
- Kayhan, N., & Fekri-Ershad, S. (2021). Content based image retrieval based on weighted fusion of texture and color features derived from modified local binary patterns and local neighborhood difference patterns. *Multimedia Tools and Applications*, *80*(21-23), 32763-32790. <https://doi.org/10.1007/s11042-021-11217-z>
- Ke, Y., & Sukthankar, R. (2004, June 27 - July 2). *PCA-SIFT: A more distinctive representation for local image descriptors*. [Paper presentation]. Proceedings of the 2004 IEEE Computer Society Conference on Computer Vision and Pattern Recognition, 2004. CVPR 2004., 2, Washington, USA. <https://doi.org/10.1109/CVPR.2004.1315206>
- Latif, A., Rasheed, A., Sajid, U., Ahmed, J., Ali, N., Ratyal, N. I., Zafar, B., Dar, S. H., Sajid, M., & Khalil, T. (2019). Content-based image retrieval and feature extraction: A comprehensive review. *Mathematical Problems in Engineering*, *2019*, Article 9658350. <https://doi.org/10.1155/2019/9658350>
- Lazzara, G., & Géraud, T. (2014). Efficient multiscale Sauvola's binarization. *International Journal on Document Analysis and Recognition (IJ DAR)*, *17*(2), 105-123. <https://doi.org/10.1007/s10032-013-0209-0>
- Lee, J., Jin, R., Jain, A., & Tong, W. (2012). Image retrieval in forensics: Tattoo image database application. *IEEE Multimedia*, *19*(1), 40-49. <https://doi.org/10.1109/MMUL.2011.59>
- Leutenegger, S., Chli, M., & Siegwart, R. Y. (2011, November 6-13). *BRISK: Binary Robust invariant scalable keypoints*. [Paper presentation]. 2011 International Conference on Computer Vision, Barcelona, Spain. <https://doi.org/10.1109/ICCV.2011.6126542>

- Li, J., & Wang, J. Z. (2003). Automatic linguistic indexing of pictures by a statistical modeling approach. *IEEE Transactions on Pattern Analysis and Machine Intelligence*, 25(9), 1075–1088. <https://doi.org/10.1109/TPAMI.2003.1227984>
- Loupias, E., Sebe, N., Bres, S., & Jolion, J. M. (2000, September 10-13). *Wavelet-based salient points for image retrieval*. [Paper presentation]. Proceedings 2000 International Conference on Image Processing (Cat. No.00CH37101), Vancouver, Canada. <https://doi.org/10.1109/ICIP.2000.899469>
- Lowe, D. G. (2004). Distinctive image features from scale-invariant keypoints. *International Journal of Computer Vision*, 60(2), 91-110. <https://doi.org/10.1023/B:VISI.0000029664.99615.94>
- Manjunath, B. S., & Ma, W. Y. (1996). Texture features for browsing and retrieval of image data. *IEEE Transactions on Pattern Analysis and Machine Intelligence*, 18(8), 837-842. <https://doi.org/10.1109/34.531803>
- Matas, J., Chum, O., Urban, M., & Pajdla, T. (2004). Robust wide-baseline stereo from maximally stable extremal regions. *Image and Vision Computing*, 22(10), 761-767. <https://doi.org/https://doi.org/10.1016/j.imavis.2004.02.006>
- Mehmood, Z., Abbas, F., Mahmood, T., Javid, M. A., Rehman, A., & Nawaz, T. (2018). Content-based image retrieval based on visual words fusion versus features fusion of local and global features. *Arabian Journal for Science and Engineering*, 43(12), 7265-7284. <https://doi.org/10.1007/s13369-018-3062-0>
- Mikolajczyk, K., & Schmid, C. (2001, July 7-14). *Indexing based on scale invariant interest points*. [Paper presentation]. Proceedings Eighth IEEE International Conference on Computer Vision. ICCV 2001, Vancouver, Canada. <https://doi.org/10.1109/ICCV.2001.937561>
- Mikolajczyk, K., & Schmid, C. (2002). An affine invariant interest point detector. In A. Heyden, G. Sparr, M. Nielsen & P. Johansen (Eds.), *Computer vision – ECCV 2002* (pp. 128-142). Springer. https://doi.org/10.1007/3-540-47969-4_9
- Mistry, Y., Ingole, D. T., & Ingole, M. D. (2016, April 28-30). *Efficient content based image retrieval using transform and spatial feature level fusion*. [Paper presentation]. 2016 2nd International Conference on Control, Automation and Robotics (ICCAR), Hong Kong, China. <https://doi.org/10.1109/ICCAR.2016.7486744>
- Müller, H. (2020, June 8-11). *Medical image retrieval: applications and resources*. [Paper presentation]. ICMR '20: Proceedings of the 2020 International Conference on Multimedia Retrieval, New York, USA. <https://doi.org/10.1145/3372278.3390668>
- Murala, S., Maheshwari, R. P., & Balasubramanian, R. (2012a). Local tetra patterns: A new feature descriptor for content-based image retrieval. *IEEE Transactions on Image Processing*, 21(5), 2874-2886. <https://doi.org/10.1109/TIP.2012.2188809>
- Murala, S., Maheshwari, R. P., & Balasubramanian, R. (2012b). Directional local extrema patterns: A new descriptor for content based image retrieval. *International Journal of Multimedia Information Retrieval*, 1(3), 191-203. <https://doi.org/10.1007/s13735-012-0008-2>
- Nene, S. A., Nayar, S. K., & Murase, H. (n.d.). *Columbia Object Image Library (COIL-20)*. Retrieved July 20, 2019, from http://www.cs.columbia.edu/CAVE/publications/pdfs/Nene_TR96.pdf

- Ojala, T., Pietikäinen, M., & Harwood, D. (1996). A comparative study of texture measures with classification based on featured distributions. *Pattern Recognition*, 29(1), 51-59. [https://doi.org/10.1016/0031-3203\(95\)00067-4](https://doi.org/10.1016/0031-3203(95)00067-4)
- Pass, G., Zabih, R., & Miller, J. (1996, November 18-22). *Comparing images using color coherence vectors*. [Paper presentation]. MM96: The Fourth ACM International Multimedia Conference, Massachusetts, USA. <https://doi.org/10.1145/244130.244148>
- Rosten, E., & Drummond, T. (2006). Machine learning for high-speed corner detection. In A. Leonardis, H. Bischof, & A. Pinz (Eds.), *Computer vision - ECCV 2006* (pp. 430-443). Springer. https://doi.org/10.1007/11744023_34
- Rublee, E., Rabaud, V., Konolige, K., & Bradski, G. (2011, November 6-13). *ORB: An efficient alternative to SIFT or SURF*. [Paper presentation]. 2011 International Conference on Computer Vision, Barcelona, Spain. <https://doi.org/10.1109/ICCV.2011.6126544>
- Sauvola, J., & Pietikäinen, M. (2000). Adaptive document image binarization. *Pattern Recognition*, 33(2), 225-236. [https://doi.org/10.1016/S0031-3203\(99\)00055-2](https://doi.org/10.1016/S0031-3203(99)00055-2)
- Shao, H., Wu, Y., Cui, W., & Zhang, J. (2008, November 18-21). *Image retrieval based on MPEG-7 dominant color descriptor*. [Paper presentation]. 2008 The 9th International Conference for Young Computer Scientists, Hunan China. <https://doi.org/10.1109/ICYCS.2008.89>
- Shi, J., & Tomasi. (1994, June 21-23). *Good features to track*. [Paper presentation]. Proceedings of IEEE Conference on Computer Vision and Pattern Recognition, Seattle, USA. <https://doi.org/10.1109/CVPR.1994.323794>
- Shifa, A., Afgan, M. S., Asghar, M. N., Fleury, M., Memon, I., Abdullah, S., & Rasheed, N. (2018). Joint crypto-stego scheme for enhanced image protection with nearest-centroid clustering. *IEEE Access*, 6, 16189-16206. <https://doi.org/10.1109/ACCESS.2018.2815037>
- Singh, V. P., & Srivastava, R. (2018). Effective image retrieval based on hybrid features with weighted similarity measure and query image classification. *International Journal of Computational Vision and Robotics*, 8(2), Article 98. <https://doi.org/10.1504/IJCVR.2018.091979>
- Smith, S. M., & Brady, J. M. (1997). SUSAN-A new approach to low level image processing. *International Journal of Computer Vision*, 23(1), 45-78. <https://doi.org/10.1023/A:1007963824710>
- Srivastava, P., & Khare, A. (2018). Utilizing multiscale local binary pattern for content-based image retrieval. *Multimedia Tools and Applications*, 77(10), 12377-12403. <https://doi.org/10.1007/s11042-017-4894-4>
- Sumana, I. J., Islam, M. M., Zhang, D., & Lu, G. (2008, October 8-10). *Content based image retrieval using curvelet transform*. [Paper presentation]. 2008 IEEE 10th Workshop on Multimedia Signal Processing, Cairns, Australia. <https://doi.org/10.1109/MMSP.2008.4665041>
- Sun, J., & Wu, X. (2006, December 18-20). *Chain code distribution-based image retrieval*. [Paper presentation]. 2006 International Conference on Intelligent Information Hiding and Multimedia, California, USA . <https://doi.org/10.1109/IIH-MSP.2006.264973>
- Tamura, H., Mori, S., & Yamawaki, T. (1978). Textural features corresponding to visual perception. *IEEE Transactions on Systems, Man, and Cybernetics*, 8(6), 460-473. <https://doi.org/10.1109/TSMC.1978.4309999>

- Tarawneh, A. S., Hassanat, A. B. A., Celik, C., Chetverikov, D., Rahman, M. S., & Verma, C. (2018). *Deep Face Image Retrieval: A Comparative Study with Dictionary Learning*. ArXiv. <http://arxiv.org/abs/1812.05490>
- Tunio, M. H., Memon, I., Mallah, G. A., Shaikh, N. A., Shaikh, R. A., & Magsi, Y. (2020, February 8-9). *Automation of traffic control system using image morphological operations*. [Paper presentation]. 2020 International Conference on Information Science and Communication Technology (ICISCT), Karachi, India. <https://doi.org/10.1109/ICISCT49550.2020.9080051>
- Van De Sande, K., Gevers, T., & Snoek, C. (2010). Evaluating color descriptors for object and scene recognition. *IEEE Transactions on Pattern Analysis and Machine Intelligence*, 32(9), 1582-1596. <https://doi.org/10.1109/TPAMI.2009.154>
- Varish, N., Pal, A. K., Hassan, R., Hasan, M. K., Khan, A., Parveen, N., Banerjee, D., Pellakuri, V., Haqis, A. U., & Memon, I. (2020). Image retrieval scheme using quantized bins of color image components and adaptive tetrolet transform. *IEEE Access*, 8, 117639-117665. <https://doi.org/10.1109/ACCESS.2020.3003911>
- Wang, J., Wang, L., Liu, X., Ren, Y., & Yuan, Y. (2018). Color-based image retrieval using proximity space theory. *Algorithms*, 11(8), Article 115. <https://doi.org/10.3390/a11080115>
- Wang, J. Z., Li, J., & Wiederhold, G. (2001). SIMPLiCity: Semantics-sensitive integrated matching for picture libraries. *IEEE Transactions on Pattern Analysis and Machine Intelligence*, 23(9), 947-963. <https://doi.org/10.1109/34.955109>
- Xiaoling, W., & Kanglin, X. (2004, September 16). *A novel direction chain code-based image retrieval*. [Paper presentation]. The Fourth International Conference On Computer and Information Technology, 2004. CIT '04., Wuhan, China. <https://doi.org/10.1109/CIT.2004.1357195>
- Yang, Z., Ge, Y., Huang, Z., & Xiong, C. (2021, March 26-28). *Supervised hashing with kernel based on feature fusion for remote sensing image retrieval*. [Paper presentation]. 2021 IEEE 2nd International Conference on Big Data, Artificial Intelligence and Internet of Things Engineering (ICBAIE), Nanchang, China. <https://doi.org/10.1109/ICBAIE52039.2021.9389931>
- Yu, G., & Morel, J. M. (2011). ASIFT: An algorithm for fully affine invariant comparison. *Image Processing On Line*, 1, 11-38. <https://doi.org/10.5201/ipol.2011.my-asift>
- Yu, J., Qin, Z., Wan, T., & Zhang, X. (2013). Feature integration analysis of bag-of-features model for image retrieval. *Neurocomputing*, 120, 355-364. <https://doi.org/10.1016/j.neucom.2012.08.061>
- Zhang, B., Gao, Y., Zhao, S., & Liu, J. (2010). Local derivative pattern versus local binary pattern: Face recognition with high-order local pattern descriptor. *IEEE Transactions on Image Processing*, 19(2), 533-544. <https://doi.org/10.1109/TIP.2009.2035882>
- Zhang, S., Tian, Q., Lu, K., Huang, Q., & Gao, W. (2013). Edge-SIFT: Discriminative binary descriptor for scalable partial-duplicate mobile search. *IEEE Transactions on Image Processing*, 22(7), 2889-2902. <https://doi.org/10.1109/TIP.2013.2251650>

On Estimating the Parameters of the Generalised Gamma Distribution Based on the Modified Internal Rate of Return for Long-Term Investment Strategy

Amani Idris Ahmed Sayed* and Shamsul Rijal Muhammad Sabri

School of Mathematical Sciences, Universiti Sains Malaysia, 11800 USM, Pulau Pinang, Malaysia

ABSTRACT

The generalised gamma distribution (GGD) is one of the most widely used statistical distributions used extensively in several scientific and engineering application areas due to its high adaptability with the normal and exponential, lognormal distributions, among others. However, the estimation of the unknown parameters of the model is a challenging task. Many algorithms were developed for parameter estimation, but none can find the best solution. In this study, a simulated annealing (SA) algorithm is proposed for the assessment of effectiveness in determining the parameters for the GDD using modified internal rate of return (MIRR) data extracted from the financial report of the publicly traded Malaysian property companies for long term investment periods (2010–2019). The performance of the SA is compared to the moment method (MM) based on mean absolute error (MAE) and root mean squares errors (RMSE) based on the MIRR data set. The performance of this study reveals that the SA algorithm has a better estimate with the increases in sample size (long-term investment periods) compared to MM, which reveals a better estimate with a small sample size (short-time investment periods). The results show that the SA algorithm approach provides better estimates for GGD parameters based on the MIRR data set for the long-term investment period.

Keywords: Generalised gamma distribution, modified internal rate of return, moment methods, simulated annealing algorithm

ARTICLE INFO

Article history:

Received: 31 May 2022

Accepted: 02 November 2022

Published: 13 July 2023

DOI: <https://doi.org/10.47836/pjst.31.5.07>

E-mail addresses:

amani.sayd983@yahoo.com (Amani Idris Ahmed Sayed)

rijal@usm.my (Shamsul Rijal Muhammad Sabri)

* Corresponding author

INTRODUCTION

Recently, one of the major concerns in the investment decision is stock assessment and forecasting. An investment decision is one of the vital activities in business performance.

Both shareholders and investors can use stock valuation models to evaluate their shares and make stock trading decisions accordingly. Major shareholders carried out investment valuations to drive them to make decisions using various models. Managers must have a correct grasp of the influential resources to construct an investment model for stock valuation, which is a vital aspect of a company's performance in stock valuation.

Investment modelling is all about building and analysing mathematical models to depict the processes by which money flows into and out of a company. It takes various quantitative techniques to "make financial sense of the future." Investors may use a variety of models when selecting stocks and evaluating the performance of their stock portfolios. Stock valuation is a strategy used in determining the worth of a firm, which may provide information to potential investors about the company's profitability constraints (Besley & Brigham, 2015).

Stock valuations are widely conducted based on traditional accounting methods. It includes the Net Present Value (NPV) and the Internal Rate of Return (IRR), and the Profitability Index (PI) (Bonazzi & Iotti, 2016). The implementation of IRR calculation, in which a single investment project came with multiple values, is one of the major flaws of traditional accounting methods (Kierulff, 2008; Osborne, 2010; Sabri & Sarsour, 2019). This problem is overcome by the application of the MIRR, which was rediscovered in the 1950s after its development during the 18th century, and which accounts for the periodic free cash flows by assuming reinvestment of cash inflows at the reinvestment rate (Baldwin, 1959; Biondi, 2006; Kierulff, 2008; Sabri & Sarsour, 2019).

The MIRR is defined as the rate at which the NPV equals zero, that is, where the Present Value (PV) of the investment fund's terminal value (future value of cash inflows assumed to be reinvested at the firm's required rate of return) equals the present value of the investment outlays (cash outflows over the investment period) when discounted at the firm's required rate of return (Besley & Brigham, 2015; Quiry et al., 2005). The investment rate of return might be accomplished using an iterative procedure to locate the root, such as the Newton-Raphson algorithm (Ahmad, 2015) or the modified Newton-Raphson method (Pascual et al., 2018).

However, some problems arise when utilising this procedure since it does not account for all relevant aspects that affect the investment return, rendering their methods ineffective for measuring stock performance (Brealey et al., 2006; Markowitz, 1952; Ross et al., 2010). As a result, several researchers have devised alternate investment appraisal methodologies to address this issue (Sabri & Sarsour, 2019; Satyasai, 2009; Sayed & Sabri, 2022). Sabri and Sarsour (2019) formulate an effective approach for determining the rate of return from long-term investments considering a variety of financial parameters, including stock price, reinvested dividends, and share issuances such as splits and bonuses issues. Investment returns were more realistically shown in the stock investment model since it revealed the calculation of the MIRR using a yearly annuity-style approach to contributions.

Sayed and Sabri (2022) extend the process of calculating the MIRR by incorporating treasury share dividends, which may significantly affect the investment's rate of return. Moreover, the study suggests transforming the MIRR by adding the value of one to prevent any negative return since the return estimated on any investment appears to be more than minus one. Being a random variable, the rate of return will follow some statistical distribution. The normal distribution in finance is often used to model asset returns. For example, Sharpe (1964) assumed that the return follows a normal distribution while describing the theory of market equilibrium and Capital Asset Pricing Models. However, returns on financial assets do not exhibit the normal distribution (Cont, 2001). As a result, other distributions should be employed (Fama, 1963).

The gamma distribution is extensively employed in several scientific and technical disciplines, such as banking, networking, and meteorological research (Kellison, 2009; Kim et al., 2003) due to its high degree of adaptability with the normal and exponential distributions, among others (Eric et al., 2021). This distribution is used to represent positive continuous variables. It logically models the waiting durations between events, like Sabri and Sarsours (2019), who modelled a framework with positive and continuous variables. A unique and flexible form of the gamma distribution is the GGD which includes special cases of some distributions such as the Weibull distribution, the gamma distribution, the exponential distribution, and the lognormal distribution (Kiche et al., 2019; Khodabina & Ahmadabadi, 2010; Stacy & Mihram, 1965).

Various approaches, such as the method of moment and maximum-likelihood function, exist to estimate the three parameters of the GGD, namely, shape, scale, and growth rate (Naji & Rasheed, 2019). Estimating the GGD parameters based on the numerical methods is problematic due to the difficulty in deriving their values from the mean and variance equations unless the value of one parameter is fixed and the values of the other two are calculated. Also, utilising the maximum-likelihood function to estimate the three parameters simultaneously is a mathematically complex procedure since it is difficult to derive a simple differentiation of the log-likelihood function concerning the shape parameter (Gomes et al., 2008; Lakshmi & Vaidyanathan, 2016; Özsoy et al., 2020). Hence, the SA algorithm, which uses the log-likelihood function as an objective function and seeks to maximise it, may be incorporated as an alternative parameter estimation method (Idris & Muhammad, 2022).

The SA algorithm attempts to produce novel solutions to a particular problem based on a random process and a series of probability distributions. This random procedure does not necessarily improve the objective function but may still be accepted (Franzin & Stützle, 2019). The algorithm was first employed in metallurgy as an optimisation procedure to attain minimal energy by progressively lowering atomic mobility, decreasing lattice defects' uniformity, and reducing metal temperature (Du & Swamy, 2016). It is unaffected by any restraint at any local minimum and accepts any changes in the objective function with

indulgence, making it useful in many fields, including finance, mathematics and statistics (Abubakar & Sabri, 2021a, 2021b; Crama & Schyns, 2003; Orús et al., 2019).

The method of moments (MM) is a technique for estimating the parameters of a statistical model. It works by finding values of the parameters that result in a match between the sample moments and the population moments (as implied by the model). The MM is used as quick information about the unknown parameter or an initial guess for a numerical search for MLE estimates (Malá et al., 2022). Various researchers conducted the estimates of various statistical distributions based on MM. It includes the work of Hosking et al. (1985), who used the method of probability-weighted moments to derive estimators of the parameters and quantiles of the generalised extreme-value distribution. Greenstein et al. (1999) used MM to estimate the Ricean K-factor from measured power versus time, which is relatively cumbersome and time-consuming. Chang (2011) used MM compared with other numerical methods in estimating Weibull parameters for wind energy applications based on Monte Carlo simulation and analysis of actual wind speed. Bílková (2012) compare MM with L-moments based on lognormal distribution. Rocha et al. (2012) analysed and compared 7 (seven) numerical methods to assess effectiveness in determining the parameters for the Weibull distribution using wind speed data. Munkhammar et al. (2017) proposed a procedure based on the is based on MM, which is set up algorithmically to aid applicability in estimating N th-degree polynomial approximations to be unknown (or known) probability density functions (PDFs) based on N statistical moments from each distribution. Tizgui et al. (2017) compare moment methods with other estimation methods for Weibull parameters in the Agadir region in Morocco. Chaurasiya et al. (2018) examine the effectiveness of nine different numerical methods in calculating the parameters of Weibull distribution for wind power density. Honore et al. (2020) introduce measures on how each moment contributes to the precision of parameter estimates in generalised MM settings.

This study aims to demonstrate the SA algorithm's efficacy in estimating the parameters of the GGD modelled on the transformed MIRR as formulated in Sayed and Sabri (2022) compared with the MM. The data relates to long-term investments in the stocks of 62 publicly listed Malaysian property companies from 2010 to 2019, considering varying cases of one to eight-year investment periods.

MATERIALS AND METHODS

Modified Internal Rate of Return

The MIRR model in this paper was introduced by Sabri and Sarsour (2019) and developed by Abubakar and Sabri (2021a) and Sayed and Sabri (2022). The MIRR model framework is a good fit for a long-term investment. Therefore, it requires a comprehensive search to collect more in-depth financial information about the companies under study, such as the

yearly updated dividend rate, stock issuance and daily updated stock price. It is crucial to focus on the form of the dividend declared for the shareholders because that tends to differ from one company to another, thus affecting the accumulation of their share unit g .

In the investment theory, some companies are found practising the share split. For example, suppose each ordinary share is split into 2 (*i. eg* = 2). In that case, the number of the share units earned by the shareholder will be multiplied by two, thereby reducing the stock price to half to enhance the liquidity of the share capital traded in the market without any change in the investor's capital. On the contrary, the bonus issue in which the company distributes the accumulated shares to the shareholders depends on the number of their shares. For instance, in a bonus issue of one share for two existing ordinary shares, the company distributes half of the accumulative share units to 1.5 share units at the end of the year. With such a bonus issue, the shareholder will earn $2 \times (1 + \frac{1}{2} \times 1) = 3$ that makes $g = 3$.

Furthermore, companies issue treasury shares or mandatory treasury shares in which the company distributes dividends for shareholders in cash, which does not affect the accumulation of the share unit g . If the company does not announce any share issuance for any year, then $g = 1$. The accumulation of share units g for a particular year is calculated by adding any share split or bonus issue in the same year and any treasury shares activity.

The long-term investment strategy associated with the MIRR model requires holding the cash out at the same level as at the beginning of every year for k years and reinvesting the cash dividend to increase the share units. After the desired investment's time ends, the investor earns the capital with the profit of the investment after k years. If the investor gets less cash than the total contribution, then the MIRR may come negative. The process of calculating the MIRR is represented in a few steps as follows:

1. Set the investment time K .
2. Calculate the respective terminal investment $F(K)$ (Equation 1), which is the terminal value of the invested fund at the end of year K ,

$$F(K) = S_K^{(2)} P_{u_{K+1,2}} + B_K + DIV_K \tag{1}$$

where $u_{K,1}$ is the date of share purchased and sold; $u_{K,2}$ is the date of dividend and share issued based on the stock reported for year k ; $P_{u_{k,2}}$ is the stock price at the date $u_{k,2}$; B_K is the cash balance of year k ; DIV_K is the cash dividend at year k , and r is the MIRR and C is the yearly fixed contribution used in Equation 2. Assuming the NPV at time zero is equal to zero, computed for MIRR as follows,

$$NPV = [S_K^{(2)} P_{u_{K+1,2}} + B_K + DIV_K](1 + r)^{\frac{u_{K+1,1} - u_{1,1}}{365}} - C \sum_{k=1}^{K+1} a_k (1 + r)^{\frac{u_{k,1} - u_{1,1}}{365}} \tag{2}$$

For the year $k = 1, \dots, K$, $S_K^{(2)}$ is the accumulated share unit after share issuance at the end of year k , defined as Equation 3,

$$S_K^{(2)} = g_k \times S_k^{(1)} \tag{3}$$

where g_k is the function of share issuance, and $S_k^{(1)}$ is the share units at the beginning of year k .

In a long-term investment based on the MIRR model, choosing the promising stock or the right time for investing is ineffective since the MIRR differs when holding a stock for an extended investment period. Also, tracking the best investment timing is difficult, as the MIRR measure can only be spotted annually. Therefore, this study assumes that the MIRR for all stocks and the time for starting an investment are common. For computation purposes, we define the MIRR by R_{tiK} , where $i = 1, \dots, n$ stocks, $t = t_1, \dots, t_T$ years of investment start, and K is the investment period so that $K \leq T$.

The investors either expect a positive return (profit) from an investment or, in the worst case, they can get zero return which leads to work with a non-negative MIRR. The non-negative transformed rate of return was introduced by Sabri and Sarsour (2019) as Equation 4:

$$X_{tiK} = 1 + R_{tiK} \tag{4}$$

where K is the investment period, $R_{tiK} > 1$ is defined as the MIRR, $i = 1, \dots, n$ stocks, $t = t_1, \dots, t_T$ years of investment start, and K is the investment period. The non-negative transformed MIRR X_{tiK} , being a random variable, should be distributed with a non-negative distribution such as the GGD, which will be explained in the next section.

Generalised Gamma Distribution

The non-negative MIRR or the random variable X_{tiK} for the i -th stock at investment year t over the investment period of K years may be distributed by the three parameters of the GGD, namely α and θ with the growth rate parameter γ . By letting $X_{tiK} = (1 + \gamma)^{K-1} X_{ti1}$, the probability density function (PDF) of the distribution is presented as Equation 5

$$f_{X_{tiK}}(x; \alpha, (1 + \gamma)^{K-1}\theta) = \begin{cases} \frac{1}{\Gamma(\alpha)} \left[\frac{1}{(1 + \gamma)^{K-1}\theta} \right]^\alpha x^{\alpha-1} e^{-\frac{x}{(1+\gamma)^{K-1}\theta}}, & x > 0 \\ 0, & \text{otherwise.} \end{cases} \tag{5}$$

with the mean and the variance presented in Equations 6 and 7, respectively, as follows,

$$\mu = \alpha(1 + \gamma)^{K-1}\theta \tag{6}$$

$$\sigma^2 = \alpha[(1 + \gamma)^{K-1}\theta]^2 \tag{7}$$

The likelihood function of Equation 5 is defined as Equation 8,

$$L(\alpha_K, (1 + \gamma)^{K-1}\theta_K | x_{tiK}) = -\ln[\Gamma(\alpha_K)] - \alpha_K \ln((1 + \gamma)^{K-1}\theta_K) + \ln(x_K^{\alpha_K-1}) - \frac{x_K}{(1+\gamma)^{K-1}\theta_K} \tag{8}$$

$$l(\alpha_K, (1 + \gamma)^{K-1}\theta_K | x_{tiK}) = -\sum_{K=1}^{K^*} \ln[\Gamma(\alpha_K)] - \sum_{K=1}^{K^*} [\alpha_K \ln((1 + \gamma)^{K-1}\theta_K)] + \sum_{K=1}^{K^*} \ln(x_K^{\alpha_K-1}) - \sum_{K=1}^{K^*} \frac{x_K}{(1+\gamma)^{K-1}\theta_K}. \tag{9}$$

Method of Moment (MM)

The MM is one of the existing methods used in estimating the parameters of the statistical distribution function. However, estimating the three parameters of Equation 5 using the MM is not ideal because of the difficulty of constructing the values of the three parameters from the mean and variance equations unless one of the values is fixed and solved for the other two. Therefore, in this study, we fix the value of the growth rate parameter γ to estimate the shape parameter α and the scale parameter θ using the MM. The fixed value of the growth parameter γ should be selected precisely to provide us with a closer estimation of α and θ to their true values. For the period of investment, K , the MM estimates of μ s and σ s can be defined as Equations 10 and 11:

$$\alpha\theta = \frac{\sum \sum_{i=1}^n x_i}{n} = m_{1K} \tag{10}$$

$$\alpha\theta^2 + (\alpha\theta)^2 = \frac{\sum \sum_{i=1}^n x_i^2}{n} = m_{2K} \tag{11}$$

Thus, it gives the following Equations 12 and 13

$$\hat{\theta} = \frac{m_{2K} - m_{1K}^2}{m_{2K}} \tag{12}$$

$$\hat{\alpha} = \frac{m_{1K}^2}{m_{2K} - m_{1K}^2} \tag{13}$$

Simulated Annealing Algorithm (SA)

The Simulated Annealing (SA) algorithm is a heuristic technique proposed separately by Kirkpatrick et al. (1983) and Cerny (1985). It is one of the most popular metaheuristics algorithms that rely on logic and rules to optimise model parameters. This process is based on Physical Annealing, which mimics the physical melting process of heating a material

to its melting point and then slowly cooling it to achieve the required structure. The SA algorithm optimises by systematically decreasing the temperature and minimising the search region.

Estimating the parameters using the SA algorithm requires selecting values of control parameters, such as the temperature parameter and the initial set of the modelling parameters that meet the study purpose. Since this study focuses on estimating the GGD parameters to maximise the likelihood function, choosing a high enough temperature parameter is necessary. The likelihood function should be multiplied by (-1) to be appropriately maximised. Such persuading can be done using MATLAB programming. The SA algorithm adopted in this paper was explained in-depth in Abubakar and Sabri (2021a) and Idris and Muhammad (2022) and summed up here as follows:

- (i) Start the function folder with a big enough sample of data X and the problem function $f = (Y, X)$ where Y is the maximum likelihood function.
- (ii) Select controlling parameters for the SA, for example, S_0, S_1, S_2, S_3 such that while $S_1 > S_0, S_1 = S_2 \times S_1$
- (iii) Generate random values $a, b,$ and c within the initial lower and upper bounds.
- (iv) Compute the likelihood function (L) at $a, b,$ and c using Equation 8
- (v) Generate neighbour values $a_1, b_1,$ and c_1 within the initial lower and upper bounds.
- (vi) Compute the likelihood function L_1 at $a_1, b_1,$ and c_1 .
- (vii) If $L_1 > L$ then $L_1 = L$ and $a = a_1, b = b_1,$ and $c = c_1$.
- (viii) Else generate a random value $m \in (0,1)$.
- (ix) -if $e^{-\frac{(L_1-L)}{S_1}} > m$ then $a = a_1, b = b_1,$ and $c = c_1$.
- (x) Print $a, b,$ and $c,$ which are $\alpha, \theta,$ and γ .

Data Collection and Experiment

The data in this study was extracted from property companies based on the Malaysian market from 2010 to 2019. The company's financial data and stock prices were collected from trusted resources, such as the Bursa Malaysia website (www.bursama-laysia.com) and The Wall Street Journal website (www.wsj.com). The data analysis involved Excel modelling, starting from listed companies' historical stock prices, the dividends declared yearly, and their share issuance for calculating the MIRR in annuity form for each year of the ten years using Equation 2. After that, the collected MIRR data was transformed into a non-negative form according to Equation 4. Since the study supports a long-term investment method, the investor is expected to hold on to a share for a minimum of one year to a maximum of ten years. Each data sample with different sizes was obtained (620, 558, 496, 434, 372, 310, 248, 186).

This study aims at modelling the MIRR data distribution on the assumption of GGD. There is a need for a good estimator to estimate the distribution parameters (α, θ, γ). In this

experiment, the two parameters α and θ of the distribution are estimated using the SA and MM, considering the fixed values (-0.0001, 0.0001) of the third parameter γ to get an initial impression of the parameters. Based on this information, the SA algorithm explained above estimates the three parameters of our model. We can finally determine our SA algorithm's effectiveness by obtaining parameters close enough to the initial parameters to maximise the likelihood function and minimise the variance nicely. To measure the closeness of the estimated parameters to the initial ones, we compute the mean absolute errors (MAE) and root mean square errors (RMSE) for each investment period of the estimated parameters according to Equations 14 and 15 respectively,

$$MAE = \frac{1}{n} \sum_{i=1}^n |\hat{V}_i - V| \tag{14}$$

$$RMSE_{V_i} = \sqrt{\frac{\sum(\hat{V}_i - V)^2}{n}}, \tag{15}$$

where $i = 1, \dots, n$ is the number of observations, V is the observed value and \hat{V} is the predicted value of the distribution.

RESULTS AND DISCUSSION

The parameters of the GGD are estimated based on the transformed modified internal rate of return datasets using a SA in comparison with MM for investment modelling. The estimated results are presented in Tables 1 and 2. The results in Tables 1 and 2 are plotted in Figures 1 and 2 for further analysis.

Table 1 shows the initial parameters estimation of the transformed MIRR distributed using GGD as in Equation 1, with two unknown parameters α and θ and the fixed growth parameter $\gamma = -0.0001, 0, 0.001$ over eight years investment periods of 62 property sector stocks in Malaysia from 2010 to 2019, using the method of the moment. From Table 1, it is observed that the estimated values α and θ are close to the actual values. Moreover, the mean, variance and maximum-likelihood function values are very close to different growth rate parameter values for each investment period, thus providing a steady initial assumption of the parameters generated.

Table 2 displays the estimated values for the three parameters GGD using SA. According to the trends, it is noticed that the larger the data set (Investment periods), the closer the estimated parameters are to the initial parameters. It is further observed that the estimated parameters based on SA maximise the maximum-likelihood function and minimise the variance in most cases, emphasising the efficiency of using the SA algorithm in estimating the parameters for the GGD based on MIRR data from the Malaysian property sector.

Figure 1 depicts the trends of the MAE values of the estimation methods used in this study in estimating the parameters of GGD using MIRR data from the property sector in

Table 1
 Estimated parameters via method of moment

	Investment Periods							
K	1	2	3	4	5	6	7	8
n_K	620	558	496	434	372	310	248	186
m_{1K}	1.12037	1.07290	1.06335	1.05949	1.04194	1.02725	1.01692	1.01046
m_{2K}	1.67559	1.26850	1.19862	1.17247	1.12006	1.07969	1.05239	1.03564
	$\gamma = 0$							
$E(X_K)$	1.1204	1.0729	1.0633	1.0595	1.0419	1.0273	1.0169	1.0105
$Var(X_K)$	0.4204	0.1174	0.0679	0.0499	0.0344	0.0244	0.0183	0.0146
α_K	2.9861	9.8058	16.6495	22.4730	31.5448	43.1858	56.5871	69.8467
θ_K	0.3752	0.1094	0.0639	0.0471	0.0330	0.0238	0.0180	0.0145
$l(\alpha_K, \theta_K, \gamma_K)$	-416.81	-115.37	3.8792	57.630	108.29	136.876	142.16	125.92
	$\gamma = -0.0001$							
$E(X_K)$	1.1204	1.0727	1.0629	1.0589	1.0411	1.0262	1.0157	1.0090
$Var(X_K)$	0.4204	0.1173	0.0679	0.0499	0.0344	0.0244	0.0182	0.0146
α_K	2.9861	9.8058	16.6495	22.4730	31.5448	43.1858	56.5871	69.8467
θ_K	0.3752	0.1094	0.0639	0.0471	0.0330	0.0238	0.0180	0.0145
$l(\alpha_K, \theta_K, \gamma_K)$	-416.81	-115.37	3.8785	57.629	108.28	136.870	142.15	125.90
	$\gamma = 0.0001$							
$E(X_K)$	1.1204	1.0731	1.0638	1.0638	1.0428	1.0283	1.0181	1.0119
$Var(X_K)$	0.4204	0.1174	0.0680	0.0680	0.0345	0.0245	0.0183	0.0147
α_K	2.9861	9.8058	16.649	22.473	31.544	43.1858	56.587	69.846
θ_K	0.3752	0.1094	0.0639	0.0472	0.0330	0.0238	0.0180	0.0145
$l(\alpha_K, \theta_K, \gamma_K)$	-416.81	-115.37	3.8785	57.629	108.28	136.870	142.15	125.90

Note. $n_K = n(T - K + 1)$; $n = 62$ and $T = 8$. Furthermore, $l(\alpha_K, \theta_K, \gamma_K)$ indicate log-likelihood

Table 2
 Estimated parameters via simulated annealing

	Investment Periods							
K	1	2	3	4	5	6	7	8
n_K	620	558	496	434	372	310	248	186
α_K	2.9299	9.6941	17.3998	22.5085	32.4969	43.6111	57.2080	70.2149
θ_K	0.3709	0.1071	0.0610	0.0473	0.0321	0.0235	0.0177	0.0143
γ_K	-0.000098	-0.000085	-0.000098	-0.00009	-0.00009	-0.00009	-0.00009	-0.00009
$E(X_K)$	1.0866	1.0384	1.0619	1.0652	1.0432	1.0244	1.0128	1.0045
$Var(X_K)$ 0.4030	0.1112	0.0648	0.0504	0.0335	0.0241	0.0179	0.0144	
$l(\alpha_K, \theta_K, \gamma_K)$ - 421.107	-119.065	5.0878	57.5151	108.3712	136.807	142.003	125.672	

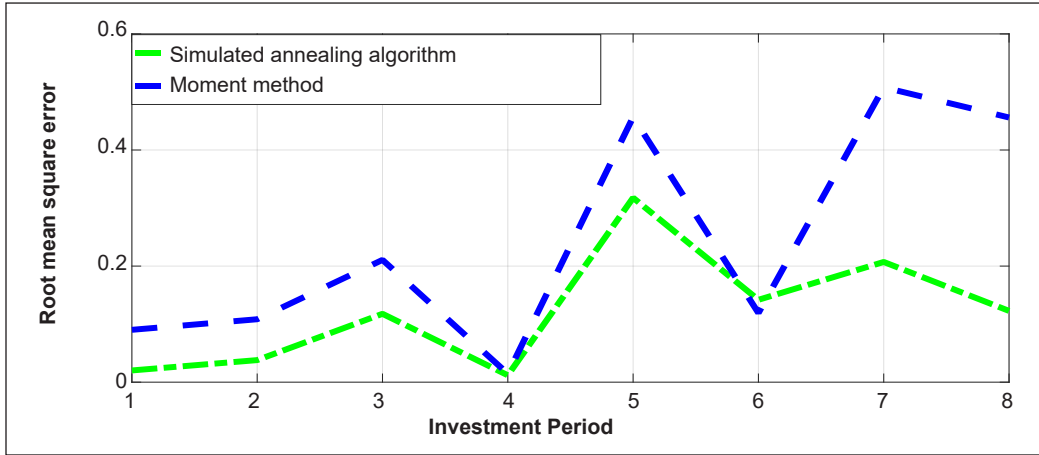


Figure 1. Comparing MAE of the estimation methods

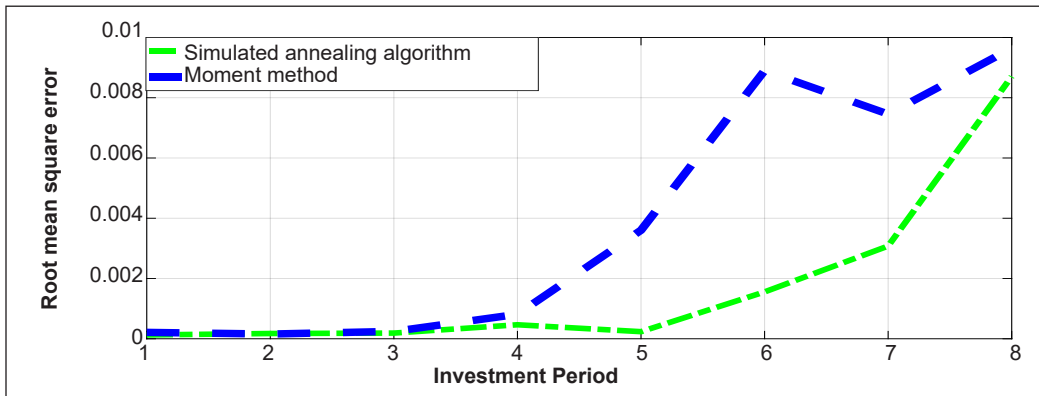


Figure 2. Comparing the RMSE_{v_i} of the estimation methods

Malaysia. The estimated parameters in both SA and MM approaches are close to the initial parameters as the values of their MAE approaches are zero. The SA approach’s performance improved with the investment period increase.

In Figure 2, the performance of SA and MM is displayed in terms of their RMSE accumulations throughout the investment periods. According to the trends, it can be observed that both the SA and MM have lower RMSE accumulation which is close to zero. The two methods’ understudy exhibits similar trends as the initial investment period but disagrees as the investment period grows. The SA algorithm utilised to estimate the GGD parameters provides efficient results by displaying lower error accumulation even with a larger sample size. Moreover, the longer the investment period, the lower the RMSE because holding on to a stock for a longer period minimises the variance and hence the risk recommended in stock investment. The SA employs an optimisation strategy similar to how metallurgy and glass are produced. SA varies from most other iterative improvement

algorithms in that, depending on a pseudo-temperature variable, candidate solutions of poorer quality than present can be allowed during the algorithm's iterations. However, SA's performance is better than MM's, especially when the sample size is large (long-term investment period). It indicates that SA can be used for parameter estimation when a large sample is used. The process is relatively easy and fast compared to traditional estimation methods.

CONCLUSION

This study's results demonstrate the SA's capability to estimate the parameters of the GGD using the transformed MIRR data. It reveals how the SA parameters are close to the initial ones and can be utilised to maximise the likelihood function and minimise the variance. Moreover, comparing the values of the SA estimated parameters with the initial parameters validates our long-term investment strategy. Such an algorithm performs better with the initial assumptions about the parameters. We used the MM to estimate our model's shape and scale parameters while keeping the growth rate parameter values fixed. It provided us with suitable initial parameters to use with SA. The results reveal the efficacy of the SA algorithm in parameter estimation problems. Hence, the algorithm can be applied to multiple generalised distributions belonging to the same family, thereby assisting in resolving modelling difficulties associated with real-world data. In addition, the performance of SA can be improved by hybridising with other estimation methods, such as the Election algorithm, variable neighbourhood search, and differential evolution algorithm, to achieve more robust and more efficient implementations.

ACKNOWLEDGEMENT

The authors are thankful to the Jazan University Saudi Arabia for sponsorship.

REFERENCES

- Abubakar, H., & Sabri, S. R. M. (2021a). Incorporating simulated annealing algorithm in the Weibull distribution for valuation of investment return of Malaysian property development sector. *International Journal for Simulation and Multidisciplinary Design Optimization*, 12, Article 22. <https://doi.org/10.1051-/smdo/2021023>
- Abubakar, H., & Sabri, S. R. M. (2021b). Simulation study on modified weibull distribution for modelling of investment return. *Pertanika Journal of Science and Technology*, 29(4), 2767-2790. <https://doi.org/10.47836/pjst.29.4.29>
- Ahmad, A. G. (2015). Comparative study of bisection and Newton-Rhapson methods of root-finding problems. *International Journal of Mathematics Trends and Technology*, 19(2), 121-129. <https://doi.org/10.14445/22315373/ijmtt-v19p516>
- Baldwin, R. H. (1959). How to assess investment proposals. *Harvard Business Review*, 37(3), 98-104.

- Besley, S., & Brigham, E. F. (2015). *CFIN4 (with Finance CourseMate)*. Cengage Learning.
- Bílková, D. (2012). Lognormal distribution and using L-moment method for estimating its parameters. *International Journal of Mathematical Models and Methods in Applied Sciences*, 6(1), 30-44.
- Biondi, Y. (2006). The double emergence of the modified internal rate of return: The neglected financial work of Duvillard (1755 - 1832) in a comparative perspective. *The European Journal of the History of Economic Thought*, 13(3), 311-335. <https://doi.org/10.1080/09672560600875281>
- Bonazzi, G., & Iotti, M. (2016). Evaluation of investment in renovation to increase the quality of buildings: A specific Discounted Cash Flow (DCF) approach of appraisal. *Sustainability*, 8(3), Article 268. <https://doi.org/10.3390/su8030268>
- Brealey, R. A., Myers, S. C., & Allen, F. (2006). *Principles of Corporate Finance*. IrwinMcGrawHill.
- Černý, V. (1985). Thermodynamical approach to the traveling salesman problem: An efficient simulation algorithm. *Journal of Optimization Theory and Applications*, 45(1), 41-51.
- Chang, T. P. (2011). Performance comparison of six numerical methods in estimating Weibull parameters for wind energy application. *Applied Energy*, 88(1), 272-282.
- Chaurasiya, P. K., Ahmed, S., & Warudkar, V. (2018). Study of different parameters estimation methods of Weibull distribution to determine wind power density using ground based Doppler SODAR instrument. *Alexandria Engineering Journal*, 57(4), 2299-2311. <https://doi.org/10.1016/j.aej.2017.08.008>
- Cont, R. (2001). Empirical properties of asset returns: Stylised facts and statistical issues. *Quantitative Finance*, 1(2), 223-236. <https://doi.org/10.1080/713-665670>
- Crama, Y., & Schyns, M. (2003). Simulated annealing for complex portfolio selection problems. *European Journal of Operational Research*, 150(3), 546-571. [https://doi.org/10.1016/S0377-2217\(02\)00784-1](https://doi.org/10.1016/S0377-2217(02)00784-1)
- Du, K. L., & Swamy, M. N. S. (2016). Simulated annealing. In *Search and Optimisation by Metaheuristics* (pp. 29-36). Birkhauser. https://doi.org/10.1007/978-3-319-41192-7_2
- Eric, U., Olusola, O. M. O., & Eze, F. C. (2021). A study of properties and applications of gamma distribution. *African Journal of Mathematics and Statistics Studies*, 4(2), 52-65. <https://doi.org/10.52589/ajmss-mr0dq1dg>
- Fama, E. F. (1963). Mandelbrot and the stable Paretian hypothesis. *The Journal of Business*, 36(4), 420-429. <https://doi.org/10.1086/294633>
- Franzin, A., & Stützle, T. (2019). Revisiting simulated annealing: A component-based analysis. *Computers and Operations Research*, 104, 191-206. <https://doi.org/10.1016/j.cor.2018.12.015>
- Gomes, O., Combes, C., & Dussauchoy, A. (2008). Parameter estimation of the generalized gamma distribution. *Mathematics and Computers in Simulation*, 79(4), 955-963. <https://doi.org/10.1016/j.matcom.2008.02.006>
- Greenstein, L. J., Michelson, D. G., & Erceg, V. (1999). Moment-method estimation of the Ricean K-factor. *IEEE Communications Letters*, 3(6), 175-176. <https://doi.org/10.1109/4234.769521>
- Honore, B., Jørgensen, T., & de Paula, A. (2020). The informativeness of estimation moments. *Journal of Applied Econometrics*, 35(7), 797-813. <https://doi.org/10.1002/jae.2779>

- Hosking, J. R. M., Wallis, J. R., & Wood, E. F. (1985). Estimation of the generalized extreme-value distribution by the method of probability-weighted moments. *Technometrics*, 27(3), 251-261.
- Idris, A. A., & Muhammad, S. S. R (2022). A simulation study on the simulated annealing algorithm in estimating the parameters of generalized gamma distribution. *Science and Technology Indonesia*, 7(1), 84-90. <https://doi.org/10.26554/sti.2022.7.1.84-90>
- Kellison, S. G. (2009). *The Theory of Interest*. McGraw Hill Education.
- Khodabina, M., & Ahmadabadi, A. (2010). Some properties of generalized gamma distribution. *Mathematical Sciences*, 4(1), 9-28.
- Kiche, J., Ngesa, O., & Orwa, G. (2019). On generalized gamma distribution and its application to survival data. *International Journal of Statistics and Probability*, 8(5), 1927-7040. <https://doi.org/10.5539/ijsp.v8n5p85>
- Kierulff, H. (2008). MIRR: A better measure. *Business Horizons*, 51(4), 321-329. <https://doi.org/10.1016/j.bushor.2008.02.005>
- Kim, S., Lee, J. Y., & Sung, D. K., (2003). A shifted gamma distribution model for long-range dependent internet traffic. *IEEE Communications Letters*, 7(3), 124-126. <https://doi.org/10.1109/lcomm.2002.808400>
- Kirkpatrick, S., Gelatt Jr, C. D., & Vecchi, M. P. (1983). Optimization by simulated annealing. *Science*, 220(4598), 671-680. <https://doi.org/10.1126/science.220.4598.67>
- Lakshmi, R. V., & Vaidyanathan, V. S. (2016). Three-parameter gamma distribution: Estimation using likelihood, spacings and least squares approach. *Journal of Statistics and Management Systems*, 19(1), 37-53. <https://doi.org/10.1080/09720510.2014.986927>
- Malá, I., Sládek, V., & Habarta, F. (2022). Comparison of estimates using L and TL moments and other robust characteristics of distributional shape and tail heaviness. *REVSTAT-Statistical Journal*, 20(5), 529-546. <https://doi.org/10.57805/revstat.v20i5.386>
- Markowitz, H. (1952). Portfolio selection. *The Journal of Finance*, 7(1), 77-91. <https://doi.org/10.1111/j.1540-6261.1952.tb01525.x>
- Munkhammar, J., Mattsson, L., & Rydén, J. (2017). Polynomial probability distribution estimation using the method of moments. *PloS One*, 12(4), Article e0174573. <https://doi.org/10.1371/journal.pone.0174573>
- Naji, L. F., & Rasheed, H. A. (2019). Estimate the two parameters of gamma distribution under entropy loss function. *Iraqi Journal of Science*, 60(1), 127-134. <https://doi.org/10.24996/ij.s.2019.60.1.14>
- Orús, R., Mugel, S., & Lizaso, E. (2019). Quantum computing for finance: Overview and prospects. *Reviews in Physics*, 4, Article 100028. <https://doi.org/10.1016-/j.revip.-2019.100028>
- Osborne, M. J. (2010). A resolution to the NPV–IRR debate? *The Quarterly Review of Economics and Finance*, 50(2), 234-239. <https://doi.org/10.1016/j.qref.2010.01.002>
- Özsoy, V. S., Ünsal, M. G., & Örkücü, H. H. (2020). Use of the heuristic optimization in the parameter estimation of generalized gamma distribution: Comparison of GA, DE, PSO and SA methods. *Computational Statistics*, 35(4), 1895-1925. <https://doi.org/10.1007/s00180-020-00966-4>

- Pascual, N., Sison, A. M., Gerardo, B. D., & Medina, R. (2018). Calculating internal rate of return (IRR) in practice using improved newton-raphson algorithm. *Philippine Computing Journal*, 13(2), 17-21. <https://pcj.csp.org.ph/index.php/pcj/issue/view/28>
- Quiry, P., Dallochio, M., LeFur, Y., & Salvi, A. (2005). *Corporate Finance: Theory and Practice* (6th Ed). John Wiley & Sons Ltd.
- Rocha, P. A. C., de Sousa, R. C., de Andrade, C. F., & da Silva, M. E. V. (2012). Comparison of seven numerical methods for determining Weibull parameters for wind energy generation in the northeast region of Brazil. *Applied Energy*, 89(1), 395-400. <https://doi.org/10.1016/j.apenergy.2011.08.003>
- Ross, A. S., Westerfield, R. W., & Jordan, B. D. (2010). *Fundamentals of Corporate Finance*. The McGraw-Hill Companies, Inc.
- Sabri, S. R. M., & Sarsour, W. M. (2019). Modelling on stock investment valuation for long-term strategy. *Journal of Investment and Management*, 8(3), 60-66. <https://doi.org/10.11648/j.jim.20190803.11>
- Satyasai, K. J. S. (2009). Application of modified internal rate of return method for watershed evaluation. *Agricultural Economics Research Review*, 22, 401-406.
- Sayed, A. I. A., & Sabri, S. R. M. (2022). Transformed modified internal rate of return on gamma distribution for long term stock investment. *Journal of Management Information and Decision Sciences*, 25(S2), 1-17
- Sharpe, W. F. (1964). Capital asset prices: A theory of market equilibrium under conditions of risk. *The Journal of Finance*, 19(3), 425-442. <https://doi.org/10.1111/j.1540-6261.1964.tb02865.x>
- Stacy, E. W., & Mihram, G. A. (1965). Parameter estimation for a generalized gamma distribution. *Technometrics*, 7(3), 349-358. <https://doi.org/10.1080/00401706.1965.10268>
- Tizgui, I., El Guezar, F., Bouzahir, H., & Benaïd, B. (2017). Comparison of methods in estimating Weibull parameters for wind energy applications. *International Journal of Energy Sector Management*, 11(4), 650-663. <https://doi.org/10.1108/IJESM-06-2017-0002>



Underdetermined Blind Source Separation of Bioacoustic Signals

Norsalina Hassan¹ and Dzati Athiar Ramli^{2*}

¹Department of Electrical Engineering, Politeknik Seberang Perai, 13700 Jalan Permatang Pauh, Pulau Pinang, Malaysia

²School of Electrical & Electronic Engineering, Universiti Sains Malaysia, Nibong Tebal, 14300, Pulau Pinang, Malaysia

ABSTRACT

Bioacoustic signals have been used as a modality in environmental monitoring and biodiversity research. These signals also carry species or individual information, thus allowing the recognition of species and individuals based on vocals. Nevertheless, vocal communication in a crowded social environment is a challenging problem for automated bioacoustic recogniser systems due to interference problems in concurrent signals from multiple individuals. The bioacoustics sources are separated from the mixtures of multiple individual signals using a technique known as Blind source separation (BSS) to address the abovementioned issue. In this work, we explored the BSS of an underdetermined mixture based on a two-stage sparse component analysis (SCA) approach that consisted of (1) mixing matrix estimation and (2) source estimation. The key point of our procedure was to investigate the algorithm's robustness to noise and the effect of increasing the number of sources. Using the two-stage SCA technique, the performances of the estimated mixing matrix and the estimated source were evaluated and discussed at various signal-to-noise ratios (SNRs). The use of different sources is also validated. Given its robustness, the SCA algorithm presented a stable and reliable performance in a noisy environment with small error changes when the noise level was increased.

Keywords: Bioacoustic signals, blind source separation, sparse component analysis, underdetermined mixtures

ARTICLE INFO

Article history:

Received: 06 June 2022

Accepted: 25 January 2023

Published: 13 July 2023

DOI: <https://doi.org/10.47836/pjst.31.5.08>

E-mail addresses:

nizlin7374@gmail.com (Norsalina Hassan)

dzati@usm.my (Dzati Athiar Ramli)

* Corresponding author

INTRODUCTION

Bioacoustics can be defined as the study of animal sound communication and can be considered one of the most effective methods in environmental monitoring applications and biodiversity research (Huang et al., 2009). In particular, vocalising

animals, such as frogs, primarily rely on sound to interact with conspecifics or other species by making a range of different calls for various purposes. Humans can use such sounds to extract additional detailed species information and identify species (Stevenson et al., 2015). Most studies on animal call recognition focused on animal species identification. However, identifying different animal species in accordance with recorded calls, which frequently contain vocalisations from more than one individual, is difficult (Hassan & Ramli, 2018). This situation makes identifying the source data from a given mixture of data challenging. Therefore, postprocessing approaches are needed to separate individual bioacoustic sources from sound mixtures to enhance the process further. Blind source separation (BSS) is often used in audio, digital communication, biomedical, and signal processing to separate source signals from mixed signals (Santamaria, 2013).

Depending on the number of sources, N and the number of sensors, M , BSS can be classified into determined ($N = M$), overdetermined ($N < M$) and underdetermined ($N > M$) cases. In determined cases, the mixing matrix A can be invertible as it is a square matrix. Therefore, the source can be recovered easily by multiplying the mixture with the inverse of A after discovering the mixing matrix. Independent component analysis is a well-known method for determining cases (Hyvarinen, 2012). For overdetermined cases, the mixing matrix can be transformed into a square using principal component analysis (Winter et al., 2006). Underdetermined cases are the most popular among these three cases because they best fit the practical application. For underdetermined mixtures cases, the mixing matrix is not square and is therefore insufficient for reconstructing the sources because of the noninvertible mixing matrix. Therefore, the algorithms used for the determined and overdetermined cases may not work when dealing with a complex problem, such as underdetermined mixtures. Therefore, important prior information from sources, such as sparsity, is required to resolve the underdetermined problem. If an appropriate linear transformation is applied, the sources not sparse in the time domain can be sparse in the time-frequency (TF) domain. Some algorithms for achieving sparsity in the transform domain, namely short-time Fourier transform (STFT) (Linh-Trung et al., 2005; Lu et al., 2019; Su et al., 2017) and wavelet packet transform (Li et al., 2003; Miao et al., 2021; Sadhu et al., 2011), have been proposed thus far.

The main method for underdetermined cases is Sparse Component Analysis (SCA) (Li et al., 2003). Most existing SCA algorithms that exploit the sparse representation of the mixtures $X(t)$ are composed of two stages, as shown in Figure 1.

The underdetermined problem is solved by estimating the sources from the observed signals using the mixing matrix estimated in the first stage. If the mixing matrix is identified as inaccurate, the source cannot recover. Hence, the first stage is very important. The mixing matrix estimation method can further be classified into two categories, i.e., single source point (SSP) detection and clustering. In the second stage, a series of least-squares

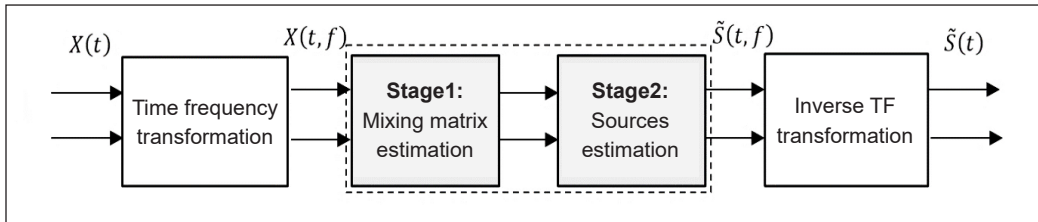


Figure 1. Two-stage method for SCA

problems is used to recover the estimated sources. Recently, many studies have focused on underdetermined problems based on the SCA framework. For example, the works of (Reju et al., 2009) identified SSPs by the fact that the absolute orientations of the real and imaginary sections of the Fourier transform coefficient vectors of the mixed signals are the same. The detected SSPs are then used to estimate the mixing matrix using hierarchical clustering. Finally, the degenerate unmixing estimation algorithm introduced by (Jourjine et al., 2000) recovers the source signals based on the ratio of the observed mixing signals' TF transforms.

The performances of the algorithms (Jourjine et al., 2000; Reju et al., 2009) depend on this ratio to detect SSPs. (Li et al., 2016) present an improved algorithm by utilising the TF coefficients of the mixed signals and complex conjugates of the coefficient for identifying SSPs. On the other hand, most SSPs-based underdetermined mixtures only consider a single SSP and ignore the relationship between SSPs. As a result of this situation, SSPs have low identification accuracy, particularly in noisy cases. The work of (Zhen et al., 2017) introduced blind source separation for underdetermined mixtures based on STFT, with SSPs identified using sparse coding. This method can exhibit excellent estimation performance even in low signal-to-noise ratio (SNR) cases, as the sparse coding strategy considers the linear relations between SSPs. This work aims to investigate the performance of BSS for underdetermined mixtures using the method of (Zhen et al., 2017) on our bioacoustic signals. As in real life, the underdetermined mixtures are formed by a pair of random mixing matrices with different selected source vectors. The mixture of sources is dynamic because the position of sources and the sensors are subject to change with time.

METHODOLOGY

The underdetermined mixtures' linear instantaneous mixed model can be written as Equation 1:

$$X(t) = AS(t), \quad [1]$$

where $X(t) = [X_1, X_2, \dots, X_M]^T$ and $S(t) = [S_1, S_2, \dots, S_N]^T$ are the vectors of the mixtures and sources in the time domain of transposition operation. M and N are the numbers of

mixed and source signals, respectively, where M is lesser than N . $A = [a_1, a_2, \dots, a_N]$ is the mixing matrix. The entries of each matrix A are determined by several characteristics, which include source locations, sensor locations, and acoustical properties. The BSS of underdetermined mixtures aims to estimate the source signals when A and S are unknown.

Data Preparation

Seven bioacoustic sources from an in-house database are used in this experiment. Figure 2 presents the dataset of the bioacoustic signals $S_N(t)$ employed in this study. The species name of each source is given below:

Source 1: *Ameerega trivittata*

Source 2: *Adenomera andre*

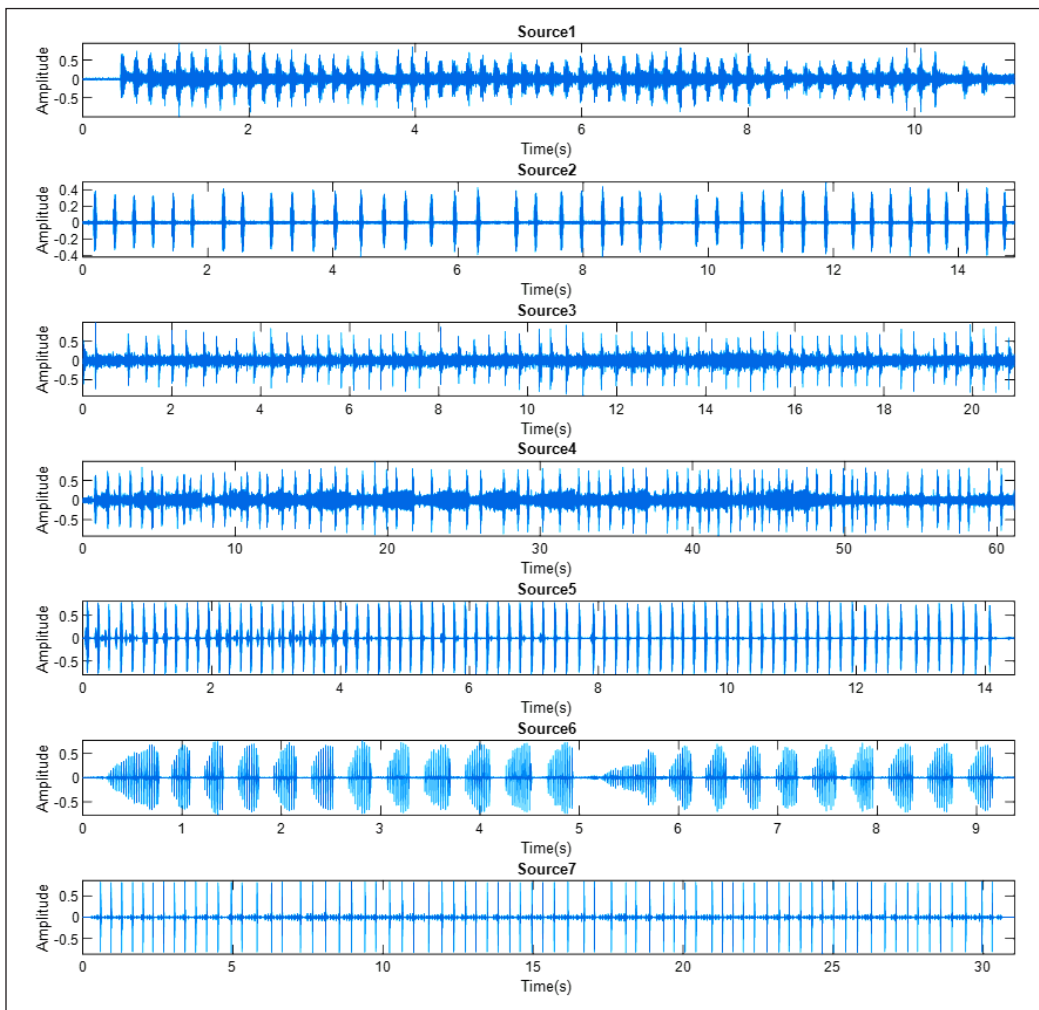


Figure 2. Dataset of bioacoustic source signals

- Source 3: *Leptodactylus hylaedactylus*
- Source 4: *Leptodactylus fuscus*
- Source 5: *Geocrinia victoriana*
- Source 6: *Geocrinia victoriana*
- Source 7: *Limnodynastes convexiusculus*

The signals were recorded in wav format in the monochannel at 16-bit and 16 kHz.

Mixed Signal Generation

In a real-life environment, the nature of mixtures varies in accordance with the position of animals and sensors. Mixed signals were generated using Equation 1 with the random selection of sources from 1: N and with a random mixing matrix ($M \times N$) to mimic the behaviour of the real-life system. Each generated mixed signal $X(t)$ had a different entry of sources and mixing matrix. To our knowledge, no standard way exists for the dynamic/nonstatic underdetermined mixtures of bioacoustic signals. In our case, the term dynamic indicates that the sources and weight are not static but subject to change. Therefore, we decided to create one based on our data through the procedure illustrated in Figure 3. Here, A represents the weight from a source to a sensor, and the different selections of sources represent the different locations of sources.

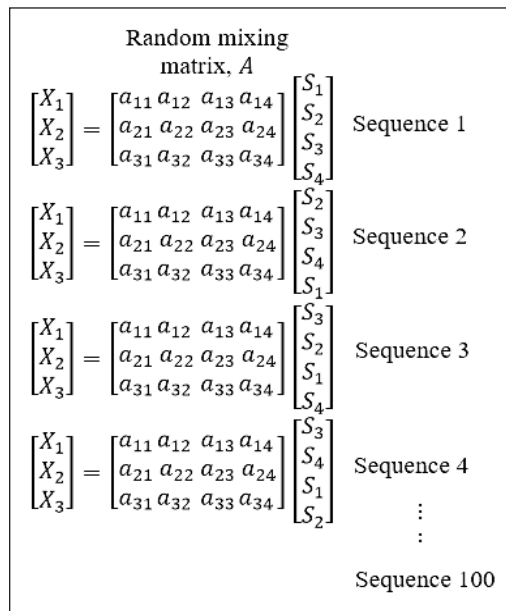


Figure 3. The procedure of mixed-signal generation

Domain Transformation

Natural signals, such as bioacoustic ones, are sparse in the time domain. Therefore, the STFT transformation was applied to Equation 1 to increase the sparsity of source signals. The STFT of the m -th mixture $x_m(t)$ is given by Equation 2:

$$X_m(t, f) = \int_{-\infty}^{\infty} x_m(\tau)h(t - \tau)e^{-j2\pi f\tau} d\tau \quad [2]$$

where $h(t)$ is the window function. Given that A is constant and that STFT is used on both sides of Equation 1, the mixing model in the time-frequency domain is obtained as Equation 3:

$$\tilde{X}(t, f) = A\tilde{S}(t, f) \tag{3}$$

where $\tilde{X}(t, f) = [\tilde{X}_1(t, f), \tilde{X}_2(t, f), \dots, \tilde{X}_M]^T$ and $\tilde{S}(t, f) = [\tilde{S}_1(t, f), \tilde{S}_2(t, f), \dots, \tilde{S}_N]^T$ represent the STFT complex coefficients of $X(t)$ and $S(t)$ at TF point (t, f) , respectively. The underdetermined mixtures in the time domain and the TF domain of three mixtures and four sources are illustrated in Figures 4 and 5, respectively. Figure 4 shows that the mixtures' direction is unclear due to the sources' weak sparsity. After the STFT is addressed, the scatter plot in Figure 5 clearly shows the column directions of the mixing matrix.

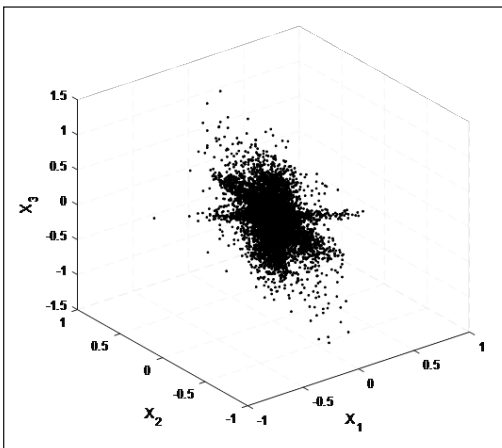


Figure 4. Mixed bioacoustic signals in the time-domain

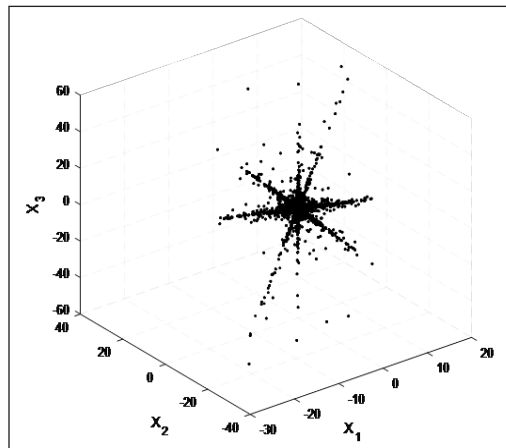


Figure 5. Mixed bioacoustic signals in the TF domain

The Mixing Matrix Estimation

The mixing matrix was estimated using the TF domain mixing model. Mixing matrix estimation is an important procedure in SCA and can be improved in two ways: SSP detection and clustering. Two assumptions were made to estimate the mixing matrix:

- A1) Any column vector is linearly independent in the mixing matrix A .
- A2) There are some TF points (t, f) for each source s'_i in which only s'_i is dominant, $|\tilde{S}_i(t, f)| \geq |\tilde{S}_j(t, f)| \forall j \neq i$.

The stability of SSP detection can be increased by using both assumptions. The steps of mixing matrix estimation can be summarised as follows:

1. Generate the underdetermined mixtures.
2. Transform the time domain underdetermined mixtures $X(t)$ into the TF domain $\tilde{X}(t, f)$.
3. Detect the SSP: Compute the sparse coding coefficients
4. Through l_1 -norm optimisation to detect the SSP for each of the TF vectorisation.

The problem of sparse coding can be formulated as Equation 4:

$$J(c_i; \lambda) = \frac{1}{2} \|y_i - Y_{c_i}\|_2^2 + \lambda \|c_i\|_1 \text{ s.t. } c_{ii} = 0, \quad [4]$$

where c_i is the $\|c_i\|_1$ l_1 -norm and $y_i - Y_{c_i}$ is the reconstruction error between each mixture TF vector and the linear combination of it. The SSP is the sparse coding coefficient with only one nonzero element at the TF point.

Apply the hierarchical clustering technique to the detected single-source mixture TF vectors to obtain clustering centres, which can then be used to calculate the estimated mixing matrix \tilde{A} .

The Source Recovery Estimation

Following the estimation of the mixing matrix, the bioacoustic source \tilde{S} is estimated. Given that Equation 1 is underdetermined, its solution is not unique even when \tilde{A} is known. Assumption A2 is needed to achieve source recovery. Let \mathbf{A} be a set consisting of all $M \times (M - 1)$ submatrices of \tilde{A} (Equation 5):

$$\mathbf{A} = \{\mathbf{A}_i | \mathbf{A}_i = [\hat{\mathbf{a}}_{\theta_1}, \hat{\mathbf{a}}_{\theta_2}, \dots, \hat{\mathbf{a}}_{\theta_{M-1}}]\}. \quad [5]$$

Then, for any TF point (t, f) there must exist a matrix element

$$\mathbf{A}_* = \{\mathbf{A}_i | \mathbf{A}_i = [\hat{\mathbf{a}}_{\theta_1}, \hat{\mathbf{a}}_{\theta_2}, \dots, \hat{\mathbf{a}}_{\theta_{M-1}}]\} \text{ that fulfils Equation 6:}$$

$$\tilde{X}(t, f) = \mathbf{A}_* \mathbf{A}_*^\dagger \tilde{X}(t, f), \quad [6]$$

where \dagger is the pseudoinverse of \mathbf{A}_* . Then, Equation 7 can estimate source signals:

$$\tilde{S}_j(t, f) = \begin{cases} i, & \text{if } j = \theta_1 \\ 0, & \text{otherwise} \end{cases}, \quad [7]$$

where $e = [e_1, e_2, \dots, e_{M-1}]^T = \mathbf{A}_*^\dagger \tilde{X}(t, f)$ and \mathbf{A}_* is produced by Equation 8:

$$\mathbf{A}_* = \underset{\mathbf{A}_i \in \mathbf{A}}{\text{arg min}} \|\tilde{X}(t, f) - \mathbf{A}_* \mathbf{A}_*^\dagger \tilde{X}(t, f)\|_2. \quad [8]$$

Finally, using inverse STFT, the time domain of the estimated bioacoustic signal $S(t)$ can be easily obtained.

RESULTS AND DISCUSSION

Experimental Setup

For the experimental setup, randomly selected sources from 1: N of $S(t)$ were mixed with 100 random mixing matrices using Equation 1 to generate 100 random mixtures $X(t)$.

This setup was intended to represent a real environment wherein some sensors are placed in different positions to receive mixed signals. The algorithm was implemented on each mixture signal to separate the bioacoustic source signals. The STFT size of each mixture signal was set to 1024 with the time step was 512, and the weighting function was a Hamming window. The averages of 100 Monte Carlo simulation tests were obtained to evaluate the performance of the SCA method. We performed the following at each stage of the SCA algorithm:

- (1) We investigated the algorithm's robustness concerning the noise by evaluating system performance at different SNRs. Compared to background noise, SNR is a metric that measures the level of the desired signal with that of the background.
- (2) We also assessed the algorithm's performance by using the setting of different numbers of mixtures M and the numbers of sources N where $M \times N = 3 \times 4, 3 \times 5, 3 \times 6, 4 \times 5, 4 \times 6$.

$3 \times 4, 3 \times 5$ and 3×6 indicate that four, five, and six sources are received by three sensors, respectively, whereas $4 \times 5, 4 \times 6$, and 4×7 indicate that five, six and seven sources are received by four sensors, respectively.

First Stage: Performance of Mixing Matrix Estimation

The following Equation 9 was used to quantify the performance of mixing matrix estimation:

$$Error = \frac{1}{N} \sum_{t=1}^n \left(1 - \frac{a_i^T \hat{a}_i}{\|a_i\| \|\hat{a}_i\|} \right), \quad [9]$$

where the number of sources is represented by N and \hat{a}_i represents the estimation of mixing vector \hat{a}_i . As the error decreases, the accuracy of mixing matrix estimation increases. Gaussian white noise is added to the mixed signal to compare how robust the method is to noise. The noise performance of the algorithm at various signal-to-noise ratios (SNR) ranging from 5 dB to 45 dB was tested.

Figures 6 and 7 show the averaged error obtained by 100 Monte Carlo tests in estimating the mixing matrix for three and four mixtures with different numbers of sources, respectively. As inferred from Figure 6, the error values tended to decrease as the SNR was increased in all settings. Figure 7 also illustrates the same trend. This result indicated that the mixing matrix's accuracy improved as the SNR value was increased. The robustness of SCA concerning noise was demonstrated here, given that it presented a stable and reliable performance when the noise level was increased from 45 dB to 5 dB with error changes less than 0.15. Comparing the performances of different settings in Figures 6 and 7 revealed that the three mixture settings obtained small average errors at the SNR of 45 dB. This result showed that mixing matrix estimation in the three-mixture setting was superior to that in the four-mixture setting. Figures 6 and 7 illustrated that the performances under

different sensor settings degraded when the number of sources was increased. This finding indicated that the number of sources and sensors strongly correlates with performance.

Next, the three-mixture setting using Zhen's method, which utilised sparse coding to identify the SSPs, was chosen for a quantitative comparison in estimating the mixing matrix with V.G. Reju's (Reju et al., 2009) and the TIFROM (Abrard & Deville, 2005) methods. We applied the same setting to both comparison methods. Figure 8 compares the performance of different mixing matrix estimation methods after 100 Monte Carlo trials for bioacoustic signals. Observing the error with changes in SNR from 5 to 45dB shows that all errors from different approaches diminish with rising SNR for bioacoustic signals. The estimation performance of V.G. Reju, TIFROM and the method proposed by Zhen differs significantly when the SNR is less than 30 dB. All methods have lower estimation performance when the SNR is greater than 30dB. The three-mixture setting using Zhen's method has a more consistent and dependable performance. In the noisy case, the three-mixture setting using Zhen's method outperforms V.G. Reju and TIFROM by more than 0.5dB in error when SNR declines from 45dB to 5dB. The suggested technique provides a low error rate when implemented for bioacoustic signals.

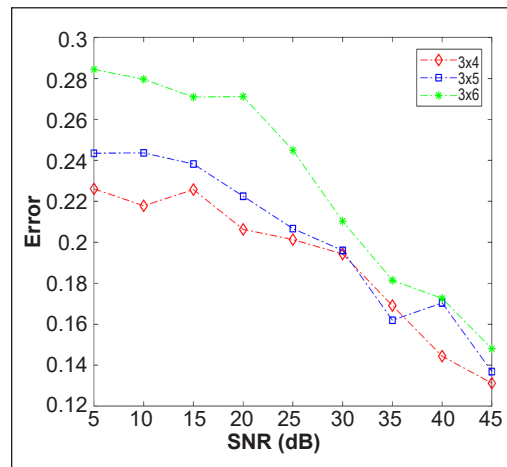


Figure 6. Comparison of the mixing matrix estimation performances of three mixtures with different numbers of sources at different SNRs

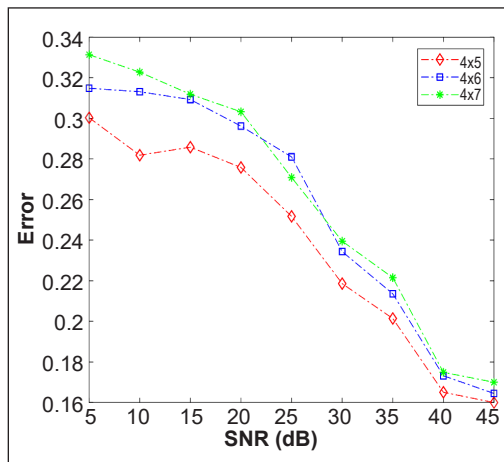


Figure 7. Comparison of the mixing matrix estimation performances of four mixtures with different numbers of sources at different SNRs

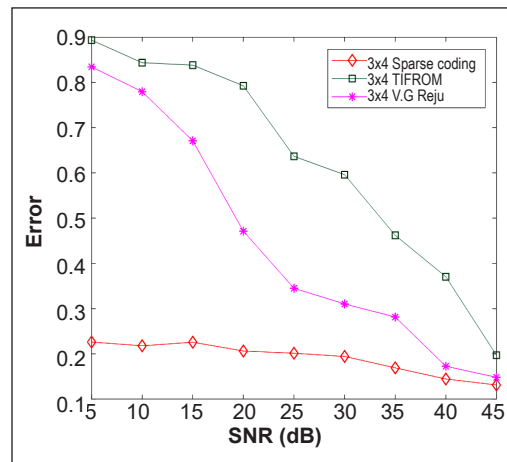


Figure 8. Comparison of the mixing matrix estimation performances of three mixtures for different methods at different SNRs

Second Stage: The Source Recovery Estimation

After estimating the mixing matrix, the source recovery was quantified. The accuracy of source recovery is determined by how well we estimate the mixing matrix. The quality of the separation was tested by using the following measures to achieve bioacoustic source recovery (Equation 10):

$$\text{Mean Squared Error, MSE} = 10\log_{10}\left(\frac{1}{n}\sum_{t=1}^{nt} \min_{\delta} \frac{\|s'_i - \delta \tilde{s}'_i\|_2^2}{\|s'_i\|_2^2}\right), \quad [10]$$

where s'_i represents the i th source, \tilde{s}'_i is the estimated source, and δ is a scalar that reflects the scalar ambiguity. Figures 9 and 10 show the comparison of the performances of the three and four mixtures with different numbers of sources in source recoveries at different SNRs. The average results were taken from 100 Monte Carlo simulations. The trend in Figures 9 and 10 showed that as the SNR was increased, the MSE decreased under all settings, in agreement with the finding reported by (Zhen et al., 2017). At 45dB SNR, the three-mixture setting provided a smaller MSE value than the four-mixture setting. A small MSE indicates high accuracy in source recovery. Figures 9 and 10 indicate that accuracy degraded when the number of sources was increased. When additional sources were used, the performance degradation may be attributed to the difficulty in satisfying the restriction in assumption A2, wherein only one source is active at any TF point.

We evaluated performance by using three metrics, namely, signal-to-distortion ratio (SDR), signal-to-interferences ratio (SIR), and signal-to-artefacts ratio (SAR), to measure the quality of the separated bioacoustic source signals (Vincent et al., 2006). High values of the metrics indicate good quality of separation. The results summarised in Figure 11

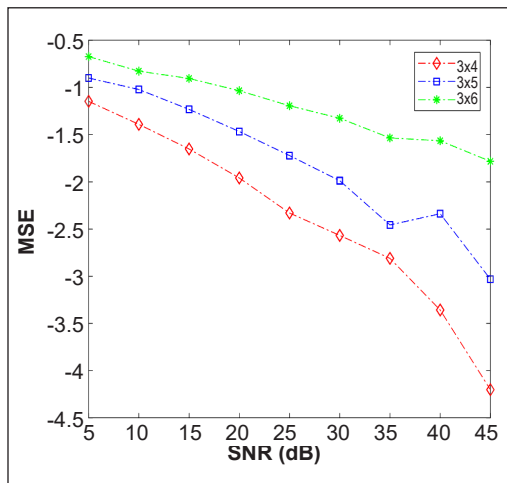


Figure 9. Comparison of source recovery performances by the three-mixture setting with different numbers of sources at different SNRs

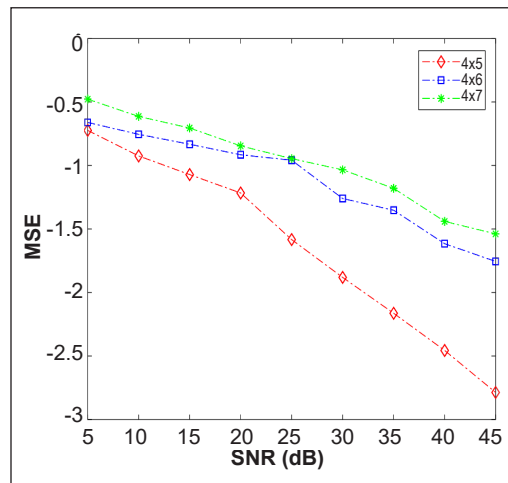


Figure 10. Comparison of the source recovery performances of the four-mixture setting with different numbers of sources at different SNRs

demonstrated that 3×4 and 3×5 exhibited high SDR, SIR, and SAR values under all settings, thus showing that the sources were well separated. On the other hand, the 3×6 setting obtained low SDR and SIR values for Source 2. This situation showed that the increasing number of sources does impact the source recovery performance. Figure 12 depicts that for each setting, 4×5 can separate all the sources well, whereas the setting for 4×6 can only separate sources 2 and 3, and 4×7 can only separate source 1. In short, the discrepancy between the number of sources and the number of sensors influences the separation performance of our underdetermined bioacoustic mixtures.

Some simulation results are also presented to illustrate the performance of the separation algorithms. The simulation results related to the performance in Figure 11 are shown in Figures 13, 14, and 15. Figure 13 presents the simulation result of separating four sources from three mixtures. All estimated sources were sufficiently close to the sources. Figure 14 provides the simulation result of separating five sources from three mixtures. Given the simulation results, the estimated source 5 was not fully recovered but can still be identified as source 5. Figure 15 gives the simulation result of separating six sources from three mixtures, indicating that four sources were effectively recovered while source 2 was incompletely recovered. The simulation results related to the performance depicted in Figure 12 are shown in Figures 16, 17, and 18, illustrating the results of separating five, six, and seven sources from four mixtures, respectively. In Figure 16, all estimated sources were fully recovered except for estimated source 5. Figure 17 shows that only estimated sources 2 and 4 were recognisable. Meanwhile, in Figure 18, only estimated source 1 was recovered. The results indicated that the SCA algorithm using our bioacoustic signals performed best with three mixtures with increasing numbers of sources at different SNRs.

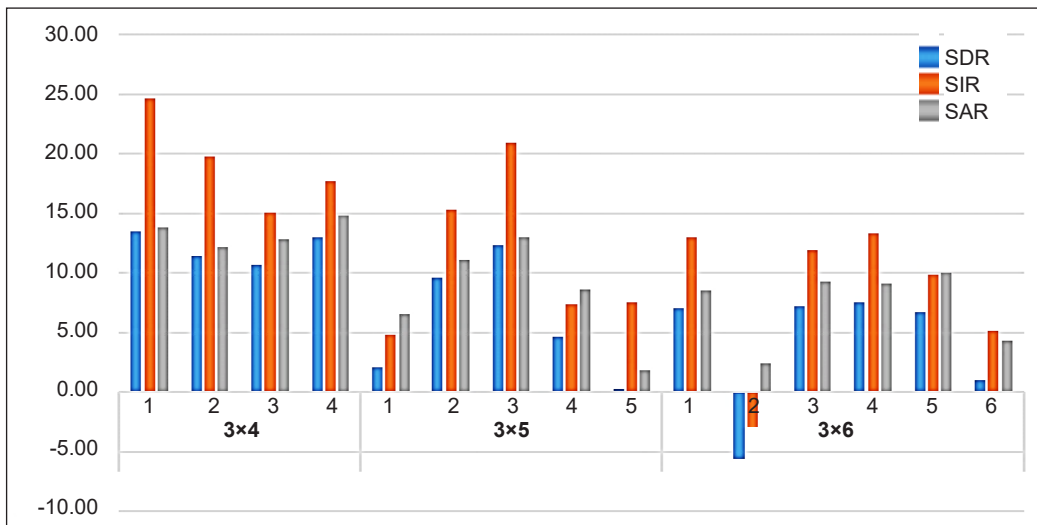


Figure 11. Comparison of the bioacoustic signal separation performances of three mixtures with different numbers of sources

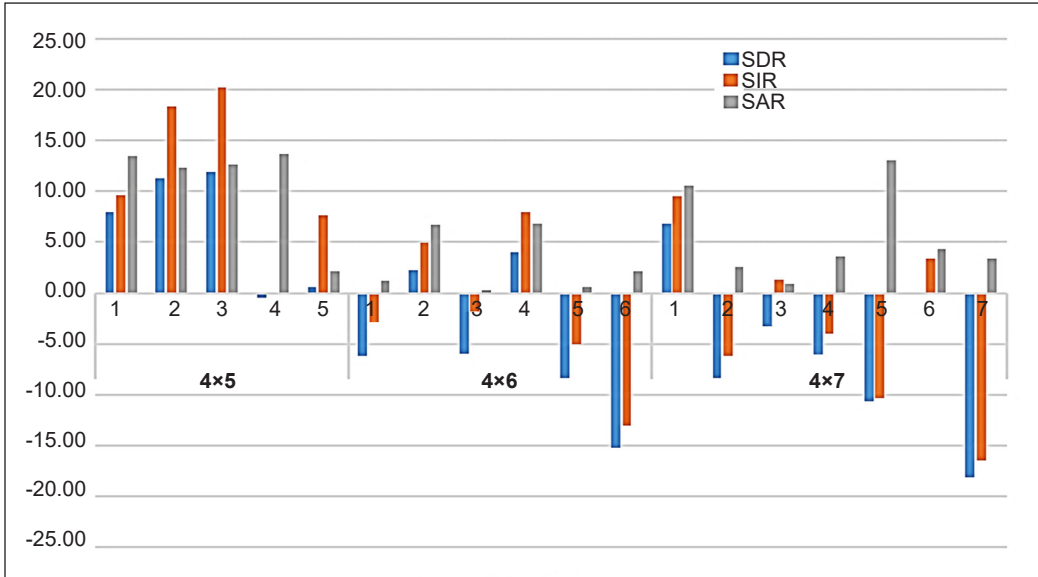


Figure 12. Comparison of the bioacoustic signal separation performances of four mixtures with different numbers of sources

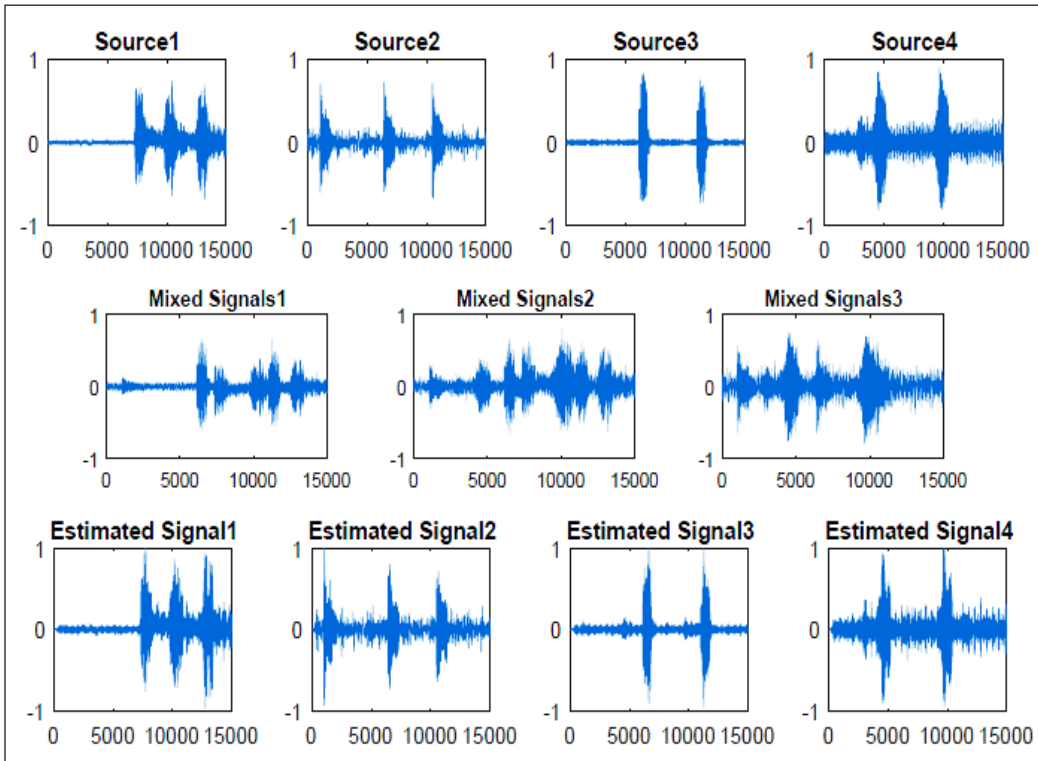


Figure 13. Simulation result of the separation of four sources from three mixtures. First row: Bioacoustic source signals. Second row: Mixtures. Third row: Estimated source signals

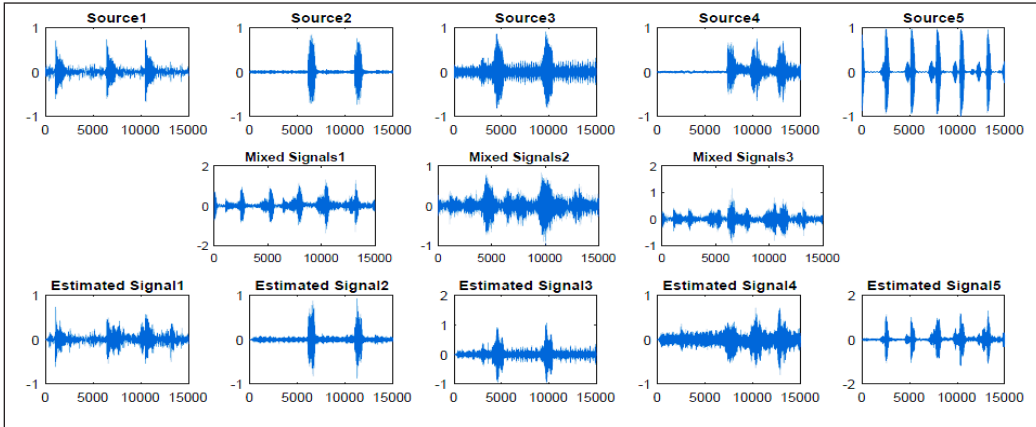


Figure 14. Simulation result of separating five sources from three mixtures. First row: Bioacoustic source signals. Second row: Mixtures. Third row: Estimated source signals

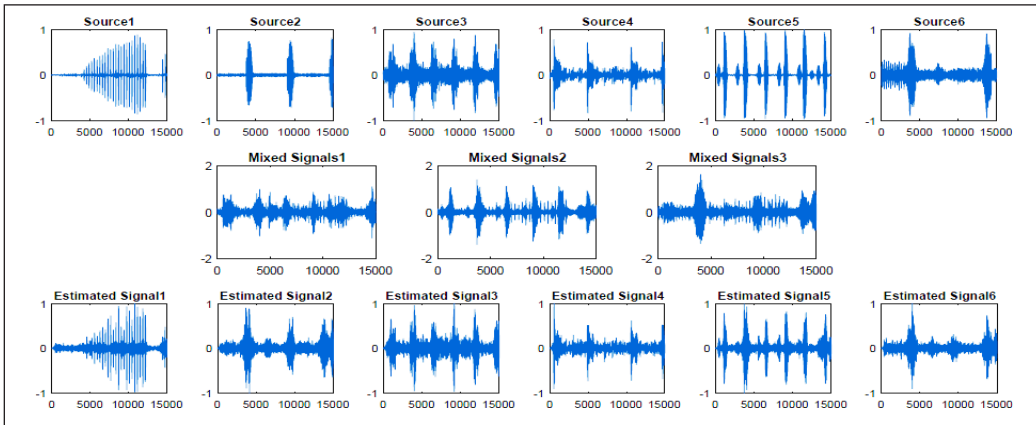


Figure 15. Simulation result of separating six sources from three mixtures. First row: Bioacoustic source signals. Second row: Mixtures. Third row: Estimated source signals

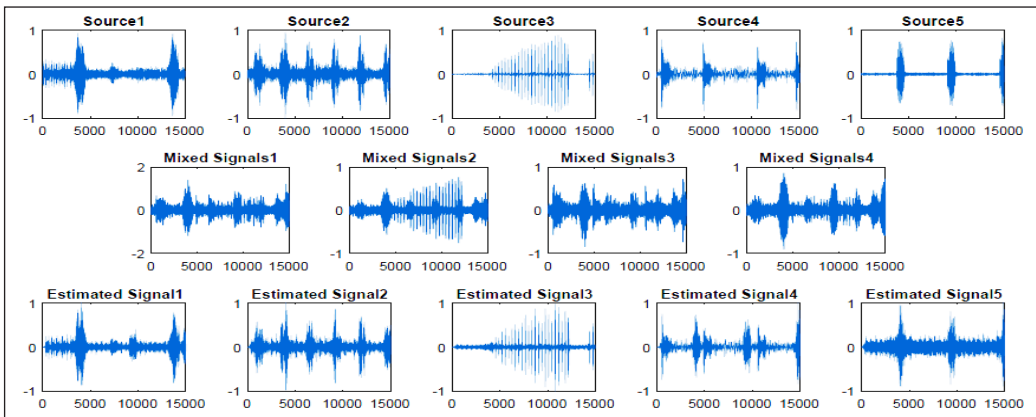


Figure 16. Simulation result of separating five sources from four mixtures. First row: Bioacoustic source signals. Second row: Mixtures. Third row: Estimated source signals

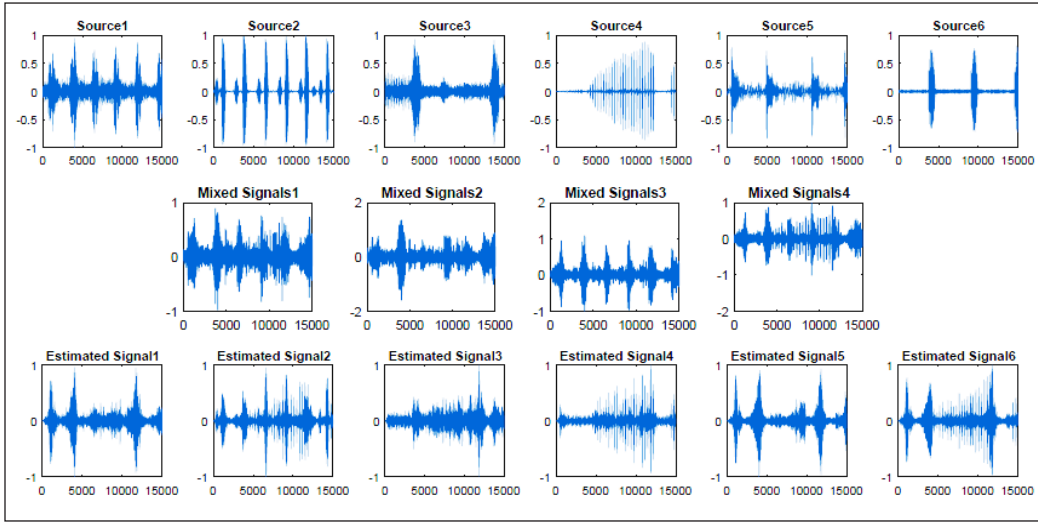


Figure 17. Simulation result of separating six sources from four mixtures. First row: Bioacoustic source signals. Second row: Mixtures. Third row: Estimated source signals

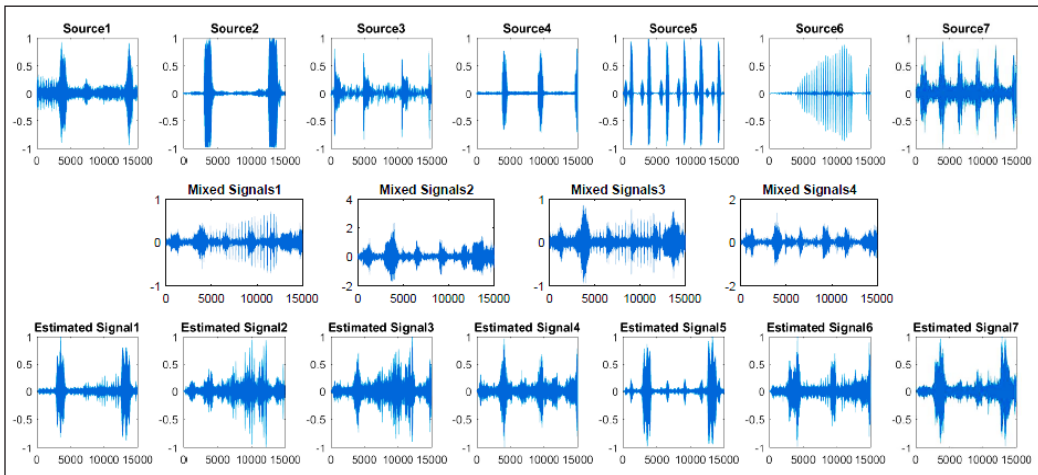


Figure 18. Simulation result of separating seven sources from four mixtures. First row: Bioacoustic source signals. Second row: Mixtures. Third row: Estimated source signals

CONCLUSION

This study exploited the SCA algorithm miming the real environment procedure for underdetermined bioacoustic mixtures. The sources in the underdetermined mixtures presented here exhibited sparse behaviour after being transformed into the TF domain using STFT. SSPs were discovered by estimating the mixing matrix with sparse coding. A series of least-square problems were used to recover the estimated sources. The robustness of the SCA algorithm also demonstrated that the algorithm presented a stable and reliable

performance in a noisy environment with small error changes when the SNR was increased. The influences of different numbers of sources and sensors on the SCA algorithm were examined. The experimental results revealed that the performances varied when different numbers of sources and sensors were used. Moreover, the performances of the SCA algorithm using bioacoustic signals degraded when the number of sources was increased, and the number of sensors was fixed.

ACKNOWLEDGEMENT

This work was supported by Universiti Sains Malaysia, Malaysia, under Research University Grant (RU) 1001/PELECT/8014057.

REFERENCES

- Abrard, F., & Deville, Y. (2005). A time–frequency blind signal separation method applicable to underdetermined mixtures of dependent sources. *Signal Processing*, *85*(7), 1389-1403. <https://doi.org/10.1016/j.sigpro.2005.02.010>
- Hassan, N., & Ramli, D. A. (2018). A Comparative study of blind source separation for bioacoustics sounds based on FastICA, PCA and NMF. *Procedia Computer Science*, *126*, 363-372. <https://doi.org/10.1016/j.procs.2018.07.270>
- Huang, C. J., Yang, Y. J., Yang, D. X., & Chen, Y. J. (2009). Frog classification using machine learning techniques. *Expert Systems with Applications*, *36*(2), 3737-3743. <https://doi.org/10.1016/j.eswa.2008.02.059>
- Hyvarinen, A. (2012). Independent component analysis: Recent advances. *Philosophical Transactions of the Royal Society A: Mathematical, Physical and Engineering Sciences*, *371*(1984), 20110534-20110534. <https://doi.org/10.1098/rsta.2011.0534>
- Jourjine, A., Rickard, S., & Yilmaz, O. (2000, June 5-9). *Blind separation of disjoint orthogonal signals Demixing n sources from 2 mixtures*. [Paper presentation]. 2000 IEEE International Conference on Acoustics, Speech, and Signal Processing. Proceedings (Cat. No. 00CH37100), Istanbul, Turkey. <https://doi.org/10.1109/ICASSP.2000.861162>
- Li, Y., Cichocki, A., & Amari, S. I. (2003, April 1-4). *Sparse component analysis for blind source separation with less sensors than sources*. [Paper presentation]. 4th International Symposium on Independent Component Analysis and Blind Signal Separation (ECA2003), Nara, Japan.
- Li, Y., Nie, W., Ye, F., & Lin, Y. (2016). A mixing matrix estimation algorithm for underdetermined blind source separation. *Circuits, Systems, and Signal Processing*, *35*(9), 3367-3379. <https://doi.org/10.1007/s00034-015-0198-y>
- Linh-Trung, N., El Bey, A. A., Abed-Meraim, K., & Belouchrani, A. (2005, August 28-31). *Underdetermined blind source separation of non-disjoint nonstationary sources in the time-frequency domain*. [Paper presentation]. 8th International Symposium on Signal Processing and its Applications, (ISSPA), Sydney, Australia. <https://doi.org/10.1109/ISSPA.2005.1580192>

- Lu, J., Cheng, W., He, D., & Zi, Y. (2019). A novel underdetermined blind source separation method with noise and unknown source number. *Journal of Sound and Vibration*, 457, 67-91. <https://doi.org/10.1016/j.jsv.2019.05.037>
- Miao, F., Zhao, R., Jia, L., & Wang, X. (2021). Multisource fault signal separation of rotating machinery based on wavelet packet and fast independent component analysis. *International Journal of Rotating Machinery*, 2021, Article 9914724. <https://doi.org/10.1155/2021/9914724>
- Reju, V. G., Koh, S. N., & Soon, I. Y. (2009). An algorithm for mixing matrix estimation in instantaneous blind source separation. *Signal Processing*, 89(9), 1762-1773. <https://doi.org/10.1016/j.sigpro.2009.03.017>
- Sadhu, A., Hazra, B., Narasimhan, S., & Pandey, M. D. (2011). Decentralized modal identification using sparse blind source separation. *Smart Materials and Structures*, 20(12), Article 125009. <https://doi.org/10.1088/0964-1726/20/12/125009>
- Santamaria, I. (2013). Handbook of blind source separation: Independent component analysis and applications (Common, P. and Jutten, ; 2010 [Book Review]. *IEEE Signal Processing Magazine*, 30(2), 133-134. <https://doi.org/10.1109/msp.2012.2230552>
- Stevenson, B. C., Borchers, D. L., Altwegg, R., Swift, R. J., Gillespie, D. M., & Measey, G. J. (2015). A general framework for animal density estimation from acoustic detections across a fixed microphone array. *Methods in Ecology and Evolution*, 6(1), 38-48. <https://doi.org/10.1111/2041-210X.12291>
- Su, Q., Shen, Y., Wei, Y., & Deng, C. (2017). Underdetermined blind source separation by a novel time-frequency method. *AEU - International Journal of Electronics and Communications*, 77, 43-49. <https://doi.org/10.1016/j.aeue.2017.04.025>
- Vincent, E., Gribonval, R., & Févotte, C. (2006). Performance measurement in blind audio source separation. *IEEE Transactions on Audio, Speech and Language Processing*, 14(4), 1462-1469. <https://doi.org/10.1109/TSA.2005.858005>
- Winter, S., Sawada, H., & Makino, S. (2006). Geometrical interpretation of the PCA subspace approach for overdetermined blind source separation. *Eurasip Journal on Applied Signal Processing*, 2006, 1-11. <https://doi.org/10.1155/ASP/2006/71632>
- Zhen, L., Peng, D., Yi, Z., Xiang, Y., & Chen, P. (2017). Underdetermined blind source separation using sparse coding. *IEEE Transactions on Neural Networks and Learning Systems*, 28(12), 3102-3108. <https://doi.org/10.1109/TNNLS.2016.2610960>

Correlation Studies and Kinetic Modelling of Electrocoagulation Treatment of Pepper Wastewater

Puteri Nurain Megat Ahmad Azman¹, Rosnah Shamsudin^{1,2*}, Hasfalina Che Man³ and Mohammad Effendy Ya'acob¹

¹Department of Process and Food Engineering, Faculty of Engineering, Universiti Putra Malaysia, 43400 UPM, Serdang, Selangor, Malaysia

²Institute of Plantations Studies, Universiti Putra Malaysia, 43400 UPM, Serdang, Selangor, Malaysia

³Department of Biological and Agricultural Engineering, Faculty of Engineering, Universiti Putra Malaysia, 43400 UPM, Serdang, Selangor, Malaysia

ABSTRACT

Pepper processing is one of the largest productions that significantly contribute (98%) to Sarawak, Malaysia's economic and agricultural sectors. The prolonged retting process of pepper berries would cause undesirable dark colour and acidic wastewater. This study aims to evaluate the performance of an electrocoagulation treatment using nickel and copper electrodes for the changes in turbidity and pH of pepper wastewater. Some analyses (correlation studies and kinetic modelling) were studied. The electrocoagulation treatment was conducted by having two conditions nickel and copper electrodes immersed in 400 mL of pepper wastewater for 30 minutes. Every 5 minutes, it was monitored, and the sample was taken for further analysis. The results indicated a significant decrease in the turbidity of pepper wastewater for nickel (98.25%) and copper electrodes (86.32%) was noticed with the increase in the electrocoagulation treatment time. At the same time, the pH values for nickel and copper electrodes were increased by 27.43% and 31%,

respectively. The results were evaluated by using Principal Component Analysis (PCA). PCA describes the correlation between the wastewater qualities in this study within less time. Among four models (zero, first and second-order) applied in this study, the turbidity for nickel and copper electrodes had the highest R^2 values (0.9457 and 0.9899) in the zero-order model. For pH, the second-order model had the highest R^2 values (0.9508 and 0.9657) for nickel and

ARTICLE INFO

Article history:

Received: 09 June 2022

Accepted: 11 October 2022

Published: 13 July 2023

DOI: <https://doi.org/10.47836/pjst.31.5.09>

E-mail addresses:

puteri.nurain@gmail.com (Puteri Nurain Megat Ahmad Azman)

rosnahs@upm.edu.my (Rosnah Shamsudin)

hasfalina@upm.edu.my (Hasfalina Che Man)

m_effendy@upm.edu.my (Mohammad Effendy Ya'acob)

* Corresponding author

copper electrodes. Electrocoagulation using nickel and process electrodes is a practical method to treat pepper wastewater.

Keywords: Correlation, electrocoagulation, kinetic, pepper, pH, treatment, turbidity, wastewater

INTRODUCTION

Pepper is known as the 'King of Spices', which has a sharp, pungent aroma and flavour and light colour. The pepper processing is one of the largest productions in Sarawak, Malaysia, by 98% (Rosnah & Chan, 2014). According to International Pepper Community and Malaysian Pepper Board, Malaysia was the fifth-largest pepper producer in the world production. The retting process is necessary to soften the pericarp of mature pepper berries to produce the white pepper. The main source of water pollution is bioactive compounds and organic matter leached into the water during the prolonged retting process of pepper berries and pericarp degradation (Aziz et al., 2019). It was caused by the high turbidity of wastewater, which was the presence of suspended particulates in water inhabiting the passage of light that caused the dark colour produced (Mandal, 2014). Meanwhile, the low pH would be produced acidic wastewater. At the same time, the inorganic matter and microorganisms in the water produced low-quality wastewater. The low quality of wastewater produced harms the environment and living things. Pepper wastewater should be treated before discharge to minimise its negative effects on the environment and living things. There are national standards of turbidity and pH for wastewater discharge limit by the Department of Environment (DOE). Therefore, the standard discharge limit for turbidity and pH is 50 NTU and 6-9, respectively.

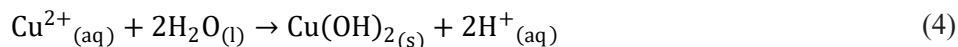
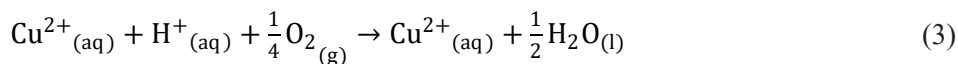
In order to treat the pepper wastewater, electrocoagulation is used to reduce the turbidity and increase the pH. Electrocoagulation implies simple equipment that can be performed in small and tiny treatment facilities (Dura, 2013). In its most basic form, an electrochemical cell consists of two electrodes, the anode and the cathode. It is immersed in a conducting solution or electrolyte and connected by an electrical circuit with a current source and control device. The reduction occurred at the cathode, while oxidation occurred at the anode. There are three electrocoagulation stages: coagulation, destabilisation of contaminants and particulate suspension, and floatation (Dura, 2013). According to Danial et al. (2017), Liu et al. (2017) and Bakshi et al. (2019), the following are the chemical reactions that occurred at the anode and cathode as shown in Equations 1 to 4.

For cathode:



For anode:





Since the turbidity and pH of pepper wastewater were changed during the electrocoagulation treatment, the correlation between wastewater qualities and treatment time was studied. The experimental results were also evaluated using statistical analysis such as Principal Component Analysis (PCA). PCA includes identifying the significant parameters in the experiment and determining the correct relationship between the parameters within less time (Patil & Dwivedi, 2020).

The kinetic orders of reactions, such as the zero, first and second-order models, are used to predict changes in turbidity and pH. The rate equations for zero, first and second-order mathematically express the changes (Li et al., 2022). The orders of reaction are included in the rate equation. There is a lack of studies about the changes in turbidity and pH of pepper wastewater during the electrocoagulation treatment using nickel and copper electrodes. As a result, the objectives of this study were to (1) determine the changes in turbidity and pH of pepper wastewater during the electrocoagulation treatment, (2) perform PCA in determining the clustering turbidity and pH of pepper wastewater within nickel and copper electrodes used during the electrocoagulation treatment and (3) develop kinetic models that express the changes in turbidity and pH of the wastewater.

MATERIALS AND METHODS

Sample Preparation

The wastewater produced from the retting process of pepper berries after 7 days were collected and used as a sample.

Experimental Set-Up

This study conducted the electrocoagulation treatment of wastewater from the retting process of pepper berries using a laboratory scale. The container was made up of transparent plexiglass with dimensions of 12.5 cm (height) × 8 cm (diameter). The experiment of the electrocoagulation treatment of pepper wastewater was set up (Figure 1).

About 400 mL of wastewater was placed into the container with two vertical electrode

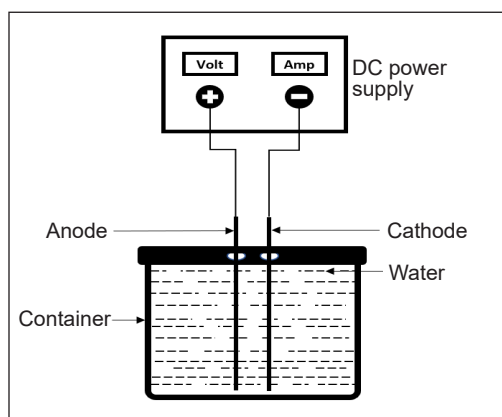


Figure 1. Schematic diagram of the electrocoagulation treatment of pepper wastewater

plates as an anode and cathode with an interspacing distance of 0.5 cm (Tharmalingam et al., 2017). The electrodes used were made of nickel and copper with the dimensions of 15 cm (length) × 5 cm (width) × 0.1 cm (thickness) (Che et al., 2020). A DC-regulated power supply (MCP M10-SP6005 L) provided current intensities in 0-1A. All runs were done at room temperature. The electrocoagulation treatment was monitored for 30 minutes. The samples were taken at different retention times (0, 5, 10, 15, 20, 25, and 30 minutes) to evaluate the performance of the changes in turbidity and pH of the wastewater using nickel and copper electrodes. After electrocoagulation treatment, the wastewater was allowed to settle for 30 minutes before being collected for analysing turbidity and pH. The electrodes were properly washed with deionised water between runs to remove any solid residue on the surface. Determining turbidity and pH of wastewater were recorded and replicated five times.

Determination of Turbidity

The change in turbidity of wastewater during the electrocoagulation treatment was evaluated using a turbidity meter (2100 Q, HACH, USA). About 10 mL of the wastewater was used to determine turbidity every 5 minutes.

Determination of pH

The change in pH of wastewater during the electrocoagulation treatment was investigated using a pH meter (Spear pH Tester, China). About 30 mL of the wastewater was used to determine pH every 5 minutes.

Turbidity and pH removal efficiencies after each treatment were calculated using Equation 5 (Tharmalingam et al., 2017):

$$\text{Removal efficiency} = \frac{C_0 - C}{C_0} \times 100\% \quad (5)$$

where C_0 and C are turbidity or pH of wastewater before and after treatment.

Kinetic Study

In this study, zero, first, and second-order models described the kinetics of the changes in turbidity and pH determined for wastewater during the electrocoagulation treatment. The coefficient (R^2) was determined to evaluate the best kinetic model-fitting analysis. The zero, first and second-order kinetic models were expressed as Equations 6 to 8 (Azman et al., 2020):

$$\text{Zero order} = C = -kt + C_0 \quad (6)$$

$$\text{First order} = C = -kt + \ln C_0 \quad (7)$$

$$\text{Second order} = \frac{1}{C} = kt + \frac{1}{C_0} \quad (8)$$

where C = the measured value for each parameter (turbidity and pH); C_0 = the initial value of the measured turbidity and pH of wastewater; k = rate constant; t = time of electrocoagulation treatment.

Statistical Analysis

A Tukey's test was applied to all data as a function of time by performing a one-way Analysis of Variance (ANOVA) analysis to differentiate and determine the significance of the mean values. Each analysis was analysed for triplicate data, and the mean and standard were reported. The confidence limits were considered as 95% ($p < 0.05$). Correlations between each parameter, including turbidity and pH of wastewater, were assessed by performing the Pearson correlation coefficient ($p < 0.05$). Statistical analyses, including PCA, were performed using Minitab Statistic 16 Edition.

RESULTS AND DISCUSSION

Turbidity and pH of pepper wastewater are the most important factors affecting white pepper quality. Therefore, the pepper wastewater should be monitored and evaluated to ensure that its discharge was followed according to the discharge limit standards by DOE. Table 1 shows the changes in turbidity and pH of wastewater during the electrocoagulation treatment using nickel and copper electrodes.

Determination of Turbidity

The initial turbidity of wastewater for nickel electrodes was 830.67 ± 0.58 NTU. Based on Table 1, the turbidity of wastewater for nickel electrodes had decreased steadily with the value of 558.00 ± 1.00 NTU after 5 minutes of electrocoagulation treatment. It continued to decrease until it reached 14.53 ± 0.58 NTU after 30 minutes of the treatment with a removal efficiency of 98.25%. Next, copper electrodes had the same value of turbidity as nickel electrodes. The wastewater turbidity attained after 5 minutes for copper electrodes was 721.00 ± 1.00 NTU. After 30 minutes of electrocoagulation treatment, it decreased gradually by 86.32% with a value of 113.67 ± 0.58 NTU.

As can be seen in Figure 2(a), the turbidity of wastewater significantly ($p < 0.05$) decreased from 5 minutes until it reached the lowest value after 30 minutes of electrocoagulation treatment using nickel and copper electrodes. The percentage of turbidity removal efficiency for nickel (98.25%) and copper electrodes (86.32%) could be observed with electrocoagulation treatment. The increment in OH^- ions production and hydrogen gas concentration affected this turbidity removal efficiency. The lightweight flocks were forced

to float towards the surface, and the large and heavy flocks settled under the gravitational force. From the results (Table 1), electrocoagulation treatment using nickel electrodes proved to be better than copper electrodes in reducing the turbidity of pepper wastewater. Furthermore, the previous work of Tharmalingam et al. (2017) had 90.76% of turbidity removal by using aluminium during the electrocoagulation treatment of pepper wastewater. Therefore, the nickel electrodes had the highest turbidity removal of pepper wastewater compared to the aluminium and copper electrodes.

Table 1
Mean values for turbidity and pH of wastewater during 30 minutes of electrocoagulation treatment

Time (min)	Properties of soaking water			
	Turbidity (NTU)		pH	
	Ni	Cu	Ni	Cu
0	830.67 ±0.58 ^a	830.67 ±0.58 ^a	4.92 ±0.01 ^g	4.92 ±0.01 ^g
5	558.00 ±1.00 ^b	721.00 ±1.00 ^b	4.95 ±0.01 ^f	5.07 ±0.01 ^f
10	457.67 ±0.58 ^c	604.67 ±0.58 ^c	5.11 ±0.01 ^e	5.26 ±0.02 ^e
15	334.67 ±0.58 ^d	440.33 ±0.58 ^d	5.34 ±0.01 ^d	5.61 ±0.01 ^d
20	89.00 ±0.58 ^e	282.67 ±0.58 ^e	5.99 ±0.02 ^c	6.46 ±0.01 ^c
25	43.00 ±0.58 ^f	212.33 ±0.58 ^f	6.24 ±0.01 ^b	6.76 ±0.02 ^b
30	14.53 ±0.58 ^g	113.67 ±0.58 ^g	6.78 ±0.01 ^a	7.13 ±0.02 ^a

Note. Data are expressed mean ±SD; turbidity (NTU); pH; Ni, nickel electrodes; Cu, copper electrodes. Different letters indicate statistically significant differences exist $p < 0.01$ for each column. The means that do not share a letter is significantly different. Tukey's test was applied with 95% simultaneous confidence intervals.

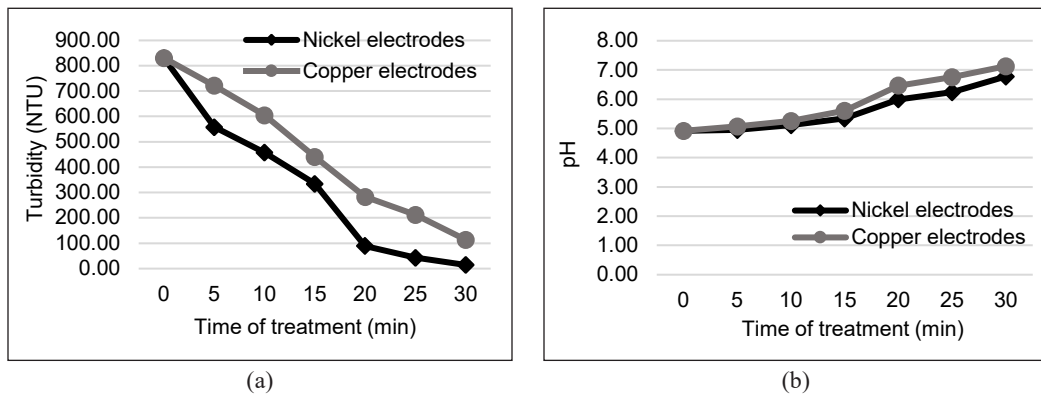


Figure 2. Graph of the effect of electrocoagulation treatment using nickel and copper electrodes on (a) Turbidity; and (b) pH of pepper wastewater

Determination of pH

The initial pH of wastewater for nickel and copper electrodes was acidic, with a value of 4.92 ± 0.01 . The pH of wastewater for nickel electrodes had increased gradually with the value of 4.95 ± 0.01 after 5 minutes of electrocoagulation treatment, as shown in Table 1.

It continued to increase until it reached 6.78 ± 0.01 after 30 minutes of the treatment with an increment efficiency of 27.43%. Next, the pH of wastewater attained after 5 minutes for copper electrodes was 5.07 ± 0.01 . After 30 minutes of electrocoagulation treatment, it increased steadily by 31% at 7.13 ± 0.02 .

As indicated in Figure 2(b), the pH of wastewater was significantly ($p < 0.05$) increased from 5 minutes until it reached the highest value after 30 minutes of electrocoagulation treatment using nickel and copper electrodes. Therefore, the percentage of pH increment efficiency for nickel (27.43%) and copper electrodes (31%) could be observed with electrocoagulation treatment after 30 minutes. Overall, electrocoagulation using copper electrodes proved to be better than nickel electrodes in increasing the pH of pepper wastewater. However, the aluminium electrodes in the previous work had the highest pH increment of pepper wastewater by 37.22% compared to the nickel and copper electrodes (Tharmalingam et al., 2017).

Correlations for Turbidity and pH of Wastewater During the Electrocoagulation Treatment

The correlation analysis showed significant ($p < 0.05$) wastewater qualities for the electrocoagulation treatment using nickel and copper electrodes, as shown in Table 2. For nickel electrodes, the correlation coefficient between turbidity and pH was highly negative, with a value of -0.907 ($p < 0.05$). Also, the turbidity was highly negatively correlated with the pH ($r = -0.977$, $p < 0.01$) for copper electrodes. Therefore, the turbidity decreased proportionally with the increased pH applied for nickel and copper electrodes.

Table 2
Correlations for turbidity and pH of wastewater attribute during the electrocoagulation treatment

Electrode	Ni		Cu	
Parameter	Turbidity (NTU)	pH	Turbidity (NTU)	pH
Turbidity (NTU)	1		1	
pH	-0.907^{**}	1	-0.977^{***}	1

Note. Data are expressed turbidity (NTU); pH; Ni, nickel electrodes; Cu, copper electrodes

*Not significant, **Significant at $p < 0.05$, ***Significant at $p < 0.01$

Principal Component Analysis for Turbidity and pH of Pepper Wastewater During the Electrocoagulation Treatment

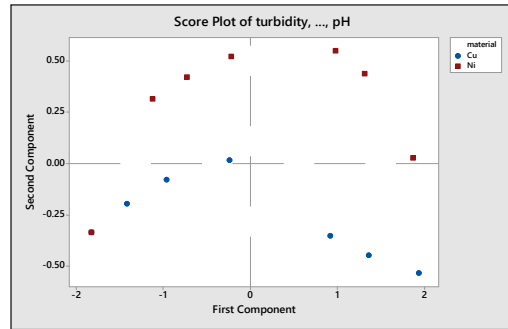
PCA was done to determine the clustering turbidity and pH within the electrocoagulation treatment's two different electrodes (nickel and copper). According to Figure 3(a), PC1 explained 92.60% of the total variance of turbidity and pH. Also, PC1 was dominant compared to PC2. Based on the PCA score plot [Figure 3(a)], PC1 and PC2 were used to demonstrate the PCA results. They specified a clear and scattered separation between the

two electrodes based on the turbidity and pH during the electrocoagulation treatment of pepper wastewater. Theoretically, the PCA results demonstrated that the turbidity and pH could discriminate the influence of the different electrodes used during the electrocoagulation treatment. Hence, their changes were verified by classifying the two electrodes used during the electrocoagulation treatment.

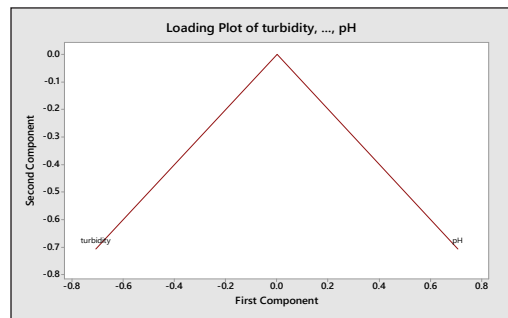
The PCA loading plot of the turbidity and pH is shown in Figure 3(b). The loading plot delivered information on the correlations among the turbidity and pH during the electrocoagulation treatment using nickel and copper electrodes. Based on Figure 3(b), the pH was loaded positively on PC1, whereas turbidity was loaded negatively on PC1 and PC2, respectively. Figure 3(c) shows the eigenvalues for each PC, which resulted in the scree plot. Figure 3(c) shows that the PC1 has an eigenvalue greater than 1. As a result, a straight line formed in the scree plot, in which only PC1 and PC2 were involved.

Kinetic Study of Changes in Turbidity and pH of Wastewater

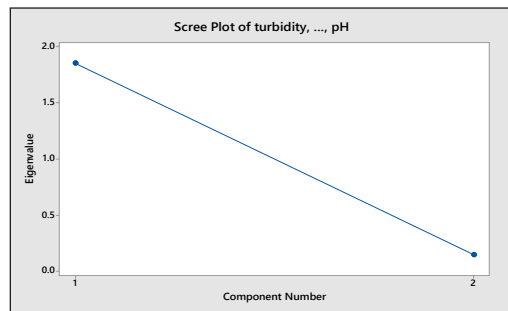
The kinetic parameters for the quality changes in wastewater for nickel and copper electrodes are indicated in Table 3. The turbidity of pepper wastewater agreed with the zero-order model based on the highest R^2 values (0.9457 and 0.9899 for nickel and copper electrodes, respectively) obtained compared to the values of the first and second-order kinetic models. The rate constant (k) value of the zero-order model for turbidity using nickel electrodes was 27.479 NTU min^{-1} , which indicated that the turbidity reduction of pepper wastewater occurred faster than copper electrodes during the electrocoagulation treatment (Table 3). For the pH of pepper wastewater, the second-order model had the highest R^2 values (0.9508 and 0.9657



(a)



(b)



(c)

Figure 3. The PCA graph of the turbidity and pH during the electrocoagulation treatment of pepper wastewater. (a) Score plot; (b) Loading plot; and (c) Scree plot

for nickel and copper electrodes, respectively) obtained compared to the values of the zero and first-order kinetic models. The k value of the second-order model for pH using copper electrodes was $0.0023 \text{ NTU}^{-1} \text{ min}^{-1}$, which indicated that the pH increment of pepper wastewater occurred slightly faster than nickel electrodes during the electrocoagulation treatment.

Table 3
Kinetics of the changes in turbidity and pH of pepper wastewater during the electrocoagulation treatment

Parameter	Type of electrodes	Zero-order model		First-order model		Second-order model	
		$k \text{ (NTU min}^{-1}\text{)}$	R^2	$k \text{ (min}^{-1}\text{)}$	R^2	$k \text{ (NTU}^{-1} \text{ min}^{-1}\text{)}$	R^2
Turbidity	Ni	27.479	0.9457	0.1350	0.9296	0.0018	0.6361
	Cu	24.931	0.9899	0.0655	0.9563	0.0002	0.7947
Parameter	Type of electrodes	Zero-order model		First-order model		Second-order model	
		$k \text{ (min}^{-1}\text{)}$	R^2	$k \text{ (min}^{-1}\text{)}$	R^2	$k \text{ (min}^{-1}\text{)}$	R^2
pH	Ni	0.0646	0.9301	0.0113	0.9417	0.0020	0.9508
	Cu	0.0802	0.9529	0.0678	0.9604	0.0023	0.9657

Note. Data are expressed Ni, nickel electrodes; Cu, copper electrodes; k , rate constant (min^{-1}); R^2 , coefficient.

CONCLUSION

The statistical analysis of the changes in turbidity and pH of wastewater showed significant differences ($p < 0.05$). Overall, nickel electrodes were the most affected in turbidity reduction (98.25%) by the treatment time compared to copper electrodes. Meanwhile, copper electrodes had the highest (31%) pH increment after the electrocoagulation treatment compared to nickel electrodes. The correlations indicated that the turbidity was highly negatively correlated with the pH of pepper wastewater for nickel and copper electrodes. PCA very precisely describes the correlation among the wastewater qualities in the study. Also, PCA supports the hypothesis of the study. Furthermore, a kinetic model that expressed the quality changes in wastewater is presented in this study. The wastewater quality changes in turbidity and pH during the electrocoagulation treatment were adequately expressed by zero, first and second-order kinetic models. The changes in turbidity and pH of pepper wastewater using electrocoagulation treatment were evaluated effectively. Electrocoagulation using nickel and copper electrodes is a practical method to treat wastewater from the retting process of pepper berries. The experimental data from this study is estimated to be significant for evaluating wastewater's turbidity and pH changes during the electrocoagulation treatment.

ACKNOWLEDGEMENT

The authors thank Universiti Putra Malaysia, Malaysia, for the financial and technical support while conducting this research. Also, we thank the 9th International Symposium

on Applied Engineering and Sciences 2021 (SAES2021) for giving this publication the opportunity and financial support.

REFERENCES

- Aziz, N. S., Sofian-Seng, N. S., Razali, N. S. M., Lim, S. J., & Mustapha, W. A. W. (2019). A review on conventional and biotechnological approaches in white pepper production. *Journal of the Science of Food and Agriculture*, 99(6), 2665-2676. <https://doi.org/10.1002/jsfa.9481>
- Azman, P. N. M. A., Shamsudin, R., Man, H. C., & Ya'acob, M. E. (2020). Kinetics of quality changes in soaking water during the retting process of pepper berries (*Piper nigrum* L.). *Processes*, 8(10), Article 1255. <https://doi.org/10.3390/pr8101255>
- Bakshi, A., Verma, A. K., & Dash, A. K. (2019). Electrocoagulation for removal of phosphate from aqueous solution: Statistical modeling and techno-economic study. *Journal of Cleaner Production*, 246, Article 118988. <https://doi.org/10.1016/j.jclepro.2019.118988>
- Che, H., Yun, C., Faezah, K., Mohammed, A., & Hazwan, M. (2020). Optimizing hydrogen production from the landfill leachate by electro-coagulation technique. *Journal of Agricultural and Food Engineering*, 1(3), 1-7. <https://doi.org/10.37865/jafe.2020.0020>
- Danial, R., Abdullah, L. C., & Sobri, S. (2017). Potential of copper electrodes in electrocoagulation process for glyphosate herbicide removal. *MATEC Web of Conferences*, 103, Article 06019. <https://doi.org/10.1051/mateconf/201710306019>
- Dura, A. (2013). *Electrocoagulation for Water Treatment: The Removal of Pollutants using Aluminium Alloys, Stainless Steels and Iron Anodes Table of Contents* (Master thesis). National University of Ireland Maynooth, Ireland. <https://www.proquest.com/docview/1535031150?pq-origsite=gscholar&fromopenview=true>
- Li, F., Shean, T., Choong, Y., Soltani, S., Chuah, L., Nurul, S., & Jamil, A. (2022). Kinetic study of fenton-like degradation of methylene blue in aqueous solution using calcium peroxide. *Pertanika Journal of Science & Technology*, 30(2), 1087-1102. <https://doi.org/10.47836/pjst.30.2.13>
- Liu, Y., Jiang, W., Yang, J., Li, Y., & Chen, M. (2017). Experimental study on evaluation and optimization of tilt angle of parallel-plate electrodes using electrocoagulation device for oily water demulsification. *Chemosphere*, 181, 142-149. <https://doi.org/10.1016/j.chemosphere.2017.03.141>
- Mandal, H. K. (2014). Influence of wastewater pH on turbidity. *International Journal of Environmental Research and Development*, 4(2), 2249-3131. <http://www.ripublication.com/ijerd.htm>
- Patil, H., & Dwivedi, A. (2020). Prediction of properties of the cement incorporated with nanoparticles by principal component analysis (PCA) and response surface regression (RSR). *Materials Today: Proceedings*, 43, 1358-1367. <https://doi.org/10.1016/j.matpr.2020.09.170>
- Rosnah, S., & Chan, S. (2014). Enzymatic rettings of green pepper berries for white pepper production. *International Food Research Journal*, 21(1), 237-245.
- Tharmalingam, M. A., Gunawardana, M., Mowjood, M. I. M., & Dharmasena, D. A. N. (2017). Coagulation-flocculation treatment of white pepper (*Piper nigrum* L.) processing wastewater. *Tropical Agricultural Research*, 28(4), 435-446. <https://doi.org/10.4038/tar.v28i4.8244>

Short Communication

The Digestibility and Bacterial Growth Rates of Microwave Treated Sago (*Metroxylon sagu*) Starch

Mohd Alhafizh Zailani^{1,2}, Hanisah Kamilah^{1,3}, Ahmad Husaini⁴, Awang Zulfikar Rizal Awang Seruji⁵ and Shahrul Razid Sarbini^{1,3*}

¹Department of Crop Science, Faculty of Agricultural Science and Forestry, Universiti Putra Malaysia Kampus Bintulu, 97008 UPM, Bintulu, Sarawak, Malaysia

²Centre for Pre-University Studies, Universiti Malaysia Sarawak, 94300 UNIMAS, Kota Samarahan, Sarawak, Malaysia

³Halal Products Research Institute, Universiti Putra Malaysia, 43400 UPM, Serdang, Selangor, Malaysia

⁴Department of Molecular Biology, Faculty of Resource Science and Technology, Universiti Malaysia Sarawak, 94300 UNIMAS, Kota Samarahan, Sarawak, Malaysia

⁵CRAUN Research Sdn. Bhd., Jalan Sultan Tengah, Petra Jaya, 93050 Kuching, Sarawak, Malaysia

ABSTRACT

Sago starch is rich in resistant starch (RS) but less utilised than other commercial starches. Hence, modification is essential to give an add-on value to the starch. Thus, the objective was to determine the influence of microwave heat treatment (MHT) on the digestibility and probiotic growth rates of sago starch. In this study, the starch was treated by MHT for durations of up to 20 min. The digestibility and bacterial growth rates increase as the treatment duration increases to 15 min. It implies the potential of the MHT in increasing the digestibility of the sago starch and improving its prebiotic property based on probiotic growth rates.

Keywords: Functional food, glycaemic, prebiotic, resistant starch, starch modification

ARTICLE INFO

Article history:

Received: 15 June 2022

Accepted: 11 October 2022

Published: 13 July 2023

DOI: <https://doi.org/10.47836/pjst.31.5.10>

E-mail addresses:

zmalhafizh@unimas.my (Mohd Alhafizh Zailani)

hanisahkamilah@upm.edu.my (Hanisah Kamilah)

haahmad@unimas.my (Ahmad Husaini)

azras1975@gmail.com (Awang Zulfikar Rizal Awang Seruji)

shahrulrazid@upm.edu.my (Shahrul Razid Sarbini)

* Corresponding author

INTRODUCTION

Sago starch is acquired from the wet milling of the *Metroxylon sagu* plant, a native of Southeast Asia (Zhu, 2019). Nowadays, this plant has been cultivated in various countries, including Malaysia (Achudan et al., 2020). A single pith of the sago palm can yield up to 82% of sago starch (Zhu, 2019). Nevertheless, this starch is underutilised

compared to potato and maize starches, which led to its modifications (Singh & Nath, 2012; Sondari, 2018). The modification is essential to improve the starch's physicochemical and functional food properties, adding value to the starch and increasing its utilisation.

Physical treatment is known for its simple and cost-effective elements among modification techniques. Among them, microwave heat treatment has been used widely for its heating efficiency and time-saving features. Microwave starch treatment has been performed on Bambara groundnut, corn, and potato starches (Oyeyinka et al., 2019; Wang et al., 2019). The microwave irradiation caused changes in the granules' surface of starch (Oyeyinka et al., 2019). Changes on the granule surface will impact starch's physicochemical, functionality, and digestibility due to the formation of pinholes, fractures, pores, or a destroyed granule structure.

Regarding digestibility, starch is categorised into rapidly digestible, slowly digestible, and resistant starch. Sago starch contains a high resistant starch content of up to 62% (Arshad et al., 2018). The slowly digestible and resistant starches are favoured in food formulations, contributing to their low glycaemic properties, which are valuable for diabetic patients (Chung et al., 2008). Moreover, resistant starch is linked to the prebiotic properties of starch. A prebiotic is a substance that can promote the growth of good gut bacteria and suppress pathogenic bacteria (Zaman & Sarbini, 2015). Prebiotics is digested by good gut bacteria such as *Lactobacillus* spp. and *Bifidobacterium* spp. producing by-products, short-chain fatty acids useful to the host's health. The resistant starch has mutual characteristics with the prebiotic, which can withstand digestion by the human digestive system and cannot be absorbed by the small intestine (Zaman & Sarbini, 2015). This statement was supported by an *in vivo* study in which resistant starch from maize flour was used; it displayed an increase in *Lactobacillus* bacteria while decreasing *Escherichia coli* (Khan et al., 2022). In another study, the resistant starch obtained from potato starch exhibited an increase in *Lactiplantibacillus plantarum* subsp. *plantarum* and butyric acid content (Wang et al., 2022). Meanwhile, previous studies on sago starch treated by enzymatic debranching followed by autoclaving, cooling and annealing have shown the highest *Lactobacillus* sp. count compared to control, fructo-oligosaccharide (Loo et al., 2010).

However, heating starch as a modification treatment reduces the resistant starch content (Chen et al., 2017). Lowering the resistant starch content may also lower the prebiotic properties of sago starch. Therefore, this study evaluated the effect of microwave heat treatment on digestibility and bacterial growth rates of sago starch.

MATERIALS AND METHODS

Materials

Food-grade native sago starch in the current study was obtained from CRAUN Research Sdn. Bhd., Kuching, Malaysia. The resistant starch assay kit was acquired from Megazyme,

Ireland, which is AOAC Method 2002.02 and AACC Method 32-40.01 complied. Chemicals used in the current study were purchased from a local supplier and were in analytical reagent grade. *Lactobacillus casei*, *Bifidobacterium lactis*, and *Escherichia coli* were acquired from the biology laboratory, Centre for Pre-University Studies, Universiti Malaysia Sarawak.

Modification of Sago Starch

The modification of native sago starch started with adjusting its moisture content by adding distilled water to 30%. The starch was sealed and maintained at 4 °C overnight. It was followed by the microwave heat treatment with a 20% power setting for 5, 10, 15, or 20 minutes using a microwave oven (EMO-2505, 900 W, ELBA). The treated starch was then oven-dried (Heraeus T12 oven, Thermo Scientific) at 50 °C overnight. The modified starches were labelled M5 (Microwave heat treatment for 5 minutes), M10 (Microwave heat treatment for 10 minutes), M15 (Microwave heat treatment for 15 minutes), and M20 (Microwave heat treatment for 20 minutes) and kept in a sealed airtight bag at ambient temperature away from direct sunlight and heat until further use (Zailani et al., 2021).

Resistant Starch Content

Determining resistant starch content in uncooked and cooked modified starches was performed using Megazyme Resistant Starch Assay Kit (K-RSTAR). The starch sample was used as it is for the uncooked sample. Meanwhile, for the cooked sample, the modified starch was cooked by boiling and cooled before digestion. The samples were digested using a mixture of amylase and amyloglucosidase in a shaking incubator (16 h, 37 °C, 200 strokes/min). Ethanol solution was added to wash and remove non-resistant starch, followed by centrifugation. The pellet obtained was mixed with potassium hydroxide in an ice bath and stirred continuously. Sodium acetate buffer (pH 3.8, 1.2 M) was added to the mixture, followed by amyloglucosidase solution (3,300 U/mL), with heating at 50 °C for 30 min. Glucose oxidase/peroxidase reagent was mixed with the sample mixture, and their absorbance was recorded at 510 nm using a UV-Vis spectrometer.

Bacterial Growth Rates

Meanwhile, Okolie et al. (2019) used a method to determine the bacterial growth rates of *Lactobacillus casei*, *Bifidobacterium lactis*, and *Escherichia coli*. The bacteria were cultured in a De Man, Rogosa and Sharpe (MRS) broth for 24–48 h in an incubator at 37 °C. The culture was streaked onto a sterilised MRS agar and incubated overnight. A single bacteria colony was transferred into MRS broth and incubated for 24–48 h. Prior

to use, the optical density of the bacteria was adjusted to 1.0 at a wavelength of 620 nm using a UV-Vis spectrometer. This study was performed on resistant starch fractions of uncooked and cooked samples. The sample preparation followed the digestion process as the determination of resistant starch. The sample was mixed into a sterilised MRS broth to a concentration of 0.1 and 0.5% w/v. Positive and negative controls were inulin and glucose, respectively, and prepared at 0.1 and 0.5% w/v of concentration. Aliquots of 200 μ L of samples and controls were placed into a 96-well plate separately. 7.5 μ L of bacterium culture was added and sealed with parafilm in each well. Incubation of the plate was conducted at 37 °C for 24 h. The optical density at 620 nm was measured every 30 min using a microplate reader. Graphs were plotted to determine the bacterial growth rates as described by Okolie et al. (2019).

Statistical Analysis

One-way ANOVA was used to analyse the data, which was then analysed by Tukey's test (Zailani et al., 2021). Meanwhile, a correlation study was performed using Pearson's Correlation. The significant level was set at 0.05. Statistical Package for Social Sciences (IBM® SPSS® Statistics Version 20) was used for the statistical analyses.

RESULTS AND DISCUSSION

The starch treated by microwave heating with different treatment duration displayed a decrease in the resistant starch content (Figure 1). A strong negative correlation ($r = -0.748$, $p = 0.033$) between the resistant starch content and treatment duration was observed for the uncooked samples. The decline in the resistant starch content may be caused by the formation of pinholes, cracks, and rough granule surfaces (Oyeyinka et al., 2019). These disruptions in the starch granule structure permitted the digestion enzymes to access the internal structure of the granules resulting in the digestion of the starch (Li et al., 2020). Among the modified starches, M5 had the highest resistant starch content. The short treatment duration might have had a low impact on the granule structure and retaining parts resistant to digestion. Meanwhile, the resistant starch contents were drastically lower for the cooked samples compared to the uncooked counterparts. No significant difference was observed between the

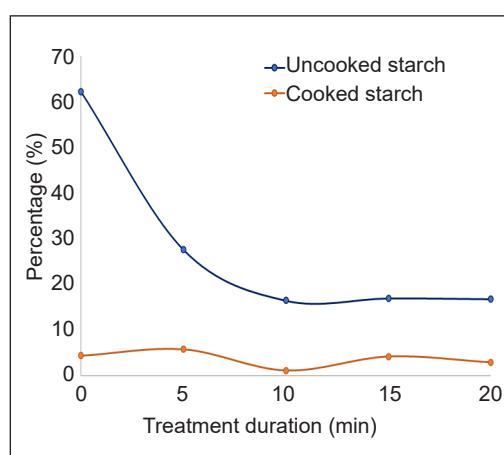


Figure 1. The resistant starch content of sago starches against microwave treatment duration

cooked sample content of resistant starch. Cooking the starch destroyed the granule's structure by undergoing gelatinisation. As the sago starch has a gelatinisation temperature of around 79 °C, this process was possible during the preparation of cooked starch samples (Ying et al., 2020). The gelatinisation process caused the leaching of amylose and low molecular weight amylopectin chains (Li et al., 2020; Fan et al., 2019). It causes the components to be susceptible to enzymatic digestion, lowering the resistant starch content.

Meanwhile, the bacterial growth rates of starches at different treatment duration were lower than the positive standard used, inulin. However, the resistant starch samples showed an interesting pattern of growth rates as the treatment duration increased. The resistant starch of cooked samples with a treatment duration of 15 minutes showed the highest bacterial growth rates among the cooked samples. The growth rates of uncooked resistant starch samples showed a decreasing pattern against treatment duration, as seen in correlation for *B. lactis* ($r = -0.841$, $p = 0.001$) and *E. coli* ($r = -0.814$, $p = 0.001$) (Figure 2). It is possibly linked to the formation of double helices between

amylose molecules, which were produced by the breakage of α -(1,6)- and α -(1,4)-glycosidic bonding and with amylopectin molecules (Yang et al., 2017). These double helices form during the cooling and storage of the sample, where the retrogradation process occurs. The double helix structure may limit the bacteria's fermentation of the starch components. Meanwhile, moderate positive correlations between cooked resistant starch samples and treatment durations were observed for *L. casei* ($r = 0.600$, $p = 0.039$) and *B. lactis* ($r = 0.583$, $p = 0.047$) growth rates. The cooked RS of M10 (*L. casei*) and M15 (*L. casei* and *B. lactis*) exhibited higher growth rates than the native starch. Probably

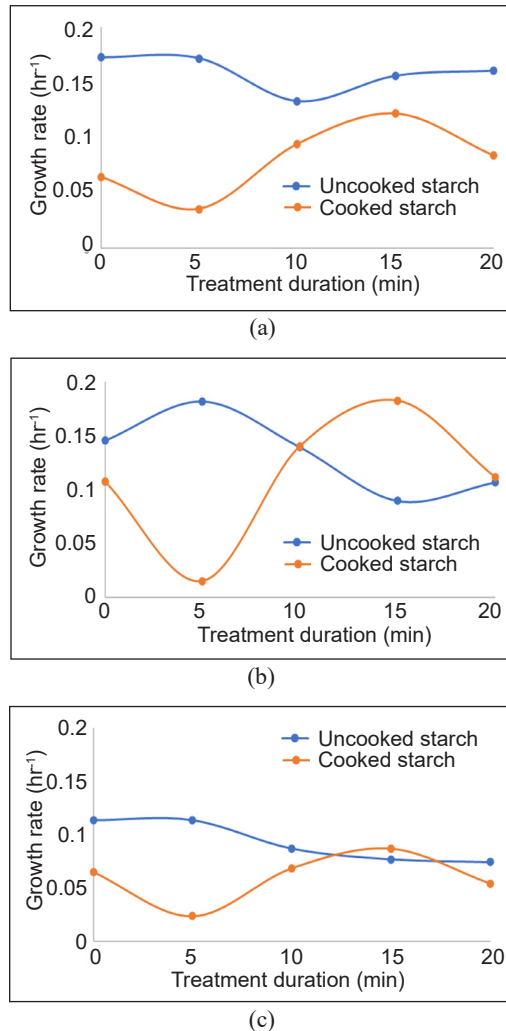


Figure 2. (a) *Lactobacillus casei*, (b) *Bifidobacterium lactis* and (c) *Escherichia coli* growth rates for uncooked and cooked resistant starch samples of microwave-treated sago starch

cooking the sample reduces the mixture's complexity and enables bacteria's fermentation of the components. Meanwhile, M5 cooked resistant starch had its bacterial growth rates decreased, which may be associated with the short treatment duration, which reduces the chances of reducing the entanglement of its complex mixture. Slight changes were seen in uncooked resistant starch of M10 (*L. casei*), M15 (*E. coli*), and M20 (*E. coli*) bacterial growth rates compared to the native starch.

CONCLUSION

In conclusion, the microwave heat treatment with different treatment duration on sago starch changes its digestibility by digestive enzymes and fermentation by tested bacteria. The treatment causes a decrease in the resistant starch fractions by changing the starch granules' structure. An increase in the treatment duration influences the amount of resistant starch in each sample, linked to a higher number of pinholes and pores on the surface of the granules. Additionally, the treatment also improves the growth rates of *L. casei* and *B. lactis* for cooked-resistant starch samples. It suggests that the microwave heat treatment can enhance the digestibility and prebiotic property of the sago starch, especially for the cooked samples.

ACKNOWLEDGEMENT

The authors thank Sarawak Research and Development Council, Kuching, Malaysia for their financial support *via* a Catalyst research grant (RDCRG/CAT/2019/26). The authors also thank the Ministry of Higher Education Malaysia for providing a scholarship to a PhD candidate.

REFERENCES

- Achudan, S. N., Mohamed, A. M., Rashid, R. S., & Mittis, P. (2020). Yield and physicochemical properties of starch at different sago palm stages. *Materials Today: Proceedings*, 31, 122-126. <https://doi.org/10.1016/j.matpr.2020.01.341>
- Arshad, N., Zaman, S., Rawi, M., & Sarbini, S. (2018). Resistant starch evaluation and *in vitro* fermentation of *lemantak* (native sago starch), for prebiotic assessment. *International Food Research Journal*, 25(3), 951-957.
- Chen, Y., Yang, Q., Xu, X., Qi, L., Donga, Z., Luo, Z., Lu, X., & Peng, X. (2017). Structural changes of waxy and normal maize starches modified by heat moisture treatment and their relationship with starch digestibility. *Carbohydrate Polymers*, 177, 232-240. <https://doi.org/10.1016/j.carbpol.2017.08.121>
- Chung, H. J., Shin, D. H., & Lim, S. T. (2008). *In vitro* starch digestibility and estimated glycemic index of chemically modified corn starch. *Food Research International*, 41, 579-585. <https://doi.org/10.1016/j.foodres.2008.04.006>
- Fan, M., Huang, Q., Zhong, S., Li, X., Xiong, S., Xie, J., Yin, T., Zhang, B., & Zhao, S. (2019). Gel properties of myofibrillar protein as affected by gelatinization and retrogradation behaviours of modified starches with

- different crosslinking and acetylation degree. *Food Hydrocolloids*, *96*, 604-616. <https://doi.org/10.1016/j.foodhyd.2019.05.045>
- Khan, A., Ali, H., Rehman, U. U., Belduz, A. O., Bibi, A., Abdurahman, M. A., Shah, A. A., Badshah, M., Hasan, F., Kilic, A. O., Ullah, A., Jahan, S., Ur Rehman, M. M., Mansoor, R., & Khan, S. (2022). Prebiotic potential of enzymatically prepared resistant starch in reshaping gut microbiota and their respond to body physiology. *Plos One*, *17*(5), Article e0267318. <https://doi.org/10.1371/journal.pone.0267318>
- Li, H., Wang, R., Liu, J., Zhang, Q., Li, G., Shan, Y., & Ding, S. (2020). Effects of heat-moisture and acid treatments on the structural, physicochemical, and *in vitro* digestibility properties of lily starch. *International Journal of Biological Macromolecules*, *148*, 956-968. <https://doi.org/10.1016/j.ijbiomac.2020.01.181>
- Loo, S. W., Tan, Z. N., Karim, A. A., Hani, N. M., & Rosma, A. (2010). Fermentation of *Metroxylon sagu* resistant starch type III by *Lactobacillus* sp. and *Bifidobacterium bifidum*. *Journal of Agricultural and Food Chemistry*, *58*(4), 2274-2278. <https://doi.org/10.1021/jf903820s>
- Okolie, C. L., Mason, B., Mohan, A., Pitts, N., & Udenigwe, C. C. (2019). The comparative influence of novel extraction technologies on *in vitro* prebiotic-inducing chemical properties of fucoidan extracts from *Ascophyllum nodosum*. *Food Hydrocolloids*, *90*, 462-471. <https://doi.org/10.1016/j.foodhyd.2018.12.053>
- Oyeyinka, S. A., Umaru, E., Olatunde, S. J., & Joseph, J. K. (2019). Effect of short microwave heating time in the physicochemical and functional properties of Bambara groundnut starch. *Food Bioscience*, *28*, 36-41. <https://doi.org/10.1016/j.fbio.2019.01.005>
- Singh, A. V., & Nath, L. K. (2012). Synthesis and evaluation of physicochemical properties of cross-linked sago starch. *International Journal of Biological Macromolecules*, *50*, 14-18. <https://doi.org/10.1016/j.ijbiomac.2011.09.003>
- Sondari, D. (2018). Modification of sago starch for edible coating. *IOP Conference Series: Materials Science and Engineering*, *543*, Article 012013. <https://doi.org/10.1088/1757-899X/543/1/012013>
- Wang, M., Chen, X., Zhou, L., Li, Y., Yang, J., Ji, N., Xiong, L., & Sun, Q. (2022). Prebiotic effects of resistant starch nanoparticles on growth and proliferation of the probiotic *Lactiplantibacillus plantarum* subsp. *plantarum*. *LWT - Food Science and Technology*, *154*, Article 112572. <https://doi.org/10.1016/j.lwt.2021.112572>
- Wang, M., Sun, M., Zhang, Y., Chen, Y., Wu, Y., & Ouyang, J. (2019). Effect of microwave irradiation-retrogradation treatment on the digestive and physicochemical properties of starches with different crystallinity. *Food Chemistry*, *298*, Article 125015. <https://doi.org/10.1016/j.foodchem.2019.125015>
- Yang, Q., Qi, L., Luo, Z., Kong, X., Xiao, Z., Wang, P., & Peng, X. (2017). Effect of microwave irradiation on internal molecular structure and physical properties of waxy maize starch. *Food Hydrocolloids*, *69*, 473-482. <https://doi.org/10.1016/j.foodhyd.2017.03.011>
- Ying, B. Z., Kamilah, H., Karim, A. A., & Utra, U. (2020). Effects of heat-moisture and alkali treatment on the enzymatic hydrolysis of porous sago (*Metroxylon sagu*) starch. *Journal of Food Processing and Preservation*, *44*(5), Article e14419. <https://doi.org/10.1111/jfpp.14419>

- Zailani, M. A., Kamilah, H., Husaini, A., & Sarbini, S. R. (2021). Physicochemical properties of microwave heated sago (*Metroxylon sago*) starch. *CyTA - Journal of Food*, *19*(1), 596-605. <https://doi.org/10.1080/19476337.2021.1934550>
- Zaman, S. A., & Sarbini, S. R. (2015). The potential of resistant starch as prebiotic. *Critical Reviews in Biotechnology*, *36*(3), 578-584. <https://doi.org/10.3109/07388551.2014.993590>
- Zhu, F. (2019). Recent advances in modifications and applications of sago starch. *Food Hydrocolloids*, *96*, 412-423. <https://doi.org/10.1016/j.foodhyd.2019.05.035>

Effects of Microwave Power and Carrier Materials on Anthocyanins, Antioxidants, and Total Phenolic Content of Encapsulated *Clitoria ternatea* Flower Extract

Nurul Asyikin Md Zaki^{1,2*}, Junaidah Jai¹, Mohd Hakim Syuwari Hasan¹, Nur Qistina Mohamad Kamarul Azman¹, Syafiza Abd Hashib¹, Nozieana Khairuddin³, Norashikin Mat Zain⁴ and Nurul Hidayah Samsulrizal⁵

¹School of Chemical Engineering, College of Engineering, Universiti Teknologi MARA, 40450 UiTM, Shah Alam, Selangor, Malaysia

²Food Process Engineering Research Group, Universiti Teknologi MARA, 40450 UiTM, Shah Alam, Selangor, Malaysia

³Department of Science and Technology, Faculty of Humanities, Management and Science, Universiti Putra Malaysia, Bintulu Sarawak Campus, 97008 UPMKB, Bintulu, Malaysia

⁴Faculty of Chemical and Process Engineering Technology, College of Engineering Technology, Universiti Malaysia Pahang, 26300 UMP, Kuantan, Pahang, Malaysia

⁵Department of Plant Science, Kulliyah of Science, International Islamic University Malaysia, 25200 IIUM, Kuantan, Pahang, Malaysia

ABSTRACT

Clitoria ternatea, also famously known as the blue pea flower (local name: *bunga telang*), has attracted interest among researchers due to its plethora of biological and pharmacological properties. It is rich in anthocyanin and widely used as a natural food colourant. However, the poor stability of active compounds may affect the therapeutic benefits and limit their application in the pharmaceutical and food industries. Hence, this work aims to study

the effects of microwave encapsulation on the anthocyanins, antioxidants, and total phenolic content of *Clitoria ternatea* flower extract (CTFE). Microwave-assisted encapsulation (MAEC) was carried out at three different powers (300, 450, and 600 W) with different formulations of Gum Arabic (GA) and Maltodextrin Dextrose (MD) as carrier materials from 40% to 70% w/v. The total phenolic content (TPC), antioxidant activity, and anthocyanins in encapsulates were analysed for the formulations. The

ARTICLE INFO

Article history:

Received: 20 June 2022

Accepted: 25 January 2023

Published: 13 July 2023

DOI: <https://doi.org/10.47836/pjst.31.5.11>

E-mail addresses:

asyikin6760@uitm.edu.my (Nurul Asyikin Md Zaki)

junejai@uitm.edu.my (Junaidah Jai)

hakim25syuwari@gmail.com (Mohd Hakim Syuwari Hasan)

nqistinaa72@gmail.com (Nur Qistina Mohamad Kamarul Azman)

syafiza0358@uitm.edu.my (Syafiza Abd Hashib)

nozieana@upm.edu.my (Nozieana Khairuddin)

shikin@ump.edu.my (Norashikin Mat Zain)

hidayahsamsulrizal@iiium.edu.my (Nurul Hidayah Samsulrizal)

* Corresponding author

findings showed that increased microwave power increased TPC and antioxidant activity ($P < 0.05$). However, adding carrier materials concentration above 60% reduced TPC and the antioxidant activity of microwave-encapsulated anthocyanin from CTFE. The best microwave-assisted encapsulation conditions of CTFE were found at 600 W microwave power with 50% w/v carrier materials GA/MD (ratio 1:1) concentration. The retention of anthocyanins, antioxidant activity, and TPC increased significantly ($P < 0.05$) with increased microwave power and lower concentration of carrier materials. The MAEC approach to enhance the stability of anthocyanin in CTFE presents a high potential to expand its application as a high-value-added natural colourant.

Keywords: Active compounds, anthocyanins, blue pea flower, microwave encapsulation, total phenolic content

INTRODUCTION

Clitoria ternatea, or the blue pea flower, is popular as a colourant for food and delicacies. Additionally, the *Clitoria ternatea* flower has been widely used in traditional medicine, particularly as a supplement to enhance cognitive functions and alleviate symptoms of numerous ailments, including fever, inflammation, pain, and diabetes (Mukherjee et al., 2008). The blue pea flower is very popular among traditional Chinese and Ayurvedic medicine and has been consumed for centuries as a memory enhancer, brain booster, anti-stress and insomnia (Anthika et al., 2015; Salleh & Pa'ee, 2021; Mukherjee et al., 2008; Verma et al., 2013). The major phytoconstituents found in extracts from *Clitoria ternatea* flowers are pentacyclic triterpenoids such as taraxerol and taraxerone (Swathi et al., 2021). Furthermore, various phytochemicals such as kaempferol, quercetin, myricetin glycosides, and anthocyanins have been successfully isolated from *Clitoria ternatea* flowers (Jeyaraj et al., 2021). Thus, *Clitoria ternatea* flower extract (CTFE) has the potential to be used for functional food applications due to its plethora of biological and pharmacological properties.

The stability of polyphenols from CTFE has been reported to be very poor, especially in the human gastrointestinal tract. Therefore, it is important to develop a protective method to increase the stability of polyphenols and investigate their encapsulation under simulated gastrointestinal conditions. Microencapsulation of polyphenols from *Clitoria ternatea* flower petals using calcium alginate found that polyphenol degradation has been successfully reduced, while the biological activity increased after gastrointestinal digestion (Pasukamonset et al., 2016). According to Bringas-Lantigua (2011), encapsulation of CTFE may enhance the bioavailability of antioxidants and anthocyanins in the extracts. It is often used to protect the natural plant extract pigments from degradation and, thus, extend the shelf-life of these active compounds. Encapsulation is important and relevant in food and pharmaceutical industries as it protects food ingredients sensitive to degradation,

denaturation, and loss of volatile compounds. There are many encapsulation techniques, such as coacervation, spray drying, nanoencapsulation, microencapsulation, and microwave encapsulation.

Among the encapsulation techniques, microwave-assisted encapsulation is an alternative technology that uses microwave radiation to stimulate molecular motion and a constant dipole to rotate the molecules to generate volumetric heating. Time and energy consumption can be reduced significantly during microwave treatment due to its uniform heat distribution onto the material surfaces. Microwave technology is considered an economical method of preserving plant extract, as this method provides quality for the final product, is easy to operate, and could reduce water activity in the final products. Furthermore, the microwave-assisted technique has excelled in encapsulating natural colourants from dragon fruit (Zaidel et al., 2015), purple sweet potatoes (Nawi et al., 2015), as well as from hibiscus, lavender, and blackberry (Perez-Grijalva et al., 2018). The advantages of encapsulation via microwave technology are enhancement of antimicrobial activity, prolonged effects, and stability improvement towards the encapsulated plant extracts. However, the microwave technique is not widely used as there are still limited references on the microwave-assisted encapsulation (MAEC) process. Hence, this work aimed to evaluate the effects of microwave encapsulation on the anthocyanins, antioxidants, and total phenolic content of *Clitoria ternatea* flower extract.

METHODOLOGY

Materials

The dried blue pea flower was purchased from a local supplier around Klang Valley, Malaysia. Distilled water, maltodextrin, Gum Arabic, ethanol, hydrochloride acid, sodium hydroxide, potassium chloride, sodium acetate buffer, Folin-Ciocalteu phenol reagents, gallic acid, and sodium carbonate solution were purchased from Sigma Aldrich (USA).

Preparation of *Clitoria ternatea* Flower Extract

Clitoria ternatea flower was extracted by weighing 5 g each before being diluted in 100 ml of water (1:20) for 5 min and undergoing extraction. The extraction process was conducted using microwave-assisted extraction at 600 W power for 2 min. The *Clitoria ternatea* flower extract (CTFE) was then centrifuged at 7000 rpm for 15 min and ready to be further encapsulated using the microwave.

Microwave-Assisted Encapsulation of *Clitoria ternatea* Flower Extract

The carrier materials were mixed and diluted with water at various concentrations (40%, 50%, 60% and 70%) of Arabic Gum (GA) and Maltodextrin Dextrose (MD). The carrier

materials, GA and MD (1:1), were mixed with extracted sample (1:5) in the beaker and stirred for 20 min. The sample was then encapsulated in the microwave using the microwave-assisted encapsulation (MAEC) method using three power levels (300 W, 450 W, and 600 W) for 7 to 10 min until powder forms. The MAEC method was modified by Marsin et al. (2020).

Analysis of Total Phenolic Content

The total phenolic content (TPC) was measured using the Folin-Ciocalteu method modified by Bei et al. (2018), in which 1 ml of extract was mixed with 0.5 ml of Folin-Ciocalteu reagent. After 5 min being kept in the dark at 26°C, 1 ml of sodium carbonate was added with 9 ml of distilled water. The absorbance was measured at 760 nm after 30 min incubation period in the dark. The results were expressed in mg of Gallic Acid Equivalent (GAE)/g of dry weight sample of BPF (mg GAE/g). All samples were analysed in triplicates. The formula of TPC is shown in Equation 1:

$$\text{TPC} = C \times \frac{v}{m} \quad (1)$$

where C is the rate constant, v is the pre-exponential factor, and m is the activation energy.

Analysis of Total Anthocyanin Content

The anthocyanin was measured using a pH differential method using a potassium chloride with pH 1.0 and a sodium acetate buffer with pH 4.5 (Nawi et al., 2015). An amount of 1 ml of extract was mixed with 9 ml of each buffer to produce 10 ml of solution, which was then incubated at 37°C for 15 to 60 min. All the experiments were carried out in triplicates. Both the solutions were measured at 520 nm and 700 nm, and the absorbance (A) and total anthocyanin were calculated using Equations 2 and 3:

$$A = (A_{520nm} - A_{700nm})_{pH1} - (A_{520nm} - A_{700nm})_{pH4.5} \quad (2)$$

$$\text{TAC} = \frac{A \times \text{MW} \times \text{DF} \times 1000}{\epsilon \times 1} \quad (3)$$

where: A is the absorbance at a specified wavelength, MW is the molecular weight for cyanidin-3-glucoside (449.2 g/mol), DF is the dilution factor, and $\epsilon = 26,900$ molar extinction coefficients in L/mol/cm.

Determination of Antioxidant Activity

The CTFE antioxidant scavenging activity was measured using 2,2'-diphenyl-1-picrylhydrazyl radical (DPPH) following procedures of Alwi et al. (2017) with some

modifications. First, an amount of 1 ml extract was mixed with 1 ml of DPPH solution and 4 ml of 80% ethanol and incubated at 37°C for 30 min. All the experiments were carried out in triplicates. The absorbance was measured at 501 nm, and DPPH inhibition was determined using Equation 4:

$$\text{Inhibition (\%)} = \frac{A_0 - A_1}{A_0} \times 100\% \quad (4)$$

where: A_0 is the absorbance of the control solution (DPPH and ethanol solution without the CTFE sample), and A_1 is the absorbance of the sample.

Statistical Analysis

Statistical analysis was performed using Microsoft® Excel® for Microsoft 365 MSO (Version 2208 Build 16.0.15601.20072). A one-way analysis of variance (ANOVA) followed by a post hoc t-test was carried out to determine the statistical differences between encapsulated CTFE for each tested parameter. The significance level used was 0.05.

RESULTS AND DISCUSSION

Total Phenolic Content of Encapsulated CTFE

Figure 1 shows the total phenolic content (TPC) of encapsulated CTFE with different concentrations of carrier materials at various microwave powers. The results found a significant influence of GA/MD concentration on the total phenolic content ($P < 0.05$). The TPC increased gradually as the microwave power increased from 300 W to 600 W. However, at 50% GA/MD concentration, TPC showed no significant difference from 300 to 600 W. The highest TPC was obtained at 600 W and 40% concentration, which was 780 mg GAE/g. At high power, the microwave can speed up the encapsulation process.

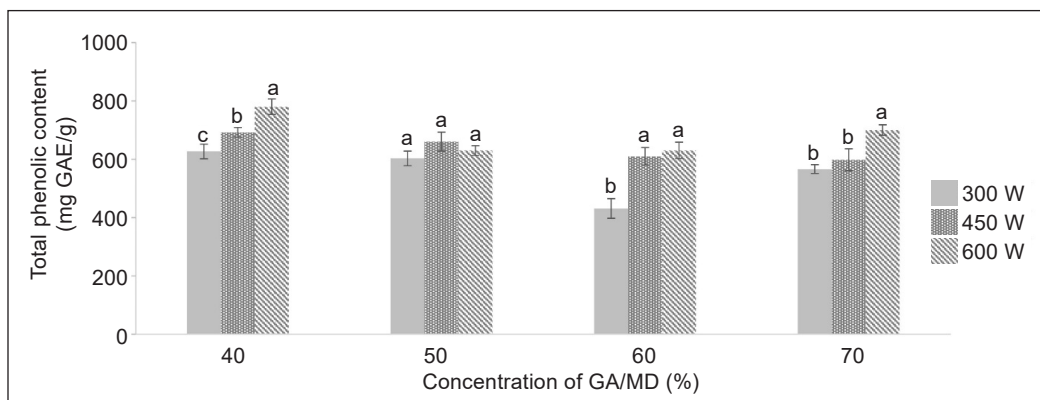


Figure 1. Total phenolic content of encapsulated CTFE at a microwave power of 300 W, 450 W, 600 W and GA/MD 40%, 50%, 60%, and 70% concentration. Bars with different letters indicate significant differences in microwave power within the same GA/MD concentration ($P < 0.05$).

Thus, the targeted bioactive compounds can be protected from heat exposure for a long time. However, it can also cause the decomposition of certain molecules and damage the bioactive compounds due to heat generated by the high power. For the comparison of the extract samples before and after encapsulation, it was observed that the TPC amount after encapsulation was higher compared to the number of fresh extracts. The encapsulation process exposed the extracts to microwave radiation, thus, increasing the temperature of the materials and the exposure to heat caused damage to the bioactive compounds. It was also reported that plant phenols could degrade at high temperatures during the encapsulation or extraction process (Sulaiman et al., 2017).

The amount of TPC decreased significantly ($P < 0.05$) as the carrier materials concentration increased. The decreasing pattern of TPC against the carrier material concentration was observed at a microwave power of 450 W. The coating agent protects the phenol compounds from degradation at constant microwave power. MD, as a polymeric coat, could assist in retaining bioactive compounds in the encapsulated extract (Sablania & Bosco, 2018). Besides, the encapsulation technique involves a defensive mechanism of the wall membrane that covers the particles of the encapsulated material to ensure that no active ingredients or phenolic compounds leak from the carrier materials (Mozafari, 2008). However, the TPC of CTFE with 40% GA/MD was the highest, although it contained the lowest carrier materials. It might be attributed to the accumulation and sedimentation of gum arabic in the suspension with a higher concentration of GA/MD prior to MAEC. The phenomenon could lead to reduced GA/MD in the sample and result in less encapsulation of TPC. This finding was similar to the encapsulation of isoflavone with milk, maltodextrin, and gum acacia (Mazumder & Ranganathan, 2020). Several factors could affect encapsulation, such as the chemical properties of carrier materials and extracts, emulsion characters, and encapsulation parameters.

Total Anthocyanin Content of Encapsulated CTFE

The total anthocyanin content (TAC) of encapsulated CTFE with a 40% concentration of GA/MD at various microwave powers is shown in Figure 2. This condition was chosen based on the highest TPC obtained during the MAEC. The highest TAC was obtained when the encapsulation was performed using 600 W at 7 min encapsulation time. It was observed that the amount of TAC increased as the microwave power increased

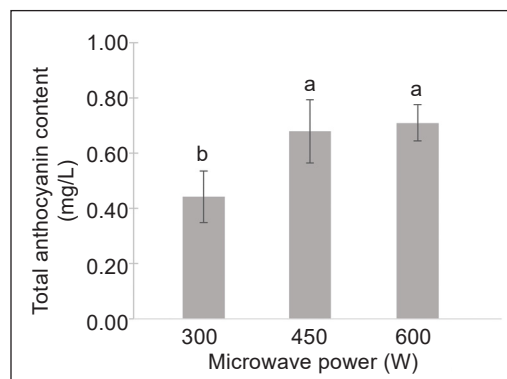


Figure 2. Total anthocyanin content of encapsulated CTFE with 40% concentration of GA/MD at microwave powers of 300 W, 450 W, and 600 W ($P < 0.05$)

for the encapsulation of CTFE with a 40% concentration of GA/MD. Low microwave power resulted in longer encapsulation time due to low heat generated throughout the process. Thus, anthocyanins monomeric may decompose during this long encapsulation time (Marsin et al., 2020).

Figure 3 shows the TAC of encapsulated CTFE with different concentrations of carrier materials at 600 W microwave power. The results found a significant effect of GA/MD concentration on TAC values

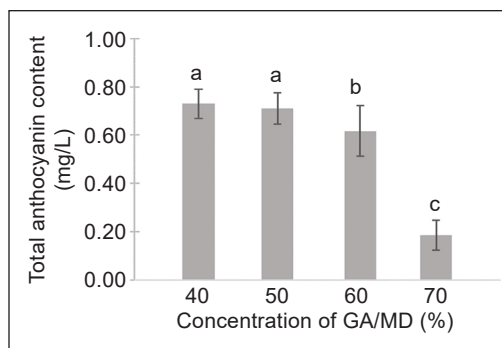


Figure 3. Total anthocyanin content of encapsulated CTFE with different concentrations of GA/MD at 600 W ($P < 0.05$)

on the encapsulated CTFE ($P < 0.05$). In this study, based on the overall TAC obtained at various concentrations and microwave power, the highest TAC was obtained when the CTFE was encapsulated with 40% GA/MD (0.73 ± 0.06). This finding could be attributed to using GA/MD as the carrier material that covers and protects the extracted compounds from the environment. Encapsulation reduces the core reactivity of the environmental factors and the transmission rate of the core material to the outside environment by forming a physical barrier between the core compound and the other external compound of the product (Jyothi et al., 2010). Nonetheless, TAC was reduced when the GA/MD was increased. An increase in GA/MD concentration decreased the total anthocyanin content in blue pea powder due to adding dried solids to the mixture (Hariadi, 2018). The ratio of carrier materials to the CTFE increased, thus, possibly causing the accumulation and sedimentation of the carrier materials in the suspension with a higher concentration of GA/MD. It affected the protective characteristic of anthocyanin and necessarily decreased its content.

The TAC of the initial extract was 0.9184 mg/L. The encapsulation resulted in a huge loss of anthocyanins from the initial extract due to the heat exposure to CTFE during MAEC. However, the encapsulation of CTFE is important to protect the anthocyanins from degradation during storage. Factors such as storage with access to light and air did not cause significant degradation of anthocyanins in encapsulated samples due to efficient coating by carrier materials (Pieczycolan & Kurek, 2019). Furthermore, the degradation of anthocyanins occurs on the surface, and the encapsulated extract is adequately protected against the transfer of oxygen through the density of the matrix and the distance from the degradation factor (Tonon et al., 2010).

Antioxidant Activity of Encapsulated CTFE

Figure 4 shows the percentage of inhibition demonstrated by encapsulated CTFE at various microwave power for encapsulation with a 40% concentration of GA/MD. The highest

inhibition was exhibited by encapsulated CTFE at 600 W, which accounted for 78%. The lowest inhibition was observed as 70% at 300 W. These findings demonstrated that using the microwave to encapsulate CTFE can retain most of the antioxidant activity. Therefore, the antioxidant activity of CTFE peaks at a microwave power of 600 W. However, when it reaches the optimum condition, the value decreases or becomes negligible up to a certain point due to exposure to a higher temperature. A study on the antioxidant activity of dried ginger reported an increase in microwave power of 0.6 W/g–0.9 W/g. However, it decreased when the microwave power was further increased to 1.2 W/g, which may be related to the degradation of active substances under high microwave power (Zeng et al., 2023).

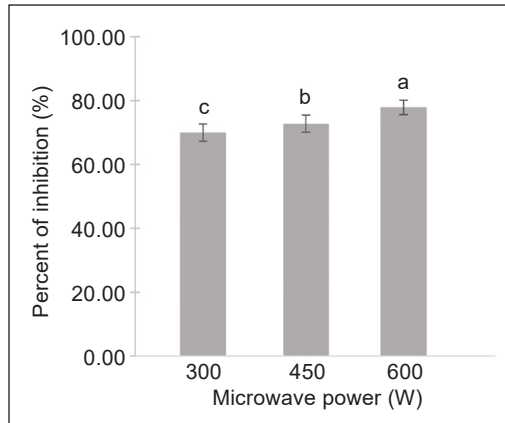


Figure 4. Antioxidant activity of CTFE encapsulated with 40% concentration of GA/MD at microwave powers of 300 W, 450 W, and 600 W ($P < 0.05$)

High microwave power results in a faster encapsulation and may retain higher antioxidants than low microwave power (Marsin et al., 2020). The encapsulation rate may be lower due to low microwave power. It will affect the encapsulation efficiency of the end product. The heat penetration will also be low, thus causing longer encapsulation time; prolonged exposure to heat during the encapsulation process results in the degradation of antioxidants. However, a single microwave process may also cause non-uniform heating and a low penetration rate of microwave energy (Ng et al., 2020).

The encapsulation process might affect the polyphenol activity of the extract, which in turn affects the antioxidant activity. It was found that MAEC provided high retention of antioxidant activity, which might be due to the shorter time at a lower temperature process, which reduced the degradation of phenolic compounds (Parthasarathi et al., 2013). Furthermore, polyphenols extracted from apple pomace and fermented apples using microwave-assisted extraction at 60°C obtained higher antioxidant activity than samples extracted at different temperatures (30, 40, 50, 70, and 80°C) (Ajila et al., 2011).

Encapsulation Efficiency of Encapsulated CTFE

Figure 5 shows the encapsulation efficiency of encapsulated CTFE with various concentrations of GA/MD at 600 W. The best encapsulation efficiency was 40% and 50% of GA/MD concentrations at 600 W microwave power, with 76% and 78% values, respectively. This percentage is high enough to confirm that GA/MD is an appropriate combination for carrier material encapsulating CTFE. The encapsulation efficiency of

Clitoria ternatea flowers is 60.22%, 63.38% and 95.74% for ultrasonic spray drying (outlet temperature 100°C), convection oven drying (80°C), and freeze-drying (-80°C), respectively (Liew et al., 2020). The encapsulation was unstable above 50% concentration of carrier materials. Therefore, the encapsulation efficiency decreased when encapsulation was done with carrier materials above 50% concentration (Marsin et al., 2020) which might be due to the accumulation and sedimentation of excess carrier materials in the suspension because the solubility of arabic gum is 43–48% in water. It shows that the encapsulation has reached saturation at 50% concentration of GA/MD and limits its capacity.

The higher encapsulation efficiency can be attributed to the electrostatic ionic interaction between magnesium and potassium cations in gum arabic polysaccharides. A similar study on the encapsulation of anthocyanin from *Syzygium cumini* found that arabic gum provided higher encapsulation efficiency than chitosan, maltodextrin, and sodium alginate (Abdin et al., 2021). Arabic gum forms a dry coating around the core material, preventing contact between the core material and air, whereas maltodextrin develops an amorphous glass structure during encapsulation (Yadav et al., 2020).

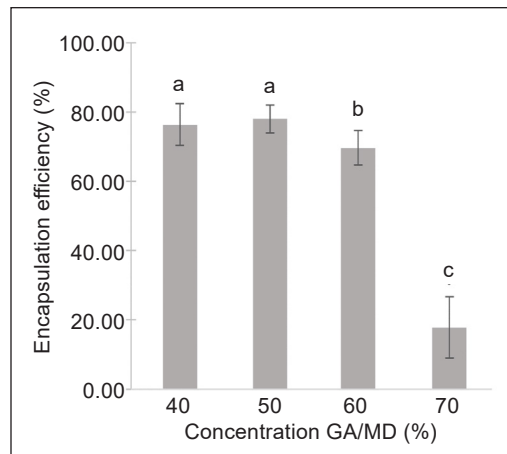


Figure 5. Encapsulation efficiency of CTFE encapsulated with 40%, 50%, 60%, and 70% concentrations of GA/MD at 600 W ($P < 0.05$)

CONCLUSION

In conclusion, the best concentration of carrier materials for encapsulating CTFE with arabic gum and maltodextrin dextrose is 50%, which provides higher encapsulation efficiency, shorter time, and stable preservation of bioactive compounds. Based on the findings, the optimum condition for encapsulation efficiency was achieved at 600 W of microwave power and 50% of GA/MD concentration. Microwave power, exposure time, and concentration of carrier materials significantly affect the retaining of anthocyanins, antioxidants and total phenolic content of *Clitoria ternatea* flower extract. Anthocyanin retention increases with microwave power and lower concentration of carrier materials. Therefore, the microwave-assisted encapsulation approach to enhance the stability of anthocyanin in CTFE presents a high potential to expand its application as a high-value-added natural colourant.

ACKNOWLEDGEMENTS

This work was financially supported by Universiti Teknologi MARA, Shah Alam, Malaysia, through its Sustainable Research Collaboration Grant Scheme (600-RMC/SRC/5/3 (050/2020)) and the Ministry of Higher Education through the Fundamental Research Grant Scheme (FRGS/1/2018/TK05/UPM/02/8).

REFERENCES

- Abdin, M., Salama, M. A., Gawad, R. M. A., Fathi, M. A., & Alnadari, F. (2021). Two-steps of gelation system enhanced the stability of *Syzygium cumini* anthocyanins by encapsulation with sodium alginate, maltodextrin, chitosan and gum Arabic. *Journal of Polymers and the Environment*, 29, 3679-3692. <https://doi.org/10.1007/s10924-021-02140-3>
- Ajila, C. M., Brar, S. K., Verma, M., Tyagi, R. D., & Valéro, J. R. (2011). Solid-state fermentation of apple pomace using *Phanerocheate chrysosporium* - Liberation and extraction of phenolic antioxidants. *Food Chemistry*, 126(3), 1071-1080. <https://doi.org/10.1016/j.foodchem.2010.11.129>
- Alwi, H., Zaki, N. A. M., Radzi, N. C., Rodhi, M. N. M., Ami, M. A., & Hamid, K. H. K. (2017). Heat effects from far-infrared source towards antioxidant activity in *Aquilaria subintegra* leaves. *Materials Science Forum*, 890, 146-149. <https://doi.org/10.4028/www.scientific.net/msf.890.146>
- Anthika, B., Kusumocahyo, S. P., & Sutanto, H. (2015). Ultrasonic approach in *Clitoria ternatea* (Butterfly Pea) extraction in water and extract sterilization by ultrafiltration for eye drop active ingredient. *Procedia Chemistry*, 16, 237-244. <https://doi.org/10.1016/j.proche.2015.12.046>
- Bei, Q., Chen, G., Liu, Y., Zhang, Y., & Wu, Z. (2018). Improving phenolic compositions and bioactivity of oats by enzymatic hydrolysis and microbial fermentation. *Journal of Functional Foods*, 47, 512-520. <https://doi.org/10.1016/j.jff.2018.06.008>
- Bringas-Lantigua, M., Expósito-Molina, I., Reineccius, G. A., López-Hernández, O., & Pino, J. A. (2011). Influence of spray-dryer air temperatures on encapsulated Mandarin oil. *Drying Technology*, 29(5), 520-526. <https://doi.org/10.1080/07373937.2010.513780>
- Hariadi, H., Sunyoto, M., Nurhadi, B., & Karuniawan, A. (2018). Comparison of phytochemical characteristics pigment extract (Antosianin) sweet purple potatoes powder (*Ipomea batatas* L) and clitoria flower (*Clitoria ternatea*) as natural dye powder. *Journal of Pharmacognosy and Phytochemistry*, 7(4), 3420-3429.
- Jeyaraj, E. J., Lim, Y. Y., & Choo, W. S. (2021). Extraction methods of butterfly pea (*Clitoria ternatea*) flower and biological activities of its phytochemicals. *Journal of Food Science and Technology*, 58(6), 2054-2067. <https://doi.org/10.1007/s13197-020-04745-3>
- Jyothi, N. V. N., Prasanna, P. M., Sakarkar, S. N., Prabha, K. S., Ramaiah, P. S., & Srawam, H. Y. (2010). Microencapsulation techniques, factors influencing encapsulation efficiency. *Journal of Microencapsulation*, 27(3), 187-197. <https://doi.org/10.3109/02652040903131301>
- Liew, S. Y., Zin, Z. M., Maidin, N. M. M., Mamat, H., & Zainol, M. K. (2020). Effect of the different encapsulation methods on the physicochemical and biological properties of *Clitoria ternatea* flowers microencapsulated in gelatine. *Food Research*, 4(4), 1098-1108. [https://doi.org/10.26656/fr.2017.4\(4\).033](https://doi.org/10.26656/fr.2017.4(4).033)

- Marsin, A. M., Jusoh, Y. M. M., Zaidel, D. N. A., Hashim, Z., Yusof, A. H. M., & Muhamad, I. I. (2020). Microwave-assisted Encapsulation of Blue Pea Flower. *Chemical Engineering Transactions*, 78, 199-204. <https://doi.org/10.3303/CET2078034>
- Mazumder, M. A. R., & Ranganathan, T. V. (2020). Encapsulation of isoflavone with milk, maltodextrin and gum acacia improves its stability. *Current Research in Food Science*, 2, 77-83. <https://doi.org/10.1016/j.crfs.2019.12.003>.
- Mozafari, M. R., Khosravi-Darani, K., Borazan, G. G., Cui, J., Pardakhty, A., & Yurdugul, S. (2008). Encapsulation of food ingredients using nanoliposome technology. *International Journal of Food Properties*, 11(4), 833-844. <https://doi.org/10.1080/10942910701648115>
- Mukherjee, P. K., Kumar, V., Kumar, N. S., & Heinrich, M. (2008). The ayurvedic medicine *Clitoria ternatea* - from traditional use to scientific assessment. *Journal of Ethnopharmacology*, 120(3), 291-301. <https://doi.org/10.1016/j.jep.2008.09.009>
- Nawi, N. M., Muhamad, I. I., & Marsin, A. M. (2015). The physicochemical properties of microwave-assisted encapsulated anthocyanins from *Ipomoea batatas* as affected by different wall materials. *Science and Nutrition*, 3(2), 91-99. <https://doi.org/10.1002/fsn3.132>
- Ng, Z. X., Yong, P. H., & Lim, S. Y. (2020). Customized drying treatments increased the extraction of phytochemicals and antioxidant activity from economically viable medicinal plants. *Industrial Crops and Products*, 155, Article 112815. <https://doi.org/10.1016/j.indcrop.2020.112815>
- Parthasarathi, S., Ezhilarasi, P. N., Jena, B. S., & Anandharamakrishnan, C. (2013). A comparative study on conventional and microwave-assisted extraction for microencapsulation of Garcinia fruit extract. *Food and Bioprocess Processing*, 91(2), 103-110. <https://doi.org/10.1016/j.fbp.2012.10.004>
- Pasukamonset, P., Kwon, O., & Adisakwattana, S. (2016). Alginate-based encapsulation of polyphenols from *Clitoria ternatea* petal flower extract enhances stability and biological activity under simulated gastrointestinal conditions. *Food Hydrocolloids*, 61, 772-779. <https://dx.doi.org/10.1016/j.foodhyd.2016.06.039>
- Perez-Grijalva, B., Herrera-Sotero, M., Mora-Escobedo, R., Zebadúa-García, J. C., Silva-Hernández, E., Oliart-Ros, R., Pérez-Cruz, C., & Guzmán-Gerónimo, R. (2018). Effect of microwaves and ultrasound on bioactive compounds and microbiological quality of blackberry juice. *LWT*, 87, 47-53. <https://doi.org/10.1016/j.lwt.2017.08.059>
- Pieczykolan, E., & Kurek, M. A. (2019). Use of guar gum, gum arabic, pectin, beta-glucan and inulin for microencapsulation of anthocyanins from chokeberry. *International Journal of Biological Macromolecules*, 129, 665-671. <https://doi.org/10.1016/j.ijbiomac.2019.02.073>
- Sablania, V., & Bosco, S. J. D. (2018). Optimization of spray drying parameters for *Murraya koenigii* (Linn) leaves extract using response surface methodology. *Powder Technology*, 335, 35-41. <https://doi.org/10.1016/j.powtec.2018.05.009>
- Salleh, N. A. M., & Pa'ee, F. (2021). Effect of various immersion time and water temperature on seed germination of *Clitoria ternatea* and *Momordica charantia*. *Pertanika Journal of Tropical Agricultural Science*, 44(4), 745-753. <https://doi.org/10.47836/pjtas.44.4.03>

- Sulaiman, I. S. C., Basri, M., Masoumi, H. R. F., Chee, W. J., Ashari, S. E., & Ismail, M. (2017). Effects of temperature, time, and solvent ratio on the extraction of phenolic compounds and the antiradical activity of *Clinacanthus nutas* Lindau leaves by response surface methodology. *Chemistry Central Journal*, *11*, Article 54. <https://doi.org/10.1186/s13065-017-0285-1>
- Swathi, K. P., Jayaram, S., Sugumar, D., & Rymbai, E. (2021). Evaluation of anti-inflammatory and anti-arthritis property of ethanolic extract of *Clitoria ternatea*. *Chinese Herbal Medicines*, *13*, 243-249. <https://doi.org/10.1016/j.chmed.2020.11.004>
- Tonon, R.V., Brabet, C., & Hubinger, M.D. (2010). Anthocyanin stability and antioxidant activity of spray-dried açai (*Euterpe oleracea* Mart.) juice produced with different carrier agents. *Food Research International*, *43*(3), 907-914. <https://doi.org/10.1016/j.foodres.2009.12.013>
- Verma, P. R., Itankar, P. R., & Arora, S. K. (2013). Evaluation of antidiabetic antihyperlipidemic and pancreatic regeneration, potential of aerial parts of *Clitoria ternatea*. *Revista Brasileira de Farmacognosia*, *23*(5), 819-829. <https://doi.org/10.1590/S0102-695X2013000500015>
- Yadav, K., Bajaj, R. K., Mandal, S., & Mann, B. (2020). Encapsulation of grape seed extract phenolics using whey protein concentrate, maltodextrin and gum arabica blends. *Journal of Food Science & Technology*, *57*(2), 426-434. <https://doi.org/10.1007/s13197-019-04070-4>
- Zeng, S., Wang, B., Lv, W., & Wu, Y. (2023). Effects of microwave power and hot air temperature on the physicochemical properties of dried ginger (*Zingiber officinale*) using microwave hot-air rolling drying. *Food Chemistry*, *404*, Article 134741. <https://doi.org/10.1016/j.foodchem.2022.134741>

Utilization of Water Hyacinth and Spent Coffee Ground as Raw Materials to Produce Bio-Compost

Thanakorn Saengsanga* and Napat Noinumsai

Environmental Science Program, Faculty of Science and Technology, Nakhon Ratchasima Rajabhat University, Nakhon Ratchasima 30000, Thailand

ABSTRACT

The study aims to utilize water hyacinth and spent coffee grounds (SGC) as raw materials to produce bio-compost and its effects on rice growth. Four different bio-compost formulations were produced. The water hyacinth (6 kg) and dried cow manure (2 kg) were thoroughly mixed and added with SGC+EM (Trial 1), SGC+water (Trial 2), EM (Trial 3), and water (Trial 4). At the end of fermentation, the 3 types of macronutrients (N, P, and K) were determined. Germination percentage and growth in response to this bio-compost were also assessed. The results found that the bio-compost consisted of N, P, and K, ranging from 311–350, 154–197, and 23–25 mg/100 g, respectively. All bio-composts had a favorable effect on the germination percentage, root and shoot lengths, and vigor index of rice seedlings in the seed germination assay. Trial 2 gave the highest root and shoot lengths of 7.32 and 4.35 cm, respectively, and the greatest value of 1051 of the vigor index. At 45 DAS, the results revealed that all trials of bio-compost had a beneficial influence on the development of rice seedlings by increasing root and shoot lengths and fresh and dried weights of rice seedlings, especially Trial 2, which consisted of SGC when compared to the controls. In this phenomenon, the presence of SGC at low concentrations could encourage rice growth.

Keywords: Bio-compost, rice, spent coffee ground (SCG), water hyacinth

ARTICLE INFO

Article history:

Received: 01 July 2022

Accepted: 14 November 2022

Published: 13 July 2023

DOI: <https://doi.org/10.47836/pjst.31.5.12>

E-mail addresses:

thanakorn.s@nrru.ac.th (Thanakorn Saengsanga)

noinumsai@windowslive.com (Napat Noinumsai)

* Corresponding author

INTRODUCTION

One resource for restoring soil fertility and promoting plant growth is non-traditional organic materials like weeds. Water hyacinth (*Pontederia crassipes*, formerly *Eichhornia crassipes*) is one of the most invasive weed species, causing

enormous economic and ecological destruction, especially in tropical and subtropical regions (Jafari, 2010). Water hyacinth can spread rapidly with a daily growth rate of 220 kg/ha and may increase twice after 5–15 days (Islam et al., 2021). Water hyacinth is composed of 74–84 % organic matter, 0.26–0.53% P, 18.5– 27.6% C, 1.18–2.9% N, 2.27–4.53% K, and 15.8–25.1 C/N ratio on a dry matter basis (Su et al., 2018) which a suitable C/N ratio for microorganisms is 15–30 (Haug, 1993). Additionally, the plant has a high concentration of plant hormone, gibberellin, which can boost the growth of plants (Ummah & Rahayu, 2019).

The utilization of water hyacinth as a source of raw materials to produce compost has been studied. As composted material, water hyacinth is increasingly utilized as a source of nutrients (Malik, 2007). Applying bio-compost increases the nutrient storage capacity, water binding capacity, cation exchange capacity, and micro-aggregation in soils. It may reduce the effects of over-fertilization by gradually releasing nutrients (Khan & Sarwar, 2002). Furthermore, manure can improve compost quality, soil fertility, soil productivity, soil organic carbon content, soil microorganisms, soil crumb structure, soil nutrient status, and crop production. Organic manure is particularly economical and effective as a source of nitrogen for long-term crop development (Singh & Kalamdhad, 2015).

Additionally, spent coffee grounds (SCGs) are the residues from the coffee-making process that contain several high-value products. SCGs are generated approximately 6 million tons annually globally (Mussatto, Carneiro, et al., 2011). SCGs mostly consist of polysaccharides, particularly cellulose and hemicellulose, constituting over 50% of the SCG's dry mass. Lignin and protein comprise approximately 20% of the dry mass (Ballesteros et al., 2014) and contain a high value of N, P, and K ranging from 1.2–2.8%, 0.02–0.5%, and 0.35, respectively (Mussatto, Machado, et al., 2011; Cruz et al., 2012). SCGs are used as biomass fuel, organic fertilizer, and soil amendment. Kasongo et al. (2011) reported that the addition of SCGs provides macro- and micronutrients and improves the pH and electrical conductivity of the soil (Cruz et al., 2012) and recommend using it as a soil amendment or fertilizer in agriculture (Cervera-Mata et al., 2018; Gomes et al., 2013). Thai jasmine rice (*Oryza sativa* L. var. KDML105) is among the most popular and economically important cultivars widely produced in northeastern Thailand, where there is soil salinity and low soil fertility. Although applying chemical fertilizers to increase agricultural productivity is a successful strategy, overusing them can harm the environment (Saengsanga, 2018). Consequently, applying organic fertilizers to accelerate soil fertility and increase crop yield is important in sustainable agriculture. Hence, this study aims at assessing the effects of bio-composts produced from water hyacinth and spent ground coffee on the growth of Thai jasmine rice seedlings.

MATERIALS AND METHODS

Harvesting of Water Hyacinth and Collecting of Spent Coffee Grounds

The water hyacinth was collected from the stabilization pond of the Municipal Wastewater Pumping Station (14.9641606N, 102.12496E), Nakhon Ratchasima province. The samples were washed and cut into pieces 3–5 cm long to enlarge the surface area for microbial action. SCG was obtained from a local coffee shop and air-dried to reduce its water content.

Production of Bio-Compost

Four different treatments of bio-compost from water hyacinth and SCG, according to Table 1, all components were mixed and prepared in a plastic bucket of 120 L capacity. Compost was turned out every 14 days, and moisture was maintained at 50–60%. The temperature was taken with a digital thermometer. The color and odor of bio-compost were also observed.

The experiment was performed under natural conditions for 12 weeks until the temperature gradually dropped to ambient air temperatures.

Table 1
Different treatments of bio-compost from water hyacinth

Treatments	Water hyacinth (kg)	Dried cow manure (kg)	SCG (kg)	EM (L)	Water (L)
Trial 1	6	2	0.25	1	0
Trial 2	6	2	0.25	0	1
Trial 3	6	2	0	1	0
Trial 4	6	2	0	0	1

Nutrient Contents

At the end of the composting process, we determined the levels of total N and P according to the method of Bremner et al. (1982) as well as Bray and Kurtz (1945); K was analyzed by atomic absorption spectrophotometer (AAS) (Spectra Ad 55B, Varian).

Determination of the Bio-Compost Maturity by Seed Germination Assay

Phytotoxicity was performed through seed germination assay to assess bio-compost maturity. The plant used in this experiment was jasmine rice (*Oryza sativa* L. var. KDML105). Rice seeds were drenched for 3 min in 90% EtOH and 30 min in 3.5% NaOCl. In the final step, rice seeds were cleaned 3 times with sterile ddH₂O. Each bio-compost sample was diluted with ddH₂O in a concentration of 10% and filtered using filter paper. Sterilized seeds (20/ plate) were germinated in filtrated solution, as mentioned before, in a Petri dish and incubated for 7 days under ambient conditions. Rice plants were irrigated with 3 mL of ddH₂O every 2 days. Germination percentage was observed at 4 days after

sowing (DAS). Root and shoot lengths were determined at 7 DAS, and the vigor index of rice seedlings was also calculated according to Equations 1 and 2 (Saengsanga, 2018).

$$\% \text{ Germination} = (\text{Seed germinated} / \text{Total seed}) \times 100 \quad (1)$$

$$\text{Vigor index} = \% \text{ germination} \times (\text{root length} + \text{shoot length}) \quad (2)$$

Effects of Bio-Composts on the Growth of Rice Seedlings

A soil sample was collected from BuaYai District, Nakhon Ratchasima Province, Thailand, to evaluate bio-compost on the growth of rice seedlings by pot experiment. After 7 days of germination, rice was transplanted in a 6-inch pot containing 0.5 kg of soil and fertilized with each bio-compost (50 g/pot). Irrigation was performed, and flooding was 2–5 cm over the soil. At 45 DAS, the growth parameters were collected, including root and shoot lengths and root and shoot dry weight. Vernier calipers determined plant height and weight by analytical balance 4 digits (Denver Instrument, USA) after drying at 70°C for 2 days.

Statistical Analysis

To determine the significance of the experiments, we presented the results as the mean \pm SD of three replicates. Comparison of mean was performed using one-way analysis of variance (ANOVA) with Duncan’s multiple range test (DMRT), and $p < 0.05$ was considered to be statistically significant.

RESULTS AND DISCUSSION

Physical and Chemical Properties

Bio-compost samples were gathered after 12 weeks of maturation to examine the main crop nutrients. The compost sample had a range of colors. Trials 1 and 2 were dark brown, while 3 and 4 were light brown (Figure 1).

The bio-compost’s N, P, and K contents varied from 311–350, 154–197, and 23–25 mg/100 g, respectively. Furthermore, the pH value of the bio-compost ranged from 8.1–8.4,

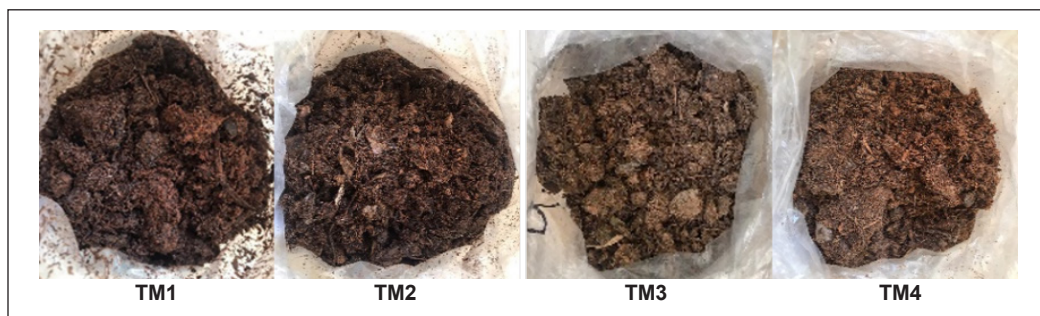


Figure 1. Characteristics of bio-compost

and EC was 4.18–6.29 ds/m (Table 2). Nutrient concentrations often rise due to the net loss of dry mass throughout the composting process (Singh & Kalamdhad, 2015). Besides, the result suggests that adding SCG in an insufficient quantity did not affect the nutritional content of the bio-compost. As a result, adding organic wastes could improve the quality of bio-compost. Islam et al. (2021) claimed that supplementing black liquor and kitchen bio-waste could improve the N, P, and K contents of the water hyacinth bio-compost. A combination of water hyacinth and corncob has various nutrients, including C, N, K, and C/N. At the same time, bio-compost from a combination of water hyacinth and soybean dregs contained more P content (Fitrihidajati et al., 2021).

Table 2
Chemical properties of the bio-compost

Treatments	N (mg/100 g)	P (mg/100 g)	K (mg/100 g)	EC _(5:1)	pH _(2:1)
Trial 1	323.42±5.26	179.92±4.84	24.32±0.46	5.78	8.4
Trial 2	311.15±2.98	174.12±4.75	23.32±0.20	6.29	8.7
Trial 3	343.62±4.82	194.97±3.39	25.28±0.03	4.18	8.1
Trial 4	350.67±4.29	197.70±2.36	24.46±0.08	4.68	8.5

Effects of Bio-Compost on Rice Seed Germination

Effects of different bio-composts on germination percentage, plant heights, and vigor index were evaluated, and the result is shown in Table 3. The finding was that all formulations of bio-extract displayed a beneficial effect on germination rate, root and shoot lengths, and vigor index ($p > 0.05$). Trial 2 gave the maximum root and shoot lengths of 7.32 and 4.35 cm, respectively.

Again, Trial 2 was the most efficient stimulator for rice plants, having a maximum vigor index of 1051. The germination assay showed that the bio-compost had no phytotoxicity issues, indicating that these bio-composts produced from water hyacinth and combined with SCG were mature and had no phytotoxicity to inhibit plant growth. It has been documented that SCG at a low concentration (2.5–5%) stimulates plant growth (Gomes et al., 2013).

Table 3
Effects of bio-compost on the germination of KDML 105 rice seeds

Treatments	Germination (%)	Root length (cm)	Shoot length (cm)	Total length (cm)	Vigor index
Control	86.65 ^a	6.63±0.62 ^a	3.71±0.95 ^a	9.78±1.21 ^a	847 ^b
Trial 1	91.65 ^{bc}	6.79±0.52 ^{ab}	3.85±0.30 ^a	10.64±0.59 ^{ab}	975 ^{ab}
Trial 2	90.00 ^{ab}	7.32±0.82 ^b	4.35±0.33 ^a	11.67±0.70 ^b	1051 ^a
Trial 3	93.35 ^{bc}	6.17±0.80 ^{ab}	4.14±0.28 ^a	10.32±1.08 ^{ab}	963 ^{ab}
Trial 4	91.65 ^{bc}	7.09±0.17 ^{ab}	4.01±0.11 ^a	11.09±0.17 ^{ab}	1017 ^a

Note. Values are mean ±SD of 3 replicates with lowercase letters indicating statistically significant differences at $p < 0.05$ (DMRT).

Effects of Bio-Compost on the Growth of Rice Seedlings

We investigated the bio-compost’s effects on rice growth under a pot experiment. After 45 DAS, all tested bio-composts boosted the growth of rice seedlings by increasing root and shoot lengths and plant weights ($p < 0.05$) (Figure 2). Rice seedlings fertilized with Trial 2 had the greatest shoot and root lengths and biomass, followed by those with Trial 3.

However, all seedlings’ exposure to bio-compost was revealed to be higher than the controls, suggesting bio-compost accelerates the development of the rice seedlings. The utilization of water hyacinth compost can improve the growth and flowering of *Crossandra* and some vegetables compared to untreated plants (Gajalakshmi & Abbasi, 2002). Beesigamukama et al. (2018) reported that water hyacinth bio-compost enhanced maize yield. Hence, water hyacinth-based compost is a good option to improve soil quality and increase plant productivity.

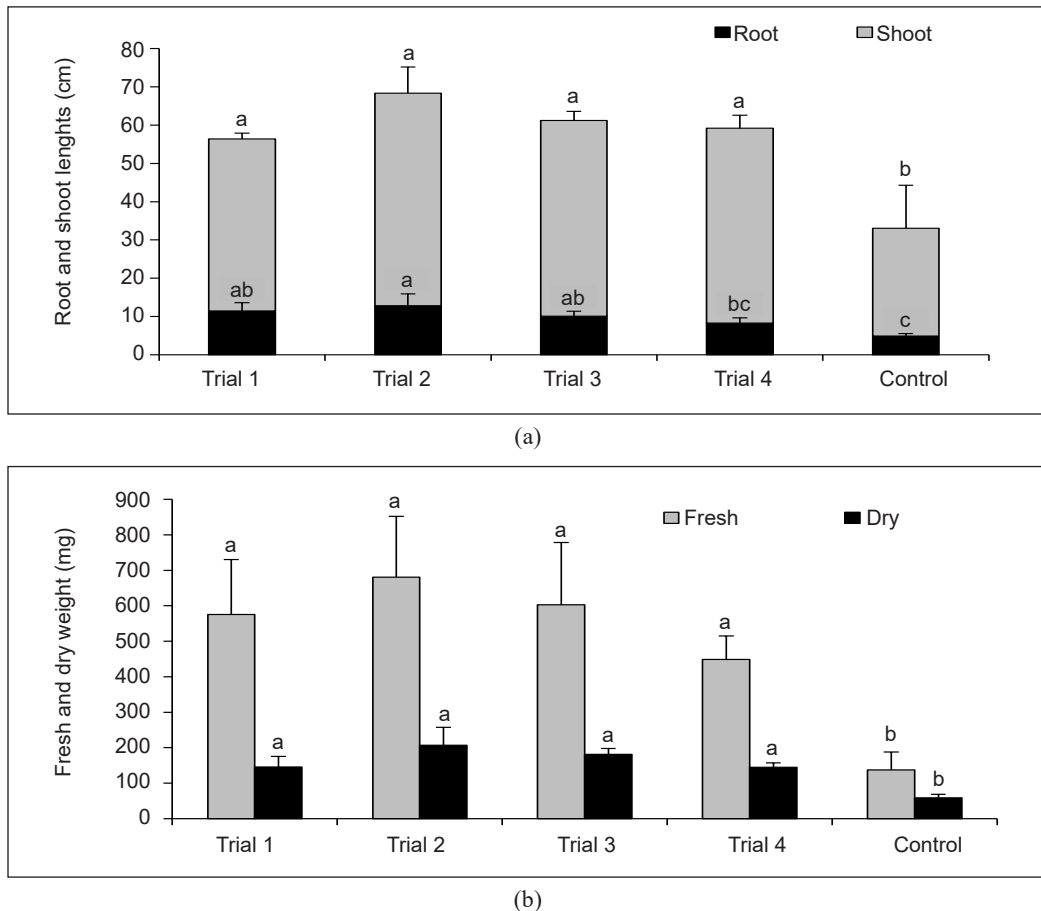


Figure 2. Effects of the bio-composts on the growth of rice seedlings at 45 DAS. Root and shoot lengths (a), fresh and dried weights (b). Values are the mean \pm SD of three replicates with the lowercase letters above the bar, indicating statistically significant differences at $p < 0.05$ (DMRT)

CONCLUSION

The outcomes of this investigation have illustrated that the bio-compost derived from water hyacinth and a combination of SCGs is a good soil enrichment to promote jasmine rice plant growth at the seedling stage. Our results revealed that all bio-compost trials had encouraged rice growth, particularly Trial 2 (Water hyacinth: Dried cow manure: SCG: Water = 6: 2: 0.25: 1), having the highest performance. Future investigations should examine the additions of nutrient-rich organic wastes to enhance their qualities.

ACKNOWLEDGEMENTS

The authors acknowledge the support of the Nakhon Ratchasima Rajabhat University, Thailand, for this manuscript completion. The authors would also like to thank Miss Jiratikorn Jinda and Miss Thanpitcha Jantai for their assistance and service.

REFERENCES

- Ballesteros, L. F., Teixeira, J. A., & Mussatto, S. I. (2014). Chemical, functional, and structural properties of spent coffee grounds and coffee silverskin. *Food and Bioprocess Technology*, 7, 3493-3503. <https://doi.org/10.1007/s11947-014-1349-z>
- Beesigamukama, D., Amoding-Katusabe, A., Tumuhairwe, J. B., Muoma, J., Maingi, J. M., Ombori, O., Nakanwagi, J., & Mukaminega, D. (2018). Agronomic effectiveness of water hyacinth-based composts. *African Journal of Agricultural Research*, 13(39), 2055-2062. <https://doi.org/10.5897/AJAR2018.13440>
- Bray, R. H., & Kurtz, L. T. (1945). Determination of total, organic, and available forms of phosphorus in soils. *Soil Science*, 59, 39-45.
- Bremner, J. M., & Mulvaney, C. S. (1982). Nitrogen-Total. In A. L. Page, R. H. Miller & D. R. Keeney (Eds.), *Methods of Soil Analysis Part 2 Chemical and Microbiological Properties* (pp. 595-942). American Society of Agronomy Inc, Soil Science Society of America Inc.
- Cervera-Mata, A., Pastoriza, S., Rufián-Henares, J. A., Párraga, J., Martín-García, J. M., & Delgado, G. (2018). Impact of spent coffee grounds as organic amendment on soil fertility and lettuce growth in two Mediterranean agricultural soils. *Archives of Agronomy and Soil Science*, 64(6), 790-804. <https://doi.org/10.1080/03650340.2017.1387651>
- Cruz, R., Baptista, P., Cunha, S., Pereira, J. A., & Casal, S. (2012). Carotenoids of lettuce (*Lactuca sativa* L.) grown on soil enriched with spent coffee grounds. *Molecules*, 17, 1535-1547. <https://doi.org/10.3390/molecules17021535>
- Fitrihidajati, H., Rachmadiarti, F., Winarsih, Purnomo, T., & Kuntjoro, S. (2021). Quality of organic fertilizer made from water hyacinth with the addition of corncobs waste and soybean dregs. *Journal of Physics: Conference Series*, 1899, Article 012024. doi:10.1088/1742-6596/1899/1/012024
- Gajalakshmi, S., & Abbasi, S. A. (2002). Effect of the application of water hyacinth compost/ vermicompost on the growth and flowering of *Crossandra undulataefolia*, and on several vegetables. *Bioresource Technology*, 85(2), 197-199. [https://doi.org/10.1016/S0960-8524\(02\)00096-2](https://doi.org/10.1016/S0960-8524(02)00096-2)

- Gomes, T., Pereira, J.A., Ramalhosa, E., Casal, S., & Baptista, P. (2013). Effect of fresh and composted spent coffee grounds on lettuce growth, photosynthetic pigments and mineral composition. In *VII Congreso Ibérico de Agroingeniería y Ciencias Hortícolas* (pp. 1-5). SECH e SEAgIng.
- Haug, R. T. (1993). *The Practical Handbook of Compost Engineering*. Lewis Publishers.
- Islam, M. N., Rahman, F., Papri, S. A., Faruk, M. O., Das, A. K., Adhikary, N., Debrot, A. O., & Ahsan, M. N. (2021). Water hyacinth (*Eichhornia crassipes* (Mart.) Solms.) as an alternative raw material for the production of bio-compost and handmade paper. *Journal of Environmental Management*, 294, Article 113036. <https://doi.org/10.1016/j.jenvman.2021.113036>
- Jafari, N. (2010). Ecological and socio-economic utilization of water hyacinth (*Eichhornia crassipes* Mart Solms). *Journal of Applied Sciences and Environmental Management*, 14(2), 43-49.
- Kasongo, R. K., Verdoodt, A., Kanyankagote, P., Baert, G., & Van Ranst, E. (2011). Coffee waste as an alternative fertilizer with soil improving properties for sandy soils in humid tropical environments. *Soil Use and Management*, 27, 94-102. <https://doi.org/10.1111/j.1475-2743.2010.00315.x>
- Khan, S., & Sarwar, K. S. (2002). Effect of water-hyacinth compost on physical, physico-chemical properties of soil and on rice yield. *Journal of Agronomy*, 1, 64-65. <https://doi.org/10.3923/ja.2002.64.65>
- Malik, A. (2007). Environmental challenge vis a vis opportunity: The case of water hyacinth. *Environment International*, 33(1), 122-138. <https://doi.org/10.1016/j.envint.2006.08.004>
- Mussatto, S. I., Carneiro, L. M., Silva, J. P. A., Roberto, I.C., & Teixeira, J. A. (2011). A study on chemical constituents and sugars extraction from spent coffee grounds. *Carbohydrate Polymers*, 83, 368-374. <https://doi.org/10.1016/j.carbpol.2010.07.063>
- Mussatto, S. I., Machado, E. M. S., Martins, S., & Teixeira, J. A. (2011). Production, composition, and application of coffee and its industrial residues. *Food and Bioprocess Technology*, 4, 661-672. <https://doi.org/10.1007/s11947-011-0565-z>
- Saengsanga, T. (2018). Isolation and characterization of indigenous plant growth-promoting rhizobacteria and their effects on growth at the early stage of Thai jasmine rice (*Oryza sativa* L. KDML105). *Arabian Journal for Science and Engineering*, 43, 3359-3369. <https://doi.org/10.1007/s13369-017-2999-8>
- Singh, J., & Kalamdhad, A. S. (2015). Assessment of compost quality in agitated pile composting of water hyacinth collected from different sources. *International Journal of Recycling of Organic Waste in Agriculture*, 4, 175-183. <https://doi.org/10.1007/s40093-015-0097-z>
- Su, W., Sun, Q., Xia, M., Wen, Z., & Yao, Z. (2018). The resource utilization of water hyacinth (*Eichhornia crassipes* [Mart.] Solms) and its challenges. *Resources*, 7(3), Article 46. <https://doi.org/10.3390/resources7030046>
- Ummah, K., & Rahayu, Y. S. (2019). The effect of gibberellin extracted from *Eichhornia crassipes* root on the viability and duration of hard seed germination. *Journal of Physics: Conference Series*, 1417, Article 012037. <https://doi.org/10.1088/1742-6596/1417/1/012037>

Effect of Pre-Treatment Methods on the Extractability of *Christia vespertilionis* by Supercritical Carbon Dioxide

Izni Atikah Abd Hamid¹, Najla Laazizi², Ana Najwa Mustapa^{3,4*} and Norazah Abd Rahman³

¹Centre for Bioprocessing Engineering, Faculty of Engineering, Built Environment and Information Technology, SEGi University, Jalan Teknologi, Kota Damansara, 47810 Petaling Jaya, Selangor, Malaysia

²EMINES - School of Industrial Management, Mohammed VI Polytechnic University, Ben Guerir, Morocco

³School of Chemical Engineering, College of Engineering, Universiti Teknologi MARA, 40450 Shah Alam, Malaysia

⁴Centre of Lipids Engineering and Applied Research (CLEAR), Ibnu Sina Institute for Scientific and Industrial Research, Universiti Teknologi Malaysia, 81310 UTM Johor Bahru, Johor, Malaysia

ABSTRACT

Christia vespertilionis is a medicinal herb traditionally used as a complementary and alternative medicine to treat cancer and malaria. This study investigated the effect of pre-treatments of the *Christia vespertilionis* plant on supercritical CO₂ extraction yield and solubility. Four pre-treatments were studied: drying and grinding, doping with absolute ethanol (99%) and 80% (v/v) of ethanol/water, and microwave pre-treatment. The supercritical CO₂ extraction was conducted at a constant 13.8 MPa, 40°C with 24 mL/min flow rate in 40 min of extraction time. It was found that the dried sample after drying and grinding pre-treatment produced the highest yield of 4.56 mg/g, whereas the lowest yield was obtained for the fresh leaves' samples treated with microwave irradiation (1.26 mg/g). Doping techniques with absolute ethanol and 80% (v/v) were comparable in the 2.64 to 2.94 mg/g. GCMS results revealed that *Christia vespertilionis* extract comprises antioxidants, mainly phytol, limonene, and other medicinal compounds such as α -monolaurin and l-ascorbyl 2,6-dipalmitate. This study indicates that adding co-solvent was not the primary technique in supercritical CO₂ extraction to increase the extractability of compounds of interest from plant matrices.

ARTICLE INFO

Article history:

Received: 03 July 2022

Accepted: 05 October 2022

Published: 13 July 2023

DOI: <https://doi.org/10.47836/pjst.31.5.13>

E-mail addresses:

iznihamid@segi.edu.my (Izni Atikah Abd Hamid)

najlaa3012@gmail.com (Najla Laazizi)

anajwa@uitm.edu.my (Ana Najwa Mustapa)

noraza695@uitm.edu.my (Norazah Abd Rahman)

* Corresponding author

Keywords: Carbon dioxide, *Christia vespertilionis*, co-solvent, medicinal compounds, pre-treatment, supercritical extraction

INTRODUCTION

The red butterfly wing plant has received increasing public attention due to its medicinal properties in treating several critical diseases. The plant is scientifically known as *Christia vespertilionis* (L.) Bakh. from the Fabaceae family. It was reported that the plant could treat cancer (Wu et al., 2012) and malaria diseases (Upadhyay et al., 2013). Numerous studies on the traditional applications of *C. vespertilionis*, such as healing tuberculosis, bronchitis, colds, muscle weakness, and poor blood circulation (Whiting, 2007), fever treatment (Chassagne et al., 2016), and healing scabies disease (Cambie & Ash, 1994) were done and shown potential medicinal benefits. The plant extract was also reported to possess anti-proliferative potential due to the high content of bioactive compounds, mainly triterpenes, alkaloids, fatty acids, phenol, and long-chained alcohols (Hofer et al., 2013). In another aspect, the alkaloids from the *C. vespertilionis* plant exhibited as an anti-cancer agent for neuroendocrine tumors (Lu et al., 2012) and as a tumor inhibitor when tested on a mouse (Wu et al., 2012). The extract was found could prolong the life span of the tumor-bearing mice. In addition, the plant also possesses strong antiplasmodial activity, where it can act as an antidote against diseases caused by the Plasmodium genus, such as malaria (Dash, 2016). The noble compound responsible for the anti-plasmodial agent found in *C. vespertilionis* extract was named christene with the IUPAC name of 7-isopropylidene-1-methyl-1,2,6,7,8,9-hexahydronaphthalene (Nguyen-Pouplin et al., 2007; Upadhyay et al., 2013). These findings indicate the high potential of the medicinal plant as a complementary and alternative natural medicine for the pharmaceutical industry. Most recent studies have discovered that the root *C. vespertilionis* extracts have shown remarkable anti-breast cancer activity (Ismail et al., 2021; Lee et al., 2020).

However, all the studies on the *C. vespertilionis* plant were based on conventional extraction methods, i.e., organic solvent extraction to extract the bioactive compounds. The technique is not suitable and unsafe for edible products due to the use of toxic chemicals as solvent extraction. The major drawbacks of solvent extraction include compound degradation (due to the elevated temperature), product impurities, extensive extraction duration, and exposure to toxic fumes in surroundings, which will cause health problems and create dirty environments (Rombaut et al., 2014).

The extraction of bioactive compounds from *C. vespertilionis* using supercritical carbon dioxide (SC-CO₂) is scarcely available in the open literature. SC-CO₂ extraction was recognized as a green method, employing high-purity carbon dioxide (CO₂), i.e., 99.99%, as its solvent extraction. CO₂ is an ideal solvent for extracting functional foods and medicines since it is non-toxic, non-corrosive, inert (where it would not affect the extraction output), and safer for consumers and the environment (Mukhopadhyay, 2000). It is due to the advantages owned by SC-CO₂, such as faster extraction time (where the extraction could be completed within 1 to 2h compared to 8 to 12h of solvent extraction method),

the mild operating temperature used (ability to extract, and preserve thermosensitive and volatile compounds), organic solvent-free (no chemical solvent involves except for a certain extraction condition such as additional of co-solvent with a very minimum amount of possible) and clean extract produced where CO₂ can easily be removed by releasing the pressure at the end of the extraction process.

C. vespertilionis, which belongs to the Fabaceae family, is categorized as a plant containing essential oil. In principle, essential oil from plant matrices is difficult to be extracted. According to the plant anatomy of leaves, glandular trichomes (i.e., glandular hairs on the leaf's surface) contain volatile oils and other plant secretions (Beck, 2010). Therefore, breaking the plant sample's glandular cells and cell walls is crucial for easy access to the oil to the extraction solvent before the extraction process.

Numerous studies were reported on enhancing oil extractability in obtaining maximum yield. The method is called sample pre-treatment, such as drying, grinding, microwave, ultrasound, and high-pressure pre-treatments. Drying pre-treatment is necessary to remove the moisture content from the plant's material since fresh plant contains high moisture that will compete with the solvent during the extraction process. Many authors agreed that the ideal moisture content for plant material should be between 3 to 12% (wet basis moisture) (Ivanovic et al., 2014). Reducing sample size is also important for successfully applying SC-CO₂, which could be obtained by grinding, chopping, or flaking the sample material (Mustapa et al., 2009). They found that the grinding pre-treatment technique could rupture the glandular cells and wall cells. In addition, a larger surface area can be obtained by decreasing the particle size, increasing the extraction yield due to the increasing solvent-oil contact and accessibility. The distance between solute-solvent contact was reduced to fasten the extraction process. Another technique to improve the extraction efficiency is microwave pre-treatment before being subjected to SC-CO₂ extraction. Theoretically, by exposing plant materials to microwave radiation, a greater extraction yield could be obtained (Uquiche et al., 2008). This phenomenon occurred due to the breaking of plant cell walls by irradiation, generating permanent pores in the sample. Thus, enabling the oil to move out through the permeable cell walls makes it easier to be extracted using the SC-CO₂ method.

For the sample treated using the ultrasound method, many studies had shown that the quality of the extract improved when the concentration of the compound increased through the cavitation phenomenon. Cavitation occurs when the ultrasonic wave passes through the sample degrading the plant cell walls (Herrero et al., 2015). As for the high-pressure pre-treatment method, the exposure of the plant sample to high pressure can lead to higher solvent permeation in the inner cells, and therefore higher and faster extraction will be achieved (Vidović et al., 2014). Overall, the purpose of sample pre-treatments above is to destroy the cell walls and disrupt the plant structures since the methods will be assisted in releasing the oil from cells, leading to the higher recovery of oil from SC-CO₂ extraction.

Another technique to enhance extraction efficiency is adding a small amount of polar co-solvent to the system. This technique is expected could increase the solvent power of supercritical fluid, thus enhancing the ability of CO₂ to dissolve compounds. In this study, several techniques of sample pre-treatments: (1) drying and grinding, (2) microwave pre-treatment on fresh leaves, (3) doping with absolute ethanol (99%), and (4) doping with 80% (v/v) of ethanol/water was employed to the *C. vespertilionis* plant prior to the SC-CO₂ extraction at 13.8 MPa and 40°C for 40 min. The study investigates the effect of different sample pre-treatments on the SC-CO₂ extraction of *C. vespertilionis* yield, solubility, and extracted phytochemicals.

MATERIAL AND METHODS

Materials

C. vespertilionis plant samples containing only leaves were purchased from Pure Rerama Leaf in Bukit Subang, Shah Alam, Malaysia. Absolute ethanol of 99% was purchased from Merck, and carbon dioxide (CO₂) of supercritical fluid grade with a purity of 99.99% used in supercritical fluid extraction was purchased from Air Liquide in Singapore.

Sample Pre-Treatment and Preparation

Samples were prepared accordingly for different pre-treatments.

Drying and Grinding. Fresh leaves were oven-dried at 40°C for 24h to reduce their moisture content from 59% to 8% wet basis. The dried leaves were ground using Waring Laboratory Blender and sieved through Endecotts Octagon 2000 Digital Sieve Shaker. Samples with 0.3 mm of particle size were then kept in the air-tight bag until used for SC-CO₂ extraction. The dried samples prepared by this treatment are labeled as D.

Microwave Pre-Treatment. Fresh leaves with 59 wt% moisture content were cut into small pieces (2×2 cm) and placed in a microwave (SHARP, Model R202ZS) to disrupt the plant cell wall over 320 W in the 50s and without any addition of solvent or water. The parameter condition of the microwave used was selected according to the available literature (Yu et al., 2016). After the microwave pre-treatment, the sample was placed in the cotton cloth to extract oil using SC-CO₂. The samples treated with this preparation are classed as M.

Doping with Absolute Ethanol (99%). The samples prepared from the D treatment (i.e., drying and grinding) were doped with a 1:2 weight ratio of absolute ethanol (99%) to samples and mixed before the SC-CO₂ extraction. This sample is labeled as A.

Doping with 80% (v/v) of Ethanol/Water. A similar procedure to sample A was applied for this sample pre-treatment. About 1:2 weight ratio of 80% (v/v) ethanol/water was doped to the dried samples prepared and labeled as W samples.

Supercritical Carbon Dioxide Extraction

SC-CO₂ extraction of *C. vespertilionis* was performed using SFT-100 from Supercritical Fluid Technologies, Inc. (USA) with the maximum pressure and temperature are 68.9 MPa and 150°C, respectively. Figure 1 shows the result of extraction yield for different pre-treatment methods. The CO₂ liquid with 99.99% of purity was used for SFT-100 with a long dip tube and 5.5–6.2 MPa of tank pressure. From each pre-treatment sample, about 5 g of *C. vespertilionis* sample was inserted into an extraction bag (i.e., cotton cloth) and placed in a 25 mL pressurized extraction vessel. The sample was put in the cotton cloth to prevent pressure channeling when the SC-CO₂ fluid passed through the sample. High pressure of liquid CO₂ was pumped into the extractor and regulated by a back-pressure regulator unit. Once the system has equilibrated for a certain set time and at the set temperature and pressure, a dynamic valve was gently opened to allow a continuous flow of SC-CO₂ fluid for 10 minutes. The samples were carefully collected by placing the tubing collection inside the test tube and designing it to pass through the test tube cap. This technique was done for all sample types of pre-treatment. This work conducted the extraction process within 40 min extraction time, 24 mL/min of CO₂ flowrate, 13.8 MPa, and 40°C. The extraction temperature and pressure used in this study were chosen according to the previous history available in the literature (Almeida et al., 2013; Cargnin et al., 2010).

The desired flow rate of SC-CO₂ through the sample was achieved by opening the restrictor valve slowly at 5 mL/min. The extracted oil was collected gravimetrically and measured every 10 min at time intervals by placing a glass vial at the outlet of the restrictor. The CO₂ was decompressed into atmospheric pressure. The amount of extracted oil was weighed using the analytical balance Model Mettler Toledo AB204-S with an accuracy of 0.0001 g. The extraction was repeated three times at identical operating conditions, and the average value with the standard error was

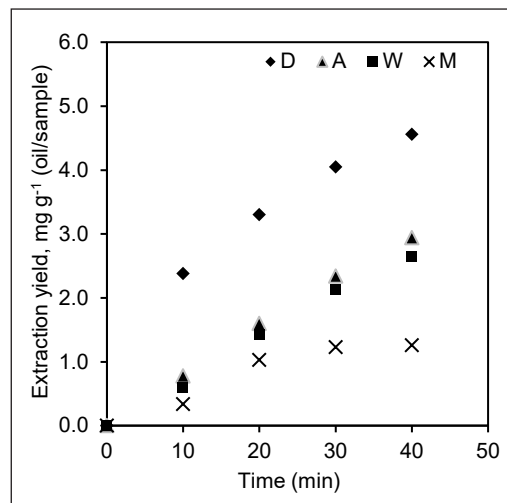


Figure 1. Extraction yield of different sample pre-treatments: dried and ground sample (D), doping with 80% (v/v) ethanol/water (W), doping with absolute ethanol sample (A), and microwave sample (M) at constant SC-CO₂ conditions; 13.8 MPa, 40°C, CO₂ flowrate of 24 mL/min and 40 min extraction time

used for extraction yield determination. The extraction yield was reported as the oil weight in mg per feed sample weight in grams (g). The solubility of oil in SC-CO₂ in each experiment was calculated as a ratio of the mass of extracted oil in mg to the mass of CO₂ consumed in grams (g). Experiments were repeated three times for each sample pre-treatment and calculated as an average and standard deviation.

Scanning Electron Microscopy (SEM)

The surface morphology of the non-processed and SC-CO₂ extraction processed samples (at 40°C, 13.8 MPa, and 40 min) of the dry and microwave pre-treatments samples (i.e., samples D and M) were analyzed by scanning electron microscopy (SEM) model Hitachi S-3400N. The purpose of this method is to observe the morphological changes of the vegetal structures before and after the extraction process. Samples were sputter-coated with gold and examined at 1000 to 2500× magnifications. An acceleration potential of 15 kV was used during the micrograph.

GCMS Analysis

The *C. vespertilionis* extracts were analyzed by gas chromatography-mass spectrometer (GCMS) Model Varian. The qualitative analyses of the extracts were performed using a stationary phase BP-5MS non-polar column with 30 m length × 0.25 mm internal diameter and 0.25 µm thickness from General Separation Technologies Inc. USA. The gas chromatography settings were as follows: 2 min at 60°C, then a progressive increase to 150°C at a rate of 10 °C/min, a further increase to 250°C at a rate of 3°C/min, and finally holds for 1 min. A 1 µL aliquot sample in methanol dilution was injected into the column with a split ratio of 1:10. Helium was used as a carrier gas with a 1 mL/min flow rate in the column. The injector and detector temperatures were 260 and 270°C, respectively. The mass spectrometer was operated in the electron-impact ionization mode at an energy level of 70 eV with a scanning range of 50–500 amu. The components of the extracted oil were identified by comparing their mass spectra (MS) with those available in the NIST (National Institute of Standards and Technologies) MS library and with blank methanol. The analyses were repeated twice for each extract of the pre-treatment sample.

RESULTS AND DISCUSSION

Extraction Yield and Solubility

Figure 1 shows the extraction yield of *C. vespertilionis* oil recovered by SC-CO₂ extraction as a function of the mass of extracted oil per mass of sample used (mg/g). Four different pre-treatments were studied to the sample before introducing it to the SC-CO₂ extraction at 13.8 MPa, 40°C, 24 mL/min CO₂ flowrate, and 40 minutes of extraction time. The sample

pre-treatments used are D: drying and grinding, M: fresh leaves with microwave pre-treatment, A: doping with absolute ethanol, and W: doping with 80% (v/v) ethanol/water.

According to Figure 1, the result revealed that the extraction using the dried sample (D) method (i.e., drying and grinding) produced the highest yield of 4.56 mg/g, followed by the A samples (doping with absolute ethanol) with 2.94 mg/g, W samples (doping with 80% (v/v) ethanol/water) with 2.64 mg/g and the microwave pre-treatment sample (M) of 1.26 mg/g. Nevertheless, the extraction yield obtained from samples A and W were comparable and did not significantly enhance the extractability of essential oil from the plant

compared to the D sample treated with drying and grinding. The lowest yield obtained after the microwave pre-treatment (M) was opposite to the finding reported by Mustapa et al. (2015), who found that the highest yield was obtained with an improved extraction rate when the medicinal plant was extracted by microwave technique.

In principle, adding polar co-solvent to the SC-CO₂ can increase the solvent power of the SC-CO₂ by enhancing the polarity of the fluid, hence increasing the extraction yield of the essential oil. However, contradictory results are shown in this study. The A sample doping with absolute ethanol yielded less than the D sample. Several studies demonstrated that adding ethanol increased oil extraction from its plants (Vidović et al., 2014). It could be due to the variation of phytochemicals compositions consisting of the high amount of non-polar compounds in the *C. vespertilionis* leaves extracts. Until today, there are no research reports on the thorough phytochemicals compositions of the *C. vespertilionis* plant. The previous study by Upadhyay et al. (2013) stated that the major components in the *C. vespertilionis* plant are comprised of triterpenes, alkaloids, fatty acids, phenols, alkanes, and long-chained alcohols. However, the composition of the polar and non-polar compounds is unavailable. Therefore, based on the result presented in this work, we hypothesize that the non-polar compounds present in the samples are higher than the amount of the polar compounds. Thus, the addition of polar co-solvent did not improve the extraction yield of the essential oil. Furthermore, the use of co-solvent was found cannot significantly increase the extraction yield. A similar result was obtained by Calvo et al.

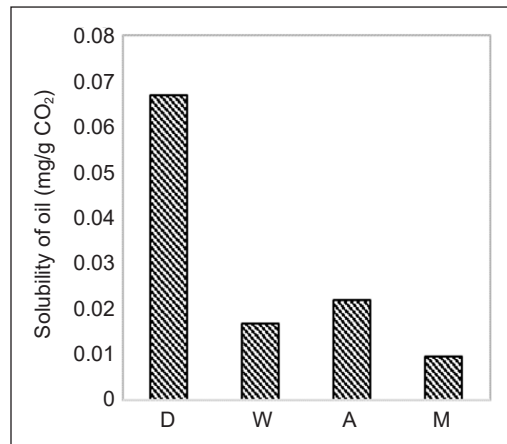


Figure 2. Solubility of *Christia vespertilionis* oil in SC-CO₂ of different sample pre-treatments: dried and ground sample (D), doping with 80% (v/v) ethanol/water (W), doping with absolute ethanol sample (A), and microwave sample (M) at constant SC-CO₂ conditions; 13.8 MPa, 40°C, CO₂ flowrate of 24 mL/min and 40 min extraction time

(2017), where adding ethanol reduced the selectivity of SC-CO₂. As studied by Reverchon and De Marco (2006), the co-solvent could increase the SC-CO₂ solvent power towards polar compounds. Nevertheless, it also could lower the fluid selectivity.

We divided dried samples into two groups to investigate how moisture content affects the supercritical extraction of *C. vespertilionis* oil. One group was treated with 80% (v/v) ethanol/water and labeled as the “W sample,” while the other group was treated with absolute ethanol and labeled as the “A sample.” The extraction yield of W and A *C. vespertilionis* samples was comparable, with 2.94 and 2.64 mg/g yield, respectively. The slight variation could be explained by the moisture content of the samples, as indicated in Table 1. Adding 80% (v/v) ethanol/water to the dried sample has increased the water content to 9% wet from the dried sample’s original moisture content (8% wet basis). Consequently, the yield of the W sample decreased to 2.64 mg/g due to the higher amount of water that hindered the extraction process. In this case, adding water to the sample increased the mass transfer resistance of the supercritical fluid to penetrate the solid particles to extract the oil. The water acts as a solvent that competes with SC-CO₂, reducing the extraction yield (Liteanu et al., 2013).

Table 1
The moisture content of samples after each pre-treatment

Types of sample pre-treatment	Moisture content (%) Wet Basis	Extraction yield (mg/g)
D	8	4.56 ± 0.52
A	8.25	2.94 ± 0.13
W	9	2.64 ± 0.08
M	59	1.26 ± 0.30

Note. D = dried and ground sample, A = doping with absolute ethanol, W = doping with 80% (v/v) ethanol/water and M = microwave pre-treatment sample

In this work, using absolute ethanol as the co-solvent in the A sample could not improve the solute solubility in SC-CO₂. It can be seen in Figure 2, which shows the solubility of *C. vespertilionis* oil in SC-CO₂ extraction for all types of sample pre-treatments. The solubility of oil from the A sample of 0.022 mg oil/g CO₂ was lower than that of the D sample (0.067 mg oil/g CO₂) when ethanol was added. The finding was similar to the work done by Calvo et al. (2017), where adding 5% (v/v) ethanol co-solvent in the SC-CO₂ extraction process did not improve the yield. It indicates that the 8% wet basis of initial moisture content of the D sample was sufficient to enhance the solubility of *C. vespertilionis* oil into supercritical fluids and facilitate the resistance of solid-fluid mass transfer (Balachandran et al., 2006). On the other hand, between A and W samples, the solubility of extract in the A sample (i.e., 0.022 mg oil/g CO₂ used) was found to be comparable to the solubility of extract in the W sample (i.e., 0.017 mg oil/g CO₂ used) due to the close moisture content owned by each other.

Among all the pre-treatment samples studied in this work, the *C. vespertilionis* sample that was treated with microwave (M) before the SC-CO₂ extraction exhibited the lowest yield of 1.26 mg/g in comparison to other pre-treatment samples (Table 1). Note that the M sample used in this study was fresh leaves with moisture content as high as 59 wt%. The leaves were used as it was collected without reducing their moisture content before being treated with microwave irradiation. The purpose of using fresh leaves without any water reduction is to promote high microwave energy absorption by the water, increasing the temperature inside the sample and leading to the expansion and rupture of the cell walls. This phenomenon is called superheating, where the water within the plant matrix facilitates the extraction via energy absorption and cell rupture (Wang & Weller, 2006). However, the lowest extraction yield obtained by the M sample showed the opposite behavior. It could be due to the substantially high-water content in the M sample acting as a barrier and increasing the mass transfer resistance for the SC-CO₂ to extract the essential oil (Pourmortazavi & Hajimirsadeghi, 2007). Furthermore, a bigger sample size of 5 mm diameter on average may also result in low yield compared to other samples. The reduction of sample particle size will shorten the intermolecular distance and increase the mass transfer rate of solutes to the solvent. Shorter distances between particles have made the diffusion process of solutes reach the solid surface higher, thus improving the yield (Santos et al., 2015).

Evaluation of SEM Images

The scanning electron microscopy (SEM) images of the dried sample (D) and microwave pre-treatment sample (M) before and after SC-CO₂ extraction are shown in Figures 3(a)–(d). Figures 3(a) and (b) show the SEM images of sample D (which was prepared by drying and grinding processes) before and after SC-CO₂ extraction. As shown in Figure 3(a), the micrograph of the non-treated sample shows a cloudy and rough surface covered with an oil layer. On the other hand, Figure 3(b) presents sample D after SC-CO₂ extraction. It is observed that the structure seems to be more porous with the deflated surfaces due to the losses of oil during the SC-CO₂ process. Grinding pre-treatment seems to destroy the epidermis of *C. vespertilionis* plant cells revealing accessible solutes to be extracted by SC-CO₂ fluid (Yahya et al., 2010).

As for the sample treated under microwave radiation (sample M) before being submitted to the SC-CO₂ extraction process, the SEM image is shown in Figure 3(c). The magnification of 2500× was used to observe the effect of irradiation on the sample. There was no difference in the structure of the sample. However, for sample M after SC-CO₂ extraction, the SEM image showed a cracked image on the leaf's surface, as shown in Figure 3(d). The extraction pressure was believed to have broken the plant's cell walls, which helped release solutes during SC-CO₂ extraction. As studied by Čolnik et al. (2016),

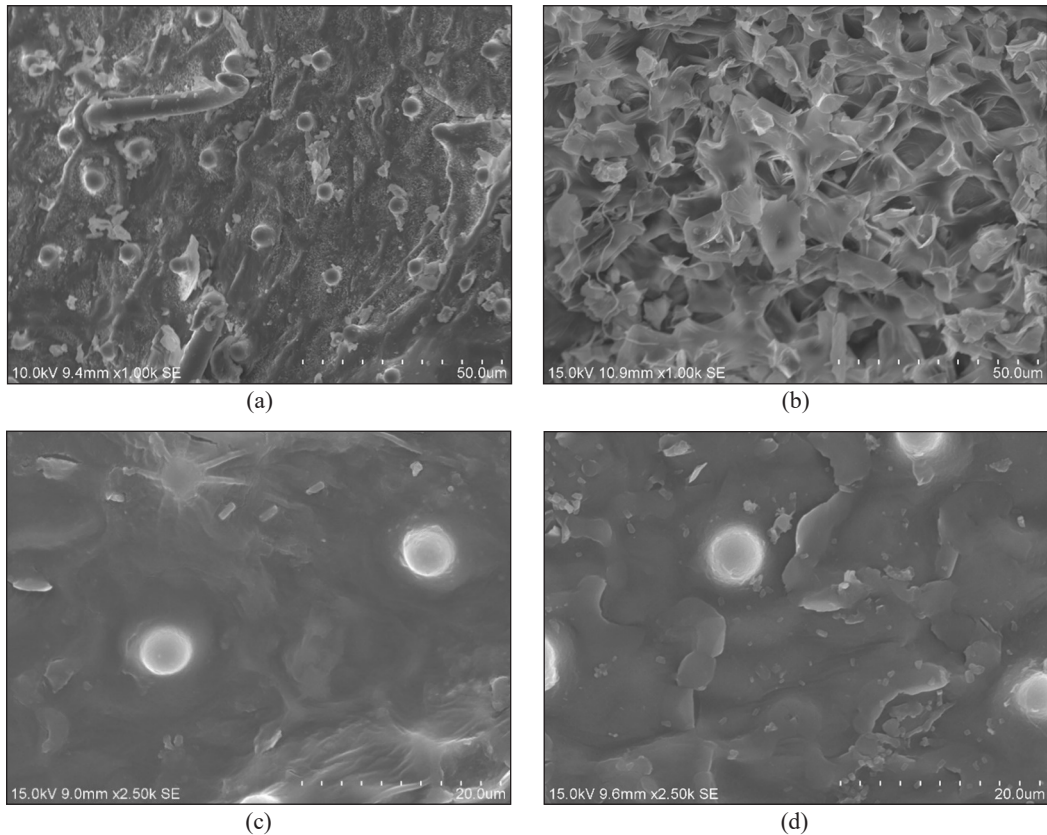


Figure 3. SEM images of (a) sample D before SC-CO₂ extraction, (b) sample D after SC-CO₂ extraction, (c) sample M before SC-CO₂ extraction, and (d) sample M after SC-CO₂ extraction. Note. Sample D: dry sample which undergoes drying and grinding processes; sample M: microwave pre-treatment sample using fresh leaves without drying and grinding processes

the SC-CO₂ extraction allows the fluid to penetrate and damage the cell walls, releasing the active compounds. However, the depletion of oil in sample M was not much occurred as compared to sample D. This result relates to the extraction yield obtained by sample M, i.e., 1.26 mg/g, which was lower than sample D (4.56 mg/g). It was assumed that the high-water content in the fresh sample had lowered the yield. A similar result was obtained by Viguera et al. (2016), where the microwave pre-treatment was not useful for the wet sample since the water created a barrier during the extraction process.

Phytochemicals Characterization Analysis

All extracts obtained from the D, A, W, and M of *C. vespertilionis* samples were analyzed by GCMS to determine the major compounds present in the essential oil and to determine the effect of sample pre-treatment on the phytochemicals extracted. The GCMS analysis revealed six major compounds in the *C. vespertilionis* extracted under SC-CO₂ extraction

at 13.8 MPa, 40°C, 24 mL/min, and 40 min extraction time. Phytochemical compounds are identified based on the peak area, retention time, and molecular formula using methanol as a blank injection sample.

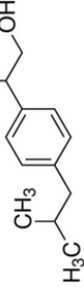
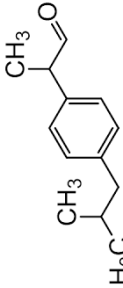

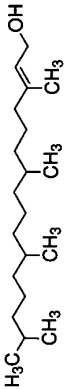
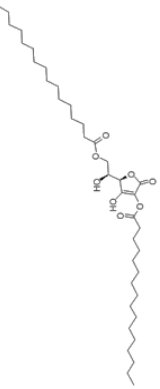
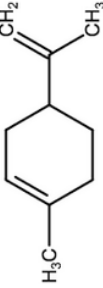
The components' names, percentage peak area, chemical structure, retention time, and component biological activity were tabulated in Table 2. The major constituents in the *C. vespertilionis* extracts were ibuprofen alcohol, 2-(4-isobutylphenyl) propanal, cis-phytol, α -monolaurin, phytol, l-ascorbyl 2,6-dipalmitate, and limonene. Similar phytochemicals were reported elsewhere from *C. vespertilionis* extracted by Soxhlet and maceration techniques (Zambari et al., 2021).

Note that three components, i.e., ibuprofen alcohol, 2-(4-isobutylphenyl) propanal, and phytol, were identified in all samples except the sample from the microwave pre-treatment (M). One component detected from the chromatography analysis of the M sample and extracted by SC-CO₂ extraction was l-ascorbyl 2,6-dipalmitate. It can be explained by the substantially low yield obtained due to its high moisture content. The water may hinder the flow of SC-CO₂ fluid through the sample, decreasing the contact surface between solutes and solvent and making it difficult to extract other compounds. Too high water content in the sample reduced the extraction efficiency and thus lowered the yield. The result was supported by the solubility data of the microwave sample, as shown in Figure 2, where it is the lowest solubility among all samples.

On the other hand, 2-(4-isobutylphenyl) propanol and 2-(4-isobutylphenyl) propanal, which are the impurities of ibuprofen, were found in all *C. vespertilionis* samples except the microwave pre-treatment technique (M sample). The 2-(4-isobutylphenyl) propanol is also known as ibuprofen alcohol or ibuprofenol (Chen & Rosazza, 1994). There are many types of ibuprofen impurities. The one discovered in this work is ibuprofen impurities which is the ibuprofen alcohol, and another is an in-house ibuprofen impurity known as 2-(4-isobutylphenyl) propanal. The compounds were commonly used as reference standards to study the separation and synthesis of ibuprofen drugs and were mainly applied in the pharmaceutical field (Giacomini et al., 2007). Ibuprofen is a non-steroidal anti-inflammatory drug (NSAID) normally used as a painkiller.

Another bioactive compound isolated from *C. vespertilionis* is the phytol compound. Phytol is a bioactive component derived from the chlorophyll of green plants. The compound was found in many plant extracts, such as *Majorana hortensis Moench*, *Thymus vulgaris* L., *Achillea ligustica*, *Marchantia convolute*, and *Porophyllum ruderale* (Conde-Hernández et al., 2017). Islam et al. (2015), in their review on the importance of phytol in the pharmaceutical industry, have reported that phytol portrayed numerous medicinal properties such as cytotoxic, anti-tumorous, anti-mutagenic, anti-teratogenic, antidiabetic, lipid-lowering, antispasmodic, anticonvulsant, anti-nociceptive, anxiolytic, antidepressant, hair growth facilitator, hair fall defense and antidandruff activities. Phytol is a non-polar compound; the SC-CO₂ tends to solubilize the compound from the plant materials. The

Table 2
Bioactive compounds identified in SC-CO₂ extraction of Christia vespertilionis using GCMS for different sample pre-treatments (D, A, W & M)

Compounds Names	Retention Time (min)	Percentage Area (%)	Formula	Molecular Weight (g/mol)	Chemical Structure	Biological Activity	References
Ibuprofen alcohol	A: 14.78	A: 2.37	C ₁₃ H ₂₀ O	192.30		Ibuprofen impurity P was used in the pharmaceutical study.	(Giacomini et al., 2007)
	W: 14.80	W: 6.89					
	D: 14.79	D: 7.97					
	M: -	M: -					
2-(4-isobutylphenyl) propanal	A: 17.01	A: 4.54	C ₁₃ H ₁₈ O	190.28		Synthesis of ibuprofen	(Roy, 2011)
	W: 17.05	W: 8.06					
	D: 17.04	D: 10.19					
	M: -	M: -					
α-Monolaurin	A: 22.64	A: 27.01	C ₁₃ H ₃₀ O ₄	274.40		Anti-bacterial Antiviral Antimicrobial	(Lieberman et al., 2006)
	W: -	W: -					
	D: -	D: -					
	M: -	M: -					
Cis-phytol and Phytol	A: 29.95	A: 16.68	C ₂₀ H ₄₀ O	296.54		Antimicrobial Anti-cancer Anti-inflammatory Antioxidant Anti-bacterial	(Pejin et al., 2014) (Kalaivani et al., 2012) (Okwu & Ighodaro, 2010)
	W: 30.61	W: 10.61					
	D: 30.46	D: 17.05					
	M: -	M: -					
L-ascorbyl 2,6-dipalmitate	A: -	A: -	C ₃₈ H ₆₈ O ₈	652.94			
	W: 22.81	W: 8.20					
	D: 22.76	D: 6.38					
	M: 22.58	M: 4.13					
Limonene	A: -	A: -	C ₁₀ H ₁₆	136.24		Antioxidant	(Bagheri et al., 2014)
	W: -	W: -					
	D: 5.44	D: 17.57					
	M: -	M: -					

highest peak area of phytol of 17.05% was obtained in the D sample compared to the A and W samples. It indicates that the doping technique with ethanol did not enhance the extraction of the phytol into the SC-CO₂. The phytol appeared at the retention time ranging from 21.22 to 22.00 min (not shown in Table 2), corresponding to isomer cis-phytol. In contrast, the phytol was identified at 29.95, 30.61, and 30.46 for the A, W, and D samples.

On the other hand, the maximum peak area of 27.01% that corresponds to the α -monolaurin appeared merely in the sample doped with absolute ethanol (A sample). The presence of the α -monolaurin was possibly due to the addition of ethanol, which increases the solvating power of the SC-CO₂ fluid to dissolve polar components in the *C. vespertilionis* plant. Although the oil yield of the A sample is slightly lower than the D sample, the oil quality was enhanced when the ethanol was added via doping technique, enabling the extraction of a polar compound from the plant. The discovery of α -monolaurin from *C. vespertilionis* was the first time discovered and reported in this study. This compound possesses many potential benefits that promote good health sustainability. A review study by Lieberman et al. (2006) has summarized that monolaurin compounds exhibit anti-bacterial, anti-fungal, and anti-virus effects, which are useful in treating infections caused by harmful organisms. The study on the anti-fungal activity of monolaurin was further continued by Seleem et al. (2016), where monolaurin was found could treat *Candida albicans*, i.e., a type of pathogen that existed in the gastrointestinal tract and mouth of the human body. According to a clinical study, the major source of monolaurin comes from the mother's breast milk which possesses an effective immune potion to protect newborn babies from bacterial infections due to the antimicrobial activity owned by the monolaurin compound.

On the other hand, l-ascorbic acid 2,6-dihexadecanoate, also known as l-ascorbyl 2,6-dipalmitate (ADP), was merely identified in D, W, and M samples with a peak area range from 4 to 8%. The absence of the ADP in the A sample could be due to its high molecular weight that hindered its solubility into the SC-CO₂, which cannot be improved even though it was doped with absolute ethanol. Sethupathy et al. (2017) demonstrated that ADP exhibits anti-biofilm, anti-pathogenic and anti-carotenogenic agents. The compound was also found in the leaf extract of *Alstonia boonei* and had anti-bacterial activity (Okwu & Ighodaro, 2010). Another study by Selvamangai and Bhaskar (2012) on the extraction of *Shorea robusta* leaves L. under methanolic extraction isolated the ascorbic compound and reported the compound possesses antioxidant, anti-scorbutic, anti-inflammatory, anti-nociceptive, anti-mutagenic and wound healing property.

Furthermore, *C. vespertilionis* extract contained L-limonene, classified as a cyclic terpene. Nevertheless, this compound was merely discovered from the dried and ground sample (D). The compound was detected at 5.44 min of retention time and had the highest relative abundance of 17.57% peak area compared to other compounds. Limonene is naturally a non-polar compound, thus, making it easy to solubilize in the SC-CO₂. The

discovery of limonene in the *C. vespertilionis* was in correspondence with the previous study conducted by Upadhyay et al. (2013), where the authors proved that limonene is present as one of the major components in *C. vespertilionis*. Terpenes were known to be the primary constituents of the essential oils of many types of medicinal plants.

The chemical structure of limonene comprises an alkene compound with double bonds that are insoluble in a polar solvent such as water or ethanol. It explains that limonene was not found in the extracts of the samples doped with absolute ethanol (A sample) and ethanol/water (W sample). A previous study demonstrated that the limonene compound could be extracted without additional co-solvent (Nautiyal, 2016). Another possible reason for the absence of limonene in the W and A type sample was the evaporation of the compounds during the sample collection. Therefore, it is suggested to place the test tube of the sample collector in an ice bath to reduce the loss of the volatile compounds at room temperature, as demonstrated by Conde-Hernández et al. (2017). As for the microwave pre-treatment (M sample), the limonene could not be identified. It could be due to the high amount of moisture in the sample that might prevent the SC-CO₂ from reaching the solute in solid particles during the extraction process.

CONCLUSION

The effect of different sample pre-treatments on the *C. vespertilionis* plant was reported in this work, including drying and grinding, the doping technique with absolute ethanol, 80% (v/v) ethanol/water as co-solvent, and the microwave pre-treatment. The findings showed that drying and grinding the sample without additional co-solvents obtained the highest extraction yield of 4.56 mg/g and solubility of 0.067 mg oil/g CO₂. Furthermore, applying microwave pre-treatment on fresh leaves prior to the SC-CO₂ did not enhance the oil yield and solubility. The best pre-treatment method for SC-CO₂ extraction of *C. vespertilionis* was by drying the fresh leaves to reduce their moisture content, then grinding them into smaller particle sizes. This technique has considerably increased the oil yield and solubility. The phytochemicals analysis of the *C. vespertilionis* extracts discovered the identification of four medicinal compounds with phytol present as the major component, followed by α -monolaurin, l-ascorbyl 2,6-dipalmitate, and limonene. The variation of compounds discovered from different types of sample pre-treatment methods suggests that the extraction of compounds of interest can be optimized by applying the appropriate techniques to increase their extractability from specific plant matrices.

ACKNOWLEDGMENTS

The authors are grateful to the School of Chemical Engineering in Universiti Teknologi MARA (UiTM), Shah Alam, Malaysia, for the facilities to carry out the project and the Pure Rerama Leaf for providing the sample.

REFERENCES

- Almeida, R. N., Neto, R. G., Barros, F. M. C., Cassel, E., von Poser, G. L., & Vargas, R. M. F. (2013). Supercritical extraction of *Hypericum caprifoliatum* using carbon dioxide and ethanol+water as co-solvent. *Chemical Engineering and Processing: Process Intensification*, 70, 95-102. <https://doi.org/10.1016/j.cep.2013.05.002>
- Bagheri, H., Manap, M. Y. A., & Solati, Z. (2014). Antioxidant activity of *Piper nigrum* L. essential oil extracted by supercritical CO₂ extraction and hydro-distillation. *Talanta*, 121, 220-228. <http://dx.doi.org/10.1016/j.talanta.2014.01.007>
- Balachandran, S., Kentish, S. E., & Mawson, R. (2006). The effects of both preparation method and season on the supercritical extraction of ginger. *Separation and Purification Technology*, 48(2), 94-105. <http://dx.doi.org/10.1016/j.seppur.2005.07.008>
- Beck, C. B. (2010). *An Introduction to Plant Structure and Development: Plant Anatomy for the Twenty-First Century*. Cambridge University Press.
- Calvo, A., Morante, J., Plánder, S., & Székely, E. (2017). Fractionation of biologically active components of grape seed (*Vitis vinifera*) by supercritical fluid extraction. *Acta Alimentaria*, 46(1), 27-34. <https://doi.org/10.1556/066.2017.46.1.4>
- Cambie, R., & Ash, J. (1994). *Fijian Medicinal Plants*. Csiro Publishing.
- Cargnin, S. T., de Matos Nunes, J., Haas, J. S., Baladão, L. F., Cassel, E., Vargas, R. F., Rech, S. B., & von Poser, G. L. (2010). Supercritical fluid extraction and high performance liquid chromatographic determination of benzopyrans and phloroglucinol derivative in *Hypericum polyanthemum*. *Journal of Chromatography B*, 878(1), 83-87. <https://doi.org/10.1016/j.jchromb.2009.11.012>
- Chassagne, F., Hul, S., Deharo, E., & Bourdy, G. (2016). Natural remedies used by Bunong people in Mondulkiri province (Northeast Cambodia) with special reference to the treatment of 11 most common ailments. *Journal of Ethnopharmacology*, 191, 41-70. <https://doi.org/10.1016/j.jep.2016.06.003>
- Chen, Y., & Rosazza, J. P. (1994). Microbial transformation of Ibuprofen by a nocardia species. *Applied and Environmental Microbiology*, 60(4), 1292-1296. <https://doi.org/10.1128/aem.60.4.1292-1296.1994>
- Čolnik, M., Primožič, M., Knez, Ž., & Leitgeb, M. (2016). Use of non-conventional cell disruption method for extraction of proteins from black yeasts. *Frontiers in Bioengineering and Biotechnology*, 4, Article 33. <https://doi.org/10.3389/fbioe.2016.00033>
- Conde-Hernández, L. A., Espinosa-Victoria, J. R., & Guerrero-Beltrán, J. Á. (2017). Supercritical extraction of essential oils of *Piper auritum* and *Porophyllum ruderale*. *The Journal of Supercritical Fluids*, 127, 97-102. <https://doi.org/10.1016/j.supflu.2017.03.026>
- Dash, G. K. (2016). An appraisal of *Christia vespertilionis* (L. F.) Bakh. F.: A promising medicinal plant. *International Journal of Pharmacognosy and Phytochemical Research*, 8(6), 1037-1039.
- Giacomini, D., Galletti, P., Quintavalla, A., Gucciardo, G., & Paradisi, F. (2007). Highly efficient asymmetric reduction of arylpropionic aldehydes by Horse Liver Alcohol Dehydrogenase through dynamic kinetic resolution. *Chemical Communications*, 39, 4038-4040. <https://doi.org/10.1039/B712290J>

- Herrero, M., del Pilar Sánchez-Camargo, A., Cifuentes, A., & Ibáñez, E. (2015). Plants, seaweeds, microalgae and food by-products as natural sources of functional ingredients obtained using pressurized liquid extraction and supercritical fluid extraction. *TrAC Trends in Analytical Chemistry*, 71, 26-38. <https://doi.org/10.1016/j.trac.2015.01.018>
- Hofer, D., Schwach, G., Tabrizi-Wizsy, N. G., Sadjak, A., Sturm, S., Stuppner, H., & Pfragner, R. (2013). *Christia vespertilionis* plant extracts as novel antiproliferative agent against human neuroendocrine tumor cells. *Oncology Reports*, 29(6), 2219-2226. <https://doi.org/10.3892/or.2013.2367>
- Islam, M. T., de Alencar, M. V. O. B., da Conceição Machado, K., da Conceição Machado, K., de Carvalho Melo-Cavalcante, A. A., de Sousa, D. P., & de Freitas, R. M. (2015). Phytol in a pharma-medico-stance. *Chemico-Biological Interactions*, 240, 60-73. <https://doi.org/10.1016/j.cbi.2015.07.010>
- Ismail, N. Z., Adebayo, I. A., Mohamed, W. A. S., Zain, N. N. M., & Arsad, H. (2021). *Christia vespertilionis* extract induced antiproliferation and apoptosis in breast cancer (MCF7) cells. *Molecular Biology Reports*, 48, 7361-7370. <https://doi.org/10.1007/s11033-021-06743-w>
- Ivanovic, J., Meyer, F., Stamenic, M., Jaeger, P., Zizovic, I., & Eggers, R. (2014). Pretreatment of natural materials used for supercritical fluid extraction of commercial phytopharmaceuticals. *Chemical Engineering & Technology*, 37(9), 1606-1611. <https://doi.org/10.1002/ceat.201300715>
- Kalaivani, C. S., Sathish, S. S., Janakiraman, N., & Johnson, M. (2012). GC-MS studies on *Andrographis paniculata* (Burm. f.) wall. ex Nees - A medicinally important plant. *International Journal of Medicinal and Aromatic Plants*, 2(1), 69-74.
- Lee, J. J., Saiful Yazan, L., Kassim, N. K., Abdullah, C. A. C., Esa, N., Lim, P. C., & Tan, D. C. (2020). Cytotoxic Activity of *Christia vespertilionis* root and leaf extracts and fractions against breast cancer cell lines. *Molecules*, 25(11), Article 2610. <https://doi.org/10.3390/molecules25112610>
- Lieberman, S., Enig, M. G., & Preuss, H. G. (2006). A review of monolaurin and lauric acid: Natural virucidal and bactericidal agents. *Alternative and Complementary Therapies*, 12(6), 310-314. <https://doi.org/10.1089/act.2006.12.310>
- Liteanu, E., Spiers, C. J., & de Bresser, J. H. P. (2013). The influence of water and supercritical CO₂ on the failure behavior of chalk. *Tectonophysics*, 599, 157-169. <https://doi.org/10.1016/j.tecto.2013.04.013>
- Lu, J. J., Bao, J. L., Chen, X. P., Huang, M., & Wang, Y. T. (2012). Alkaloids isolated from natural herbs as the anticancer agents. *Evidence-Based Complementary and Alternative Medicine*, 2012, Article 485042. <https://doi.org/10.1155/2012/485042>
- Mukhopadhyay, M. (2000). *Natural Extracts using Supercritical Carbon Dioxide*. CRC Press LLC.
- Mustapa, A. N., Manan, Z. A., Azizi, C. Y. M., Norulaini, N. A. N., & Omar, A. K. M. (2009). Effects of parameters on yield for sub-critical R134a extraction of palm oil. *Journal of Food Engineering*, 95(4), 606-616. <http://dx.doi.org/10.1016/j.jfoodeng.2009.06.025>
- Mustapa, A. N., Martin, A., Gallego, J. R., Mato, R. B., & Cocero, M. J. (2015). Microwave-assisted extraction of polyphenols from *Clinacanthus nutans* Lindau medicinal plant: Energy perspective and kinetics modeling. *Chemical Engineering and Processing: Process Intensification*, 97, 66-74. <http://dx.doi.org/10.1016/j.cep.2015.08.013>

- Mustapa, A. N., Martin, Á., Mato, R. B., & Cocero, M. J. (2015). Extraction of phytochemicals from the medicinal plant *Clinacanthus nutans* Lindau by microwave-assisted extraction and supercritical carbon dioxide extraction. *Industrial Crops and Products*, 74, 83-94. <http://dx.doi.org/10.1016/j.indcrop.2015.04.035>
- Nautiyal, O. H. (2016). Food processing by supercritical carbon dioxide-review. *EC Chemistry*, 2(1), 111-135.
- Nguyen-Pouplin, J., Tran, H., Phan, T. A., Dolecek, C., Farrar, J., Tran, T. H., Caron, P., Bodo, B., & Grellier, P. (2007). Antimalarial and cytotoxic activities of ethnopharmacologically selected medicinal plants from South Vietnam. *Journal of Ethnopharmacology*, 109(3), 417-427. <https://doi.org/10.1016/j.jep.2006.08.011>
- Okwu, D. E., & Ighodaro, B. U. (2010). GC-MS evaluation of bioactive compounds and antibacterial activity of the oil fraction from the leaves of *Alstonia boonei* De Wild. *Pharma Chemica*, 2(1), 261-272.
- Pejin, B., Savic, A., Sokovic, M., Glamoclija, J., Ciric, A., Nikolic, M., Radotic, K., & Mojovic, M. (2014). Further in vitro evaluation of antiradical and antimicrobial activities of phytol. *Natural Product Research*, 28(6), 372-376. <https://doi.org/10.1080/14786419.2013.869692>
- Pourmortazavi, S. M., & Hajimirsadeghi, S. S. (2007). Supercritical fluid extraction in plant essential and volatile oil analysis. *Journal of Chromatography A*, 1163(1), 2-24. <https://doi.org/10.1016/j.chroma.2007.06.021>
- Reverchon, E., & De Marco, I. (2006). Supercritical fluid extraction and fractionation of natural matter. *The Journal of Supercritical Fluids*, 38(2), 146-166. <http://dx.doi.org/10.1016/j.supflu.2006.03.020>
- Rombaut, N., Savoie, R., Thomasset, B., Bélliard, T., Castello, J., Van Hecke, É., & Lanoisellé, J. L. (2014). Grape seed oil extraction: Interest of supercritical fluid extraction and gas-assisted mechanical extraction for enhancing polyphenol co-extraction in oil. *Comptes Rendus Chimie*, 17(3), 284-292. <http://dx.doi.org/10.1016/j.crci.2013.11.014>
- Roy, J. (2011). *An Introduction to Pharmaceutical Sciences: Production, Chemistry, Techniques and Technology*. Woodhead Publishing.
- Santos, P., Aguiar, A. C., Barbero, G. F., Rezende, C. A., & Martínez, J. (2015). Supercritical carbon dioxide extraction of capsaicinoids from malagueta pepper (*Capsicum frutescens* L.) assisted by ultrasound. *Ultrasonics Sonochemistry*, 22(0), 78-88. <https://doi.org/http://dx.doi.org/10.1016/j.ultsonch.2014.05.001>
- Seleem, D., Chen, E., Benso, B., Pardi, V., & Murata, R. M. (2016). In vitro evaluation of antifungal activity of monolaurin against *Candida albicans* biofilms. *PeerJ*, 4, Article e2148. <https://doi.org/10.7717/peerj.2148>
- Selvamangai, G., & Bhaskar, A. (2012). GC-MS analysis of phytochemicals in the methanolic extract of *Eupatorium triplinerve*. *Asian Pacific Journal of Tropical Biomedicine*, 2(3), S1329-S1332. [https://doi.org/https://doi.org/10.1016/S2221-1691\(12\)60410-9](https://doi.org/https://doi.org/10.1016/S2221-1691(12)60410-9)
- Sethupathy, S., Vigneshwari, L., Valliammai, A., Balamurugan, K., & Pandian, S. K. (2017). l-Ascorbyl 2,6-dipalmitate inhibits biofilm formation and virulence in methicillin-resistant *Staphylococcus aureus* and prevents triacylglyceride accumulation in *Caenorhabditis elegans*. *RSC Advances*, 7(38), 23392-23406. <https://doi.org/10.1039/C7RA02934A>

- Upadhyay, H. C., Sisodia, B. S., Cheema, H. S., Agrawal, J., Pal, A., Darokar, M. P., & Srivastava, S. K. (2013). Novel antiplasmodial agents from *Christia vespertilionis*. *Natural Product Communications*, 8(11), 1591-1594. <https://doi.org/10.1177/1934578X1300801123>
- Uquiche, E., Jeréz, M., & Ortíz, J. (2008). Effect of pretreatment with microwaves on mechanical extraction yield and quality of vegetable oil from Chilean hazelnuts (*Gevuina avellana* Mol). *Innovative Food Science & Emerging Technologies*, 9(4), 495-500. <http://dx.doi.org/10.1016/j.ifset.2008.05.004>
- Vidović, S., Zeković, Z., Marošanić, B., Todorović, M. P., & Vladić, J. (2014). Influence of pre-treatments on yield, chemical composition and antioxidant activity of *Satureja montana* extracts obtained by supercritical carbon dioxide. *The Journal of Supercritical Fluids*, 95, 468-473. <http://dx.doi.org/10.1016/j.supflu.2014.10.019>
- Viguera, M., Marti, A., Masca, F., Prieto, C., & Calvo, L. (2016). The process parameters and solid conditions that affect the supercritical CO₂ extraction of the lipids produced by microalgae. *The Journal of Supercritical Fluids*, 113, 16-22. <http://dx.doi.org/10.1016/j.supflu.2016.03.001>
- Wang, L., & Weller, C. L. (2006). Recent advances in extraction of nutraceuticals from plants. *Trends in Food Science & Technology*, 17(6), 300-312. <https://doi.org/http://dx.doi.org/10.1016/j.tifs.2005.12.004>
- Whiting, P. A. (2007). *Commercial production of Christia Subcordata Moench by establishing cultural practices and by applying plant growth regulators* [Unpublished master thesis]. University of Georgia, USA. https://getd.libs.uga.edu/pdfs/whiting_paula_a_200712_ms.pdf
- Wu, X. Y., Tang, A. C., & Lu, Q. Y. (2012). Study on antitumor effect of the extract from *Christia vespertilionis* in vivo. *Chinese Journal of Experimental Traditional Medical Formulae*, 8, 202-204.
- Yahya, F., Lu, T., Santos, R. C. D., Fryer, P. J., & Bakalis, S. (2010). Supercritical carbon dioxide and solvent extraction of 2-acetyl-1-pyrroline from Pandan leaf: The effect of pre-treatment. *The Journal of Supercritical Fluids*, 55(1), 200-207. <https://doi.org/10.1016/j.supflu.2010.05.027>
- Yu, Q., Duan, W., Liu, B., Duan, Z., & Shang, F. F. (2016). Microwave-assisted extraction of bioactive substance from *Clinacanthus nutans*. In *Proceedings of the 2015 4th international conference on sustainable energy and environmental engineering* (pp. 748-754). Atlantis Press. <https://doi.org/10.2991/icseee-15.2016.128>
- Zambari, I. F., Hafid, S. R. A., & Muhamad, N. A. (2021). Optimisation of extraction method and phytochemical compounds of green *Christia vespertilionis* leaves using GC-MS. *International Journal of Pharmaceutical Sciences Review and Research*, 70(1), 1-8. <https://doi.org/10.47583/ijpsrr.2021.v70i01.001>

Spatial Distribution of Malaysian Storks Determined Based on Citizen Science (eBird) Data

Ain Afifah Tolohah, Fatihah Najihah Arazmi, Shukor Md. Nor and Mohammad Saiful Mansor*

Department of Biological Sciences and Biotechnology, Faculty of Science and Technology, Universiti Kebangsaan Malaysia, 43600 Bangi, Selangor, Malaysia

ABSTRACT

Waterbird populations are rapidly declining worldwide, including in many countries in Southeast Asia. Massive land use changes in Peninsular Malaysia are a major threat to biodiversity due to habitat loss and alteration, affecting the populations of many waterbird species. This study was conducted to determine the spatial distribution of three stork species, the Asian Openbill *Anastomus oscitans*, Painted Stork *Mycteria leucocephala* and Milky Stork *Mycteria cinerea*, in Peninsular Malaysia using the citizen science database, eBird. About 86,881 occurrences of the Asian Openbill, 2,391 occurrences of the Painted Stork and 242 occurrences of the Milky Stork were identified in the eBird database throughout Peninsular Malaysia between 2019 and 2021, suggesting major differences in occurrence size between the three species. Map generated from ArcGIS and a statistically significant difference in the population distribution of the three stork species across Peninsular Malaysia indicate habitat segregation. The populations of these stork species should be carefully monitored and managed to avoid imbalance with other waterbird populations.

Keywords: Citizen science data, distribution, Peninsular Malaysia, storks, waterbirds

ARTICLE INFO

Article history:

Received: 29 July 2022

Accepted: 14 November 2022

Published: 13 July 2023

DOI: <https://doi.org/10.47836/pjst.31.5.14>

E-mail addresses:

ainurafifah2963@gmail.com (Ain Afifah Tolohah)

n.fatihahnajihah@gmail.com (Fatihah Najihah Arazmi)

shukor@ukm.edu.my (Shukor Md. Nor)

msaifulmansor@gmail.com (Mohammad Saiful Mansor)

* Corresponding author

INTRODUCTION

Malaysia supports diverse ecosystems, including tropical rainforests and aquatic ecosystems with estuaries and mangrove forests, and is one of the world's megadiverse countries rich in flora and fauna. However, land use changes and anthropogenic activities in Peninsular Malaysia threaten the country's biodiversity (Darren et al.,

2021; Rahman et al., 2014), and many waterbird species are affected due to habitat loss and limited food resources in coastal and freshwater areas. Waterbird populations are severely declining worldwide, especially in Southeast Asia, because of anthropogenic activities, such as habitat destruction, pollution, hunting, and recreation, which intensify the effects of disturbance on certain waterbird species (Robinson & Cranswick, 2003).

Twenty species of stork (family Ciconiidae) have been identified worldwide, of which four are considered endangered (IUCN, 2022). Of the 11 stork species in tropical Asia, three found in Southeast Asia are endangered: the Greater Adjutant, *Leptoptilos dubius*; Storm's Stork, *Ciconia stormi*; and Milky Stork, *Mycteria cinerea* (BirdLife International, 2016). The Milky Stork's Malay name is "Botak Upeh," is native species to Malaysia and has an estimated 5,500 individuals surviving worldwide (BirdLife International, 2022). In Peninsular Malaysia, the wild population of Milky Storks are restricted to Matang Mangrove Forest Reserve near Kuala Gula, Perak, since the mangrove forest is the most suitable habitat for these species to survive (Ismail & Rahman, 2012). This species was part of a captive breeding and release programme in Zoo Negara, located in Peninsular Malaysia, between 1998 and 2004 to restore the population in the wild (Ismail et al., 2011). In 2005, Zoo Negara in Hulu Kelang, Selangor, became a successful sanctuary for about one hundred individuals of Milky Storks that lived and bred in captivity (Ismail & Rahman, 2012). Unfortunately, their wild population faces major threats from hazardous chemicals such as heavy metals ingested via food and water (Rahman et al., 2017; Rahman et al., 2014), habitat destruction, poaching by humans, high rates of predation and disturbance caused by anthropogenic activities (Ismail & Rahman, 2012).

The Asian Openbill (*Anastomus oscitans*) has recently been recognised as a native waterbird of Peninsular Malaysia and is commonly known as "Botak Asia" or "Upeh Paruh Sepit" by local bird guides. The migration of this species from southern Thailand to Peninsular Malaysia began during the dry season in early 2013 and was a major cause of its presence in Peninsular Malaysia (Chuah, 2013; Low et al., 2013; Tan & Murali, 2013). The population of Asian Openbill in Malaysia is considered to be in decline. However, the species is not listed as endangered as its populations in other countries, such as Nepal, Pakistan and India, are still at a high level (Abidin et al., 2017).

The Painted Stork's Malay name is "Botak Padi" (*Mycteria leucocephala*), a vagrant species in Peninsular Malaysia, may be classified as the most abundant of Asian storks (Zakaria & Nor, 2019). Previously, the Painted Stork was an introduced species brought to Malaysia (Zoo Negara) in 1965 from Sri Lanka. Then, after a few years in captivity, this species was let loose outside Zoo Negara, able to survive and spread rapidly in the lakes and ponds all over Selangor and Kuala Lumpur (Zakaria & Nor, 2019). However, its numbers have been declining for years in South Asia and Southeast Asia, and it was classified as Near Threatened in 2004 (IUCN, 2021) due to several factors, including deforestation, water pollution, wetland drainage and hunting (Koli et al., 2013).

This study determined the spatial distribution sizes of the Asian Openbill, Painted Stork and Milky Stork in Peninsular Malaysia using eBird, the citizen science database. Their similar habitat preferences, particularly for freshwater areas, raise the question of how these three stork species are spatially distributed in Peninsular Malaysia. eBird, which provides over 140 million accurate records contributed by 150,000 different researchers from around the world (Callaghan & Gawlik, 2015), is an important resource for obtaining comprehensive information on the presence of stork species in Peninsular Malaysia because data have been recorded for many locations throughout the country.

MATERIALS AND METHODS

Study Area

Malaysia consists of two regions, Peninsular Malaysia and Malaysian Borneo (East Malaysia). This study covered all states of Peninsular Malaysia, which is 131,598 km² in area and comprises 11 of the 13 states and two of the three federal territories (i.e., Wilayah Persekutuan Kuala Lumpur and Wilayah Persekutuan Putrajaya) of Malaysia (Figure 1). Peninsular Malaysia extends from southern Thailand to Singapore. It is surrounded by the sea and separated from Sumatra in the west by the Straits of Malacca and East Malaysia by the South China Sea.

eBird Data

Data were obtained from the eBird website, which provides specific information to identify the occurrences and estimate the distribution patterns of the three species of stork in Peninsular Malaysia. eBird, whose citizen science data have been used by scientific researchers worldwide, provides data for over 180,000 locations across the landscape, easily accessible at any time. Data were downloaded from eBird to identify the distributions and to compare the abundance

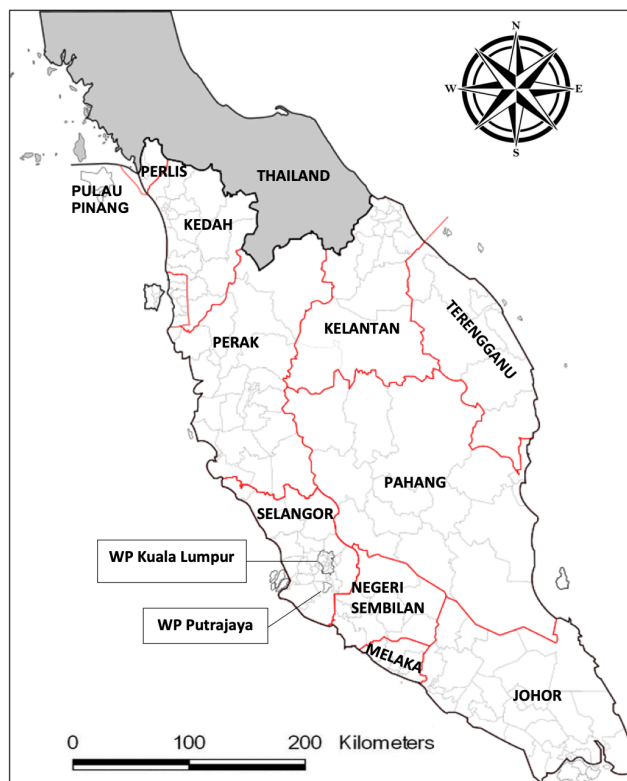


Figure 1. The map of Peninsular Malaysia

and distribution sizes of the Asian Openbill, Painted Stork and Milky Stork in all states in Peninsular Malaysia. The data set received from eBird included validated observation dates, observer identification, exact locations, coordinates, and observation counts. Only 'complete' checklists were included in this study after the downloaded data were vetted. A species checklist was defined as 'complete' if the 'stationary', 'travelling', or 'exhaustive' protocol was followed (Sullivan et al., 2014). Checklists with 'group identifiers' were excluded from the study since they duplicated data. The data for the abundances of the three stork species were collected from January 2019 to March 2021. They were grouped according to the 10 states of Peninsular Malaysia and the two federals' territories. According to the data obtained, the study area included states and territories extending from the north to the south of Peninsular Malaysia in the direction of the west coast: Johor (MY-01), Kedah (MY-02), Kelantan (MY-03), Melaka (MY-04), Negeri Sembilan (MY-05), Pahang (MY-06), Pulau Pinang (MY-07), Perak (MY-08), Perlis (MY-09), Selangor (MY-10), Terengganu (MY-11), Wilayah Persekutuan Kuala Lumpur (MY-14), and Wilayah Persekutuan Putrajaya (MY-16).

Data Analyses

Data for the distribution of the three selected species of stork were analysed using ArcGIS Desktop 10.8 to address estimated position error (ESRI, Redlands, CA, USA) to ensure that the occurrences were within 100 m of the border of Peninsular Malaysia (Arazmi et al., 2022). The Kernel Density Tool was used to determine the density and distribution pattern of the three stork species in Peninsular Malaysia. The kernels were analysed using a UTM Zone 48N projection at 1 km resolution. The Arc Toolbox was used to generate a map of the occurrence of each species, map the overlaps of the occurrences, and identify which areas received bird visits throughout the study period. Kernel output was stretched using a histogram equaliser and resampled with the bilinear interpolation technique to enhance the appearance and smoothness of the raster data.

The data were normally distributed (determined using quantile–quantile plots and the Shapiro–Wilk test). According to states, the Kruskal–Wallis test was used to compare the distribution of the occurrences of the three stork species across Peninsular Malaysia. All analyses were performed using Minitab 19 software.

RESULTS

A total of 86,881 occurrences of the Asian Openbill, 2,391 occurrences of the Painted Stork and 242 occurrences of the Milky Stork were identified across Peninsular Malaysia between 2019 and 2020 (Figure 2). The Asian Openbill was present in 10 states and one federal territory. The largest number of records of Asian Openbills was for Melaka, with 32,784 occurrences, while the smallest number was for Wilayah Persekutuan Kuala

Lumpur, with 250 occurrences (Figure 3). Painted Storks were recorded in five states and federal territories, with the highest number in Selangor, 2,013 occurrences and the lowest in Seremban and Pahang, with one and two occurrences, respectively (Figure 3). The highest number of Milky Storks was recorded in Perak, with 211 occurrences (Figure 3). Meanwhile, for Terengganu, zero individual was recorded for all three species of storks (Figure 2).

The distributions of the three stork species in Peninsular Malaysia differed significantly (Kruskal–Wallis test: $H = 6.893, p = 0.027$). The three species showed habitat segregation

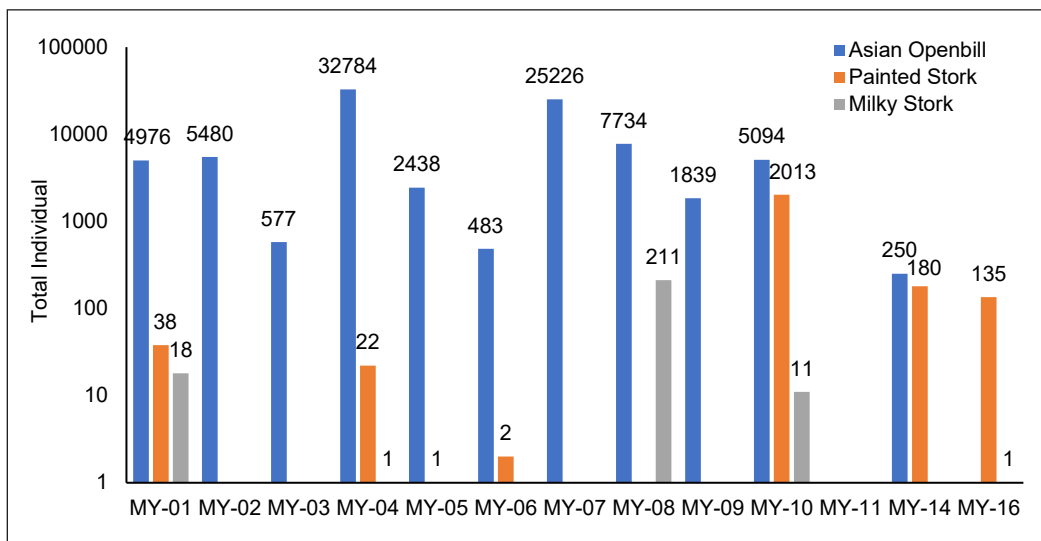


Figure 2. An abundance of Asian Openbill, Painted Storks and Milky Stork recorded in Peninsular Malaysia from January 2019 until March 2021

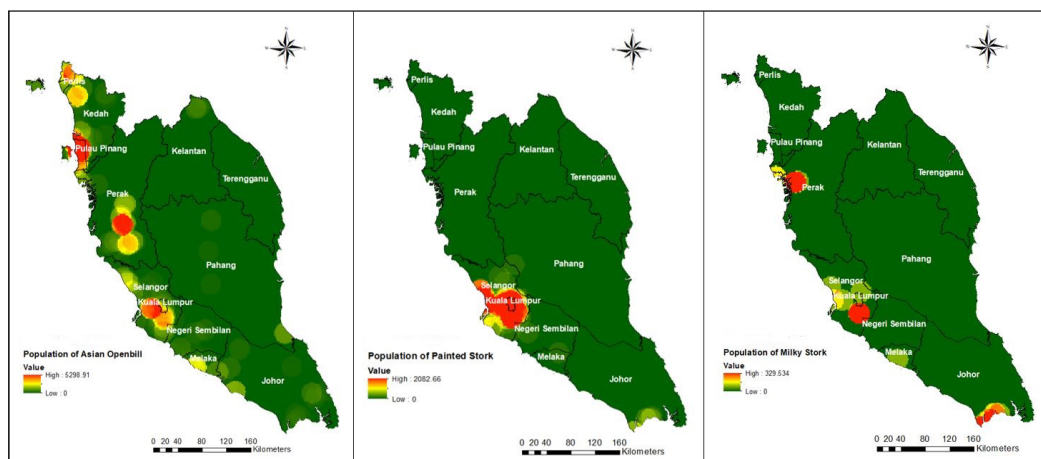


Figure 3. Distribution of Asian Openbill, Painted Stork and Milky Stork in Peninsular Malaysia between 2019 and 2021

across Peninsular Malaysia, with the Asian Openbill distributed from the northwest to the southwest, the Painted Stork concentrated in the central west, and the Milky Stork with three isolated populations in the northwest, the central east and the south (Figure 4).

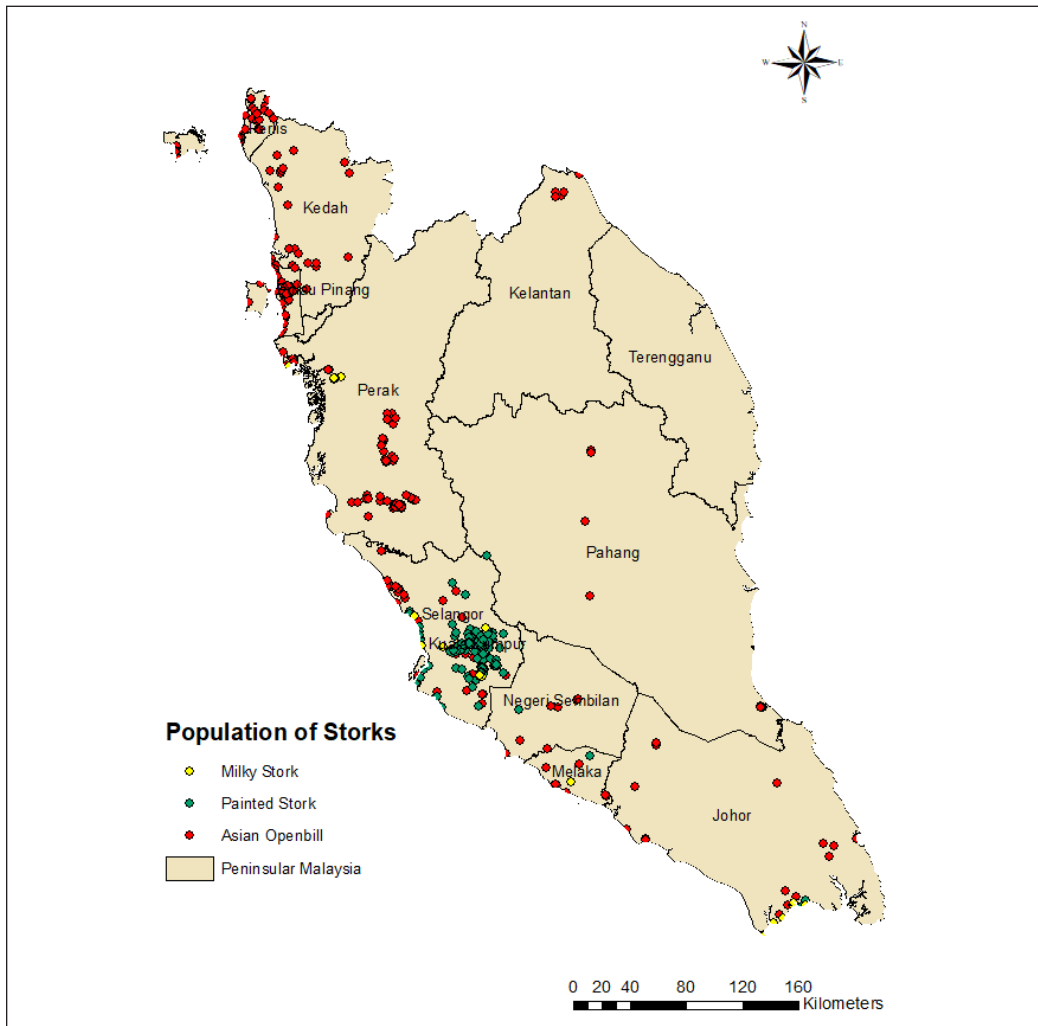


Figure 4. Habitat overlapping by Asian Openbill, Painted Stork and Milky Stork in Peninsular Malaysia between 2019 and 2021

DISCUSSION

This study shows that the Asian Openbill has a larger observation number in Peninsular Malaysia than the other two stork species. It indicates its success in dispersing from southern Thailand to the north and south of Peninsular Malaysia. Infestation of paddy fields by the invasive golden apple snail (*Pomacea canaliculata*), particularly at the early stages of rice cultivation, promotes its spread and population success but pressures its breeding

colonies, causing this species to migrate further to potential new sites. The population of this species greatly increased, particularly during the floods of 2011 in central Thailand, and depleted the snail population, which led to a food shortage and forced some colonies to abandon their original sites. About 522,112 hectares of actively cultivated rice fields in Peninsular Malaysia have facilitated the southward migration of the species (Jabatan Pertanian Semenanjung Malaysia, 2021). All areas in Peninsular Malaysia with records of Asian Openbills are mostly covered with shallowly flooded rice fields, where the conditions are moist and conducive to foraging by this species.

The high concentration of Painted Storks in Selangor, including Kuala Lumpur and Putrajaya, is related to Zoo Negara's captive breeding and release programme in 1965 (Koli et al., 2013). After 40 years, this species has bred, and its population rapidly increased in Selangor and surrounding areas, but it has not spread tremendously across other states. This species preferred migrating and building new colonies nearby wetland areas such as Putrajaya Wetland and other main lakes in Shah Alam and the Saujana Golf Resort (Zakaria & Nor, 2019). Painted Storks are mostly concentrated on the west coast of Peninsular Malaysia and nearby areas with large freshwater bodies, such as artificial lakes for recreational activities and wetland areas (e.g., the Putrajaya Wetland).

The Milky Stork has the smallest observation numbers of the three stork species, with only 242 occurrences across Peninsular Malaysia, which confirms the Endangered conservation status rank of this species (IUCN, 2021). The larger Milky Stork occurrence recorded in Perak may be due to the conservation programme of captive breeding and re-introduction implemented in the Kuala Gula Bird Sanctuary. About 50 Milky Storks were released in Kuala Gula between 2007 and 2014 (Ismail & Rahman, 2016). The large mangrove area in the Matang Mangrove Forest in Perak provides a release site and makes it possible to aid the survival of this species. This species shows high habitat specificity in mangrove areas. However, the west coast of Peninsular Malaysia is likely to have experienced pollution from heavy metals, insecticides, organochlorine mixtures, and other harmful pollutants categorised as toxins that may be absorbed into gastropods and fish, which are the main food sources of the Milky Stork (Ismail et al., 2011; Rahman et al., 2014; Samsi et al., 2017). Continuous consumption of contaminated prey will likely harm the birds and lead to low population numbers in Peninsular Malaysia.

In general, the three stork species were simultaneously present in three states, Selangor, Melaka and Johor, throughout 2019 and 2020. However, this overlap was highly concentrated in Selangor due to Zoo Negara's captive breeding programmes for the Painted Stork and the Milky Stork. However, they were re-introduced at different times in different areas: the Painted Stork in the Zoo Negara area in 1965 and the Milky Stork in Kuala Selangor Nature Park (KSNP) in 1998 and 2003 (Ismail & Rahman, 2016; Zakaria & Nor, 2019). The Zoo Negara area was selected as the release site for the Painted Stork because

of the presence of many artificial freshwater lakes and urban parks with large trees, which made it a more suitable breeding habitat. KSNP was selected as the early release site of the Milky Stork because it is close to Zoo Negara and has a mangrove habitat. At the same time, the Asian Openbill migrated across western Peninsular Malaysia, where they visited the paddy fields in Sekinchan and Sabak Bernam in Selangor state (Ali et al., 2020). These sites highlight the presence of the three stork species in the same region but at different localities and demonstrate their different habitat preferences—the Painted Stork prefers artificial freshwater lakes. In contrast, the Milky Stork favours mangrove habitat and the Asian Openbill paddy fields. Habitat segregation could reduce the competition rates by decreasing the number of niche overlaps between the related and trophically similar species (Mansor et al., 2015). However, in some regions, they overlap; thus, identifying their diets in the same habitat is crucial (Figure 4). Competition between the stork species might be avoided by dietary segregation, which could be revealed by a differential selection of major prey types (Mansor et al., 2020).

CONCLUSION

We conclude that the distribution of Malaysian storks relies significantly on the availability of their preferred habitats. The maintenance of urban lakes with suitable trees supports Painted Storks; the protection of mangrove habitat supports Milky Storks; and paddy fields sustain the Asian Openbill. However, paddy fields should be controlled and well managed to avoid large-scale natural habitat loss and overpopulation by the Asian Openbill, which could disrupt other native birds that also consume small aquatic animals. Citizen science data has become reliable for the public and researchers to measure, analyse, manage, conserve, and preserve wildlife and its habitat. Our spatial distribution model can be integrated with appropriate parameters in future studies to predict the species' potential distribution corresponding to land use changes. Additionally, further study is required to obtain detailed information about the diets of storks and other sympatric waterbird species.

ACKNOWLEDGEMENTS

This study was funded by the Fundamental Research Grant Scheme (FRGS), Ministry of Higher Education Malaysia (MOHE), under grant FRGS/1/2020/STG03/UKM/02/5. We thank the numerous contributors to eBird, including observers, the project team, and data reviewers.

REFERENCES

- Abidin, M. K. Z., Taib, F. S. M., & Nor, S. M. (2017). Distribution and habitat selection of the Asian Openbill (*Anastomus oscitans*) in Peninsular Malaysia. *Malayan Nature Journal*, 69(3), 169-181. <https://doi.org/10.5281/ZENODO.4005270>

- Ali, N. I. M., Ibrahim, N. I., Aiyub, K., & Kasavan, S. (2020). Pelaksanaan amalan pertanian baik (GAP) dalam kalangan pesawah padi di Sekinchan, Sabak Bernam, Selangor [Implementation of good agricultural practices (GAP) among paddy farmers in Sekinchan, Sabak Bernam, Selangor]. *Geografia*, 16(3), 247-262. <https://doi.org/10.17576/geo-2020-1603-18>
- Arazmi, F. N., Ismail, N. A., Daud, U. N. S., Abidin, K. Z., Nor, S. M., & Mansor, M. S. (2022). Spread of the invasive Javan myna along an urban-suburban gradient in Peninsular Malaysia. *Urban Ecosystems*, 25(3), 1007-1014. <https://doi.org/10.1007/s11252-022-01216-9>
- BirdLife International. (2016). *The IUCN Red List of Threatened Species 2016*. <https://dx.doi.org/10.2305/IUCN.UK.2016-3.RLTS.T22697651A93627701.en>
- BirdLife International. (2022). *Species Factsheet: Mycteria cinerea*. <http://www.birdlife.org>
- Callaghan, C. T., & Gawlik, D. E. (2015). Efficacy of eBird data as an aid in conservation planning and monitoring. *Journal of Field Ornithology*, 86(4), 298-304. <https://doi.org/10.1111/jof.12121>
- Chuah, B. K. (2013, January 22). Malaysia: Birder's instinct pays off. *New Straits Times*. <https://wildsingaporenews.blogspot.com/2013/01/malaysia-birders-instinct-pays-off.html?m=1>
- Darren, H. J. A., Ismail, M. H., Muharam, F. M., & Alias, M. A. (2021). Evaluating the impacts of land use/land cover changes across topography against land surface temperature in Cameron Highlands. *Plos One*, 16(5), Article e0252111. <https://doi.org/10.1371/journal.pone.0252111>
- Ismail, A., & Rahman, F. (2012). An urgent need for Milky Stork study in Malaysia. *Pertanika Journal of Tropical Agricultural Science*, 35(3), 407-4012.
- Ismail, A., & Rahman, F. (2016). Current status of the Milky Stork re-introduction programme in Malaysia and its challenges. *Tropical Life Sciences Research*, 27(2), 13-24. <https://doi.org/10.21315/tlsr2016.27.2.2>
- Ismail, A., Rahman, F., Kin, D. K. S., Ramli, M. N. H., & Ngah, M. (2011). Current status of the Milky Stork captive breeding program in Zoo Negara and its importance to the stork population in Malaysia. *Tropical Natural History*, 11(1), 75-80.
- IUCN. (2021). *The IUCN Red List of Threatened Species. Version 2021*. <https://www.iucnredlist.org>
- IUCN. (2022). *The IUCN Red List of Threatened Species. Version 2022*. <https://www.iucnredlist.org>
- Jabatan Pertanian Semenanjung Malaysia. (2021). *Booklet Statistik Tanaman (Sub-Sektor Tanaman Makanan) 2021* [Crop Statistics Booklet (Food Crop Sub-Sector) 2021]. http://www.doa.gov.my/index/resources/aktiviti_sumber/sumber_awam/maklumat_pertanian/perangkaan_tanaman/booklet_statistik_tanaman_2020. [25.08.2021-30.08.20]
- Koli, V. K., Yaseen, M., & Bhatnagar, C. (2013). Population status of Painted stork *Mycteria leucocephala* and Black-headed Ibis *Threskiornis melanocephalus* in southern Rajasthan, India. *Indian Birds*, 8(2), 39-41.
- Low, B. W., Lim, K. S., Yap, F., Lee, T. K., Lim, K. C., & Yong, D. L. (2013). First record of the Asian Openbill, *Anastomus oscitans* (Aves: Ciconiidae) in Singapore, with notes on foraging and dispersive movements. *Nature in Singapore*, 6, 25-29.
- Mansor, M. S., Halim, M. R. A., Abdullah, N. A., Ramli, R., & Cranbrook, E. O. (2020). Barn swallows *Hirundo rustica* in Peninsular Malaysia: Urban winter roost counts after 50 years, and dietary segregation from

- house-farmed swiftlets *Aerodramus* sp. *Raffles Bulletin of Zoology*, 68, 238-248. <https://doi.org/10.26107/RBZ-2020-0021>
- Mansor, M. S., Ramli, R., & Sah, S. A. M. (2015). The foraging tactics of Chestnut-winged babbler (*Stachyris erythroptera*) and Abbott's babbler (*Malacocincla abbotti*) in a lowland rainforest, Malaysia. *Sains Malaysiana*, 44(5), 687-692.
- Rahman, F., Ismail, A., Omar, H., & Hussin, M. Z. (2017). Exposure of the endangered Milky Stork population to cadmium and lead via food and water intake in Kuala Gula Bird Sanctuary, Perak, Malaysia. *Toxicology Reports*, 4, 502-506. <https://doi.org/10.1016/j.toxrep.2017.09.003>
- Rahman, F., Ismail, A., & Yusof, S. (2014). Metals contamination in the foraging area of Milky Stork: Evidence of anthropogenic inputs in the aquatic environment of Kuala Gula, Malaysia. *Toxicological & Environmental Chemistry*, 95(9), 1499-1505. <https://doi.org/10.1080/02772248.2014.892941>
- Robinson, J., & Cranswick, P. (2003). Large-scale monitoring of the effects of human disturbance on waterbirds: A review and recommendations for survey design. *Ornis Hungarica*, 12(13), 199-207.
- Samsi, A. N., Asaf, R., Santi, A., & Wamnebo, M. I. (2017). Gastropods as a bioindicator and biomonitoring metal pollution. *Aquacultura Indonesiana*, 18(1), 1-8. <http://dx.doi.org/10.21534/ai.v18i1.42>
- Sullivan, B. L., Aycrigg, J. L., Barry, J. H., Bonney, R. E., Bruns, N., Cooper, C. B., Damoulas, T., Dhondt, A. A., Dietterich, T., & Farnsworth, A. (2014). The eBird enterprise: An integrated approach to development and application of citizen science. *Biological Conservation*, 169, 31-40. <https://doi.org/10.1016/j.biocon.2013.11.003>
- Tan, C. L., & Murali, R. S. N. (2013, January 17). Malaysia not out of stork. *The Star*. <https://www.thestar.com.my/news/nation/2013/01/17/malaysia-not-out-of-stork>
- Zakaria, M. A., & Nor, S. M. (2019). Population estimate of painted stork (*Mycteria leucocephala*) in three main breeding sites Peninsular Malaysia. In *AIP Conference Proceedings* (Vol. 2111, No. 1, p. 060005). AIP Publishing LLC. <https://doi.org/10.1063/1.5111267>

Review Article

Analysis of Environmental Stresses on the Mechanical Properties of Laminated Glass Composites: A Review of Experimental Results and Outlook

Ufuoma Joseph Udi¹, Mustafasanie M. Yussof^{1*}, Felix Nkapheeyan Isa¹ and Luqman Chuah Abdullah²

¹*School of Civil Engineering, Engineering Campus, Universiti Sains Malaysia, 14300 USM, Nibong Tebal, Pulau Pinang, Malaysia*

²*Department of Chemical and Environmental Engineering, Faculty of Engineering, Universiti Putra Malaysia, 3400 UPM, Serdang, Selangor, Malaysia*

ABSTRACT

Laminated glass composites are composed of two or more layers of glass and a thermoplastic elastomeric interlayer securely glued together in an autoclave at high temperature and pressure. This composite material which significantly enhances the performance of glass before and after breakage, is desirable for various engineering applications. The main elastomeric interlayer comprises Polyvinyl butyral (PVB), SentryGlas (SG), Ethylene-vinyl acetate (EVA), and Thermoplastic Polyethylene (TPU). These interlayer materials have different unique features which offer a variety of performance benefits for engineering purposes. However, the structural response of laminated glass composites' elements and polymeric interlayers is typically prone to structural modifications relative to temperature applications and other environmental actions such as humidity and solar irradiation. This review compares the weathering resistance of the most common interlayers used in laminated glass composites based on available experimental literature findings. The main mechanical and accelerated ageing tests of laminates with different interlayer materials are summarised, giving evidence of the impact of these environmental actions on the

viscoelastic and mechanical properties of laminated glass composites plates. This research provides valuable references for predicting the long-term behaviour and risk evaluation of laminated glass composites under diverse ageing conditions.

Keywords: Ageing resistance, environmental stresses, interlayer, laminated glass composites, mechanical properties, polymeric materials

ARTICLE INFO

Article history:

Received: 13 June 2022

Accepted: 07 September 2022

Published: 21 July 2023

DOI: <https://doi.org/10.47836/pjst.31.5.15>

E-mail addresses:

udiufuomajoseph@student.usm.my (Udi Ufuoma Joseph)

cemustafa@usm.my (Mustafasanie M. Yussof)

nkapheeyan@student.usm.my (Felix Nkapheeyan Isa)

chuah@upm.edu.my (Luqman Chuah Abdullah)

*Corresponding author

INTRODUCTION

Glass is a widely used material in engineering and architectural applications due to its remarkable advantages such as desirable aesthetics, high transparency, good chemical and mechanical durability, as well as its excellent corrosion resistance and considerably small energy consumption for its manufacturing. During the formative years of glass production, the primary objective was fixated on manufacturing annealed (AN) float, representing the primary base material primarily utilised as window glass. Compared to most building materials, the strength of annealed glass is limited, with tensile resistance of up to 45 MPa (Kozlowski et al., 2018). Chemical or thermal procedures can then be employed to improve the strength of AN glass, resulting in toughened glass-tensile resistance up to 120 MPa-and is mostly employed for demanding applications like solar cell covers, façades or other load-bearing components (Kamarudin et al., 2018; Yussof et al., 2020). The structural use of glass is also receiving widespread recognition in many areas, such as aircraft and automotive industries, where laminated glass windshields may be a contributing factor to the overall vehicle crashworthiness while also being representative of the structural glass applications in buildings (Kozlowski et al., 2018).

Judging by industry market surveys, the global demand for these types of glasses is projected again to expand at a rate of 6.7% per annum over the next few years (Figure 1). Between 2012 and 2019, the global glass sector is estimated to have utilised 75 million metric tons of flat glass per year (Subagio, 2020). The construction and automotive sectors consumed a large share (70%) of the entire flat glass produced. Since flat glass usage has expanded in recent years, the proportion employed in the construction sector is expected to rise. In addition, the building sector of the Asia-Pacific region, in particular-which, has seen

rapid expansion in recent years due largely to a combination of fast-growing economies, increased infrastructure expenditures, rapid urbanisation, and the sustained rise in popularity of smart city schemes-is expected to be the driving force of flat glass demand.

Laminated glass (LG) composites in this context, is typically characterised by a combination of two or more glass sheets glued together by intermediate bonding polymeric material, which acts as a form of flexible shear connections (Castori & Speranzini, 2017). Polymeric materials such as Polyvinyl butyral (PVB) foils are the most commonly used in LG elements,

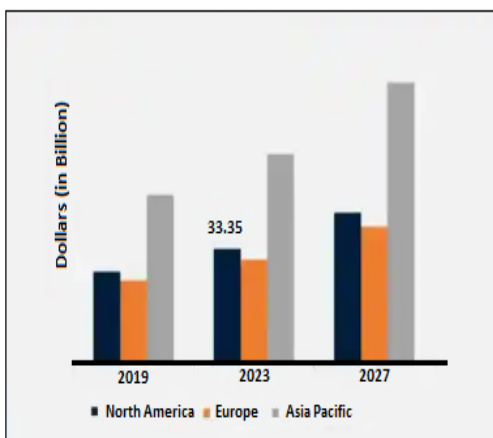


Figure 1. Global glass demand trend. Statistics from Data and Records Sheet (2021)

although they can also comprise Ethylene-vinyl acetate (EVA) or SentryGlas (SG) polymers (Hála et al., 2022; Mohagheghian et al., 2018; Zemanová et al., 2022; Zhang et al., 2020). However, the mechanical and thermos-viscoelastic properties of the polymeric materials, as well as their adhesion with glass, may be affected by exposure to other environmental stresses like UV radiation, thermal cycles or humidity conditions (Martín et al., 2020; Yang et al., 2022). Adhesive and laminated connection between parts is particularly examined for ageing variables and their impact on the durability and strength of LG elements and systems. The experimental determination of the viscoelastic properties of polymeric materials is of vital importance; in particular, bonding films utilised as interlayers in laminated connections are susceptible to thermal variations required in the laminate process (Giovanna et al., 2017; Yang et al., 2022). Moreover, previous observations have indicated the potential of various deterioration factors, each with varying degrees of impact on the rheological structure of the interlayers and, as a result, on the mechanical properties of the materials; it is entirely plausible that distinct consequences dominate at various stages during in-service conditions of LG elements.

This paper proposes a critical review of the ageing consequences on the thermos-viscoelastic properties of commonly used laminated glass polymers. The research works considered in this present study are by no means exhaustive of available scholarly publications; rather, they were selected to reflect a variety of experimental techniques to the challenge of determining interlayer properties subjected to the weathering phenomena. Particular focus is devoted to the applications, mechanical characterisation, and weathering resistance of PVB, SG, and EVA-based interlayers under diverse ageing conditions. The review ends by presenting the remaining issues that should be resolved to provide better information and develop solutions for environmentally impacted LG elements in structural applications.

LAMINATED GLASS COMPOSITES AND POLYMERIC INTERLAYERS

Laminated glass composites, or laminated safety glass, represents an arrangement of usually two plies of glass glued together by foils comprising certain types of bonding films commonly known as interlayers (Joseph Udi et al., 2023). The transition from two separate materials to a composite laminate is achieved by creating the vacuum between layers, usually with vacuum bags, and then applying pressure and temperature, usually in an autoclave, in order to create a chemical bond between glass and interlayer (Centelles et al., 2021). As a general rule, the resistant cross-section of the laminate is intended to conform as a composite in reaction to the extrinsic load. Thus, there is better mechanical performance in both elastic and post-cracking phases than in a single glass pane (Alsaed & Jalham, 2012). A tacit benefit of laminated glass composites in structural applications from a mechanical perspective is that two or more glass sheets can be glued together (Biolzi et al.,

2020; Hána et al., 2020; Zhao et al., 2021). Therefore, the necessary degree of strength and stiffness could be achieved by utilising standard glass thickness accessible in the market. Moreover, due to the advent of bonding films, laminated glass has been the conventional safety option in buildings for decades because the interlayer can strap glass fragments together in the event of collapse (Delincé et al., 2007; Hidallana-Gamage et al., 2015).

Bonding films usually comprise a PVB interlayer. Over the last several decades, PVB has been arguably the most prevalent interlayer used in the construction glass industry (Chen et al., 2022; Hána et al., 2019; Vedrtam & Pawar, 2018). Following its introduction in the 1930s, innovative attempts have centred on measures to make the interlayer less expensive to manufacture, less vulnerable to irregularities during lamination, easier to handle, or to improve some of its characteristics. Many optimised PVB products with unique features such as structural function, solar reflectiveness, acoustic insulation, tighter bond, and greater adhesion to glass, as well as security and decorative functions, have appeared due to the maturity of PVB as an interlayer in laminated glass composites (Desloir et al., 2019). These advancements have enabled it to be used in automotive windshields, PV solar cells, structural glass components, security glass, and its application in laminated doors and windows (Chen et al., 2018; Kozlowski et al., 2018).

Several other interlayers could also be employed besides PVB, such as SentryGlas (SG), Ethylene-vinyl acetate (EVA), and Thermoplastic Polyethylene (TPU), which were incorporated into the laminated glass composites industry to fulfil the high-performance resistance requirement for hurricane glazing (Bennison et al., 2008). SG is an interlayer form of ionic resin or Ionoplast which provides high stiffness and transparency over a broad temperature range (elastic modulus of about 100 MPa for temperatures up to 50°C) (Bati et al., 2010; Belis et al., 2009). EVA is a sturdy foil made using a plasticised PVB. This material provides excellent flexibility, elasticity, toughness, stress-crack resistance, and clarity as an interlayer material. EVA also possesses distinctive characteristics such as high optical transmission, excellent electrical resistivity, resilience to weather conditions, and low fusion and polymerisation temperature (Pankhardt & Balázs, 2010). The chemical structure of the interlayers used in laminated glass composites is the same for all manufacturers. Nonetheless, the unique attributes of each interlayer sheet are dependent on the interlayer type, manufacturer, and composition of the interlayer sheet (Table 1) (Martín et al., 2020).

However, as highlighted by several scholars, a typical feature of these elastomeric materials is that these films are usually governed by their viscous nature in addition to their distinct constitutive principles; thus, they are typically prone to chemical modifications relative to the ambient conditions they are exposed to over time (Hartwell & Overend, 2020; Kothe & Weller, 2014; Louter et al., 2012; Ranocchiali et al., 2016, 2018). Hence, the mechanical and thermos-viscoelastic properties of the polymeric materials, as well as their adhesion with glass or another substrate such as steel, may be affected by exposure

Table 1

Main properties of laminated glass composites interlayers (PVB, SG, and EVA) (Martín et al., 2020)

Parameter		PVB	SG	EVA
Price	€/m ²	4.02–4.82	n.a.	1.74–1.91
Coefficient of thermal expansion	10 ⁻⁵ cm/cm°C	22–40	10–15	160–190
Water absorption (ASTM D-570)	wt.%	3.6	n.a.	0.15–0.5
Density	kg/m ³	915–1070	950	945–955
Ultimate tensile strength	MPa	20.8	34.5	9.5–10
Poisson's ratio	–	0.5	0.442–0.500*	0.47–0.49
Transmittance	%	88–89	n.a.	90–92
Elongation at failure	%	190–350	400	880–930
Glass transition temperature	°C	8–42	55	–77 to –69
Yellowness index	–	12.5	2.5	1.9
Young modulus	MPa	2–5	300–480	7–9
Joining technique	–	Lamination, UV curing	Lamination	Vacuum Lamination, autoclave, or vacuum bags

* Directly proportional to time and temperature

to other environmental stresses like UV radiation, thermal cycles or humidity conditions (Andreozzi et al., 2015; Centelles, Castro et al., 2020) The coupling capability between the different components may also be altered by additional factors such as failure of the bonding layer, material degradation or delamination (Figure 2). Thus, the interlayer properties, in addition to the weathering resistance and durability, have an enormous influence on the overall structural integrity of LG composites. On account of that, LG composites and polymeric materials have garnered significant attention in recent years. The behaviour of polymeric interlayers, and thus LG composites systems can be evaluated in three ways: experimental research, numerical simulation, or theoretical study.

The mechanical behaviour of LG composites could be determined experimentally using Dynamic Mechanical Analysis (DMA) (Giovanna et al., 2017; Hána et al., 2020; Lu et al., 2021), which enables a thorough characterisation of the viscoelastic properties of the interlayers. The viscoelastic properties of polymers employed in interlayer LG composites can be analysed using a variety of experimental approaches. The ISO-6721-1

(2019) presents numerous dynamic procedures to experimentally determine the mechanical properties of polymeric materials; the draft standard EN 16613 (2013) offers three different test procedures to address specific issues pertaining to various types of polymeric materials. Moreover, many researchers have proposed different experimental techniques for simulating ageing action on LG composites in order to define thermos-viscoelastic properties and to properly reflect the short and long-term behaviour of LG composites using an effective modulus of elasticity which is dependent on the working temperature and time loading (Giovanna et al., 2017). In any case, observations from the literature findings have demonstrated that the shear stiffness of interlayers used in LG composites differs so much from the stiffness of component glass that minor inconsistency in determining this property results in significant deviations in evaluating the bending behaviour of LG composites. However, the many different methods proposed in the literature to determine the viscoelastic properties of polymeric materials make it difficult to compare results. In the following sections, we aim to highlight the disparities to identify the peculiarities associated with determining thermos-viscoelastic and mechanical properties of LG composites due to environmental stresses, summarising what different researchers agree on; and outlining the potential direction for future studies.



Figure 2. Delamination of LG panels (a) framed window glass (b) Point fixed glass (CPNI EBP 04/13, 2013)

EXPERIMENTAL RESEARCH ON PROPERTIES OF LG INTERLAYERS

The thermos-viscoelastic properties of polymeric materials used in LG composites are vital in evaluating the structural response of LG composites, and therefore, knowledge of its long-term behaviour is essential for the fail-safe design of structural components utilising LG elements to avert disastrous failures. Consequently, it is paramount that the structure meets serviceability conditions, ensuring that unexpected failure of any glass component does not cause the entire structure to collapse and that a minimum load-bearing capacity is maintained pending evacuation or replacement. In this regard, numerous attempts have

been made to characterise polymeric materials' material properties and ascertain their long-term performance under diverse ageing scenarios. In the following sections, particular emphasis will be on consequential and more recent experimental results to adequately describe the material properties of commonly used polymeric interlayers under varying environmental stress conditions and provide useful data for structural LG design involving long-term effects.

Effect of Environmental Stresses

The first consequential studies on the impact of environmental stresses on the properties of structural glass systems came to light towards the end of the 1950s because of the enormous usage of glass materials as windowpanes. However, many of these research efforts focused on the investigation of thermal stress breakage—indicative of the leading cause of fracture in window glass (Bedon, 2017; Wang, 2020). It is common knowledge that polymeric materials are susceptible to weathering agents and may alter their rheological properties. Hence, the durability of LG elements and their polymeric interlayers against environmental stresses is of significant concern in ensuring its practicability for safety design purposes. The causes and processes of glass weathering have been extensively studied for several decades. Weathering can occur as a result of either mechanical or chemical action on a glass plate. Mechanical action can be caused as a result of wind debris or abrasion (Datsiou & Overend, 2017). In contrast, chemical action is due chiefly to the effects of environmental parameters such as temperature, atmospheric water vapour (relative humidity), or UV radiation.

Accelerated ageing tests—which are used to expedite the process of natural weathering—can be employed to investigate the effects of each weathering agent on polymeric interlayers. It can be achieved by combining weathering agents in environmental chambers—such as controlled temperature or high humidity—or other ageing processes to simulate a realistic natural weathering process (Datsiou & Overend, 2016; Lombardo et al., 2005; Reiß et al., 2019). Different weathering processes may produce varying degrees of modifications in interlayer properties, and for this reason, it is vital to utilise standard procedures (ISO-6721-1, 2019) so that different results can be compared. In the following paragraphs, the different experimental ageing techniques, standard and non-standard techniques reported in the literature, are identified, categorised, and summarised. Many experimental research available in the literature has shown that weathering has a considerable impact on the physicochemical properties of polymeric materials as well as the mechanism of degradation of LG composites in general.

For example, Kothe and Weller (2014) described an experimental campaign in which LG units having different polymeric interlayers like PVB, TPU, SG, and EVA were exposed to environmental stresses such as UV radiation, corrosion by saline fog, and a combination

of humidity and temperature produced in an environmental chamber. While the authors reported considerable delamination on the edges of tested specimens after 21 days of exposure to UV radiation, the material behaviour of the interlayers did not exhibit significant changes up to the glass transition temperature compared to un-weathered specimens. Prior to this, Serafinavicius et al. (2014) investigated the weathering resistance of LG units glued with different polymeric materials, i.e., SG, EVA, and PVB, on exposure to different weathering agents in a climatic chamber. Long-term bending tests at different temperature conditions indicated that PVB interlayers had the highest mid-span deflection results at the highest temperature conditions, while SG interlayers posted the lowest deflection results at various temperatures. Humidity was also shown to have the least impact on the middle span deflection of tested specimens.

However, the maximum displacement values could not be compared due to the unreported load level in the creep tests. In a different study, Andreozzi et al. (2015) conducted an articulated experimental campaign wherein laminates with PVB interlayers were subjected to different artificial ageing processes and tested with DMA. In doing so, a thorough thermo-viscoelastic behaviour of the polymeric material was obtained both before and after the ageing processes. Delamination was observed only on specimens exposed to humidity-220 days in total in a thermostatic bath—over an extended period. It was also shown that thermal cycles performed under well-defined conditions and ISO-12543-4 (2021) have no significant effect on the rheological response of the PVB material. However, UV radiation was observed to have modified the rheological structure of the material, as evidenced by the modification of the interlayer master curves. These modifications have a direct impact on the long-term performance of LG composites. Changes were also observed in the bulk response of the polymeric material, concluding that further experimental research is needed to separately analyse these features.

In a more recent study, Centelles, Castro et al. (2020) evaluated the influence of various polymeric materials-PVB, Safflex, SG, and EVASAFE—on the bond behaviour of LG units after being exposed to different levels of environmental stresses, i.e., humidity, UV radiation, and thermal cycles. Results from the study gave evidence and under prior literature findings (Andreozzi et al., 2015; Delincé et al., 2007) of a loss in adhesion in PVB specimens on exposure to humidity conditions, as well as producing a stiffer material after exposure to UV and thermal cycles (Figure 3). EVASAFE and SG specimens, however, showed better resistance performance to weathering actions. In another study, the same authors (Centelles, Martín, et al., 2020) reported high moisture absorption in PVB and SG laminates compared to EVA and TPU laminated specimens after immersing said specimens in a thermostatic bath and following ISO-62 (2008) and ISO-175 (2010) over an extended period (367 h in total). The study concluded that SG and PVB with minimum plasticiser are the best choices for LG composites in structural applications due partly to their maximum

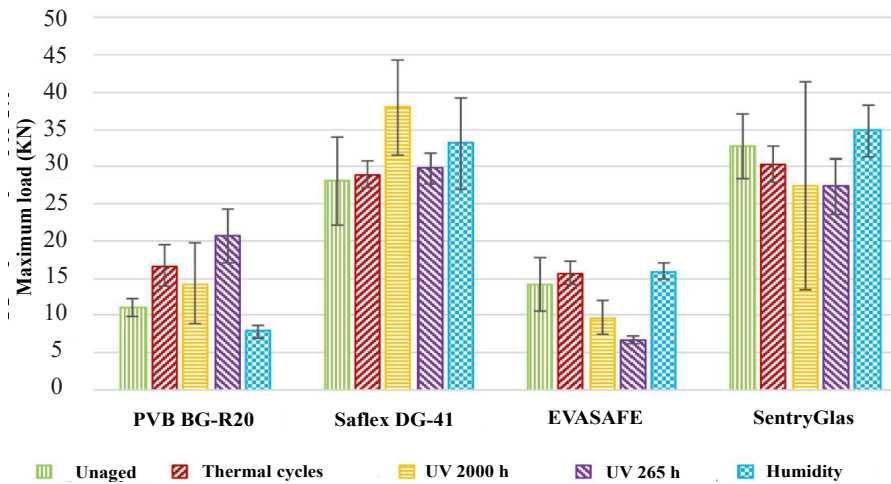


Figure 3. Weathering consequences on LG pane with different interlayer materials (Centelles, Castro et al., 2020)

stresses and high initial stiffness when not exposed to humidity conditions. The authors, however, emphasised that the performance of polymeric materials for LG composites may differ after the laminating processes, suggesting more dynamic experiments at various temperature levels to investigate the thermo-viscoelastic behaviour of these polymeric materials.

Note that, even though a significant number of experimental tests have been performed and the findings are obtainable, these studies are difficult to compare, not only because the artificial ageing processes were performed using different procedures but also because the experiments are frequently superimposing dissimilar environmental stresses in order to determine an effective rheological parameter. It is also worth highlighting a significant difference between LG composites exposed to a controlled environmental chamber (such as controlled humidity and temperature) and the exterior environment. The external environment exposes the glass to various levels of solar radiation, periodic condensation of water films due to humidity cycles, and the deposition of aerosol particles on the glass. All of these factors can influence the rate of alteration of the polymeric materials, hence, a different mechanism in the deterioration of LG composites.

Although several experimental studies have focused on the degradation of LG panes and interlayers as a constructional material due to environmental stresses, limited literature efforts are still available on the outdoor natural weathering of laminated glass (Table 2). As far as the authors know, outdoor weathering of LG composites has been performed only by Ensslen (2007). The author reported an extensive experimental evaluation on the behaviour of circular LG units 100 x 100 mm and 300 x 300 mm, their nominal sizes glued together by PVB foils and exposed to environmental stresses. Some samples were exposed to weathering processes in humidity and temperature mixed conditions in a climatic

chamber, another set of samples were exposed to UV radiation in a solarium, while others were simply exposed to outdoor environmental conditions for up to two years at various climatic locations. The monotonic shear test was used to compare specimens that had been weathered artificially to those that had been subjected to the outdoor environment. In general, results from the study demonstrated large increments in moisture absorption of artificially aged specimens but no significant increase in moisture absorption of naturally weathered specimens. Shear test results indicated that a stiffer and more brittle PVB foil, as well as adhesion loss and delamination at the edges of LG units, could also be observed in artificially aged specimens.

On the other hand, the naturally weathered specimens showed only minor derivations in overall shear performance. However, at low test speeds, it could also be observed at the edge of specimens naturally weathered in extreme climatic conditions. The actual behaviour of such glasses, as expected from the test conditions, was closely linked to local instabilities, i.e., buckling, thus, requiring more rigorous experimental analysis of naturally weathered LG units and systems.

Mechanical Characterisation

The mechanical performance of LG composites and systems relies on the deformability of the constituent polymeric material; hence, mechanical analysis cannot be achieved without considering interlayer cohesive behaviour (Hooper et al., 2012; Mohagheghian et al., 2018; Zhang et al., 2019). Furthermore, as such, the experimental techniques developed to evaluate the mechanical response of the polymeric interlayer alone and the LG composite, in general, are quite diverse and dissimilar in the existing literature. Testing methods to evaluate the mechanical properties of LG composite include most notably, the four-point bending test (Delincé et al., 2007; Louter et al., 2012; Serafinavičius et al., 2013), shear test (Centelles, Castro et al., 2020; Serafinavičius et al., 2013), peel test (Louter et al., 2012), and pull-out test (Louter et al., 2012).

Taking into account the complete LG composites, for example, Delincé et al. (2007) were among the first to conduct an extensive experimental campaign to study the effect of artificial weathering on the shear-bond properties of LG panels 1100 x 360 mm their nominal sizes with PVB and SG interlayers using two different types of mechanical tests, i.e., shear test and bending tests. Observations from the shear tests indicated that while the level of adhesion of the LG panels decreased slightly after the weathering processes, there was a slight increase in stiffness. However, the reverse trend was observed from the bending tests, in addition to the SG and PVB specimens having quite a similar failure behaviour in terms of adhesion of broken glass pieces to the interlayer. Similar observations were also noted by Serafinavičius et al. (2013), who also reported experimental results of four-point tests conducted on laminates glued with various polymeric materials PVB, SG, and EVA

after imposing sustained loading at different temperature ranges, i.e., 20°C, 30°C, and 40°C. Monolithic tempered glass sheets were also included in the set of experiments. The authors gave evidence and under prior findings (Delincé et al., 2007; Louter et al., 2012; Serafinavičius et al., 2013) that while all the tested LG specimens have a similar level of influence on the resistance and behaviour of LG composites, laminates with SG interlayer (maximum failure load at 7.8 kN) could be considered safer at the same residual stiffness of failed glass panels. The maximum load for PVB specimens was 6.5 kN (first load at failure of the bottom of the glass sheet) at a maximum displacement of about 50 mm. The maximum load of EVA specimens was similar to that of the PVB specimens (6.7 kN), but the displacement was much smaller at the same failure load (Figure 4). Nonetheless, the findings demonstrated how the interlayers' viscoelastic behaviour influences the coupling capability of LG panels.

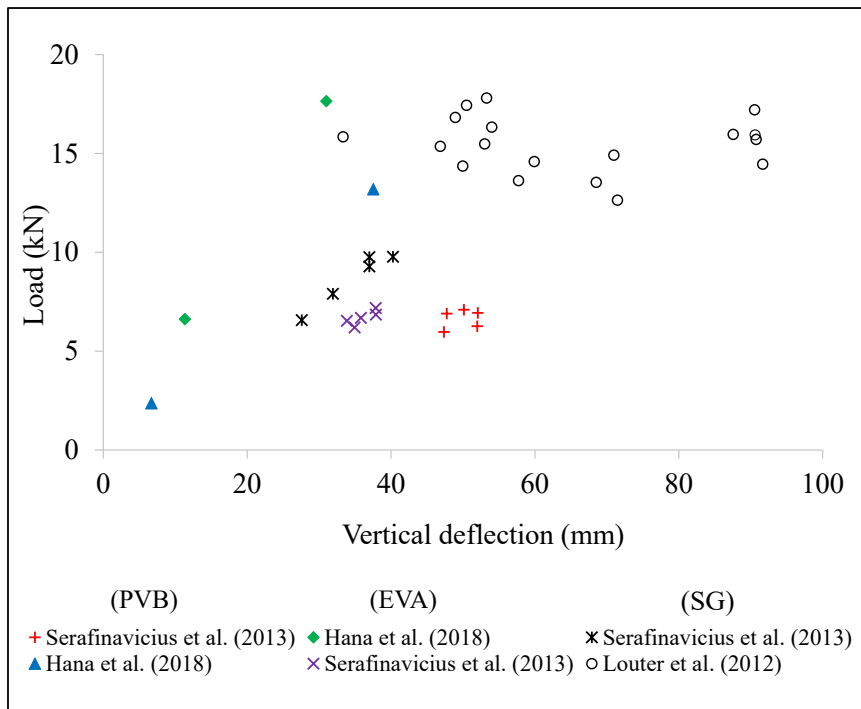


Figure 4. Load deflection relationship from four-point bending test of LG specimens with different interlayers as derived from experimental literature

Sable et al. (2019) and Hána et al. (2018) also tested LG units in a short-term controlled four-point bending test under constant temperature with three different interlayers, i.e., PVB, SG, and EVA. The authors demonstrated that the maximum load and stiffness were impacted by the type of polymeric material and the fracture pattern and breakage mechanisms. In the study by Hána et al. (2018), their experiments indicated that LG units with EVA polymers

not only revealed larger ultimate load values (Figure 4) but also demonstrated higher bending stiffness than laminates with PVB polymers. However, Sable et al. (2019) noted that the stiffness of LG units with EVA polymers was comparable with PVB specimens, and EVA materials could be utilised in the same settings as PVB polymers, requiring further detailed investigations of these tests and materials. For the sake of clarity, Figure 4 presents a comparison among experimental literature results. The comparison is made in terms of laminates with PVB, EVA, and SG interlayers used in each campaign. The comparison is only made among results with similar test conditions (four-point bending tests). As shown in Figure 4, the distribution of LG strength is highly scattered, mainly due to the different geometry and material properties used for the different campaigns.

In studying the mechanical response of a polymer material, one can usually categorise experiments into two regimes in terms of strain rate and dynamic modulus: Uniaxial tensile strength tests (Belis et al., 2009; Centelles, Martín et al., 2020; Chen et al., 2018; Hooper et al., 2012; Liu et al., 2012; Sable et al., 2017; Zhang et al., 2015) and dynamic mechanical analysis (Andreozzi et al., 2015; Liu et al., 2014; Lu et al., 2021; Pelayo et al., 2017). In characterising the strain rate-dependent behaviour, for example, Liu et al. (2012) described an articulated campaign for both compression and tensile strength tests of PVB laminates using four different strain rates, i.e., 10, 50, 100, and 200 mm/min. The authors observed that while the PVB behaviour can be best described as viscoelastic under compression loads in both dynamic and quasi-static scenarios, however, under tensile loading, the material can be described as viscoelastic in quasi-static loadings and elastic-plastic in dynamic loadings. Observations from the study indicated that, while increasing strain rates made little difference in the failure stresses (16.9, 16.5, 16.5, 14.5 MPa, respectively), the failure strain decreased from 1.8 to 2.8, a 36% drop. The authors also defined and divided the PVB constitutive model into three regimes: linear-elastic stage, bi-exponent stage and failure stage.

A similar observation was also noted in (Belis et al., 2009), where the failure behaviour of LG sheets with SG interlayers was experimentally investigated. Results from the tensile tests loading speed ranging from 5 mm/min to 100 mm/min indicated an elastic-plastic material behaviour at failure (approximately 350%), which was affected by strain rates. Despite the relatively good material properties of the interlayer, the post-failure behaviour following prior studies was below expectations (i.e., failure strength above 32 N/mm²). However, the observed failure mechanism varied significantly from that of LG with PVB interlayer tested in prior studies. In complement, Zhang et al. (2015) conducted tensile tests on LG specimens with SG interlayers, ranging from low (10 mm/min to 100 mm/min) to high (0.1 m/s to 20 m/s) strain rates. Observation from the test results indicated that, while the failure strain at low rates varied from 22 MPa to 47 MPa, the specimens were less ductile with an increasing strain rate. The authors also derived the initial modulus of the

LG specimens with SG interlayers, and this value was found at 200-300 MPa at low strain rates and reduced to approximately 150 MPa at the high strain rate. The study concluded that the SentryGlas interlayer indicated a viscous material behaviour under uniaxial tension.

Centelles, Martín et al. (2020) also studied the tensile behaviour of LG units glued together with different polymer materials such as PVB (three different variations), EVASAFE, SG, and TPU. Following the standard set in ASTM D638 (2014) and ISO-527 (2006), tests were conducted under constant displacement rates of 10 mm/min, 50 mm/min, and 100 mm/min. In general, the authors gave evidence of similar stress-strain curves for PVB and SG laminates, with a softening zone preceded by an initial non-linear small region and a second region with smaller stiffness than the initial region. Whilst the TPU specimens had an initial elastic region coupled with a progressive softening and finally a linear region until breakage, the EVASAFE specimens proved to be the most ductile among all tested specimens. Figure 5 presents a comparison among experimental literature results. The comparison is made in terms of laminates with PVB and SG interlayers used in the different campaigns. The comparison is only made among results with similar test conditions (uniaxial tensile strength tests) and similar strain rates (10 mm/min). Remarkably and despite the different geometry and material properties, a similar trend is observed for most of the experimental results considered for the normalised tensile strength.

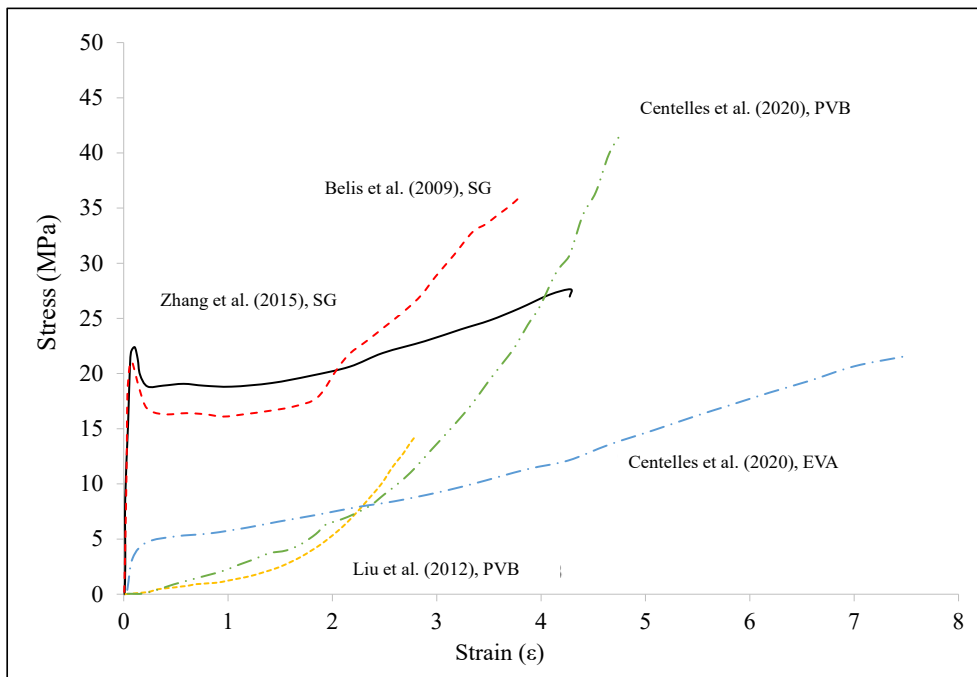


Figure 5. The stress-strain behaviour of LG interlayers in uniaxial tension test derived from experimental literature

In the case of DMA, several experiments have been conducted to study the time-temperature-dependent behaviour and hence the mechanical properties of LG interlayers. For example, Andreozzi et al. (2014) used the DMA technique to report that the PVB interlayer is in the glass transition region between 0°C and 50°C. Furthermore, as such, its dynamic modulus shows significant variations in temperature and vibration frequency. By contrast, an experiment by Liu et al. (2014) indicated that in the glassy and rubbery state, PVB shows brittleness and little variations in the dynamic modulus with temperature and vibration frequency variations. Using an identical technique, Pelayo et al. (2017) observed that the glass transition zone of standard PVB begins from 8-10°C. Thus, more studies on DMA analysis on LG interlayers, particularly for SG and EVA interlayers, are needed to verify the mechanical response of LG interlayers under different temperature conditions.

Table 2

Impact of environmental stresses on LG panes: Summary of some selected experimental research studies

Reference	Year	Interlayer type	Stress condition	Test Evaluation
Kothe and Weller	2014	PVB, EVA, SG, TPU	UV radiation, Corrosion, Temperature, Humidity	Visual inspection, Dynamic mechanical analysis
Andreozzi et al.	2015	PVB	Humidity, UV radiation, Temperature	Visual inspection, Dynamic torsion tests
Serafinavičius et al.	2013	PVB, EVA, SG	UV radiation, Temperature, Humidity	Long-term bending tests
Ensslen	2007	PVB	Temperature, Humidity, UV radiation, Natural outdoor weathering	Visual inspection, Shear Test
Louter et al.	2012	SG	Temperature, humidity, thermal cycling	Four-point bending tests
Hána et al.	2018	EVA, PVB	Controlled temperature	Short-term four-point bending tests
Sable et al.	2019	EVA, PVB, SG	Controlled temperature	Four-point bending tests
Centelles, Martín et al.	2020	PVB, EVASAFE, SG, TPU	Temperature, Humidity, UV radiation, Load–duration: 10, 50, 100 mm/min	Uniaxial tensile strength test
Centelles, Castro et al.	2020	PVB, Saflex, SG, and EVASAFE	Humidity, Thermal cycles, UV radiation	Double-lap shear tests

Table 2 (Continue)

Reference	Year	Interlayer type	Stress condition	Test Evaluation
Liu et al.	2012	PVB	Load–duration: 10, 50, 100, 200 mm/min	Uniaxial tensile strength test
Belis et al.	2009	SG	Load–duration: 5, 10, 20, 50, 100 mm/min	Uniaxial tensile strength test
Zhang et al.	2015	SG	Load–duration: Low speed; 10, 100, 250, 500, 750, 1000 mm/min High speed; 0.1, 0.5, 1, 2, 3, 5, 7, 10, 15, 20 m/s.	Uniaxial tensile strength test

CONCLUDING REMARKS AND OUTLOOK

In many applications, laminated glass composites elements are repetitively exposed to environmental stresses as well as frequent mechanical and chemical cleaning procedures, which can lead to changes in the rheological properties of the interlayer. Hence, the efficiency of the products decreases with age. Such deterioration and ageing processes are mainly determined by various environmental stress conditions such as relative humidity, thermal cycles and UV radiation. This paper presents the assessment of laminated glass composites against such ageing scenarios based on available literature findings. Only experimental studies are included in the comparison to make it more practical and consistent.

By reviewing major and other recent experimental works, several remaining questions are summarized from the authors' viewpoint. The artificial ageing actions documented in the literature and reviewed in this present study are often not comparable because the procedures were performed using different ageing processes and frequently superimposing different weathering scenarios. In addition, when mechanical tests were conducted, the goal was frequently to compare specimens exposed to different types and intensities of environmental stresses and not to determine an effective rheological parameter. As a result, it is quite difficult to compare experimental data reported by different authors. The ISO -12543-4 (2021) addresses the durability of LG composites, however, it lacks sufficient evaluation methodologies to investigate the impact of environmental stresses on the interlayers' optical, mechanical, and adhesive capabilities. It can be deduced that for comparison among weathering experiments of LG elements with diverse interlayers, a unified technique must be devised.

Nonetheless, significant inferences can be drawn from the summaries of what different scholars reported in their studies. Different researchers agree that UV radiation appears to have the most significant consequences, particularly for PVB materials, as a stiffer material is produced after the ageing action. However, more detailed experimental tests to investigate the damages produced by UV radiation on various LG interlayers are required, so as to

identify possible diverse deterioration mechanisms in these interlayers. Humidity affects the interlayer in two ways; high absorption in the polymers which also acts as a plasticizer and also delivering a softer bulk property, which may inadvertently compromise its adhesion to glass. Based on the above, more detailed investigations are required to determine the impact of environmental stresses on the occurrence of bubbling and delamination phenomena. Temperature effects require further examination, since thermal variations may have quite diverse impacts on the various types of interlayers, depending on the transition temperature of each interlayer. The findings reported by different authors do not appear to be indicative of this phenomenon.

Lastly, the tremendous advancement in technology within the LG industry is already witnessing rapid growth in the production and supply chain of innovative polymeric materials in the glazing market. Irrespective of the interlayer type, LG elements are exposed to different environmental conditions, loading scenarios or working temperatures and this may affect how they respond and behave in LG systems. The weathering effect on its mechanical performance should be continually investigated in order to gain better knowledge of LG composites under environmental stress conditions. In addition, artificial ageing techniques currently have a great deal of inconsistency in estimating the long-term performance of LG composites, owing to the lack of an artificial ageing mechanism that is consistent with the real-world accumulated damages. In light of these considerations, further monitoring and tests of naturally weathered LG elements and systems are still required to aid in the prediction of weathering resistance, risk assessment, and safety of laminated glass composites in structural applications.

ACKNOWLEDGMENTS

The authors acknowledge with gratitude the financial support provided for this study by the Ministry of Higher Education Malaysia in the form of the Fundamental Research Grant Scheme, FRGS/1/2018/TK06/USM/02/3. We sincerely thank UPM-Kyutech International Symposium on Applied Engineering and Sciences 2021 (SAES2021) and Universiti Putra Malaysia for their support in covering the publication fee.

REFERENCES

- Alsaed, O., & Jalham, I. S. (2012). Polyvinyl butyral (PVB) and ethyl vinyl acetate (EVA) as a binding material for laminated glass. *Jordan Journal of Mechanical and Industrial Engineering*, 6(2), 127-133.
- Andreozzi, L., Bati, S. B., Fagone, M., Ranocchiai, G., & Zulli, F. (2014). Dynamic torsion tests to characterize the thermo-viscoelastic properties of polymeric interlayers for laminated glass. *Construction and Building Materials*, 65, 1-13. <https://doi.org/10.1016/j.conbuildmat.2014.04.003>
- Andreozzi, L., Bati, S. B., Fagone, M., Ranocchiai, G., & Zulli, F. (2015). Weathering action on thermo-viscoelastic properties of polymer interlayers for laminated glass. *Construction and Building Materials*, 98, 757-766. <https://doi.org/10.1016/j.conbuildmat.2015.08.010>

- ASTM D638. (2014). *Standard Test Method for Tensile Properties of Plastics*. <https://www.astm.org/d0638-14.html>
- Bati, S. B., Ranocchiai, G., Reale, C., & Rovero, L. (2010). Time-dependent behavior of laminated glass. *Journal of Materials in Civil Engineering*, 22(4), 389-396. [https://doi.org/10.1061/\(asce\)mt.1943-5533.0000032](https://doi.org/10.1061/(asce)mt.1943-5533.0000032)
- Bedon, C. (2017). Structural glass systems under fire: Overview of design issues, experimental research, and developments. *Advances in Civil Engineering*, 2017, Article 2120570. <https://doi.org/10.1155/2017/2120570>
- Belis, J., Depauw, J., Callewaert, D., Delincé, D., & Van Impe, R. (2009). Failure mechanisms and residual capacity of annealed glass/SGP laminated beams at room temperature. *Engineering Failure Analysis*, 16(6), 1866-1875. <https://doi.org/10.1016/j.engfailanal.2008.09.023>
- Biolzi, L., Cattaneo, S., Orlando, M., Piscitelli, L. R., & Spinelli, P. (2020). Constitutive relationships of different interlayer materials for laminated glass. *Composite Structures*, 244, Article 112221. <https://doi.org/10.1016/j.compstruct.2020.112221>
- Castori, G., & Speranzini, E. (2017). Structural analysis of failure behavior of laminated glass. *Composites Part B: Engineering*, 125, 89-99. <https://doi.org/10.1016/j.compositesb.2017.05.062>
- Centelles, X., Castro, J. R., & Cabeza, L. F. (2020). Double-lap shear test on laminated glass specimens under diverse ageing conditions. *Construction and Building Materials*, 249, Article 118784. <https://doi.org/10.1016/j.conbuildmat.2020.118784>
- Centelles, X., Martín, M., Solé, A., Castro, J. R., & Cabeza, L. F. (2020). Tensile test on interlayer materials for laminated glass under diverse ageing conditions and strain rates. *Construction and Building Materials*, 243, Article 118230. <https://doi.org/10.1016/j.conbuildmat.2020.118230>
- Centelles, X., Pelayo, F., Lamela-Rey, M. J., Fernández, A. I., Salgado-Pizarro, R., Castro, J. R., & Cabeza, L. F. (2021). Viscoelastic characterization of seven laminated glass interlayer materials from static tests. *Construction and Building Materials*, 279, Article 122503. <https://doi.org/10.1016/j.conbuildmat.2021.122503>
- Chen, S., Chen, X., & Wu, X. (2018). The mechanical behaviour of polyvinyl butyral at intermediate strain rates and different temperatures. *Construction and Building Materials*, 182, 66-79. <https://doi.org/10.1016/j.conbuildmat.2018.06.080>
- Chen, S., Chen, Z., Chen, X., & Schneider, J. (2022). Evaluation of the delamination performance of polyvinylbutyral laminated glass by through-cracked tensile tests. *Construction and Building Materials*, 341, Article 127914. <https://doi.org/10.1016/J.CONBUILDMAT.2022.127914>
- CPNI EBP 04/13 (2013). *Influence of delamination of laminated glass on its blast performance*. National Protective Security Authority. <https://www.npsa.gov.uk/system/files/documents/4d/8f/Delamination-of-laminated-glass.pdf>
- Datsiou, K. C., & Overend, M. (2017). Artificial ageing of glass with sand abrasion. *Construction and Building Materials*, 142, 536-551. <https://doi.org/10.1016/j.conbuildmat.2017.03.094>
- Datsiou, K. C., & Overend, M. (2016). Evaluation of artificial ageing methods for glass. In J. Belis, F. Bos & C. Louter (Eds.), *Challenging Glass Conference Proceedings - Challenging Glass 5: Conference on Architectural and Structural Applications of Glass, CGC 2016* (pp 581-592). CGC, Ghent University. <https://doi.org/10.7480/cgc.5.2431>

- Delincé, D., Belis, J., Zarmati, G., & Parmentier, B. (2007). Structural behaviour of laminated glass elements-a step towards standardization. In *Glass Performance Days proceedings* (pp. 658-663). Tamglass Ltd. Oy. <http://dx.doi.org/10.13140/2.1.3592.6084>
- Desloir, M., Benoit, C., Bendaoud, A., Alcouffe, P., & Carrot, C. (2019). Plasticization of poly(vinyl butyral) by water: Glass transition temperature and mechanical properties. *Journal of Applied Polymer Science*, 136(12), Article 47230. <https://doi.org/10.1002/app.47230>
- Draft prEN 16613:2013. (2013). *Glass in building - Laminated glass and laminated safety glass - Determination of Interlayer Mechanical Properties*. <https://standards.iteh.ai/catalog/standards/sist/9a700c79-a2cc-4ce8-b931-6a274861c16a/osist-pren-16613-2013>
- Ensslen, F. (2007). Influences of laboratory and natural weathering on the durability of laminated safety glass. *Glass Performance Days*, 2, 584-590.
- Giovanna, R., Zulli, F., Andreozzi, L., & Fagone, M. (2017). Test methods for the determination of interlayer properties in laminated glass. *Journal of Materials in Civil Engineering*, 29(4), Article 04016268. [https://doi.org/10.1061/\(asce\)mt.1943-5533.0001802](https://doi.org/10.1061/(asce)mt.1943-5533.0001802)
- Hála, P., Zemanová, A., Plachý, T., Konrád, P., & Sovják, R. (2022). Experimental modal analysis of glass and laminated glass large panels with EVA or PVB interlayer at room temperature. *Materials Today: Proceedings*, 62, 2421-2428. <https://doi.org/10.1016/j.matpr.2022.02.578>
- Hána, T., Eliášová, M., & Sokol, Z. (2018). Structural performance of double laminated glass panels with EVA and PVB interlayer in four-point bending tests. *International Journal of Structural Glass and Advanced Materials Research*, 2(1), 164-177. <https://doi.org/10.3844/sgamrsp.2018.164.177>
- Hána, T., Eliášová, M., Vokáč, M., & Machalická, K. V. (2020). Viscoelastic properties of EVA interlayer used in laminated glass structures. In *IOP Conference Series: Materials Science and Engineering* (Vol. 800, p. 012021). IOP Publishing. <https://doi.org/10.1088/1757-899X/800/1/012021>
- Hána, T., Janda, T., Schmidt, J., Zemanová, A., Šejnoha, M., Eliášová, M., & Vokáč, M. (2019). Experimental and numerical study of viscoelastic properties of polymeric interlayers used for laminated glass: Determination of material parameters. *Materials*, 12(14), Article 2241. <https://doi.org/10.3390/ma12142241>
- Hartwell, R., & Overend, M. (2020). Effects of humidity and the presence of moisture at the bond-line on the interfacial separation of laminated glass for flat glass re-use. In J. Belis, F. Bos & C. Louter (Eds.), *Challenging Glass Conference Proceedings* (Vol. 7, pp. 1-15). CGC, Tu Delft Open. <https://doi.org/10.7480/CGC.7.4727>
- Hidallana-Gamage, H. D., Thambiratnam, D. P., & Perera, N. J. (2015). Influence of interlayer properties on the blast performance of laminated glass panels. *Construction and Building Materials*, 98, 502-518. <https://doi.org/10.1016/j.conbuildmat.2015.08.129>
- Hooper, P. A., Blackman, B. R. K., & Dear, J. P. (2012). The mechanical behaviour of poly(vinyl butyral) at different strain magnitudes and strain rates. *Journal of Materials Science*, 47, 3564-3576. <https://doi.org/10.1007/s10853-011-6202-4>
- ISO-6721-1. (2019). *Plastics - Determination of dynamic mechanical properties - Part 1: General principles*. <https://www.iso.org/standard/73142.html>
- ISO-62. (2008). *Plastics - Determination of water absorption*. <https://www.iso.org/standard/41672.html>
- ISO-12543-4. (2021). *Glass in building - Laminated glass and laminated safety glass - Part 4: Test methods for durability*. <https://www.iso.org/standard/75499.html>

- ISO-175. (2010). *Plastics - Methods of test for the determination of the effects of immersion in liquid chemicals*. <https://www.iso.org/standard/55483.html>
- ISO-527-1. (2019). *Plastics - Determination of tensile properties - Part 1: General principles*. <https://www.iso.org/standard/75824.html>
- Joseph Udi, U., Yussof, M. M., Musa Ayagi, K., Bedon, C., & Khairul Kamarudin, M. (2023). Environmental degradation of structural glass systems: A review of experimental research and main influencing parameters. *Ain Shams Engineering Journal*, 14(5), 101970. <https://doi.org/10.1016/j.asej.2022.101970>
- Kamarudin, M. K., Yusoff, M. M., Disney, P., & Parke, G. A. R. (2018). Experimental and numerical investigation of the buckling performance of tubular glass columns under compression. *Structures*, 15, 355-369. <https://doi.org/10.1016/j.istruc.2018.08.002>
- Kothe, M., & Weller, B. (2014). Influence of environmental stresses to the ageing behaviour of interlayer. In C. Louter, F. Bos, J. Belis & J. P. Lebet (Eds.), *Challenging Glass 4 and COST Action TU0905 Final Conference - Proceedings of the Challenging Glass 4 and Cost Action TU0905 Final Conference* (pp. 439-446). CRC Press.
- Kozłowski, M., Bedon, C., & Honfi, D. (2018). Numerical analysis and 1D/2D sensitivity study for monolithic and laminated structural glass elements under thermal exposure. *Materials*, 11(8), Article 1447. <https://doi.org/10.3390/ma11081447>
- Liu, B., Sun, Y., Li, Y., Wang, Y., Ge, D., & Xu, J. (2012). Systematic experimental study on mechanical behavior of PVB (polyvinyl butyral) material under various loading conditions. *Polymer Engineering and Science*, 52(5), 1137-1147. <https://doi.org/10.1002/pen.22175>
- Liu, B., Xu, J., & Li, Y. (2014). Constitutive investigation on viscoelasticity of PolyVinyl Butyral: Experiments based on dynamic mechanical analysis method. *Advances in Materials Science and Engineering*, 2014, Article 794568. <https://doi.org/10.1155/2014/794568>
- Lombardo, T., Chabas, A., Lefèvre, R. A., Verità, M., & Geotti-Bianchini, F. (2005). Weathering of float glass exposed outdoors in an urban area. *Glass Technology*, 46(3), 271-276.
- Louter, C., Belis, J., Veer, F., & Lebet, J. P. (2012). Durability of SG-laminated reinforced glass beams: Effects of temperature, thermal cycling, humidity and load-duration. *Construction and Building Materials*, 27(1), 280-292. <https://doi.org/10.1016/j.conbuildmat.2011.07.046>
- Lu, Y., Chen, S., & Shao, X. (2021). Shear modulus of ionomer interlayer: Effects of time, temperature and strain rate. *Construction and Building Materials*, 302, Article 124224. <https://doi.org/10.1016/j.conbuildmat.2021.124224>
- Martín, M., Centelles, X., Solé, A., Barreneche, C., Fernández, A. I., & Cabeza, L. F. (2020). Polymeric interlayer materials for laminated glass: A review. *Construction and Building Materials*, 230, Article 116897. <https://doi.org/10.1016/j.conbuildmat.2019.116897>
- Mohagheghian, I., Charalambides, M. N., Wang, Y., Jiang, L., Zhang, X., Yan, Y., Kinloch, A. J., & Dear, J. P. (2018). Effect of the polymer interlayer on the high-velocity soft impact response of laminated glass plates. *International Journal of Impact Engineering*, 120, 150-170. <https://doi.org/10.1016/j.ijimpeng.2018.06.002>
- Pankhardt, K., & Balázs, G. L. (2010). Temperature dependent load bearing capacity of laminated glass panes. *Periodica Polytechnica Civil Engineering*, 54(1), 11-22. <https://doi.org/10.3311/pp.ci.2010-1.02>
- Pelayo, F., Lamela-Rey, M. J., Muniz-Calvente, M., López-Aenlle, M., Álvarez-Vázquez, A., & Fernández-Canteli, A. (2017). Study of the time-temperature-dependent behaviour of PVB: Application to laminated glass elements. *Thin-Walled Structures*, 119, 324-331. <https://doi.org/10.1016/j.tws.2017.06.030>

- Ranocchiali, G., Andreozzi, L., Zulli, F., & Fagone, M. (2016). Effects of interlayer weathering on the structural behaviour of laminated glass structures. In J. Belis, F. Bos & C. Louter (Eds.), *Challenging Glass Conference Proceedings - Challenging Glass 5: Conference on Architectural and Structural Applications of Glass, CGC 2016* (pp. 385-390). CGC, Ghent University. <https://doi.org/10.7480/CGC.5.2264>
- Ranocchiali, G., Sciarpi, F., & Fagone, M. (2018). Laminated glass beams subjected to artificial solar radiation. In C. Louter, F. Bos & J. Belis (Eds.), *Challenging Glass 6: Conference on Architectural and Structural Applications of Glass, CGC 2018 - Proceedings* (pp. 447-452). CGC, TU Delft Open. <https://doi.org/10.7480/cgc.6.2167>
- Reiß, S., Krischok, S., & Rädlein, E. (2019). Comparative study of weather induced corrosion mechanisms of toughened and normal float glasses. *Glass Technology: European Journal of Glass Science and Technology Part A*, 60(2), 33-44. <https://doi.org/10.13036/17533546.60.2.020>
- Bennison, S. J., Qin, M. H. X., & Davis, P. (2008, May). High-performance laminated glass for structurally efficient glazing. [Paper Presented]. *Proceedings of Innovative Light-Weight Structures and Sustainable Facades Conference, Hong Kong*.
- Sable, L., Kinsella, D., & Kozłowski, M. (2019). Influence of EVA, PVB and Ionoplast interlayers on the structural behaviour and fracture pattern of laminated glass. *International Journal of Structural Glass and Advanced Materials Research*, 3(1), 62-78. <https://doi.org/10.3844/sgamrsp.2019.62.78>
- Sable, L., Skukis, E., Japins, G., & Kalnins, K. (2017). Correlation between Numerical and experimental tests of laminated glass panels with visco-elastic interlayer. *Procedia Engineering*, 172, 945-952. <https://doi.org/10.1016/j.proeng.2017.02.107>
- Serafinavicius, T., Kvedaras, A. K., & Sauciūvenas, G. (2013). Bending behavior of structural glass laminated with different interlayers. *Mechanics of Composite Materials*, 49(4), 437-446. <https://doi.org/10.1007/s11029-013-9360-4>
- Serafinavicius, T., Lebet, J. P., Louter, C., Kuranovas, A., & Lenkimas, T. (2014, January). The effects of environmental impacts on durability of laminated glass plates with interlayers (SG, EVA, PVB). In *Challenging Glass 4 & COST Action TU0905 Final Conference* (pp. 455-462). CRC Press.
- Serafinavičius, T., Lebet, J. P., Louter, C., Lenkimas, T., & Kuranovas, A. (2013). Long-term laminated glass four point bending test with PVB, EVA and SG interlayers at different temperatures. *Procedia Engineering*, 57, 996-1004. <https://doi.org/10.1016/j.proeng.2013.04.126>
- Subagio, R. (2020). Developing value innovation strategy in the “Blue Ocean Shift” framework at the flat glass industry in Indonesia. *IKAT: The Indonesian Journal of Southeast Asian Studies*, 4(1), 47-62. <https://doi.org/10.22146/ikat.v4i1.54657>
- Vedrtam, A., & Pawar, S. J. (2018). Experimental and simulation studies on fatigue behavior of laminated glass having polyvinyl butyral and ethyl vinyl acetate interlayers. *Fatigue and Fracture of Engineering Materials and Structures*, 41(6), 1437-1446. <https://doi.org/10.1111/ffe.12788>
- Wang, Y. (2020). The breakage behavior of different types of glazing in a fire. In *The Proceedings of 11th Asia-Oceania Symposium on Fire Science and Technology* (pp. 549-560). Springer. https://doi.org/10.1007/978-981-32-9139-3_40
- Yang, J., Wang, Y., Wang, X. E., Hou, X., Zhao, C., & Ye, J. (2022). Local bridging effect of fractured laminated glass with EVA based hybrid interlayers under weathering actions. *Construction and Building Materials*, 314, Article 125595. <https://doi.org/10.1016/j.conbuildmat.2021.125595>

- Yussof, M. M., Lim, S. H., & Kamarudin, M. K. (2020). The effect of short-term exposure to natural outdoor environment on the strength of tempered glass panel. In *Proceedings of AICCE'19: Transforming the Nation for a Sustainable Tomorrow 4* (pp. 997-1005). Springer International Publishing. https://doi.org/10.1007/978-3-030-32816-0_74
- Zemanová, A., Hála, P., Konrád, P., Janda, T., & Hlůžek, R. (2022). The influence of interlayer properties on the response of laminated glass to low-velocity hard-object impact. *International Journal of Impact Engineering*, *159*, Article 104036. <https://doi.org/10.1016/j.ijimpeng.2021.104036>
- Zhang, X., Liu, H., Maharaj, C., Zheng, M., Mohagheghian, I., Zhang, G., Yan, Y., & Dear, J. P. (2020). Impact response of laminated glass with varying interlayer materials. *International Journal of Impact Engineering*, *139*, Article 103505. <https://doi.org/10.1016/j.ijimpeng.2020.103505>
- Zhang, X., Mohammed, I. K., Zheng, M., Wu, N., Mohagheghian, I., Zhang, G., Yan, Y., & Dear, J. P. (2019). Temperature effects on the low velocity impact response of laminated glass with different types of interlayer materials. *International Journal of Impact Engineering*, *124*, 9-22. <https://doi.org/10.1016/j.ijimpeng.2018.09.004>
- Zhang, X., Shi, Y., Hao, H., & Cui, J. (2015). The mechanical properties of ionoplast interlayer material at high strain rates. *Materials and Design*, *83*, 387-399. <https://doi.org/10.1016/j.matdes.2015.06.076>
- Zhao, C., Yang, J., Wang, X.-E., Ren, M., & Azim, I. (2021). Investigation into short term behaviors of embedded laminated glass connections with various configurations. *Construction and Building Materials*, *297*, Article 123687. <https://doi.org/10.1016/j.conbuildmat.2021.123687>



Thermal Properties of Kenaf Fiber Reinforced Polyamide 6 Composites by Melt Processing

Norihan Abdullah^{1*}, Khalina Abdan¹, Mohd Huzaifah Mohd Roslim², Mohd Nazren Radzuan³, Lee Ching Hao¹ and Ayu Rafiqah Shafi¹

¹Laboratory of Biocomposite Technology, Institute of Tropical Forestry and Forest Products (INTROP), Universiti Putra Malaysia, 43400 UPM, Serdang, Selangor, Malaysia

²Department of Crop Science, Faculty of Engineering, Universiti Putra Malaysia, 97008 UPMKB, Bintulu Campus Sarawak, Malaysia

³Department of Biological and Agricultural Engineering, Faculty of Engineering, Universiti Putra Malaysia, 43400 UPM, Serdang, Selangor, Malaysia

ABSTRACT

In recent years, there has been much effort to find cost-effective ways to replace petroleum-based commodity plastics with biodegradable polymers with comparable thermal characteristics. The 5 wt.%, 10 wt.%, and 15 wt.% kenaf fiber were melted, and blended with polyamide-6 via a Brabender mixer, followed by compression molding. To evaluate the thermal properties of composites, thermogravimetric analysis (TGA), differential scanning calorimetry (DSC), and dynamic thermomechanical analysis (DMA) were conducted. According to the TGA results, increased kenaf fiber contents decreased the composite's thermal stability. Neat PA6 matrix decomposed rapidly at 425°C, which was comparatively higher than PA6 composites. From the DSC analysis, the addition of natural fibers resulted in quantified changes in the glass transition temperature (T_g), melting temperature (T_m), and crystallization temperature (T_c) of the PA6 composites. According to the DMA, the storage modulus of neat PA6 was 1177 MPa and decreased to 1076 MPa for 5 wt% of kenaf fiber in PA6 composite. The Kenaf fiber/polyamide 6 composites appeared to have lower thermal stability than neat PA6. This study demonstrated that the kenaf fiber/polyamide 6 composites were successfully prepared, and a detailed thermal analysis was conducted. Improving the KF/PA6 composites can be further studied to increase thermal stability.

Keywords: Composites, kenaf fiber, natural fiber, polyamide 6, polymer, thermal properties

ARTICLE INFO

Article history:

Received: 27 June 2022

Accepted: 05 October 2022

Published: 21 July 2023

DOI: <https://doi.org/10.47836/pjst.31.5.16>

E-mail addresses:

norihanjannah@gmail.com (Norihan Abdullah)

khalina@upm.edu.my (Khalina Abdan)

muhammadhuzaifah@upm.edu.my (Mohd Huzaifah Mohd Roslim)

mohdnazren@upm.edu.my (Mohd Nazren Radzuan)

leechinghao@upm.edu.my (Lee Ching Hao)

ayu.rafiqah@yahoo.com (Ayu Rafiqah Shafi)

*Corresponding author

INTRODUCTION

As the world strives to become more 'green,' the importance of global involvement is desperately needed to protect the environment and make it more economical to live in (Devnani & Sinha, 2019; Sanjay et al., 2018). The need for biocomposite has become imminent because of interest in using plant fiber as an environment-friendly reinforcement and potential replacement for synthetic fiber material in the composite polymer industry (Karthi et al., 2019; Sanjay & Yogesha, 2017). The abundance of readily available natural fibers is the perfect substitute for synthetic fibers like glass and carbon, which are typically more expensive, ecologically unfriendly, and nonrenewable (Mustafa et al., 2018). The natural fibers in composites are generally lighter, less expensive, and abundantly available, all of which contribute to the viability of a circular economy by significantly reducing carbon emissions and improving the mechanical performance of biopolymers (Atiqah et al., 2020; Kamarudin et al., 2020; Mohammed et al., 2015; Sanjay et al., 2015; Srinivas et al., 2017).

There has been growing interest in thermoplastic-based natural fiber composites (NFRCS) for high-performance engineering applications (Balla et al., 2019), with successful proof of their application to various structural and non-structural applications, especially for automotive (Boland et al., 2015; Vinayagamoorthy & Manoj, 2018), packaging (Sánchez-safont et al., 2018) and the construction industry (Mochane et al., 2019; Tadimetri, 2019). Thermoplastics offered better design flexibility and relatively simple processing techniques than thermoset and elastomer polymers. Thermoplastics such as polyethylene (PE), polypropylene (PP), nylon, high-density polyethylene (HDPE), and polyvinyl chloride (PVC) could compound with natural fibers (such as wood, kenaf, flax, hemp, cotton, oil palm, sisal, jute, and straw) to produce composites with elevated temperature (Mohammed et al., 2015; Sanjay et al., 2017; Siakeng et al., 2018; Gowda et al., 2018).

Kenaf (*Hibiscus Cannabinus*, L. family *Malvaceae*) is a cellulosic source that can be cultivated in various climate conditions. It is often produced in tropical and subtropical countries like Malaysia (Akil et al., 2011; Bhambure & Rao, 2021). Kenaf fiber has surprisingly increased worldwide because it has been appraised as environmentally beneficial and has high commercial interests. Many researchers in Malaysia are exploring kenaf fibers as a low-cost, low-density, renewable, recyclable, non-abrasive behavior, and biodegradable alternative to synthetic fibers (Guillou et al., 2018; Saba et al., 2015; Salem et al., 2017). Kenaf fiber's biodegradability contributes significantly to sustainable ecology, while it is low cost and good performance resolved the manufacturer's economic concerns. Numerous studies have examined using kenaf fiber polymer composites (Bledzki et al., 2015; El-shekeil, Sapuan, Abdan, et al., 2012; Hamidon, 2019; Sood & Dwivedi, 2018; Sreenivas et al., 2020; Thiruchitrabalam et al., 2012). Bledzki et al. (2015) researched four types of natural fibers typically used in the polymer industry (softwood, abaca, jute, and kenaf), and kenaf fiber reinforcement provides a remarkable strength for biocomposites.

Recent studies emphasize increasing the properties of engineering polymers such as polyamides reinforced with natural fiber, accounting for their excellent mechanical properties, thermal properties, and chemical stability compared to PE and PP (Zhang et al., 2020). When compared to thermoset polymers (epoxy & polyester), polyamide 6 (PA6) has attracted much interest because of its resilience to high temperatures, oils, and corrosive chemicals, relative strength-to-weight ratio, and better recyclability, which is significant for life cycle analysis (LCA) (Kiziltas et al., 2016). Correspondingly, its favorable thermo-mechanical qualities have been regarded as a conventional matrix material for natural fiber-reinforced composites. Kunchimon et al. (2019) also concluded its excellent compatibility with lignocellulosic fillers due to their similar hydrophilicity (Xu et al., 2018).

This study aims to determine the effect of various kenaf fiber contents on the thermal properties of PA6 composites. A thorough study of the thermal behavior of kenaf / polyamide 6 composites in terms of TGA, DMA, and DSC shall be discussed. This paper presents the experimental setup of the composite materials and their respective thermal testing. Results of the thermal behavior on kenaf/ polyamide 6 composites will be discussed.

MATERIALS AND METHODS

Materials

In this research, kenaf fiber was supplied by National Kenaf and Tobacco Board (LKTN) Perlis, Malaysia and was dried in the oven for 24 hr at 60°C. The kenaf fiber size of 40 mesh (400 µm) was used in this study. Meanwhile, Polyamide 6 was supplied by Polycomposite Sdn. Bhd (Perlis) with a density of 1.13 g.cm⁻³.

Kenaf Fiber / Polyamide 6 Composite Fabrication

The kenaf fiber / PA6 composites were prepared in two steps: melt compounded using the Haake Polydrive R600 internal mixer followed by Vecho Vation 40 tonnes compression molding based on composite compositions of 5%, 10%, and 15% (Table 1). Before feeding the components into the mixer, all components were manually mixed. The mixing process involves processing temperatures of 230°C, 235°C, 240°C, and 245°C with a 5-min duration and a rotating speed of 50 RPM. All

composite formulations resulting from the compounding procedure were hot pressed for 5 min at 220°C with dimensions of 150 mm × 150 mm x 3 mm (width x length x thickness).

Table 1
Formulations of kenaf fiber / polyamide 6 composites

Samples	PA6 (wt.%)	Kenaf fiber (wt.%)
PA6	100	0
5% KF	95	5
10% KF	90	10
15% KF	85	15

Thermal Stability

Thermal Gravimetric Analysis (TGA). Thermal gravimetric analysis (TGA) was conducted using the TA instrument Q500 (New Castle, DE, USA) in accordance with ASTM E1131-08 (2014). These tests were performed at room temperature ranging from room temperature to 600°C at a heating rate of 10°C/min. The sample weighed 5 to 6 mg under a nitrogen atmosphere that flowed at 50 mL/min.

Differential Scanning Calorimeter (DSC). A differential scanning calorimeter (DSC) test was evaluated with a TA instrument Q20 based on an adaptation of the ASTM D3418-15 standard (2015). In DSC, the samples weighing 5 and 6 mg were heated from room temperature to 250°C at 10°C/min throughout the heating cycle. The melting and crystallization behavior of materials was studied using a DSC thermograph. Equation 1 is used to calculate the percentage of crystallinity for each curve. The peaks of fusion values were applied to calculate the crystallinity degree (X_c) by fusion enthalpy values (ΔH_m). The theoretical 100% crystalline ($\Delta H_{100\%}$) heat fusion of PA6 equals 230 J/g (Milot et al., 2015).

$$X_c = (\Delta H_m / \Delta H_{100\%}) \cdot 100 \quad [1]$$

Dynamic Thermomechanical Analysis (DMA). Kenaf fiber / polyamide 6 composites were subjected to dynamic thermomechanical analysis (DMA) to measure the glass transition temperature (T_g), storage modulus (E'), loss modulus (E''), and loss factor ($\tan \delta$) using the TA instrument Q800 following ASTM D4065-12 (2012). The test temperature ranged from room temperature to 200°C, a heating rate of 3°C/min, a frequency of 1 Hz, an amplitude of 15 m, and specimens of 60 mm x 12 mm x 3 mm. Three samples were tested, and the findings are reported as an average of tested samples.

RESULTS AND DISCUSSION

Thermogravimetric Analysis (TGA)

The weight loss (TG) and its derivative (DTG) curves of neat PA6 and KF/PA6 composites are shown in Figures 1 and 2, respectively. The neat PA6 and KF/PA6 composites had found only one stage of the degradation process above 250°C. Increments in degradation temperature were observed with the increase in kenaf fiber content loading. The TG curve shows three mass loss steps. The first mass loss step for the neat PA6 and the KF/PA6 composites was in the range of 30-130°C, which is attributed to absorbed moisture evaporation (El-shekeil, Sapuan, Abdan, et al., 2012; Şeker Hirçin et al., 2020; Xu et al., 2019) and the neat PA6 showed more mass loss up to 4% compared to less than 3% in the kenaf fiber/PA6 composites. Besides, the degradation of the three main components of kenaf fibers, lignin, hemicellulose, and cellulose, are due to the second and third mass loss phases at 200–430°C and 360–480°C, respectively.

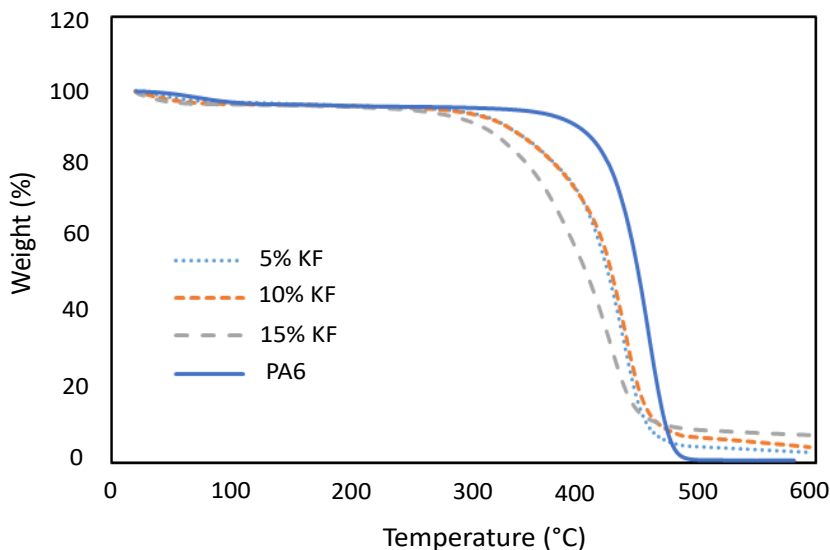


Figure 1. The weight loss (TG) curves of neat PA6 and KF / PA6 composites for various KF loadings

The thermal stability of the neat PA6 and KF/PA6 composites can be seen by their thermal decomposition temperature at the initial (T_{initial}) and final (T_{final}) as well as maximum decomposition temperature (T_{max}) (Kamarudin et al., 2020). The temperature of maximal deterioration for neat PA6 and KF/PA6 composites appears to be approximately 350°C – 450°C, similar to past researchers' findings (Kiziltas et al., 2016). Figure 2 shows thermal stability profiles for neat PA6 and KF/PA6 composites via derivative percentage weight thermograms (DTG). From the figure, the neat PA6 matrix decomposed rapidly at 425°C, which was comparatively higher than the KF/PA6 composites. The initial degradation temperature of neat PA6 was recorded at 249°C, and the degradation was completed at 457°C, with a weight loss of about 95.03%. Upon blending PA6 and kenaf fiber, the KF/PA6 composites decompose at a temperature less than neat PA6—initial and final temperatures of 15wt.% kenaf fiber showed the lowest values compared to 5 wt.% and 10 wt.% kenaf fiber. It reflected the lower thermal stability compared to 5 wt.% and 10 wt.% kenaf fiber. It also showed the lowest decomposition temperature at 361°C with a weight loss of about 88.6%.

The increase in kenaf fiber contents had recorded decreased thermal and summarized in Table 2. Lower thermal stability for all KF/PA6 composites is probably due to kenaf fiber's lower decomposition temperature behavior. It may have accelerated the disintegration of PA6's crystalline form, thereby reducing the composite's thermal stability (Kamarudin et al., 2020). Since some of PA6 has been replaced with less thermally stable kenaf fiber, the thermal stability of PA6 has been reduced. Furthermore, that may be because PA6's relative molecular mass has reduced (Zhu et al., 2020). Most researchers used chemical

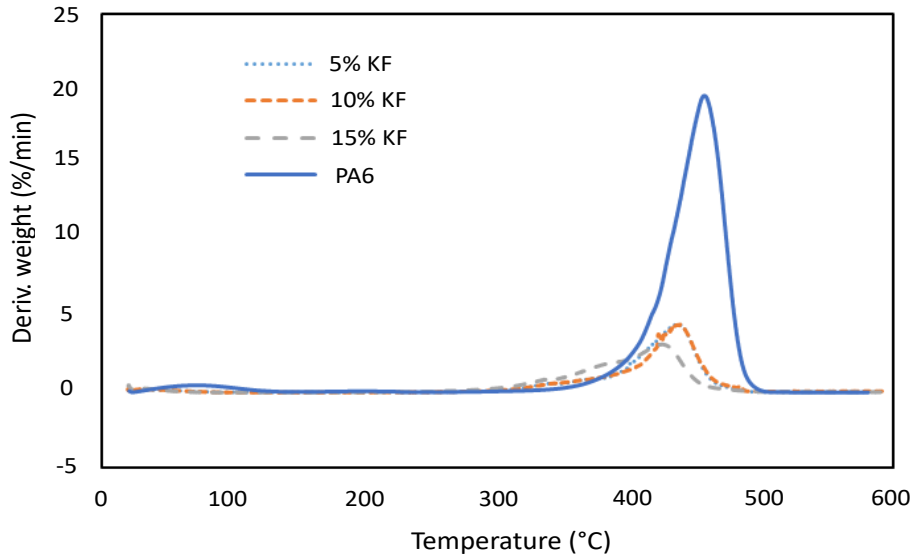


Figure 2. Derivatives percentage weight thermogram (DTG) curves of neat PA6 and KF/PA6 composites for various KF loadings

fiber modifications to overcome the composite's thermal stability (Hashim et al., 2017). One of the studies by Akhtar et al. (2016) stated that due to a higher decomposition temperature, treated composites are more thermally stable than untreated composites. The alkali treatment increases the thermal stability of natural fiber composites (El-shekeil, Sapuan, Khalina, et al., 2012). The residue weight of the composite samples at the end of the TGA measurement increased proportionally from around 0.8% (neat PA6) to 7.6% (15wt.% kenaf fiber), showing that the higher residue for higher natural fiber contents is due to the more lignin constituent in the components. The lignin forms char and maintains the structural integrity of the composite. Therefore, a higher residue was found.

Table 2

TGA results of neat PA6 and KF/PA6 composite for various kenaf fiber loadings

Sample	T _{initial} (°C)	T _{final} (°C)	T _{max} (°C)	Weight loss (%)	Residue at 600°C (%)
PA6	249.81	457.29	425.72	95.03	0.808
5% KF	163.64	437.12	394.80	94.77	2.985
10% KF	129.92	438.20	395.46	92.00	4.430
15% KF	105.13	425.32	361.69	88.76	7.657

Dynamic Mechanical Analysis (DMA)

Figure 3 shows the neat PA6 and KF/PA6 storage modulus. As the temperature increases, the storage modulus decreases due to kenaf fiber stiffness loss. The storage modulus of neat PA6 was 1177 MPa, while the KF/PA6 composite decreased to 1076 MPa with 5 wt.% kenaf fiber contents. The results showed that all KF/PA6 composites have lower storage modulus values than neat PA6. The damage to the matrix, degraded interfacial adhesion, and bonding strength between the matrix and fiber might be caused the storage modulus to reduce. The storage modulus of composites with poor adhesion has been found to produce composites with weak interfacial bonding (Akil et al., 2011). However, the 15 wt.% of kenaf fiber reinforcement was attributed to better stress transfer at the fiber interface, resulting in a higher modulus than 5 wt.% and 10 wt.%.

Figure 4 shows the loss modulus of neat PA6 and KF/PA6 composites. The loss modulus of the neat PA6 shows the highest values of 111 MPa and followed by 15 wt.%, 10 wt.%, and 5 wt.% kenaf fiber insertion composites with 89 MPa, 88 MPa, and 82 MPa, respectively. When kenaf fiber concentration is higher (15 wt.%), the polymer chain mobility's restriction becomes severe. Under external stress, the kenaf fiber particles and the PA6 matrix rubbed against one another across the interface, increasing energy consumption compared to the neat PA6 molecular chain's movement as well as the loss modulus of the composite (Zhu et al., 2020). From the overall observation, the thermal-mechanical characteristics of kenaf fiber-reinforced polyamide 6 Composites were decreased in terms of storage modulus and loss modulus.

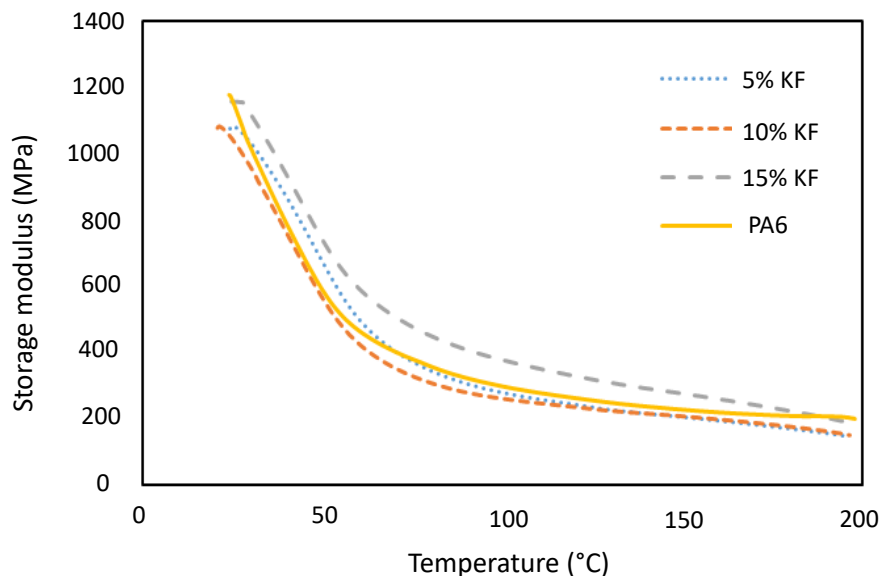


Figure 3. Storage modulus, E' of neat PA6 and KF/PA6 composites for various KF loadings

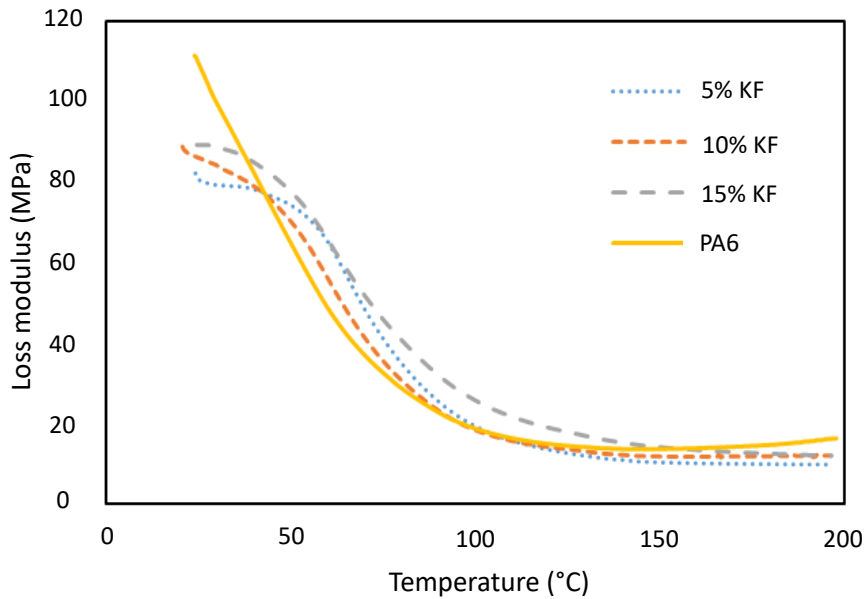


Figure 4. Loss modulus, E'' of neat PA6 and KF/PA6 composites for various KF loadings

Figure 5 shows the $\tan \delta$ (damping) of neat PA6 and KF/PA6 composites for various KF loadings. The glass transition temperature, T_g , corresponds to the $\tan \delta$ peak, and the damping is defined as the ratio of the loss modulus to the storage modulus. The KF/PA6 composite's absolute value increased when the main $\tan \delta$ peak moved to a higher temperature. The neat PA6 showed a $\tan \delta$ max peak temperature of around 52°C, whereas the KF/PA6 composites ranged from 57 to 61°C, with the presence of the 5 wt.% kenaf fiber, it is shown that there was a shift in T_g to a higher temperature. The decreased mobility of the PA6 chains due to the appearance of kenaf fiber may explain the phenomena. The highest peak of the $\tan \delta$ curve is observed on 10 wt% KF composite, indicating a greater damping property. Table 3 reports the DMA results for neat PA6 and KF/PA6 composites for various kenaf fiber loadings. The thermal properties of composites can be improved by improving fiber morphology during the treatment process (El-shekeil, Sapuan, Khalina, et al., 2012). The DMA of treated kenaf fiber improved the bondability and wettability between the polymer matrix and cellulosic reinforcement, according to Verma and Shukla (2018). It improves the load-carrying capacity of these green polymer composites.

Differential Scanning Calorimeter (DSC)

Figure 6 illustrates the DSC curves of neat PA6 and KF/PA6 composites for various KF, and Table 4 reports the DSC results for neat PA6 and KF/PA6 composites for different kenaf fiber loadings. The melting point of the neat PA6 was found to be 220°C. KF/PA6 composites ranged between 218°C and 214°C, implying that the kenaf fiber had little

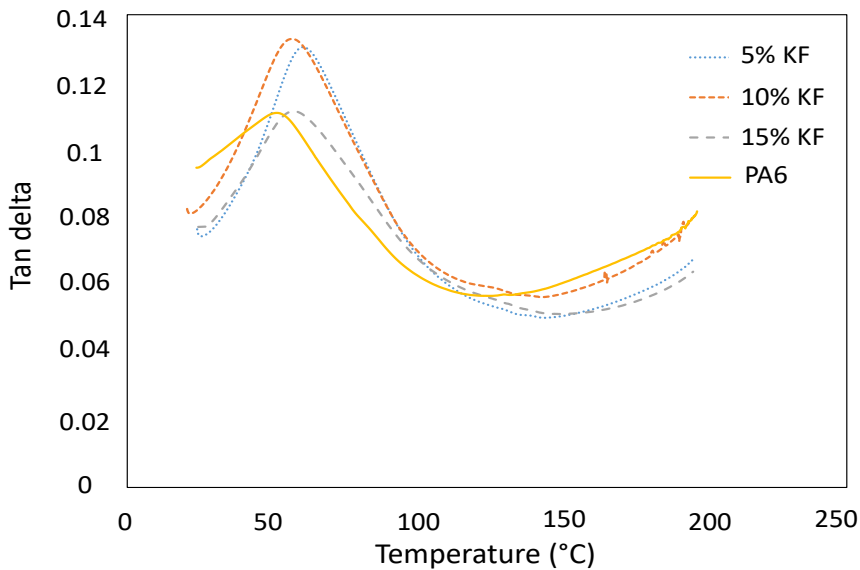


Figure 5. Tan δ (damping) of neat PA6 and KF/PA6 composites for various KF loadings

Table 3

DMA results of neat PA6 and KF/PA6 composites for various kenaf fiber loadings

Sample	Storage modulus, E' (MPa)	Loss modulus, E'' (MPa)	Tan Delta, δ
PA6	1177.49	111.49	0.1103
5% KF	1076.02	82.26	0.1303
10% KF	1077.74	88.89	0.1328
15% KF	1157.41	89.29	0.1113

influence on the T_m of the KF/PA6 composites. T_c values of neat PA6 were 208°C, and KF/PA6 composites were between 200°C and 205°C. As a result, the addition of 5 wt.%, 10 wt.%, and 15 wt.% kenaf fiber had little on the T_c of KF/PA6 composites. When the kenaf fiber was added to the PA6, the T_c value for the neat PA6 composites decreased. Adding kenaf fiber to the polymer prevents PA6 molecular chains from migrating and diffusing in the composites (Cheung et al., 2009; Huda et al., 2008). Thus, it has a negative effect on polymer crystallization, which results in a reduction in T_c . The kenaf fiber acted as a nucleating agent for the polymer to accelerate crystallization (Kamarudin et al., 2020).

The results showed that the addition of 5 wt.%, 10 wt.%, and 15 wt.% kenaf fiber in the PA6 matrix reduced the T_m . The kenaf fiber prevented the mobility of the PA6 molecular chains, resulting in partial crystals, which explains the KF/PA6 composite's decrease in

crystallinity. The fillers are good nucleating agents in polymer composites, influencing crystallization behavior significantly (Kamarudin et al., 2020). The kenaf fiber acts as a nucleating site for PA6 crystallization but can also act as a barrier to crystal development. Hence the composites have a lower crystallinity index than neat PA6.

The T_g represented the mobility of the PA6 molecular chain in the amorphous area. The T_g of neat PA6 is 52°C. After adding 5% kenaf fiber, the T_g value was increased to 160°C. T_g was detected at a low temperature since neat PA6 had no compatibility constraints, and the molecular chain motion was not hindered (Kiziltas et al., 2016). The kenaf fiber particles hindered the neat PA6 molecular chain's mobility, which required high energy and free volume to achieve the glass transition. As a result, T_g rises in KF/PA6 composites compared to neat PA6.

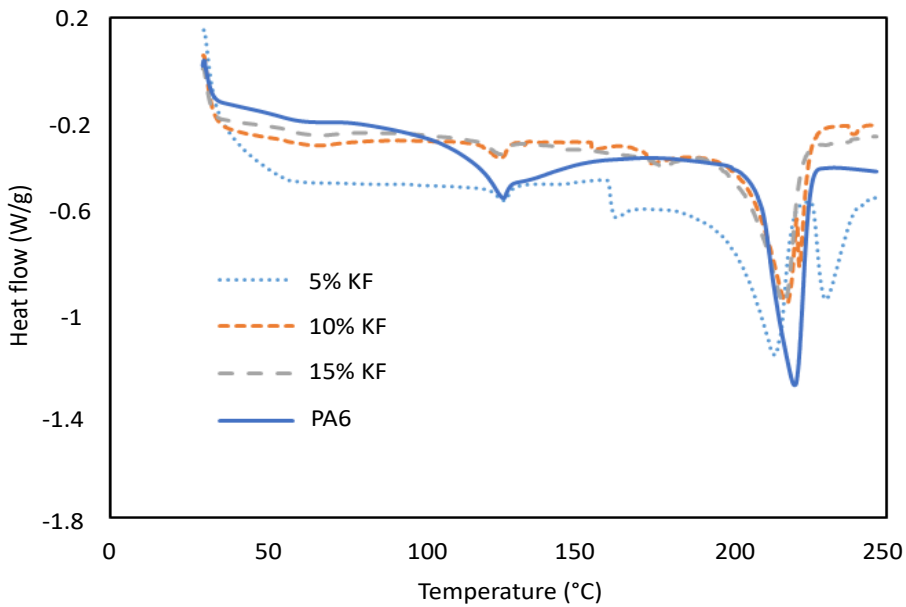


Figure 6. DSC thermograms of neat PA6 and KF/PA6 composites for various KF loadings

Table 4

DSC results of neat PA6 and KF/PA6 composites for various kenaf fiber loadings

Sample	Melting temperature, T_m (°C)	Crystallization temperature, T_c (°C)	Glass transition, T_g (°C)	Crystallinity index, X_c (%)
PA6	220.52	208.40	52.71	26.37
5% KF	214.31	200.16	160.68	22.11

Table 4 (Continue)

Sample	Melting temperature, T_m (°C)	Crystallization temperature, T_c (°C)	Glass transition, T_g (°C)	Crystallinity index, X_c (%)
10% KF	218.41	205.45	151.73	23.00
15% KF	217.13	204.15	144.03	20.28

CONCLUSION

In this study, KF/PA6 composites with different contents of KF were prepared by melt compounded, and their thermal properties were investigated in terms of TGA, DMA, and DSC. The TGA analysis proved that the kenaf fiber reinforcement had decreased the thermal stability with evidence of decreased initial and final decomposition temperature. The DMA results showed that the thermal-mechanical characteristics of kenaf fiber composites have deteriorated in terms of storage and loss modulus. However, the DSC results depicted that the glass transition temperature (T_g) of KF/PA6 composites was shifted to a higher temperature due to the affection of the crystallization behavior in KF/PA6 composites. The results showed that the addition of 5 wt.%, 10 wt.%, and 15 wt.% kenaf fiber in the PA6 matrix reduced the T_m . The composites have a lower crystallinity index than neat PA6. In conclusion, the thermal stability was decreased by increasing kenaf fiber loading. It is expected that lignocellulosic natural fibers always have higher flammability than polymer resins. Thus, improving the KF/PA6 composites can be further studied to increase thermal stability, such as through fiber treatment.

ACKNOWLEDGEMENTS

The authors thank Putra Grant Berimpak (GBP/2020/9691300) for aiding this research. We also thank the UPM-Kyutech International Symposium on Applied Engineering and Sciences 2021 (SAES2021) and Universiti Putra Malaysia for supporting the publication fee.

REFERENCES

- Akhtar, M. N., Sulong, A. B., Radzi, M. K. F., Ismail, N. F., Raza, M. R., Muhamad, N., & Khan, M. A. (2016). Influence of alkaline treatment and fiber loading on the physical and mechanical properties of kenaf/polypropylene composites for variety of applications. *Progress in Natural Science: Materials International*, 26(6), 657-664. <https://doi.org/10.1016/j.pnsc.2016.12.004>
- Akil, H. M., Omar, M. F., Mazuki, A. A. M., Safiee, S., Ishak, Z. A. M., & Bakar, A. A. (2011). Kenaf fiber reinforced composites: A review. *Materials and Design*, 32(8-9), 4107-4121. <https://doi.org/10.1016/j.matdes.2011.04.008>

- ASTM D4065-12. (2012). Standard Practice for Plastics: Dynamic Mechanical Properties: Determination and Report of Procedures, ASTM International, West Conshohocken, PA, 2012.
- ASTM D3418-15. (2015). Standard Test Method for Transition Temperatures and Enthalpies of Fusion and Crystallization of Polymers by Differential Scanning Calorimetry, ASTM International, West Conshohocken, PA, 2015.
- ASTM E1131-08. (2014). Standard Test Methods for Compositional Analysis by Thermogravimetry, ASTM International, West Conshohocken, PA, 2014.
- Atiqah, A., Chandrasekar, M., Kumar, T. S. M., Senthilkumar, K., & Ansari, M. N. M. (2020). Characterization and interface of natural and synthetic hybrid composites. *Encyclopedia of Renewable and Sustainable Materials*, 4, 389-400. <https://doi.org/10.1016/b978-0-12-803581-8.10805-7>
- Balla, V. K., Kate, K. H., Satyavolu, J., Singh, P., & Tadimeti, J. G. D. (2019). Additive manufacturing of natural fiber reinforced polymer composites: Processing and prospects. *Composites Part B: Engineering*, 174, Article 106956. <https://doi.org/10.1016/j.compositesb.2019.106956>
- Bhambure, S., & Rao, A. S. (2021). Experimental investigation of impact strength of kenaf fiber reinforced polyester composite. *Materials Today: Proceedings*, 46(part 2), 1134-1138. <https://doi.org/10.1016/j.matpr.2021.02.055>
- Bledzki, A. K., Franciszczak, P., Osman, Z., & Elbadawi, M. (2015). Polypropylene biocomposites reinforced with softwood, abaca, jute, and kenaf fibers. *Industrial Crops and Products*, 70, 91-99. <https://doi.org/10.1016/j.indcrop.2015.03.013>
- Boland, C. S., De Kleine, R., Keoleian, G. A., Lee, E. C., Kim, H. C., & Wallington, T. J. (2015). Life cycle impacts of natural fiber composites for automotive applications effects of renewable energy content and lightweighting. *Journal of Industrial Ecology*, 20(1), 179-189. <https://doi.org/10.1111/jiec.12286>
- Cheung, H. Y., Ho, M. P., Lau, K. T., Cardona, F., & Hui, D. (2009). Natural fibre-reinforced composites for bioengineering and environmental engineering applications. *Composites Part B: Engineering*, 40(7), 655-663. <https://doi.org/10.1016/j.compositesb.2009.04.014>
- Devnani, G. L., & Sinha, S. (2019). Effect of nanofillers on the properties of natural fiber reinforced polymer composites. *Materials Today: Proceedings*, 18(part 3), 647-654. <https://doi.org/10.1016/j.matpr.2019.06.460>
- El-Shekeil, Y. A., Sapuan, S. M., Abdan, K., & Zainudin, E. S. (2012). Influence of fiber content on the mechanical and thermal properties of Kenaf fiber reinforced thermoplastic polyurethane composites. *Materials and Design*, 40, 299-303. <https://doi.org/10.1016/j.matdes.2012.04.003>
- El-Shekeil, Y. A., Sapuan, S. M., Khalina, A., Zainudin, E. S., & Al-Shuja'a, O. M. (2012). Effect of alkali treatment on mechanical and thermal properties of kenaf fiber-reinforced thermoplastic polyurethane composite. *Journal of Thermal Analysis and Calorimetry*, 109(3), 1435-1443. <https://doi.org/10.1007/s10973-012-2258-x>
- Guillou, J., Lavadiya, D. N., Munro, T., Fronk, T., & Ban, H. (2018). From lignocellulose to biocomposite: Multi-level modelling and experimental investigation of the thermal properties of kenaf fiber reinforced composites based on constituent materials. *Applied Thermal Engineering*, 128, 1372-1381. <https://doi.org/10.1016/j.applthermaleng.2017.09.095>
- Gowda, T. G. Y., Sanjay, M. R., Bhat, K. S., Madhu, P., Senthamaraiannan, P., & Yogesha, B. (2018). Polymer Matrix-Natural Fiber Composites: An Overview. *Cogent Engineering*, 5(1), Article 1446667. <https://doi.org/10.1080/23311916.2018.1446667>

- Hamidon, M. H., Sultan, M. T. H., Ariffin, A. H., & Shah, A. U. M. (2019). Effects of fibre treatment on mechanical properties of kenaf fibre reinforced composites: A review. *Journal of Material Research and Technology*, 8(3), 3327-3337. <https://doi.org/10.1016/j.jmrt.2019.04.012>
- Hashim, M. Y., Amin, A. M., Marwah, O. M. F., Othman, M. H., Yunus, M. R. M., & Huat, N. C. (2017). The effect of alkali treatment under various conditions on physical properties of kenaf fiber. In *Journal of Physics: Conference Series* (Vol. 914, Article 012030). IOP Publishing. <https://doi.org/10.1088/1742-6596/914/1/012030>
- Huda, M. S., Drzal, L. T., Mohanty, A. K., & Misra, M. (2008). Effect of fiber surface-treatments on the properties of laminated biocomposites from poly (lactic acid) (PLA) and kenaf fibers. *Composite Science and Technology*, 68(2), 424-432. <https://doi.org/10.1016/j.compscitech.2007.06.022>
- Kamarudin, S. H., Abdullah, L. C., Aung, M. M., & Ratnam, C. T. (2020). Thermal and structural analysis of epoxidized jatropa oil and alkaline treated kenaf fiber reinforced poly(Lactic acid) biocomposites. *Polymers*, 12(11), Article 2604. <https://doi.org/10.3390/polym12112604>
- Karthi, N., Kumaresan, K., Sathish, S., Gokulkumar, S., Prabhu, L., & Vigneshkumar, N. (2019). An overview: Natural fiber reinforced hybrid composites, chemical treatments and application areas. *Materials Today: Proceedings*, 27(part 3), 2828-2834. <https://doi.org/10.1016/j.matpr.2020.01.011>
- Kiziltas, E. E., Yang, H. S., Kiziltas, A., Boran, S., Ozen, E., & Gardner, D. J. (2016). Thermal analysis of polyamide 6 composites filled by natural fiber blend. *BioResources*, 11(2), 4758-4769. <https://doi.org/10.15376/biores.11.2.4758-4769>
- Mochane, M. J., Mokhena, T. C., Mokhothu, T. H., Mtibe, A., Sadiku, E. R., Ray, S. S., Ibrahim, I. D., & Daramola, O. O. (2019). Recent progress on natural fiber hybrid composites for advanced applications : A review. *EXPRESS Polymer Letters*, 13(2), 159-198. <https://doi.org/10.3144/expresspolymlett.2019.15>
- Mohammed, L., Ansari, M. N. M., Pua, G., Jawaid, M., & Islam, M. S. (2015). A review on natural fiber reinforced polymer composite and its applications. *International Journal of Polymer Science*, 2015, Article 243947. <https://doi.org/10.1155/2015/243947>
- Mustafa, W. A., Saidi, S. A., Zainal, M., & Santiagoo, R. (2018). Experimental study of composites material based on thermal analysis. *Akademia Baru*, 43(1), 37-44.
- Saba, N., Paridah, M. T., & Jawaid, M. (2015). Mechanical properties of kenaf fibre reinforced polymer composite: A review. *Construction and Building Materials*, 76, 87-96. <https://doi.org/10.1016/j.conbuildmat.2014.11.043>
- Salem, I. A. S., Rozyanty, A. R., Betar, B. O., Adam, T., Mohammed, M., & Mohammed, A. M. (2017). Study of the effect of surface treatment of kenaf fiber on chemical structure and water absorption of kenaf filled unsaturated polyester composite. In *Journal of Physics: Conference Series* (Vol.908, Article 012001). IOP Publishing. <https://doi.org/10.1088/1742-6596/908/1/012001>
- Sánchez-safont, E. L., Aldureid, A., & Lagarón, J. M. (2018). Biocomposites of different lignocellulosic wastes for sustainable food packaging applications. *Composites Part B: Engineering*, 145, 215-225. . <https://doi.org/10.1016/j.compositesb.2018.03.037>
- Sanjay, M. R., Arpitha, G. R., & Yogesha, B. (2015). Study on mechanical properties of natural - glass fibre reinforced polymer hybrid composites: A review. *Materials Today: Proceedings*, 2(4-5), 2959-2967. <https://doi.org/10.1016/j.matpr.2015.07.264>

- Sanjay, M. R., Madhu, P., Jawaid, M., Sentharamaikkannan, P., Senthil, S., & Pradeep, S. (2018). Characterization and properties of natural fiber polymer composites: A comprehensive review. *Journal of Cleaner Production*, 172, 566-581. <https://doi.org/10.1016/j.jclepro.2017.10.101>
- Sanjay, M., & Yogesha, B. (2017). Studies on natural/glass fiber reinforced polymer hybrid composites: An evolution. *Materials Today: Proceedings*, 4(2), 2739-2747. <https://doi.org/10.1016/j.matpr.2017.02.151>
- Hirçin, B. S., Yörür, H., & Mengeloğlu, F. (2020). Effects of filler type and content on the mechanical, morphological, and thermal properties of waste casting polyamide 6 (W-PA6G)-based wood plastic composites. *BioResources*, 16(1), 655-668. <https://doi.org/10.15376/biores.16.1.655-668>
- Siakeng, R., Jawaid, M., Ariffin, H., Sapuan, S. M., Asim, M., & Saba, N. (2018). Natural fiber reinforced polylactic acid composites: A review. *Polymer Composites*, 40(2), 446-463. <https://doi.org/10.1002/pc.24747>
- Sood, M., & Dwivedi, G. (2018). Effect of fiber treatment on flexural properties of natural fiber reinforced composites: A review. *Egyptian Journal of Petroleum*, 27(4), 775-783. <https://doi.org/10.1016/j.ejpe.2017.11.005>
- Sreenivas, H. T., Krishnamurthy, N., & Arpitha, G. R. (2020). A comprehensive review on light weight kenaf fiber for automobiles. *International Journal of Lightweight Materials and Manufacture*, 3(4), 328-337. <https://doi.org/10.1016/j.ijlmm.2020.05.003>
- Srinivas, K., Naidu, A. L., & Bahubalendruni, M. V. A. R. (2017). A review on chemical and mechanical properties of natural fiber reinforced polymer composites. *International Journal of Performability Engineering*, 13(2), 189-200. <https://doi.org/10.23940/ijpe.17.02.p8.189200>
- Thiruchitrabalam, M., Alavudeen, A., & Venkateshwaran, N. (2012). Review on kenaf fiber composites. *Reviews on Advanced Materials Science*, 32(2), 106-112.
- Verma, R., & Shukla, M. (2018). Characterization of mechanical properties of short Kenaf fiber-HDPE green composites. *Materials Today: Proceedings*, 5(2), 3257-3264. <https://doi.org/10.1016/j.matpr.2017.11.567>
- Vinayagamoorthy, R., & Manoj, I. V. (2018). Natural fiber for green technology in automotive industry : A brief review Natural fiber for green technology in automotive industry: A brief review. In *IOP Conference Series: Materials Science and Engineering* (Vol.368, Article 012012). IOP Publishing. <https://doi.org/10.1088/1757-899X/368/1/012012>
- Xu, K., Zheng, Z., Du, G., Zhang, Y., Wang, Z., Zhong, T., Xie, L., & Wang, S. (2019). Effects of polyamide 6 reinforcement on the compatibility of high-density polyethylene/environmental-friendly modified wood fiber composites. *Journal of Applied Polymer Science*, 136(38), Article 47984. <https://doi.org/10.1002/app.47984>
- Xu, S., Fang, Y., Yi, S., He, J., Zhai, X., Song, Y., Wang, H., & Wang, Q. (2018). Effects of lithium chloride and chain extender on the properties of wood fiber reinforced polyamide 6 composites. *Polymer Testing*, 72, 132-139. <https://doi.org/10.1016/j.polymertesting.2018.10.005>
- Zhang, J., Koubaa, A., Xing, D., Liu, W., Wang, Q., Wang, X. M., & Wang, H. (2020). Improving lignocellulose thermal stability by chemical modification with boric acid for incorporating into polyamide. *Materials and Design*, 191, Article 108589. <https://doi.org/10.1016/j.matdes.2020.108589>
- Zhu, S., Guo, Y., Chen, Y., & Liu, S. (2020). Low water absorption, high-strength polyamide 6 composites blended with sustainable bamboo-based biochar. *Nanomaterials*, 10(7), Article 1367. <https://doi.org/10.3390/nano10071367>

Innovative Formulation and Characterisation of Grease Made from Waste Engine Oil

Muhammad Auni Hairunnaja¹, Mohd Aizudin Abd Aziz^{1*}, Nurul Waheeda Abdu Rahman¹, Mohd Azmir Arifin¹, Khairuddin Md Isa² and Umi Fazara Md Ali²

¹Faculty of Chemical & Process Engineering Technology, Universiti Malaysia Pahang, Lebuhraya Tun Razak, 26300 UMP, Gambang, Pahang, Malaysia

²Faculty of Chemical Engineering Technology, Universiti Malaysia Perlis, Kompleks Pusat Pengajian Jejawi 3, 02600 UNIMAP, Arau, Perlis, Malaysia

ABSTRACT

Lubricating grease is usually produced from mineral oil, making the relationship between grease and mineral oil unavoidable. Formulation of grease from waste oil can reduce the dependency of the grease industry on mineral oil as well as help to reduce the waste generation of used oil. This study aims to produce fumed silica (FS) grease from waste engine oil (WEO) and analyse the properties of the formulated grease. The method started with treating WEO to remove any contaminants in the used oil. After that, the greases are produced using a weight percentage ratio before being examined for consistency, oil separation, oil bleeding, FTIR (Fourier transform infrared spectroscopy) analysis, and corrosiveness. In terms of uniformity, oil separation, and oil bleeding, WEO percentage content had a substantial impact on the findings. The FTIR demonstrated that synthetic greases had the same spectra when evaluated between 500 cm⁻¹ and 4000 cm⁻¹. The grease's corrosiveness is low, as determined by class 1 corrosiveness toward the copper strip. However, the grease properties differ when consistency, oil bleeding and oil separation test is done. Higher oil content in grease produced high oil bleeding and separation

but low consistency. As a conclusion of the results, fumed silica grease with oil percentages of 83 and 82 have the most grease-like features, showing that the grease fits the traits' requirements. Based on the investigation's findings, it was established that WEO may be used as a base oil in grease formulation and that the grease's properties are satisfactory.

Keywords: Fumed Silica (FS), grease formulation, waste engine oil (WEO)

ARTICLE INFO

Article history:

Received: 03 August 2022

Accepted: 30 November 2022

Published: 21 July 2023

DOI: <https://doi.org/10.47836/pjst.31.5.17>

E-mail addresses:

mauliduni97@gmail.com (Muhammad Auni Hairunnaja)

maizudin@ump.edu.my (Mohd Aizudin Abd Aziz)

waheedarahman95@gmail.com (Nurul Waheeda Abdu Rahman)

m.azmir@ump.edu.my (Mohd Azmir Arifin)

khairudin@unimap.edu.my (Khairuddin Md Isa)

umifazara@unimap.edu.my (Umi Fazara Md Ali)

*Corresponding author

INTRODUCTION

Lubricating grease is primarily composed of lubricating base fluid, a specific type of thickening agent, and an additive chosen based on the function of the grease. The base fluid is a lubricant, and the thickening acts as a sponge, holding the base fluid together. The base fluid used in grease is typically mineral oil, with a few instances of synthetic-base oil being utilised depending on the application. It is mostly because mineral oil may function satisfactorily as grease in industrial applications (Misozi et al., 2018). Metallic soap is the most common form of thickening used in grease production, which contains lithium, polyurea, aluminium, sodium, clay, and calcium (Daniel & Paulus, 2019). It will provide critical grease properties such as chemical and thermal stability, mechanical stability, and rheology. It also acts as a sponge, retaining the main fluid (Fan et al., 2018). Grease formulation also includes an additive addition which enhances the grease performance depending on the type of grease used. Incorporating additives into the grease improves properties such as high temperature, high pressure, water resistance, and anti-wear. Molybdenum Disulphate (MoS_2) is a common additive found in grease. According to Epshteyn and Risdon (2010), MoS_2 is a powder that ranges from dark grey to black. It is extensively employed in a wide range of non-aerospace applications. It was historically used as grease for bit lubrication and has long been a great solid lubricant (Fink, 2021).

Lubricating grease is preferred in difficult-to-reach areas of mechanically rubbing or sophisticated machinery. Grease has several properties that allow it to retain stability in water, have highly consistent shear stability, and deal with viscosity fluctuations despite changes in temperature and pressure—all of which contribute to its functionality as a storage medium for base oil and additives (Adhvaryu et al., 2005). Grease is divided into numerous varieties based on its use, such as insoluble-solid thickened greases, polymer-thickened greases, soap-thickened greases, and lithium and aluminium grease (Casserly et al., 2018).

Using waste oil as the primary oil in grease formulation is a new and emerging trend. Waste oil is petroleum-based or synthetic oil that has deteriorated due to pollution. It has lost its original properties due to pollutants (Japar, Aziz, & Razali, 2018; Japar, Aziz, Razali, & Rahman, 2018). The most frequent type of waste oil is automobile lubricant waste oil, abbreviated WEO. WEO is produced using motor oil. Motor oil waste is a high-contaminated commodity that must be treated with caution. Depletion of additives, metallic components, particle dirt and grits, and other asphaltic particles are examples of waste motor oil pollution (Tsai, 2011). Discharging waste oil into the ground or water streams, including sewage, can harm the environment. It could contaminate groundwater and soil (Hegazi et al., 2017).

Many previous studies discovered that WEO might be utilised as a base oil in grease formulation. Except for sulfation, the properties of WEO after treatment are nearly identical to those of fresh engine oil. The current study intends to produce grease from WEO and

then analyse the properties of the greases based on the results. The current trend in non-soap grease manufacturing is to maximise the ability of Fumed silica (FS), known for its significantly small particle size and thickening effect, making it an excellent thickener. Because of its high surface energy, it is used in a wide range of industrial applications. Due to the flame reaction that occurs when silicon tetrachloride and oxygen come into contact, fumed silica is also known as pyrogenic silica (Ha et al., 2013). It is non-toxic and available in the form of white powder. It is commonly used as a thickening and anti-caking agent. According to Rahman et al. (2018), it is composed of amorphous silicon dioxide with silanol groups all over it (Vansant et al., 1995). Because the silanol groups are so highly reactive, they can be used to start chemical reactions. Its reactivity surface is determined by the number of silanol groups surrounding the surfaces of FS powder. Aside from that, as opposed to a large surface area, Barthel et al. (2005) claimed that the structure of FS is related to having space-filling particle characteristics. Aside from that, FS is free of swelling or chemical inertness, making it an effective thickening agent (Barthel et al., 2005). It is one of the advantages available when compared to FS. Table 2 lists the numerous trials where FS was used as a grease thickener and additive.

In other words, fumed silica (FS) is a white powder with an exceptionally low density. This thickener is non-melt and can be mixed with base oil. When FS is dispersed in oil, it has a texture similar to gel and is colourless. Furthermore, according to Whitby (2020), the network synthesis by FS in WCO increases the mixture's viscosity and thickens the structure stability. FS is resistant to oxidation, has a high-temperature tolerance, and has a significant thickening effect. Additionally, at relatively low concentrations, the FS particles can form the unique 3D network found in fumed silica (Santos et al., 2011).

It demonstrated that using fumed silica as a grease thickener is advantageous and improves the characteristics of the grease. Due to the fibrous matrix of the pore structure of FS, has tendency to entrap the base oil entirely until may turn from liquid into semi-solid state. FS grease has excellent stability with minimal oil leakage and separation. The way of formulating grease also affects the homogenization process between base oil and thickener itself. An appropriate composition of grease gives significant effects especially in term of grease consistency, oil bleeding and oil separation. The FTIR analysis is also essential since it helps in defining the type of desired or undesired impurities availability since they have a tendency in effecting the corrosiveness of the grease due to corrosive agents like sulphur and metal content. Therefore, many criteria considerations should be taken in formulating grease to ensure it meets the commercial grease standard.

MATERIALS AND METHODS

Materials

In this study, waste engine oil (WEO) with black visual colour and 0.8751 g/mL of density was acquired from a workshop in Kuantan, Pahang. Meanwhile, the fumed silica (FS)

of low-density white powder with 99% purities from R&M Chemical Kuala Lumpur, Malaysia was selected to be used in this study. The FS is supposed to have a high melting point of up to 1600°C.

Grease Formulation

Pre-Treatment of WEO. The sedimentation of any large, suspended substance starts the process. The filtering operation was then started using a vacuum filter and a glass microfiber filter with a pore size of 1.2 µm. The filtration eliminated any small, suspended particles in the WEO. Evaporation was the final procedure, which helped to remove any moisture in the WEO by heating it for 1 hour at 120°C. The altered WEO was saved in a container for future usage.

Preparation of Grease Using WEO. Abdulbari et al. (2008) developed the methodical process which leads to the production of FS grease, which begins with heating WEO for a minimum of one hour at a constant temperature of 120°C. Throughout the one-hour duration, the WEO is stirred to remove all moisture. The temperature is then lowered to 80°C - 90°C in gradual phases before the gradual inclusion of FS begins. Both processes are done gradually to ensure thorough homogenisation (Abdulbari et al., 2008).

The next step is to allow homogenisation, which is accomplished by allowing the homogeniser to run at a minimum speed of 4000 rpm for three hours. When a substance similar to gel is produced, the grease production process is considered complete. The grease is then allowed to cool at room temperature. Following that, it must be kept in a closed container. Two days must elapse before testing to ensure complete cooling of the grease. It is to ensure that the test results are consistent, as the characteristics of the grease change with the presence of heat,

Table 1

Grease formulation ratio

Sample	WEO	Thickener (FS)
FG ₈₅	85	15
FG ₈₄	84	16
FG ₈₃	83	17
FG ₈₂	82	18
FG ₈₁	81	19
FG ₈₀	80	20

particularly grease consistency. The grease formulation ratio employed in this study is shown in Table 1.

Grease Analysis

Several studies were carried out on the grease produced to establish its properties. The test includes consistency, oil separation, oil bleeding, FTIR (Fourier transform infrared spectroscopy) analysis, and corrosion testing.

Consistency Test

This test was performed using an SKF Grease Test Kit TGKT 1 set. The two glass plates were placed between a fixed amount of grease, which was then pushed for 15 seconds with the weight. Then, using a calibrated measuring scale with an NLGI grade, the consistency of the grease strain was inspected and assessed. This test procedure complied with ISO 2137 (Japar et al., 2014), which details techniques for assessing the consistency of lubricating greases when only limited samples are available. Each grease's consistency level is shown by the NLGI results.

Oil Separation

Oil separation testing was done in accordance with ASTM D-1742 (Standard Test Method for Oil Separation from Lubricating Grease during Storage) to determine the propensity of oil to separate from grease during storage. The grease sample was kept at room temperature for a month in a sealed container.

Oil Bleeding

In this part, the SKF Grease Test Kit TGKT 1 was used as an alternative technique for the oil bleeding test, requiring only modest volumes of samples (Lugt, 2013). In accordance with the instructions in the SKF manual 1, a sample of fresh grease was placed on blotting paper and heated for 2 hr at 60°C using a hot plate. Using the bleed area and the percentage difference between the bleed areas of fresh grease and used grease, Equations 1 and 2 were used to determine the amount of oil stain formed on the paper. Grease that has been aged under two controlled conditions for 10 days at room temperature and at 70°C is referred to as used grease.

$$S_i = 0.785 \times (D_{AVI}^2 - 100) \quad (1)$$

$$\%Diff = 100 \times \frac{(S_{used} - S_{Fresh})}{S_{Fresh}} \quad (2)$$

S_i denotes the difference between the bled areas from the fresh and used samples, DAV denotes the bleeding area's average diameter, and $\%Diff$ denotes the bled area's difference between the two samples.

FTIR (Fourier Transform Infrared Spectroscopy) Analysis

All the grease sample base oil and thickener types were determined using the Fourier transform infrared (FTIR) spectroscopy. The FTIR spectrum can reveal any changes and contamination in a grease sample by contrasting it with a fresh grease reference and a used

grease sample. Grease and oil characteristics were analysed in this experiment with wave numbers ranging from 500 to 4000 cm^{-1} .

Corrosion Testing

The extent of the grease's corrosiveness toward copper strips was assessed using a corrosion test. This procedure was carried out in accordance with ASTM D4048 (Test Method for Detecting Copper Corrosion from Lubricating Grease by the Copper Strip Tarnish Test). The grease sample is placed on a copper strip prepared for this purpose and then heated in an oven or liquid bath at a predetermined temperature for a predetermined amount of time. After the test, the strips were removed from the sample, washed, and compared to the ASTM Copper Strip Corrosion Standards (ASTM D4048, 2018).

RESULT AND DISCUSSION

Grease Consistency

The most grease-like and beneficial greases have an NLGI grade 2-3 consistency or 220 - 295 mm/10 penetration (Rizvi, 2009). The grease can be dislodged from its intended location if the surface is too smooth, and it may move to the intended spot to fail. The findings of the grease consistency study are shown in Table 2. According to the research, a higher quantity of WEO used in grease formulation resulted in softer grease. It is evidenced by the zero consistency of FG85 greases and the five consistency of FG80 greases. It supports Doyle's conclusion that the quantity of thickening used directly impacts the grease's consistency (Doyle, 2015). The trend was consistent when compared to data produced by Japar et al. (2019). According to the results of Japar et al. (2019), the consistency of the grease rose as the fumed silica content increased. However, because Japar et al. (2019) utilised transformer oil for grease formation, the data differs from the findings of this study. Table 2 summarises the findings of this investigation on grease characteristics.

Table 2

Properties of formulated grease

FS grease	NLGI grade	Oil separation (%)	Oil bleeding (%)	
			At ambient	at 70°C
FG ₈₅	0	5.7543	-	-
FG ₈₄	1-2	4.3875	-16.4835	4.3269
FG ₈₃	2	2.9645	-5.0251	1.6304
FG ₈₂	3	1.0056	-3.2609	-1.6484
FG ₈₁	4-5	0	2.9557	-2.4631
FG ₈₀	5	0	2.8846	-2.5126

The consistency of the grease decreased as the ratio of WEO to thickener increased due to a low sponge-like structure that could hold the base oil. The oil became loosely held and easily separated from the thickening matrix system when the attraction between the thickening and the base oil decreased (Japar et al., 2019). When forced, the lower the viscosity of the grease, the more probable it is to spill oil (Abdulbari et al., 2011).

Oil Separation

When the grease was exposed to specific conditions, oil separation, also known as static oil bleeding or puddling, occurred. The low tension causes the grease to leak a small amount of oil. Oil separation can occur spontaneously in greases, and the rate is determined by the grease's composition. Oil separation is a grease that has released oil under static (storage) or typical running circumstances. Small pools of oil indicate static oil separation, especially if the grease surface is not smooth or uniform. Oil separation can happen when oil heated for a long time. This incident might occur either by keeping the grease in a warm atmosphere or by being exposed to pressure and altitude fluctuations within a warm environment storage. Grease having a poor consistency, as compared to firmer grease, is expected to have a higher proportion of oil separation (Zakani et al., 2018).

Table 2 summarises the findings of this experiment, which indicates the percentage of oil separation throughout storage duration. The oil separation values for FG81 and FG80 in Table 2 are unavailable since the grease consistency ranges between 4 and 5, necessitating a high matrix thickening force to hold the oil together. The more solid the grease becomes, the less probable it is to separate from the oil. However, due to oil separation, a thin layer of oil with a consistency of NLGI grade > 4 may be observed on top of the grease. As a consequence, the oil is gathered and weighed. Figure 1 depicts the results of an investigation into the effect of WEO content on grease oil separation. The value of oil separation increases as the WEO content in grease increases. It happened because there was no thickening matrix to keep the WEO contained inside the grease, causing the grease to flow.

According to the research, the oil separation is maximum at 85% WEO concentration, with a 5.75% oil separation. It is because of the high base oil concentration occurring during the formulation process. Since 80% WEO has the lowest base oil concentration, oil separation does not occur during the study. It occurred because the thickening in the grease held the oil together, reducing the potential of the oil to separate from the matrix thickener. A previous study by Japar et al. (2019) also demonstrated that grease with a high FS percentage did not remove the oil from the thickening matrix.

Oil Bleeding

Oil bleeding, commonly called dynamic oil bleeding, is the controlled release of basic oils and additives in response to mechanical and thermal stress. Grease's ability to bleed

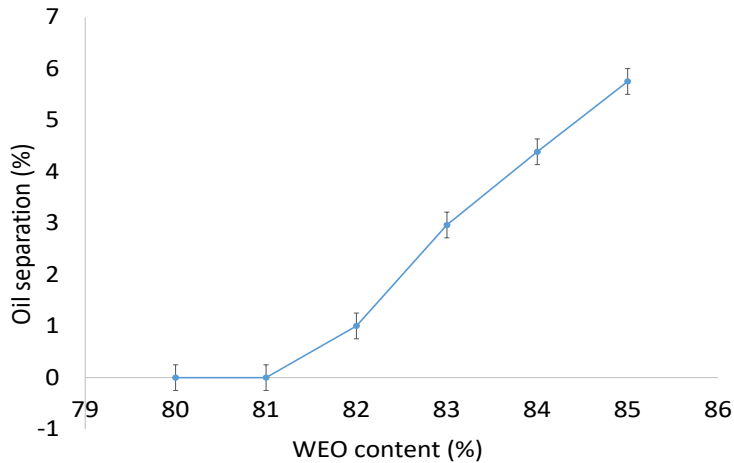


Figure 1. Effect of WEO content on FS greases' oil separation

is important since it lubricates machines at specified temperatures and conditions. On the other hand, uncontrolled oil bleeding will cause grease to leak out, causing the grease to dry out. As a result, a specific percentage of oil bleeding, ranging from -15 to +15%, is optimal (Rahman et al., 2019). A hidden meaning exists between positive and negative signs of oil bleeding values. The positive sign value of oil bleeding indicates that the grease structure is soft and prone to bleed when applied. Meanwhile, the negative sign value indicates the hardness of the grease structure, which is unlikely to bleed even at high temperatures. The oil bleeding rate is quietly related to the amount of thickener in the grease composition. The higher the amount of thickener, the lower the tendency of oil bleeding rates (Gonçalves et al., 2015). This restriction applies to both new and old grease and indicates the grease's ability to operate without re-lubrication.

Table 2 and Figure 2 show the findings of our inquiry on the link between WEO content and oil bleeding. However, due to the 0 consistency of the grease, the oil leakage percentage for FG85 is not calculated. A low NLGI grade may cause grease to leak, resulting in inaccurate figures. The results showed that when the WEO level increased, so did the proportion of FS grease oil leakage. It is because there are only a limited number of fibrous networks of thickening that can help in the retention of the base oil within the grease. Because of the limited number of fibrous networks, grease's resistance to oil flow was reduced, increasing grease permeability (Gonçalves et al., 2015).

One reason for conducting separate analyses at both temperatures (at room temperature and 70°C) is to distinguish the oil bleeding rate between normal and extreme conditions for the old grease. One of the conditions showed the grease characteristics after being used or exposed to high temperatures for a duration, while the other showed how the grease behaved after being stored for a duration of time. The grease condition and ability

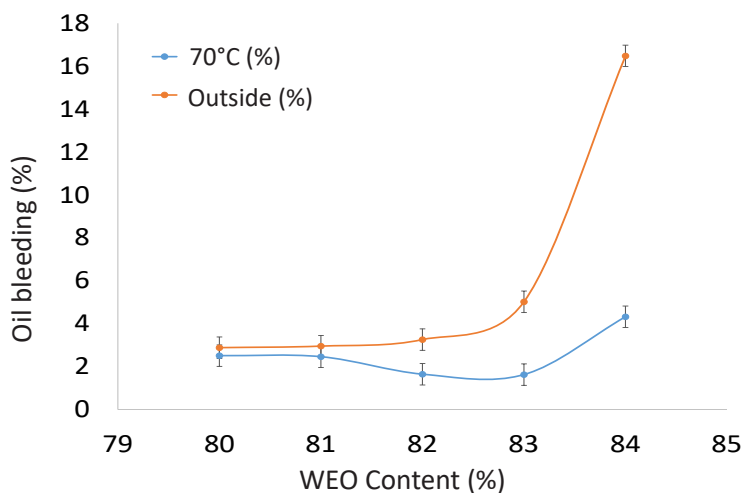


Figure 2. Effect of WEO content on FS greases' oil bleeding

to release oil after high-temperature exposure is expected to decrease compared to normal aged grease due to grease drying out and oil leakage during high-temperature exposure.

Japar et al. (2019) discovered that when heated at 70°C and ambient temperature, the oil leakage of the grease is larger for grease with higher FS concentration. However, this study found the contrary. The results indicated that at 80% WEO concentration, the oil bleeding is 2.5% at 70°C and 2.88% at ambient temperature, while at 84% WEO content, the oil bleeding is 4.3% at 70°C and 16.48% at ambient temperature. It could be due to the oil used, which imparts different qualities to the formed grease. Japar et al. (2019) utilised waste transformer oil as the base fluid in their investigation, which has different qualities from the WEO used in this study.

FTIR Analysis

A useful tool for understanding chemical component availability in certain materials or goods is the Fourier Transform Infrared (FTIR) Spectroscopy. This equipment can also perform quantitative and qualitative organic and inorganic substance analyses. Several chemical compound groupings can be found in the oil, including additives, contaminants, and chemical modifications. The FTIR analysis of a grease sample is used to evaluate its content, such as additives, impurities, product degradation, and components. Figure 3 depicts the FTIR spectrum of the tested FS grease. The FS grease spectrum revealed similarities and differences between the greases. It is because the components used in the grease composition are comparable. The only distinction between the two is the proportion of each constituent.

The spectra of FS greases indicated a strong peak in the 2800 – 3000 cm^{-1} region, showing that C-H stretched (Nabi et al., 2013). The peaks continued in the 1450 – 1460 cm^{-1} spectrum area, exhibiting CN stretch, and the 1350 – 1380 cm^{-1} spectrum area, exhibiting C-H symmetrical bend (Cyriac et al., 2016). The peak on the spectrum 1080 – 2000 cm^{-1} showed the presence of a Si-O-Si stretch inside the FS greases, and the peak on the spectrum 800 – 810 cm^{-1} indicated the presence of an S-S stretch which indicates the presence of diesel that usually exist in used oil as a contaminant as well as thickener inside the grease, and the peak on the spectrum 450 – 460 cm^{-1} indicated the presence of halogen within the grease (Mudalip et al., 2012). However, the grease formulation is expected to have the minimum amount of impurities that have a lower effect on the grease properties.

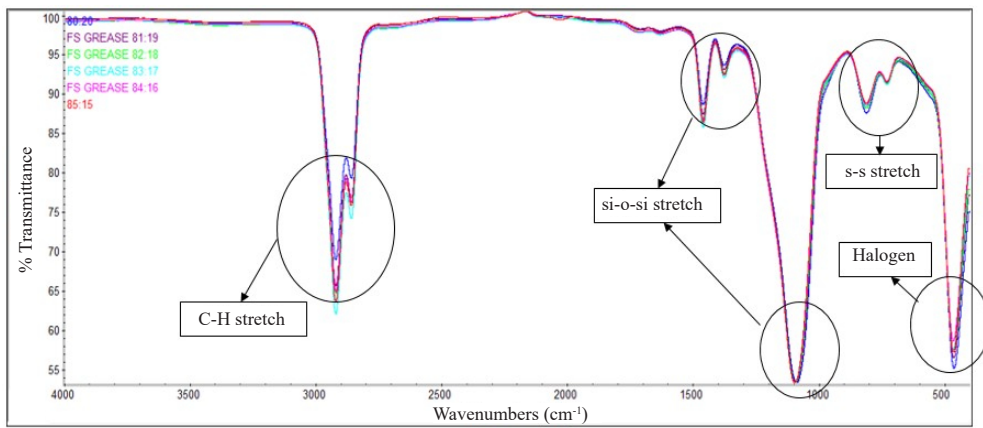


Figure 3. FTIR spectrum of FS greases

Corrosion

A corrosion test can be done to predict the risk of an attack on lubricated goods containing copper or copper alloy. The ASTM D4048 standard determines how corrosive the grease is to the copper strip. The results of corrosion experiments on FS grease are shown in Table 3.

Table 3

FS grease corrosiveness level towards the copper strip

Sample	Results	Strip appearances
Freshly-polished strip		
FG ₈₅	1b – slight tarnish (dark orange)	
FG ₈₄	1b – slight tarnish (dark orange)	

Table 3 (Continue)





Sample	Results	Strip appearances
FG ₈₃	1b – slight tarnish (dark orange)	
FG ₈₂	1b – slight tarnish (dark orange)	
FG ₈₁	1b – slight tarnish (dark orange)	
FG ₈₀	1b – slight tarnish (dark orange)	

Table 3 demonstrates that the formulated grease is not corrosive to the copper strip. All copper strips were corrosive in class 1 or above, specifically 1b, where only a small tarnish occurred on the tested copper strip and the strip's colour is dark orange.

CONCLUSION

In terms of WEO content, the grease produced by WEO was also high quality. WEO concentration has been proven to be related to oil bleeding and separation but is inversely proportional to grease consistency. According to the study findings, the FTIR analysis of the grease revealed no contaminant. It proved that the WEO treatment technique could eliminate contaminants found in WEO. Despite achieving only class 1 was achieved throughout this experiment, the formulated grease demonstrated decreased corrosiveness on the copper strip. According to the data acquired throughout the trial, FG83 and FG82 have the most grease-like features, showing that the grease meets the standards for the traits. More study is also required to learn to discover more about the properties of grease.

ACKNOWLEDGEMENT

The authors wished to acknowledge the financial support from the Ministry of Higher Education, Malaysia, for funding this research under FRGS (RDU 210147) and the University Malaysia Pahang research fund (RDU 190398 & PGRS 200356).

REFERENCES

- Abdulbari, H. A., Abid, R. T., & Mohammad, A. H. A. (2008). Fume silica base grease. *Journal of Applied Sciences*, 8(4), 687-691. <https://doi.org/10.3923/jas.2008.687.691>
- Abdulbari, H. A., Rosli, M. Y., Abdurrahman, H. N., & Nizam, M. K. (2011). Lubricating grease from spent bleaching earth and waste cooking oil: Tribology properties. *Academic Journals*, 6(20), 4695-4699. <https://doi.org/10.5897/IJPS11.561>
- Adhvaryu, A., Sung, C., & Erhan, S. (2005). Fatty acids and antioxidant effects on grease microstructures. *Industrial Crops and Products*, 21(3), 285-291. <https://doi.org/10.1016/j.indcrop.2004.03.003>

- ASTM D4048-16e1. (2018). Standard Test method for detection of copper corrosion. *ASTM International*. <http://www.astm.org/>
- Barthel, H., Rösch, L., & Weis, J. (2005). Fumed silica - Production, properties, and applications. In N. Auner, & J. Weis (Eds.), *Organosilicon Chemistry Set: From Molecules to Materials* (pp. 761-778). Wiley. <https://doi.org/10.1002/9783527620777.ch91a>
- Casserly, E., Langlais, T., Springer, S. P., Kumar, A., & Mallory, B. (2018). The effect of base oils on thickening and physical properties of lubricating greases. *The European Lubricants Industry Magazine*, 144, 32-37.
- Cyriac, F., Lugt, P. M., Bosman, R., Padberg, C. J., & Venner, C. H. (2016). Effect of thickener particle geometry and concentration on the grease EHL film thickness at medium speeds. *Tribology Letters*, 61, Article 18.
- Daniel, R., & Paulus, T. (2018). *Lock gates and other closures in hydraulic projects*. Butterworth-Heinemann.
- Doyle, D. (2015). *General Grease Overview and Bearing Lubrication*. ALS Tribology.
- Ephsteyn, Y., & Risdon, T. J. (2010, January 28-30). Molybdenum disulfide in lubricant applications - A review. In *Proceedings of the 12 Lubricating Grease Conference*. Goa, India. <http://www.nlgi-india.org/images/PDF/Yakov%20Ephsteyn.pdf>
- Fan, X., Li, W., Li, H., Zhu, M., Xia, Y., & Wang, J. (2018). Probing the effect of thickener on tribological properties of lubricating greases. *Tribology International*, 118, 128-139. <https://doi.org/10.1016/j.triboint.2017.09.025>
- Fink, J. (2021). *Petroleum engineer's guide to oil field chemicals and fluids* (3rd ed.). Gulf Professional Publishing. <https://doi.org/10.1016/C2020-0-02705-2>
- Gonçalves, D., Graça, B., Campos, A. V., Seabra, J., Leckner, J., & Westbroek, R. (2015). Formulation, rheology and thermal ageing of polymer greases - Part I: Influence of the thickener content. *Tribology International*, 87, 160-170. <https://doi.org/10.1016/j.triboint.2015.02.018>
- Ha, S. W., Weitzmann, M. N., & Beck, G. R., Jr. (2013). Chapter 4 - Dental and skeletal applications of silica-based nanomaterials. In K. Subramani, W. Ahmed, & J. K. Hartsfield, Jr. (Eds.), *Nanobiomaterials in Clinical Dentistry* (pp. 69-91). William Andrew Publishing. <https://doi.org/10.1016/B978-1-4557-3127-5.00004-0>
- Hegazi, S. E. F., Mohamd, Y. A., & Hassan, M. I. (2017). Recycling of waste engine oil using different acids as washing agents. *International Journal of Oil, Gas and Coal Engineering*, 5(5), 69-74. <https://doi.org/10.11648/j.ogce.20170505.11>
- Japar, N. S. A., Aziz, M. A. A., & Razali, M. N. (2014). Formulation of lubricating grease using Beeswax thickener. In *IOP Conference Series: Materials Science and Engineering* (Vol. 342, No. 1, p. 012007). IOP Publishing. <https://doi.org/10.1088/1757-899X/342/1/012007>
- Japar, N. S. A., Aziz, M. A. A., & Razali, M. N. (2018, August 28-29). Fundamental study of waste oil potential as base oil alternative in grease formulation. In *Proceeding of 2018 National Conference for Postgraduate Research* (pp. 208-212). Pahang, Malaysia.
- Japar, N. S. A., Aziz, M. A. A., Razali, M. N., & Rahman, N. W. A. (2018). Grease and its application on electrical equipment: A review. *International Journal of Engineering & Technology*, 7(3.26), 23-39. <https://doi.org/http://dx.doi.org/10.14419/ijet.v7i3.26.17455>

- Japar, N. S. A., Aziz, M. A. A., & Razali, M. N. (2019). Formulation of fumed silica grease from waste transformer oil as base oil. *Egyptian Journal of Petroleum*, 28(1), 91-96. <https://doi.org/10.1016/j.ejpe.2018.12.001>
- Japar, N. S. A., Aziz, M. A. A., Razali, M. N., Zakaria, N. A., & Rahman, N. W. A. (2019). Preparation of grease using organic thickener. *Materials Today: Proceedings*, 19(4), 1303-1308. <https://doi.org/10.1016/j.matpr.2019.11.141>
- Lugt, P. M. (2013). Condition monitoring and maintenance. In *Grease Lubrication in Rolling Bearings* (pp. 283-337). Wiley.
- Misozi, D. M., Victor, M., Ebelia, M., & Chanda, T. P. (2018). Mineral base oil recovery from waste lubricant grease. *Rwanda Journal of Engineering Science Technology and Environment*, 1(1), 1-7. <https://doi.org/10.4314/rjeste.v1i1.7S>
- Mudalip, S. K. A., Yeung, S. L. C., Sazwani, S., & Yunus, R. M. (2012). Production of high temperature grease from waste lubricant sludge and silicone oil. *Journal of Applied Sciences*, 12(11), 1171-1175. <https://doi.org/10.3923/jas.2012.1171.1175>
- Nabi, M. N., Akhter, M. S., & Rahman, M. A. (2013). Waste transformer oil as an alternative fuel for diesel engine. *Procedia Engineering*, 56, 401-406. <https://doi.org/10.1016/j.proeng.2013.03.139>
- Rahman, M. R., Hui, J. L. C., & Hamdan, S. B. (2018). 5 - Nanoclay dispersed phenol formaldehyde/fumed silica nanocomposites: Effect of diverse clays on physicomechanical and thermal properties. In M. R. Rahman (Ed.), *Silica and Clay Dispersed Polymer Nanocomposites (Preparation, Properties and Applications)* (pp. 59-70). Woodhead Publishing. <https://doi.org/10.1016/B978-0-08-102129-3.00005-1>
- Rahman, N. W. A., Japar, N. S. A., Aziz, M. A. A., Razik, A. H. A., & Yunus, M. Y. M. (2019). Sodium grease formulation from waste engine oil. In *2019 9th International Conference on Future Environment an Energy, IOP Conference Series: Earth and Environmental Science* (Vol. 257, Article 012018). IOP Publishing.
- Rizvi, S. Q. A. (2009). *A Comprehensive Review of Lubricant Chemistry, Technology, Selection, and Design*. ASTM. <https://doi.org/10.1520/mnl59-eb>
- Santos, P. H. S., Carignano, M. A., & Campanella, O. H. (2011). Qualitative study of thixotropy in gelled hydrocarbon fuels. *Engineering Letters*, 19(1), 13-19.
- Vansant, E. F., Van der Voort, P., & Vrancken, K. C. (1995). *Characterization and chemical modification of the silica surface*. Elsevier.
- Tsai, W. T. (2011). An analysis of used lubricant recycling, energy utilization and its environmental benefit in Taiwan. *Energy*, 36(7), 4333-4339. <https://doi.org/10.1016/j.energy.2011.04.008>
- Whitby, C. P. (2020). Structuring edible oils with fumed silica particles. *Frontiers in Sustainable Food Systems*, 4, Article 585160. <https://doi.org/10.3389/fsufs.2020.585160>
- Zakani, B., Ansari, M., & Grecov, D. (2018). Dynamic rheological properties of a fumed silica grease. *Rheologica Acta*, 57, 83-94. <https://doi.org/10.1007/s00397-017-1064-6>



A Study on Bio-Stabilisation of Sub-Standard Soil by Indigenous Soil Urease-Producing Bacteria

Abdulaziz Dardau Aliyu^{1,2}, Muskhazli Mustafa^{1*}, Nor Azwady Abd Aziz¹ and Najaatu Shehu Hadi¹

¹Department of Biology, Faculty of Science, Universiti Putra Malaysia, 43400 UPM, Serdang, Selangor, Malaysia

²Department of Microbiology, Faculty of Science, Federal University of Lafia, Akunza 950101, Nasarawa State, Nigeria

ABSTRACT

Sub-standard soils are of great concern worldwide due to diverse economic losses and the possibility of severe environmental hazards ranging from catastrophic landslides, building collapse, and erosion to loss of lives and properties. This study explored the potential of urease-producing bacteria, *Bacillus cereus* and *Bacillus paramycooides*, to stabilise sub-standard soil bio-stabilisation. The maximum urease activity measured by *B. cereus* and *B. paramycooides* was 665 U/mL and 620 U/mL, respectively. *B. cereus* and *B. paramycooides* precipitated 943 ± 57 mg/L and 793 ± 51 mg/L of CaCO₃ at an optical density (425 nm) of 1.01 and 1.09 and pH 8.83 and 8.59, respectively, after 96 hours of incubation. SEM microstructural analysis of the precipitated CaCO₃ revealed crystals of various sizes (2.0–23.0 μm) with different morphologies. XRD analysis confirmed that the precipitated CaCO₃ comprised calcite and aragonite crystals. SEM analysis of the microstructure of organic and sandy clay soils treated with *B. cereus* and *B. paramycooides* showed the formation of bio-precipitated calcium carbonate deposits on the soil particles (biocementing soil grains), with *B. cereus* precipitating more CaCO₃ crystals with a better biocementing effect compared to *B. paramycooides*. Overall, the experimental results attributed CaCO₃ formation to bacterial-associated processes, suggesting that soil ureolytic bacteria are potentially useful to stabilise sub-standard soil.

Keywords: Bio-stabilisation, calcite, calcium carbonate, micp, urease enzyme, ureolysis

ARTICLE INFO

Article history:

Received: 15 August 2022

Accepted: 25 January 2023

Published: 21 July 2023

DOI: <https://doi.org/10.47836/pjst.31.5.18>

E-mail addresses:

aliyuabdulaziz23@gmail.com (Abdulaziz Dardau Aliyu)

muskhazli@upm.edu.my (Muskhazli Mustafa)

azwady@upm.edu.my (Nor Azwady Abd Aziz)

Shehuhadinajaatu@gmail.com (Najaatu Shehu Hadi)

*Corresponding author

INTRODUCTION

There is a high demand for land for civil infrastructure, particularly in urban areas, due to rapid population growth in both developing and developed nations (Sinha & Chattopadhyay, 2016). On the contrary, landmass for various construction purposes continues to become relatively scarce (Bernardi et al., 2014). This rapid growth enhances the high demand for land utilisation to meet various basic human needs, necessitating infrastructural development on sub-standard soils (Chang et al., 2016). Geotechnical engineers define a sub-standard soil type as having inferior engineering features and cannot be effectively utilised for construction without an improvement technique (Rabenhorst et al., 2020). Indeed, there is an estimated global financial loss of up to seven billion US dollars annually due to the failure of various geotechnical structures built on sub-standard soils (Singh et al., 2020).

In Malaysia, the Department of Environment reported that 2.56 million hectares of land (representing 7.74%) are covered with sub-standard peat soils, mostly distributed within Sarawak (1,697,847 hectares) and Selangor (164,708 hectares) states (Wahab et al., 2019; Sapar et al., 2020). Furthermore, during the last two decades, there have been more than 400 landslides comprising over 30 major landslides involving both natural and cut slopes, which have destroyed properties worth billions of ringgits and claimed over 200 lives due to the high compressibility and low shear strength of these tropical peatland sub-standard soils (Makinda et al., 2018). The poor soil characteristics may affect the foundations of multi-storey buildings, pavements, retaining walls and dams with devastating consequences such as slip failures, local sinking and massive settlements. Thus, an urgent need is to develop an effective, less evasive, durable and relatively environment-friendly soil stabilisation method.

Despite the numerous advances in using conventional materials and methods for soil stabilisation, challenges remain to overcome (Nawarathna et al., 2018). Industrial manufacturing of mineral additives such as cement has economic and environmental concerns, such as high energy consumption and CO₂ emission accounting for 7% of the world's anthropogenic emissions (Nawarathna et al., 2018; Nething et al., 2020), which contributes to climate change (Wong, 2015). An alternative method to stabilise sub-standard soil is microbial urease enzyme technology known as Microbially Induced Calcite Precipitation (MICP).

MICP utilises eco-friendly features of urease-producing bacteria to hydrolyse urea (ureolysis) in a series of complex biochemical reactions to generate ammonium and carbonate ions. The ammonium ions favour precipitation by increasing the pH (Terzis & Laloui, 2019; Filet et al., 2020). The bacteria cell surface has a net negative charge as a negative zeta potential (Renner & Weibel, 2011), thus providing binding sites for carbonate

ions with available divalent calcium ions within the micro-environment under sufficient supersaturation conditions, hence precipitating cementitious calcite crystals on the cell surface (Dardau et al., 2021). These precipitated inorganic carbonate crystals further cement soil grains together, filling inter-particle voids, thereby improving the physical and mechanical properties of sub-standard soils (Lutfian et al., 2020). The success of the MICP process is promoted primarily by *in situ* conditions such as particle size and distribution, temperature, water content and treatment conditions like cementation solution and bacterial concentrations (Dadda et al., 2018).

MICP is considered one of the most effective soil stabilisation technologies (Ghosh et al., 2019; Ivanov et al., 2020), thus, has the potential to address a wide range of geoenvironmental and geotechnical issues (Miftah et al., 2020), including erosion control in coastal areas, enhancing the stability of non-piled and piled foundations, pavement surface treatment, reducing dust levels on exposed loose soil surfaces by binding the dust particles together, and reinforcing soil to improve underground constructions (Wath & Pusadkar, 2016). Furthermore, the technique can also be applied to various soil types ranging from coarse and well-graded sands to finer soils, but it is more effective for coarse and well-graded sands (Mortensen et al., 2011). Although previous literature presented encouraging and impressive results on the stabilisation of sub-standard soils via exogenous ureolytic bacterial strains procured commercially from microbial culturing centres (Jain & Arnapalli, 2019; Hoang et al., 2019), the introduction of such strains to the soil environment may adversely disturb the natural eco-system balance (indigenous bacterial strains present).

Furthermore, bacterial cultivation, special precautions required during mixing, the survivability of the exogenous bacteria and the long time required for the permeation of the bacteria render this process costly, thus challenging for large-scale implementation (Tiwari et al., 2021). However, very limited studies focus on the potential of indigenous ureolytic bacterial strains distributed within the soil (Bibi et al., 2018). Hence, this study focuses on the potential of indigenous soil urease-producing bacterial strains to reduce costs.

This study focused on the potential MICP treatment of organic and sandy clay soils by indigenous ureolytic bacteria. It is also the first study involving the application of MICP using indigenous *B. paramycoides* for sub-standard soil stabilisation. The maximum urease activity of *B. cereus* and *B. paramycoides* were measured, and the bio-precipitated CaCO_3 crystals were evaluated to prove the biocementing effect of both bacterial species as potential MICP agents to stabilise sandy clay and organic soils. The study outcomes are expected to serve as a reference for an improved, simple natural bio-mediated soil stabilisation method via the precipitation of calcium carbonate by ureolytic bacteria.

MATERIALS AND METHODS

Bacterial Culture

Two bacterial species, *Bacillus cereus* (https://www.ncbi.nlm.nih.gov/nuccore/NR_115714.1) and *Bacillus paramycooides* (https://www.ncbi.nlm.nih.gov/nuccore/NR_157734.1) were isolated from sub-standard soil on a farm at Universiti Putra Malaysia in Selangor, Malaysia. The bacterial species stocks were maintained in sterilised microcentrifuge tubes at -82°C in 30% sterile glycerol, and the bacterial cells were activated by cultivation on calcium carbonate precipitation agar containing 10 g/L NH_4Cl , 3 g/L nutrient agar, 20 g/L agar, 20 g/L urea and 2.12 g/L NaHCO_3 for 24 hr at $28 \pm 0.5^{\circ}\text{C}$ before use (Wei et al., 2015; Bibi et al., 2018).

Urease Activity

The urease activity was quantified by the phenol hypochlorite assay as previously described by Chahal et al. (2011). The mixture was measured at an optical density of 626 nm, and ammonium chloride (50 to 100 μM) was used as a standard, with one unit of urease defined as the amount of enzyme hydrolysing 1 μmol urea/minute.

Quantification of Precipitated Crystals

The method adapted from Wei et al. (2015) was used to quantify the precipitated carbonate crystals produced by *B. cereus* and *B. paramycooides*. The bacterial isolates were grown in 100 mL of calcium carbonate precipitation (CCP) broth and incubated for 96 hr at $28 \pm 0.5^{\circ}\text{C}$, with an uninoculated CCP medium used as a control. After incubation, the bacterial cultures were centrifuged at 4,000 g for 4 min. The pellet containing precipitated CaCO_3 and the ureolytic bacteria cells were resuspended in 50 mL TE buffer (pH 8.5, 10 mM Tris, 1 mM EDTA) before 1 mg/mL lysozyme was added and incubated for 60 min at $37 \pm 0.5^{\circ}\text{C}$ to break down the ureolytic bacteria cell walls. The suspension was centrifuged to remove cell debris, and the pellet was washed with distilled water (pH 8.5), then air dried for 48 hr at $40 \pm 0.5^{\circ}\text{C}$ and weighed to quantify the precipitated carbonate crystals. The quick acid test, according to the method by Richardson et al. (2014), was then performed to confirm the formation of carbonate crystals. The precipitated carbonate crystals were placed in dried sterile test tubes before the dropwise addition of 10% (v/v) of hydrogen chloride. The rapid effervescence with bubble formation confirmed carbonate crystals.

Characterisation of the Precipitated Crystals

The CaCO_3 crystals were characterised by a scanning electron microscope (SEM) and X-ray diffraction (XRD) (Dhami et al., 2016; Liu et al., 2017). The samples were crushed to evenly distribute the particles before mounting them on the stub. The sample was then

gold sputtered (BAL - TEC SCD 005, Williston, USA) for 3 min to increase conductivity, and the stub was mounted onto the JSM-IT100 InTouch Scope™ (Tokyo, Japan). The XRD spectra of the crushed dried samples were obtained using Shimadzu 6000 Diffractometer (Kyoto, Japan) to identify the crystalline phase composition and crystalline nature (calcite, vaterite, aragonite or amorphous calcium carbonate crystals). The samples were scanned at 2.00 (deg/min) from 20.00 – 70.00 2 θ with the Cu anode at 30 kV and 30 mA.

Analysis of the Role of Ureolytic Bacteria in MICP

The texture of the treated soil samples was determined as described by Towner (1974) and Ritchey et al. (2015), while the potential deposition of carbonate crystals by *B. cereus* and *B. paramycoides* to stabilise sandy clay soil and organic soil was studied based on the previously described method by Bibi et al. (2018). Approximately 50 mL cultures of urea medium containing 0.6 g of soil, 20 g/L of urea and 3.7 g/L of CaCl₂.2H₂O was used to inoculate ureolytic bacterial isolates with an initial concentration of 0.1 at an optical density of 600 nm. The culture was incubated at 28 ± 0.5°C at 120 rpm for 30 days on a controlled temperature incubator shaker (Infors Ecotron, Bottmingen, Switzerland). Ten experimental setups in triplicates were prepared, as shown in Table 1. *B. cereus* and *B. paramycoides* were cultured in tests A, B and C, D, respectively. On the 30th day, treated samples were washed three times with distilled water, and the pellets were oven dried at 40 ± 0.5°C for 48 hr. Dried-treated soil samples were analysed using SEM and XRD to confirm CaCO₃ (Dhami et al., 2016; Liu et al., 2017).

Table 1

The experimental setup for analysis of ureolytic bacteria's role in calcite precipitation

Test	Medium	Soil type	Isolate
A	Urea + CaCl ₂ .2H ₂ O	Sandy clay soil	<i>Bacillus cereus</i>
B	Urea + CaCl ₂ .2H ₂ O	Organic soil	<i>Bacillus cereus</i>
C	Urea + CaCl ₂ .2H ₂ O	Sandy clay soil	<i>Bacillus paramycoides</i>
D	Urea + CaCl ₂ .2H ₂ O	Organic soil	<i>Bacillus paramycoides</i>
E	Urea + CaCl ₂ .2H ₂ O	Organic soil	-
F	Urea + CaCl ₂ .2H ₂ O	-	-
G	Urea	Sandy clay soil	-
H	Urea	Organic soil	-
I	Distilled water	Sandy clay soil	-
J	Distilled water	Organic soil	-
K	Distilled water	-	-

RESULTS AND DISCUSSION

Bacterial Culture and Measurement of Urease Activity

There are diverse bacterial species inhabiting the soil, among which ureolytic bacteria are particularly abundant (Hasan, 2000; Oshiki et al., 2018). In the present study, *B. cereus* and *B. paramycooides* were isolated from farm soils, as such soils are rich in urea due to the frequent use of organic manure and synthetic urea fertilisers, which improve microbial activity through stimulating *in situ* urease-producing bacteria within the soil pores (Zhu & Dittrich, 2016). Farm soils contain urea for urease-producing bacteria to utilise as sole nitrogen and energy sources, thus, enhancing the rapid distribution, diversity and adaptability of these microbes within the soil environment (San Pablo et al., 2020; Svane et al., 2020).

As shown in Figure 1, there was a steady increase in *B. cereus* and *B. paramycooides* urease activity with incubation time reaching a maximum urease activity of 665 U/mL and 620 U/mL, respectively, indicating their suitability as potential agents for MICP soil stabilisation. By comparison, the study by Chahal et al. (2011) reported unidentified soil ureolytic bacterial isolates with maximum urease activity of 598 U/mL, 593 U/mL and 589 U/mL, respectively. Similarly, Li et al. (2015) reported that *B. megaterium* recorded maximum urease activity of 592 U/mL after 120 hr incubation. According to the study, *B. megaterium* increases the unconfined compressive strength of the urease-based treated sand sample to 1002 KPa with a decrease in permeability to $2.0 \times 10^{-7} \text{ ms}^{-1}$ due to the high urease activity recorded. The steady decrease in urease activity observed in this study after 96 hr and 120 hr is probably due to cell death, metabolism inhibition, exhaustion of nutrients, and enzyme degradation with time, leading to an irreversible loss of urease activity (Jiang et al., 2016). Sub-standard soil stabilisation via MICP is initiated by the microbial enzyme urease, which catalyses urea decomposition (Bzura & Koncki, 2019), consequently increasing the pH and production of inorganic mineral carbonate crystals, such as calcite (Omorieg et al., 2019; Jiang et al., 2020).

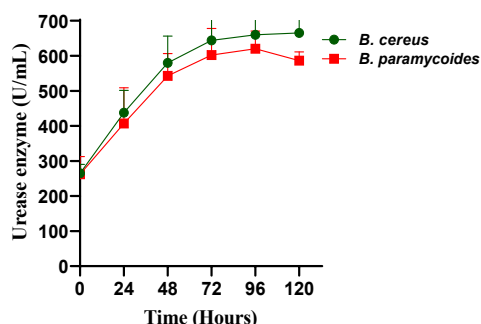


Figure 1. Urease activity (optical density 626 nm) of *B. cereus* and *B. paramycooides*. Error bars represent the standard deviation of the mean

Quantification of Precipitated Crystals

Individual ureolytic bacterial strains have different urease production rates, influencing the amount of CaCO_3 precipitated (Qabany et al., 2011). Thus, it becomes paramount to determine the amount of CaCO_3 produced by the ureolytic bacteria to evaluate its calcifying potential. Therefore, the CaCO_3

precipitated at 96 hr incubation time by *B. cereus* and *B. paramycooides* was quantified and studied in relation to cell growth (Figure 2) and pH (Figure 3). As observed from Figure 2, the amount of CaCO₃ precipitated by *B. cereus* and *B. paramycooides* were 655 mg/L and 546 mg/L at a bacterial growth of 0.83 and 0.76 at the optical density of 425 nm within 48 hr, respectively, while at 96 hr, the precipitated CaCO₃ increased to 943 mg/L and 793 mg/L with a corresponding increase in bacterial growth to 1.01 and 1.09 respectively.

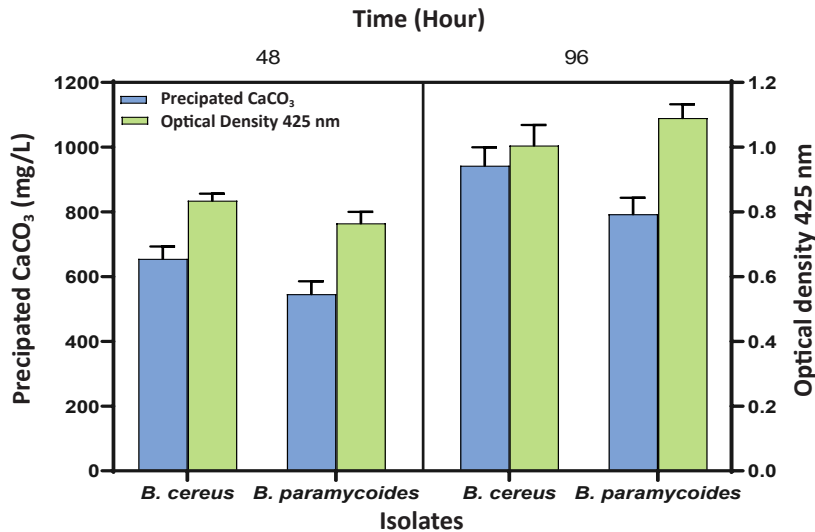


Figure 2. Comparison of the bacterial growth and potential of calcium carbonate precipitation among *B. cereus* and *B. paramycooides*. Error bars represent the standard deviation of the mean.

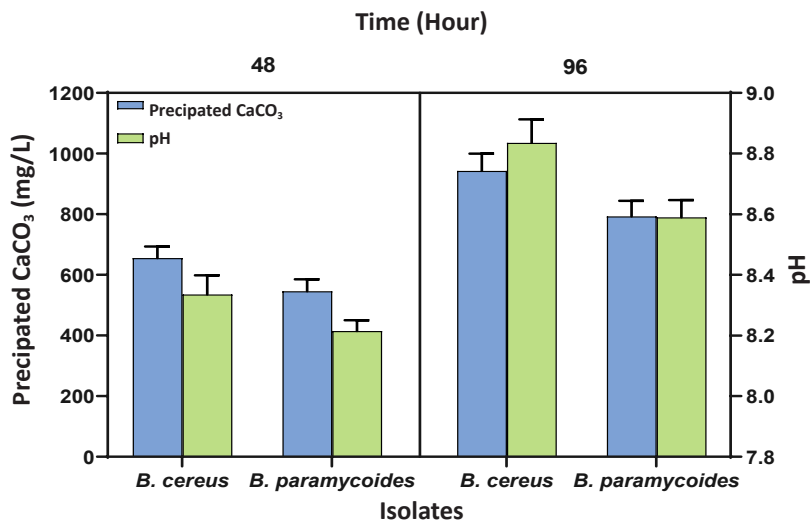


Figure 3. Comparison of the pH and potential of calcium carbonate precipitation among *B. cereus* and *B. paramycooides*. Error bars represent the standard deviation of the mean.

Although both isolates recorded an increase in precipitation with time, *B. cereus* precipitated more CaCO_3 than *B. paramycooides*. Further, most of the precipitated CaCO_3 by both isolates was produced within the first 48 hr, in contrast to the study of Kim et al. (2018), which reported that most calcite precipitation by *Staphylococcus saprophyticus* and *Sporosarcina pasteurii* occurred within 72 hr. This study adopted a 96 hr incubation based on the maximum precipitation period achieved by both bacteria. Wei et al. (2015) reported that *B. lentus*, *B. diminuta* and *S. soli* precipitated 931 mg/L, 842 mg/L and 456 mg/L of CaCO_3 . Noteworthy, findings from previous reports and the current study reveal that individual ureolytic bacterial species precipitated different amounts of CaCO_3 despite being incubated under similar growth and cultural conditions (Wei et al., 2015; Kim & Youn, 2016; Kim et al., 2018). This variation in the quantity of CaCO_3 crystals precipitated across individual ureolytic bacterial species might be due to individual differences in bacterial urease activity, favouring CO_3^{2-} concentrations generated during urea breakdown and resulting in differences in CaCO_3 precipitation. Thus, the higher precipitation achieved by *B. cereus* compared to *B. paramycooides* in this study was expected based on the highest urease activity recorded (Figure 1), which was in relatively good agreement with the amount of calcium carbonate precipitated (Figure 2).

The increased CaCO_3 precipitation by both isolates corresponds to an individual increase in bacterial growth with increasing incubation over 96 hr. Further, *B. paramycooides* grew faster after 48 hr recording higher bacterial growth of 1.09 after 96 hr but precipitated less CaCO_3 than *B. cereus*. It implies that higher bacterial cell growth may not correspond to higher urease activity which does not necessarily translate to a higher CaCO_3 yield (Bibi et al., 2018) because urease activity is the main factor favouring a higher CaCO_3 yield during MICP (Mwandira et al., 2019; Tang et al., 2020).

Optimum proteolysis occurs at a pH favouring bacterial growth and metabolism, and the pH of the bacterial medium plays a significant role in inducing microbial morphological changes, affecting its stability and instigating enzyme secretion (Omoregie et al., 2017). Urea hydrolysis occurs due to the secretion of urease by the bacteria, which generates carbonate ions precipitated as CaCO_3 crystals (Wu et al., 2017). As shown in Figure 3, *B. cereus* and *B. paramycooides* increased the medium pH to 8.33 and 8.21, respectively, after 48 h, indicating that both isolates require an alkaline pH for maximum CaCO_3 precipitation. The medium alkaline pH enhances the physiological conditions favourable for the ureolytic bacterial cell wall acting as the nucleation site for mass CaCO_3 precipitation (Imran et al., 2019). After 96 hr, the CaCO_3 precipitation reached a plateau pH of 8.83 and 8.59, respectively, implying that CaCO_3 precipitation corresponds with an increase in pH over the incubation period, and this has been well documented in several studies (Park et al., 2010; Keykha et al., 2017). The steady increase in pH may enhance the transportation of growth factors and other essential nutrients across the bacterial cell membrane, probably

by facilitating active transport or diffusion (Wiley & Stokes, 1963; Morsdorf & Kaltwasser, 1989), favouring mass CaCO_3 precipitation which enhances the MICP treatment of sub-standard soils (Wu et al., 2017).

By comparison, Kim et al. (2018) reported maximum CaCO_3 precipitation by *Staphylococcus saprophyticus* and *S. pasteurii* at pH 7.0, and Wei et al. (2015) reported a pH of 9.6 for *B. lentus*. It implies that individual ureolytic bacteria have their unique peak pH favouring maximum calcite precipitation, which varies from neutral to an alkaline pH.

Characterisation of the Precipitated Crystals

Precipitated CaCO_3 by both *B. cereus* and *B. paramycoides* was confirmed by a quick acid test (Figure 4) (Richardson et al., 2014). CaCO_3 precipitated by *B. cereus* was visualised under a light microscope showing that some rhombohedral crystals formed aggregates, as shown in Figure 4a, while no precipitates were formed in the uninoculated medium. These precipitates were formed by supersaturation within the medium, with the bacterial cell wall acting as nucleation sites (Wang et al., 2017). The morphology of the CaCO_3 crystals observed in this study was relatively similar to the rhombohedral CaCO_3 crystals previously observed in aggregates, as reported by the study of Al-Thawadi and Cord-Ruwisch (2012). Noteworthy, in the present study, only calcite crystals were visualised under the light microscope, justifying further adaptation of the SEM-XRD technique for a more detailed microstructural analysis which confirmed the presence of aragonite crystals.

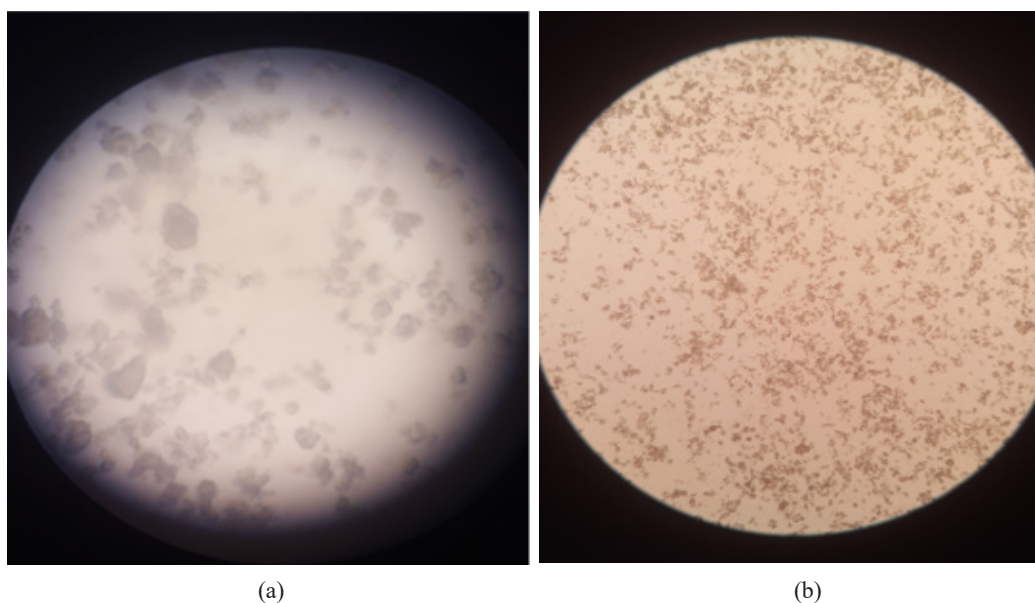


Figure 4. Microscopic images of precipitated calcium carbonates viewed under Light microscope (a) *Bacillus cereus* (b) *Bacillus paramycoides*.

The XRD spectra of *B. cereus* precipitated CaCO_3 (Figure 5a) showed distinct peaks at 23.2° , 29.6° , 36.1° , 39.6° , 48.6° , 57.5° , 60.8° and 64.8° attributed to the typical calcite structure abundantly precipitated with aragonite identified at 2theta diffraction angle of 43.3° . Further, *B. paramycoides* CaCO_3 XRD spectra (Figure 5b) showed characteristic diffraction peaks at an angle of 29.6° , 36.2° , 39.6° , 48.7° and 57.6° , 60.8° , revealing that the most precipitated bio-product was calcite. In comparison, only a 2theta diffraction angle of 43.3° was identified as aragonite. Therefore, calcite crystals were the most abundant precipitated CaCO_3 polymorph by both *B. cereus* and *B. paramycoides*.

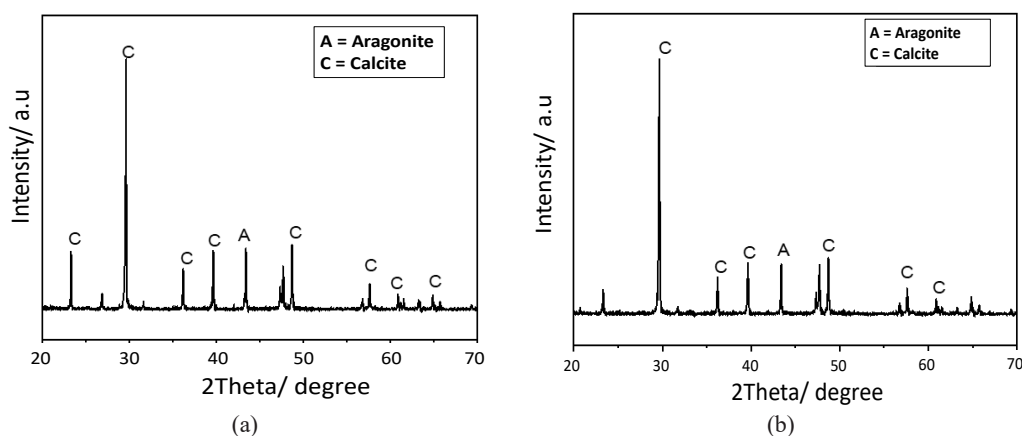


Figure 5. XRD spectra of precipitated calcium carbonate crystals by (a) *B. cereus* and (b) *B. paramycoides*

The *B. cereus* precipitated calcite minerals of different morphology comprised clustered rhombohedral crystals, cubic crystals of roughly similar sizes and a few irregular calcite crystals (Figure 6 a-c). Other crystals were also observed, like flower-shaped calcite up to $8.0\ \mu\text{m}$ in diameter (Figure 6c). The findings from this study were consistent with previous observations by Wei et al. (2015), Oral and Ercan (2018) and Wen et al. (2020). The irregular calcite crystals were amorphous with several tiny holes on the surface ($2.7\text{--}3.4\ \mu\text{m}$). By contrast, Luo and Qian (2016) observed larger irregular calcite crystals of $50\ \mu\text{m}$ diameter. Furthermore, the cubic crystals have smooth surfaces ranging from 2.0 to $2.7\ \mu\text{m}$. On the contrary, Zhang et al. (2019) reported larger irregular cubic crystals ($53.4\ \mu\text{m}$). Irregular cubic and spherical crystals favour better soil biocementation (Tang et al., 2020).

In contrast, the precipitated mineral induced by *B. paramycoides* was composed mainly of irregular calcite particles of different sizes (Figure 6f) and agglomerated rhomboids (Figure 6 d-e). The agglomerated rhombohedral calcite crystals were similar to those produced by *B. cereus* and similar to previous observations (Kakelar et al., 2016). Furthermore, the irregular calcite crystals ($4.6\text{--}23.0\ \mu\text{m}$) induced by *B. paramycoides* had

a rough surface and were larger than the irregular calcite crystals (2.7–3.4 μm) precipitated by *B. cereus*.

The differences in CaCO_3 morphology are observed in numerous MICP processes and are usually influenced by several factors, such as differences in bacterial urease activity, which might be strain-specific (Kim & Lee, 2019), concentration and composition of the cementation solution, extracellular polymeric substances available on bacterial cell surfaces, rate of carbonation, CO_2 concentration, temperature and pH (Cizer et al., 2008; Tang et al., 2020). Various CaCO_3 crystal morphologies have been observed, including rhombic hexahedrons (Duo et al., 2018), ellipsoidal, spherical, rhombohedral (Dhami et al., 2013), flower-like, agglomerated rhomboids (Kakelar et al., 2016), lamellar rhombohedral (Zhang et al., 2019), irregular carbonate particles (Oral & Ercan, 2018), orthorhombic (Warren et al., 2001), hexagonal (Choi et al., 2017), framboidal aggregates (Mwandira et al., 2017), sponge-like (Srivastava et al., 2014) and capsule shape (Nawarathna et al., 2019).

Based on the SEM micrographs, no bacterial cells were visualised on crystals due to the lysozyme enzyme added to the medium after incubation, which breakdown all bacterial cell walls for clear differentiation of the crystals. By contrast, other authors observed bacterial cells embedded on similarly precipitated CaCO_3 crystals of different morphologies, as reported in this study. It demonstrated the direct involvement of the bacterial cell walls as nucleation sites for crystal formation (Bang et al., 2001; Duo et al., 2018). Interestingly, calcite formation from the recrystallisation of spherical vaterite crystals (2.9–5.3 μm) was partially observed in precipitated CaCO_3 by both *B. cereus* and *B. paramycooides* (Figure 6). It suggests that the calcite crystals were formed by the transformational disintegration and dissolution of earlier spherical vaterite crystals. Biocementation may commence with the initial formation of vaterite spherical crystals, which are meta-stable (Al-Thawadi & Cord-Ruwisch, 2012) but may gradually dissolve to recrystallise and form a more stable rhombohedral permanent calcite structure under a longer incubation period (Warren et al., 2001; Cheng et al., 2014).

However, the mechanism of rhombohedral crystal formation from spherical crystals remains unclear. Oral and Ercan (2018) observed the polymorphic transformation of vaterite to calcite with increased pH, indicating that this phenomenon might be related to supersaturation changes upon pH alteration. Kakelar et al. (2016) suggested that (1) vaterite crystals formation is kinetically favoured at higher urease activity, but when the urea is exhausted, there is a continuous decrease in urease activity, favouring calcite crystals formation and (2) the longer nucleation phase quickly decreases saturation which accelerates recrystallisation and dissolution, thus, favouring calcite abundance over vaterite. It may explain why no vaterite crystals were observed in the current study. Of note, factors influencing the polymorphic form of ureolytic bacterial CaCO_3 precipitation include the temperature of the solution, pH, precipitation time, degree of saturation, presence of

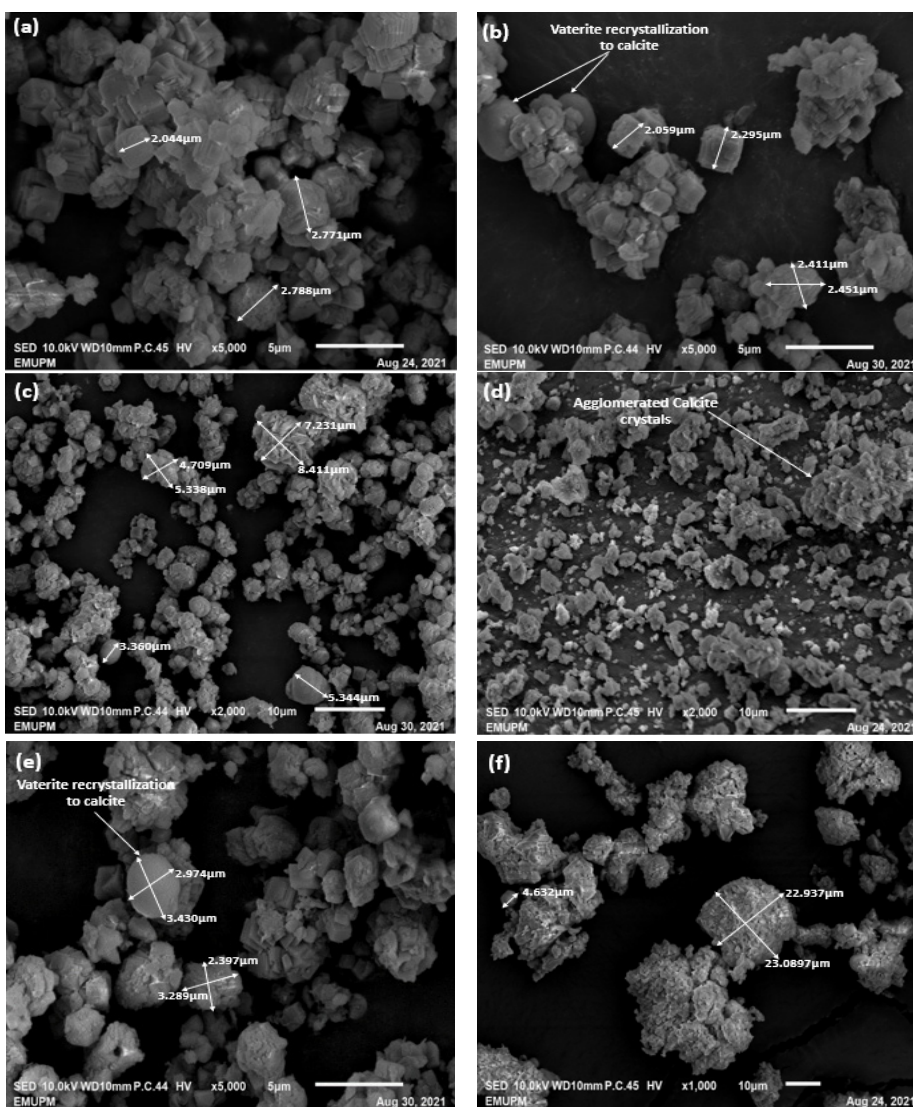


Figure 6. SEM micrographs showing different morphologies of precipitated calcium carbonate crystals by (a, b, c) *Bacillus cereus* and (d, e, f) *Bacillus paramycooides*

additives, the solvent used to dissolve precursors and stirring velocity (Oral & Ercan, 2018). In summary, the characterisation of CaCO_3 crystals induced by different ureolytic bacterial species favours the selection of the optimal species, thus, maximising the MICP efficiency. Further, photographs from SEM microanalysis have shown CaCO_3 crystals of different morphologies, confirmed by XRD to be mostly calcite precipitated by both *B. cereus* and *B. paramycooides*.

Analysis of the Role of Ureolytic Bacteria in MICP

Applying MICP to sub-standard soil will eventually result in the binding of the soil grains and the filling of inter-particle voids to stabilise the soil (Muthukkumaran & Shashank, 2016). In the current study, two soil types, sandy clay soil and organic soil, were treated with *B. cereus* and *B. paramycoides*. Figure 7 depicts treated organic and sandy clay soil by *B. cereus* formed flat, irregularly shaped solids of 24 mm and 22 mm in diameter, respectively; hence, indicating that *B. cereus* precipitated more CaCO_3 compared to *B. paramycoides*. Thus, consistent with previous results (Figure 2). It has been shown that larger CaCO_3 crystals favour coarse-grained soil cementation, while smaller CaCO_3 crystals are more conducive to fine-grained soil biocementation of the treated soils (Tang et al., 2020).

By comparison, based on this study, *B. cereus* precipitated much smaller CaCO_3 crystals of 2.0–8.0 μm in diameter (Figure 6 a-c) than *B. paramycoides* which precipitated larger CaCO_3 crystals of 4.6–23.0 μm in diameter (Figure 6 e-f). Notably, the texture of organic and sandy clay soil treated in this study is silky and fine, therefore more favourable to biocementation with smaller CaCO_3 crystals. It is because fine-grained sands have smaller intergranular distances and more intergranular contacts. Hence, most of the smaller CaCO_3 coats the contact points, which could eventually enhance the overall cementation efficiency (Tang et al., 2020). It also might have further favoured *B. cereus*'s visible bio-cementation effect (Figure 7) over *B. paramycoides* because *B. cereus* precipitated much smaller CaCO_3 crystals. A detailed future study on factors influencing soil biocementation should be conducted to clarify the discrepancy in calcite crystal biocementation potential.

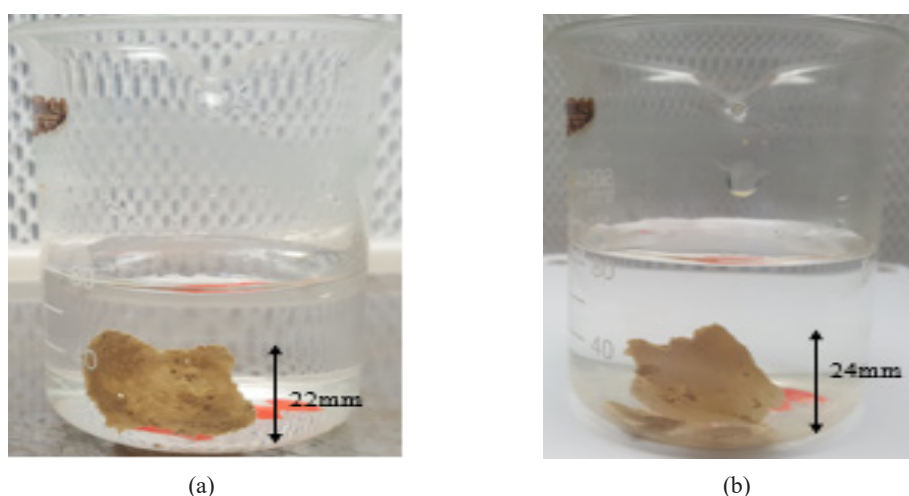


Figure 7. Biocementation of soil samples treated by *Bacillus cereus* (a) sandy clay soil and (b) organic soil

The SEM-XRD microstructural analysis confirmed the deposition of bio-precipitated CaCO_3 on the treated soil grains by both bacterial species. The microstructural analysis of untreated soil samples (Figure 8 a and b) showed that the particle surfaces were smooth and distributed with large pores. By comparison, the inter-particle voids of all treated soil samples in Figure 8 (c, d, e, f) were densely filled and cemented by precipitated CaCO_3 . SEM images of the treated soil samples in Figure 8f with only urea-calcium chloride medium showed particles surrounded with CaCO_3 even though the soil was not treated with any ureolytic bacteria under study.

XRD results of untreated soil showed characteristic diffraction peaks at 24.9° , 26.86° , 50.34° , 60.12° and 62.62° identified as defernite crystalline minerals which may be found in soil (Figure 9a) (Taner & Martin, 2013). The current study confirmed no CaCO_3 crystals in the untreated soil sample. Furthermore, the XRD results of treated soil samples with only urea-calcium chloride medium showed (Figure 9b) 2theta diffraction angles of 24.9° , 26.7° , 50.2° and 55.0° , which were attributed to defernite mineral. In comparison, distinct peaks at 20.9° and 62.3° were identified as vaterite and calcite, respectively. The abundant defernite minerals observed are part of the natural soil composition, as similarly observed in the untreated soil sample (Figure 9a), while the few calcite and vaterite crystals found may have been precipitated by the soil indigenous ureolytic bacteria since no CaCO_3 was introduced into the medium throughout the incubation period.

It is contrary to the study by Bibi et al. (2018), who reported no crystals or amorphous calcium carbonate precipitated after 30 days of incubation with only urea-calcium chloride medium on sampled soil from the Qatar desert. However, the present findings were expected as the sampled soils were urea-rich due to the frequent application of synthetic urea and organic manure during crop cultivation. Hence, such soils favour biodiversity and abundant distribution of *in situ* ureolytic bacteria (Zhu & Dittrich, 2016).

The microstructural analysis of sandy clay soil treated with *B. cereus* and *B. paramycooides* (Figure 8 c-f) showed pore spaces of soil grains surrounded by CaCO_3 . The morphology of individual CaCO_3 crystals was not visible due to the dense formation of CaCO_3 clusters. However, the distribution of CaCO_3 bonds was qualitatively visualised, covering soil grains and forming bridges between grains. It is similar to the findings utilising pure cultures such as *B. licheniformis* (Helmi et al., 2016), *S. pasteurii* (Liu et al., 2021), *B. subtilis*, *S. pasteurii* and *B. sphaericus* (Sharma et al., 2021). The XRD spectra of *B. cereus* treated sandy clay soil (Figure 9c) showed distinct peaks at 29.6° , 36.1° , 39.6° , 48.7° , 57.6° and 61.0° attributed to calcite abundantly precipitated with some aragonite identified at 2theta diffraction angle of 43.4° in addition to peaks at 23.2° , 26.8° and 47.7° attributed to defernite crystals believed present in the soil. Furthermore, *B. paramycooides* treated sandy clay soil (Figure 9d) showed characteristic diffraction peaks at an angle of 29.4° , 36.0° , 39.4° , 43.1° , 48.4° and 57.4° revealing that the most precipitated bio-product

was calcite. In comparison, the only 2theta diffraction angle of 47.5° was identified as scawtite, a carbonised calcium silicate hydrate crystalline mineral believed to be in the soil (Grice, 2005).

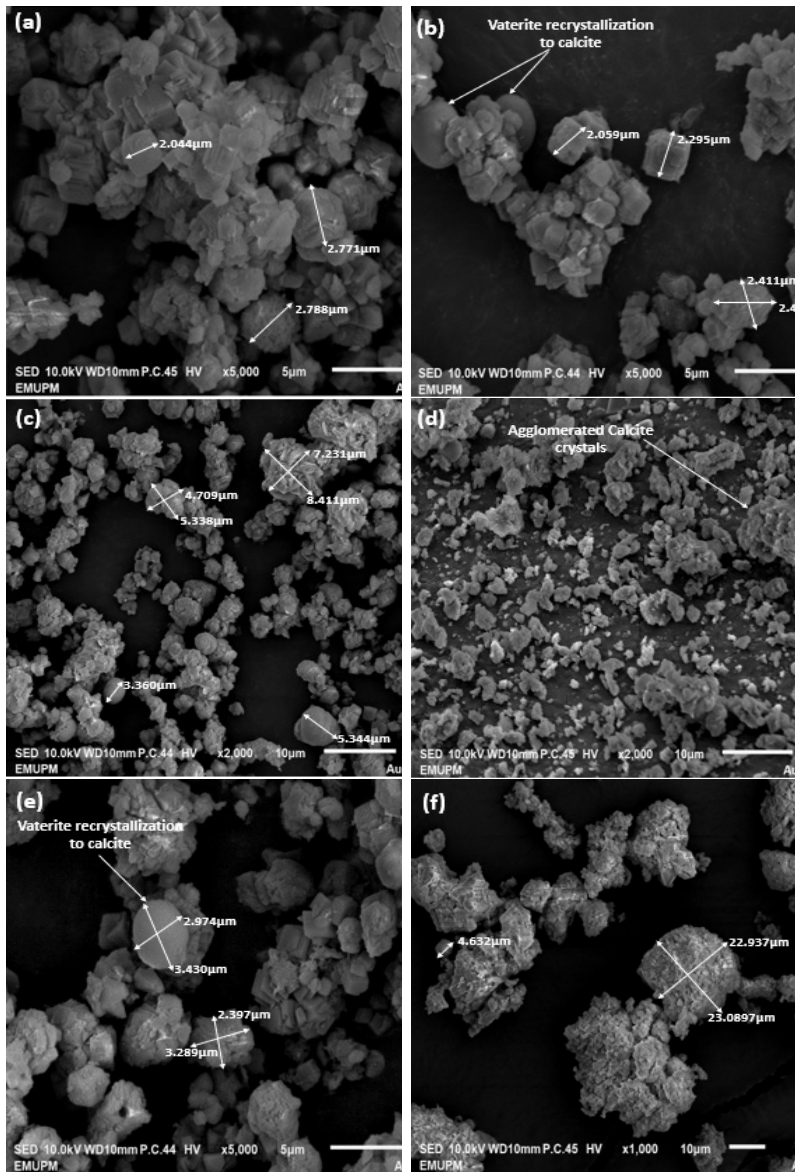
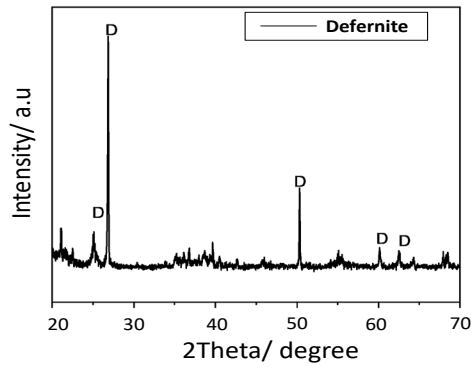
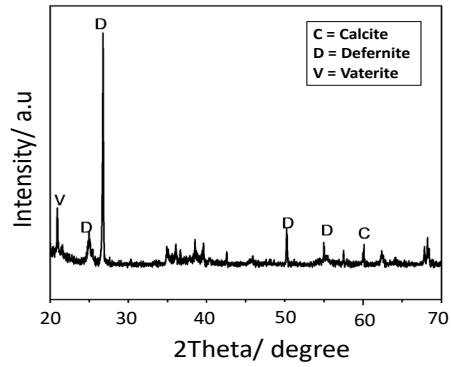


Figure 8. SEM micrographs of untreated/treated soil samples after 30 days of incubation at $28^\circ\text{C} \pm 0.5^\circ\text{C}$. (a) Untreated sandy clay soil sample, (b) Treated sandy clay soil by *Bacillus cereus*, (c) Treated sandy clay soil by *Bacillus paramycooides*, (d) Treated organic soil by *Bacillus cereus*, (e) Treated organic soil by *Bacillus paramycooides*, and (f) Treated soil sample with urea–calcium chloride medium only.

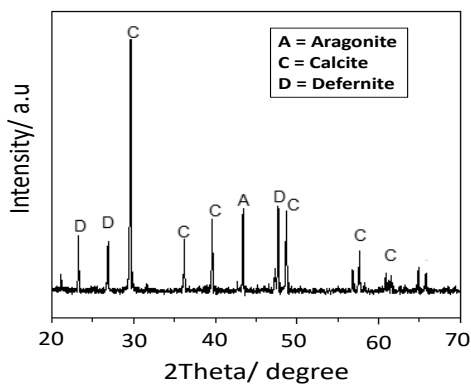
Figure 8 (b, c, d & e) shows the SEM images of biocemented organic soil treated with *B. cereus* and *B. paramycooides*, respectively, with bio-precipitated CaCO₃ on the surfaces and contact points of soil particles. The CaCO₃ crystals were integrated tightly around the entire soil grain structure, with a decreased distance between the grains. Duo et al. (2018) found that the CaCO₃ crystals between soil particles improved the strength, enhanced the bearing capacity and reduced the permeability of the soil structure. The XRD spectra (Figure 9e) confirmed calcite to be the most abundant precipitated CaCO₃ polymorph by *B. cereus* with distinct peaks at 29.6°, 36.1°, 39.6°, 48.6°, 57.6° and 61.0°, with aragonite identified at peak 43.3°, in addition to peaks at 23.2°, 26.7° and 47.6° attributed to defernite. *B. paramycooides* precipitated calcite most at 2theta diffraction angles of 29.8°, 39.8° and 43.5°, while vaterite and aragonite were identified at 27.0°, 61.4° and 36.3°, 48.9° respectively in addition to scawtite at a diffraction angle of 23.5°, 47.8° and 57.8° (Figure 9f).



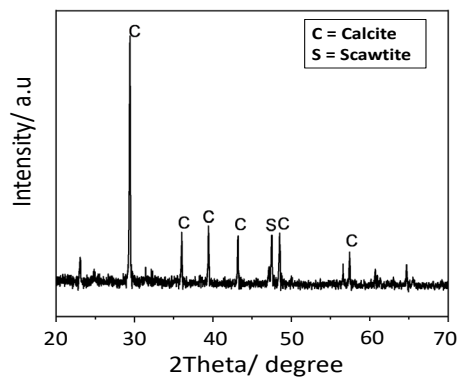
(a)



(b)



(c)



(d)

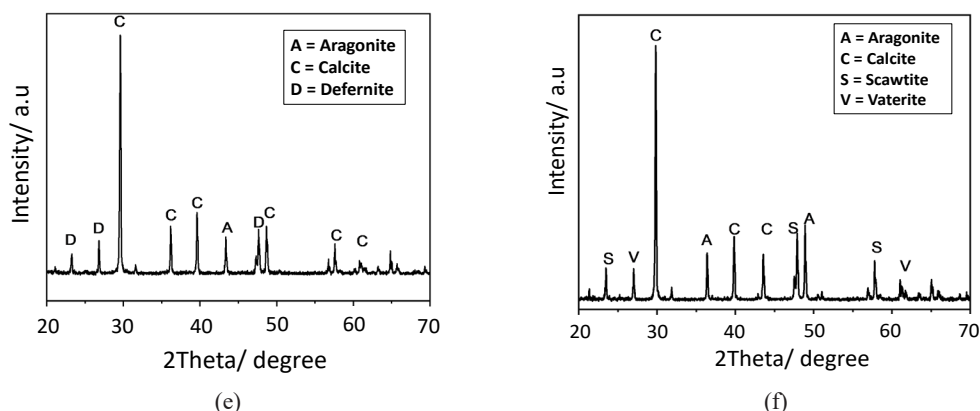


Figure 9. XRD spectra of (a) Untreated soil sample, (b) Treated soil sample with Urea + $\text{CaCl}_2 \cdot 2\text{H}_2\text{O}$, (c) Treated sandy clay soil sample by *B. cereus*, (d) Treated sandy clay soil sample by *B. paramycoides*, (e) Treated organic soil sample by *B. cereus*, (f) Treated organic soil sample by *B. paramycoides*

In the present study, all three polymorphic forms of crystalline CaCO_3 (calcite, vaterite and aragonite) were precipitated, with calcite being the most abundant CaCO_3 polymorph deposited onto the soil grains by both *B. cereus* and *B. paramycoides*, followed by vaterite and aragonite. Of note, vaterite is not naturally abundant but is an important precursor in calcite formation (Mwandira et al., 2017). Meanwhile, *B. cereus* precipitated more calcite than *B. paramycoides* in all treatments in this study. Consistent with our findings, most studies conducted through ureolysis-driven MICP confirmed calcite and vaterite crystalline polymorphic forms as the most precipitated (Al-Thawadi & Cord-Ruwisch, 2012; Algaifi et al., 2020). Calcite is the most preferable in MICP as it is the most thermodynamically stable polymorph (Chang et al., 2017). The solubility of CaCO_3 polymorphs increases in the order of calcite, aragonite, vaterite and amorphous calcium carbonate (Chang et al., 2017). Therefore, the lower solubility of aragonite and vaterite makes it difficult to obtain these polymorphs (Oral & Ercan, 2018). The characteristics mentioned above-favoured calcite over other CaCO_3 polymorphs in MICP for an effective soil stabilisation method. Although little is known with regard to what causes the bacterial precipitation of a particular polymorphic form of CaCO_3 , previous investigations have shown that the selective precipitation of a specific polymorphic form is influenced by complex processes governed by several biotic and abiotic factors ranging from pH, urease enzyme specific amino acid sequence, medium composition to bacterial extracellular polymeric substances (Wei et al., 2015).

The calcite crystals observed in this study as the most precipitated polymorphic form of CaCO_3 in all treatments with *B. cereus* and *B. paramycoides* agreed with numerous studies (Bang et al., 2010; Achal et al., 2013). However, studies by Akyol et al. (2017) reported vaterite as the most precipitated form of CaCO_3 , while Zhang et al. (2019) reported

aragonite as the most precipitated. Other polymorphic forms of bio-precipitated calcium carbonate include amorphous calcium carbonate and two hydrated crystalline phases: hexahydrocalcite ($\text{CaCO}_3 \cdot 6\text{H}_2\text{O}$) and monohydrocalcite ($\text{CaCO}_3 \cdot \text{H}_2\text{O}$) (Anitha et al., 2018). Therefore, future comprehensive investigation of the parameters determining the formation of the polymorphic forms of CaCO_3 should be conducted.

In all cases, CaCO_3 mineral formation was bacteria associated, as none of the cultures had introduced CaCO_3 sources, and no mineral formation was detected in a medium without bacteria. Hence, the dynamic process of MICP leading to CaCO_3 precipitation is not chemically induced but microbially induced and directly linked with urea hydrolysis by bacterial urease activity (Alonso et al., 2018; Badiee et al., 2019; Osinubi et al., 2019).

CONCLUSION

B. cereus and *B. paramycooides* demonstrated high urease activity and precipitated large amounts of CaCO_3 , including the three polymorphic forms of calcite, vaterite and aragonite. Since it is the most thermodynamically stable polymorph, calcite crystals were the most precipitated and preferable in MICP. Applying *B. cereus* and *B. paramycooides* to treat both organic and sandy clay soils results in the dense formation of CaCO_3 biocementing soil grains and filling inter-particle voids. Of note, *B. cereus* recorded the highest urease activity and precipitated more calcite with a better biocementing effect than *B. paramycooides*. Therefore, *B. cereus* is the preferred MICP bacterial candidate with the highest potential to be utilised as an agent for soil bio-stabilisation. This study established the presence of active indigenous urease CaCO_3 precipitating bacteria within the soil and their promising potential application as potential MICP agents for soil stabilisation.

ACKNOWLEDGEMENT

This work was financially supported by Universiti Putra Malaysia through Geran Universiti Putra Malaysia (Grant No: GP-IPS/2020/9691000). The authors express their appreciation for the support of all the laboratory science officers of the Faculty of Science, Universiti Putra Malaysia, for providing all the necessary assistance.

REFERENCES

- Achal, V., Mukerjee, A., & Reddy, M. S. (2013). Biogenic treatment improves the durability and remediates the cracks of concrete structures. *Construction and Building Materials*, 48, 1-5. <https://doi.org/10.1016/j.conbuildmat.2013.06.061>
- Akyol, E., Bozkaya, O., & Dogan, N. M. (2017). Strengthening sandy soils by microbial methods. *Arab Journal of Geoscience*, 10, Article 327. <https://doi.org/10.1007/s12517-017-3123-9>
- Algaifi, H. A., Sam, A. R. M., Bakar, S. A., Abidin, R. Z., & Shahir, S. (2020). Screening of native ureolytic bacteria for self-healing in cementitious materials. In *IOP Conference Series: Material Science and Engineering* (Vol. 849, pp. 1-8). IOP Publishing. <https://doi.org/10.1088/1757-899X/849/1/012074>

- Alonso, M. J. C., Ortiz, C. E. L., Perez, S. O. G., Narayanasamy, R., Miguel, G. D. J. F. S., Hernández, H. H., & Balagurusamy, N. (2018). Improved strength and durability of concrete through metabolic activity of ureolytic bacteria. *Environmental Science and Pollution Research*, 25, 21451-21458. <https://doi.org/10.1007/s11356-017-9347-0>
- Al-Thawadi, S., & Cord-Ruwisch, R. (2012). Calcium carbonate crystals formation by ureolytic bacteria isolated from Australian soil and sludge. *Journal of Advanced Science and Engineering Research*, 2, 12-26.
- Anitha, V., Abinaya, K., Prakash, S., Rao, A. S., & Vanavil, B. (2018). *Bacillus cereus* KLUVAA mediated biocement production using hard water and urea. *Chemical and Biochemical Engineering Quarterly*, 32(2), 257-266. <https://doi.org/10.15255/CABEQ.2017.1096>
- Badiee, H., Sabermahani, M., Tabandeh, F., & Javadi, A. S. (2019). Application of an indigenous bacterium in comparison with *Sporosarcina pasteurii* for improvement of fine granular soil. *International Journal of Environmental Science and Technology*, 16(12), 8389-8400. <https://doi.org/10.1007/s13762-019-02292-9>
- Bang, S. S., Galinat, J. K., & Ramakrishnan, V. (2001). Calcite precipitation induced by polyurethane-immobilized *Bacillus pasteurii*. *Enzyme and Microbial Technology*, 28(4-5), 404-409. [https://doi.org/10.1016/S0141-0229\(00\)00348-3](https://doi.org/10.1016/S0141-0229(00)00348-3)
- Bang, S. S., Lippert, J. J., Yerra, U., & Mulukutla, S. (2010). Microbial calcite, a bio-based smart nanomaterial in concrete remediation. *International Journal of Smart and Nano Materials*, 1(1), 28-39. <https://doi.org/10.1080/19475411003593451>
- Bernardi, D., Dejong, J. T., Montoya, B. M., & Martinez, B. C. (2014). Bio-bricks: Biologically cemented sandstone bricks. *Construction and Building Materials*, 55, 462-469. <https://doi.org/10.1016/j.conbuildmat.2014.01.019>
- Bibi, S., Oualha, M., Ashfaq, M. Y., Suleiman, M. T., & Zouari, N. (2018). Isolation, differentiation and biodiversity of ureolytic bacteria of Qatari soil and their potential in microbially induced calcite precipitation (MICP) for soil stabilization. *RSC Advances*, 8(11), 5854-5863. <https://doi.org/10.1039/C7RA12758H>
- Bzura, J., & Koncki, R. (2019). A mechanized urease activity assay. *Enzyme and Microbial Technology*, 123, 1-7. <https://doi.org/10.1016/j.enzmictec.2019.01.001>
- Chahal, N., Rajor, A., & Siddique, R. (2011). Calcium carbonate precipitation by different bacterial strains. *African Journal of Biotechnology*, 10(42), 8359-8372. <https://doi.org/10.5897/ajb11.345>
- Chang, I., Im, J., & Cho, G. C. (2016). Introduction of microbial biopolymers in soil treatment for future environmentally-friendly and sustainable geotechnical engineering. *Sustainability*, 8(3), Article 251. <https://doi.org/10.3390/su8030251>
- Chang, R., Kim, S., Lee, S., Choi, S., Kim, M., & Park, Y. (2017). Calcium carbonate precipitation for CO₂ storage and utilization: A Review of the carbonate crystallization and polymorphism. *Frontiers in Energy Research*, 5, Article 17. <https://doi.org/10.3389/fenrg.2017.00017>
- Cheng, L., Shahin, M. A., & Cord-Ruwisch, R. (2014). Bio-cementation of sandy soil using microbially induced carbonate precipitation for marine environments. *Geotechnique*, 64(12), 1010-1013. <https://doi.org/10.1680/geot.14.T.025>
- Choi, S. G., Wang, K., Wen, Z., & Chu, J. (2017). Mortar crack repair using microbial induced calcite precipitation method. *Cement and Concrete Composites*, 83, 209-221. <https://doi.org/10.1016/j.cemconcomp.2017.07.013>

- Cizer, O., Van Balen, K., Elsen, J., & Van Gemert, D. (2008). Crystal morphology of precipitated calcite crystals from accelerated carbonation of lime binders. In *2nd International Conference on Accelerated Carbonation for Environmental and Materials Engineering (ACEME08)* (pp. 149-158). University of Rome.
- Dadda, A., Geindreau, C., Emeriault, F., du Roscoat, S. R., Filet, A. E., & Garandet, A. (2018). Characterization of contact properties in biocemented sand using 3D X-ray micro-tomography. *Acta Geotechnica*, *14*, 597-613. <https://doi.org/10.1007/s11440-018-0744-4>
- Dardau, A. A., Mustafa, M., & Abdaziz, N. A. (2021). Microbial-induced calcite precipitation: A milestone towards soil improvement. *Malaysian Applied Biology Journal*, *50*(1), 11-27. <https://doi.org/10.55230/mabjournal.v50i1.8>
- Dhami, K. N., Mukherjee, A., & Reddy, M. S. (2016). Micrographical, mineralogical and nano-mechanical characterisation of microbial carbonates from urease and carbonic anhydrase producing bacteria. *Ecological Engineering*, *94*, 443-454. <https://doi.org/10.1016/j.ecoleng.2016.06.013>
- Dhami, N. K., Reddy, M. S., & Mukherjee, M. S. (2013). Biomineralization of calcium carbonates and their engineered applications: A review. *Frontiers in Microbiology*, *4*, 314-327. <https://doi.org/10.3389/fmicb.2013.00314>
- Filet, A. E., Gutjahr, I., Garandet, A., Viglino, A., Béguin, R., Sibourg, O., Monier, J. M., Martins, J., Oxarango, L., Spadini, L., Geindreau, C., Emeriault F., & Perthuisot, S. C. (2020). BOREAL, Bio-reinforcement of embankments by biocalcification. In *E3S Web of Conferences* (Vol. 195, p. 05001). EDP Sciences.. <https://doi.org/10.1051/e3sconf/202019505001>
- Ghosh, T., Bhaduri, S., Montemagno, C., & Kumar, A. (2019). *Sporosarcina pasteurii* can form nanoscale calcium carbonate crystals on cell surface. *Plos One*, *14*(1), Article e0210339. <https://doi.org/10.1371/journal.pone.0210339>
- Grice, J. D. (2005). The structure of spurrite, tilleyite and scawtite, and relationships to other silicate-carbonate minerals. *The Canadian Mineralogist*, *43*(5), 1489-1500. <https://doi.org/10.2113/gscanmin.43.5.1489>
- Helmi, F. M., Elmitwalli, H. R., Elnagdy, S. M., & El-Hagrassy, A. F. (2016). Calcium carbonate precipitation induced by ureolytic bacteria *Bacillus licheniformis*. *Ecological Engineering*, *90*, 367-371. <https://doi.org/10.1016/j.ecoleng.2016.01.044>
- Hoang, T., Alleman, J., Cetin, B., Ikuma, K., & Choi, S. G. (2019). Sand and silty sand soil stabilization using bacterial enzyme induced calcite precipitation (BEICP). *Canadian Geotechnical Journal*, *56*(6), 808-822. <https://doi.org/10.1139/cgj-2018-0191>
- Imran, M. A., Kimura, S., Nakashima, K., Evelpidou, N., & Kawasaki, S. (2019). Feasibility study of native ureolytic bacteria for biocementation towards coastal erosion protection by MICP method. *Applied Sciences*, *9*(20), Article 4462. <https://doi.org/10.3390/app9204462>
- Ivanov, V., Stabnikov, V., Stabnikova, O., & Ahmed, Z. (2020). Biocementation technology for construction of artificial oasis in sandy desert. *Journal of King Saud University - Engineering Sciences*, *32*(8), 491-494. <https://doi.org/10.1016/j.jksues.2019.07.003>
- Jiang, N. J., Tang, C. S., Hata, T., Courcelles, B., Dawoud, O., & Singh, D. N. (2020). Bio-mediated soil improvement: The way forward. *Soil Use and Management*, *36*(2), 185-188. <https://doi.org/10.1111/sum.12571>
- Jiang, N. J., Yoshioka, H., Yamamoto, K., & Soga, K. (2016). Ureolytic activities of a urease-producing bacterium and purified urease enzyme in the anoxic condition: Implication for subseafloor sand production control by microbially induced carbonate precipitation (MICP). *Ecological Engineering*, *90*, 96-104. <https://doi.org/10.1016/j.ecoleng.2016.01.073>

- Kakelar, M. M., Ebrahimi, S., & Hosseini, M. (2016). Improvement in soil grouting by biocementation through injection method. *Asia-Pacific Journal of Chemical Engineering*, *11*(6), 930-938. <https://doi.org/10.1002/apj.2027>
- Keykha, H. A., Asadi, A., & Zareian, M. (2017). Environmental factors affecting the compressive strength of microbiologically induced calcite precipitation treated soil. *Geomicrobiology Journal*, *34*(10), 889-894. <https://doi.org/10.1080/01490451.2017.1291772>
- Kim, G., & Youn, H. (2016). Microbially induced calcite precipitation employing environmental isolates. *Materials*, *9*(6), Article 468. <https://doi.org/10.3390/ma9060468>
- Kim, G., Kim, J., & Youn, H. (2018). Effect of temperature, pH, and reaction duration on microbially induced calcite precipitation. *Applied Sciences*, *8*(8), Article 1277. <https://doi.org/10.3390/app8081277>
- Kim, J. H., & Lee, J. Y. (2019). An optimum condition of MICP indigenous bacteria with contaminated wastes of heavy metal. *Journal of Material Cycles and Waste Management*, *21*, 239-247. <https://doi.org/10.1007/s10163-018-0779-5>
- Li, D., Tian, K. L., Zhang, H. L., Wu, Y. Y., Nie, K. Y., & Zhang, S. C. (2018). Experimental investigation of solidifying desert aeolian sand using microbially induced calcite precipitation. *Construction and Building Materials*, *172*, 251-262. <https://doi.org/10.1016/j.conbuildmat.2018.03.255>
- Li, M., Fu, Q. L., Zhang, Q., Achal, V., & Kawasaki, S. (2015). Bio-grout based on microbially induced sand solidification by means of asparaginase activity. *Scientific Reports*, *5*, Article 16128. <https://doi.org/10.1038/srep16128>
- Liu, B., Xie, Y. H., Tang, C. S., Pan, X. H., Jiang, N. J., Singh, D. N., Cheng, Y. J., & Shi, B. (2021). Bio-mediated method for improving surface erosion resistance of clayey soils. *Engineering Geology*, *293*, Article 106295. <https://doi.org/10.1016/j.enggeo.2021.106295>
- Liu, Y., Chen, Y., Huang, X., & Wu, G. (2017). Biomimetic synthesis of calcium carbonate with different morphologies and polymorphs in the presence of bovine serum albumin and soluble starch. *Materials Science and Engineering: C*, *79*, 457-464. <https://doi.org/10.1016/j.msec.2017.05.085>
- Luo, M., & Qian, C. X. (2016). Performance of two bacteria-based additives used for self-healing concrete. *Journal of Materials in Civil Engineering*, *28*(12), Article 04016151. [https://doi.org/10.1061/\(asce\)mt.1943-5533.0001673](https://doi.org/10.1061/(asce)mt.1943-5533.0001673)
- Makinda, J., Gungat, L., Rao, N. S. V. K., & Sulis, S. (2018). Compressibility behaviour of Borneo tropical peat stabilized with lime-sand column. *International Journal on Advanced Science, Engineering and Information Technology*, *8*(1), 172-177. <https://doi.org/10.18517/ijaseit.8.1.4169>
- Miftah, A., Tirkolaei, H. K., & Bilsel, H. (2020). Biocementation of calcareous beach sand using enzymatic calcium carbonate precipitation. *Crystals*, *10*(10), Article 888. <https://doi.org/10.3390/cryst10100888>
- Morsdorf, G., & Kaltwasser, H. (1989). Ammonium assimilation in *Proteus vulgaris*, *Bacillus pasteurii*, and *Sporosarcina ureae*. *Archives of Microbiology*, *152*, 125-131. <https://doi.org/10.1007/BF00456089>
- Mortensen, B. M., Haber, M. J., Dejong, J. T., Caslake, L. F., & Nelson, D. C. (2011). Effects of environmental factors on microbial induced calcium carbonate precipitation. *Journal of Applied Microbiology*, *111*(2), 338-349. <https://doi.org/10.1111/j.1365-2672.2011.05065.x>
- Muthukkumaran, K., & Shashank, B. S. (2016). Durability of microbially induced calcite precipitation (MICP) treated cohesionless soils. *Japanese Geotechnical Society Special Publication*, *2*(56), 1946-1949. <https://doi.org/10.3208/jgsssp.IND-23>

- Mwandira, W., Nakashima, K., & Kawasaki, S. (2017). Bioremediation of lead-contaminated mine waste by *Pararhodobacter* sp. based on the microbially induced calcium carbonate precipitation technique and its effects on strength of coarse and fine grained sand. *Ecological Engineering*, 109(Pt. A), 57-64. <https://doi.org/10.1016/j.ecoleng.2017.09.011>
- Mwandira, W., Nakashima, K., Kawasaki, S., Ito, M., Sato, T., Igarashi, T., Chirwa, M., Banda, K., Nyambe, I., Nakayama, S., Nakata, H., & Ishizuka, M. (2019). Solidification of sand by Pb(II)-tolerant bacteria for capping mine waste to control metallic dust: Case of the abandoned Kabwe Mine, Zambia. *Chemosphere*, 228, 17-25. <https://doi.org/10.1016/j.chemosphere.2019.04.107>
- Nawarathna, T. H. K., Nakashima, K., & Kawasaki, S. (2018). Enhancement of microbially induced carbonate precipitation using organic biopolymer. *International Journal of Geomate*, 14(41), 7-12. <https://doi.org/10.21660/2018.41.7223>
- Nawarathna, T. H. K., Nakashima, K., & Kawasaki, S. (2019). Chitosan enhances calcium carbonate precipitation and solidification mediated by bacteria. *International Journal of Biological Macromolecules*, 133, 867-874. <https://doi.org/10.1016/j.ijbiomac.2019.04.172>
- Nething, C., Smirnova, M., Gröning, J. A. D., Haase, W., Stolz, A., & Sobek, W. (2020). A method for 3D printing bio-cemented spatial structures using sand and urease active calcium carbonate powder. *Materials and Design*, 195, Article 109032. <https://doi.org/10.1016/j.matdes.2020.109032>
- Omoregie, A. I., Ngu, L. H., Ong, D. E. L., & Nissom, P. M. (2019). Low-cost cultivation of *Sporosarcina pasteurii* strain in food-grade yeast extract medium for microbially induced carbonate precipitation (MICP) application. *Biocatalysis and Agricultural Biotechnology*, 17, 247-255. <https://doi.org/10.1016/j.bcab.2018.11.030>
- Omoregie, A., Khoshdelnezamiha, G., Ong, D. E. L., & Nissom, P. M. (2017). Microbial-induced carbonate precipitation using a sustainable treatment technique. *International Journal of Service Management and Sustainability*, 2(1), 17-31. <http://dx.doi.org/10.24191/ijSMS.v2i1.6045>
- Oral, Ç. M., & Ercan, B. (2018). Influence of pH on morphology, size and polymorph of room temperature synthesized calcium carbonate particles. *Powder Technology*, 339, 781-788. <https://doi.org/10.1016/j.powtec.2018.08.066>
- Oshiki, M., Araki, M., Hirakata, Y., Hatamoto, M., Yamaguchi, T., & Araki, N. (2018). Ureolytic prokaryotes in soil: Community abundance and diversity. *Microbes and Environments*, 33(2), 230-233. <https://doi.org/10.1264/jSM2.ME17188>
- Osinubi, K. J., Eberemu, A. O., Gadzama, E. W., & Ijimdiya, T. S. (2019). Plasticity characteristics of lateritic soil treated with *Sporosarcina pasteurii* in microbial-induced calcite precipitation application. *SN Applied Sciences*, 1, Article 829. <https://doi.org/10.1007/s42452-019-0868-7>
- Pablo, A. C. M. S., Lee, M., Graddy, C. M. R., Kolbus, C. M., Khan, M., Zamani, A., Martin, N., Acuff, C., Dejong, J. T., Gomez, M. G., & Nelson, D. C. (2020). Meter-scale biocementation experiments to advance process control and reduce impacts: Examining spatial control, ammonium by-product removal, and chemical reductions. *Journal of Geotechnical and Geoenvironmental Engineering*, 146(11), 1-14. [https://doi.org/10.1061/\(ASCE\)GT.1943-5606.0002377](https://doi.org/10.1061/(ASCE)GT.1943-5606.0002377)
- Park, S. J., Park, Y. M., Chun, W. Y., Kim, W. J., & Ghim, S. Y. (2010). Calcite-forming bacteria for compressive strength improvement in mortar. *Journal of Microbiology and Biotechnology*, 20(4), 782-788.
- Qabany, A. A., Soga, K., & Santamarina, C. (2011). Factors affecting efficiency of microbially induced calcite precipitation. *Journal of Geotechnical and Geoenvironmental Engineering*, 138(8), 992-1001. [https://doi.org/10.1061/\(asce\)gt.1943-5606.0000666](https://doi.org/10.1061/(asce)gt.1943-5606.0000666)

- Rabenhorst, M., Buchanan, A., Morozov, E., Shay, J., & Mack, S. (2020). Field test for identifying problematic red parent materials. *Soil Science Society of American Journal*, 84(3), 1006-1010. <https://doi.org/10.1002/saj2.20066>
- Renner, L. D., & Weibel, D. B. (2011). Physicochemical regulation of biofilm formation. *MRS Bulletin*, 36, 347-355. <https://doi.org/10.1557/mrs.2011.65>
- Richardson, A., Coventry, K. A., Forster, A. M., & Jamison, C. (2014). Surface consolidation of natural stone materials using microbial induced calcite precipitation. *Structural Survey*, 32(3), 265-278. <https://doi.org/10.1108/SS-07-2013-0028>
- Ritchey, E. L., McGrath, J. M., & Gehring, D. (2015). *Determining soil texture by feel*. Agriculture and Natural Resources Publications.
- Sapar, N. I. F., Matlan, S. J., Mohamad, H. M., Alias, R., & Ibrahim, A. (2020). A study on physical and morphological characteristics of tropical peat in Sabah. *International Journal of Advanced Research in Engineering and Technology (IJARET)*, 11(11), 542-553.
- Sharma, M., Satyam, N., & Reddy, K. R. (2021). Investigation of various gram-positive bacteria for MICP in Narmada Sand, India. *International Journal of Geotechnical Engineering*, 15(2), 220-234. <https://doi.org/10.1080/19386362.2019.1691322>
- Singh, M. J., Weiqiang, F., Dong-Sheng, X., & Borana, L. (2020). Experimental study of compression behavior of Indian black cotton soil in oedometer condition. *International Journal of Geosynthetics and Ground Engineering*, 6, Article 30. <https://doi.org/10.1007/s40891-020-00207-0>
- Sinha, S., & Chattopadhyay, S. (2016). A study on application of renewable energy technologies for mitigating the adverse environmental impacts generated from power generation units in Himalayan region. *International Journal for Innovative Research in Science & Technology*, 3(1), 212-232.
- Srivastava, S., Bharti, R. K., & Thakur, I. S. (2014). Characterization of bacteria isolated from palaeoproterozoic metasediments for sequestration of carbon dioxide and formation of calcium carbonate. *Environmental Science and Pollution Research*, 22, 1499-1511. <https://doi.org/10.1007/s11356-014-3442-2>
- Svane, S., Sigurdarson, J. J., Finkenwirth, F., Eitinger, T., & Karring, H. (2020). Inhibition of urease activity by different compounds provides insight into the modulation and association of bacterial nickel import and ureolysis. *Scientific Reports*, 10, Article 8503. <https://doi.org/10.1038/s41598-020-65107-9>
- Taner, F. M., Martin, R. F. & Gault, R. A. (2013). The mineralogy of skarns of the spurrite-merwinite subfacies, sanidine facies, Guneyce-ikizdere area, eastern black sea, Turkey. *The Canadian Mineralogist*, 51(6), 893-911. <https://doi.org/10.3749/canmin.51.6.893>
- Tang, C. S., Yin, L. Y., Jiang, N. J., Zhu, C., Zeng, H., Li, H., & Shi, B. (2020). Factors affecting the performance of microbial-induced carbonate precipitation (MICP) treated soil: A review. *Environmental Earth Sciences*, 79, Article 94. <https://doi.org/10.1007/s12665-020-8840-9>
- Terzis, D., & Laloui, L. (2019). Cell-free soil bio-cementation with strength, dilatancy and fabric characterization. *Acta Geotechnica*, 14, 639-656. <https://doi.org/10.1007/s11440-019-00764-3>
- Towner, G. D. (1974). The assessment of soil texture from soil strength measurements. *Journal of Soil Science*, 25(3), 298-306. <https://doi.org/10.1111/j.1365-2389.1974.tb01125.x>
- Wahab, N., Talib, M. K. A., & Rohani, M. M. (2019). An introduction of tropical peat and its history of shear strength in Malaysia. *International Journal of Civil Engineering and Technology (IJCIET)*, 10(5), 695-705.

- Wang, Z., Zhang, N., Cai, G., Jin, Y., Ding, N., & Shen, D. (2017). Review of ground improvement using microbial induced carbonate precipitation (MICP). *Marine Georesources and Geotechnology*, 35(8), 1135-1146. <https://doi.org/10.1080/1064119X.2017.1297877>
- Warren, L. A., Maurice, P. A., Parmar, N., & Ferris, F. G. (2001). Microbially mediated calcium carbonate precipitation: Implications for interpreting calcite precipitation and for solid-phase capture of inorganic contaminants. *Geomicrobiology Journal*, 18(1), 93-115. <https://doi.org/10.1080/01490450151079833>
- Wath, R. B., & Pusadkar, S. S. (2016). Soil improvement using microbial: A review. In T. Thyagaraj (Ed.), *Lecture Notes in Civil Engineering: Vol. 14. Ground Improvement Techniques and Geosynthetics* (pp. 329-335). Springer. https://doi.org/10.1007/978-981-13-0559-7_37
- Wei, S., Cui, H., Jiang, Z., Hao, L., He, H., & Fang, N. (2015). Biomineralization processes of calcite induced by bacteria isolated from marine sediments. *Brazilian Journal of Microbiology*, 46(2), 455-464. <https://doi.org/10.1590/2F51517-838246220140533>
- Wen, K., Li, Y., Amini, F., & Li, L. (2020). Impact of bacteria and urease concentration on precipitation kinetics and crystal morphology of calcium carbonate. *Acta Geotechnica*, 15, 17-27. <https://doi.org/10.1007/s11440-019-00899-3>
- Wiley, W. R., & Stokes, J. L. (1963). Effect of pH and ammonium ions on the permeability of *Bacillus pasteurii*. *Journal of Bacteriology*, 86, 1152-1156. <https://doi.org/10.1128/jb.86.6.1152-1156.1963>
- Wong, L. S. (2015). Microbial cementation of ureolytic bacteria from the genus *Bacillus*: A review of the bacterial application on cement based materials for cleaner production. *Journal of Cleaner Production*, 93, 5-17. <https://doi.org/10.1016/j.jclepro.2015.01.019>
- Wu, J., Wang, X. B., Wang, H. F., & Zeng, R. J. (2017). Microbially induced calcium carbonate precipitation driven by ureolysis to enhance oil recovery. *RSC Advances*, 7(59), 37382-37391. <https://doi.org/10.1039/c7ra05748b>
- Zhang, J., Zhao, C., Zhou, A., Yang, C., Zhao, L., & Li, Z. (2019). Aragonite formation induced by open cultures of microbial consortia to heal cracks in concrete: Insights into healing mechanisms and crystal polymorphs. *Construction and Building Materials*, 224, 815-822. <https://doi.org/10.1016/j.conbuildmat.2019.07.129>
- Zhu, T., & Dittrich, M. (2016). Carbonate precipitation through microbial activities in natural environment, and their potential in biotechnology: A review. *Frontiers in Bioengineering and Biotechnology*, 4, Article 4. <https://doi.org/10.3389/fbioe.2016.00004>

Occupational Formaldehyde Exposure and the Health Symptoms Among Histopathology Laboratory Workers in North Borneo

Alif Ramli^{1,2}, Shamsul Bahari Shamsudin^{1*}, Jac Fang Lim¹ and Mei Ching Lim¹

¹Department of Public Health Medicine, Faculty of Medical and Health Sciences, Universiti Malaysia Sabah, 88400 UMS Road, Kota Kinabalu, Sabah, Malaysia

²Occupational Safety and Health Unit, Medical Development Department, Ministry of Health Malaysia, 62590 Putrajaya, Malaysia

ABSTRACT

In hospitals, the chemical formaldehyde is commonly utilised to preserve tissues. The healthcare personnel exposed to formaldehyde the most work in histopathology laboratories. This study aims to determine the health effects of everyday formaldehyde exposure on healthcare professionals in the histopathology laboratory. Cross-sectional comparative research was used for the study design. The 8-hour time-weighted-average (TWA₈) formaldehyde level was measured at the histopathology laboratory at Hospital Queen Elizabeth in Sabah and the administration office (control) using the real-time colorimetric tube method. Workers in both places were required to answer a questionnaire on their health status. The TWA₈ formaldehyde level was higher in the exposed area (0.113 ppm) than in the unexposed area (0.031 ppm). Air samplings showed that formaldehyde exposure levels in the exposed area (0.108 ± 0.026 ppm) were significantly higher than in an unexposed area (0.028 ± 0.018 ppm) at $p < 0.001$. Symptoms closely related to formaldehyde exposure were 51% in the histopathology laboratory workers, greater than 35% in the control group ($p < 0.05$). The workers showed six symptoms: irritated eyes, sore throat, cough, runny nose, sneezing and headache. Although the level of occupational workplace exposure to formaldehyde in the histopathology laboratory was below the recommended limit, the

health symptoms related to formaldehyde among the exposed group were detected. Enhancing control measures for indoor air quality improvement in the working area is required to minimise the health risk among laboratory workers.

Keywords: Health symptoms, healthcare workers, histopathology, occupational formaldehyde exposure

ARTICLE INFO

Article history:

Received: 21 August 2022

Accepted: 25 January 2023

Published: 21 July 2023

DOI: <https://doi.org/10.47836/pjst.31.5.19>

E-mail addresses:

dr.alif@moh.gov.my (Alif Ramli)

alifperdana87@gmail.com (Shamsul Bahari Shamsudin)

dr_ljfl@yahoo.com (Jac Fang Lim)

jennmclim@gmail.com (Mei Ching Lim)

*Corresponding author

INTRODUCTION

Formaldehyde is a combustible, colourless, pungent-smelling, and easily polymerised gas at standard room temperature and pressure (WHO, 2000). Despite having the potential to cause cancer, it is often applied in medical settings around the globe, including as a disinfectant in surgical units, a sterilising agent, and the preservation of tissues in histopathology laboratories (Bono et al., 2012; Xu & Zhang, 2003). Many healthcare workers are exposed to formaldehyde during occupational activities (Kim et al., 2011). Formaldehyde, an occupational indoor air pollutant, is quickly volatilised and released into the workplace atmosphere (Jerusalem & Galarpe, 2015; Norbäck et al., 2017).

Health practitioners who work in histopathological and anatomical laboratories are more at risk compared to other laboratory workers due to the higher levels of formaldehyde exposed to them every day as a result of their routine, whether by inhaling or direct contact with their skin (Zain et al., 2019). Symptoms linked to exposure to formaldehyde among healthcare workers can be acute or chronic (Binawara et al., 2010; Hauptmann et al., 2009). According to some studies, brief and long-term exposure by inhaling formaldehyde is correlated to respiratory disorder manifestations and eye, nasal, and throat discomfort (Takahashi et al., 2007).

Based on a recent study investigating formaldehyde exposure and health symptoms in several hospitals in the Klang Valley of Malaysia, 37% of personnel working in the histopathology laboratories and 16% of unexposed workers thought their symptoms were connected to their present working environment (Zain et al., 2019). A formaldehyde exposure level beyond the permitted amount degrades the air quality and increases the risk to workers' health (Elshaer & Mahmoud, 2017), especially in hospital pathology laboratories (Ghasemkhani et al., 2005; Jerusalem & Galarpe, 2015).

There are numerous standards for evaluating hazards and risk assessments in the workplace. Aside from broad standards in Malaysia, special criteria for substances that are often used or are primarily dangerous should be followed (Malaysia DOSH, 2018). Under the requirements of the Occupational Safety and Health (Use and Standard of Exposure of Chemicals Hazardous to Health) (OSH (USECHH)) Regulations 2000, the amount of formaldehyde in the air should not exceed 0.3 ppm (ceiling limit of airborne concentration) throughout a working hour (Malaysia DOSH, 2000). However, the OSH (USECHH) Regulations 2000 does not state the formaldehyde level airborne that a worker may be exposed to over an 8-hour day (TWA_8). Among the standards proposed by the international organisation for formaldehyde, TWA_8 limit values are 0.75 ppm by the Occupational Safety and Health Administration (OSHA-USA) and 0.1 ppm by the American Conference of Governmental Industrial Hygienists (ACGIH-USA), which is similar to the Malaysia Industry Code of Practice on Indoor Air Quality (ICOP) 2010 (Ministry of Human Resources, 2010; Motta et al., 2021; Salthammer et al., 2010). Employers are required and

accountable under OSH (USECHH) Regulation 2000 to complete Chemical Health Risk Assessments (CHRA) on any chemicals used at the workplace (Malaysia DOSH, 2018). Additionally, under specific conditions, the employer must carry out Chemical Exposure Monitoring (CEM) to track chemicals and Medical Surveillance to monitor exposed workers' health (MOH, 2010).

The exposure to formaldehyde and its relation to health symptoms among healthcare workers in histopathology laboratories in North Borneo still needs to be adequately studied. Hence, to fill in the knowledge gap, this study aims to assess the exposure to formaldehyde and determine the association between formaldehyde exposure and health symptoms among healthcare workers in the histopathology laboratory in North Borneo.

METHODOLOGY

Cross-sectional comparative research was used for the study design to determine formaldehyde exposure and health symptoms among healthcare workers in the histopathology laboratory in comparison to the staff of the administration office (as control) in Hospital Queen Elizabeth, Sabah, Malaysia. The study was performed from March 2021 until May 2021, involving air sampling measurements and a survey on health symptoms.

Workplace exposure was measured from 8 a.m. to 5 p.m., i.e., the standard working hour to reflect the 8-hr time-weighted-average (TWA_8) formaldehyde level. Real-time formaldehyde exposure levels were collected from the histopathology laboratory and the administrative office using Dräger-Tube pump type accuro with the selection of colorimetric Dräger tubes of 0.2/a (0.2 to 5 ppm) with activation tube. All samples were collected during working days as the sampling strategy is based on a similar exposure group (Clerc et al., 2020; Parikh et al., 2009).

The formaldehyde level of exposure was measured by employing the real-time method. This sampling method complied with the standard recommended by the Department of Occupational Safety and Health (DOSH) Malaysia (Ministry of Human Resources, 2010). The research team was trained by a certified industrial hygienist to avoid measurement bias. The instrument was calibrated before use, and the colorimetric tubes had not passed their expiration date. Data collection was conducted by positioning the instrument at the middle point of the workspace area. Sampling was done at the height of 1.5 meters of the sampling areas, namely the administrative office and the histopathology laboratory.

The sampling procedure for the survey on health symptoms is non-probability purposive sampling among healthcare workers in the histopathology laboratory and administrative office in Hospital Queen Elizabeth, Sabah. The healthcare workers were asked for consent before filling in sociodemographic data and answering the questionnaire. The questionnaire assessing symptoms of formaldehyde exposure among healthcare workers listed the symptoms linked to occupational formaldehyde exposure (Zain et al., 2019). Follow-up

on responses from the healthcare workers was carried out by sending reminders from time to time to control non-response bias.

Data were analysed using Microsoft Excel. Statistical analysis was done using IBM Statistical Packages for Social Sciences (SPSS) version 20.0. Descriptive statistics were computed to examine and characterise the data. The first hypothesis, the difference in formaldehyde exposure levels between the histopathology laboratory (exposed) and administrative office (unexposed), was assessed using the Mann-Whitney U test. The second hypothesis, the relationship between categorical variables of symptoms and formaldehyde exposure, was evaluated using the chi-square or Fisher's exact test. Every statistical test was performed with a 95% confidence interval and p -value of 0.05.

RESULTS

A total of 20 samples of formaldehyde exposure levels were measured, with 10 samples from the histopathology laboratory (exposed area) and 10 samples from the administrative office (unexposed area). The measurements in both areas are less than Malaysia's Occupational Safety and Health Act 1994 permitted level (Table 1).

Table 1

Formaldehyde exposure levels in histopathology laboratory and administration office

	Histopathology Laboratory (ppm)	Administration Office (ppm)
1 hour before 8 working hours	0.125	0
8 working hours:		
Hour-1	0.125	0
Hour-2	0.125	0.05
Hour-3	0.125	0.05
Hour-4	0.1	0.025
Hour-5	0.1	0.025
Hour-6	0.125	0.025
Hour-7	0.125	0.05
Hour-8	0.075	0.025
1 hour after 8 working hours	0.05	0.025
TWA ₈	0.113	0.031
Reference limit	0.750^a	0.3^b

^aThe United States Occupational Safety and Health Administration (US OSHA) Permissible Exposure Limit (PEL), 1993.

^bMalaysia Occupational Safety and Health Act 1994 (Act 514) Ceiling Limit Airborne Concentration, 2000.

The TWA₈ level of formaldehyde exposure recorded in the histopathology laboratory was higher than in the administrative office (unexposed) at 0.113 ppm and 0.031 ppm, respectively. This result stipulated that the amount of formaldehyde exposure for the histopathology laboratory was 365% greater than the administrative office.

Formaldehyde exposure levels in the histopathology laboratory were greater ($p < 0.001$) compared to the administrative office in Hospital Queen Elizabeth with the means of 0.108 ± 0.026 ppm and 0.028 ± 0.018 ppm, respectively (Table 2).

Table 2

Formaldehyde exposure in the histopathology laboratory compared to the administration office in Hospital Queen Elizabeth

Variable	Histopathology laboratory (n = 10*)	Administration office (n = 10*)	Z value	p-value
	Mean \pm S.D.			
Formaldehyde exposure (ppm)	0.108 \pm 0.026	0.028 \pm 0.018	-3.762	< .001**

* Results should be interpreted cautiously due to the small sample sizes ($n < 40$)

** Significant at $p < 0.01$ (Mann-Whitney U Test)

There were 205 survey participants, comprising 164 from the histopathology laboratory and 41 from the administrative office. The distribution of responses (Table 3) corresponds to the socio-demographic characteristics of both groups. The 73.8% and 75.6% of healthcare workers, respectively, were predominately female. The age range of 31 to 40 made up 57.6% of the respondents. Almost all the respondents were non-smoking.

Table 3

Socio-demography characteristics of the histopathology laboratory workers and administration office staff

	Histopathology Laboratory workers N = 41, n (%)	Administration Office staff N = 164, n (%)
Gender		
Female	31 (75.6%)	121 (73.8%)
Male	10 (24.4%)	43 (26.2%)
Age group		
21 – 30	-	24 (14.6%)
31 – 40	35 (85.4%)	83 (50.6%)
41 – 50	5 (12.2%)	39 (23.8%)
51 – 60	1 (2.4%)	18 (11.0%)

Table 3 (Continue)

	Histopathology Laboratory workers N = 41, n (%)	Administration Office staff N = 164, n (%)
Ethnicity		
Chinese	6 (14.6%)	7 (4.3%)
Indian	3 (7.3%)	1 (0.6%)
Malay	12 (29.3%)	29 (17.7%)
Sabahan	20 (48.8%)	127 (77.4%)
Smoking		
No	39 (95.1%)	158 (96.3%)
Yes	2 (4.9%)	6 (3.7%)

Table 4 shows the distribution of respondents according to their occupational backgrounds in both groups. In terms of occupation, 63.4% of the unexposed group were general workers or clerks, whereas 34.1% of the exposed group worked were medical laboratory technologists, and 43.9% were medical officers. The total number of participants working at the same workplace for over a year was 92.2%.

Table 4

Occupational backgrounds of the histopathology laboratory workers and administration office staff of Hospital Queen Elizabeth, Sabah, Malaysia

	Administration Office staff N = 164, n (%)	Histopathology Laboratory workers N = 41, n (%)
Duration of years working at current workplace		
< 1	19 (11.6%)	5 (12.2%)
1 – 2	59 (36.0%)	12 (29.3%)
3 – 4	22 (13.4%)	2 (4.9%)
5 – 6	18 (11.0%)	8 (19.5%)
7 – 8	22 (13.4%)	1 (2.4%)
9 – 10	9 (5.5%)	4 (9.8%)
> 10	15 (9.1%)	9 (22%)
Job title		
Medical laboratory technologist	-	14 (34.1%)
Medical officer	2 (1.2%)	18 (43.9%)
Science officer	-	2 (4.9%)

Table 4 (Continue)

	Administration Office staff N = 164, n (%)	Histopathology Laboratory workers N = 41, n (%)
Medical laboratory technologist	-	14 (34.1%)
Attendant	13 (7.9%)	1 (2.4%)
Clerk	104 (63.4%)	6 (14.6%)
Accountant	4 (2.4%)	-
Medical assistant	6 (3.7%)	-
Nurse	4 (2.4%)	-
Others	31 (18.9%)	-

Strained eyes symptom was reported by 51% of the laboratory workers and 35% of the administration staff while working at their current job area, as shown in Table 5. Strained eyes were the most common symptom in both groups (> 35%), whereas wheezing was the least common (< 3%). There is a significant association between formaldehyde exposure and health symptoms among the workers in the histopathology laboratory. There are six symptoms (irritated eyes, sore throat, cough, runny nose, sneezing and headache) that were significantly more prevalent in the exposed group than the unexposed group ($p < 0.05$).

Table 5

Formaldehyde exposure symptoms of histopathology laboratory and administration office

Formaldehyde exposure-related symptoms	Administration Office staff n (%)	Histopathology Laboratory workers n (%)	X ²	p-value
Irritated eyes	20 (12.2%)	15 (36.6%)	13.782	0.001 ^a
Strained eyes	57 (34.8%)	21 (51.2%)	3.772	0.052 ^a
Sore or dry throat	13 (7.9%)	16 (39.0%)	26.117	0.001^a
Cough	5 (3.0%)	10 (24.4%)	22.029	0.001^a
Shortness of breath	4 (2.4%)	3 (7.3%)	2.367	0.145 ^b
Chest tightness	5 (3.0%)	3 (7.3%)	1.593	0.201 ^b
Wheezing	2 (1.2%)	1 (2.4%)	0.338	0.491 ^b
Runny nose	17 (10.4%)	10 (24.4%)	5.641	0.018^a
Sneezing	16 (9.8%)	9 (22.0%)	4.556	0.033^a
Headache	34 (20.7%)	17 (41.5%)	7.543	0.006^a
Stress or irritability	35 (21.3%)	12 (29.3%)	1.166	0.28 ^a
Drowsiness	33 (20.1%)	11 (26.8%)	0.875	0.349 ^a

Table 5 (Continue)

Formaldehyde exposure-related symptoms	Administration Office staff n (%)	Histopathology Laboratory workers n (%)	X ²	p-value
Shoulder pain	53 (32.3%)	20 (48.8%)	3.877	0.05 ^a
Difficulty in concentrating	19 (11.6%)	3 (7.3%)	0.624	0.578 ^b
Feeling depressed	6 (3.7%)	2 (4.9%)	0.13	0.662 ^b

^a Pearson Chi Square test, $p < 0.05$; ^b Fisher's Exact Test, $p < 0.05$.

DISCUSSION

Occupational formaldehyde exposure in hospital facilities has been the subject of some research in various countries, including a couple of studies that have been performed in Malaysia, as shown in Table 6 (Ahmed, 2011; Bono et al., 2012; Ghasemkhani et al., 2005; Jerusalem & Galarpe, 2015; Ladeira et al., 2011; Ogawa et al., 2019; Orsière et al., 2006; Ya'acob et al., 2013; Zain et al., 2019). Concerning methodology and sample area, this research is comparable to the work (Zain et al., 2019). The TWA₈ level of formaldehyde exposure described in this study with the range of 0.082 to 0.134 ppm was within the range of values of 0.076 to 0.252 ppm reported by (Zain et al., 2019). The TWA₈ values with a wider range from 0.01 to 0.51 ppm were obtained by other studies (Bono et al., 2012; Viegas et al., 2010; Ya'acob et al., 2013). Conversely, higher TWA₈ levels ranging from 0.1 to 1.19 ppm were recorded (Jerusalem & Galarpe, 2015; Orsière et al., 2006). Ghasemkhani et al. (2005) discovered that formaldehyde concentrations in pathology laboratories surpassed the recommended limits.

Table 6

Comparing occupational formaldehyde exposure in Hospital Queen Elizabeth, Sabah, Malaysia with other studies

Location	Method	Sampling area	TWA ₈ concentration (ppm)	Reference
Sabah, Malaysia	Colorimetric tube	Histopathology laboratory	0.113 Range: 0.082 – 0.134	This study
		Administrative office	0.031 Range: 0.01 – 0.046	
Klang Valley, Malaysia	OSHA 52 and NIOSH 2541	Histopathology laboratory	0.076 – 0.252	Zain et al. (2019)

Table 6 (Continue)

Location	Method	Sampling area	TWA ₈ concentration (ppm)	Reference
Cagayan de Oro, Philippines	DNPH and DNPH-coated silica	Histopathology laboratory	0.14 – 1.03	Jerusalem and Galarpe (2015)
Selangor, Malaysia	NIOSH 2541	Anatomy laboratory	0.10 – 0.17	Ya'acob et al. (2013)
Piedmont region, Italy	NIOSH 2016	Pathology laboratory	0.012 – 0.454	Bono et al. (2012)
The University of Sharjah, United Arab Emirates	NIOSH 3500	Anatomy laboratory	0.013 – 0.105	Ahmed (2011)
Lisbon and Tagus Valley, Portugal	NIOSH 2541	Histopathology laboratory	0.04 – 0.51	Ladeira et al. (2011)
South of France	Passive air monitoring badges	Pathology and anatomy laboratory	0.1 – 0.7	Orsière et al. (2006)
Tehran, Iran	NIOSH 3500	Pathology laboratory	0.73 – 1.19	Ghasemkhani et al. (2005)

The TWA₈ levels of formaldehyde exposure in the histopathology laboratory and the administrative office in this study were still lower than the limit of 0.75 ppm, an acceptable exposure level for workplace formaldehyde exposure set by the OSHA-USA or 0.3 ppm as imposed by the Malaysia Occupational Safety and Health Act 1994 (Act 514) Ceiling Limit Airborne Concentration, 2000 and close to 0.1 ppm as imposed by the Malaysia ICOP 2010.

Formaldehyde is routinely utilised in Malaysian hospitals, specifically histopathology units, to preserve human tissue samples. As a result of laboratory activities, high levels of formaldehyde vapours are introduced to laboratory workers. The existence of formaldehyde in the administrative office might be ascribed to a variety of sources, including pressed wood materials, glue, paints, furnishings, flooring, and other indoor objects (Du et al., 2014; Salthammer et al., 2010).

Respondents from the administrative office and histopathology laboratory reported health symptoms in this study. Symptoms experienced by administrative office employees might be related to their job role since well over 60% of those employed as general workers or clerks use or have exposure to computers, laser printing machine, or copier regularly. Numerous volatile organic compounds (VOCs) are also emitted by these devices, such

as formaldehyde (Viegas et al., 2010). As a result of their regular job processes, the exposure of these VOCs to the workers could have caused their symptoms. Irritated eyes, sore throat, cough, runny nose, sneezing, and headache based on statistical analysis were all shown to be more among workers in histopathology laboratory in which the exposure of formaldehyde concentrations was higher than unexposed individuals in this research. Irritated eyes and upper respiratory tract are key indicators of acute formaldehyde effects (WHO, 2010). According to the United States Department of Labour, formaldehyde levels between 0.05 and 0.5 ppm irritate the eyes, including burning, itching, redness, and tears (USDOL, 2021). The WHO stated that 0.293 ppm of formaldehyde for 4 hr is the minimum amount documented to produce irritated eyes in individuals (WHO, 2010).

It justifies the significant symptoms of irritated eyes in this study since the exposure to formaldehyde was higher in the histopathology laboratory than in the administrative office. Ocular and irritated nasal were the very often documented symptoms (55%) after exposure to formaldehyde when dissecting in an anatomical laboratory, according to another research (Ya'acob et al., 2013). Over 50% of employees in an anatomical laboratory reported cough, sore throat, and runny nose, while irritated eyes were recorded by 48% (Azari et al., 2012). Other studies have found a substantial difference in the occurrence of irritated eyes, irritated nose, dyspnoea, headache, throat dryness, and chest tightness for the duration of dissection periods versus nonworking periods (Ya'acob et al., 2013). Latex gloves, a 3-ply mask, a plastic apron, a lab coat, and cover shoes were frequently utilised by laboratory personnel, even though this personal protective equipment is not appropriate for handling formaldehyde. Unsuitable personal protective equipment in the laboratory had been ineffective as a control device in reducing formaldehyde exposure. As an individual adjusts to formaldehyde exposure, they become less sensitive to the odour and less discomfort in the eyes. Overexposure to formaldehyde might result if workers assume that typical formaldehyde characteristics would alert them to probable exposure (Amoore & Hautala, 1983).

This study was conducted in the pathology department of Hospital Queen Elizabeth, Sabah, Malaysia which is one of the important tertiary government hospitals under the Ministry of Health Malaysia. The pathology department is separated from the main ward building. The histopathology laboratory complies with international and national quality standards of IS 9002, ISO 15189 and MSQH hospital quality accreditation. It also follows the Guidelines on Chemical Management in Health Care Facilities Ministry of Health in which CHRA are conducted under the requirement of OSH USECHH regulation 2000 (MOH, 2010). The control of hazardous chemicals was also practised in the guidelines according to the OSH hierarchy of control, which includes elimination, substitution, engineering controls, administrative controls and personal protective equipment.

The amount of formaldehyde in this study was shown to be substantially impacted by the control measures, workplace area, and environmental settings. According to a study by the Institute of Medical Research (IMR), TWA_8 concentrations were lower in two hospitals which used a mechanical exhaust ventilator, fume hoods, a ducted backdraft grossing station, and appropriate specimen storage than in another two hospitals which used fewer control measures (Zain et al., 2019). An investigation was conducted on the efficiency of five ventilation methods in pathology laboratories to minimise exposure to formaldehyde (Xu & Stewart, 2016). The study discovered that the most effective control measures were ducted backdraft grossing stations, and this should be utilised instead of other types of grossing stations to reduce formaldehyde exposure during the grossing procedure. The leading causes of elevated formaldehyde levels in the sampling areas were inadequate processing measures, such as local exhaust ventilation in pathology laboratories (Ghasemkhani et al., 2005; Ogawa et al., 2019; Orsière et al., 2006).

When not in use, chemical containers, for example, must be kept away from the work site into storage areas or chemical cabinets. An airtight and leak-proof screw cap container is advised when storing formaldehyde-containing specimens since it can minimise the quantity of formaldehyde emitted into the air. Before being disposed of, all specimens should be kept in isolation in a separate room at a safe distance from the work area or in a formalin storage cabinet. These engineering control and administrative control of good work practice methods help to reduce the possible health risks to workers.

Even though every attempt was made to ensure that the study was free of biases and errors, the following limitations were noted when analysing the findings. The assumption by the study was that environmental hazard exposure constantly existed the whole year. Another assumption is that the activities done during working hours are also constant throughout the year. Recall bias exists in self-report questionnaires, but it was reduced by applying a brief recall interval in which the suggested time to complete the questionnaire is 15 min. On the other hand, the formaldehyde exposure level assessment can only capture exposure at work and does not account for exposure happening in the household or during off-duty hours. Financial constraints limited the amount of formaldehyde exposure level assessments. Scarce resources limited the researchers to utilise available tools. Cross-sectional research merely summarises the current health state and cannot identify causal relationships. The findings of this study represent Sabah as the sole histopathology laboratory under the Ministry of Health Malaysia located in the state, which may not be fully representative of histopathology laboratories all over Malaysia. Despite the limitation, the sampling size was sufficient to give a reliable result backed up by several studies.

Nevertheless, this study contributes to additional knowledge on occupational formaldehyde exposure and health symptoms in the histopathology laboratory in Hospital Queen Elizabeth, Sabah, Malaysia. Future health intervention planning and health education programmes may utilise the findings of this study as a baseline.

CONCLUSION

The specific activity performed by the employees, working place environment and control measures have notable impacts on formaldehyde exposure levels. Although the levels of occupational workplace exposure to formaldehyde were under the recommended limit, the laboratory workers had considerable symptoms, implying high formaldehyde exposure. Several control measures may be applied based on the findings to lessen the hazard linked to laboratory employees' occupational exposure to formaldehyde in terms of work process and environment. A program such as good work practices, health promotion to increase awareness and educational activities can be considered in addition to the existing control measures for reducing the risk from occupational formaldehyde exposure.

ACKNOWLEDGEMENT

The authors thank the Director General of Health Malaysia for his permission to publish this article. This study received ethical approvals from the Ethical Committee of Faculty Medical and Health Science, Universiti Malaysia Sabah (Approval code: JKEtika 1/21 (7)) and the Ethical Committee of the Ministry of Health Malaysia (Ethical approval: NMRR-21-213-58518 (IIR)). We sincerely thank the Institute for Medical Research and Hospital Queen Elizabeth, Sabah, Malaysia for their cooperation and support.

REFERENCES

- Ahmed, H. O. (2011). Preliminary study: Formaldehyde exposure in laboratories of Sharjah University in UAE. *Indian Journal of Occupational and Environmental Medicine*, 15(1), 33-37. <https://doi.org/10.4103/0019-5278.82997>
- Amoore, J. E., & Hautala, E. (1983). Odor as an aid to chemical safety: Odor thresholds compared with threshold limit values and volatilities for 214 industrial chemicals in air and water dilution. *Journal of Applied Toxicology*, 3(6), 272-290. <https://doi.org/10.1002/JAT.2550030603>
- Azari, M., Asadi, P., Jafari, M., Soori, H., & Hosseini, V. (2012). Occupational exposure of a medical school staff to formaldehyde in Tehran. *Tanaffos*, 11(3), 36-41.
- Binawara, B. K., Rajnee., Choudhary, S., Mathur, K. C., Sharma, H., & Goyal, K. (2010). Acute effect of formalin on pulmonary function tests in medical students. *Pakistan Journal of Physiology*, 6(2), 8-10.
- Bono, R., Romanazzi, V., Pirro, V., Degan, R., Pignata, C., Suppo, E., Pazzi, M., & Vincenti, M. (2012). Formaldehyde and tobacco smoke as alkylating agents: The formation of N-methylvaline in pathologists and in plastic laminate workers. *Science of the Total Environment*, 414, 701-707. <https://doi.org/10.1016/j.scitotenv.2011.10.047>
- Clerc, F., Emili, A., & Mater, G. (2020). AltrexChimie, a web application for the management and the interpretation of occupational exposure measurements to chemical substances. *International Journal of Environmental Research and Public Health*, 17(10), Article 3375. <https://doi.org/10.3390/IJERPH17103375>

- Du, Z., Mo, J., Zhang, Y., & Xu, Q. (2014). Benzene, toluene and xylenes in newly renovated homes and associated health risk in Guangzhou, China. *Building and Environment*, 72, 75-81. <https://doi.org/10.1016/J.BUILDENV.2013.10.013>
- Elshaer, N. S. M., & Mahmoud, M. A. E. (2017). Toxic effects of formalin-treated cadaver on medical students, staff members, and workers in the Alexandria Faculty of Medicine. *Alexandria Journal of Medicine* 53(4), 337-343. <https://doi.org/10.1016/j.ajme.2016.11.006>
- Ghasemkhani, M., Jahanpeyma, F., & Azam, K. (2005). Formaldehyde exposure in some educational hospitals of Tehran. *Industrial Health*, 43(4), 703-707. <https://doi.org/10.2486/indhealth.43.703>
- Hauptmann, M., Stewart, P. A., Lubin, J. H., Freeman, A. E. B., Hornung, R. W., Herrick, R. F., Hoover, R. N., Fraumeni, J. F., Blair Jr, A., & Hayes, R. B. (2009). Mortality from lymphohematopoietic malignancies and brain cancer among embalmers exposed to formaldehyde. *Journal of the National Cancer Institute*, 101(24), 1696-1708. <https://doi.org/10.1093/jnci/djp416>
- Jerusalem, J. G., & Galarpe, V. R. K. R. (2015). Determination of formaldehyde in air in selected hospital-histopathology laboratories in Cagayan de Oro, Philippines. *Journal of Chemical Health and Safety*, 22(1), 10-14. <https://doi.org/10.1016/j.jchas.2014.07.012>
- Kim, K. H., Jahan, S. A., & Lee, J. T. (2011). Exposure to formaldehyde and its potential human health Hazards. *Journal of Environmental Science and Health - Part C Environmental Carcinogenesis and Ecotoxicology Reviews*, 29(4), 277-299. <https://doi.org/10.1080/10590501.2011.629972>
- Ladeira, C., Viegas, S., Carolino, E., Prista, J., Gomes, M. C., & Brito, M. (2011). Genotoxicity biomarkers in occupational exposure to formaldehyde-The case of histopathology laboratories. *Mutation Research - Genetic Toxicology and Environmental Mutagenesis*, 721(1), 15-20. <https://doi.org/10.1016/j.mrgentox.2010.11.015>
- Malaysia DOSH. (2000). *Malaysia Occupational Safety and Health Act and Regulations Act 514 (1994) Use and Standards of Exposure of Chemicals Hazardous to Health Regulations 2000*. Malaysia DOSH. <https://www.dosh.gov.my/index.php/legislation/regulations/regulations-under-occupational-safety-and-health-act-1994-act-514/522-pua-131-2000-1/file>
- Malaysia DOSH. (2018). *Assessment of the health risk arising from the use of chemicals hazardous to health at the workplace*. Malaysia DOSH. <https://www.dosh.gov.my/index.php/legislation/guidelines/chemical/2874-01-a-manual-of-recommended-practice-on-assessment-of-the-health-risks-arising-from-the-use-of-chemicals-hazardous-to-health-at-the-workplace-3rd-edition/file>
- Ministry of Human Resources Malaysia (2010). Questionnaire for building occupants. In *Industry Code of Practice on Indoor Air* (pp. 36-38). Department of Occupational Safety and Health.
- MOH. (2010). *Guidelines on chemical management in health care facilities Ministry of Health*. MOH. https://www.moh.gov.my/moh/images/gallery/Garispanduan/Guidelines_on_Chemical-1.pdf
- Motta, O., Charlier, B., De Caro, F., Coglianese, A., De Rosa, F., Moccia, G., Pironti, C., Capunzo, M., Borrelli, A., Filippelli, A., & Izzo, V. (2021). Environmental and biological monitoring of formaldehyde inside a hospital setting: A combined approach to manage chemical risk in workplaces. *Journal of Public Health Research*, 10(1), jphr.2021.2012. <https://doi.org/10.4081/JPHR.2021.2012>
- Norbäck, D., Hashim, J., Hashim, Z., & Ali, F. (2017). Volatile organic compounds (VOC), formaldehyde and nitrogen dioxide (NO₂) in schools in Johor Bahru, Malaysia: Associations with rhinitis, ocular, throat and dermal symptoms, headache and fatigue. *The Science of the Total Environment*, 592, 153-160. <https://doi.org/10.1016/J.SCITOTENV.2017.02.215>

- Ogawa, M., Kabe, I., Terauchi, Y., & Tanaka, S. (2019). A strategy for the reduction of formaldehyde concentration in a hospital pathology laboratory. *Journal of Occupational Health*, 61(1), 135-142. <https://doi.org/10.1002/1348-9585.12018>
- Orsière, T., Sari-Minodier, I., Iarmarcovai, G., & Botta, A. (2006). Genotoxic risk assessment of pathology and anatomy laboratory workers exposed to formaldehyde by use of personal air sampling and analysis of DNA damage in peripheral lymphocytes. *Mutation Research - Genetic Toxicology and Environmental Mutagenesis*, 605(1-2), 30-41. <https://doi.org/10.1016/j.mrgentox.2006.01.006>
- Parikh, J., Ly, L., & Tkaczuk, M. (2009, December 5-9). *Respirable quartz exposure monitoring in South Australian quarries*. [Paper presentation]. AIOH2009 Conference, Canberra, Australia.
- Salthammer, T., Mentese, S., & Marutzky, R. (2010). Formaldehyde in the Indoor Environment. *Chemical Reviews*, 110(4), 2536-2572. <https://doi.org/10.1021/CR800399G>
- Takahashi, S., Tsuji, K., Fujii, K., Okazaki, F., Takigawa, T., Ohtsuka, A., & Iwatsuki, K. (2007). Prospective study of clinical symptoms and skin test reactions in medical students exposed to formaldehyde gas. *The Journal of Dermatology*, 34(5), 283-289. <https://doi.org/10.1111/j.1346-8138.2007.00274.x>
- USDOL. (2021). *1910.1048 App C - Medical surveillance - Formaldehyde | Occupational safety and health administration*. US OSHA Official Website. <https://www.osha.gov/laws-regs/regulations/standardnumber/1910/1910.1048AppC>
- Viegas, S., Ladeira, C., Nunes, C., Malta-Vacas, J., Gomes, M., Brito, M., Mendonça, P., & Prista, J. (2010). Genotoxic effects in occupational exposure to formaldehyde: A study in anatomy and pathology laboratories and formaldehyde-resins production. *Journal of Occupational Medicine and Toxicology*, 5(1), 1-8. <https://doi.org/10.1186/1745-6673-5-25>
- WHO. (2000). Chapter 5.8 formaldehyde. In *Air quality guidelines for Europe* (2nd ed., pp.87-91). WHO Regional Publication.
- WHO. (2010). *WHO guidelines for indoor air quality: Selected pollutants*. WHO Regional Office for Europe. <http://www.who.int/iris/handle/10665/260127>
- Xu, W., & Stewart, E. J. (2016). A comparison of engineering controls for formaldehyde exposure during grossing activities in health care anatomic pathology laboratories. *Journal of Occupational and Environmental Hygiene*, 13(7), 529-537. <https://doi.org/10.1080/15459624.2016.1149182>
- Xu, Y., & Zhang, Y. (2003). An improved mass transfer based model for analyzing VOC emissions from building materials. *Atmospheric Environment*, 37(18), 2497-2505. [https://doi.org/10.1016/S1352-2310\(03\)00160-2](https://doi.org/10.1016/S1352-2310(03)00160-2)
- Ya'acob, S. J., Suis, A. J., Awang, N., & Sahani, M. (2013). Exposure assessment of formaldehyde and its symptoms among anatomy laboratory workers and medical students. *Asian Journal of Applied Sciences*, 6(1), 50-55. <https://doi.org/10.3923/ajaps.2013.50.55>
- Zain, S. M. S. M., Azmi, W. N. F. W., Veloo, Y., & Shaharudin, R. (2019). Formaldehyde exposure, health symptoms and risk assessment among hospital workers in Malaysia. *Journal of Environmental Protection*, 10(06), 861-879. <https://doi.org/10.4236/jep.2019.106051>

Estimating Disability-Free Life Expectancy of Malaysian Population Using the Sullivan's Approach

Khairunnisa Mokhtar¹, Syazreen Niza Shair^{2*} and Norazliani Md Lazam²

¹*School of Computing, Faculty of Computing and Engineering, Quest International University, No.227, Jalan Raja Permaisuri Bainun, 30250 Ipoh, Perak, Malaysia*

²*Centre for Actuarial Studies, Faculty of Computer and Mathematical Sciences, Universiti Teknologi MARA, 40450, Shah Alam, Selangor, Malaysia*

ABSTRACT

As we age, the chances of becoming disabled tend to increase due to an accumulation of health risks from a lifetime of illness, injury, and disability. This research examines the increasing life expectancy of the Malaysian population in relation to their disability status from 2015 to 2019. Disability-free life expectancy (DFLE) was computed using the Sullivan's approach; subsequently, compression or expansion of disability over the two observation years, 2015 and 2019, were analysed. Malaysian disability prevalence rates by age groups for 2015 and 2019 were used to execute this research. In addition, the respective mortality rates by age were gathered from the Department of Statistics of Malaysia. Results showed that, as life expectancy increases, the number of years lived without a disability would rise significantly while the anticipated number of years with a disability will be concurrently declining, suggesting evidence of disability compression. It was also observed that the median age at which the number of years spent with a disability

higher than without a disability was 55 in 2015, then delayed to 67.5 in 2019. This study informs medical practitioners and health policymakers about the average lifespan of Malaysians without disabilities, which can indicate the population's general health status.

ARTICLE INFO

Article history:

Received: 22 August 2022

Accepted: 14 November 2022

Published: 21 July 2023

DOI: <https://doi.org/10.47836/pjst.31.5.20>

E-mail addresses:

khairunnisamokhtar8@gmail.com (Khairunnisa Mokhtar)

syazreen@uitm.edu.my (Syazreen Niza Shair)

norazliani@uitm.edu.my (Norazliani Md Lazam)

*Corresponding author

Keywords: Disability, disability-free life expectancy, life table, morbidity, Sullivan's method

INTRODUCTION

Malaysia is moving towards an ageing nation as the percentage of older people aged sixty and above increased tremendously over the last four decades. One of the elderly population's concerns is that they tend to become disabled due to an accumulation of health problems. They face some obstacles in performing daily routines, limiting their full capabilities, thus requiring dependability from family members to perform their daily activities (ADLs) (Prina et al., 2020).

Statistics showed that the life expectancy of the Malaysian population has been increasing remarkably over the years, from 53.52 in 1950 to 76.51 in 2021 (Macrotrends.net, 2023). Despite the COVID-19 outbreak that emerged at the end of 2019, the Malaysian population's life expectancy at birth has continued to rise. (Ministry of Economy, 2021). The increase in life expectancy raises the important question of whether the population lives longer in good or poor health. According to Moreno et al. (2020), changes in lifestyle and medical technology have contributed to the increase in life expectancy of the population and, at the same time, delayed the onset of chronic illness and disability, leading to a compression of morbidity at older ages. On the other hand, the increase in life expectancy at older ages also expands morbidity as this group of people is likely to associate with ageing-related diseases commonly experienced by the elderly (Jagger et al., 2014). These two theories can be absolute and relative, whereby the increase in life expectancy can be with or without disability (Moreno et al., 2020). An in-depth study on assessing and analysing the life expectancy with and without a disability is crucial in planning for social and health policies, particularly related to the elderly.

The Healthy Life Expectancy (HLE) theory addresses how many years of life were spent in good rather than poor health. HLE measures population health by integrating mortality and morbidity levels of a population and partitions years of life lived at a particular age into healthy and unhealthy years. The disability-free life expectancy (DFLE) is one measure of HLE, which indicates the remaining years of life spent in an able state and can perform daily activities independently without assistance from the carers (Moreno et al., 2018). Existing research on HLE and DFLE of various populations and periods has often reached inconsistent conclusions about the competing nature of mortality and morbidity. In Brazil, for instance, the proportion of healthy years lost increases significantly with age due to long-term disease or disability that limits daily activities, regardless of the difficulty and severity of the functional limitations (Romero et al., 2005). In Japan, the gains before 1995 were in years of good health, while the gains in life expectancy after 1995 were in poor health (Yong & Saito, 2009). Moreover, Belgian women had a DFLE at birth of 66.6 years out of a total life expectancy of 81.4 years, leading to 82% of their lifespan free of disability (Stiefel et al., 2010).

The computation of the person-years lived in the health state requires longitudinal data to estimate the probability of transitioning from healthy to poorer health or death. The subject of interest may frequently enter and leave states repeatedly, in which this dynamic can only be captured through a long-term follow-up study (Dudel & Myrskylä, 2020). Even though longitudinal data can be used to evaluate healthy life expectancy using the Markov model, access to this data is generally limited and inaccessible. As a result, the Sullivan method serves as an alternative strategy that allows for readily available secondary data. According to Jagger et al. (2007), both approaches yield comparable outcomes if all rates are smooth over time. The Sullivan method is an advantage as it can generally be used for its simplicity, relative accuracy and ease of interpretation. Sullivan's method explored the association between mortality and morbidity or disability in a single summary measure of a population's health status (Jagger et al., 2007). It has been used extensively to estimate the DFLE in various populations at the national level. This method remains the most widely used method among researchers and government officials for estimating DFLE. See, for example, Imai and Soneji (2012), Brønnum-Hansen et al. (2017) and Minagawa and Saito (2018). Sullivan's method mainly combines the period life table, the primary method to calculate life expectancy, with the age-specific disability prevalence obtained from cross-sectional national survey data. In particular, the method divides the total number of person-years lived, generated from the period life table, into the expected life expectancy with and without disabilities depending on the fraction of people with disabilities.

In Malaysia, the application of Sullivan's method has been extended for cancer patients to estimate cancer-free life expectancy (Omar et al., 2019). In addition, a study from Mathers et al. (2000) estimated DFLE for Malaysian aged 81 to 96 years old. However, the analyses were based on data year 1999 which is outdated and does not represent Malaysia's current perspective on disability. Up to today, the study on the trends of disability experience for Malaysian population is still lacking.

Therefore, this research aims to estimate disability-free life expectancy for the Malaysian population using the Sullivan's approach and extends the analysis starting from 18 years old and above, using recent NHMS survey datasets for year 2015 and 2019. The results of DFLE in two respective years are compared, and the compression of disability is further analysed. The trends of disability between the two years provide valuable insights into the disability burden, prevalence, and overall health status of Malaysian population.

MATERIALS AND METHODS

In order to estimate disability-free life expectancy for the Malaysian population, this research adopts the Sullivan's method, which requires two types of secondary data, including age-specific disability prevalence rates and age-specific mortality rates.

Data Collection

Disability prevalence rates according to age were obtained from the National Institute of Health (2019) report. The NHMS survey was conducted by the Malaysia Institute of Public Health once every four years. The survey, specifically on disability, was available only in 2015 and 2019. The disability prevalence estimates by age group for 2019 were obtained directly from the National Health & Morbidity Survey report (National Institute of Health, 2019). The sample included people aged 18 and older and were national representatives. The disability prevalence rates by age group for 2015 were retrieved from (Ahmad et al., 2017), as data by age group were not available directly in the NHMS (2015) report. Ahmad et al. (2017) surveyed the NHMS disability module in 2015, including people aged 18 and above and published the disability prevalence data by age group. The questionnaires were based on the International Classification of Functioning, Disability and Health (ICF) framework by the Washington Group on Disability Statistics (WG). Participants were classified as without disability or with a disability according to the following questions:

- "Do you have difficulty in hearing, even if using a hearing aid?"
- "Do you have difficulty in walking or climbing steps?"
- "Do you have difficulty in remembering or concentrating?"
- "Do you have difficulty with self-care such as washing all over or dressing?"
- "Using your usual (customary) language, do you have difficulty in communicating?"

The response categories:(1) No, no difficulty, (2) Yes, some difficulty, (3) Yes, many difficulties and (4) Cannot do it at all. The most important quantity for calculating DFLE is the person-years lived in each age group. Several deaths of the population are required. Thus, age and gender-specific central mortality rates for the Malaysian population in 2015 and 2019 were obtained from the Department of Statistics Malaysia (DOSM). The mortality data were in the quinquennial age range from 0, 1–4, 5–9.....,75–79 and 80+.

Table 1
Age-specific disability prevalence rate among adults in Malaysia for 2015

Age	Prevalence (%)
18–30	4.21
31–40	5.31
41–50	10.07
51–60	19.24
61 & above	41

Source. Ahmad et al. (2017)

Table 2
The age-specific disability prevalence rate among adults in Malaysia for 2019

Age	Prevalence (%)
18–29	3.5
30–39	4.7
40–49	8.6
50–59	15.6
60–69	25.7
70–79	45.7
80 & above	78.4

Source. NHMS (2019)

The disability prevalence rates for 2015 and 2019 in Tables 1 and 2 were inconsistent in terms of age group range. Thus, these disability prevalence and mortality data were transformed into single-age data using the interpolation technique.

Estimation of Life Expectancy Using the Life Table Approach

The life table measures the expectation of life using the estimates of age-specific mortality rates representing a notional population, typically per 100,000 people (Imai & Soneji, 2012). A period life table is developed based on the following stationarity assumptions of the population (Imai & Soneji, 2012): (1) The age-specific mortality rate is constant throughout a year, (2) the birth rate is constant over time and, (3) the net migration rates are zero at all ages. The assumptions also imply that the number of survivors is constant over time. Therefore, the total size of the hypothetical cohort is assumed to remain constant over time.

Using the collected age-specific central mortality rates data, ${}_n m_x$, the period life table is developed following Equations 1 to 6:

Number of survivors at age x : l_x (1)

Probability of dying between age x and $x + n$: ${}_n q_x$ (2)

Number of deaths between ages x and $x + n$: ${}_n d_x = l_x \times {}_n q_x$ (3)

Number of person-years lived between x and $x + n$: ${}_n L_x = \frac{{}_n d_x}{{}_n m_x}$ (4)

Total number of person-years lived after age x : $T_x = \sum {}_n L_x$ (5)

Life expectancy at age x : $e_x = \frac{T_x}{L_x}$ (6)

Estimation of Disability-Free Life Expectancy (DFLE) Using Sullivan's Method

Unlike life expectancy, DFLE cannot be calculated only from a period life table without additional data on the prevalence of disabilities. Sullivan's method estimates DFLE by segmenting the person-years lived into the proportion with and without disability. After developing the life table above, the disability prevalence is applied to calculate the disability-free life expectancy.

Sullivan's method relies on a period life table structure. The assumptions of Sullivan's model inherit the three stationarity assumptions of the population such that (1) The age-specific mortality rate is constant throughout a year, (2) the birth rate is constant over time, and (3) the net migration rates are zero at all ages. In addition, the age-specific disability

prevalence rate is assumed to be stationary. To estimate DFLE, first, the life expectancy for Malaysia's population needs to be calculated. Then the DFLE can be measured by applying the disability prevalence rate data in the DFLE formula. The steps in finding the DLFE are represented in Equations 7 to 11.

Disability prevalence rate for age x . π_x (7)

Person years lived without disability in age interval. $[1 - \pi_x] nL_x$ (8)

Total years lived without disability from age x . $\sum [1 - \pi_x] nL_x$ (9)

Disability-free life expectancy age x : $DFLE_x = \frac{1}{l_x} \sum_{i=x}^{\omega} [1 - \pi_x] nL_x$ (10)

The proportion of remaining life spent disability-free $\frac{DFLE_x}{e_x}$ (11)

Due to sample variation, the prevalence of disability varies considerably across all ages. The rate of mortality is also subject to random variation. Because the Sullivan health expectancy is derived from mortality and morbidity rates, this is also subject to random variations. Under the four stationarity assumptions, the variance of Sullivan's estimator is given by Equation 12:

$$\sigma_x^{DF} = \frac{1}{l_x^2} \sum_{i \in A_x} \frac{n_i \hat{\pi}_i (1 - n_i \hat{\pi}_i) n_i L_i^2}{n_i N_i} \tag{12}$$

Where,

- l_x = the proportion of survivors at age x
- $n_i \hat{\pi}_i$ = sample fraction of the disabled survey respondents within the age interval $[i, i + n_i)$
- $n_i L_i$ = total number of person-years lived in an interval, $[i, i + n_i)$
- $n_i N_i$ = total number of survey respondents in the age interval, $[i, i + n_i)$

RESULTS AND DISCUSSION

Tables 3 and 4 show the estimated Malaysian total life expectancy, the expected number of years lived with and without disability, and the proportion of life spent disability-free for 18 to 60+ years old for 2015 and 2019, respectively.

Results show that the life expectancy of persons aged 18–19 increased by 1.42 years from 55.51 to 56.93, while the life expectancy of elderlies aged 60 increased by 1.07 years from 16.97 to 18.04 over the observed period. This trend is consistent with the global pattern that life expectancy continues increasing over the years in which the lifespan of elderlies increased more substantially than younger population (Ibrahim et al., 2020; United Nations, 2019).

Table 3

Life Expectancy (e_x) and Disability-Free Life Expectancy (DFLE) and proportion of life with free disability for Malaysian population in 2015

Age	Life Expectancy e_x (DOSM ^a)	Life Expectancy e_x (Estimated ^b)	Expected No of Years of Life				Proportion of Life Without Disability (%)
			With Disability (DLE)		Without Disability (DFLE)		
			Years	95% CI	Years	95% CI	
18–19	56.99	55.51	19.21	(18.86, 21.14)	36.30	(35.95, 36.65)	65.40
20–24	53.59	52.14	19.10	(18.75, 21.07)	33.04	(32.70, 33.39)	63.35
25–29	48.76	47.29	18.92	(20.21, 20.90)	28.37	(29.71, 30.40)	59.40
30–34	43.96	42.45	18.72	(18.39, 19.06)	23.73	(23.39, 24.07)	55.85
35–39	39.23	37.66	18.48	(18.15, 18.81)	19.18	(18.85, 19.51)	50.87
40–44	34.62	32.97	18.18	(17.86, 18.50)	14.79	(14.47, 15.11)	44.77
45–49	30.14	28.37	17.77	(17.47, 18.07)	10.60	(10.30, 10.90)	37.23
50–54	25.83	23.91	17.25	(16.97, 17.53)	6.66	(6.38, 6.93)	27.67
55–59	21.73	19.61	16.50	(16.29, 16.70)	3.11	(2.91, 3.32)	15.59
60+	18.98	16.97	16.08	(15.96, 16.20)	0.89	(0.77, 1.01)	5.19

Note. ^aDepartment of Statistics Malaysia (2019)

^bThe life expectancy is calculated using the period life table approach

Disability-free life expectancy (DFLE) results indicate a compression in disability among the Malaysian population. As life expectancy steadily rose, the prevalence of disability experienced a profound shift, i.e., with small increases in life expectancy from 2015 to 2019, there was a substantial increase in the expected number of years lived without disability. For instance, in 2015, the 18–19 years old Malaysians had a life expectancy of 55.51 years. They were expected to live for 36.30 years without disability and the remaining 19.21 years with at least one disability condition. In comparison to 2019, when the life expectancy increased to 56.93, the expected lifetime years of 18–19 years old Malaysian

without a disability increased to 44.28, while the number of years they suffered from any disability was reduced to 12.66, resulting from disability compression. The compression of disability among the Malaysian population is consistent with (Fries et al., 2011) theory of healthy ageing that emphasises improvements in preventive medicine with the untapped potential of health promotion and prevention that led to a postponement of the onset of disability at later ages, which squeezing most of the disability in life into a shorter period.

Table 4

Life Expectancy (e_x) and Disability-Free Life Expectancy (DFLE) and proportion of life with free disability for Malaysian population in 2019

Age	Life Expectancy e_x (DOSM ^a)	Life Expectancy e_x (Estimated ^b)	Expected No of Years of Life				Proportion of Life Without Disability (%)
			With Disability (DLE)		Without Disability (DFLE)		
			Years	95% CI	Years	95% CI	
18–19	57.00	56.93	12.66	(12.18, 13.13)	44.28	(43.80, 44.75)	77.77
20–24	53.63	53.56	12.56	(12.09, 13.02)	41.01	(40.54, 41.48)	76.55
25–29	48.82	48.75	12.40	(11.93, 13.02)	36.35	(35.89, 36.82)	74.55
30–34	44.02	43.95	12.21	(11.75, 12.68)	31.74	(31.27, 32.20)	72.19
35–39	39.29	39.22	11.98	(11.51, 12.45)	27.24	(26.77, 27.71)	69.43
40–44	34.67	34.61	11.69	(11.21, 12.16)	22.92	(22.44, 23.39)	66.19
45–49	30.21	30.14	11.31	(10.83, 11.79)	18.83	(18.36, 19.31)	62.43
50–54	25.93	25.87	10.85	(10.37, 11.33)	15.02	(14.54, 15.50)	58.00
55–59	21.89	21.84	10.30	(9.81, 10.78)	11.54	(11.05, 12.02)	52.76
60–64	18.10	18.04	9.65	(9.17, 10.14)	8.39	(7.91, 8.87)	46.39
65–69	14.53	14.48	8.79	(8.31, 9.27)	5.69	(5.21, 6.17)	39.16
70–74	11.18	11.13	7.65	(7.17, 8.13)	3.48	(3.01, 3.96)	31.09
75+	8.15	9.42	7.18	(6.64, 7.72)	2.24	(1.70, 2.78)	28.34

Note. ^aDepartment of Statistics Malaysia (2019)

^bThe life expectancy is calculated using the period life table approach

A similar pattern was observed for older people aged 60. Increases in life expectancy from 2015 to 2019 resulted in an increase in the expected number of years of life free from disability from 1.19 to 8.39 and reduced the expected number of years with a disability by almost half from 17.47 to 9.65. The reduction in the number of years of life with disability among Malaysian elderlies may be due to changes in medical technology that prevent chronic illnesses and the promotion of healthy ageing that emphasise a healthy lifestyle. In addition, the high costs of long-term care and limited access to public institutions force the elderly to better care for their health and well-being while trying to avoid becoming disabled.

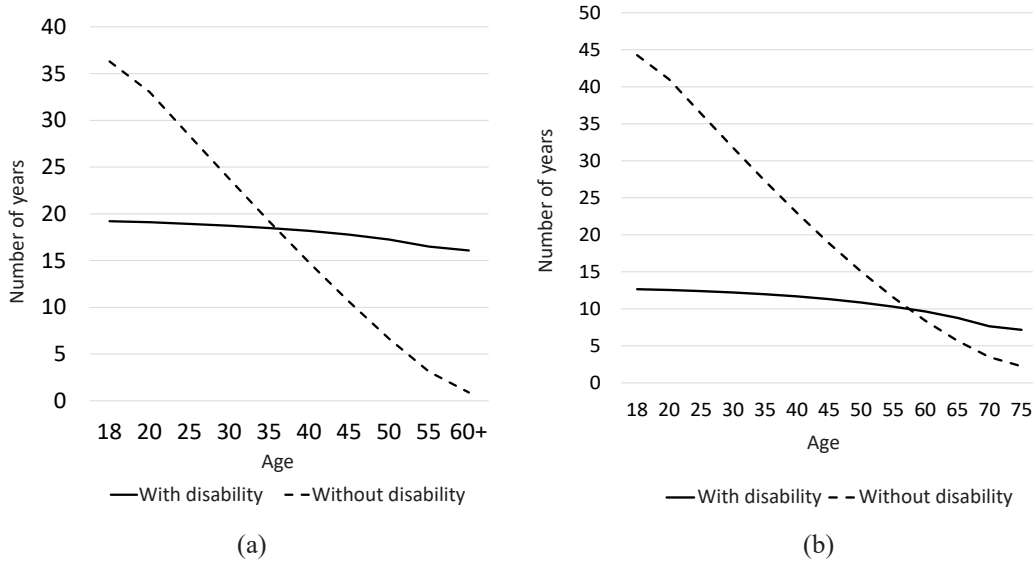
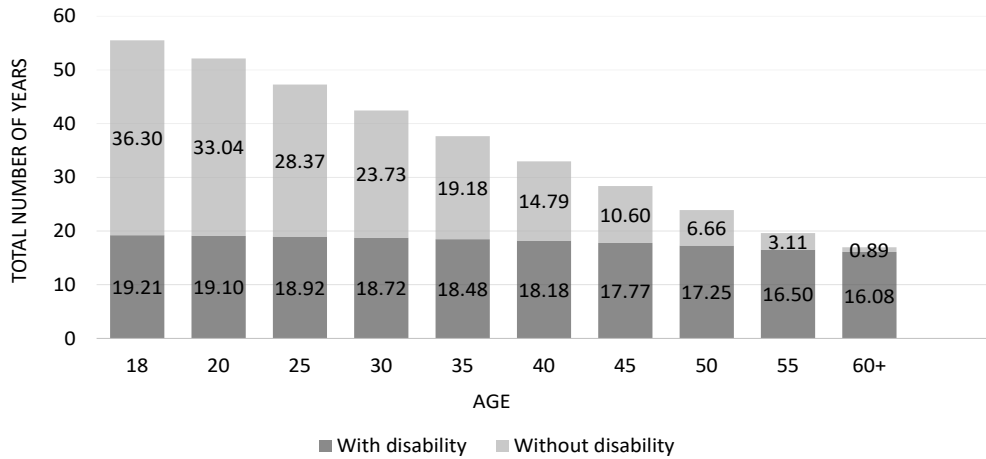


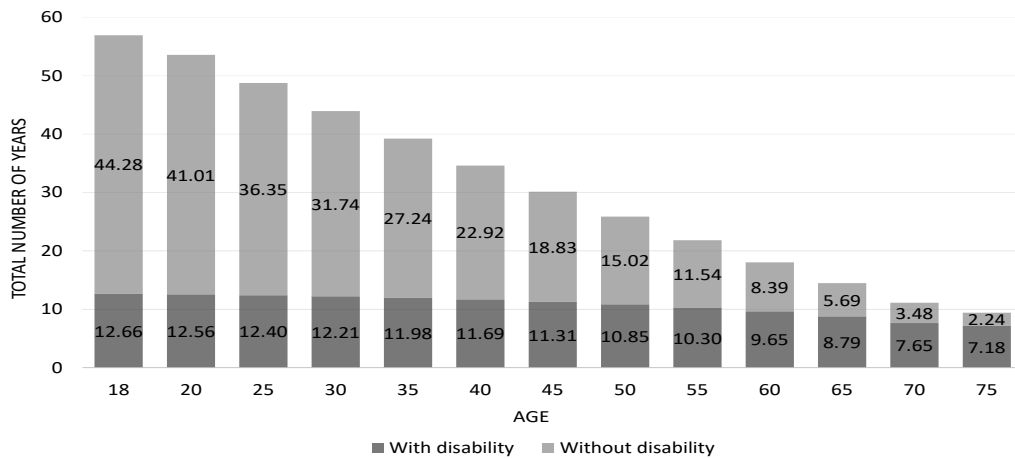
Figure 1. Disability Life Expectancy (DFLE) versus Disability-Free Life Expectancy for 2015 (a) and 2019 (b)

In addition, Figure 1 demonstrates the trends of disability life expectancy (full lines) and disability-free life expectancy (dashed lines) by age in both years. Both lines show a declining trend. It can be seen from Figure 1 that the disability-free life expectancy line is higher than the disability life expectancy for ages 18 to 35, indicating younger population live longer without a disability than with a disability. The trend depicts the same for 2019. However, the expected turning point age population in 2019 to start living with a disability longer than without a disability is delayed by 25 years, i.e., at the age of 60 years old. Compared to a study from Brown (2015), the turning point age for the English and Wales population is expected at 70 years old.

Figure 2 compares the proportion of life spent with and without disability by age groups for 2015 (a) and 2019 (b). The graph shows a declining trend from 18 to 60+ years old in both years, demonstrating that as a person ageing, the proportion of the person's life years spent in a healthy state free of disability is also decreasing. It is due to age-associated physical changes such as reduction in muscle bulk, kidney function and ventilatory capacity (Knott, 2022). According to Hairi et al. (2010), fifty per cent of those aged 75 and above need help with at least one ADL due to physical limitations. The compression of disability is apparent in that the life expectancy with disability (black bar) becomes shorter in 2019 compared to 2015. As an illustration, the life expectancy with a disability for Malaysian older adults aged 60 to 64 decreased from 16.3 years in 2015 to 9.7 years in 2019, demonstrating a 6.6-year delay in the onset of disability. This shows good indications of the population's well-being and health status, of which the proportion of years living without disability has increased tremendously over the four years under the



(a)



(b)

Figure 2. Malaysian total life expectancy by age group segregated by disability and disability-free life expectancies in 2015 (a) and 2019 (b)

study period from year 2015 to 2019. This result is consistent with a study (Fries, 2000) that indicates the postponement of the onset of disability among seniors in the United States is a minimum of 10 years due to improvement in age-specific health status as a result of a reduction in the average cumulative morbidity and disability over the life years. On the contrary, a study in the Philippines showed that an increase in life expectancy comes with a significant increase in the proportion of remaining life in an unhealthy state for all ages and genders, leading to an expansion of morbidity (Cruz et al., 2022). Comparison with these current studies concludes that Malaysia's disability data shows a solid progression in health status, with disability rates decreasing over time in conformity with morbidity compression trends in some developed nations.

In light of the morbidity compression outcomes, the proportion of life spent free from disability improved significantly between years in which the number of years spent without disability in 2019 is substantially higher than in 2015. Subsequently, the proportion of life spent with disability in 2019 is lower than in 2015. As mentioned by the Director-General of WHO "Healthy life expectancy is a key indicator of the nation's health. Increased longevity without quality of life is an empty prize" (Wolf & Laditka, 1997). The improvement in disability among Malaysian elderlies is due to government initiatives in establishing national and social strategies focusing on older people. It includes the agenda of raising the standards of living for elderlies (Department of Social Welfare, 2021).

CONCLUSION

Changes in lifestyle and medical technology that hamper the onset of chronic illness and disability has recently become a major topic of discussion among researchers and public health practitioners. The information of disability-free life expectancy has also attracted the attention of insurance firms particularly those who provide medical and health care coverage. This study explores the possibility of estimating the disability prevalence rates by observing the effect of declining trend that could delay the onset of disability at later ages. The comparison of DFLE between the two observation years, showed that as Malaysia's population lived longer with the anticipated number of years without a disability rose remarkably, and the number of years with at least one impairment condition decreased indicating disability compression towards later years. Future research could be carried out by both genders and by the severity levels of disability. Overall, this research can be a good start for future studies on DFLE in Malaysia. In order to understand the significant impact of morbidity compression on the government health care levels of spending, it would be beneficial to the country if future works investigate the relationship between the increase in disability free life expectancy and the costs for medical services.

The comparison of DFLE between the two observation years showed that as Malaysia's population lived longer, the anticipated number of years without a disability rose remarkably, and the number of years with at least one impairment condition decreased. It shows good indications of the population's well-being and health status, of which the proportion of years living without disability has increased tremendously over the four years under study (2015-2019). The results of the DFLE also revealed that almost estimations are linearly declined, demonstrating a decreasing trend across all ages. It indicates an increased risk of physical restrictions as the person ageing.

It is believed that this study would be more comprehensive and meaningful if the calculations of DFLE could be carried out on both genders and by the severity levels of disability. At the same time, initiating and incorporating social, psychological, and biological aspects in the longitudinal study is more appropriate. These additional factors

may help better identify the potential risk factors that could assist in designing and introducing more robust prospective interventions and measures.

Overall, this research can be a good start for future studies on DFLE in Malaysia. Healthy life expectancy is a key indicator of the nation's health. As the Director-General of WHO mentioned in the mid-1990s, "Increased longevity without quality of life is an empty prize" (Wolf & Laditka, 1997). In order to understand the significant impact of morbidity compression on the government health care levels of spending, it would be beneficial to the country if future works investigate the relationship between the increase in disability-free life expectancy and the costs for medical services.

ACKNOWLEDGEMENT

The authors gratefully acknowledge the support of the Universiti Teknologi MARA Shah Alam, Malaysia for support and funding to publish this research. The authors also thank the National Institute of Health (2019) for producing the information about population disability prevalence data.

REFERENCES

- Ahmad, N. A., Mohamad Kasim, N., Mahmud, N. A., Mohd Yusof, Y., Othman, S., Chan, Y. Y., Abd Razak, M. A., Yusof, M., Omar, M., Abdul Aziz, F. A., Jamaluddin, R., Ibrahim Wong, N., & Aris, T. (2017). Prevalence and determinants of disability among adults in Malaysia: Results from the National Health and Morbidity Survey (NHMS) 2015. *BMC Public Health*, 17(1), 1-10. <https://doi.org/10.1186/s12889-017-4793-7>
- Brønnum-Hansen, H., Eriksen, M. L., Andersen-Ranberg, K., & Jeune, B. (2017). Persistent social inequality in life expectancy and disability-free life expectancy: Outlook for a differential pension age in Denmark? *Scandinavian Journal of Public Health*, 45(4), 459-462. <https://doi.org/10.1177/1403494816683591>
- Brown, G. C. (2015). Living too long: Republican time in cooper's leatherstocking novels. *Nineteenth-Century Literature*, 77(1), 29-55. <https://doi.org/10.1525/ncl.2022.77.1.29>
- Cruz, G. T., Cruz, C. J. P., & Saito, Y. (2022). Is there compression or expansion of morbidity in the Philippines? *Geriatrics & Gerontology International*, 22(7), 511-515. <https://doi.org/10.1111/ggi.14398>
- Department of Social Welfare. (2021). *Older person*. Department of Social Welfare. <https://www.jkm.gov.my/jkm/index.php?r=portal/submenu&id=UkQ5T2ZCTIVkeWFYU2pJZGM5QIE5UT09>
- Dudel, C., & Myrskylä, M. (2020). Estimating the number and length of episodes in disability using a Markov chain approach. *Population Health Metrics*, 18(1), 1-9. <https://doi.org/10.1186/s12963-020-00217-0>
- Fries, J. F. (2000). Compression of morbidity in the elderly. *Vaccine*, 18(16), 1584-1589. [https://doi.org/10.1016/S0264-410X\(99\)00490-9](https://doi.org/10.1016/S0264-410X(99)00490-9)
- Fries, J. F., Bruce, B., & Chakravarty, E. (2011). Compression of morbidity 1980-2011: A focused review of paradigms and progress. *Journal of Aging Research*, 2011, Article 261702. <https://doi.org/10.4061/2011/261702>

- Hairi, N. N., Bulgiba, A., Cumming, R. G., Naganathan, V., & Mudla, I. (2010). Prevalence and correlates of physical disability and functional limitation among community dwelling older people in rural Malaysia, a middle income country. *BMC Public Health*, *10*, 1-13. <https://doi.org/10.1186/1471-2458-10-492>
- Ibrahim, N. S. M., Shair, S. N., & Yusof, A. Y. (2020). Mortality rates and life expectancy improvements among Malaysian elderlies. *Indonesian Journal of Electrical Engineering and Computer Science*, *19*(1), 134-139. <https://doi.org/10.11591/ijeecs.v19.i1.pp134-139>
- Imai, K., & Soneji, S. (2012). On the estimation of disability-free life expectancy: Sullivan's method and its extension. *Journal of the American Statistical Association*, *102*(480), 1199-1211. <https://doi.org/10.1198/016214507000000040>
- Jagger, C., Oyen, H. Van, & Robine, J. M. (2014). Health expectancy calculation by the sullivan method: A practical guide. *Newcastle University Institute of Ageing*. http://www.eurohex.eu/pdf/Sullivan_guide_pre_final_oct_2014.pdf
- Jagger, C., Robine, J. M., Van Oye, V. O., Cox, B., Cambois, E., Romieu, I., Clavel, A., & Le Roy, S. L. (2007). *Health Expectancy Calculation by the Sullivan Method: A Practical Guide* [EHEMU Technical report 2006_3]. https://webgate.ec.europa.eu/chafea_pdb/assets/files/pdb/2006109/2006109_d5sullivan_guide_final_jun2007.pdf
- Knott, L. (2022). *Disability in older people (Causes and treatment)*. Patient. <https://patient.info/doctor/disability-in-older-people>
- Macrotrends.net. (2023). Malaysia Life Expectancy 1950-2023. <https://www.macrotrends.net/countries/MYS/malaysia/life-expectancy>
- Ministry of Economy (2021). *Abridged life table, Malaysia 2019-2021*. Department of Statistics Malaysia. <chrome-extension://efaidnbmnnpkajpcglclefindmkaj/https://www.dosm.gov.my/site/downloadrelease?id=abridged-life-tables-malaysia-2019-2021&lang=English>
- Mathers, C. D. M., Sadana, R., Salomon, J. A., Murray, C. J., & Lopez, A. D. (2000). *Estimates of DALE for 191 countries: Methods and results* (Working Paper No. 16). World Health Organization. <https://www.who.int/healthinfo/paper16.pdf>
- Minagawa, Y., & Saito, Y. (2018). An analysis of factors related to disability-free life expectancy at 65 years of age across Japanese prefectures in 2010. *European Journal of Ageing*, *15*(1), 15-22. <https://doi.org/10.1007/s10433-017-0433-4>
- Moreno, X., Albala, C., Lera, L., Leyton, B., Angel, B., & Sánchez, H. (2018). Gender, nutritional status and disability-free life expectancy among older people in Santiago, Chile. *PLoS ONE*, *13*(3), 1-10. <https://doi.org/10.1371/journal.pone.0194074>
- Moreno, X., Lera, L., & Albala, C. (2020). Disability-free life expectancy and life expectancy in good self-rated health in Chile: Gender differences and compression of morbidity between 2009 and 2016. *PLoS ONE*, *15*(4), 1-12. <https://doi.org/10.1371/journal.pone.0232445>
- National Institute of Health (2019). *NCDs - Non-communicable diseases: Risk Factors and other health problems* (Technical Report Vol. 1). National Institutes of Health. chrome-extension://efaidnbmnnpkajpcglclefindmkaj/https://iku.gov.my/images/IKU/Document/REPORT/NHMS2019/Report_NHMS2019-NCD_v2.pdf

- Omar, M. H., Asmuni, N. H., & Shima, S. N. (2019). Healthy life expectancy vs health expenditure by sullivan method in Malaysia. *Indonesian Journal of Electrical Engineering and Computer Science*, 14(1), 402-406. <https://doi.org/10.11591/ijeecs.v14.i1.pp402-406>
- Prina, A. M., Wu, Y. T., Kralj, C., Acosta, D., Acosta, I., Guerra, M., Huang, Y., Jotheeswaran, A. T., Jimenez-Velazquez, I. Z., Liu, Z., Llibre Rodriguez, J. J., Salas, A., Sosa, A. L., & Prince, M. (2020). Dependence and disability-free life expectancy across eight low- and middle-income countries: A 10/66 study. *Journal of Aging and Health*, 32(5-6), 401-409. <https://doi.org/10.1177/0898264319825767>
- Romero, D. E., Leite, I. da C., & Szwarcwald, C. L. (2005). Healthy life expectancy in Brazil: applying the Sullivan method. *Cadernos de Saúde Pública / Ministério Da Saúde, Fundação Oswaldo Cruz, Escola Nacional de Saúde Pública*, 21(suppl 1), S7-S18. <https://doi.org/10.1590/s0102-311x2005000700002>
- Stiefel, M. C., Perla, R. J., & Zell, B. L. (2010). A healthy bottom line: Healthy life expectancy as an outcome measure for health improvement efforts. *The Milbank Quarterly*, 88(1), 30-53. <https://doi.org/10.1111/j.1468-0009.2010.00588.x>
- United Nations. (2019). *World population ageing 2019*. United Nations. <chrome-extension://efaidnbmnmnipccajpcgclefindmkaj/https://www.un.org/en/development/desa/population/publications/pdf/ageing/WorldPopulationAgeing2019-Highlights.pdf>
- Wolf, D. A., & Laditka, S. B. (1997). *Stochastic modeling of active life and its expectancy* [Working Paper]. Center for Policy Research. <https://surface.syr.edu/cpr/419/>
- Yong, V., & Saito, Y. (2009). Trends in healthy life expectancy in Japan: 1986-2004. *Demographic Research*, 20, 467-494. <https://doi.org/10.4054/DemRes.2009.20.19>

Effects of UV Irradiation on Electrospun PLLA and PAN in the Production of Short Electrospun Fibres Using Ultrasonication Method

Marini Sawawi*, Cheryl Rinnai Raja, Shirley Jonathan Tanjung, Sinin Hamdan, Siti Kudnie Sahari, Rohana Sapawi, Ervina Junaidi, Mahshuri Yusof and Noor Hisyam Noor Mohamed

Faculty of Engineering Universiti Malaysia Sarawak, 94300, Kota Samarahan, Sarawak, Malaysia

ABSTRACT

This work showed that exposure of ductile electrospun polymers, namely poly-*L*-Lactide acid (PLLA) and polyacrylonitrile (PAN) to UV-Ozone, leads to the embrittlement of fibres. Young's modulus for PLLA and PAN increased by 39% and 78%, respectively. Meanwhile, the ductility was reduced by 23% for PLLA and 40% for PAN. The SEM images show that the UV irradiation resulted in a surface pitted of PLLA and no changes in PAN surface morphology. The ATR-FTIR results indicate that this treatment did not change the chemical structure of the electrospun PLLA and PAN fibres. The as-spun polymers that failed to be scission directly using ultrasonication can now be fragmented into micron-length short fibres after the UV irradiation treatment. The minimum time to produce the short fibres is 18 mins for PAN and 29 mins for PLLA. It indicates ultrasonication is suitable for producing short electrospun fibres, even for ductile materials.

Keywords: Electrospun fibres, short fibres, ultrasonication

ARTICLE INFO

Article history:

Received: 29 August 2022

Accepted: 06 December 2022

Published: 21 July 2023

DOI: <https://doi.org/10.47836/pjst.31.5.21>

E-mail addresses:

smarini@unimas.my (Marini Sawawi)

cheryl.raja@gmail.com (Cheryl Rinnai Raja)

jtshirley@unimas.my (Shirley Jonathan Tanjung)

hsinin@unimas.my (Sinin Hamdan)

sskudnie@unimas.my (Siti Kudnie Sahari)

srohana@unimas.my (Rohana Sapawi)

jervina@unimas.my (Ervina Junaidi)

ymashun@unimas.my (Mahshuri Yusof)

nmnhisyam@unimas.my (Noor Hisyam Noor Mohamed)

*Corresponding author

INTRODUCTION

Electrospinning is a technique that employs electrical charge and polymer solutions to generate tiny filaments. In comparison to other conventional approaches such as drawing, template synthesis, phase separation, and self-assembly, this method has since been recognised as a quick and straightforward technique for producing continuous sub-micron to nano-sized fibres (Huang et al., 2003; Ramakrishna et al.,

2005). Natural polymers, synthetic polymers, polymer solutions, polymer melts, and biopolymers have all been employed to make fibre materials. Flexibility is one of the appealing characteristics of electrospinning. By adjusting the processing parameters, the morphology of the fibres can be easily altered with this technology, allowing the manufacture of solid, porous, and core-shell fibres (Bazilevsky et al., 2007; Sun et al., 2003).

Briefly, the electrospinning method uses the positive electric field to induce changes in the polymer solution, and once this charge build-up exceeds that of the surface tension, a Taylor cone is formed (He et al., 2008). A polymer jet erupts from the cone tip at this critical voltage, accelerating through the electric field towards the collector. The solvent evaporates as the jet travels towards the collector, and a solidified polymer fibre is collected. The electrospun fibres produced from this method have a wide range of applications, including tissue engineering, sensors, and composite reinforcement (Bhardwaj & Kundu, 2010; Huang et al., 2003; Li et al., 2019; Nakielski et al., 2022; Niemczyk-Soczynska et al., 2021; Ramakrishna et al., 2005; Zakrzewska et al., 2022).

There is little research on making individual, short nanofibres from commonly electrospun membranes. It would be useful to separate an electrospun membrane into distinct, short nanofibres because this would result in a method for making large amounts of these fibres. Short fibres are excellent for biomedical applications as injectable fibrous scaffolds for tissue engineering or drug-containment channels (Nakielski et al., 2022). Short electrospun fibres are produced quickly (in a few seconds to a few minutes) using ultrasonication (Niemczyk-Soczynska et al., 2021; Sawawi et al., 2013). Most laboratories utilise ultrasonic probes, which operate at a frequency of 20 kHz, for tasks including cleaning and mixing (Watmough, 1994). Bubbles in the fluid medium expand and contract during sonication, releasing energy as they do so. These bubbles begin with a diameter of approximately 1 μm and increase to approximately 50 μm under negative pressure (Suslick, 1988). The bubble expands under these sonication settings in 20 microseconds and collapses in nanoseconds. This technique has been used to help carbon nanotubes disperse in a solvent (Rennhofer & Zanghellini, 2021) and cause carbon nanotube scission (Hennrich et al., 2007).

There are varied degrees of success with several approaches to reinforced composite using the shortened, non-woven electrospun membrane. Mortar grinding (Deniz et al., 2011; Sancaktar & Aussawasathien, 2009) is a straightforward but unpredictable technique that is proven to work well for brittle electrospun membranes like carbonised polyacrylonitrile (Sancaktar & Aussawasathien, 2009). Better choices for scissioning electrospun membranes include rubber milling (Kim & Reneker, 1999) and cryogenic milling (Verreck et al., 2003), where the impactor of cycle and rate can be precisely regulated. Comparing the methods is challenging because the features of the resulting short fibres were not always accurately described. Short magnetic composite fibres such as methyl methacrylate-vinyl acetate

copolymer/superparamagnetic cobalt nanoparticles are created through the application of other mechanical techniques, such as razor blade cutting under nitrogen (Kriha et al., 2007). Another technique for creating distinct fibres from the electrospun membrane includes producing short nylon electrospun fibres using 1 μm step-sliced cryomicrotoming. However, it requires time-consuming, repetitive steps (Mark et al., 2008). Reduced poly(butadiene) electrospun fibre mats were made utilising UV light to degrade polymers. The UV light was shone through masks with well-defined slit diameters and inter-slit distances. The mesh is covered with mats, which result in short fibre bundles rather than single, short fibres (Stoiljkovic & Agarwal, 2008).

In this work, treatment of ductile polymers such as PLLA and PAN using UV irradiation. The electrospun membrane of these polymers will be exposed to UV irradiation, and the materials' surface morphology and chemical bonding will be investigated. Subsequently, ultrasonication of the as-spun electrospun and UV-irradiated membranes will be discussed. The ability of the ductile polymers such as PAN and PLLA to be directly scission using ultrasonication will open a venue for the methodology to produce individual short electrospun fibre in a short time and high quantities, which can be used in various applications.

MATERIAL AND METHODS

Poly(*L*-lactide) Acid (PLLA, Inherent viscosity = 0.9 - 1.2 dL/g) was purchased from Lactel, USA. Polyacrylonitrile (PAN, $M_w = 120,000$) and dodecyl trimethyl ammonium bromide (DTAB) were purchased from Sigma Aldrich, Australia. Chloroform, dimethylformamide (DMF) and acetone were bought from Merck Pty Ltd, Australia. Deionised water was obtained from the Direct-Q3 water purification system, Millipore.

Electrospun PLLA webs were made using chloroform/acetone (3:1) in 1 mM DTAB. Using 13.7 wt/v% concentration, DTAB was added to 10 mL chloroform/acetone to make a 0.1 M stock solution. A magnetic stirrer dissolved PLLA-solvent overnight. As-received PAN was mixed with DMF to make PAN solution at the concentration of 10 wt/v%. Electrospinning was done utilising a lab-built electrospinner with a Gamma High Voltage Research (USA) high voltage supply and a Razel Scientific Instruments, Inc. syringe pump (USA). The PLLA solution was spun at the feed rate of 1.6 ml/hr, a voltage of 20kV, a needle size of 18G and a working distance of 16 cm. PAN solution was prepared using the same electrospinning parameter except for the working distance, which was at 8 cm. After several optimisation processes, the electrospinning parameter was chosen to obtain a beaded fibre with a similar submicron diameter. All polymers were spun onto a flat collector (aluminium foil) and stored in a desiccator under a vacuum before use.

An ultrasonicator probe with a diameter of 13 mm (Vibracell 750W with 20kHz from Sonics & Materials, Inc, USA) is used for the ultrasonication experiment. A 1 cm^2 section

of the electrospun membrane with a ca 100 – 200 μm thickness was cut and placed in a 25 mm glass vial containing 15 ml of MiliQ water at room temperature. The sonicator was set to 80% amplitude with a 2 s ON/2 s OFF (2/2) cycle. The sonication time was halted until visible fibre breakup. After sonication, a drop of short fibres in suspension was deposited on a carbon-tape-covered stub. The material was dried prior to FESEM imaging (JEOL 7001FEG SEM),

UV-Ozone irradiation treatment was conducted using UV Ozone ProcleanerTM UV PC 220 (Bioforce, USA). The electrospun membrane was irradiated for 12 min at 14.75 mW/cm² prior to the sonication experiment.

Field Emission SEM (JEOL 7001FEG SEM) characterised fibre morphology. Before imaging, the sample was platinum-coated at 1 nm thickness (Cressington 208HR, UK). Image J programme (National Institute of Health, USA) was used to measure the diameter and length of 50 short fibres.

The mechanical testing was done with an Instron 5848 microtester (USA) at 5 mm/min and 10 N load. The 0.3-mm-thick electrospun membrane was sliced with a dogbone cutter with a gauge length of 20 mm. Five independent samples of each polymer were tested for ultimate tensile strength (UTS), Young's modulus (E), and per cent strain to failure (ductility).

The samples were further characterised by Attenuated Total Reflectance Fourier Transform Infrared (ATR-FTIR) spectroscopy (Thermo Scientific Nicolet 6700) with a scanning range of 4500 to 400 cm^{-1} and 4 cm^{-1} resolution.

RESULTS AND DISCUSSION

SEM images in Figure 1 show the untreated (as-spun) and the UV-ozone irradiated PLLA and PAN membrane at different magnifications.

Figure 1a shows that the as-spun PLLA fibre is beads-free and randomly oriented with a smooth surface (Figure 1b). Whilst the UV-Ozone treatment has changed the surface morphology of PLLA electrospun webs, where etching on the surface of the fibre can be observed (Figure 1c and d). In contrast, the PAN electrospun webs' surface morphology remains the same as for the untreated and the UV-Ozone treated webs (Figure 1f to i). The effect of UV-Ozone irradiation depends on the chemical nature of the polymer and the UV wavelength. It was reported that the carbonyl group (C=O) bond can be cleaved at the wavelength of 225 nm (Sakai & Tsutsumi, 2010), whilst the UV-Ozone cleaner used in this work has a wavelength of about 254 nm. In contrast, homolysis of alkane (C \equiv C) PAN fibres occurs at wavelengths greater than 300 nm, indicating that the UV wavelength used in this experiment is insufficient to cause chain scission.

The as-spun PLLA and PAN average fibre diameter is calculated to be 770 ± 240 nm and 740 ± 150 nm, respectively, with the fibre size distribution shown in Figure 2.

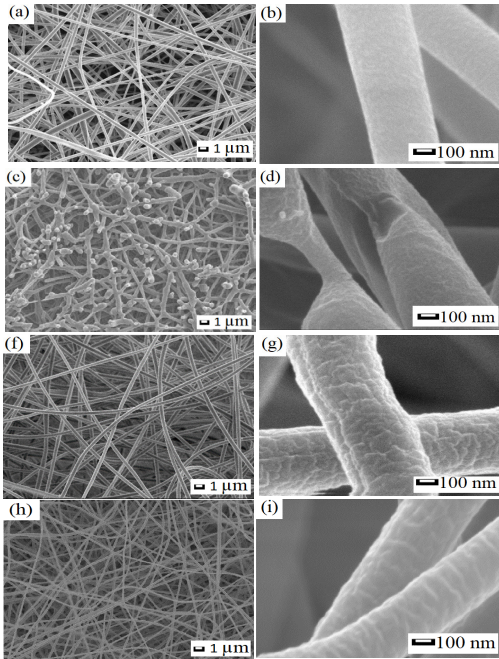


Figure 1. SEM images (a and b), untreated PLLA fibre (c and d), UV-Ozone irradiated electrospun PLLA fibre (f and g), untreated PAN fibre and UV-Ozone irradiated electrospun PAN (h and i)

It shows that the diameter of both fibres is broadly similar.

Tensile testing of the UV-Ozone irradiated and untreated electrospun PAN and PLLA was performed to study the effect of UV-Ozone on the mechanical properties. Figure 3 shows the stress-strain curves of the untreated, and UV-Ozone irradiated electrospun webs, and a summary of the average mechanical properties taken from 5 samples are presented in Table 1.

Figure 3 and Table 1 found that the UV-Ozone treatment increased Young’s modulus of both electrospun PLLA from an average of 11.1 GPa to 15.4 GPa, which is about a 39% increment. It is also similar to PAN fibres, where the modulus increased from an average of 12.2 GPa to 21.7 GPa (78% difference). The tensile strength of PAN

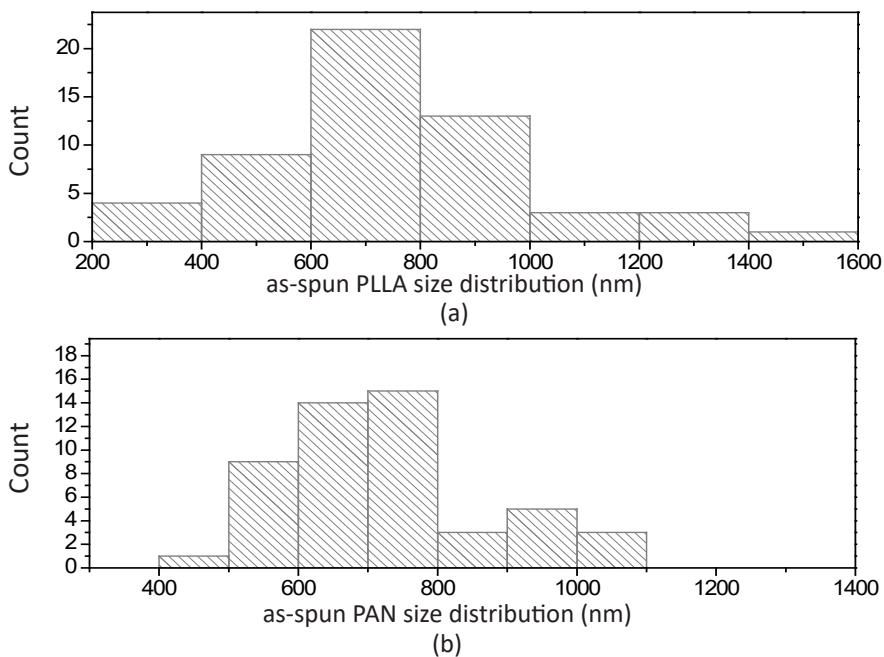


Figure 2. Size distribution of as-spun fibres (a) PLLA, (b) PAN

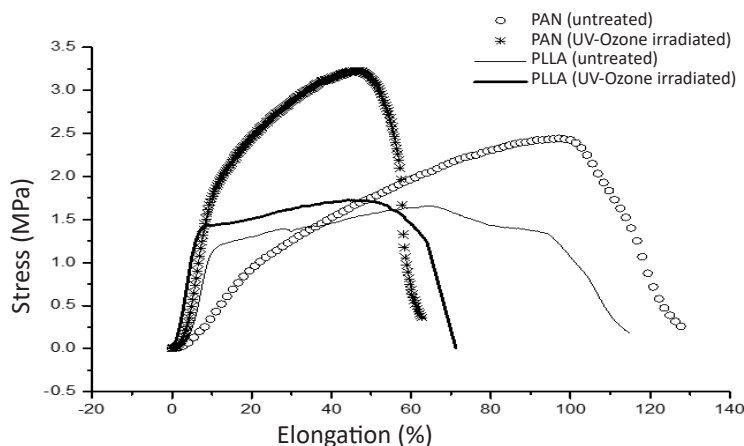


Figure 3. Stress-strain curve of the untreated and UV-Ozone irradiated PAN and PLLA

Table 1

Mechanical properties of the untreated and UV-Ozone irradiated electrospun PLLA and PAN (n=5)

Material	Young's modulus, E (GPa)	Tensile strength, σ (MPa)	Ductility (%)
PLLA (untreated)	11.1 ± 2.6	1.6 ± 0.2	79.2 ± 17.9
PLLA (UV-Ozone irradiated)	15.4 ± 2.8	1.2 ± 0.3	56.1 ± 16.9
PAN (untreated)	12.2 ± 7.7	2.5 ± 0.1	86.3 ± 22.3
PAN (UV irradiated)	21.7 ± 6.9	3.2 ± 0.3	50.2 ± 13.5

webs increased by 29% (from 2.5 MPa to 3.2 MPa) and showed a reduction in ductility of about 40% (from 86.5 to 50.2%). However, for PLLA, the tensile strength and ductility decreased by 23 % (from 1.6 MPa to 1.2 MPa) and 30% (from 79.2 to 56.1%), respectively. It was reported that the effect of UV irradiation varies depending on the polymer exposed (Guillet, 1972). The effect of UV irradiation on polymers includes discolouration, scission of the main chain, photoinduced crystallisation and crosslinking (Guillet, 1972; Sakai & Tsutsumi, 2010; Stowe et al., 1974). The UV-Ozone treatment of PLLA is likely to degrade the PLLA macromolecules, as it reduces its strength and the elongation to failure, initiating the degradation of polymer molecules and reducing the molecular weight (Yixiang et al., 2008). It could occur at the surface (since introducing surface flaws through exposure would change mechanical properties) and within the bulk. The increase in modulus observed could be due to cross-linking. Most importantly, it can be seen from these results that the UV-Ozone treatment leads to a decrease in ductility, resulting in the desired electrospun fibre embrittlement.

In this study, we investigated the impact of UV-Ozone treatment on the ultrasonication of PLLA and PAN electrospun webs. Specifically, we performed ultrasonication on webs that had been previously irradiated. Our previous work (Sawawi et al., 2013) discussed that the untreated PLLA and PAN fail to be scission using ultrasonication directly. Here, the UV-ozone-treated webs were sonicated in water at 2/2 lapsed ON/OFF time and 80% amplitude. It was found that the sonication time for the electrospun webs to break up fully is 29 min for PLLA and 18 min for PAN. The untreated electrospun webs for PLLA and PAN were also sonicated simultaneously for comparative purposes. The SEM images of the sonicated webs are shown in Figure 4.

Untreated PLLA and PAN webs (Figures 4a and 4b) could now be fractured into short fibres by ultrasonication. After 29 min of sonication, the PLLA fibre's average length is $5.2 \pm 5.4 \mu\text{m}$ (Figures 4c and 4d). PAN-treated webs can be scission in 18 minutes with a

$10.6 \pm 5.1 \mu\text{m}$ average fibre length (Figures 4h and 4i). As with untreated PLLA webs, UV-Ozone-treated sonicated fibres produced a rougher, pitted surface than the pre-sonicated sample.

This surface morphology change is also observed in sonicated untreated PAN (Figure 4f) compared to sonicated UV-Ozone treated PAN (Figure 4h). It supports the hypothesis that ductility represents the most important mechanical properties of the electrospun nanofibres in terms of the ability of sonication that cause scission. It is most likely that it is the manifestation of this ductility, which is reduced due to pitting and tensile and bending deformations that lead to the final failure.

The chemical characterisation of the untreated, pre and post-sonication UV-Ozone irradiated webs was performed using reflection mode by Attenuated Total Reflectance Fourier Transform Infrared spectroscopy (ATR-FTIR) with the spectra as shown in Figure 5.

It was observed that the as-received PLLA, UV-Ozone treated electrospun PLLA

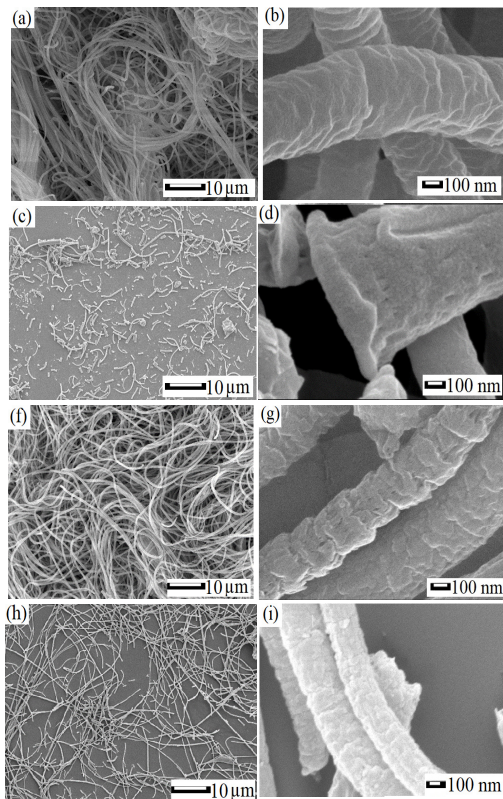


Figure 4. SEM images of sonicated (a and b), untreated PLLA $t = 29$ min (c and d), UV-Ozone irradiated PLLA $t = 29$ min (e and f), untreated PAN, $t = 18$ min and UV-Ozone irradiated PAN, $t = 18$ min (g and h)

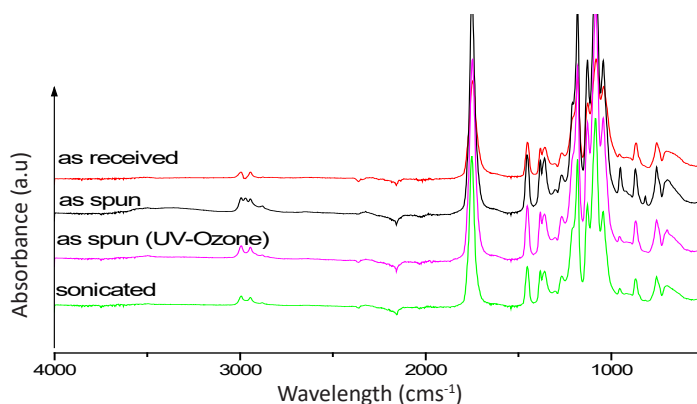


Figure 5. ATR -FTIR spectrum for as received, as-spun, as-spun with UV-Ozone treatment and sonicated PLLA (UV-Ozone treated web) in water

and sonicated UV-treated webs show a similar symmetric and asymmetric bending vibration of methyl groups at 1383 and 1456 cm⁻¹ with ester linkages appeared at 1747, 1180, 1126 cm⁻¹ which is corresponding to C=O, C-O-C and O-C-C vibration for all types of PLLA sample. However, the untreated PLLA webs showed a new band of a methyl group at 2973 cm⁻¹, whilst only symmetric and asymmetric stretching vibrations of the methyl group at 2947 and 2997 cm⁻¹ were seen for other conditions. This new peak was probably due to the solvent residue of chloroform, CHCl₃. It was noted that chloroform peaked at 2976 cm⁻¹, which appeared in the untreated spectrum. After UV-Ozone treatment, this peak disappears, which is likely due to the removal of the residual solvent during UV-Ozone exposure.

The ATR-FTIR spectra of the PAN fibre before and after UV-Ozone treatment are shown in Figure 6.

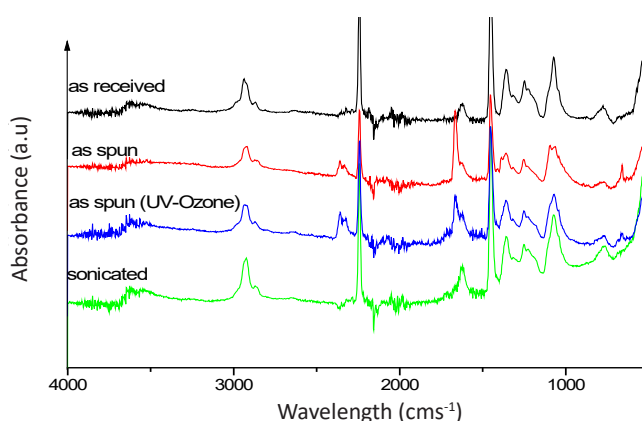


Figure 6. ATR-FTIR Spectra of PAN as received, as-spun, as-spun with UV-Ozone irradiation and sonicated PAN (UV-Ozone treated web) in water

Figure 6 shows that the as-received and sonicated electrospun webs PAN have a similar peak, where the methylene group stretching vibrations appear at 2923 and 2867 cm^{-1} . The strong peak at 2240 cm^{-1} is the characteristic vibration of the nitrile group (-CN). The stretching vibrations of carbon-carbon double bonds are shown at 1660 and 1630 cm^{-1} . The peaks at 1452 cm^{-1} and 1361 cm^{-1} are assigned to the bending vibrations of the methylene and methane groups, respectively. The 1253 cm^{-1} peak is due to the vibration of the methane group. However, an additional weak band at 2356 cm^{-1} and 2321 cm^{-1} appears in the as-spun, and as-spun (UV-Ozone) treated webs spectra due to CO_2 (could be originated from environment and contaminant) and can be neglected. UV-Ozone irradiation for PLLA and PAN did not seem to change the chemical structure of the surface and bulk polymer.

CONCLUSION

This work has shown that the UV-ozone irradiation to the surface of the electrospun fibres leads to a lower ductility resulting in embrittlement compared to the spun membrane. The embrittlement results in the ability for PLLA and PAN to be scission into short fibres down to about 5 μm using ultrasonication was unable to be achieved prior to the treatment. The ATR-FTIR results indicate no significant changes to the chemical structure of the electrospun fibres, which shows that this method can produce short electrospun fibres for other types of ductile polymers.

ACKNOWLEDGEMENT

The author thanks the Ministry of Higher Education, Malaysia, Fundamental Research Grant Scheme (FRGS/1/2020/TK0/UNIMAS/02/12) and Universiti Malaysia Sarawak (F02/FRGS/1999/2020) for supporting this work.

REFERENCES

- Bazilevsky, A. V., Yarin, A. L., & Megaridis, C. M. (2007). Co-electrospinning of core-shell fibers using a single-nozzle technique. *Langmuir*, 23(5), 2311-2314. <https://doi.org/10.1021/la063194q>
- Bhardwaj, N., & Kundu, S. C. (2010). Electrospinning: A fascinating fiber fabrication technique. *Biotechnol Advances*, 28(3), 325-347. <https://doi.org/10.1016/j.biotechadv.2010.01.004>
- Deniz, A. E., Celebioglu, A., Kayaci, F., & Uyar, T. (2011). Electrospun polymeric nanofibrous composites containing TiO_2 short nanofibers. *Materials Chemistry and Physics*, 129(3), 701-704. <https://doi.org/10.1016/j.matchemphys.2011.06.018>
- Guillet, J. (1972). Fundamental processes in the UV degradation and stabilization of polymers. *Chemical Transformations of Polymers*, 135-144. Butterworth-Heinemann. <https://doi.org/10.1016/B978-0-408-70310-9.50012-5>
- He, J. H., Liu, Y., Mo, L. F., Wan, Y. Q., & Xu, L. (2008). *Electrospun nanofibers and their applications*. iSmithers.

- Hennrich, F., Krupke, R., Arnold, K., Stutz, J. A. R., Lebedkin, S., Koch, T., Schimmel, T., & Kappes, M. M. (2007). The mechanism of cavitation-induced scission of single-walled carbon nanotubes. *The Journal of Physical Chemistry B*, *111*(8), 1932-1937. <https://doi.org/10.1021/jp065262n>
- Huang, Z. M., Zhang, Y. Z., Kotaki, M., & Ramakrishna, S. (2003). A review on polymer nanofibers by electrospinning and their applications in nanocomposites. *Composites Science and Technology*, *63*(15), 2223-2253. [https://doi.org/10.1016/S0266-3538\(03\)00178-7](https://doi.org/10.1016/S0266-3538(03)00178-7)
- Kim, J. S., & Reneker, D. H. (1999). Mechanical properties of composites using ultrafine electrospun fibers. *Polymer Composites*, *20*(1), 124-131. <https://doi.org/10.1002/pc.10340>
- Kriha, O., Becker, M., Lehmann, M., Kriha, D., Kriegelstein, J., Yosef, M., Schlecht, S., Wehrspohn, R. B., Wendorff, J. H., & Greiner, A. (2007). Connection of hippocampal neurons by magnetically controlled movement of short electrospun polymer fibers - A route to magnetic micromanipulators. *Advanced Materials*, *19*(18), 2483-2485. <https://doi.org/10.1002/adma.200601937>
- Li, Y., Yin, X., Yu, J., & Ding, B. (2019). Electrospun nanofibers for high-performance air filtration. *Composites Communications*, *15*, 6-19. <https://doi.org/10.1016/j.coco.2019.06.003>
- Mark, S. S., Stolper, S. I., Baratti, C., Park, J. Y., Taku, M. A., Santiago-Aviles, J. J., & Kricka, L. J. (2008). Bioconjugation of alkaline phosphatase to mechanically processed, aqueous suspendible electrospun polymer nanofibers for use in chemiluminescent detection assays. *Macromolecular Bioscience*, *8*(6), 484-498. <https://doi.org/10.1002/mabi.200800016>
- Nakielski, P., Rinoldi, C., Pruchniewski, M., Pawlowska, S., Gazinska, M., Strojny, B., Rybak, D., Jezierska-Woźniak, K., urbanek, O., Denis, P., Sinderewicz, E., Czelejewska, W., Staszkievicz-Chodor, J., Grodzik, M., Ziai, Y., Barczewska, M., Maksymowicz, W., & Pierini, F. (2022). Laser-assisted fabrication of injectable nanofibrous cell carriers. *Small*, *18*(2), Article e2104971. <https://doi.org/10.1002/smll.202104971>
- Niemczyk-Soczynska, B., Dulnik, J., Jeznach, O., Kolbuk, D., & Sajkiewicz, P. (2021). Shortening of electrospun PLLA fibers by ultrasonication. *Micron*, *145*, Article 103066. <https://doi.org/10.1016/j.micron.2021.103066>
- Ramakrishna, S., Fujihara, K., Teo, W. E., Lim, T. K., & Ma, Z. (2005). *An Introduction to Electrospinning and Nanofibers*. World Scientific Publishing. <https://doi.org/10.1142/5894>
- Rennhofer, H., & Zanghellini, B. (2021). Dispersion state and damage of carbon nanotubes and carbon nanofibers by ultrasonic dispersion: A review. *Nanomaterials*, *11*(6), Article 1469. <https://doi.org/10.3390/nano11061469>
- Sakai, W., & Tsutsumi, N. (2010). Photodegradation and radiation degradation. In R. A. Auras, L. T. Lim, S. E. M. Selke & H. Tsuji (Eds.), *Poly(Lactic Acid): Synthesis, Structures, Properties, Processing, Applications, and End of Life* (pp. 413-421). John Wiley & Sons. <https://doi.org/10.1002/9781119767480.ch19>
- Sancaktar, E., & Aussawasathien, D. (2009). Nanocomposites of epoxy with electrospun carbon nanofibers: Mechanical behavior. *The Journal of Adhesion*, *85*(4-5), 160-179. <https://doi.org/10.1080/00218460902881758>
- Sawawi, M., Wang, T. Y., Nisbet, D. R., & Simon, G. P. (2013). Scission of electrospun polymer fibres by ultrasonication. *Polymer*, *54*(16), 4237-4252. <https://doi.org/10.1016/j.polymer.2013.05.060>

- Stoiljkovic, A., & Agarwal, S. (2008). Short electrospun fibers by UV cutting method. *Macromolecular Materials and Engineering*, 293(11), 895-899. <https://doi.org/10.1002/mame.200800171>
- Stowe, B. S., Fornes, R. E., & Gilbert, R. D. (1974). UV degradation of Nylon 66. *Polymer-Plastics Technology and Engineering*, 3(2), 159-197. <https://doi.org/10.1080/03602557408545026>
- Sun, Z., Zussman, E., Yarin, A. L., Wendorff, J. H., & Greiner, A. (2003). Compound core-shell polymer nanofibers by co-electrospinning. *Advanced Materials*, 15(22), 1929-1932. <https://doi.org/10.1002/adma.200305136>
- Suslick, K. S. (Ed.) (1988). *Ultrasound: Its Chemical, Physical and Biological Effects*. VCH Publishers.
- Verreck, G., Chun, I., Peeters, J., Rosenblatt, J., & Brewster, M. E. (2003). Preparation and characterization of nanofibers containing amorphous drug dispersions generated by electrostatic spinning. *Pharmaceutical Research*, 20(5), 810-817. <https://doi.org/10.1023/a:1023450006281>
- Watmough, D. J. (1994). Role of ultrasonic cleaning in control of cross-infection in dentistry. *Ultrasonics*, 32(4), 315-317. [https://doi.org/10.1016/0041-624x\(94\)90012-4](https://doi.org/10.1016/0041-624x(94)90012-4)
- Yixiang, D., Yong, T., Liao, S., Chan, C. K., & Ramakrishna, S. (2008). Degradation of electrospun nanofiber scaffold by short wavelength ultraviolet radiation treatment and its potential applications in tissue engineering. *Tissue Eng Part A*, 14(8), 1321-1329. <https://doi.org/10.1089/ten.tea.2007.0395>
- Zakrzewska, A., Bayan, M. A. H., Nakielski, P., Petronella, F., De Sio, L., & Pierini, F. (2022). Nanotechnology transition roadmap toward multifunctional stimuli-responsive face masks. *ACS Appl Mater Interfaces*, 14(41), 46123-46144. <https://doi.org/10.1021/acsami.2c10335>



A Comparison of the Performance of MAPbI₃ and MASnI₃ as an Inverted Perovskite Structure Using NiO as HTL Through Numerical GPVDM Simulation

Subathra Muniandy^{1*}, Muhammad Idzdiyar Idris¹, Zul Atfyi Fauzan Mohammed Napiah¹, Zarina Baharudin Zamani¹, Marzaini Rashid² and Luke Bradley³

¹Faculty of Electronics and Computer Engineering, University Technical Malaysia Melaka (UTeM), 75450 Melaka, Malaysia

²School of Physics, University Science Malaysia, 11800 USM, Penang, Malaysia

³School of Engineering, Newcastle University, England

ABSTRACT

Perovskite solar cells (PSCs) are solar cells that have intriguing characteristics such as environmental friendliness and the capability for high power conversion efficiency, which have attracted study from both scientific investigation and analytical standpoints. However, lead toxicity has become a significant barrier to the widespread use of PSCs. Due to the serious environmental implications of lead, an environmentally compatible perovskite is required. Tin-based perovskite has a considerable impact, showing that it is a good hole extraction material with good mobility and low effective mass. In this study, we explore the impacts of perovskite and hole transporting layer (HTL) thickness, and intensity of light limitations, in inverted PSCs based on the structure of FTO/NiO/MAPbI₃/ZnO/Ag and FTO/NiO/MASnI₃/ZnO/Ag incorporating GPVDM (General-purpose Photovoltaic Device Model) to evaluate if MASnI₃ is a viable substitute to MAPbI₃. From the simulation results, the optimized parameters obtained for PCSs under 1 sun incorporating MASnI₃ were 27.97%, 0.88 a.u., 0.92 V, and 34.45 mA/cm². Instead, the optimized parameters obtained for PCSs incorporating MAPbI₃ were 24.94%, 0.88 a.u., 0.90 V, and 31.03 mA/cm². The thickness of the film of both PSC architectures was optimized to provide the best suitable result. The findings show that MASnI₃ is employed as a promising perovskite layer in PSCs instead of MAPbI₃.

ARTICLE INFO

Article history:

Received: 01 September 2022

Accepted: 25 January 2023

Published: 21 July 2023

DOI: <https://doi.org/10.47836/pjst.31.5.22>

E-mail addresses:

m022020016@student.utem.edu.my (Subathra Muniandy)

idzdiyar@utem.edu.my (Muhammad Idzdiyar Idris)

zulatfyi@utem.edu.my (Zul Atfyi Fauzan Mohammed Napiah)

zarina@utem.edu.my (Zarina Baharudin Zamani)

marzaini@usm.my (Marzaini Rashid)

luke.bradley@strath.ac.uk (Luke Bradley)

*Corresponding author

Keywords: GPVDM software, MAPbI₃, MASnI₃, nickel oxide, perovskite solar cells

Current Affiliation

Luke Bradley

Rolls Royce UTC, University of Strathclyde, Glasgow, Scotland, United Kingdom

INTRODUCTION

Solar energy offers several distinct benefits over other renewable energy sources, including the worldwide dispersion of sunshine and the decentralized nature of solar energy output (Mohtasham, 2015). Perovskite solar cells (PSCs) have emerged as the "third generation of solar cells," as alternative renewable energy to solve environmental implications such as global warming and greenhouse gases (Ibn-Mohammed et al., 2017). PSCs have been the most recent solar cell type and among the most promising thin-film PV technologies. Strong absorption coefficients, excellent charge carrier mobilities, diffusion duration, and solution processability are the desired properties that make perovskites a potentially new front-runner material for thin-film solar technology (Khadka et al., 2017). These qualities are required for their real implementation in semiconductor-based devices such as solar cells. Sustainable substitutes to present power-generating systems are critical to conserving the planetary environment by ensuring long-term economic prosperity. The recent discovery of halide perovskites as solar energy harvesting and hole-transport materials has contributed to the development of solar technology. Among the several types of PSCs, organic-inorganic metal halide PSCs have garnered substantial interest in recent years due to their high power conversion efficiency (PCE) and ease of fabrication at a cheap cost (Yongjin et al., 2020). The ABX_3 perovskite framework is used in organic-inorganic hybrid perovskite substances depending on metal halides. This architecture comprises networks of corner-sharing BX_6 octahedra, whereby B is a metal cation (usually Sn^{2+} or Pb^{2+}), and X is generally F^- , Cl^- , Br^- , or I^- . The A cation is used to equalize the overall charge or to represent a tiny molecular group (Hao et al., 2014). Methylammonium lead tri-iodide ($MAPbI_3$) has often been known to be a perovskite content and is widely employed in PSCs. Even though the efficiencies have now exceeded 20%, long-term stability is the major obstacle to commercializing PSCs on a broader level. As the lead in $MAPbI_3$ is extremely hazardous, industrial applications of $MAPbI_3$ -based PSCs are severely limited (Conings et al., 2015; Wang, Phung et al., 2019; Wang, Mujahid et al., 2019), resulting in interest in lead-free PSCs in the sector of solar technologies.

Experts refer to the idea that inorganic halide perovskites, like Sn-, Ag-, Sb-, Bi-, Cu-, and Ge-based solar cells might be employed as lead substitutes (Green et al., 2014; Song et al., 2017). A tin-based perovskite, $MASnI_3$, is a possible option for lead-free PSCs owing to its excellent bandgap of 1.3eV, which are even narrower than $MAPbI_3$ (Baig et al., 2018). It was reported that $MASnI_3$ perovskite has high absorption efficiency with excellent optical features and the broadest light-absorption spectrum compared to $MAPbI_3$ (Du et al., 2016). Sn-based perovskites are environmentally beneficial since they decompose to SnO_2 (from Sn^{4+}) when exposed to air. Sn-based perovskites and Pb-based perovskites are comparable in their fundamental physical features (Ke & Kanatzidis, 2019; Schileo & Grancini, 2021). Vishnuwaran et al. (2022) have compared the performance of $MASnI_3$

and FASnI₃ perovskite materials. Modification in thickness and temperature of the absorber layer revealed that MASnI₃ had a higher cell efficiency (23.74%) than FASnI₃ (23.11%). Germanium (Ge) is another possible replacement for lead. Recent computational and experimental research has demonstrated that Ge–Sn mixtures are an excellent candidate for enhancing the performance of Ge²⁺-based PSCs. Upon doping a tiny amount (5%) of Ge²⁺ into Ge–Sn mixed halide perovskites, an overall efficiency of 4.48% was attained (Vishnuwaran et al., 2022). The PCE grew to 6.9% after exposure to an N₂ environment for 72 hr. Simulation design and investigation of the performance of Sn-Ge-based perovskite in a planar inverter structure yield a PCE of 24.20%, such substantial enhancement established by trap density at the interface layers (Vishnuwaran et al., 2022). Furthermore, Pindolia et al. (2022) proposed an inorganic RbGeI₃-based PSC that acquired an efficiency of 10.11% and a greater fill factor (FF) of 63.68% by analyzing alternative inorganic HTL and ETL layers. Like another example of Pb-free PSCs with great promise as light-absorbing perovskite, Cs₂TiBr₆, and Cs₂PtI₆ have a good absorption coefficient, a lengthy carrier lifespan, and outstanding stability with adequate bandgaps (1.8 eV and 1.4 eV, respectively). The value can be increased by refining the interface between perovskite and HTL. For this study, MASnI₃ was chosen and tested further as a potential replacement for lead-based PSCs.

Aside from the performance of perovskite material, the functionality and maximum efficiencies of PSCs are heavily influenced by the HTL. In the optimization of PSC, HTL can improve the overall performance of PSC by reducing series resistance, enhanced fill factor (FF), and open-circuit voltage (V_{oc}) while providing a transport medium for holes to the counter electrode (Yang et al., 2017). Owing to its improved chemical stability, cheap cost, and appropriate energy level, NiO, a direct bandgap inorganic material, has lately caught the scientific community's interest as a viable HTL for stable and efficient PSCs (Hossain et al., 2020). NiO is a significant transition metal oxide that may be easily deposited using a variety of processes, including spray pyrolysis (Danjuma, 2019), sputter deposition (Mulik, 2019), thermal decomposition (Guo et al., 2018), precipitation (Chowdhury et al., 2018), hot-casting (Abzieher et al., 2018), and electrodeposition (Xi et al., 2019). NiO demonstrated good potential in organic solar cells and has a work function of between 5 and 5.6 eV, which satisfies the criteria for an HTL (Nguyen, 2018). NiO, as a p-type semiconductor material, has been effectively used in PSCs with inverted architectures, according to its adequate carrier mobility and good work functionality, which can fit perovskite materials' energy (Chen et al., 2017). The energy band diagram reveals the good positioning of the NiO in such a way as to foster hole extraction from the perovskite material (Nkele et al., 2020). Besides that, there are already many research articles experimentally showing that NiO is a potential material for HTL with good efficiency of 17.75% (Thakur et al., 2020), 19.10% (Mali et al., 2018) and 20.8% (Mahmoudi et al., 2021) which undergone different synthesis processes. In previous work, the General-Objective

Photovoltaic Devices Model (GPVDM) has been used to determine the optimal material parameter for PSCs. GPVDM is a research-leading electrical and optical solver that the electrical transfer characteristics and the optical model pattern of PSCs (MacKenzie, 2016). The PCE of PSC was reported to increase from 9.96 to 12.9% through optimization of the layer thickness using this model (Hima et al., 2018). On the other hand, the effect of the thickness of MAPbI₃ as perovskite with Spiro-OMeTAD as HTL and different ETL material (TiO₂ and SiO₂) has a significant effect on overall PSC efficiency with reported values of 5.6%, 14.5%, and 14.7%, respectively (Mishra & Shukla, 2020; Abdulsalam et al., 2018; Yasodharan et al., 2019). The best-reported efficiencies were obtained with optimal 200 nm and 300 nm ETL thicknesses, respectively. A comparative study on the effect of perovskite layer thickness and charge mobilities in PSCs was also observed with an efficiency of 18.43% (Sittirak et al., 2019). The influence of light intensity has achieved an efficiency from 8.5 to 10%, which indicates that performance can be improved by maximizing the light falling on the solar cell's surface (Mekky, 2020).

There are more solar cell models besides GPVDM that investigate PSC-based structures with MAPbI₃, MASnI₃, NiO, and ZnO Rahman et al. (2019) used SCAPS-1D to construct a p-i-n structure with three distinct ETL layers (TiO₂, ZnO, and SnO₂) and compared their properties to that of MAPbI₃ as the perovskite layer and NiO as the HTL layer. The research proved that using ZnO as the ETL allowed for the highest possible PCE of 17.84%. The identical model was also used to simulate a MASnI₃-based PSC along with NiO as the HTL and PCBM as the ETL to study the details of the device by changing the layer thickness, defect density at junctions, density of states, and metalwork efficiently (Shamna et al., 2020). It is estimated from the simulation result that the designed structure has attained an efficiency of 22.95% with the optimal absorber layer thickness of 600 nm. Another study used the Silvaco ATLAS device model to construct a lead-free titanium PSC (Cs₂TiBr₆) using TiO₂ as the ETL and comparison of three HTLs (CuPc, P₃HT, and NiO), in which NiO gaining the maximum PCE of 8.5% (Samanta et al., 2020). Although the efficiency of Cs₂TiBr₆ based-PSC is poor compared to lead-based PSCs, its long-term stability and, most significantly, its eco-friendly nature are predicted to drive it to the forefront of future solar cell application. In addition, Karimi et al. (2020) performed a comparative analysis of the SCAPS and AMPS software applications to explore the impact of ZnO and SnO₂ on PSC performances.

Aside from NiO as HTL, many inorganic materials are discovered as HTL layers to study the performance of lead-free PSCs. Anand Kumar Singh et al. (Singh et al., 2021) conducted a simulation study that focuses on MASnI₃ perovskite sandwiched between CuO₂ as HTL and TiO₂ as ETL, achieving maximum efficiency of 27.43% by varying various parameters with the aid of SCAPS-1D simulator. CZTS has recently been analyzed as HTL in tin-based PSC by optimizing layer thickness, energy bandgap, and operating temperature that acquire the best PCE of 20.28% (Reyes et al., 2021). For the first time, the inorganic

material CuSbS₂ was employed as HTL in alignment with the MASnI₃ as the active layer, and the resulting device achieved an efficiency of 24.1% and further boosting the doping concentration of MASnI₃ contributed to an increase in PCE value. (Devi & Mehra, 2019). According to the literature review, inorganic materials are now well-equipped to replace the costly Spiro-MeOTAD and demonstrate the potential to become the ideal alternative for use in the future. Several solvers programs are available, including open source and subscription to model and simulate solar cells. At the same time, certain simulation software shares a common module but varies in terms of speed, features, the quality of the user interfaces, and how easy or difficult to use (Kowsar et al., 2019). It is important to note that this study used an optimized configuration that achieved the highest possible efficiency of 27.43%, the maximum value documented for this configuration by GPVDM simulation software.

From previous work, factors such as the thickness of the film, carrier mobilities, defect density, and light intensity influence device performance optimization. This work investigated the effect of PSCs on the configuration of MASnI₃, which was investigated through GPVDM simulations. During the simulations, the thickness of perovskite, the thickness of HTL, and the light intensity were varied to attain the optimal values to maximize the PCE. A comprehensive analysis of the electrical and optical characteristics affecting each performance of MASnI₃ and MAPbI₃ as perovskite with NiO as HTL has never been described. Furthermore, the results of this inquiry may be extremely valuable and give excellent direction for the understanding of the acquired data, which will aid in revealing the primary processes of PCE rise in the structure of MASnI₃ as perovskite and NiO as HTL.

METHODOLOGY

In Figure 1, the device comprises a layered configuration made from an inverted planar structure (FTO/NiO/Perovskite/ZnO/Ag). Two absorbance layers were compared as the primary carrier producer (MASnI₃ and MAPbI₃). P-type (HTL = NiO) and n-type (ETL = ZnO) were placed on the top and bottom perovskite layers. The close boundary conditions were applied to the simulation environment, where fluorine tin oxide (FTO) was selected as a glass substrate and silver (Ag) was chosen as the back-electrode layer designated as anode and cathode, respectively. The simulation studies in this work were performed using the GPVDM tool, a freeware solar cell modeling software for photovoltaic systems. The model captures the joint movement of electrons, holes, and transport momentum equation in the orientated area to reflect the movement of loads within the device. The GPVDM software often only provides specialized simulation materials. The NiO, MAPbI₃, and MASnI₃ material was manually introduced to the GPVDM software following the technique in (MacKenzie, 2016). The absorption and refractive index data of NiO, MAPbI₃, and MASnI₃ were extracted from the previous work reported by Bakr et al. (2015) and Sun et

al. (2016). This work focuses much on the perovskite and HTL layer, which were largely set to evaluate their effectiveness as active layers.

Both device structure was simulated under one sun AM 1.5G illumination (1 kW/m²; T = 300°K). Table 1 summarizes the designed default GPVDM software variables used during the simulation. The physical parameters of MAPbI₃ and MASnI₃, such as bandgap (E_g), electron affinity (X_i), density electron states (cm⁻³), density hole states (cm⁻³), electron mobility (cm²/Vs), hole mobility (cm²/Vs) and relative permittivity (ε_r) were taken from previous experimental and simulation studies (Ahmed et al., 2019; Mohammadi et al., 2021; Hima et al., 2018; Then et al., 2021). Three different approaches were performed to find the optimum parameters of the solar cell, which are (1) different thicknesses of perovskite layer ranging from 50 to 500 nm, (2) different thicknesses of HTL layer varying from 100 to 800 nm, and (3) different values of light intensity. The activated perovskite layer and HTL layer have quite a significant effect on the efficiency of the cells.

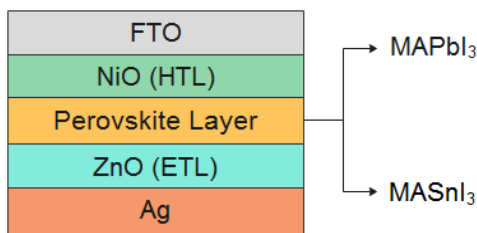


Figure 1. Schematic representation of inverted PSCs with MASnI₃ and MAPbI₃ perovskite material

RESULTS AND DISCUSSION

Optimization of the perovskite layer thickness is one of the approaches for increasing the PCE. A sufficient thickness is necessary for a successful perovskite device to achieve enough light absorbance and effective charge carrier capture. A perovskite is sufficiently thick in the region of its absorption; then, it leads to an excellent photovoltaic performance (Jakobson et al., 2021; Rai et al., 2020). The thickness of the perovskite film plays an essential part in the device for optimal carrier generation. The influence of perovskite film thickness on cell efficiency was evaluated by computational

Table 1

Simulation parameter of both perovskite layers and NiO (Ahmed et al., 2019; Du et al., 2016; Hao et al., 2014)

No.	Parameters	Layers		
		MAPbI ₃	MASnI ₃	NiO
1.	Bandgap energy, E _g (eV)	1.55	1.3	1.46
2.	Electron affinity, X _i (eV)	3.93	4.17	3.80
3.	Density electron states (cm ⁻³)	1.3x10 ²⁶	1x10 ¹⁸	-
4.	Density hole states (cm ⁻³)	9.1x10 ²⁶	1x10 ¹⁸	1x10 ¹⁸
5.	Electron mobility (cm ² /Vs)	2x10 ⁻¹	2x10 ⁻²	2.8
6.	Hole mobility (cm ² /Vs)	2x10 ⁻¹	2x10 ⁻⁴	2.8
7.	Relative permittivity, ε _r	6.5	8.2	11.7

models, with a thickness range of 50 to 500 nm (Yasodharan et al., 2019). According to Figures 2(a) and 2(d), the PSC with the MASnI₃ has the maximum PCE of 12.88% and J_{SC} of 16.74 (mA/cm²), whereas the PSC with the MAPbI₃ has the greatest PCE of 16.96% and J_{SC} of 22.53 (mA/cm²). The higher the thickness of the perovskite layer, the greater the performance of PCE produced.

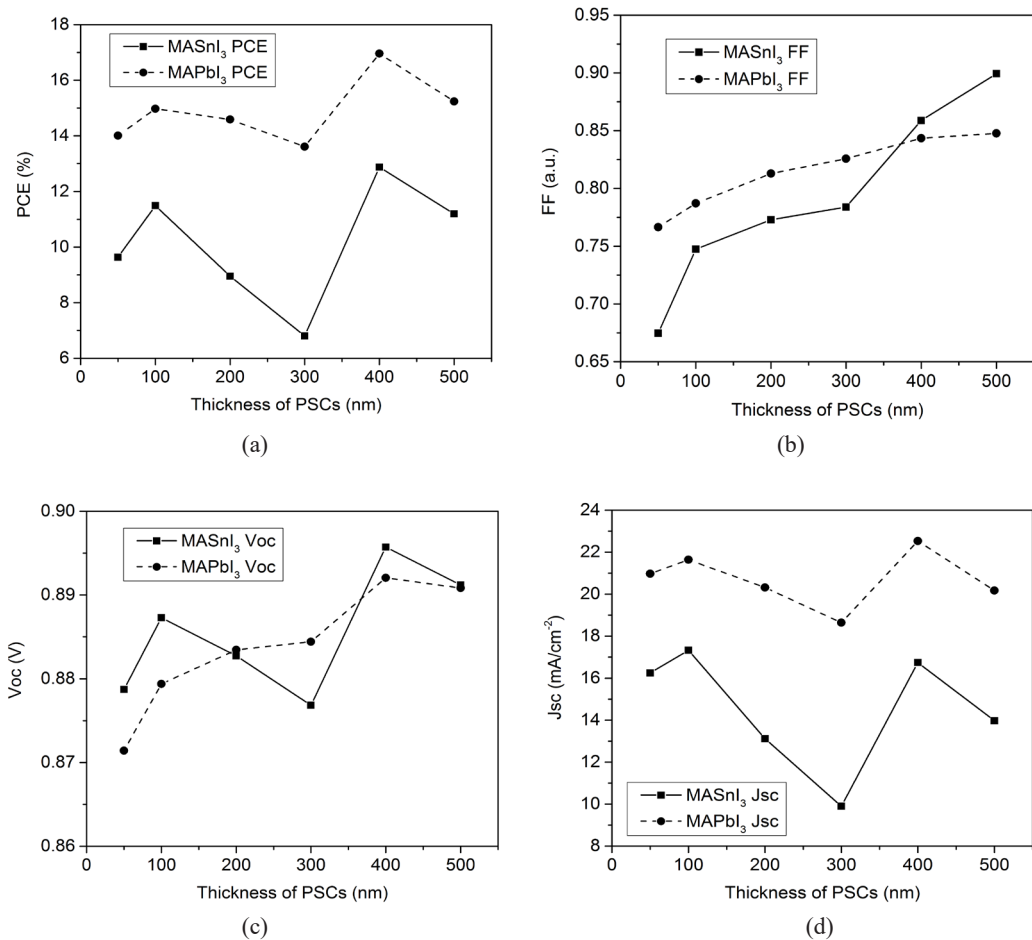


Figure 2. The optimized outcome of perovskite thickness generated by the GPVDM software focusing on the comparison between MASnI₃ and MAPbI₃ produced at 400 nm of (a) PCE, (b) FF, and (c) V_{OC}, and (d) J_{SC}

The thickness of the perovskite layer increases slowly from 50 to 100 nm, and after that, it decreases when approaching to 200 to 300 nm thickness range. It causes an abrupt drop in the V_{OC} for both perovskite layers (Figure 2c). In contrast, the PCE and J_{SC} showed the highest value at the thickness of 400 nm. It explains how, after the perovskite has reached its ideal thickness, it regulates the interfacial structuring to improve light trapping, resulting in a greater carrier concentration and, as an outcome, a higher J_{SC} (Rai et al., 2020). It is

important to mention that even though the computed J_{SC} for the $MASnI_3$ perovskite device is less efficient than that for the $MAPbI_3$ device, the greatest current density above 15 mA/cm^2 can be achieved when integrating $MASnI_3$ perovskite under the bandgap of the 1.30 eV. However, at the thickness of 500 nm, there is also a small significant decrease in PCE and V_{OC} . In contrast to PCE and V_{OC} , the outcome of FF keeps increasing with perovskite thicknesses from 50 to 500 nm (Figure 2b). It is due to the thicker perovskite layer that absorbs more significant photons using broader wavelengths, thus increasing the production of electron and hole pairs (Lin et al., 2017).

Although the PCE of $MASnI_3$ is lower compared to $MAPbI_3$, the FF of $MASnI_3$ is larger, which implies lower recombination at the interface. The V_{OC} also constantly increased as the thickness of the perovskite layer increased but dropped when it reached 500 nm, as shown in Figure 2(c). It is also the same case with the simulation study made by Hima et al. (2019), which shows that the PCE drops after the thickness of the perovskite layer reaches the optimal value at 600 nm. As the thickness of the perovskite approached its optimal value, the recombination rate increased, and the efficiency of the cell decreased as a consequence.

In addition, the current simulation study shows much better results than the preceding simulation results using $MAPbI_3$ as a perovskite in GPVDM, which were obtained about 12.83% at 200 nm (Hima et al., 2018) and 14.7% at 300nm (Abdulsalam et al., 2018). Instead, Ahmed et al. (2019) reported that the performance hit as much as 20% at a thickness of 850 nm. A thicker layer of perovskite causes it difficult for charge carriers created by photons to be carried away, reducing the device's effectiveness. This statement also agreed with the report by Nam et al. (2010) about bulk heterojunction organic solar cells and Sievers et al. (2006) regarding polymer bulk-heterojunction solar cells. The optimal thickness should be determined by a balance between the absorption range and the diffusion length of the material (Ragb et al., 2021). Besides that, the obtained result showed higher efficiency than the experimental result of Srivastava et al. (2021), using $MAPbI_3$ perovskite with obtained PCE of 14.44%. Another report also focuses on fabricating $MAPbI_3$ perovskite achieved an efficiency of 14.79% with regulated moisture of 35% in ambient air using a one-step spin coating method (Soucase et al., 2022). In conjunction, solution-processed PSCs based on $MASnI_3$ as the light-absorbing material achieved a PCE of 5.8% (Hao et al., 2014). Based on the analysis between $MAPbI_3$ and $MASnI_3$, the thickness of the perovskite layer plays a major role in increasing the performance of the photovoltaic device (Bag et al., 2020). Additionally, this work obtained efficiency much higher than the experimental outcome, which recently studied NiO nanocrystal film as HTL for Sn-Pb-based PSCs with PCE up to 18.8% (Chen et al., 2021).

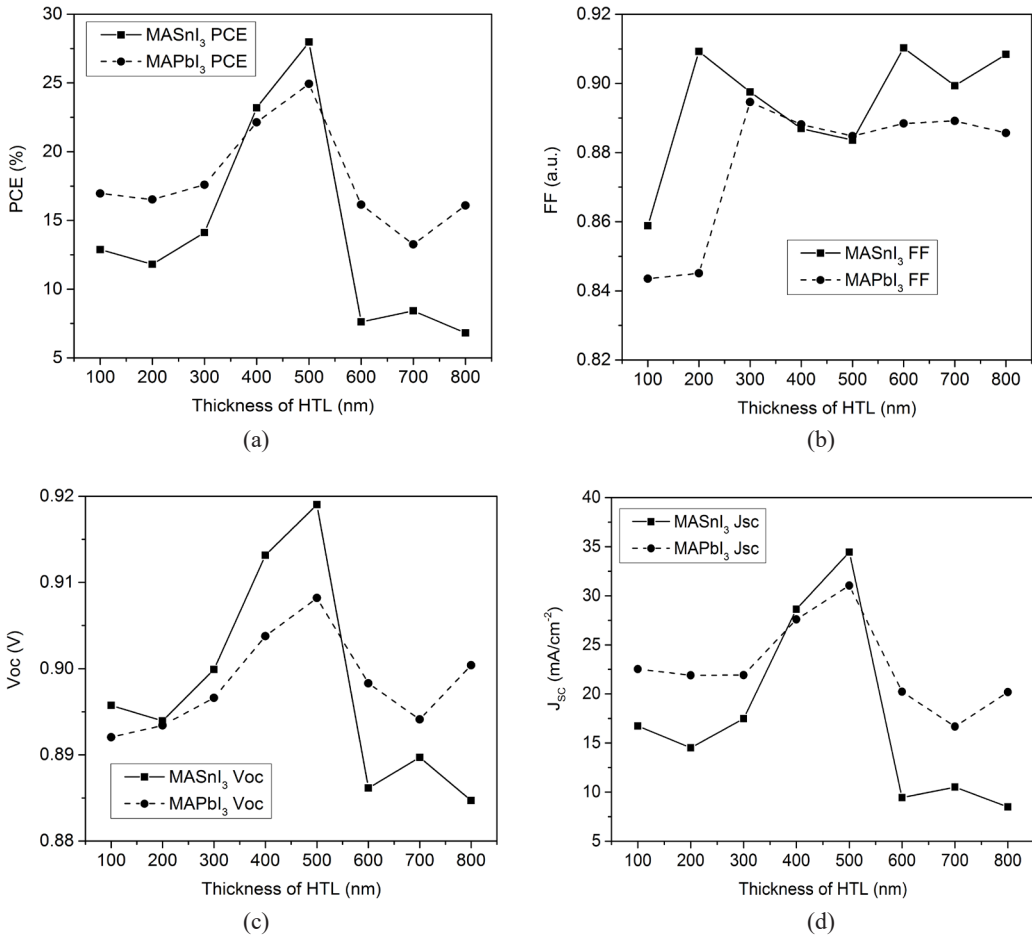


Figure 3. The optimized thickness of NiO as HTL generated by the GPVDM software focusing on the comparison of MASnI₃ and MAPbI₃ obtained at 500 nm of (a) PCE, (b) FF, (c) V_{oc}, and (d) J_{sc}

Additionally, the impact of light intensity on each solar cell affects all electrical parameters. The quantity of 1 Sun indicates the normal AM1.5 or 1 (kW/m²) lighting on a PSC. Equally, a solar cell system with 10 (kW/m²) could run at 10 suns. The PCE of MASnI₃ is much higher than that of MAPbI₃, which is at 29.90% and 26.67%, as seen in Figure 4(a). The growing levels of PCE were seen for both materials as the intensity of the light increased up to 10 (kW/m²), which has been previously found in Mekky (2020) utilizing a hybrid perovskite-based solar cell employing a GPVDM model. The above findings indicate that the PCE relies on light-intensity instances and exhibits an extraordinary increase in light-intensity energy transformation. The same trend was also observed in the graph of Figure 4(c); as the intensity of the light increased, the V_{oc} also kept increasing, which is similarly reported by Liu et al. (2017) using MAPbI₃ as a perovskite layer.

In contrast, the FF is mainly influenced by the amount of light intensity (Figure 4b). Both structure FF rise when the light intensity is less than 1 kW/m². However, when the intensity of the light hits more than 1 kW/m², the FF decreases owing to the impact of series resistance (Mekky, 2020). Figure 4(d) illustrates that the J_{SC} from a solar cell depends linearly on the light intensity, such that a device operating under 10 suns would have 10 times the J_{SC} as the same device under one sun operation. However, this effect does not increase efficiency since the incident power also increases linearly. Instead, the efficiency benefits arise from the dependence of the V_{OC} on short circuits. Subsequently, the same trend of J_{SC} was observed by Kassahun Lewetegn Damena through GPVDM in which the light intensity was varied from 1 sun to 40 suns (Damena, 2019).

The J–V curves of the devices were illustrated in Figure 5, recorded the MASnI₃ perovskite-based solid-state device exhibits the highest mean J_{SC} of 32.05 mA/cm² and

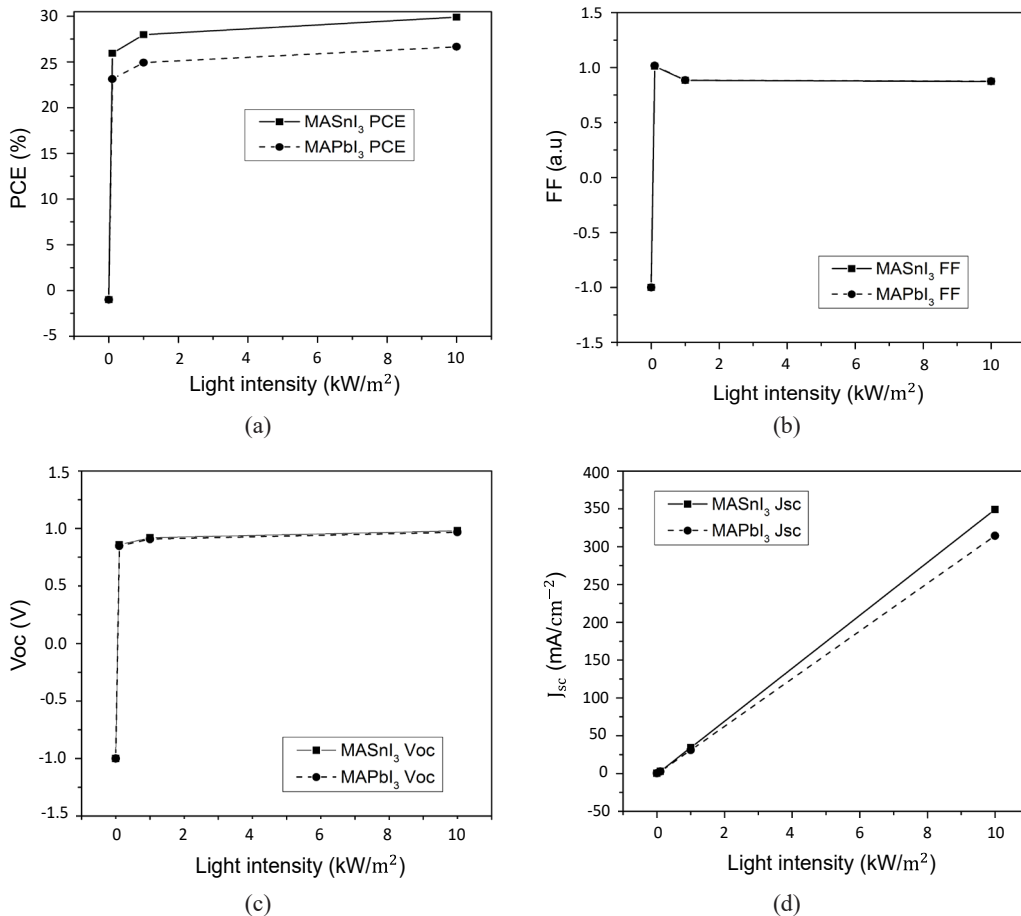


Figure 4. The influence of light intensity on MASnI₃ and MAPbI₃ perovskite achieved an optimum value at 10 (kW/cm²) of (a) PCE, (b) FF, (c) V_{OC}, and (d) J_{SC}

V_{OC} of 1.6 V under AM 1.5G solar illumination. Meanwhile, the MAPbI₃ device showed a slightly lower J_{SC} of 27.93 mA/cm² and V_{OC} of 1.2 V. A substantial rise in V_{OC} was detected in the MASnI₃ device compared to the MAPbI₃ device. The current analysis also demonstrates the potential ability of tin-based perovskite contrasted with lead-based perovskite. Previously, Mandadapu et al. (2017) presented a simulation regarding MASnI₃ PSC with the thickness of 600 nm obtained PCE, J_{SC} , and V_{OC} of 24.82 %, 25.67 mA/cm² and 1.04 V correspondingly. Nevertheless, another simulation study of MASnI₃ compared to MAPbI₃ reported by Shyma and Sellappan (2021) gained an efficiency of 24.3 % with J_{SC} of 32.30 mA/cm², which is higher than the current study yet still shows a lower V_{OC} of 1.2 V. Regardless of the simulation studies, Li et al. (2019) demonstrated an experimental result of MASnI₃ developed using a two-step technique for the deposition of solid and homogeneous perovskite layers, reaching the optimum value of PCE at 7.13 %, J_{SC} at 22.91 mA/cm² and V_{OC} at 0.486 V.

It is well known that the present simulation result of MASnI₃ PSC has enhanced the photovoltaic performances of the devices compared to the MAPbI₃ PSC. It can be supported by the fact that by integrating the AM 1.5G solar spectrum below the bandgap of MASnI₃ (1.30 eV) perovskite, the greatest current density that can be produced, despite the lower J_{SC} found for MAPbI₃ perovskite (Hao et al., 2014). Besides that, this could be owing to the perovskite's wide optical absorbance cross-section and the well-developed interstitial pore opening by the hole conductor, which allowed for this tremendous current density produced by MASnI₃ (Cao & Yan, 2021; Du et al., 2016). Additionally, the insertion of the NiO HTL in the structure significantly improves the PCE of the solar cells, which is attributed due to the suitable band alignment of the NiO and perovskite.

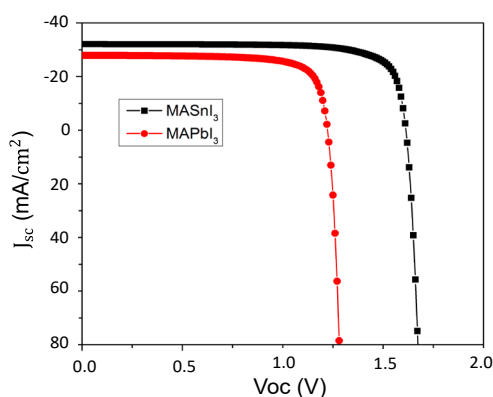
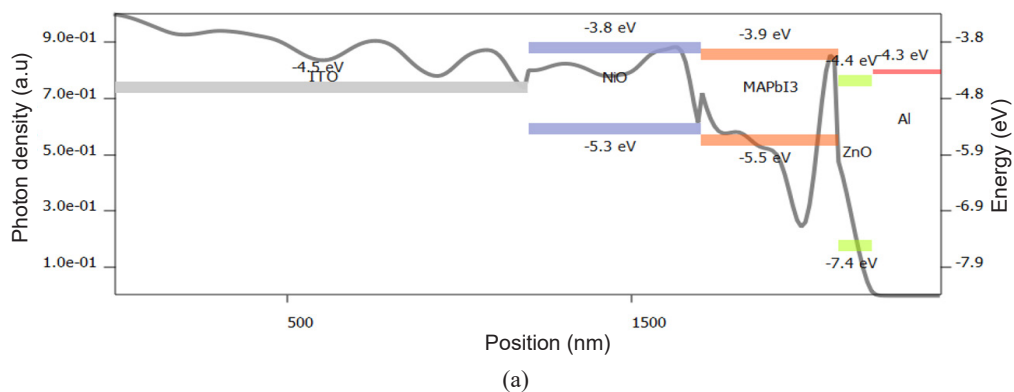


Figure 5. The optimized curve of photocurrent density-voltage (J-V) achieved higher by MASnI₃ at J_{SC} of 32.05 mA/cm² and V_{OC} of 1.6 V in parallel with MAPbI₃ obtained at J_{SC} of 27.93 mA/cm² and V_{OC} of 1.2 V as perovskite

The photon density distribution corresponding wavelength as a function of the position of the MAPbI₃ device layers was presented in Figure 6(a). Most photons are absorbed in the perovskite absorbance layer. Therefore, massive electrons and holes have promoted the device's efficiency (Said & Woon, 2019). The same trend was also observed for the MASnI₃ PSC in Figure 6(b). The photon of both PSCs was more significant from FTO and decreased after the Ag electrode was incorporated. When the light penetrates an absorber layer of the film, the process of pumping electrons through the valence band into the conduction band

occurs. The electrons quickly start to move to the ETL of the n-type ZnO, whereas the holes begin to migrate to the HTL of the p-type NiO. The ZnO has a lower work function (-4.4 eV) which matches with the lowest unoccupied molecular orbital (LUMO) energy level of MAPbI₃ perovskite film (LUMO = -3.9 eV) and MASnI₃ perovskite film (LUMO = -4.2 eV). The band structure of perovskite/ZnO further accelerates the electron transport to the Ag cathode (LUMO = -4.3 eV). NiO work function (-5.3 eV) must be aligned as closely as possible with the highest molecular orbital (HOMO) energy level of the ITO (HOMO = -4.0 eV) to deliver accurate hole direction. The minority and majority carriers are generated when a photon is absorbed. Absorbed photons at the HTL interface (NiO) showed that the MASnI₃ structure absorbs higher than the MAPbI₃ structure but decreases in time. It indicates that the stored charge at the hole-extracting interface of NiO could have a strong downward band bending on the perovskite side at the perovskite/HTL interface (Ravishankar et al., 2019). It is consistent with that tin-based perovskite produces the highest efficiency levels. The resulting shift of NiO in the work function leads to a more beneficial energy level alignment with the MASnI₃ perovskite, which is believed to facilitate charge extraction. Therefore, the photovoltaic performance is enhanced by an appropriate work function in relation to the perovskite interfaces. The downward band bending is potentially detrimental to charge extract and recombination kinetics because it sends holes back to the perovskite surface, which could increase the device's performance. The driving energy for hole injection happens from the valence band maximum of the HTL and should be greater in energy than the valence band maximum of the perovskite (Haider et al., 2022).

However, the photon density produced at the MAPbI₃ interface is higher than at the MASnI₃ interface. The MAPbI₃ perovskites have much higher radiative recombination coefficients, leading to the situation that MASnI₃ is much less charge carrier densities faced in photovoltaic at intensities around 1 sun (Kirchartz, 2019). Therefore, only a small percentage of photons will be created within the interface of MASnI₃.



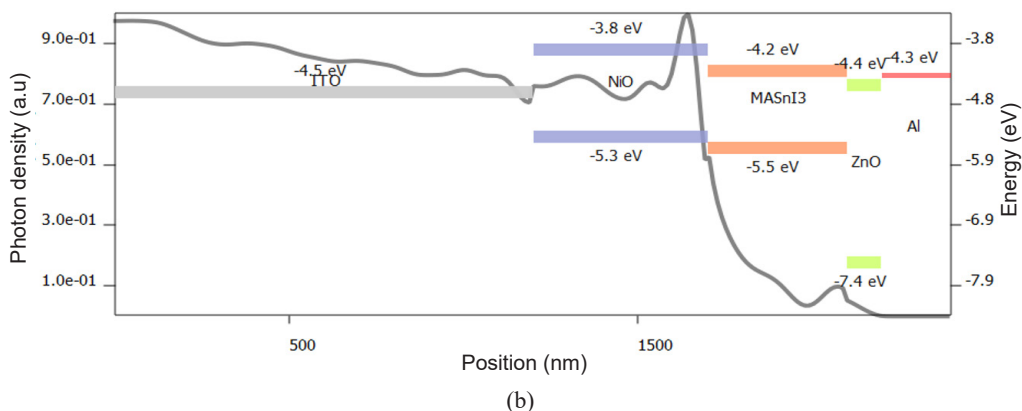


Figure 6. Photon density distributions (a) MAPbI₃ and (b) MASnI₃ as perovskite with the AM 1.5G solar spectrum interfaced with the thickness of the device

CONCLUSION

In summary, tin-based perovskites have excellent optoelectronic properties which lead to a promising candidate for efficient lead-free PSCs. Under 1 sun light intensity the tin-based perovskites have achieved the highest PCE of 27.97% while the lead-based perovskite achieved PCE at 24.94% using GPVDM software. During the optimization of perovskite layer thickness both perovskite material found at 400 nm in which the higher efficiency was attained by lead-based perovskite. Nevertheless, after the evaluation made on the HTL thickness the highest efficiency was noticed on tin-based perovskites at 500 nm with high J_{SC} and V_{OC} value. The findings imply that lead-free MASnI₃ has a huge potential as an absorber layer when combined with a robust inorganic hole transport material like NiO. Moreover, further increase of light intensity in each structure implies a progressive increase in PCE. Encouragingly, simulation models produced a maximum PCE of more than 20% that can be achieved from tin-based PSCs under optimized conditions. A deeper study on the previous simulation and experimental of each of the photovoltaic parameters such as PCE, J_{SC} , V_{OC} , and FF reveals that the Sn-based devices perform better for high efficiency in lead-free PSC. In comparison to, lead-based counterparts, tin-based PSCs have a higher V_{OC} with a record value of 1.6 V, which consider higher than previous studies. Importantly, these computational results demonstrate that the absorber and HTL layers significantly impact system efficiency. The construction of a high-efficiency tin-based PSCs will be aided by this simulation study.

ACKNOWLEDGMENTS

This work was supported by the Ministry of Higher Education Malaysia and the Technical University of Malaysia Melaka through the Fundamental Research Grant Scheme with

Project No FRGS/1/2020/FKEKK-CETRI/F00423 and PJP/2021/FTKKEE/S01822. The author also acknowledges the provider of the free version of GPVDM software.

REFERENCES

- Abdulsalam, H., Babaji, G., & Abba, H. T. (2018). The effect of temperature and active layer thickness on the performance of CH₃NH₃PbI₃ perovskite solar cell: A numerical simulation approach. *Journal for Foundations and Applications of Physics*, 5(2), 141-151. <http://sciencefront.org/ojs/index.php/jfap/article/download/89/58>
- Abzieher, T., Schwenzer, J. A., Sutterluti, F., Pfau, M., Lotter, E., Het-terich, M., Lemmer, U., Powalla, M., & Paetzold, U. W. (2018). Towards inexpensive and stable all-evaporated perovskite solar cells for industrial large-scale fabrication. In *2018 IEEE 7th World Conference on Photovoltaic Energy Conversion (WCPEC)(A Joint Conference of 45th IEEE PVSC, 28th PVSEC & 34th EU PVSEC)* (pp. 2803-2807). IEEE Publishing. <https://doi.org/10.1109/PVSC.2018.8547364>
- Ahmed, S., Shaffer, J., Harris, J., Pham, M., Daniel, A., Chowdhury, S., Ali, A., & Banerjee, S. (2019). Simulation studies of non-toxic tin-based perovskites: Critical insights into solar performance kinetics through comparison with standard lead-based devices. *Superlattices and Microstructures*, 130, 20-27. <https://doi.org/10.1016/j.spmi.2019.04.017>
- Bag, A., Radhakrishnan, R., Nekovei, R., & Jeyakumar, R. (2020). Effect of absorber layer, hole transport layer thicknesses, and its doping density on the performance of perovskite solar cells by device simulation. *Solar Energy*, 196, 177-182. <https://doi.org/10.1016/j.solener.2019.12.014>
- Baig, F., Khattak, Y. H., Mari, B., Beg, S., Ahmed, A., & Khan, K. (2018). Efficiency enhancement of CH₃NH₃SnI₃ solar cells by device modeling. *Journal of Electronic Materials*, 47, 5275-5282. <https://doi.org/10.1007/s11664-018-6406-3>
- Bakr, N. A., Salman, S. A., & Shano, A. M. (2015). Effect of co doping on structural and optical properties of NiO thin films prepared by chemical spray pyrolysis method. *International Letters of Chemistry, Physics and Astronomy*, 41, 15-30. <https://doi.org/10.56431/p-k5woe6>
- Cao, J., & Yan, F. (2021). Recent progress in tin-based perovskite solar cells. *Energy & Environmental Science*, 14(3), 1286-1325. <https://doi.org/10.1039/d0ee04007j>
- Chen, H., Peng, Z., Xu, K., Wei, Q., Yu, D., Han, C., Li, H., & Ning, Z. (2021). Band alignment towards high-efficiency NiO_x-based Sn-Pb mixed perovskite solar cells. *Science China Materials*, 64(3), 537-546. <https://doi.org/10.1007/s40843-020-1470-5>
- Chen, W., Liu, F. Z., Feng, X. Y., Djurišić, A. B., Chan, W. K., & He, Z. B. (2017). Cesium doped NiO_x as an efficient hole extraction layer for inverted planar perovskite solar cells. *Advanced Energy Materials*, 7(19), Article 1700722. <https://doi.org/https://doi.org/10.1002/aenm.201700722>
- Chowdhury, M. S., Shahahmadi, S. A., Chelvanathan, P., Tiong, S. K., Amin, N., Techato, K., Nuthammachot, N., Chowdhury, T., & Suklueng, M. (2020). Effect of deep-level defect density of the absorber layer and n/i interface in perovskite solar cells by SCAPS-1D. *Results in Physics*, 16, Article 102839. <https://doi.org/10.1016/j.rinp.2019.102839>
- Chowdhury, T. H., Kaneko, R., Kayesh, M. E., Akhtaruzzaman, M., Sopian, K. B., Lee, J. J., & Islam, A. (2018). Nanostructured NiO_x as hole transport material for low temperature processed stable perovskite solar cells. *Materials Letters*, 223, 109-111. <https://doi.org/10.1016/j.matlet.2018.04.040>

- Conings, B., Drijkoningen, J., Gauquelin, N., Babayigit, A., D'Haen, J., D'Olieslaeger, L., Ethirajan, A., Verbeeck, J., Manca, J., Mosconi, E., Angelis, F. D., & Boyen, H. G. (2015). Intrinsic thermal instability of methylammonium lead trihalide perovskite. *Advanced Energy Materials*, 5(15), Article 1500477. <https://doi.org/10.1002/aenm.201500477>
- Damena, K. L. (2019). Investigation of organic solar cell at different active layer thickness and suns using GPVDM. *International Research Journal of Engineering and Technology*, 6(12), 1615-1626. <https://www.irjet.net/archives/V6/i12/IRJET-V6I12284.pdf>
- Devi, C., & Mehra, R. (2019). Device simulation of lead-free MASnI₃ solar cell with CuSbS₂ (copper antimony sulfide). *Journal of Materials Science*, 54, 5615-5624. <https://doi.org/10.1007/s10853-018-03265-y>
- Du, H. J., Wang, W. C., & Zhu, J. Z. (2016). Device simulation of lead-free CH₃NH₃SnI₃ perovskite solar cells with high efficiency. *Chinese Physics B*, 25(10), Article 108802. <https://doi.org/10.1088/1674-1056/25/10/108802>
- Green, M. A., Ho-Baillie, A., & Snaith, H. J. (2014). The emergence of perovskite solar cells. *Nature Photonics*, 8, 506-514. <https://doi.org/10.1038/nphoton.2014.134>
- Guo, Y., Yin, X., Liu, J., Yang, Y., Chen, W., Que, M., Que, W., & Gao, B. (2018). Annealing atmosphere effect on Ni states in the thermal-decomposed NiOx films for perovskite solar cell application. *Electrochimica Acta*, 282, 81-88. <https://doi.org/10.1016/j.electacta.2018.06.019>
- Haider, M. I., Fakhruddin, A., Ahmed, S., Sultan, M., & Schmidt-Mende, L. (2022). Modulating defect density of NiO hole transport layer via tuning interfacial oxygen stoichiometry in perovskite solar cells. *Solar Energy*, 233, 326-336. <https://doi.org/10.1016/j.solener.2022.01.023>
- Hao, F., Stoumpos, C. C., Cao, D. H., Chang, R. P. H., & Kanatzidis, M. G. (2014). Lead-free solid-state organic-inorganic halide perovskite solar cells. *Nature Photonics*, 8(6), 489-494. <https://doi.org/10.1038/nphoton.2014.82>
- Hima, A., Khechekhouche, A., Kemerchou, I., Lakhdar, N., Benhaoua, B., Rogti, F., Telli, I., & Saadoun, A. (2018). GPVDM simulation of layer thickness effect on power conversion efficiency of CH₃NH₃PbI₃ based planar heterojunction solar cell. *International Journal of Energetica*, 3(1), 37-41. <https://doi.org/10.47238/ijeca.v3i1.64>
- Hima, A., Khouimes, A. K. L., Rezzoug, A., Yahkem, M. B., Khechekhouche, A., & Kemerchou, I. (2019). Simulation and optimization of CH₃NH₃PbI₃ based inverted planar heterojunction solar cell using SCAPS software. *International Journal of Energetica*, 4(1), 56-59. <https://doi.org/10.47238/ijeca.v4i1.92>
- Hossain, M. I., Hasan, A. K. M., Qarony, W., Shahiduzzaman, M., Islam, M. A., Ishikawa, Y., Uraoka, Y., Amin, N., Knipp, D., Akhtaruzzaman, M., & Tsang, Y. H. (2020). Electrical and Optical Properties of Nickel-Oxide Films for Efficient Perovskite Solar Cells. *Small Methods*, 4(9), Article 2000454. <https://doi.org/10.1002/smt.202000454>
- Iakobson, O. D., Gribkova, O. L., Tameev, A. R., & Nunzi, J. M. (2021). A common optical approach to thickness optimization in polymer and perovskite solar cells. *Scientific Reports*, 11, Article 5005. <https://doi.org/10.1038/s41598-021-84452-x>
- Ibn-Mohammed, T., Koh, S. C. L., Reaney, I. M., Acquaye, A., Schileo, G., Mustapha, K. B., & Greenough, R. (2017). Perovskite solar cells: An integrated hybrid lifecycle assessment and review in comparison with other photovoltaic technologies. *Renewable and Sustainable Energy Reviews*, 80, 1321-1344. <https://doi.org/10.1016/j.rser.2017.05.095>

- Karimi, E., & Ghorashi, S. M. B. (2020). The effect of SnO₂ and ZnO on the performance of perovskite solar cells. *Journal of Electronic Materials*, 49, 364-376. <https://doi.org/10.1007/s11664-019-07804-4>
- Ke, W., & Kanatzidis, M. G. (2019). Prospects for low-toxicity lead-free perovskite solar cells. *Nature Communications*, 10, Article 965. <https://doi.org/10.1038/s41467-019-08918-3>
- Khadka, D. B., Shirai, Y., Yanagida, M., Ryan, J. W., & Miyano, K. (2017). Exploring the effects of interfacial carrier transport layers on device performance and optoelectronic properties of planar perovskite solar cells. *Journal of Materials Chemistry C*, 5(34), 8819-8827. <https://doi.org/10.1039/C7TC02822A>
- Kim, G. W., Shinde, D. V., & Park, T. (2015). Thickness of the hole transport layer in perovskite solar cells: performance versus reproducibility. *RSC Advances*, 5(120), 99356-99360. <https://doi.org/10.1039/c5ra18648j>
- Kirchartz, T. (2019). Photon management in perovskite solar cells. *Journal of Physical Chemistry Letters*, 10(19), 5892-5896. <https://doi.org/10.1021/acs.jpcclett.9b02053>
- Kowsar, A., Billah, M., Dey, S., Debnath, S. C., Yeakin, S., & Uddin Farhad, S. F. (2019). Comparative Study on Solar Cell Simulators. In *2019 2nd International Conference on Innovation in Engineering and Technology (ICIET)* (pp 1-6). IEEE Publishing. <https://doi.org/10.1109/ICIET48527.2019.9290675>
- Lee, M. M., Teuscher, J., Miyasaka, T., Murakami, T. N., & Snaith, H. J. (2012). Efficient hybrid solar cells based on meso-superstructured organometal halide perovskites. *Science*, 338(6107), 643-647. <https://doi.org/10.1126/science.1228604>
- Li, F., Zhang, C., Huang, J. H., Fan, H., Wang, H., Wang, P., Zhan, C., Liu, C. M., Li, X., Yang, L. M., Song, Y., & Jiang, K. J. (2019). A Cation-Exchange approach for the fabrication of efficient methylammonium tin iodide perovskite solar cells. *Angewandte Chemie International Edition*, 58(20), 6688-6692. <https://doi.org/10.1002/anie.201902418>
- Lin, L., Jiang, L., Qiu, Y., & Yu, Y. (2017). Modeling and analysis of HTM-free perovskite solar cells based on ZnO electron transport layer. *Superlattices and Microstructures*, 104, 167-177. <https://doi.org/10.1016/j.spmi.2017.02.028>
- Liu, M., Endo, M., Shimazaki, A., Wakamiya, A., & Tachibana, Y. (2017). Light intensity dependence of performance of lead halide perovskite solar cells. *Journal of Photopolymer Science and Technology*, 30(5), 577-582. <https://doi.org/10.2494/photopolymer.30.577>
- Nguyen, L. (2018). *New Method of Nickel Oxide as Hole Transport Layer and Characteristics of Nickel Oxide Based Perovskite Solar Cell* [Master dissertation]. Old Dominion University, USA. <https://doi.org/10.25776/8dx3-kz45>
- MacKenzie, R. C. (2022). *GpvdM user manual v7.88*. <http://www.gpvdM.com/docs/man/man.pdf>
- Mahmoudi, T., Wang, Y., & Hahn, Y.-B. (2021). Highly stable perovskite solar cells based on perovskite/NiO-graphene composites and NiO interface with 25.9 mA/cm² photocurrent density and 20.8% efficiency. *Nano Energy*, 79, Article 105452. <https://doi.org/10.1016/j.nanoen.2020.105452>
- Mali, S. S., Kim, H., Kim, H. H., Shim, S. E., & Hong, C. K. (2018). Nanoporous p-type NiOx electrode for pin inverted perovskite solar cell toward air stability. *Materials Today*, 21(5), 483-500. <https://doi.org/10.1016/j.mattod.2017.12.002>
- Mandadapu, U., Vedanayakam, S. V., Thyagarajan, K., Reddy, M. R., & Babu, B. J. (2017). Design and simulation of high efficiency tin halide perovskite solar cell. *International Journal of Renewable Energy Research*, 7(4), 1603-1612. <https://doi.org/10.20508/ijrer.v7i4.6182.g7270>

- Mekky, A. B. H. (2020). Electrical and optical simulation of hybrid perovskite-based solar cell at various electron transport materials and light intensity. *Annales de Chimie-Science Des Matériaux*, 44(3), 179-184. <https://doi.org/10.18280/acsm.440304>
- Mishra, A. K., & Shukla, R. K. (2020). Electrical and optical simulation of typical perovskite solar cell by GPVDM software. *Materials Today: Proceedings*, 49, 3181-3186. <https://doi.org/10.1016/j.matpr.2020.11.376>
- Mohammadi, M. H., Fathi, D., & Eskandari, M. (2021). Light trapping in perovskite solar cells with plasmonic core/shell nanorod array: A numerical study. *Energy Reports*, 7, 1404-1415. <https://doi.org/10.1016/j.egy.2021.02.071>
- Mohtasham, J. (2015). Review article-renewable energies. *Energy Procedia*, 74, 1289-1297. <https://doi.org/10.1016/j.egypro.2015.07.774>
- Mouchou, R. T., Jen, T. C., Laseinde, O. T., & Ukoba, K. O. (2021). Numerical simulation and optimization of p-NiO/n-TiO₂ solar cell system using SCAPS. *Materials Today: Proceedings*, 38, 835-841. <https://doi.org/10.1016/j.matpr.2020.04.880>
- Mulik, R. N. (2019). Microstructural studies of nanocrystalline nickel oxide. *International Journal of Research and Analytical Reviews*, 6(2), 973-981.
- Nam, Y. M., Huh, J., & Jo, W. H. (2010). Optimization of thickness and morphology of active layer for high performance of bulk-heterojunction organic solar cells. *Solar Energy Materials and Solar Cells*, 94(6), 1118-1124. <https://doi.org/10.1016/j.solmat.2010.02.041>
- Nkele, A. C., Nwanya, A. C., Shinde, N. M., Ezugwu, S., Maaza, M., Shaikh, J. S., & Ezema, F. I. (2020). The use of nickel oxide as a hole transport material in perovskite solar cell configuration: Achieving a high performance and stable device. *International Journal of Energy Research*, 44(13), 9839-9863. <https://doi.org/10.1002/er.5563>
- Pindolia, G., Shinde, S. M., & Jha, P. K. (2022). Optimization of an inorganic lead free RbGeI₃ based perovskite solar cell by SCAPS-1D simulation. *Solar Energy*, 236, 802-821. <https://doi.org/10.1016/j.solener.2022.03.053>
- Reyes, A. C. P., Lázaro, R. C. A., Leyva, K. M., López, J. A. L., Méndez, J. F., Jiménez, A. H. H., Zurita, A. L. M., Carrillo, F. S., & Durán, E. O. (2021). Study of a lead-free perovskite solar cell using CZTS as HTL to achieve a 20% PCE by SCAPS-1D simulation. *Micromachines*, 12(12), Article 1508. <https://doi.org/10.3390/mi12121508>
- Ragb, O., Mohamed, M., Matbully, M. S., & Civalek, O. (2021). An accurate numerical approach for studying perovskite solar cells. *International Journal of Energy Research*, 45(11), 16456-16477. <https://doi.org/10.1002/er.6892>
- Rahman, M. S., Miah, S., Marma, M. S. W., & Sabrina, T. (2019). Simulation based investigation of inverted planar perovskite solar cell with all metal oxide inorganic transport layers. In *2019 International Conference on Electrical, Computer and Communication Engineering (ECCE)* (pp. 1-6). IEEE Publishing. <https://doi.org/10.1109/ECACE.2019.8679283>
- Rai, M., Wong, L. H., & Etgar, L. (2020). Effect of perovskite thickness on electroluminescence and solar cell conversion efficiency. *The Journal of Physical Chemistry Letters*, 11(19), 8189-8194. <https://doi.org/10.1021/acs.jpcclett.0c02363>
- Rai, S., Pandey, B. K., Garg, A., & Dwivedi, D. K. (2021). Hole transporting layer optimization for an efficient lead-free double perovskite solar cell by numerical simulation. *Optical Materials*, 121, Article 111645. <https://doi.org/10.1016/j.optmat.2021.111645>

- Ravishankar, S., Aranda, C., Sanchez, S., Bisquert, J., Saliba, M., & Garcia-Belmonte, G. (2019). Perovskite solar cell modeling using light-and voltage-modulated techniques. *The Journal of Physical Chemistry C*, 123(11), 6444–6449. <https://doi.org/10.1021/acs.jpcc.9b01187>
- Said, N. D. M., & Woon, L. C. (2019). Fill factor and power conversion efficiency simulation of heterojunction organic solar cells (P₃HT/PCBM) using ZnO and PEDOT: PSS as interfacial layer. *International Journal of Advanced Research in Technology and Innovation*, 1(2), 64-71.
- Samanta, M., Ahmed, S. I., Chattopadhyay, K. K., & Bose, C. (2020). Role of various transport layer and electrode materials in enhancing performance of stable environment-friendly Cs₂TiBr₆ solar cell. *Optik*, 217, Article 164805. <https://doi.org/10.1016/j.ijleo.2020.164805>
- Danjumma, S. G., Abubakar, Y., & Suleiman, S. (2019). Nickel Oxide (NiO) Devices and Applications: A Review. *International Journal of Engineering Research & Technology*, 8(04), 461-467. <https://doi.org/10.17577/ijertv8is040281>
- Schileo, G., & Grancini, G. (2021). Lead or no lead? Availability, toxicity, sustainability and environmental impact of lead-free perovskite solar cells. *Journal of Materials Chemistry C*, 9(1), 67-76. <https://doi.org/10.1039/D0TC04552G>
- Shamna, M. S., Nithya, K. S., & Sudheer, K. S. (2020). Simulation and optimization of CH₃NH₃SnI₃ based inverted perovskite solar cell with NiO as Hole transport material. *Materials Today: Proceedings*, 33, 1246-1251. <https://doi.org/10.1016/j.matpr.2020.03.488>
- Shyma, A. P., & Sellappan, R. (2021). *Computational probing of tin-based lead-free perovskite solar cells: Effects of absorber parameters and various ETL materials on device performance*. ResearchSquare. <https://doi.org/10.21203/rs.3.rs-658718/v1>
- Sievers, D. W., Shrotriya, V., & Yang, Y. (2006). Modeling optical effects and thickness dependent current in polymer bulk-heterojunction solar cells. *Journal of Applied Physics*, 100(11), Article 114509. <https://doi.org/10.1063/1.2388854>
- Singh, A. K., Srivastava, S., Mahapatra, A., Baral, J. K., & Pradhan, B. (2021). Performance optimization of lead free-MASnI₃ based solar cell with 27% efficiency by numerical simulation. *Optical Materials*, 117, Article 111193. <https://doi.org/10.1016/j.optmat.2021.111193>
- Sittirak, M., Ponrat, J., Thubthong, K., Kumnorkaew, P., Lek-Uthai, J., & Infahaeng, Y. (2019). The effects of layer thickness and charge mobility on performance of FAI: MABr: PbI₂: PbBr₂ perovskite solar cells: GPVDM simulation approach. In *Journal of Physics: Conference Series* (Vol. 1380, No. 1, p. 012146). IOP Publishing. <https://doi.org/10.1088/1742-6596/1380/1/012146>
- Song, T. B., Yokoyama, T., Aramaki, S., & Kanatzidis, M. G. (2017). Performance enhancement of lead-free tin-based perovskite solar cells with reducing atmosphere-assisted dispersible additive. *ACS Energy Letters*, 2(4), 897-903. <https://doi.org/10.1021/acsenergylett.7b00171>
- Soucase, B. M., Baig, F., Khattak, Y. H., Vega, E., & Mollar, M. (2022). Numerical analysis for efficiency limits of experimental perovskite solar cell. *Solar Energy*, 235, 200-208. <https://doi.org/10.1016/j.solener.2022.02.051>
- Srivastava, M., Singh, P. K., Gultekin, B., & Singh, R. C. (2021). Fabrication of room ambient perovskite solar cell using nickel oxide HTM. *Materials Today: Proceedings*, 34, 748-751. <https://doi.org/10.1016/j.matpr.2020.04.688>
- Sun, P. P., Li, Q. S., Yang, L. N., & Li, Z. S. (2016). Theoretical insights into a potential lead-free hybrid perovskite: substituting Pb²⁺ with Ge²⁺. *Nanoscale*, 8(3), 1503-1512. <https://doi.org/10.1039/c5nr05337d>

- Thakur, U. K., Kumar, P., Gusarov, S., Kobryn, A. E., Riddell, S., Goswami, A., Alam, K. M., Savela, S., Kar, P., Thundat, T., Meldrum, A., & Shankar, K. (2020). Consistently high V_{oc} values in pin type perovskite solar cells using Ni³⁺-Doped NiO nanomesh as the hole transporting layer. *ACS Applied Materials & Interfaces*, 12(10), 11467-11478. <https://doi.org/10.1021/acsami.9b18197>
- Then, F. S. X., Azhari, A. W., Halin, D. S. C., Sepeai, S., & Ludin, N. A. (2021). Simulation studies on thickness variation of perovskite absorption layer for solar cells application. In *AIP Conference Proceedings of Green Design and Manufacture* (Vol. 2339, No. 1, Article 020071). AIP Publishing. <https://doi.org/10.1063/5.0044580>
- Vishnuwaran, M., Ramachandran, K., & Roy, P. (2022). SCAPS simulated FASnI₃ and MASnI₃ based PSC solar cells: A comparison of device performance. In *IOP Conference Series: Materials Science and Engineering* (Vol. 1219, No. 1, Article 012048). IOP Publishing. <https://doi.org/10.1088/1757-899X/1219/1/012048>
- Wang, Q., Phung, N., Di Girolamo, D., Vivo, P., & Abate, A. (2019). Enhancement in lifespan of halide perovskite solar cells. *Energy & Environmental Science*, 12(3), 865-886. <https://doi.org/10.1039/c8ee02852d>
- Wang, R., Mujahid, M., Duan, Y., Wang, Z.-K., Xue, J., & Yang, Y. (2019). A review of perovskites solar cell stability. *Advanced Functional Materials*, 29(47), Article 1808843. <https://doi.org/10.1002/adfm.201808843>
- Xi, Q., Gao, G., Zhou, H., Zhao, Y., Wu, C., Wang, L., Lei, Y., & Xu, J. (2019). Highly efficient inverted perovskite solar cells mediated by electrodeposition-processed NiO NPs hole-selective contact with different energy structure and surface property. *Applied Surface Science*, 463, 1107-1116. <https://doi.org/10.1016/j.apsusc.2018.09.019>
- Yang, G., Wang, C., Lei, H., Zheng, X., Qin, P., Xiong, L., Zhao, X., Yan, Y., & Fang, G. (2017). Interface engineering in planar perovskite solar cells: Energy level alignment, perovskite morphology control and high performance achievement. *Journal of Materials Chemistry A*, 5(4), 1658-1666. <https://doi.org/10.1039/c6ta08783c>
- Yang, H., Park, H., Kim, B., Park, C., Jeong, S., Chae, W. S., Kim, W., Jeong, M., Ahn, T. K., & Shin, H. (2021). Unusual hole transfer dynamics of the NiO layer in methylammonium lead tri-iodide absorber solar cells. *The Journal of Physical Chemistry Letters*, 12(11), 2770-2779. <https://doi.org/https://doi.org/10.1021/acs.jpcclett.1c00335>
- Yasodharan, R., Senthilkumar, A. P., Ajayan, J., & Mohankumar, P. (2019). Effects of layer thickness on Power Conversion Efficiency in Perovskite solar cell: A numerical simulation approach. In *2019 5th International Conference on Advanced Computing and Communication Systems, ICACCS 2019* (pp. 1132-1135). IEEE Publishing. <https://doi.org/10.1109/ICACCS.2019.8728410>
- Yongjin, G., Xueguang, B., Yucheng, L., Binyi, Q., Qingliu, L., Qubo, J., & Pei, M. (2020). Numerical investigation energy conversion performance of tin-based perovskite solar cells using cell capacitance simulator. *Energies*, 13(22), Article 5907. <https://doi.org/https://doi.org/10.3390/en13225907>
- Zhao, P., Liu, Z., Lin, Z., Chen, D., Su, J., Zhang, C., Zhang, J., Chang, J., & Hao, Y. (2018). Device simulation of inverted CH₃NH₃PbI₃-xCl_x perovskite solar cells based on PCBM electron transport layer and NiO hole transport layer. *Solar Energy*, 169, 11-18. <https://doi.org/10.1016/j.solener.2018.04.027>



Fabrication of PES MMMs with Improved Separation Performances Using Two-Dimensional rGO/ZIF-8 and MoS₂/ZIF-8 Nanofillers

Noor Fauziyah Ishak^{1*}, Nur Hidayati Othman¹, Najihah Jamil¹, Nur Hashimah Alias¹, Fauziah Marpani¹, Munawar Zaman Shahrudin¹, Lau Woei Jye² and Ahmad Fauzi Ismail²

¹School of Chemical Engineering, College of Engineering, Universiti Teknologi MARA, 40450 UiTM, Shah Alam, Selangor, Malaysia

²Advanced Membrane Technology Research Centre (AMTEC), Universiti Teknologi Malaysia, 81310 UTM, Skudai, Johor, Malaysia

ABSTRACT

Modifying polymeric membranes using nanofiller is a promising method to enhance gas permeability and selectivity performance. This work used two types of ZIF-8 functionalized-2D nanofillers to fabricate polyethersulfone mixed matrix membranes. The rGO/ZIF-8 and MoS₂/ZIF-8 nanofillers were first synthesised and characterised using FTIR and XRD. Then, 10 wt% of each nanofillers was added to the PES solution. TGA analysis indicates that MMMs containing rGO/ZIF-8 and MoS₂/ZIF-8 exhibit improved thermal stability. No additional peaks in FTIR and XRD were observed in the MMMs, indicating that the 2D nanofillers were compatible with the PES matrix. The MMMs show significantly enhanced gas separation properties where the highest selectivity was observed for 10 wt%PRG/Pebax membrane of 35.71 with CO₂ permeability of 611 barrer and CH₄ permeability of 17.11 barrer. These results confirm the possibility of using 2D nanofillers to develop high-performance membranes for gas separation.

ARTICLE INFO

Article history:

Received: 07 September 2022

Accepted: 25 January 2023

Published: 21 July 2023

DOI: <https://doi.org/10.47836/pjst.31.5.23>

E-mail addresses:

noorfauziyah@uitm.edu.my (Noor Fauziyah Ishak)

nurhidayati0955@uitm.edu.my (Nur Hidayati Othman)

najihah_jamil90@yahoo.com (Najihah Jamil)

nurhashimah@uitm.edu.my (Nur Hashimah Alias)

fauziah176@uitm.edu.my (Fauziah Marpani)

munawar_zaman@salam.uitm.edu.my

(Munawar Zaman Shahrudin)

lwoejjye@utm.my (Lau Woei Jye)

afauzi@utm.my; fauzi.ismail@gmail.com (Ahmad Fauzi Ismail)

*Corresponding author

Keywords: 2D nanofillers, gas separation, mixed matrix membranes, MoS₂, rGO, ZIF-8

INTRODUCTION

Gas separation is extensively used in carbon capture and storage, air purification, natural gas upgrading and hydrogen recovery. The

conservative method such as cryogenic distillation, adsorption and absorption are not economically satisfied due to the high heat and energy consumption. Membrane technology, which does not need any heat, does not utilise any chemicals, has no emissions, has a smaller footprint and a simple setup, is considered a competitive technology for gas separation. Membrane separation for an ideal gas must be high permeability and selectivity to the desired gases. However, the membrane is known to be subjected to a trade-off between selectivity and permeability (Jamil et al., 2019). Achieving high gas permeation and excellent selectivity is still a big challenge today. The tremendous development of mixed matrix membranes (MMMs) for gas separation was recently discovered by academics (Kamble et al., 2021). The MMMs consist of organic-inorganic hybrid membranes, which are polymeric as substrate membranes and are incorporated with inorganic materials as filler. In this regard, inorganic filler as a two-dimensional (2D) material is extensively used in MMMs fabrication.

The developing 2D layered materials of atomic thickness have provided an extraordinary opportunity to improve high-performance membrane materials with unique nanopores and/or nanochannels (Liu et al., 2016). Graphene and its derivatives are of specific attention for molecular separation (Dong et al., 2016). However, there are many other 2D nanomaterials, such as metal-organic framework (MOF), transition metal dichalcogenide (TMD), hexagonal boron nitride (h-BN) and molybdenum disulphide (MoS_2), which possess unique and intriguing structural features suitable for membrane application that have not been widely studied. Besides material properties, these 2D materials can be massively produced using high-yield and scalable liquid-based exfoliation methods. The 2D nanosheets, single-layered or few-layered, can be stacked in parallel to form sub-nanometre channels between the sheets. Such laminate membranes usually possess exceptional molecular-sieving properties as gas transport resistance is minimised and thus maximises gas flux (Moghadam & Park, 2019).

Due to molecular-sieving properties that allow mitigation of recognised participation phenomenon in polymer membranes by strongly interacting with the polymer chains, these 2D nanosheets are preferably utilised as nanofillers. Therefore, enormous effort has been devoted to implementing zeolitic imidazolate frameworks-8 (ZIF-8) as one of the capable inorganic MOFs to enhance materials compatibility in MMMs fabrication (Amedi & Aghajani, 2017; Jusoh et al., 2016; Mei et al., 2020). For instance, Hadi et al. (2021) used 10 wt% of ZIF-8 to fabricate hollow fibre MMMs, resulting in improved O_2/N_2 gas separation with ideal selectivity of 5.25 (Hadi et al., 2021). However, excessive ZIF-8 loading in the MMMs fabrication would occur defects due to agglomeration phenomena. Recently, it has been a major challenge to prepare defect-free MMMs that implement ZIF-8 as a nanofiller.

Thus, this work aims to develop a new type of MMMs by functionalised ZIF-8 with other materials, which are reduced graphene oxide (rGO) and MoS₂ as potential 2D nanofillers. These two materials incorporated with ZIF-8 are promising as emerging 2D nanomaterials that improve gas permeability and selectivity.

MATERIALS AND METHODS

Materials

Graphite powders (MW = 12.01 g/mol), N-methyl-2-pyrrolidone (NMP, 99% purity), polyethylene glycol (PEG, MW = 400), hydrogen peroxide (H₂O₂, 30 wt%), and hydrochloric acid (HCl, 37% purity) were purchased at Merck Sdn. Bhd., Malaysia. Meanwhile, concentrated sulphuric acid (H₂SO₄, 95–98% purity) and potassium permanganate (KMnO₄, MW = 158.05 g/mol) was purchased at R&M Chemicals. Zinc nitrate hexahydrate (Zn(NO₃)₂·6H₂O, MW = 297.49 g/mol) and 2-methylimidazole (H-MeIM, MW = 82.10 g/mol) and polyethersulfone (PES) were purchased at Sigma-Aldrich (M) Sdn. Bhd., Malaysia. Sodium nitrate (NaNO₃, MW = 84.99 g/mol), L(+) ascorbic acid (C₆H₈O₆, MW = 176.13 g/mol) and methylalcohol (MeOH, MW = 32.04 g/mol) were purchased at SYSTERM. Poly (ether block amide) (PEBAX-1657) was used as a coating material to form a selective membrane layer purchased at Arkema.

Preparation of rGO/ZIF-8 and MoS₂/ZIF-8 Nanofillers

Graphene oxide (GO) and reduced graphene oxide (rGO) was synthesised by using combined chemical and mechanical method (Zainuddin et al., 2017). Firstly, GO was prepared using Hummer's method, where 5 g of graphite powder was mixed with 200 ml of H₂SO₄ and 30 g of KMnO₄. Then, 30 ml of H₂O₂ was used to stop the reaction and washed with HCl and distilled water to adjust pH to get neutral GO. The GO was deoxygenation using C₆H₈O₆ as a reducing agent to produce rGO suspension. Meanwhile, template growth of ZIF-8 was used to synthesise rGO/ZIF-8 nanofillers by stirring 4.8 g of Zn(NO₃)₂·6H₂O and 10.6 g of 2-Hmim in 180.8 ml of methanol for 1 hr. 70 mg of rGO suspension was immersed in the Zn(NO₃)₂ methanol solution and added into the previous Zn(NO₃)₂ solution. This solution was continued stirring for 8 hr and then ultrasonic for another 1 hr. Its precipitate was collected by washing with third times of 50 ml of methanol to remove the leftover precursor. The last step was to dry the rGO/ZIF-8 nanofillers for 4 hr at 60°C under vacuum conditions. All these steps were repeated for synthesising MoS₂-ZIF/8 nanofiller using MoS₂ powder to replace rGO suspension.

Preparation of rGO/ZIF-8 and MoS₂/ZIF-8 PES MMMs

PES as a based membrane was first prepared by blending with NMP as a solvent to get a dope solution. Then 10 wt% of rGO/ZIF-8 and 10 wt% MoS₂-ZIF/8 nanofillers were

added into the dope solution of PES-NMP to prepare rGO/ZIF-8 and MoS₂/ZIF-8 PES MMMs solution, respectively. Both prepared dope solutions were sonicated and degassed for 1 hr, then cast onto a glass plate using a casting knife at a gap of 200 μm. The casted MMM sheets were immersed immediately in the coagulation bath for 24 hr using the phase inversion technique, followed by a second immersion in another coagulation bath to remove any residual before being air-dried (Akhaier et al., 2017; Jamil et al., 2019). A bare PES membrane was also prepared for the comparison study without adding a nanofiller.

Preparation of Coated rGO/ZIF-8 and MoS₂/ZIF-8 PES MMMs

Pebax solution with 3 wt% concentration was prepared by dissolving 3 g of Pebax 1657 pellet in a 70/30 ethanol/water ratio. The solution was then heated at 60°C and stirred for 1 hr to achieve a homogenous solution before being cool down at room temperature. Prior to dip-coating, the Pebax solution was sonicated for 30 min. The coating process was repeated 3 times at 60s intervals. After each coating step, the membranes were dried at 60°C for 25 min to allow solvent vaporisation. Table 1 was summarised the list of abbreviations for each of the membranes coated with Pebax.

Table 1

List of abbreviations for membranes coated with 3 wt% of Pebax

Sample	List of abbreviations
Bare PES/Pebax	PB/Pebax
10 rGO/ZIF-8PES/Pebax	10 wt% PRG/Pebax
10 MOS ₂ /ZIF-8PES/Pebax	10 wt% PMZ/Pebax

Characterisation and Gas Permeation Testing

The synthesised nanofillers and fabricated MMMs were characterised using XRD (PANalytical, X'Pert Pro), FTIR (Perkin Elmer, Spectrum One) and TGA (Mettler Toledo, TGA/SDTA 851E) analysis. Then, the morphology was observed by scanning electron microscopy (SEM) (Hitachi Backs Catter Detector S-3000). An in-house 316 stainless steel gas permeation cell was used for the gas permeation testing with an effective area of 22.9 cm² at constant volume, but variable pressure was applied. The prepared MMMs were cut into desired circular shapes, and two gases were used for this method which is CO₂ (3.30 Å) and CH₄ (3.80 Å), with high purity of 99.99%. During the testing, a bubble flow meter was used to measure the permeation rate of these gas streams and repeated 3 times to get an average value. The gas permeability was determined from the following Equation 1:

$$P = \frac{Q \times L}{A \times \Delta P} \quad (1)$$

where Q and L are permeating volumetric flowrate (mol/s) and membrane thickness (m), respectively. Meanwhile, A is the effective membrane area, and ΔP is the pressure difference. Thus, the selectivity performance for gas I to gas j was calculated using Equation 2, as reported by (Jamil et al., 2019):

$$Selectivity = \frac{P_i}{P_j} \quad (2)$$

where the P_i and P_j are permeability values for gas i and j, respectively.

RESULTS AND DISCUSSION

XRD Analysis

Figure 1 illustrates the XRD of nanofillers and MMMs. It can be seen that a weak MoS₂ peak appears at 103, confirming that a successful intercalation of ZIF-8 into MoS₂ can be obtained through the sonication process. Besides that, the exfoliated MoS₂ planes in MoS₂/ZIF-8 were observed to shift to a slightly lower angle from $2\theta=39.45^\circ$ to $2\theta=39.01^\circ$ which is attributed to the increase of interlayer spacing of MoS₂ due to intercalation of ZIF-8 into MoS₂ layers (Gao et al., 2013; Ries et al., 2019). The XRD pattern for rGO/ZIF-8 was almost similar to a single ZIF-8. It indicates that the in-situ functionalization of ZIF-8 into rGO does not alter their intrinsic properties, or the amount of MoS₂ and rGO added was too small to reach the detection limit. Both nanofillers had sharper peaks compared to a single ZIF-8, indicating that the nanofillers' crystallite size was larger than ZIF-8 (Lai et al., 2016).

The XRD patterns of PB/Pebax and PES MMMs/Pebax incorporated with 10 wt% of PRG and PMZ were then compared. It was observed that the amorphous phase of the PES polymer dominated the XRD patterns of MMMs. No significant changes in the XRD pattern of 10PRG/Pebax indicate that the amount of rGO/ZIF-8 nanofillers added into the polymer matrix is quite low to affect the structure of PES. Interestingly, for 10PMZ/Pebax membranes, a weak peak of MoS₂ at $2\theta=10.82^\circ$, which is related to (002) planes, appeared, which designates that the amount of MoS₂/ZIF-8 is high enough for well-preserved the MoS₂ crystallite structure even after incorporation of them into the amorphous polymer structure.

FTIR Analysis

Figure 2 shows the functional group peaks obtained through FTIR analysis. The FTIR analysis of ZIF-8 shows spectra that are associated with C=N stretching (1596 cm^{-1}), vibration from entire ring stretching ($1434\text{--}1312\text{ cm}^{-1}$) and C-N stretching (1150 cm^{-1}). The peaks at 994 cm^{-1} and 750 cm^{-1} could also correspond to the in-plane C-N bending vibration and C-H bending mode (Feng et al., 2016), respectively. At band 690 cm^{-1} , the

ring out-of-plane bending vibration of Hmim was observed. Similarly, the very small peak was observed at a higher wavenumber (3450 cm^{-1}), which might be attributed to the N-H stretching vibration from residual Hmim. For rGO/ZIF-8, it can be observed that several major peaks of ZIF-8 spectra are retained, indicating that the in-situ functionalisation of rGO does not interrupt the coordination of 2-methylimidazole linker to the zinc(II) centres and thus the formation of ZIF-8 (Wang et al., 2017). For MoS₂/ZIF-8, the broad absorption band at 1748 cm^{-1} and 3541 cm^{-1} belongs to the carbonyl stretching vibrations (Kumar et al., 2016), and O-H stretching can be seen. Additional peaks at 1232 cm^{-1} belonging to epoxy C-O-C were also observed.

PB/Pebax spectra band shows spectra band at 1110 cm^{-1} and 1745 cm^{-1} recognised as C-O-C and -C=O stretching vibrations, respectively. Two other bands, also observed at 1640 and 3309 m^{-1} , are attributed to the existence of H-N-C=O and N-H groups in the hard polyamide (PA) segment, respectively (Cheshomi et al., 2018). The PES characteristic peaks consist of a benzene ring (2952 cm^{-1}), an ether bond, and a sulphone structure (1050 cm^{-1}) (Qu et al., 2010) that appeared in the spectra, although generally, the characteristic peak of Pebax is more prominent compared to PES, MoS₂/ZIF-8 and rGO/ZIF-8 nanofillers that were

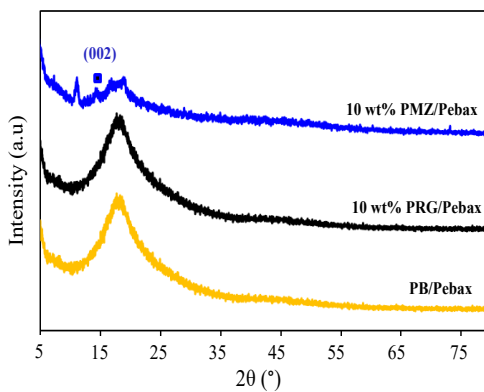
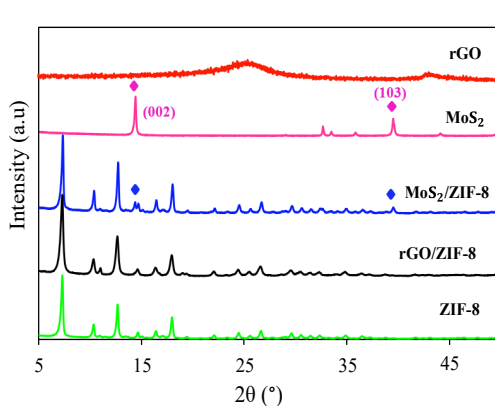


Figure 1. XRD pattern of nanofillers and MMMs

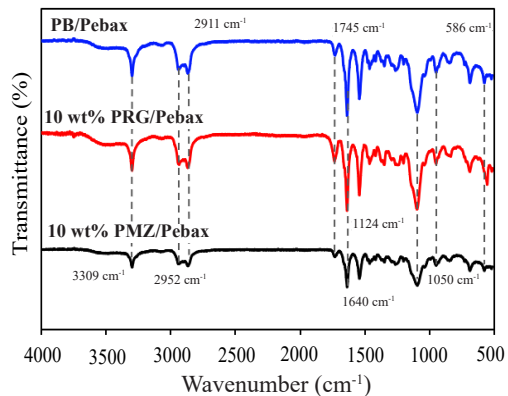
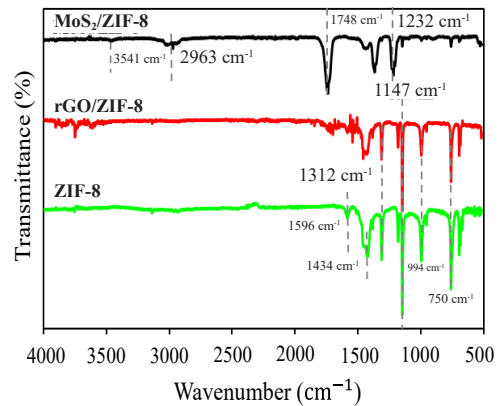


Figure 2. FTIR spectra of nanofillers and MMMs

incorporated inside the membrane. It might be due to the presence of polar pendant groups such as ethylene oxide in Pebax, where the more polar the molecule, the stronger the size of the IR spectrum.

TGA Analysis

Thermal degradation analysis is important to analyse thermal stability for materials application. Figure 3 shows the TGA analysis of nanofillers and MMMs. Single component MoS₂ and rGO are the most stable materials compared to ZIF-8. ZIF-8 is quite stable and possesses little weight loss below 350°C. However, at a temperature range of 600-800°C, it was observed that 55% of weight loss was occurred. This phenomenon indicated that ZIF-8 was converted into zinc oxide as in the thermal decomposition process (L. Dong et al., 2016). As a result, it can be observed that once rGO and MoS₂ were functionalised with ZIF-8, the thermal stability of the hybrid nanofillers was increased.

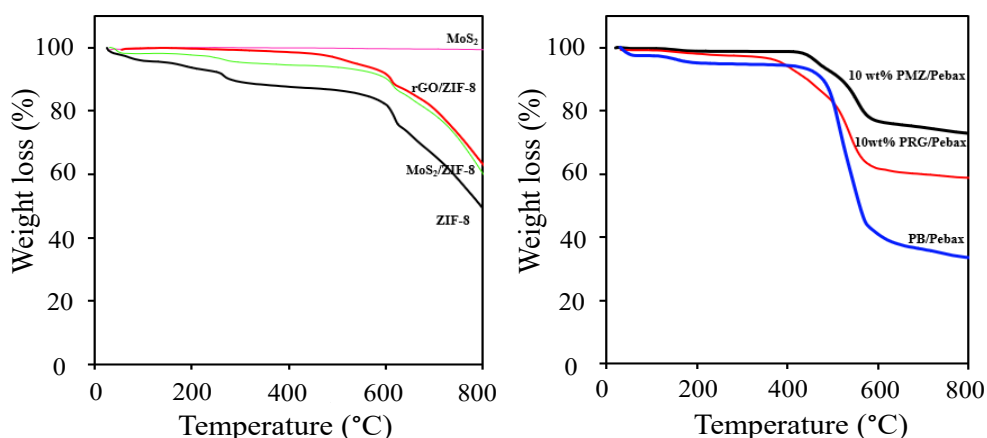


Figure 3. TGA of nanofillers and MMMs

Meanwhile, for PB/Pebax and both MMMs, there are three degradation steps, i.e. the first step is due to the removal of residual solvent and possibly adsorbed water (< 200°C), the second step is due to major polymer chain carbonisation (< 480°C) and finally the degradation of the polymer chain (> 480°C). Overall, the total weight loss for both MMMs with nanofillers was significantly lower than the PB/Pebax membrane, in which 10 wt%PMZ/Pebax membrane exhibited the most thermal stability of the total weight loss was less than 30%.

SEM Analysis

The cross-section SEM structure of the selective layer for Pebax coated on the PES and PES MMMs is presented in Figure 4. Overall, the SEM structures show that the selective layers of Pebax were uniformly coated with thicknesses of around 0.5-0.8 μm and 1.2 μm for MMMs and bare membrane, respectively. The selective layer of MMMs was thinner than bare PES (PB/Pebax). Besides that, it was noted that both MMMs exhibited straighter and more organised finger form structures than PB/Pebax due to the addition of nanofillers in MMMs fabrication. Thus, these two nanofillers were contributed in better interaction with pebax layer by forming higher adhesion force with thinner coating layer (Garcia-Fayos et al., 2018). The coating thickness of MMMs was in a good range due to higher gas permeability being performed at less selective layer thickness.

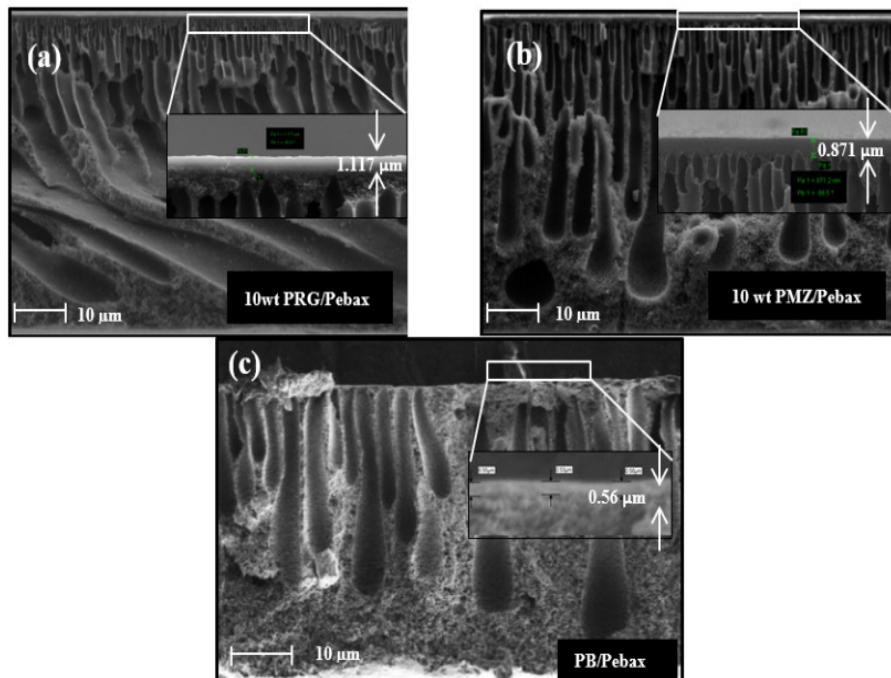


Figure 4. SEM of MMMs

Gas Permeation Measurement

The CO_2 and CH_4 gas permeabilities and their selectivity are presented in Figure 5. In general, the permeability for both gases increases with increased operating pressure. However, it was noted that at a high operating pressure of 5 bar, particularly for bare PES membrane (PB/Pebax), CH_4 permeability decreased, leading to lower CO_2/CH_4 selectivity compared to the low operating pressure of 1 bar. This trend occurred due to the polymer

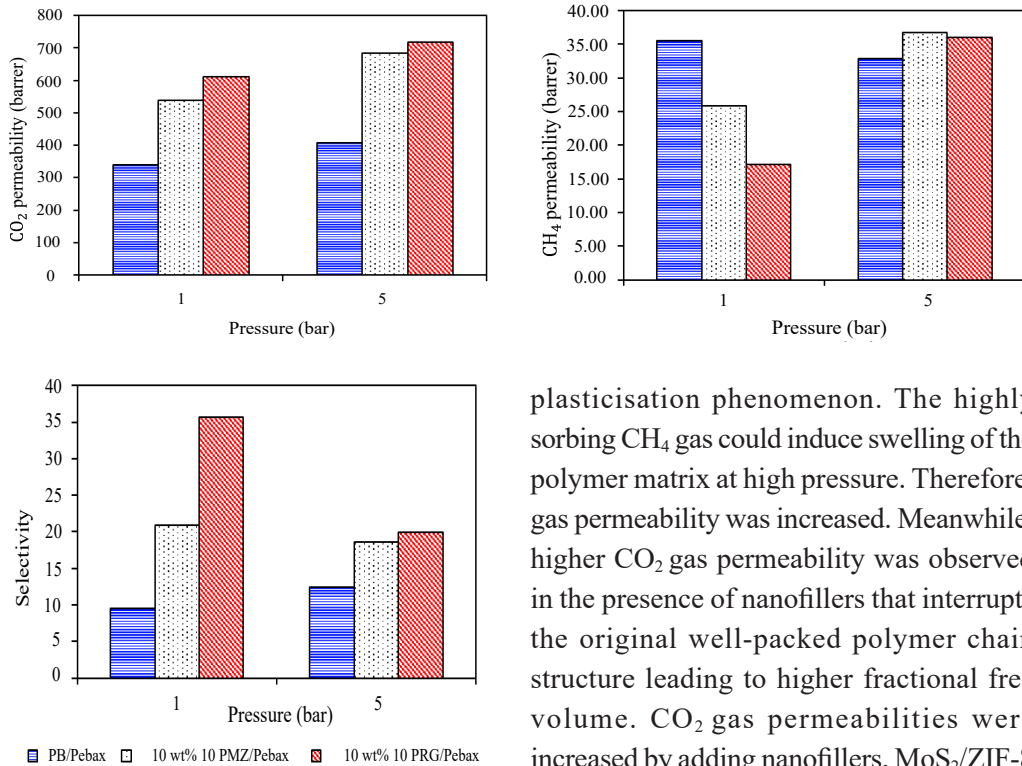


Figure 5. Permeabilities and selectivity of PB/Pebax, 10 wt% PMZ/Pebax and 10 wt% PRG/Pebax

plasticisation phenomenon. The highly sorbing CH₄ gas could induce swelling of the polymer matrix at high pressure. Therefore, gas permeability was increased. Meanwhile, higher CO₂ gas permeability was observed in the presence of nanofillers that interrupts the original well-packed polymer chain structure leading to higher fractional free volume. CO₂ gas permeabilities were increased by adding nanofillers, MoS₂/ZIF-8 and rGO/zif-8, for 10 wt% PMZ/Pebax and 10 wt% PRG/Pebax, respectively. Thus, the CO₂/CH₄ selectivities for these two MMMs

were higher at low operating pressure compared to high operating pressure. The highest selectivity of 35.71 was observed for 10 wt%PRG/Pebax membrane with CO₂ permeability of 611 barrer and CH₄ permeability of 17.11 barrer.

Meanwhile, Table 2 was illustrated for gas permeability and selectivity of MMMs with different polymers and nanofillers from the literature to compare with this work. From the literature, more studies were found to use ZIF-8 as a single nanofiller, improving gas

Table 2
Gas permeability and selectivity of MMMs with different polymers and nanofillers

Polymer	Nanofiller	Operating Pressure	CO ₂ permeability	Selectivity	Reference
6FDA-durene polymer	10 wt% of ZIF-8	1 bar	1426.75 Barrer	CO ₂ /CH ₄ selectivity of 28.70	Jusoh et al. (2016)

Table 2 (Continue)

Polymer	Nanofiller	Operating Pressure	CO ₂ permeability	Selectivity	Reference
Polysulfone (Psf)	0.15 wt% of MoS ₂	2 bar	64 Barrer	CO ₂ /N ₂ selectivity of 93	Shen et al. (2016)
Polyvinylidene Fluoride (PVDF)	0.5 wt% of GO	5 bar	0.897 Barrer	CO ₂ /CH ₄ selectivity of 40.63	Feijani et al. (2018)
Polysulfone (Psf)	0.5 wt% of aminated rGO	4 bar	65.20 Barrer	CO ₂ /CH ₄ selectivity of 14.82	Krishnan et al. (2020)
Polysulfone (Psf)	10 wt% of ZIF-8	4 bar	36.60 Barrer	CO ₂ /CH ₄ selectivity of 27.72	Mei et al. (2020)
Polysulfone (Psf)	0.25 wt% of GO	1 bar	35.42 Barrer	CO ₂ /CH ₄ selectivity of 6.42	Sainath et al. (2021)
Polyethersulfone (PES)	10 wt% of rGO/ZIF-8	1 bar	611 Barrer	CO ₂ /CH ₄ selectivity of 35.71	This work
		5 bar	725 Barrer	CO ₂ /CH ₄ selectivity of 20.14	
Polyethersulfone (PES)	10 wt% of MoS ₂ /ZIF-8	1 bar	551 Barrer	CO ₂ /CH ₄ selectivity of 21.67	This work
		5 bar	682 Barrer	CO ₂ /CH ₄ selectivity of 19.86	

permeability and selectivity. Mei et al. (2020) reported that 10 wt% of ZIF-8 was used in Psf MMM fabrication to establish CO₂ permeability of 36.60 Barrer with CO₂/CH₄ selectivity of 27.72 at an operating pressure of 4 bar. In addition, Krishnan et al. (2020) added 0.5 wt% of aminated rGO in Psf MMM fabrication, resulting in CO₂ permeability of 65.20 Barrer with CO₂/CH₄ selectivity of 14.82 at an operating pressure of 4 bar. In

this regard, the present study functionalised ZIF-8 with two different materials, rGO and MoS₂ to implement as nanofillers in PES MMMs fabrication. Therefore, both nanofillers have successfully enhanced the performance of gas permeability and selectivity at two different operating pressure (Table 2).

CONCLUSION

The demand for cost-efficient separation necessitates membranes with high gas permeability and excellent selectivity, providing the pathway for the further development of membrane materials. In this study, ZIF-8 was successfully functionalised with two different 2D materials, i.e., rGO and MoS₂ and further incorporated into the PES matrix to form MMMs. The results indicate that the 2D nanofillers can significantly increase the gas permeability, especially CO₂ while maintaining high selectivity. These nanofillers could also minimise the plasticisation effects of the membrane, especially at high operating pressure. It is due to the laminate structure of 2D materials, which minimises gas transport resistance and consequently maximises gas permeability.

ACKNOWLEDGEMENTS

The authors acknowledged the Ministry of Higher Education (MOHE) and Universiti Teknologi Mara (UiTM), Malaysia for the financial support via the FRGS grant, 600-IRMI/FRGS 5/3 (087/2017). Nur Hidayati Othman would also like to thank Professor Nalan Kabay (Ege Üniversitesi) and The Scientific and Technological Research Council of Turkey (TÜBİTAK) for 2221-Fellowship for Visiting Scientists and Scientists on Sabbatical Leave (Short-term).

REFERENCES

- Akhaier, S. S. M., Harun, Z., Jamalludin, M. R., Shuhor, M. F., Kamarudin, N. H., Yunos, M. Z., Ahmad, A., & Azhar, M. F. H. (2017). Polymer mixed matrix membrane with graphene oxide for humic acid performances. *Chemical Engineering Transactions*, 56, 697-702. <https://doi.org/10.3303/CET1756117>
- Amedi, H. R., & Aghajani, M. (2017). Aminosilane-functionalized ZIF-8/PEBA mixed matrix membrane for gas separation application. *Microporous and Mesoporous Materials*, 247, 124-135. <https://doi.org/10.1016/j.micromeso.2017.04.001>
- Cheshomi, N., Pakizeh, M., & Namvar-Mahboub, M. (2018). Preparation and characterization of TiO₂/Pebax/ (PSf-PES) thin film nanocomposite membrane for humic acid removal from water. *Polymers for Advanced Technologies*, 29(4), 1303-1312. <https://doi.org/10.1002/pat.4242>
- Dong, G., Hou, J., Wang, J., Zhang, Y., Chen, V., & Liu, J. (2016). Enhanced CO₂/N₂ separation by porous reduced graphene oxide/Pebax mixed matrix membranes. *Journal of Membrane Science*, 520, 860-868. <https://doi.org/10.1016/j.memsci.2016.08.059>

- Dong, L., Chen, M., Li, J., Shi, D., Dong, W., Li, X., & Bai, Y. (2016). Metal-organic framework-graphene oxide composites: A facile method to highly improve the CO₂ separation performance of mixed matrix membranes. *Journal of Membrane Science*, 520, 801-811. doi: <https://doi.org/10.1016/j.memsci.2016.08.043>
- Feijani, E. A., Tavassoli, A., Mahdavi, H., & Molavi, H. (2018). Effective gas separation through graphene oxide containing mixed matrix membranes. *Journal of Applied Polymer Science*, 135, Article 46271. <https://doi.org/10.1002/app.46271>
- Feng, Y., Li, Y., Xu, M., Liu, S., & Yao, J. (2016). Fast adsorption of methyl blue on zeolitic imidazolate framework-8 and its adsorption mechanism. *RSC Advances*, 6(111), 109608-109612. <https://doi.org/10.1039/C6RA23870J>
- Gao, D., Si, M., Li, J., Zhang, J., Zhang, Z., Yang, Z., & Xue, D. (2013). Ferromagnetism in freestanding MoS₂ nanosheets. *Nanoscale Research Letters*, 8(1), 1-8. <https://doi.org/10.1186/1556-276X-8-129>
- Garcia-Fayos, J., Balaguer, M., Baumann, S., & Serra, J. M. (2018). Dual-phase membrane based on LaCo_{0.2}Ni_{0.4}Fe_{0.4}O_{3-x}Ce_{0.8}Gd_{0.2}O_{2-x} composition for oxygen permeation under CO₂/SO₂-rich gas environments. *Journal of Membrane Science*, 548, 117-124. doi: <https://doi.org/10.1016/j.memsci.2017.11.006>
- Hadi, A., Karimi-Sabet, J., Nikkho, S., & Dastbaz, A. (2021). Fabrication of ZIF-8/polyethersulfone (PES) mixed matrix hollow fiber membranes for O₂/N₂ separation. *Chemical Papers*, 75, 4129-4145. <https://doi.org/10.1007/s11696-021-01642-7>
- Jamil, N., Othman, N. H., Alias, N. H., Shahrudin, M. Z., Roslan, R. A., Lau, W. J., & Ismail, A. F. (2019). Mixed matrix membranes incorporated with reduced graphene oxide (rGO) and zeolitic imidazole framework-8 (ZIF-8) nanofillers for gas separation. *Journal of Solid State Chemistry*, 270, 419-427. <https://doi.org/10.1016/j.jssc.2018.11.028>
- Jusoh, N., Yeong, Y. F., Lau, K. K., & Shariff, A. M. (2016). Mixed matrix membranes comprising of ZIF-8 nanofillers for enhanced gas transport properties. *Procedia Engineering*, 148, 1259-1265. <https://doi.org/10.1016/j.proeng.2016.06.499>
- Kamble, A. R., Patel, C. M., & Murthy, Z. V. P. (2021). A review on the recent advances in mixed matrix membranes for gas separation processes. *Renewable and Sustainable Energy Reviews*, 145, Article 111062. <https://doi.org/10.1016/j.rser.2021.111062>
- Krishnan, G., Mohtar, S. S., Aziz, F., Jaafar, J., Yusof, N., Salleh, W. N. W., & Ismail, A. F. (2020). Mixed matrix composite membranes based on amination of reduced graphene oxide for CO₂ separation: Effects of heating time and nanofiller loading. *Korean Journal of Chemical Engineering*, 37(12), 2287-2294. <https://doi.org/10.1007/s11814-020-0649-4>
- Kumar, S., Sharma, V., Bhattacharyya, K., & Krishnan, V. (2016). Synergetic effect of MoS₂-RGO doping to enhance the photocatalytic performance of ZnO nanoparticles. *New Journal of Chemistry*, 40(6), 5185-5197. <https://doi.org/10.1039/C5NJ03595C>
- Lai, L. S., Yeong, Y. F., Lau, K. K., & Shariff, A. M. (2016). Effect of synthesis parameters on the formation of ZIF-8 under microwave-assisted solvothermal. *Procedia Engineering*, 148, 35-42. <https://doi.org/10.1016/j.proeng.2016.06.481>

- Liu, G., Jin, W., & Xu, N. (2016). Two-dimensional-material membranes: A new family of high-performance separation membranes. *Angewandte Chemie International Edition*, 55(43), 13384-13397. <https://doi.org/10.1002/anie.201600438>
- Mei, X., Yang, S., Lu, P., Zhang, Y., & Zhang, J. (2020). Improving the selectivity of ZIF-8/Polysulfone-Mixed Matrix Membranes by Polydopamine Modification for H₂/CO₂ separation. *Frontiers in Chemistry*, 8, Article 528. <https://doi.org/10.3389/fchem.2020.00528>
- Moghadam, F., & Park, H. B. (2019). 2D nanoporous materials: Membrane platform for gas and liquid separations. *2D Materials*, 6(4), Article 042002. <https://doi.org/10.1088/2053-1583/ab1519>
- Qu, P., Tang, H., Gao, Y., Zhang, L., & Wang, S. (2010). Polyethersulfone composite membrane blended with cellulose fibrils. *BioResources*, 5(4), 2323-2336.
- Ries, L., Petit, E., Michel, T., Diogo, C. C., Gervais, C., Salameh, C., Bechelany, M., Balme, S., Miele, P., Onofrio, N., & Voiry, D. (2019). Enhanced sieving from exfoliated MoS₂ membranes via covalent functionalization. *Nature Materials*, 18(10), 1112-1117. <https://doi.org/10.1038/s41563-019-0464-7>
- Sainath, K., Modi, A., & Bellare, J. (2021). CO₂/CH₄ mixed gas separation using graphene oxide nanosheets embedded hollow fiber membranes: Evaluating effect of filler concentration on performance. *Chemical Engineering Journal Advances*, 5, Article 100074. <https://doi.org/10.1016/j.cej.2020.100074>
- Shen, Y., Wang, H., Zhang, X., & Zhang, Y. (2016). MoS₂ nanosheets functionalized composite mixed matrix membrane for enhanced CO₂ capture via surface drop-coating method. *ACS Applied Materials & Interfaces*, 8(35), 23371-23378. <https://doi.org/10.1021/acsami.6b07153>
- Wang, H., Wang, Y., Jia, A., Wang, C., Wu, L., Yang, Y., & Wang, Y. (2017). A novel bifunctional Pd-ZIF-8/rGO catalyst with spatially separated active sites for the tandem Knoevenagel condensation-reduction reaction. *Catalysis Science & Technology*, 7(23), 5572-5584. <https://doi.org/10.1039/C7CY01725A>
- Zainuddin, M., F., Raikhan, N. N. H., Othman, N. H., & Abdullah, W. F. H. (2017, February 15-16). *Synthesis of reduced Graphene Oxide (rGO) using different treatments of Graphene Oxide (GO)*. [Paper presentation]. IOP Conference Series: Materials Science and Engineering, Putrajaya, Malaysia. <https://doi.org/10.1088/1757-899X/358/1/012046>



The Influence of Abiotic Factors on the Occurrence of Jackfruit Dieback Disease

Nurul Hawani Idris^{1*}, Erneeza Mohd Hata², Norliza Adnan³, Sazlieya Saupi Teri¹, Mohamad Jahidi Osman¹, Ami Hassan Md Din¹ and Mohamad Hafis Izran Ishak⁴

¹Department of Geoinformation, Faculty of Built Environment and Surveying, Universiti Teknologi Malaysia, 81310 UTM, Johor Bahru, Johor, Malaysia

²Department of Plant Protection, Faculty of Agriculture, Universiti Putra Malaysia, 43400 UPM, Serdang, Selangor, Malaysia

³Department of Mathematical Science, Faculty of Science, Universiti Teknologi Malaysia, 81310 UiTM, Johor Bahru, Johor, Malaysia

⁴Faculty of Electrical Engineering, Universiti Teknologi Malaysia, 81310 UTM, Johor Bahru, Johor, Malaysia

ABSTRACT

The jackfruit (*Artocarpus heterophyllus*) is one of six high-value non-seasonal tropical fruits identified as a target for export fruit products in the Malaysia National Key Economic Area (NKEA) report. It is challenging to sustain the jackfruit crop's productivity and achieve the targets for the growth of premium fruits because of the emergence of plant diseases that can affect yields. This paper discusses the influence of abiotic factors, including landscape and weather, on the occurrence of *Erwinia carotovora* disease. This paper applied Ordinary Least Square (OLS) and hotspot analysis to understand the occurrence of the disease from the landscape and spatial perspective. The findings suggest that the rate of *E. carotovora* in jackfruit trees (based on a percentage of the area affected) is significantly affected by the

proximity of the trees to roads, rivers, and irrigation. At the same time, the frequency of *E. carotovora* is substantially dependent on rainfall levels. The Koenker (BP) statistic provides a consistent set of results that explain the relationship between variables that impact the occurrence of dieback jackfruit disease remains the same over the study area. This study helps us understand how specific landscape characteristics and climatic variables influence jackfruit dieback disease. This area of research is

ARTICLE INFO

Article history:

Received: 15 July 2022

Accepted: 06 December 2022

Published: 27 July 2023

DOI: <https://doi.org/10.47836/pjst.31.5.24>

E-mail addresses:

hawani@utm.my (Nurul Hawani Idris)

erneeza@upm.edu.my (Erneeza Mohd Hata)

orlyy2liza@gmail.com (Norliza Adnan)

sazlieya@graduate.utm.my (Sazlieya Saupi Teri)

mohamadjahidi@gmail.com (Mohamad Jahidi Osman)

amihassan@utm.my (Ami Hassan Md Din)

hafis@utm.my (Mohamad Hafis Izran Ishak)

* Corresponding author

essential so that the best land management practices can be adapted to prevent future disease occurrences.

Keywords: Abiotic factors, *Erwinia carotovora*, Koenker statistic, landscape management, spatial analysis, tropical agricultural

INTRODUCTION

Jackfruit is one of the six high-value non-seasonal tropical fruits identified as a target product in the National Key Economic Area (NKEA) report. According to 2017 data, jackfruit is one of 21 tropical fruits commercially grown in Malaysia (DOSM, 2017). Jackfruit was recorded as having a self-sufficiency level (SSL), with the country producing more than 100% (111.1%) of domestic consumer needs: over 30,000 tonnes per year (Durai, 2021; Rozhan, 2017). Pahang, Negeri Sembilan, Sabah and Johor are the states that supply the most jackfruit for Malaysian consumption and export to international markets (MAFI, 2021).

Plant diseases must be investigated to sustain jackfruit productivity and achieve the national gross per capita of premium fruits, and relevant strategies must be implemented to meet national targets. Despite the emergence of several plant pest and disease models in the past decades, pests, weeds, and diseases continue to impact agricultural industries worldwide (Jeger et al., 2018; Zulperi et al., 2017).

BACKGROUND

Jackfruit

Jackfruit (*Artocarpus heterophyllus*) is a member of the Moraceae family. The plant genus, *Artocarpus*, comprises 50 tropical species native to the Asia-Pacific region. It is a prevalent tree in home orchards where people often grow fruits and vegetables for personal consumption (Elevitch & Manner, 2006).

Many believe that the jackfruit originated from India's Western Ghats Mountain range; some studies reported finding trees in the primary forest away from human habitation. Meanwhile, another study suggests that it originated in Malaysia because of the broad diversity of jackfruit cultivars (Dickinson et al., 2020; Ranasinghe et al., 2019; Khan et al., 2010). It then spread to countries such as Australia, Brazil, and Indonesia (Ismail & Kaur, 2013). Elevitch and Manner (2006) describe how jackfruit grows well in the equatorial to subtropical maritime climates of the Indian and Pacific oceans and favours tropical moist to semi-dry forests.

Since 2001, several jackfruit clones have been grown commercially (FAMA, 2001), hence the variety of jackfruits available in Malaysia like Mastura, Mantin, Tekam Yellow, Golden Fruit, J29, N.S.1, CJ1, CJ3 and CJ6 (DOA, 2017). These clones perform well in

the Malaysian market because they are small and sweet with fleshy, smooth pulp and an attractive colour (Ismail & Kaur, 2013).

According to Elevitch and Manner (2006), jackfruit may withstand other soil types, such as shallow limestone, sand, and rocky substrates but does best in well-drained, deep soils of moderate fertility. The tree does not tolerate poor drainage or water stagnation. The tree will not bear fruit or perish if its roots come into contact with still water. The tree can grow in soils with light and medium textures (sands, sandy loams, loams, and sandy clay loams). It needs free drainage and can grow in neutral to slightly acidic soils (pH 5.0–7.5). Jackfruit may grow in infertile, shallow, and somewhat saline soils. It can also grow in rocky, laterite, and high-pH limestone soils. The jackfruit can survive three to four months of dryness but thrives with consistent and constant soil moisture (Blom-Zandstra et al., 2017).

Jackfruit Disease

The jackfruit crop is susceptible to various diseases caused by fungal and bacterial infections affecting the leaves, branches, twigs, stems, and roots (Haq, 2006; Sabtu et al., 2019). According to Borines et al. (2014), jackfruit disease incidence tends to increase during the wet season, especially in areas prone to flooding or with poor drainage. Diagnosing the cause of jackfruit decline is crucial to assist in developing disease management strategies and the industry's survival.

Several diseases that infect jackfruit are dieback (caused by *Botryodiplodia theobromae*), fruit rot (*Rhizopus artocarp*i and *Rhizopus stolonifer*), and leaf spot (caused by *Phyllosticta artocarina*), and pink disease (caused by *Botryobasidium salmonicolor* and *Corticium salmonicolor*) (Love & Paull, 2011). Other diseases such as charcoal rot (*Ustilana zonata*), collar rot (*Rosellinia arcuata*), grey blight (*Pestalotia elasticola*), and rust (*Uredo artocarp*i) also occur on jackfruit crops in some regions.

In Malaysia, the most common disease affecting the jackfruit crop is wilt/dieback disease caused by a bacterial pathogen, *Erwinia carotovora*, pink disease caused by *Erythricium salmonicolor* and fruit rot disease caused by *Phytophthora palmivora* (DOA Sarawak, 2006).

Jackfruit dieback disease is associated with different causal pathogens, *Lasiodiplodia theobromae* and *Erwinia carotovora*. *Lasiodiplodia theobromae* is a fungus capable of infecting growing shoots, causing discolouration of the bark and, in severe cases, causing the death of the jackfruit tree (Haq, 2006; Sabtu et al., 2019). However, the bacteria *E. carotovora* is also associated with dieback disease, which infects most *Artocarpus* species (Love & Paull, 2011), and this causal pathogen is the focus of this study.

Erwinia carotovora is a phytopathogenic enterobacterium that causes soft rot, blackleg, or stem rot on many crops (De Boer & Kelman, 2001). The bacterium *E. carotovora* causes

dieback resulting in leaf yellowing and gummy exudates from the stems and branches (Abhijit et al., 2012; Borines et al., 2014; Sangchote et al., 2003). White latex can be seen oozing out of the dark stains on the branches. A chocolate patch is found in the bottom when infected skin is removed. This necrotic area eventually blackens and can develop into large cavities that resemble those caused by the weevil borer. The disease spreads between branches and causes the whole tree to wilt. The fruit infected trees produce is relatively tiny and ripens prematurely compared to uninfected fruits (DOA Sarawak, 2006). Fruits can also become infected with this pathogen which insect transmits. The pathogen may infect young fruits, resulting in black, rotten, shrunken and sometimes withered fruit. Symptoms can appear before the fruit is harvested and on fruits in transit or storage. If not managed properly, these diseases can potentially damage fruit production severely.

According to Bhat et al. (2010), *E. carotovora* is a gram-negative bacterium, rod-shaped, facultatively anaerobic, catalase positive, oxidase negative and urease harmful bacteria. The optimum temperature for *E. carotovora* growth is 30°C. According to Kumar and Ragupathy (2012), a temperature range of 25°C–30°C with low relative humidity (80–85%) and the presence of susceptible hosts favours dieback disease. It allows it to proliferate (Kumar & Ragupathy, 2012).

A study by Nadarasah and Stavrinides (2011) stated that insects are one of the intermediaries that spread plant pathogens. According to Elevitch and Manner (2006), boring insects are the major pests of jackfruit in southwestern and southern Asia; these include *Batocera rufomaculata*, *Indarbela tetraonids*, *Margaronia caecalis*, and *Ochyromera artocarpio* (Rajkumar et al., 2018; Ibrahim et al., 2022; Khan et al., 2021; Khan & Khan, 2020; Sabtu et al., 2019;). According to a survey conducted between 2013 and 2016, fifty-one insect pests were found on jackfruit in the south Indian states of Karnataka, Kerala and Tamilnadu (Kallekkattil et al., 2020). Shoot-boring caterpillar (*Diaphania caesalis*) is the major pest (Elevitch & Manner, 2006; Gullan & Cranston, 2014), including mealybugs (*Nipaecoccus viridis*, *Pseudococcus corymbatus*, and *Ferrisia virgata*), spittlebug (*Cosmoscarta relata*), and jack scale (*Ceroplastes rubina*). The larva of *D. caesalis* is a voracious feeder that causes severe fruit damage. Khan and Islam (2004) reported that *D. caesalis* caused 27.44% of damage in jackfruit plantations in Bangladesh.

METHODOLOGY

The methodology applied in this study is shown in Figure 1, as this study used climatic and landscape data (Table 1). The Malaysian Meteorological Department obtained climatic data from 2011–2017. The *E. carotovora* jackfruit disease incidence data were collected from the Plant Biosecurity Division of Johor. River, irrigation, and rainfall data were obtained from the Department of Irrigation, and Drainage of Johor, and elevation data from TanDEM sentinel was 12 meters. All data were initially in different coordinate systems, such as World

Geodetic System 1984 (WGS 84) and Cassini Soldner Johor map projection. Then, the data were transformed into Malayan Rectified Skew Orthomorphic (MRSO) Kertau map projection. Eight variables were extracted from these data to analyse the relationship using Ordinary Least Square (OLS) analysis. Jackfruit disease incidence records (location), road, river, and irrigation are vector shaped. The elevation data was converted from raster to vector format, and then 20-meter contour lines were created to obtain the elevation value for jackfruit disease incidence.

The spatial database consists of all data collected in the second stage. The data were divided into either spatial or attribute data. Spatial data describes a location on the earth's surface, whereas attribute data describes a spatial object in the database. Roads, water bodies and elevation data were included in the spatial data, while the others were included in attribute data.

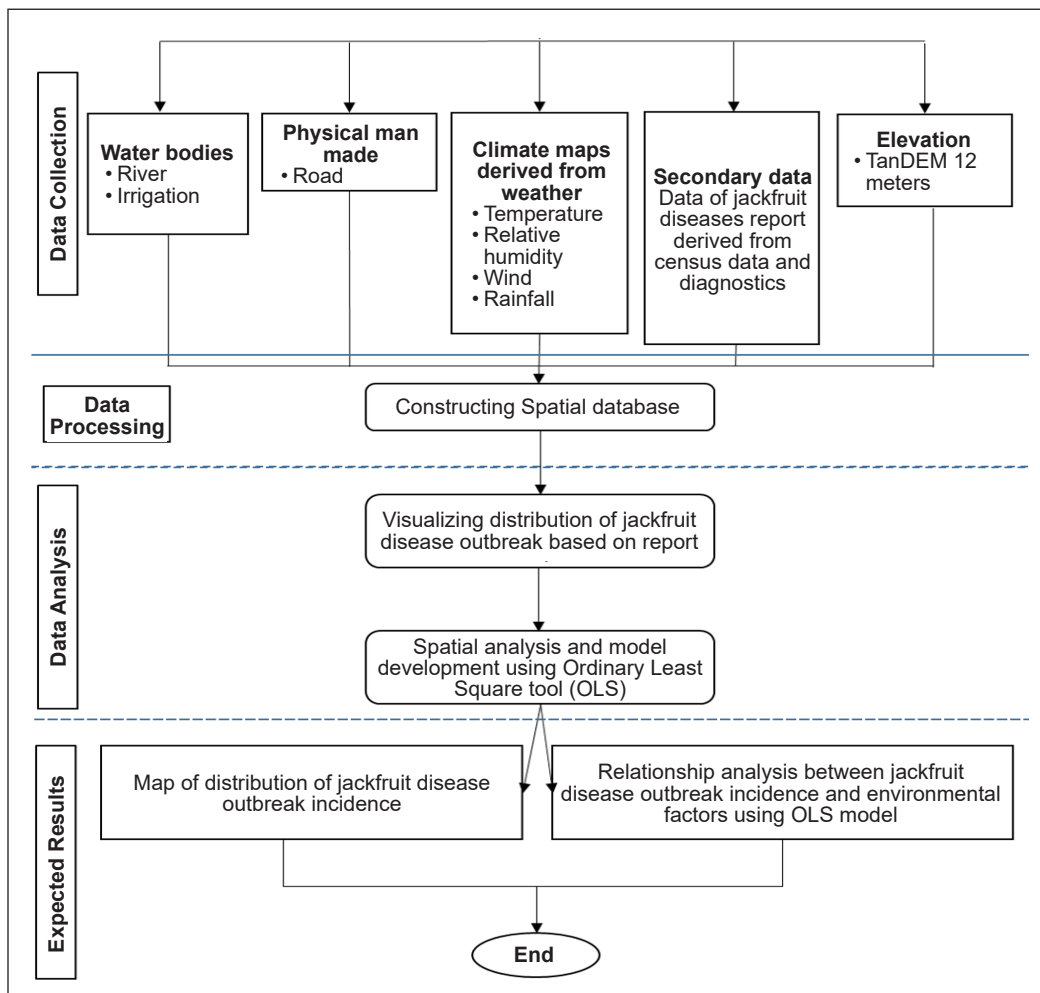


Figure 1. Methodology flowchart

Table 1
Description of each variable

Variables	Data Descriptions
Jackfruit diseases incidence records (in percentage)	Jackfruit diseases report is derived from census and diagnostics data from the year 2011 until 2017
Jackfruit diseases frequency occurrence (in quantity)	(Source: Plant Biosecurity Division of Johor)
Maximum temperature (unit degree Celsius)	The maximum temperature in every district in Johor State from the year 2011 until 2017 (Source: Malaysian Meteorological Department)
Relative humidity (unit %)	Daily relative humidity in every district in Johor State from the year 2011 until 2017 (Source: Malaysian Meteorological Department)
Maximum wind (unit meter per second)	Daily mean wind speed at every district in Johor state from the year 2011 until 2017 (Source: Malaysian Meteorological Department)
Rainfall (unit millimetre)	Daily rainfall in every district in Johor State from the year 2011 until 2017 (Source: Department of Irrigation and Drainage of Johor State)
Road (unit meter)	Road features for the entire Johor (Source: Malaysian Public Works Department)
River (unit meter)	River features for the entire Johor (Source: Department of Irrigation and Drainage of Johor State)
Irrigation (unit meter)	Irrigation features for the entire Johor (Source: Department of Irrigation and Drainage of Johor State)
Elevation (unit meter)	Elevation data is extracted from TanDEM 12 meters (Source: TanDEM)

The maximum temperature, relative humidity and wind data were gathered and displayed in Shapefile format according to their coordinates and using the “Add XY Data” function in ArcGIS 10.3.

Moran’s I spatial autocorrelation was performed on each explanatory variable to understand the distribution of data acquired from the sources (Table 1). Moran’s tool determines whether the spatial pattern is random or clustered. Statistically significant clustering under or over predictions indicates a variable is missing from the model (misspecification) (ESRI, 2016a). Hence, the OLS model that mis-specifies or provides spatially random results is not deemed reliable. Also, it is considered unreliable if the residuals are statistically significant and autocorrelated (ESRI, 2016a). Data distribution must be random, and the residual is not statistically significant or autocorrelated to meet the requirement to conduct OLS regression.

This study’s initial distance to road and elevation data shows clustered spatial autocorrelation. Random spatial autocorrelation is preferred in OLS analysis, or the output analysis cannot be trusted. From a scatter plot matrix graph, the data distribution of the dataset was non-normal. Moreover, each variable showed a few outliers. Hence, the non-normal

distribution data were transformed into a natural logarithm (ln) for all datasets, including maximum temperature, relative humidity, wind, rainfall, road distance, river, irrigation, and irrigation elevation. SPSS software was used to transform the dataset into natural log distribution. Outliers were also identified through a box-plot graph and were removed.

Next, data were processed to generate new attributes by calculating the distance of the disease records to the tested variables—the Near tool (in ArcGIS software) calculated the distance between input features. The distance calculation depends on the geometry type and coordinates system (ESRI, 2016c). The input feature is the record (point location) of *E. carotovora* jackfruit disease to the nearest road, irrigation, river, and elevation. The *E. carotovora* jackfruit disease data was in point feature while other relative features were in line. The output from this analysis was the distance value (in meters) added as a new column (namely, NEAR_DIST) in the *E. carotovora* jackfruit disease attribute table.

The distance was calculated based on these basic rules below (ESRI, 2016d):

1. The distance between two points is the straight line connecting the points.
2. The distance from a point to a line is perpendicular or the closest vertex.
3. Segment vertices determine the distance between polylines.

The variable's distance to roads, rivers and irrigation layers was calculated by measuring their proximity to *E. carotovora* jackfruit disease occurrences.

Hotspot Analysis

This study used a Kernel density tool to map the hotspot of disease occurrence. The tool calculates the density of input features within a neighbourhood. Regarding ESRI (2016b), it is the magnitude of each sample location (line or point) over a surface. A circular search area is applied for a density map to determine the distance to search for sample locations or whether to spread the values around each location and calculate a density value. Density surfaces show the concentration of point or line features.

For mapping the density of *E. carotovora* jackfruit disease, the hotspot analysis was carried out using ArcGIS software. The distribution of the disease was weighted based on the number of incidences.

Ordinary Least Square (OLS) Linear Regression

Ordinary Least Square (OLS) linear regression is a statistical method for estimation and prediction. According to ESRI (2016a), OLS linear regression estimates the unknown parameters in a linear regression model. The technique minimises the sum of squared vertical distances between observed answers in the dataset and the expected responses, utilising a linear approximation. ESRI (2016a) also state that the OLS linear regression in ArcGIS can predict and model the relationship between a dependent variable and a set of explanatory variables.

The OLS regression model analysed the relationship between *E. carotovora* and the independent variables (i.e., maximum temperature, relative humidity, rainfall, and wind speed), along with topographical surface features such as distance to the river and road and irrigation. All variables were analysed with the dependent variable and tested to identify the most influential variable concerning disease occurrence. OLS assesses the overall relationship between the dependent and independent variables. The dependent and independent factors analysed in this study are displayed in Table 2.

The modified R^2 , variance inflation factor (VIF), and coefficient values are shown in the regression tool's output to illustrate the model's performance, which comprises the tested dependent and independent variables. Several R^2 and adjusted R^2 values measure the model's performance. Adjusted R^2 always has a lower value than multiple R^2 since it indicates model complexity, according to ESRI (2016a). Because it directly relates to the data, the adjusted R^2 is a more reliable performance indicator than many other R^2 . The range of potential values is 0.0 to 1.0. Esri (2016a) recommended removing variables with VIFs greater than 7.5 from the model even though the VIF assesses redundancy among variables.

The joint-F-statistic and conventional Wald statistic values were used to determine the statistical significance of the entire model. The joint-F-statistic is reliable only when the Koenker (BP) statistic is not statistically significant (ESRI, 2016c). The Koenker (BP) statistic determines whether the model's explanatory variables are consistently related to the dependent variable regarding the available data and spatial location (ESRI, 2016c). In the studied area, the spatial process operates uniformly if the model is compatible with spatial distance.

According to ESRI (2016a), probability (p-values) reveals the statistical significance of the regression model and if the theory or common sense strongly suggests a relationship with the dependent variable. Explanatory variables must not be redundant with other explanatory factors in the model and must predominantly be linear. The p-value in a statistically significant model must be less than 0.05. The model is not statistically significant, and the model relationship is inconsistent if the p-value is higher than 0.05. The relationship variation between the predicted value and each explanatory variable remains constant if the model is consistent in the data space. Due to volatile output characteristics brought on

Table 2
List of dependent and independent variables used in the OLS tool

Type of Variable	Parameters
Dependent	<ol style="list-style-type: none"> Affected area per hectares (Severity of <i>E. carotovora</i> jackfruit disease occurrence) (in percentage) <i>E. carotovora</i> jackfruit disease occurrence (in frequency)
Explanatory (Independent Variables)	<ol style="list-style-type: none"> Maximum Temperature (annual average) Relative Humidity (yearly average) Mean Wind Speed (yearly average) Distance to Road Distance to River Distance to Irrigation Elevation (20m contour) Rainfall (yearly average)

by local multicollinearity, a regression model with statistically significant stationary values is not recommended for geographically weighted regression (GWR) research.

RESULTS AND DISCUSSION

The Mapping of *Erwinia carotovora* Jackfruit Disease

This study analyses the abiotic factors that influence *E. carotovora* jackfruit disease occurrence. A total of 162 reported *E. carotovora* jackfruit disease incidences were reported in Johor between 2011 and 2017. Figure 2 shows the temporal data of *Erwinia carotovora* jackfruit disease occurrence for the same period. 2013 shows the highest number of instances, with 44 cases recorded by the Plant Biosecurity Division of Johor. The next highest years were 2012 and 2015, with 43 and 33 cases, respectively. The lowest cases were recorded in 2017 and 2014, with five and four, respectively. Figure 3 shows the distribution of *E. carotovora* jackfruit disease in Johor state overlaid with land use and cover.

The Near tool was used for proximity analysis, summarising each explanatory variable’s lowest and maximum values. This data could benefit farmers that plant jackfruit because it can be used to reduce disease occurrences. The summary of minimum and maximum physical explanatory variables is shown in Table 3, and the visualisation of the map is shown in Figure 4.

We can roughly estimate that the crop locations that might be free from bacterial dieback disease infections are approximately within a radius of 6 km from nearby roads, 8 km from nearby rivers, 15 km from irrigation, and at an elevation of 116 meters above sea level (Table 3).

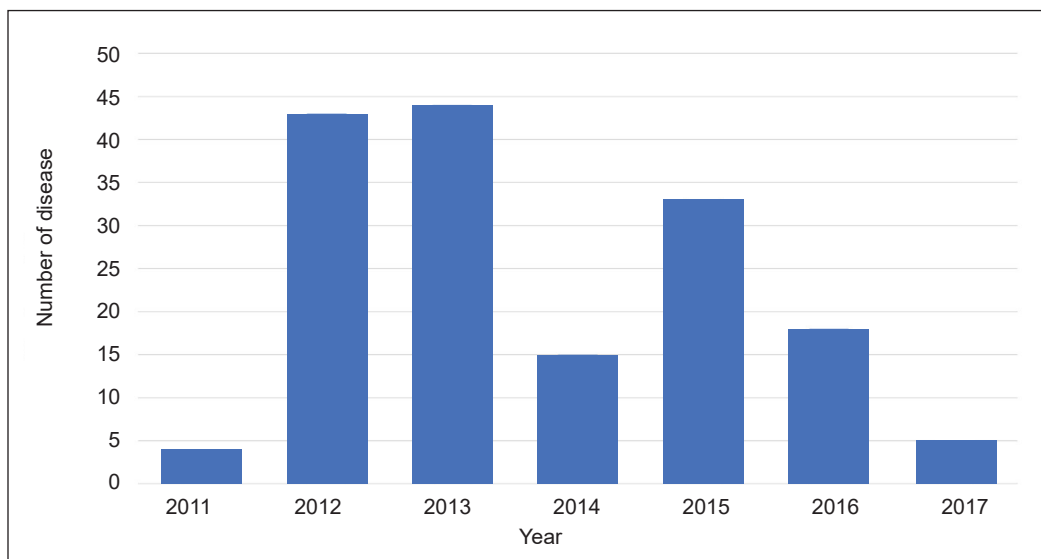


Figure 2. *E. carotovora* jackfruit disease occurrences from 2011 to 2017

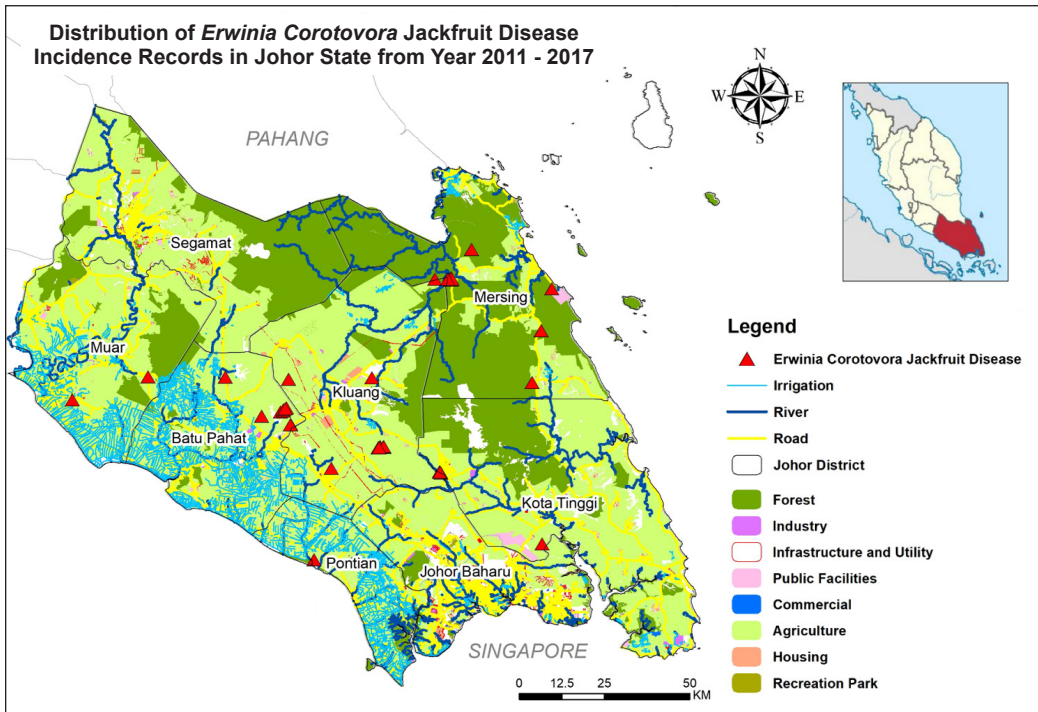


Figure 3. Distribution of *E. carotovora* jackfruit disease incidences in Johor State

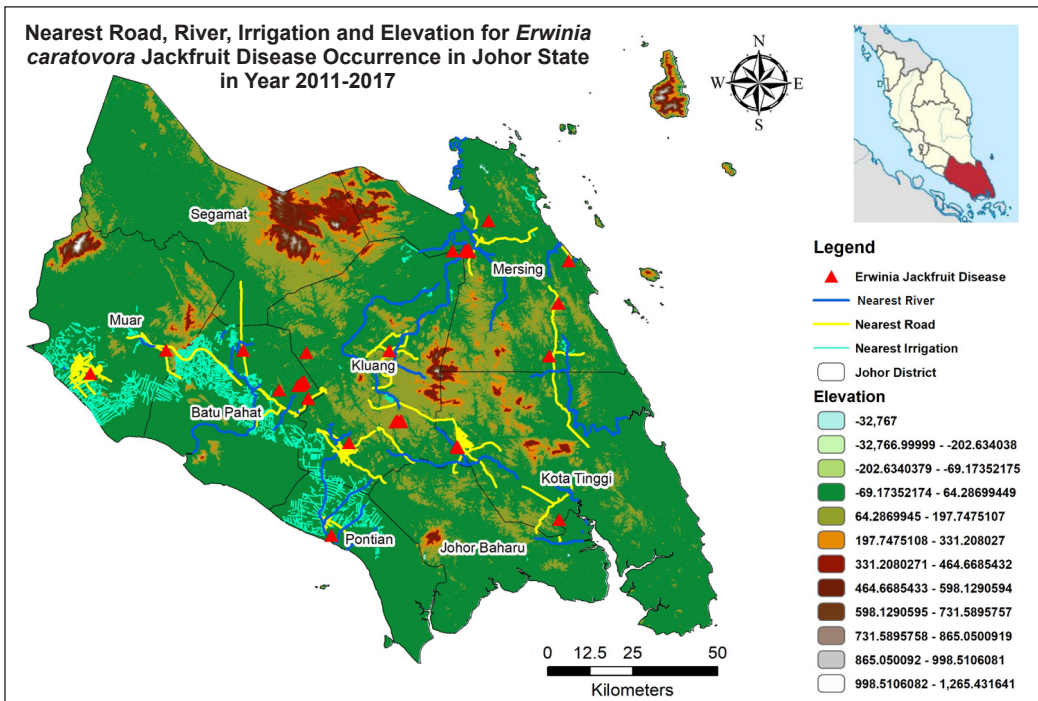


Figure 4. Topographic map for *E. carotovora* jackfruit disease occurrence

The Kernel density tool results show the hotspot for *E. carotovora* jackfruit disease in Figure 5. The gradient colour (green to red) from the figure shows the density of *E. carotovora* jackfruit disease distribution. Red cells have more records surrounding them than green cells. The higher the Kernel density value, the greater the concentration of disease incidence. In conclusion, the hotspot for *E. carotovora* jackfruit disease occurs in Ayer Hitam in Batu Pahat, Bukit Lawing in Kluang, and Felda Nitar 2 in Mersing.

Table 3
Summary of minimum and maximum physical explanatory variables

Variables	Min Value (Meters)	Max Value (Meters)
Road	5.59	5576.17
River	498.03	7637.73
Irrigation	224.79	14819.61
Elevation	10.73	115.42

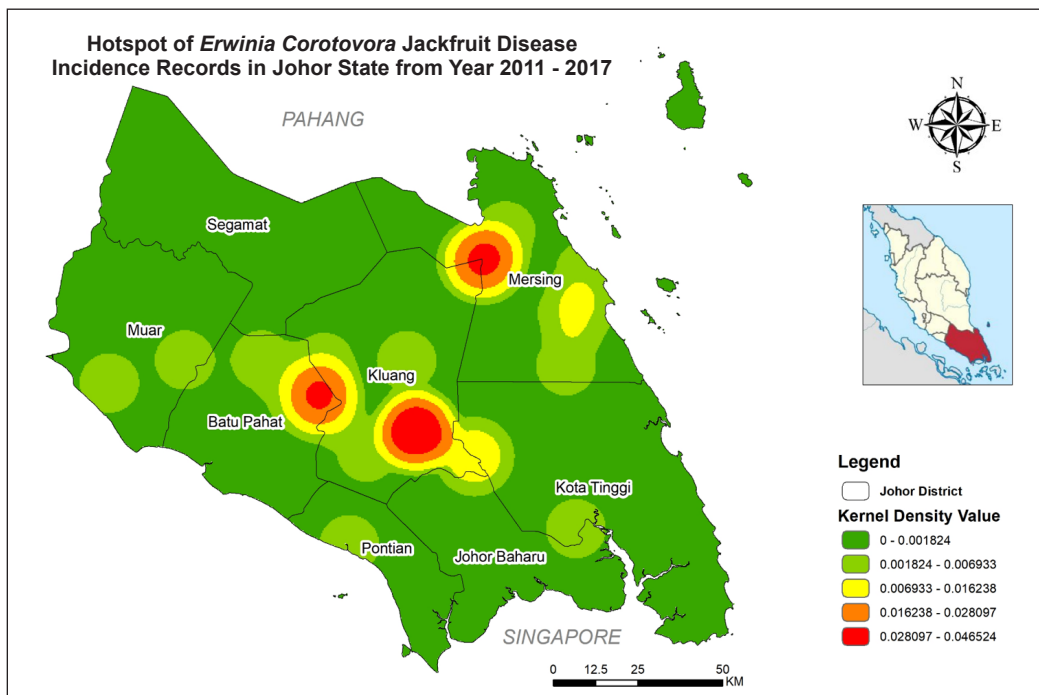


Figure 5. Hotspot area of *E. carotovora*

The Dominant Factors

Eight abiotic factors investigated their relationships with the dieback disease occurrence in this study (Table 2). According to OLS regression (Table 4), this model has a multiple R² of 0.788745 and an adjusted R² of 0.619741. As a result, this model can

Table 4
OLS diagnostics results

Multiple R-Squared	Adjusted R-Squared
0.788745	0.619741
Joint F-Statistic	p-value:
4.667013	0.013233*
Koenker (BP) Statistic	p-value:
2.441167	0.964418

account for about 61% of the variation in the explanatory variables in the entire jackfruit disease-affected area. Alshibly (2018) claims that the better the model matches the data, the greater the R².

Table 5 shows the first model tested in this study (i.e., the size of the area affected by *E. carotovora* jackfruit disease). From the model, the size of the affected area has a significant relationship with the distance to roads, rivers, and irrigation. The p-value of roads, rivers, and irrigation is less than 0.05; hence these variables are significant. Whereas Table 6 shows different dependent variables (i.e., frequency of disease incidence) and their OLS regression results where the rainfall value closely influences the frequency of disease occurrence since the p-value is significant ($p < 0.05$).

The VIF of all explanatory variables (i.e., maximum temperature, humidity, maximum wind, rainfall, river distance, road distance, irrigation distance, and elevation) are jackfruit disease incidence records in Johor state less than 7.5 (Tables 5 and 6). It implies that the explanatory variables are not mutually exclusive. The comparison of disease incidence

Table 5
OLS results of dependent variable: Diseases incidence (as the total percentage of the affected area) versus explanatory variables

Variable	Coefficient (a)	t-Statistic	Probability [b]	VIF [c]
Temperature	5.218971	0.822658	0.429871	2.065216
Humidity	3.695793	0.845752	0.417459	1.560448
Wind	1.379807	1.506446	0.162885	2.107248
Rain	0.321554	0.466808	0.650636	1.335430
Road	0.671931	4.582496	0.001013*	2.805546
River	-1.044560	-2.837530	0.017625*	1.511604
Irrigation	-0.920625	-2.551858	0.028763*	2.595937
Elevation	-0.007164	-0.013018	0.989871	2.787380

*Significant at $p < 0.05$

Table 6
OLS results of dependent variable: Diseases incidence (in frequency) versus explanatory variables

Variable	Coefficient (a)	t-Statistic	Probability [b]	VIF [c]
Temperature	8.159650	1.587765	0.143433	2.065216
Humidity	7.626628	2.154507	0.056618	1.560448
Wind	1.098949	1.481130	0.169393	2.107248
Rain	-1.677950	3.007075	0.013192*	1.335430
Road	0.035788	0.301297	0.769370	2.805546
River	-0.408323	-1.369275	0.200894	1.511604
Irrigation	0.178177	0.609685	0.555655	2.595937
Elevation	-0.764875	-1.715687	0.116985	2.787380

*Significant at $p < 0.05$

coefficient (a) according to the total percentage of the affected area and frequency versus explanatory variables were shown in Figure 6 to illustrate and explain the data better.

From the coefficient results for the first model, we can remove the variables related to the maximum temperature, humidity, wind, elevation, and rainfall since the probability is insignificant (Table 5). From the table, this study identified that the road distance variable is positively associated with the affected size area of *E. carotovora* jackfruit disease incidence. The bigger affected area is due to the greater distance from the road. In other words, road distance has no significant effect on disease incidence.

While the relationship between river distance and irrigation distance negatively affects incidence rates. Therefore, the association is inversely proportional to the size of the affected area. It aligns with a study by Mgcoyi (2011) which stated that *Erwinia* is commonly found in lakes, rivers, and reservoirs during the summer, late spring, and early autumn. The presence of these microorganisms affected the water quality. This study concludes that the larger affected area may be due to the shorter distance to the water body.

The Koenker (BP) statistic for the regression model is 2.441167, and the p-value is 0.964418, higher than 0.05. This result means the model is not statistically significant; hence the relationship of the explanatory variables is consistent. According to Chang (2008), this consistency ensures that the relationship between variables remains the same in a different area. Hence, performing geographically weighted regression (GWR) was not necessary.

Due to the Koenker (BP), the statistic is not statistically significant, and the F-statistic can be used to determine the overall model significance. The p-value of the joint F-statistic

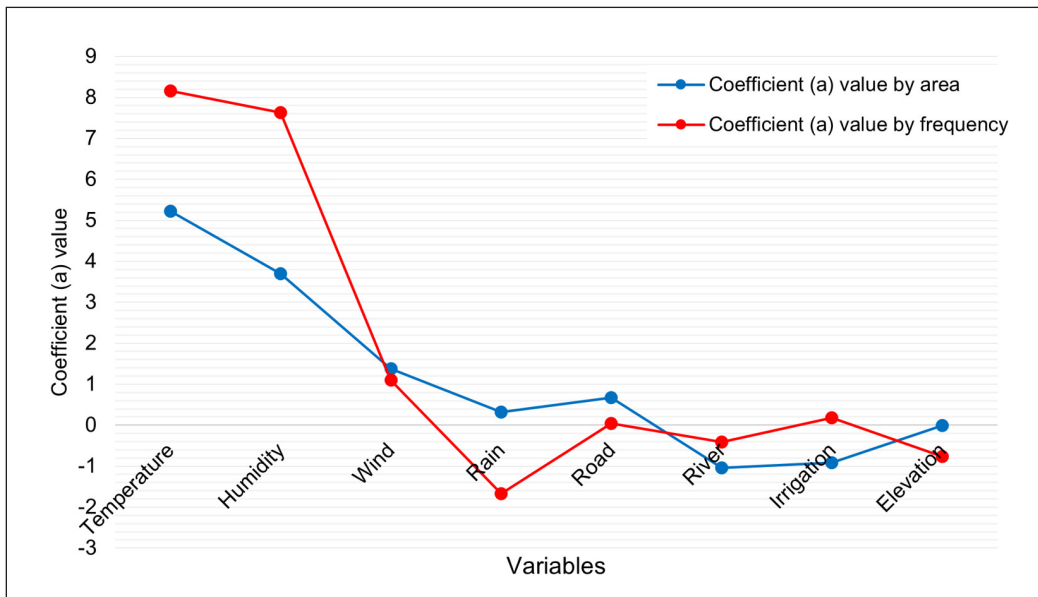


Figure 6. The comparison of the diseases incidence coefficient according to the total percentage of the affected area (blue) and frequency (red) versus explanatory variables

is 0.013233, which means the whole model is statistically significant (Table 4). According to Van Maanen and Xu (2003), rainfall is crucial to disease dispersion. The OLS results show that *E. carotovora* jackfruit disease incidence (based on the frequency of incidents) significantly depends on rainfall, where the p-value is less than 0.05 (Table 6).

CONCLUSION

This paper discusses the impact of abiotic factors that influence the occurrence of *E. carotovora* disease in jackfruit plants. The finding suggests that abiotic factors are influential regarding the presence of the disease. Most related literature frequently associates disease occurrence and severity with abiotic factors. Based on the findings in this research, it is concluded that distance from roads, distance from rivers, and distance from irrigation are the abiotic factors that determine the total percentage area of *E. carotovora* jackfruit disease. However, disease incidence data show that only rainfalls influence jackfruit dieback disease occurrence frequency. The analysis shows that distance from the river and irrigation are inversely proportional to the total percentage area of *E. carotovora* jackfruit disease incidence.

The limitation occurs of this study is the lack of temporal data to indicate the exact date of jackfruit disease occurrence. Furthermore, a lack of detailed climatic data on rainfall in the incidence area hinders the further analysis of the variable. Because of the lack of specific data, the annual average was used to perform the analysis. The model should be validated for future research to ensure reliable relationships in different samples and areas.

ACKNOWLEDGMENT

The authors thank the Department of Agriculture, specifically the Plant Biosecurity Division, Ayer Itam, Johor and Jabatan Pengairan dan Saliran Malaysia, for providing complementary data to support this study. This study is also supported by the Ministry of Higher Education Malaysia and Universiti Teknologi Malaysia through the grant awarded to the authors, GUP Tier 2 Grant 16J60 and UTMFR Vot No. 22H25.

REFERENCES

- Abhijit, G., Debashis, M., & Prasenjit, K. (2012, Disember 19-22). *Identification and management of insect pests and diseases of jackfruit (Artocarpus heterophyllus Lam.) - A documentation*. [Paper presentation]. Proceedings of the International Symposium on Minor Fruits and Medicinal Plants for Health and Ecological Security (ISMF & MP), West Bengal, India.
- Alshibly, H. H. (2018). *How to justify low R-squared and adjusted R-square values?* ResearchGate. https://www.researchgate.net/post/How_to_justify_low_R-squared_and_adjusted_R-square_values
- Bhat, K. A., Masoodi, S. D., Bhat, N. A., Ahmad, M., Zargar, M. Y., Mir, S. A., & Bhat, M. A. (2010). Studies on the effect of temperature on the development of soft rot of cabbage (*Brassica oleracea* var. capitata) caused by *Erwinia carotovora* sub sp. carotovora. *Journal of Phytology*, 2(2), 64-67.

- Blom-Zandstra, G., Nardelli, M., Chuong, N. D. X., Hien, V. T. T., Quoc, N. B., Ha, N. T. V., van der Linden, G., & Verhagen, J. (2017). *A flora of agricultural and horticultural crops: A quick scan of selected crops in the Mekong Delta* (Report WPR-688). Wageningen UR. <https://doi.org/10.18174/444768>
- Borines, L. M., Palermo, V. G., Guadalquiver, G. A., Dwyer, C., Drenth, A., Daniel, R., & Guest, D. I. (2014). Jackfruit decline caused by *Phytophthora palmivora* (Butler). *Australasian Plant Pathology*, 43(2), 123-129. <https://doi.org/10.1007/s13313-013-0241-z>
- Chang, K. T. (2008). GIS models and modelling. In *Introduction to Geographic Information Systems* (pp. 403-404). McGraw-Hill.
- De Boer, S. H., & Kelman, A. (2001). Erwinia soft rot group. In N. W. Schaad, J. B. Jones, & W. Chun (Eds.), *Laboratory Guide for Identification of Plant Pathogenic Bacteria* (3rd ed., pp. 56-71). American Phytopathological Society (APS Press).
- Dickinson, L., Noble, H., Gardner, E., Puad, A. S. A., Zakaria, W. N. F. W., & Zerega, N. J. (2020). Genetic diversity and structure of the critically endangered *Artocarpus annulatus*, a crop wild relative of jackfruit (*A. heterophyllus*). *PeerJ*, 8, Article e9897. <https://doi.org/10.7717/peerj.9897>
- DOA Sarawak. (2006). *Jackfruit - Scheme mechanics, 9MP (2006-2010) fruit industry development programme*. Department of Agriculture Sarawak. <https://doa.sarawak.gov.my/modules/web/pages.php?mod=webpage&sub=page&id=135>
- DOA. (2017). *National guidelines for the conduct of tests for distinctness, uniformity and stability – Jackfruit*. Jabatan Pertanian Malaysia. <http://pvpbktk.doa.gov.my/Test%20Guidelines/Nangka.pdf>
- DOSM. (2017). *Supply and utilisation accounts selected agricultural commodities, Malaysia 2013-2017*. Department of Statistics Malaysia. https://www.dosm.gov.my/v1/index.php?r=column/cthemeByCat&cat=164&bul_id=ZE12RXM2SDM1eGRxRXR3bU0xRThrUT09&menu_id=Z0VTZGU1UHBUT1VJMF1paXRRR0xpdz09
- Durai, A. (2021, November 12). Championing local jackfruit. *The Star*. <https://www.thestar.com.my/food/food-news/2021/11/12/championing-local-jackfruit>
- Elevitch, C. R., & Manner, H. I. (2006). *Artocarpus heterophyllus (Jackfruit)*. Permanent Agriculture Resources (PAR).
- ESRI. (2016a). *Interpreting OLS results*. ArcGIS Desktop. <http://desktop.arcgis.com/en/arcmap/10.3/tools/spatial-statistics-toolbox/interpreting-ols-results.htm#>
- ESRI. (2016b). *An overview of the density toolset*. ArcGIS Desktop. <http://desktop.arcgis.com/en/arcmap/10.3/tools/spatial-analyst-toolbox/an-overview-of-the-density-tools.htm>
- ESRI. (2016c). *How kernel density works*. ArcGIS Desktop. <http://desktop.arcgis.com/en/arcmap/10.3/tools/spatial-analyst-toolbox/how-kernel-density-works.htm>
- ESRI. (2016d). *How proximity tools calculate distance*. ArcGIS Desktop. <http://desktop.arcgis.com/en/arcmap/latest/tools/analysis-toolbox/how-near-analysis-works.htm>
- FAMA. (2001). *Siri panduan kualiti Nangka* [Jackfruit quality based on Malaysian standard.]. FAMA. <https://www.fama.gov.my/documents/20143/0/nangka+baru.pdf/15ed0e57-336a-a099-f007-ab83d3cb5bef>

- Gullan, P. J., & Cranston, P. S. (2014). *The Insects: An Outline of Entomology*. John Wiley & Sons.
- Haq, N. (2006). *Fruits for the Future 10: Jackfruit Artocarpus heterophyllus*. Southampton Centre for Underutilised Crops.
- Ibrahim, R., Ismail, S. I., Ina-Salwany, M. Y., & Zulperi, D. (2022). Biology, diagnostics, pathogenomics and mitigation strategies of jackfruit-bronzing bacterium *Pantoea stewartii* subspecies *stewartii*: What do we know so far about this culprit? *Horticulturae*, 8(8), Article 702. <https://doi.org/10.3390/horticulturae8080702>
- Ismail, N., & Kaur, B. (2013). Consumer preference for jackfruit varieties in Malaysia. *Journal of Agribusiness Marketing*, 6, 37-51.
- Jeger, M., Bragard, C., Candresse, T., Chatzivassiliou, E., Dehnen-Schmutz, K., Gilioli, G., Gregoire, J. C., Miret, J. A. J., MacLeod, A., Navarro, M. N., Niere, B., Parnell, S., Potting, R., Rafoss, T., Rossi, V., Urek, G., Bruggen, A. V., der Werf, W. V., West, J., ... & Caffier, D. (2018). Pest categorisation of *Pantoea stewartii* subsp. *stewartii*. *EFSA Journal*, 16(7), Article e05356. <https://doi.org/10.2903/j.efsa.2018.5356>
- Kallekkattil, S., Krishnamoorthy, A., & Venkatesha, M. G. (2020). Insect pest complex of jackfruit in South India. *International Journal of Tropical Insect Science*, 40(3), 513-525. <https://doi.org/10.1007/s42690-020-00099-7>
- Khan, A. U., & Khan, A. U. (2020). Infested and healthy plant and fruit of jackfruit: 12 September 2020. In *Insect Pests and Diseases of Jackfruit Plant and Fruit: A Pictorial Study* (pp. 1-23). ReseachGate.
- Khan, A. U., Choudhury, M. A. R., Maleque, M. A., Dash, C. K., Talucder, M. S. A., Maukeeb, A. R. M., Ema, I. J., & Adnan, M. (2021). Management of insect pests and diseases of jackfruit (*Artocarpus heterophyllus* L.) in agroforestry system: A review. *Acta Entomology and Zoology*, 2(1), 37-46. <https://doi.org/10.33545/27080013.2021.v2.i1a.29>
- Khan, M. A. M., & Islam, K. S. (2004). Nature and extent of damage of jackfruit borer, *Diaphania caesalis* walker in Bangladesh. *Journal of Biological Sciences*, 4(3), 327-330. <https://doi.org/10.3923/jbs.2004.327.330>
- Khan, R., Zerega, N., Hossain, S., & Zuberi, M. I. (2010). Jackfruit (*Artocarpus heterophyllus* Lam.) diversity in Bangladesh: Land use and artificial selection. *Economic Botany*, 64(2), 124-136. <https://doi.org/10.1007/s12231-010-9116-1>
- Kumar, V. B., & Ragupathy, N. (2012). *Diseases of Fruit, Plantation, Medicinal and Aromatic Crops*. Ecoursesonline. <http://ecoursesonline.iasri.res.in/course/view.php?id=575>
- Love, K., & Paull, R. E. (2011). Jackfruit. In *Fruits and Nuts* (pp.1-7). University of Hawaii.
- MAFI. (2021). *Jumlah pengeluaran, luas bertanam, luas berhasil, dan nilai pengeluaran bagi nangka* [Total production, planted area, yield area, and production value for jackfruit]. Ministry of Agriculture and Food Industry http://www.data.gov.my/data/ms_MY/dataset/jumlah-pengeluaran-luas-bertanam-luas-berhasil-dan-nilai-pengeluaran-bagi-nangka
- Mgcoyi, B. W. (2011). *Quality assessment of agricultural water used for fertigation in the boland district* [Master dissertation]. Central University of Technology, Free State. <http://hdl.handle.net/11462/174>

- Nadarasah, G., & Stavrinides, J. (2011). Insects as alternative hosts for phytopathogenic bacteria. *FEMS Microbiology Reviews*, 35(3), 555-575. <https://doi.org/10.1111/j.1574-6976.2011.00264.x>
- Rajkumar, M., Gundappa, B., Tripathi, M. M., & Rajan, S. (2018). Pests of jackfruit. In Omkar (Ed.), *Pests and their Management* (pp. 587-602). Springer. https://doi.org/10.1007/978-981-10-8687-8_18
- Ranasinghe, R. A. S. N., Maduwanthi, S. D. T., & Marapana, R. A. U. J. (2019). Nutritional and health benefits of jackfruit (*Artocarpus heterophyllus* Lam.): A review. *International Journal of Food Science*, 2019, Article 4327183. <https://doi.org/10.1155/2019/4327183>
- Rozhan, A. D. (2017). Trends in production, trade, and consumption of tropical fruit in Malaysia. *FFTC Agricultural Policy Platform*. Advance online publication.
- Sabtu, N. M., Ishak, M. H. I., & Idris, N. H. (2019). The spatial epidemiology of jackfruit pest and diseases: A review. *International Journal of Built Environment and Sustainability*, 6(1-2), 169-175. <https://doi.org/10.11113/ijbes.v6.n1-2.395>
- Sangchote, S., Wright, J. G., & Johnson, G. I. (2003). Diseases of breadfruit, jackfruit and related fruit crops. In R. C. Ploetz (Ed.), *Diseases of Tropical Fruit Crops* (pp. 135-144). CIBI Publishing. <https://doi.org/10.1079/9780851993904.0135>
- Van Maanen, A., & Xu, X. M. (2003). Modelling plant disease epidemics. *European Journal of Plant Pathology*, 109(7), 669-682. <https://doi.org/10.1023/A:1026018005613>
- Zulperi, D., Manaf, N., Ismail, S. I., Karam, D. S., & Yusof, M. T. (2017). First report of *Pantoea stewartii* subsp. *stewartii* causing fruit bronzing of jackfruit (*Artocarpus heterophyllus*), a new emerging disease in Peninsular Malaysia. *Plant Disease*, 101(5), 831-831. <https://doi.org/10.1094/PDIS-11-16-1689-PDN>



Review Article

The Grease Formulation Using Waste Substances from Palm Oil Refinery and Other Industrial Wastes: A Review

Muhammad Auni Hairunnaja¹, Mohd Aizudin Abd Aziz^{1*}, Nur Amira Fatihah Bashari¹, Mohd Azmir Arifin², Navinash Nedumaran², Khairuddin Md Isa³ and Umi Fazara Md Ali³

¹College of Engineering, University Malaysia Pahang, 26300 UMP, Gambang, Pahang, Malaysia

²Faculty of Chemical Engineering Technology, University Malaysia Pahang, 26300 UMP, Gambang, Pahang, Malaysia

³Faculty of Chemical Engineering Technology, Universiti Malaysia Perlis, 02600 UNIMAP, Arau, Perlis, Malaysia

ABSTRACT

Many applications use Spent Bleaching Earth (SBE) despite being considered hazardous waste from the palm oil refinery process. Its production increases yearly, similar to waste cooking oil (WCO). The SBE is known as a thickener in grease formulation. The same goes for red gypsum, waste motor oil, stearic acid, and lithium hydroxide monohydrate. They are all considered thickeners but have different durability in protecting base oil in grease. Then, previous studies revealed their performances with side effects detection against the environment and human bodies. Cooking oil is a heat transfer medium for serving foods with higher amounts of unsaturated fatty acids. The number of fatty acids might change after cooking oil consumption and become highly demanded due to the chemical properties of density, viscosity and fatty acids. Nowadays, people lack awareness

of the importance of recycling palm oil waste. They intend to dispose of it instead of recycling it for sustainable energy resources. Therefore, this paper will discuss the grease formulation, contaminant available in WCO, its treatment, issues regarding different thickener consumption, treatment against Spent Bleaching Earth (SBE), and propose the safe thickener and additives for future intakes. This study found that adding Fume Silica (F.S.) as a thickener and Molybdenum

ARTICLE INFO

Article history:

Received: 19 July 2022

Accepted: 14 November 2022

Published: 27 July 2023

DOI: <https://doi.org/10.47836/pjst.31.5.25>

E-mail addresses:

mauliduni97@gmail.com (Muhammad Auni Hairunnaja)

maizudin@ump.edu.my (Mohd Aizudin Abd Aziz)

amirabashari97@gmail.com (Nur Amira Fatihah Bashari)

m.azmir@ump.edu.my (Mohd Azmir Arifin)

navinash04@gmail.com (Navinash Nedumaran)

khairudin@unimap.edu.my (Khairuddin Md Isa)

umifazara@unimap.edu.my (Umi Fazara Md Ali)

* Corresponding author

Disulfide (MoS_2) enhanced the grease stability. Further treatment against SBE (remove residue oil) and WCO (metal elements, undesired impurities and water content) is necessary for providing good quality formulated grease.

Keywords: Grease formulation, spent bleaching earth, waste cooking oil

INTRODUCTION

The occurrence of environmental pollution over the years has become a big concern among scholars and researchers. The ongoing generation of waste products, whether from domestic or industrial sources, has become a significant problem. Therefore, this subject has sparked a debate among them. The waste management process is seen as expensive, and several manufactured pollutants contribute to environmental damage. Without effective management, pollution may occur and cause an ecological system imbalance. According to Lopes et al. (2020), the generation of waste cooking oil (WCO) in highly populated countries such as Japan (0.57 million tonnes), India (1.1 million tonnes), the United States of America (1.2 million tonnes), and China (5.6 million tonnes) has increased considerably. According to estimates, Malaysians squander 540 000 tonnes of WCO composed of vegetable and animal fats yearly without treating them as waste (Suzihaque et al., 2022). Meanwhile, although most households know the importance of recycling WCO, only a tiny percentage recycle it. In 2020, the Domestic Trade, Cooperatives, and Consumerism Ministry (KPDNKK) stipulated that around 45 million kg of cooking oil was utilised in a month, which means around 1.45 kg of cooking oil was consumed by each person per month (Farid et al., 2020). Meanwhile, another study found that the average monthly WCO production per family is estimated at around 2.34 kg, according to government statistics (Nizam & Misdan, 2022). Figure 1 shows the Waste Cooking Oil Production (million tonnes) within different Countries in 2019.

Pollution can have negative environmental impacts by causing eutrophication, blockage of a municipal drainage system, problems with water treatment facilities, and degradation in aquatic animals due to lack of oxygen supplied by a surface blockage by waste cooking oil (Singh-Ackbarali et al., 2017). Water contamination occurs when WCO is disposed of into the sewer system, which creates obstructions that prevent wastewater from flowing to treatment facilities. If WCO

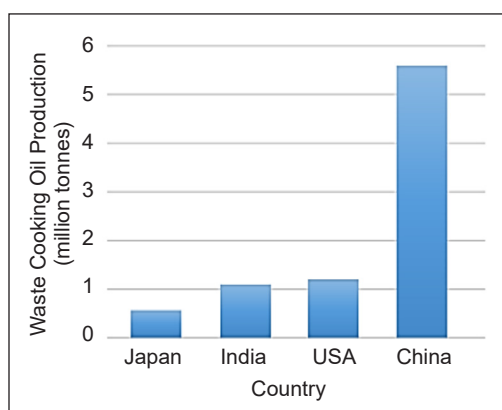


Figure 1. Bar chart for the waste cooking oil production of different countries (Lopes et al., 2020)

is disposed of in municipal solid waste landfills, it will pollute the soil (Feo et al., 2020). For example, the affected operator spends \$3.5 million yearly to clear municipal pipes of blockage caused by waste oil pollution (Vollaard, 2017). It has an impact not only on the environment but also on the cost of treatment.

Recently, many cases have been reported about improper disposal of waste cooking oil. People's lack of awareness contributes to this disposal problem. A survey of respondents in the University of Malaya Cafeteria revealed that approximately 50% threw WCO into the sink, 35% threw it as normal waste, and 20% knew of the impact of repeated consumption (Noor & Hua, 2016). The fluctuating price of mineral oil has sparked debate among academics. However, a non-linear relationship between oil prices and market deliveries due to insufficient production and spare refinery capacity was found to reduce crude oil volumes over the long term. (Dees et al., 2008). Many researchers have found the tendency of WCO as raw material in tuning new products via chemical processing, such as biodegradable polyurethane sheets, greases, bio-lubricants, soaps and alkyd resins, to address these issues (Panadare & Rathod, 2015).

Waste cooking oil (WCO) is defined as used cooking oil after the cooking process. It is generally made of edible oil containing 95% triglycerides, glycerol and fatty acids linked to hydroxyl groups via ester linkage (Vitz et al., 2021). It is categorised as lipids and results from the esterification process. Anderson (1991) states that WCO as a lubricant has been applied since ancient times. This oil acts as a lubricant during operation, reducing the frictional force between two surfaces (wheels and gears). During the Pharaonic period, around 1400 B.C., Hittite chariots used the WCO on the axle (Sharma & Singh, 2019). This application was widely used until 4000 years ago, but it was discontinued in the 19th century due to the higher chemical properties conceived by mineral oil.

Even though mineral oil outperforms waste oil in terms of chemical properties and performance, researchers still have room to find a better way to use waste products as sustainable energy. To maintain grease quality, having a good product free of unwanted impurities should be a priority in grease formulation. It impacts the appearance, colour and performance of grease produced. Furthermore, most waste oils contain undesirable impurities compared to treated crude oil. Many WCOs are taken from various resources until they can impact the tradition and method of cooking styles within various races. Furthermore, the frying period, temperature, and material used in cooking can all affect the properties and type of impurities present. It can be difficult because the process necessitates additional treatment against WCO. WCO, in particular, must be treated before being used as a base oil.

Spent Bleaching Earth (SBE) is used as a thickener known as palm oil waste. WCO is classified as palm oil waste and is used as a base oil in grease formulation. Furthermore, they can reduce environmental pollution by recycling. Not only that but red gypsum,

waste motor oil, stearic acid, and lithium hydroxide monohydrate are also considered thickeners derived from industrial waste. Unfortunately, some of them could not perform well as thickeners, and several adverse effects are found when using these substances for the grease formulation. Then, the SBE is found to be highly hazardous due to several toxicant impurities (Fattah et al., 2014). Further treatment needs to be done to remove these impurities to make it safer.

Contaminant Available in WCO

To strengthen the issues, Mannu et al. (2020) stipulated some impurities in used cooking oil (WCO), e.g., metal traces, organic molecules and spices after being heated or used. The physical properties of cooking oil also changed after use, especially in terms of colour and viscosity (Jaarin & Kamisah, 2012). Therefore, oxidation products from used oils become unfit for human consumption (Tan et al., 2011). Several investigations on fatty acids have been conducted to assess the stability of fatty acids and the efficacy of vegetable oil as a lubricant.

According to Godson and Vinoth (2015), the two most common saturated fatty acids in WCO are palmitic acid and stearic acid. Meanwhile, myristic acid, lenolenic acid, capric acid, and lauric acid are found in small amounts (Figure 2). Furthermore, not only are metal traces and impurities present, but the generation of fatty acids is also classified. According to Awogbemi et al. (2019), the number of fatty acids will degrade before and after WCO consumption. The study discovered that the percentage of oleic acid in sun foil, palm oil, and sunflower oil was the lowest but the highest in margarine. Oleic acid is known as an oxidation resistor (Hernandez, 2016). The acid may stop oxidation. Therefore, it is commonly found as the highest level per cent in WCO after consumption as it maintains the oil presence.

The theory regarding the metal element production from heating cooking oil is acceptable since many studies have traced the availability of these elements using Graphite Furnace Atomic Absorption Spectrophotometry (GFAAS). GFAAS can trace metal elements inside edible oils or foods and detect arsenic in natural medicine products (Khalid et al., 2016). Trace elements concentration of edible oils might be lower in quantity, e.g., arsenic (As), Cadmium (Cd), Lead (Pb), Selenium (Se) and Chromium (Cr). They are toxic

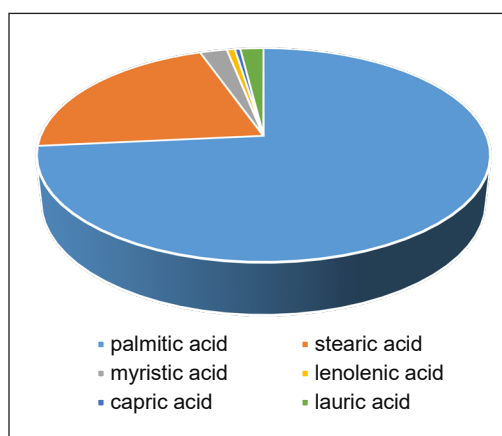


Figure 2. Pie chart of the common components in WCO (Godson & Vinoth, 2015)

and have a negative impact on consumer health (Manarattanasuwan, 2011). Copper and iron also can be detected in edible oil using (GFAAS) (De Leonardis et al., 2000). The saponification method is similar to the atomic absorption spectrophotometer (AAS) (Handajani et al., 2014).

Treatment on WCO

The treatment of WCO is crucial in removing severe undesired impurities present in it. Some researchers found the best way to remove the undesired impurities. The oil will face degradation in quality due to continuous consumption. The longer the continuous repetition of oil consumption, the higher the amount of saturated fatty acid in that oil, which may protect from oxidation easily (Hernandez, 2016). A study by Rajvanshi and Pandey (2016) purified WCO via a filtration method using filter paper. The filter paper is put into a funnel to separate severe undesired impurities. Then products from the filtering process (filtered oil) need to be appropriately kept (sealed container) to avoid a reaction from the air. Since the filtered oil is being filtered, it has similar properties to net cooking oil (Rinaldi et al., 2017). Additional treatment is required by heating the WCO within an hour to reduce moisture content. The oil must be kept in a sealed container and away from the air to prevent rancidity. Other studies also involved the treatment of WCO into a toilet cleaner product, using a filtration process with three types of absorbents (Kamaruzaman & Zin, 2019). The study also claimed similar properties between fresh and filtered cooking oil, but filtered cooking oil is highly safe to use due to less peroxide value (Kamaruzaman & Zin, 2019).

Peroxide value is the number of oxygen in peroxide, which can be measured in the oxidation process against cooking oil. Generally, it is also defined as hydro-peroxides in substances and can be used to determine the deterioration rate of oil (Gordon, 2004). Therefore, good oil quality, especially for grease formulation, depends on the amount of peroxide value related to the oxidation process, which reveals the good preservation status of oil. Fresh cooking oil (FCO) comprises a higher peroxide value due to the storage process (Almeida et al., 2019). Then, oxidation is a major problem against the selected based oil for grease formulation. The higher peroxide value can be described as being mostly available in fresh oil. First, treating WCO before reusing it to produce good quality formulated grease with minimum degradation effects is important. Awogbemi et al. (2019) stated that there would be a higher interchange of density, fatty acids and viscosity after cooking oil consumption. Using oil with a low peroxide value, “waste oil,” is recommended to avoid oxidation.

Grease Formulation

Usually, the grease formulation comprises six major steps, from collecting base oil to selecting the final grease. Grease is formulated using base oil, thickener, and additive. It is important to design these steps to make sure the generated grease product is highly defined

based on acceptable industry standards of common grease acceptable properties via the International Organization for Standardization “ISO 12924 and ISO 6743-9”. Grease is chosen based on its structure and NLGI number. The highest composition should be base oil (waste cooking oil), thickener, and additive. In order to produce grease, the heating process must be completed within three hours using a homogeniser and a hot plate. The greases produced will be tested using the American Society for Testing and Materials (ASTM) method and SKF’s grease test kit before being finalised as selected grease. However, grease performance is determined by the type of thickeners and additives used within adequate composition values. Figure 3 shows the flow chart of the general overview of the grease formulation steps.

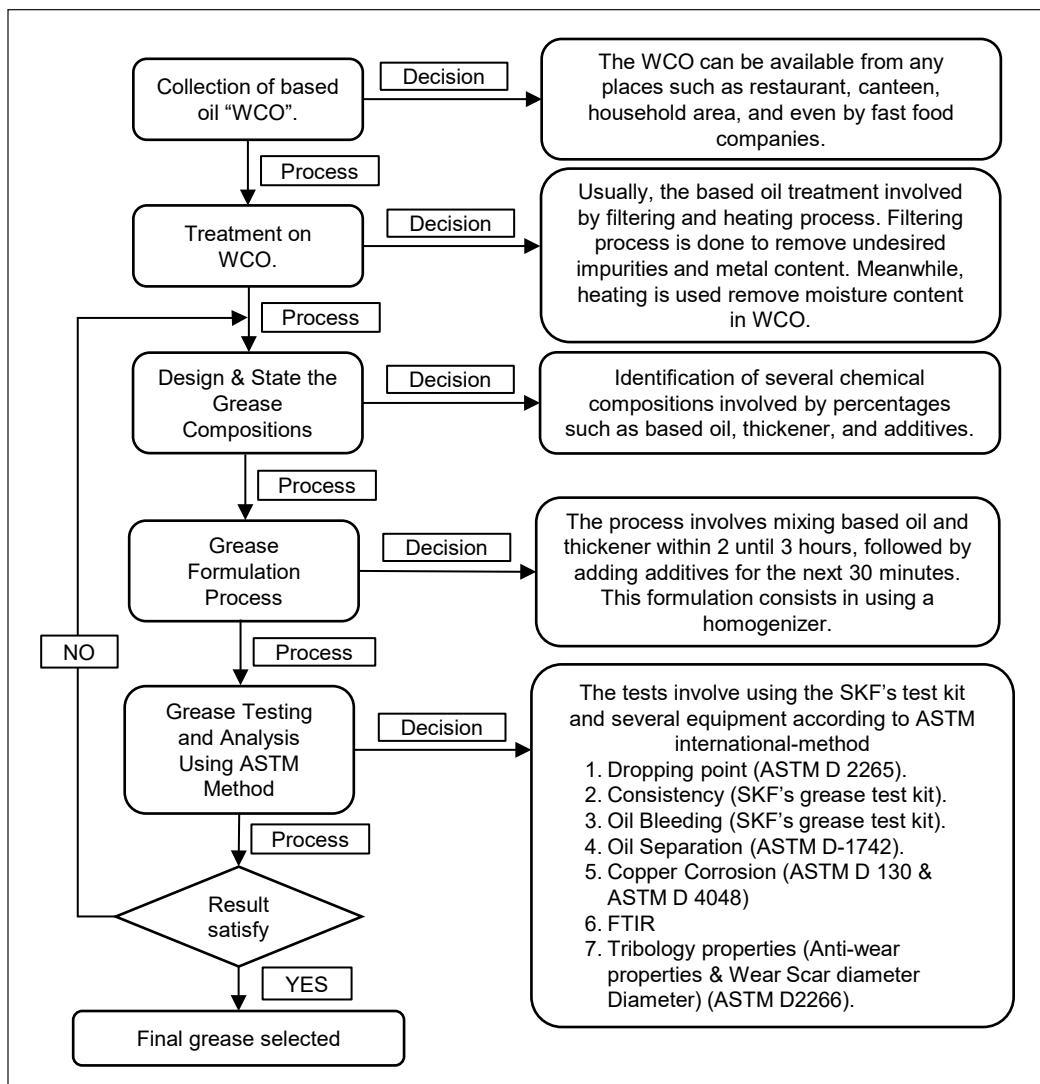


Figure 3. Flow chart of the general overview for the grease formulation steps

Issues in Using Stearic Acid and Lithium Hydroxide Monohydrate as Thickeners

A grease formulation from WCO had been produced by Othman (2009) in combining stearic acid and lithium hydroxide monohydrate as thickeners for different ratios. The study also involved maintaining WCO and sodium diethyl dithiocarbamate as an antioxidant additive. The study also discovered that increasing the thickener impacted the grease performance significantly in terms of NLGI hardness value, work penetration value, operating temperature, and dropping point value, but not for copper corrosion testing. Therefore, the thickener was directly proportional to these grease performance values. In contrast, the result showed that adding additives would significantly impact the metal corrosion up to 4c grade, which is highly corrosive. Lowering the amount of additive denoted the grease's ability to protect the metal surface from chemical attack.

Unfortunately, lithium hydroxide monohydrate is not safe to use in grease formulation due to its limitation stability under normal storage temperature conditions (Livent, 2018), which means it is vulnerable to igniting or exploding and needs to be kept in a cool and dry place. Even though it can form a high-temperature grease, the New Jersey Department of Health and Senior Service (2014) stated that it is a highly corrosive chemical that can cause irritation and burn the skin and eye, leading to eye damage. A pungent odour can irritate the nose and throat, damage the lung, and shorten the breath.

Stearic acid is an emulsifier, emollient, and lubricant that can help prevent the product from separating. It is known as a thickener and can stabilise the grease structure, which is parallel to thickener properties and helps in smoothing the grease structure (Delaneau, 2021). Even though the combination of stearic acid and lithium hydroxide monohydrate (based) can produce a thickener with fewer acidity properties (neutralisation), which is not corrosive, with high mechanical stability and excellent water resistance, the issue cannot be dismissed due to the difficulty in handling these substances during operations. Users can easily spill a bulk powder of lithium hydroxide monohydrate, causing waste and possible respiratory irritation. Another disadvantage of applying this substance is the possibility of yielding grease composition, which may result in lower than desired specifications throughout the spillage and tends to clump and form if exposed to water or high humidity storage area (Smith et al., 2000). Recently, no studies on the toxicity of the stearic acid substance were mentioned, even though it had been tested against animals (Libert, 1987). However, some studies have suggested that other side effects may occur in a few people, such as irritation of sensitive skin, the possibility of carcinogen agents (causing cancer), or toxin build-up in the brain or organs.

Issues in Using Spent Bleaching Earth as a Thickener

A WCO study using Spent Bleaching Earth (SBE) as a thickener found no significant impact on oil (Abdulbari et al., 2011). The waste can be converted into a new product but requires

specific treatments to remove most potential fire and pollution hazard impurities: 20-40% of residual oil by weight, organic compounds, and metallic impurities (Rokiah et al., 2019). Using this sticky material is brilliant since it can save costs from purchasing industrial thickeners for grease formulation while also minimising the environmental impacts of disposal issues. According to a recent study, the SBE consists of fume silica within the range of 50% to 83.05% (Dermawan & Ashari, 2018), making it an excellent thickening agent (Barthel et al., 2005) with no toxicity impact (fume silica) and as anticaking agent (Younes et al., 2018). The study discovered that while SBE can hold base oil at room temperature, it cannot hold WCO due to temperature and pressure changes. So, even though it is a fine particle of clay capable of absorbing and retaining oil, these are the criteria required by many thickeners, and this is due to the oxidative properties of WCO. Therefore, according to the final study assumption, some additives should be added to prolong this issue. SBE is also classified as solid hazardous waste because of its high organic content, which exceeds the waste acceptance criteria (WAC) for hazardous waste landfills by 6% (Fattah et al., 2014). Another issue with this substance is the difficulty in disposing of it due to the high amounts of the water-insoluble substance, diverse compositions, macro-elements, and micro-elements associated with SBE (Piotrowska-Cyplik et al., 2013). A study on mice confirmed the corrosive effect of SBE application on the skin, and the results showed its tendency to improve skin lesions (Yang et al., 2017). Even though it is classified as highly hazardous waste, the Indonesian government has declared it is only classified as non-hazardous waste if it contains less than 3% oil (Jong, 2021). Nonetheless, the study did not initially treat SBE other than by removing stone and agglomerate particles before the grease formulation. As a result, the grease produced by the SBE substance can be extremely hazardous due to its toxicity and may cause skin irritation when touched. Table 1 shows a Summarisation of using SBE as a thickener.

Table 1
Summarisation on using SBE as a thickener

Full Name	Spent Bleaching Earth (SBE)
Problem Against SBE	<ul style="list-style-type: none"> ● Most potential fire and pollution hazard impurities comprise 20-40% of residual oil by weight, organic compounds, and metallic impurities.
Characteristic of SBE	<ul style="list-style-type: none"> ● Sticky substances. ● Comprises fume silica within the range of 50% to 83.05%. ● Anticaking agent. ● SBE can hold base oil at room temperature; it cannot hold WCO due to temperature and pressure changes.
Other issues related to SBE	<ul style="list-style-type: none"> ● SBE is also classified as solid hazardous waste because of its high organic content, which exceeds the waste acceptance criteria (WAC) for hazardous waste landfills by 6%. ● Another issue with this substance is the difficulty in disposing of it due to the high amounts of the water-insoluble substance, diverse compositions, macro-elements, and micro-elements.

Table 1 (continue)

Full Name	Spent Bleaching Earth (SBE)
Research Relating to SBE	<ul style="list-style-type: none"> ● SBE can cause a corrosion effect on the skin and may ameliorate the skin lesion.
Another opinion about hazardous SBE.	<ul style="list-style-type: none"> ● The Indonesian government has declared it is only classified as non-hazardous waste if it contains less than 3% oil.
The problem with this study	<ul style="list-style-type: none"> ● The study did not initially treat SBE other than by removing stone and agglomerate particles before the grease formulation.

Issues in Using Red Gypsum/Fumed Silica (F.S.) as a Thickener

Another study of grease formation with waste oil and red gypsum/fumed silica (F.S.) within different ratios by Razali et al. (2017) has revealed the red gypsum's ability to hold different waste oils. The waste oil involved is WCO, used oil, silicon oil, and waste emulsions. After two months of storage, an oil separation occurred even with a ratio of 50% (red gypsum)/50% F.S. of WCO grease with 50 ml oil separation. In contrast, waste emulsion oil with 10 ml oil separation revealed the best result of grease within a similar ratio after the same period. As a result of its high oxidation properties, red gypsum cannot hold enough WCO structure.

Issues in Using Waste Motor Sludge as a Thickener

The study on grease from WCO and Waste Motor Sludge by Rajvanshi and Pandey (2016) proved the compatibility of WCO as a base oil for the grease production process. The study was also tested using different mixing ratios between lithium and motor sludge within various amounts of WCO and including a few quantities of molybdenum disulfide (MoS_2) as an additive. Hence, the results showed that the mixing quantity of these substances significantly impacted the increment of the dropping point and work penetration value by having directly proportional values. The grease samples also revealed a minor corrosive nature, especially under the specific static condition when tested by the ASTM method within the slightly tarnished appearance of stage 1B. Still, the dropping point decreased significantly when the amount of lithium and motor sludge was reduced while the WCO was increased. In contrast, lithium and motor sludge have been detected when lithium is very unstable and needs to be mixed with the most stabilising agent, such as "motor sludge" (Sani & Florillo, 2020). Commonly, it needs to be kept within mineral oil as it easily reacts to moisture in the air (Dye, 2021). Motor sludge can resist high temperatures due to its properties which can withstand heat. At the same time, it is highly temperature resistant as it can cause damage to the car engine when it is not frequently removed. It can be a stabilising agent in storing lithium within the sticky characteristic. Furthermore, lithium also has superior heat-transfer fluid properties, especially for high-power nuclear reactor density (Dye, 2021) with higher specific heat capacity (Szelong & Fan, 2020).

Unfortunately, lithium is still highly unstable, with a high explosion risk if not handled gently during or after grease formation. Inappropriate substance portions cause the grease to explode during operation.

The motor sludge is considered highly hazardous due to several chemical elements present in its compositions like heavy metals group, including nitrogen, chromium, Phosphorous, Potassium, Iron, Copper, Calcium, Magnesium, Cadmium, Phosphate, Chromium, barium, lead, zinc, mercury, chromium, arsenic, Zinc and Sodium (Johnson & Affam, 2019). The treatment of motor sludge can be done, but it takes a very long process to completely treat a large area (Johnson & Affam, 2019). Furthermore, the research used untreated motor sludge, a significant hazardous waste (waste lubricating oil can cause skin cancer) and lithium. This unstable chemical substance is unpredictable due to its explosive ability for the upcoming grease formulation process. Table 2 shows a summarisation of using Waste Motor Sludge as a thickener.

Table 2
Summarisation on using Waste Motor Sludge as a thickener

Full Name	Waste Motor Sludge
Characteristics of Waste Motor Sludge	<ul style="list-style-type: none"> ● Motor sludge can resist high temperatures due to its properties which can withstand heat. ● It can cause damage to the car engine when it is not frequently removed. ● Motor sludge can be a stabilising agent in storing lithium within the sticky characteristic.
Hazardous Waste Motor Sludge	<ul style="list-style-type: none"> ● It is considered highly hazardous due to several chemical elements in its compositions, like the heavy metals group.
Characteristics of Lithium	<ul style="list-style-type: none"> ● Has superior heat-transfer fluid properties, especially for high-power nuclear reactor density with higher specific heat capacity.
Hazardous of Lithium	<ul style="list-style-type: none"> ● Considered a highly unstable material, with a high explosion risk if not handled gently during or after grease formation. ● Inappropriate substance portions cause the grease to explode during operation.
Other opinions about Waste Motor Sludge	<ul style="list-style-type: none"> ● The treatment of motor sludge can be done, but it takes a very long process to treat within a large area completely.
The problem with this study	<ul style="list-style-type: none"> ● This research used untreated motor sludge, a significant hazardous waste (waste lubricating oil can cause skin cancer). ● Lithium is an unstable chemical substance, which is unpredictable due to its explosive ability for the upcoming grease formulation process.

Summarisation of Comparative Studies Between All the Mentioned Research

Table 3 summarises comparative studies of four studies in grease formulation using WCO.

Future Prospect

Recycling WCO as a base oil for grease production will encounter pollution problems due to improper waste disposal. Furthermore, using WCO to make grease is more cost-

Table 3
Summarisation of comparative studies of grease formulation

Parameters involved in grease analysis / Previous Study of WCO grease	Norasimah Mohd Othman (2009)	Abdulbari et al. (2011)	Razali et al. (2017)	Rajvanshi & Pandey (2016)
Title	Production of grease from waste cooking oil	Lubricating grease from spent bleaching earth and waste cooking oil	Synthesis of grease from waste oils and red gypsum	Lubricating grease from waste cooking oil and waste motor sludge
Thickener and Additives	Stearic acid and lithium hydroxide monohydrate (thickener) diethyl dithiocarbamate (additives)	F.S. & SBE (Thickener)	red gypsum (thickener)	lithium & motor sludge (thickener). mos ₂ (additives).
Consistency test (NLGI Grade) Cone Penetration Test	The study found that adding only LiOH may increase the NLGI value of grease. Meanwhile, having the increment combination ratios between LiOH and stearic acid may increase the work penetration test value, which defines the lower grease consistency value.	The study found that adding WCO and SBE may significantly result in up to 3 NLGI values. Nevertheless, the NLGI result will increase up to 4 when adding F.S. In order to get around 2–3 NLGI values, the SBE composition should be the major part, followed by WCO and F.S.	NGLI value is 1, which is not for the sample WCO grease	the study involved formulating grease at different mixing times. therefore, this led to the consistency of nlgi value at 1, but the consistency value dropped suddenly to 0 at the mixing time of 5 hrs.
Oil Bleeding	N/A	N/A	N/A	N/A
Oil Separation	N/A	N/A	50 ml oil still separated from grease within thickener of 50/50 fumed silica: red gypsum presence.	N/A
Dropping Point	Increasing the amount of LiOH might elevate the dropping point of the grease.	The formulated grease produced has no dropping point, meaning the grease resistance exceeds 350°C.	Applied but not on sample grease of WCO.	The formulated grease had high-temperature resistance above 200°C even at different mixing times.

Table 3 (continue)

	Norasimah Mohd Othman (2009)	Abdulbari et al. (2011)	Razali et al. (2017)	Rajvanshi & Pandey (2016)
Parameters involved in grease analysis / Previous Study of WCO grease				
Copper Corrosion	Having a huge number of additives can highly affect the corrosiveness of copper strips within grade 4c.	The corrosive test for grease within or without F.S. revealed that all the copper strips fell in class 1b (slightly tarnished).	N/A	All the grease samples appeared slightly tarnished, under 1B of the ASTM rating.
Thermal stability Analysis Using Thermogravimetric Analyzer (TGA)	N/A	Grease without F.S. possesses a temperature resistance of up to 200°C, while grease within F.S. developed a temperature resistance of up to 150 °C or more.	N/A	N/A
Tribology Properties	N/A	The formulated grease without F.S. resulted in a low frictional coefficient value (0.095) compared to the grease plus F.S. resulted in a value of (0.11). A lower frictional coefficient value is highly desirable.	N/A	N/A
Application	Bio-based grease for agriculture/farming, forestry and food processing.	Medical facilities, aircraft and other heavy industries applications.	Sealing of bearing against loss of lubricant acts as a sealant to minimise leakage.	Used to be applied at general machines without extreme pressure.
Explanation	The study found that adding LiOH may increase the NGLI and dropping point value, but adding the Stearic acid may help to get the desired grease hardness.	It is multipurpose grease designed to fit in extreme operating conditions such as high temperature or cold temperature climate and extreme pressure.	The study was to develop grease from different waste oil. Unfortunately, WCO is not compatible with red gypsum.	This study focuses on generating a new grease product from waste substances to minimise the burden of utilising conventional sources.

effective, reducing the use of non-biodegradable mineral and vegetable oils (Japar et al., 2020). The selection of an effective thickener as a viscosity enhancer of base oil follows certain criteria, such as heat resistance quality, oxidation, and thermal stability. SBE has good potential as a grease thickener due to its high-temperature stability since SBE is made of mineral clay which does not melt easily (Abdulbari et al., 2011). Formulating grease with SBE results in grease with no dropping point exceeding 350°C can widely be used in high operating temperature applications (Abdulbari et al., 2017).

Apart from that, SBE is easily accessible as an industrial waste, well-known usage in palm oil refineries and food industries, which is costly to dispose of due to its high organic matter content. Disposal of SBE in landfills has the potential to cause pollution and fire hazards due to greenhouse gases emission and auto-ignition upon degradation of residual oil, respectively. The SBE waste generally contains residual, which quickly oxidises until spontaneous auto-ignition through autocatalysis reaction by the mineral clays. The SBE must be treated from its residual oil and undesired impurities prior to converting it into sustainable energy. An estimated 600,000 tonnes of SBE are discharged globally each year, with Malaysia, one of the largest palm oil manufacturers, disposing of approximately 195,000 tonnes in landfills (Cheong et al., 2013). Moreover, incineration and land disposal will likely be impossible soon due to stricter environmental regulatory restrictions and the lack of dumping sites. Recently, Malaysia has committed to becoming a carbon-neutral nation by 2050 which simply means balancing or reducing the emission of greenhouse gases such as CO₂ (Susskind et al., 2020). Therefore, converting SBE waste as a thickener in WCO-based multi-purpose grease is an environmentally friendly, simple, and cost-effective way to convert waste to wealth and carbon-neutral.

SBE, as a thickener in WCO grease formulation, holds a major problem in the mechanical stability of the grease. The SBE and WCO do not completely homogenise, causing oil separation and sedimentation during storage (Abdulbari et al., 2017). Thus, adding fumed silica as a modifier with SBE can improve the grease strength and stability during operation with a slight increase in the coefficient of friction at the accepted range (Abdulbari et al., 2017). Other advantages also include boosting the thermal stability of grease up to 150°C without degradation and having no effect on the corrosivity towards metal. A recent study also showed that the dropping point of grease comprised waste transformer oil (WTO) and sodium stearate thickener was enhanced from 150°C to 185–200°C, which is 3.6% using fumed silica (Rahman et al., 2020). The F.S. molecules bond in a strong interaction and form a new non-melting structure in the grease.

Furthermore, wear preventative additives such as the popular molybdenum disulfide and graphite are needed to boost the performance of the formulated grease. However, there is no evident research on the performance of these additives in WCO-based grease to compete with commercial grease in the market. Over the years, Molybdenum disulfide and graphite

have demonstrated satisfactory results as corrosion inhibitors and anti-wear additives in grease formulations. Early's earlier study (Sinitsyn & Viktorova, 1968) concluded that MoS₂ has greater antifriction properties for Si and calcium-complex while denoting 30% more efficiency for Li grease than graphite. MoS₂ has a layer lattice structure, and the atoms in each layer or "basal plane" are positioned at the corners of regular hexagons, leading to higher load-carrying capacity (Mohammed, 2013).

Meanwhile, combining MoS₂ with graphite at a 60:40 ratio has a synergetic effect in increasing the weld load by 120 kg while decreasing the wear scar diameter by 22% (Antony et al., 1994). Also, these combinations at any ratio increase the extreme pressure or wear characteristics of the organoclay grease type. Without a scientific study, this synergistic effect in MoS₂ and graphite will not work on WCO-SBE-based grease. MoS₂ is more efficient and economical than graphite in Li, Ca, Na and Li-Ca grease due to its fewer wear properties. In recent years, environmental concerns have necessitated focusing on renewable resource-based components for grease composition (Abdulbari et al., 2015). Thus, recycling waste cooking oil and SBE, which are disposed of freely after expensive treatment into the environment, will be a good option to address environmental issues such as greenhouse gas emissions, odour pollution and non-biodegradable. To enhance the performance of WCO/SBE grease, rheology modifiers such as fumed silica and additives such as molybdenum disulfide can be used widely with more research support in the future.

The Treatments on Spent Bleaching Earth into Sustainable Energy

The treatment of SBE is crucial since it has sparked debate among researchers due to its hazardous properties. Many different methods are being applied to remove impurities in it. It is extremely costly within a large area requirement because SBE treatment does not only remove severe undesired impurities. Nonetheless, it can be converted into various valuable substances, including ash for the cement industry, industrial-grade oil, fatty acids, biodiesel, thickening agent, bio-fertiliser, and livestock feed.

A study by Chanrai and Burde (2004) revealed the general method of recovering oil from SBE. The recovery method was designed and invented by Narain Grirdhar Chanrai (Singapore) and Santosh Gajanan Burde (Johor). This method comprises three sub-process: reacting SBE with solvent between the temperature of 35°C and 50°C, separation of solid and liquid gained from slurry during previous steps, and extracting oil from the liquid obtained in the previous steps. The first treatment step begins with a reaction between SBE with solvent (n-hexane) from 35°C until 50°C in an agitated reactor for around 15 to 45 minutes. The main purpose of agitated reactor consumption is to dissolve oil from bleaching earth into the solvent. The standard acceptable range of slurry concentration inside the agitator's vessel is between 30% and 35%. Hence,

the typical slurry produced will be further processed into a Porous Metal Filter (PMF) associated with plates to settle solids. This process is used to separate the solid from the miscella. Miscella is known as an oil solution in the solvent. PMF will process slurries under a range of 1 bar to 4 bars. This alternative method replaces gravity settlers' and the vacuum belt filter system. Usually, there are two stages of the filtration process for PMF to improve filtration efficiency.

As mentioned above, the first PMF has the output of miscella (being recycled to Miscella Distillation), and the separated cake comprises 70% to 75% dryness. The separated cake mixing of fresh or recycled hexane is carried out in the second agitated reactor. This process aims to recover the remaining or further adsorbed oil from the cake in the second agitated reactor vessel. The second PMF is further utilised as a separator between filtered cakes to produce Deoiled Bleaching Earth (DBE) with 3% to 5% of oil content through desolventisation. Meanwhile, severe miscella generated by the first PMF will undergo the distillation process to obtain extracted oil in the distillation plant. The distillation plant consists of a rising and falling film evaporator. The reaction may cause hexane to be produced, evaporated, condensed, and recycled back to the second agitated reactor. However, the extracted oil produced from the distillation unit is processed in deodorising units to remove free fatty acid (FFA). Other products, such as industrial-grade palm oil, will be yielded from this study.

The deoiled bleaching earth is from the desolventisation unit, resulting in less residue oil presence in processed SBE. So, the product of the resultant bleaching earth is considered safe to be disposed of in landfills due to minimum ignition possibility impact. Furthermore, it can be generated into anhydrous clay through the incinerator's burning process since it is a fuel substance (Afzan et al., 2020). Nonetheless, anhydrous clay is a good raw material that can be applied in cement manufacturing industries. Figure 4 shows the steps in treating SBE and turning it into useful products.

Smallwood (2020) discovered a method to reduce the fire ignition effect of SBE. It found that the fire explosion can be avoided by adding some Granular Salt or Brine at a specific rate, which allows the spontaneous combustion problem to be eliminated. To confirm this issue, Norman J. Smallwood also identified the hygroscopic effect properties of salt by exposing the solution (SBE + salt) under the sunlight during the summer of 2012 for one week. The solution did not ignite when the salt content was as low as 35% by weight. He proposed 45% as the best salt composition, defined as the minimum required content. The pattern of this salt formulation had been designed in the form of salt-lick products, either in block or granular form. It received extremely positive feedback from five cattle producers in the U.S. States of Colorado, Missouri, and Louisiana after testing. This treatment is most commonly used to convert SBE into animal and livestock feed supplements for further nutrition development.

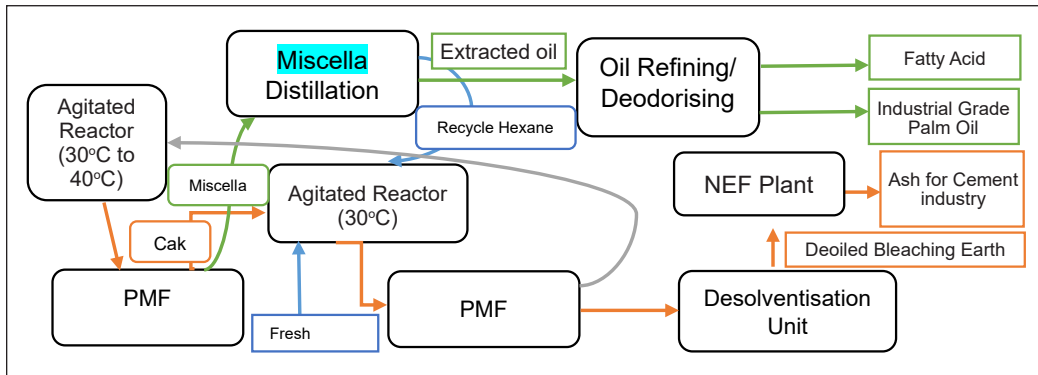


Figure 4. Steps in treating SBE into sustainable products (Chanrai & Burde, 2004)

Selection of Fumed Silica (F.S.) as Thickener for Grease Formulation

Fumed Silica is also known as pyrogenic silica because it is produced by a flame reaction between silicon tetrachloride and oxygen (Ha et al., 2013). It is available in white powder form and has non-toxic properties. It is commonly used as a thickener and anticaking agent.

Moreover, it is made up of silicon dioxide with an amorphous shape (Rahman et al., 2018) and covered in silanol groups (Vansant et al., 1995). The silanol groups are extremely reactive and may be used to initiate chemical processes. The number of silanol groups present around the surfaces of F.S. powder determines its reactivity surface (Whitby, 2020). According to Barthel et al. (2005), the structure of F.S. is related to having space-filling particle properties against a large surface area. It is associated with a small number of micropores within a range surface area between 50 and 400 m²g⁻¹. Therefore, it can be used as a free-flow additive in powder-like solids, forceful reinforcing filler in elastomers, and thickening in various liquids. In WCO, F.S. will clump together and create three-dimensional networks that can immobilise the oil by keeping its shape and constructing structural frameworks in solvents. It exists in nanoparticle form, with its surface chemistry and shape. The silanol groups on the particle surface work as molecular adsorption sites for species that establishes hydrogen bonds or interact with one another as donors or acceptors. According to Adhikari et al. (1994), the adsorption of triglyceride molecules in vegetable oils onto silica powder surfaces occurs as a result of hydrogen bonding formation between the silanol groups and the ester carbonyl groups. It will significantly reduce the silanol group that repeatedly forms hydrogen bonds. Israelachvili (2011) and Raghavan et al. (2000) stated that a 'Van der Waals' attraction is a key factor in the aggregation of F.S. in WCO. It may result in potential energy availability during mixing due to the electrostatic forces between the overlapping double layers of molecules (hydrogen bonding between silanol groups and adjacent hydrophilic

fumed silica particles). Then, it brings a semi-solid mixture forms without any leakages (Whitby, 2020).

The use of F.S. has numerous advantages. Its structure is in anisotropic network form, which resembles fats in form and mechanical properties. The network synthesis by F.S. in WCO increases the mixture viscosity and thickens structure stability (Whitby, 2020). Sugino and Kawaguchi (2017) mention that having an extra F.S. in oil can turn the liquid (oil) into gel form. Instead of thickening and anticaking agents, it can also be used as an anti-foaming and anti-blocking agent in catalysis, cosmetics, paper coating, pharmaceuticals, cable insulation, adhesive, construction, and automotive, and applied in cartridge toner for printing, stabilising agent in the food industry, bleaching cream and fire extinguisher. Therefore, selecting F.S. in grease formulation is a good idea due to its properties and physical structure, improving grease performance and meeting the industrial-grade criteria.

However, the issue regarding F.S. consumption is improper handling of this substance during operation, as Rav et al. (2020) mentioned. Several increment cases had been reported between 2015 and 2016 due to the respiratory problems caused by F.S. Commonly, Single-dose exposure to F.S. does not cause lung disease. Still, repetitive inhalation (multiple-dose) may cause a fibrogenic formation and bio-persistence process of F.S. in the lung (Sun et al., 2016). The foreign material will be present in the lung, and no treatments are currently available to remove F.S. from the lung. This problem causes patients to have difficulty breathing. The key challenges for the DOSH communities are raising awareness among stakeholders, workers, and even the public about the long-term effects of uncontrolled dust release and the magnitude of health problems caused by silicosis (Garcia et al., 2019). Therefore, proper precautions should be taken against F.S. during application. Table 4 summarises F.S. as the selected thickener for grease formulation.

Table 4
Summarisation on F.S. as a selected thickener for grease formulation

Full Name	Fumed Silica
Nomenclature	F.S.
Characteristic	<ul style="list-style-type: none"> ● It is available in white powder form and has non-toxic properties. ● Made up of silicon dioxide with an amorphous shape covered in silanol groups. ● The silanol groups are extremely reactive and may be used to initiate chemical processes. ● The structure of F.S. is related to having space-filling particle properties with a small number of micropores within a range surface area between 50 and 400 m²g⁻¹ against a large surface area.
Application	<ul style="list-style-type: none"> ● It is commonly used as a thickener and anticaking agent. ● It can also be used as an anti-foaming and anti-blocking agent in catalysis, cosmetics, paper coating, pharmaceuticals and cable insulation.

Table 4 (continue)

Full Name	Fumed Silica
Advantages	<ul style="list-style-type: none"> ● Its structure is in anisotropic network form. ● The network synthesis by F.S. in WCO increases the mixture viscosity and thickens structure stability.
Hazardous	<ul style="list-style-type: none"> ● Respiratory problems caused by F.S., according to several increment cases, had been reported between 2015 and 2016 (Rav et al., 2020). ● The repetitive inhalation (multiple-dose) may cause a fibrogenic formation and bio-persistence process of F.S. in the lung. No treatment is available to remove F.S. from the lung. ● It may cause difficulties in breathing.
Taking Action	<ul style="list-style-type: none"> ● Raising awareness among stakeholders, workers, and even the general public about the long-term effects of uncontrolled dust release and the magnitude of health problems caused by silicosis is quite challenging.

Molybdenum Disulphide as Selected Additives in Grease Formulation

MoS₂ is a dark grey to black powder (Epshteyn & Risdon, 2010). It is widely used in a variety of applications outside the aerospace industry. Other reasons for its extensive applications are layer structure, large specific area, special electronic and electrochemical properties, and good surface modification properties (Cui et al., 2016). It has also been an excellent solid lubricant for years and was traditionally used as grease for bit lubrication (Fink, 2021). MoS₂ has a solid lamellar structure composed of atomically thin planes that easily slide between each other (Savan et al., 2006). The cross-sectional area for lamellar structure within the eutectic system comprises a free surface and solid-liquid interface, enabling the structure to move smoothly with less friction. The increased lamellar spacing may result in a slower solidification rate (Bei et al., 2003). It means that the grease with semi-solid form will provide larger lamellar spacing (larger solid-liquid interface), enabling it to provide less frictional force between grease and plane (surface) due to interface gaps availability that can fit with contact surface area. According to Savan et al. (2006), there is a significant difference between lubricants within and without MoS₂ addition, where it tends to improve the adhesion to the substrate, provide higher density and viscosity of grease, and extensively possess higher purity, which are the key factors of tribology improvement properties that include wear resistance enhancement and low coefficient of friction. A study by Srinivas et al. (2017) also revealed the effectiveness of MoS₂ nanoparticles as additives in lubricant technology to commercial oil (SAE 20W-40 grade), and the result showed that the nano lubricants reduced wear and friction when compared to commercial oil. Zebox et al. (2022) also found that adding MoS₂ in grease minimised the wear part of equipment by increasing the service life at the part of the frictional unit. Table 5 summarises MoS₂ as the selected additive for grease formulation.

Table 5
Summarisation of MoS₂ as a selected additive for grease formulation

Full Name	Molybdenum Disulphide
Nomenclature	MoS ₂
Characteristic	<ul style="list-style-type: none"> ● It is a powder with a dark grey-to-black appearance. ● It has a good layer structure, a large specific area, special electronic and electrochemical properties, and good surface modification properties, which make it reasonable for extensive application. ● Comprises a solid lamellar structure.
Application	<ul style="list-style-type: none"> ● Widely used in a variety of applications outside the aerospace industry.
Advantages	<ul style="list-style-type: none"> ● It also has been an excellent solid lubricant for many years and was traditionally used as grease for bit lubrication. ● Easily slide between each other due to the presence of solid lamellar structures with atomically thin planes. ● It makes the grease structure move smoothly with less frictional forces due to the free surface and solid-liquid interface by a eutectic system of lamellar structure. ● MoS₂ improves the adhesion to the substrate, provides higher density and viscosity of grease, and extensively possesses higher purity; all of them are the key factors of tribology improvement properties that include wear resistance enhancement and low coefficient of friction.
Prove of Study for Lubricating within MoS ₂ Application.	<ul style="list-style-type: none"> ● Srinivas et al. (2017) also revealed the effectiveness of MoS₂ nanoparticles as additives in lubricant technology to commercial oil (SAE 20W-40 grade). They found that nano lubricants reduced wear and friction compared to commercial oil. ● Zebox et al. (2022) also found that adding MoS₂ in grease minimised the wear part of equipment by increasing the service life at the part of the frictional unit.

CONCLUSION

SBE as a grease thickener is better due to its sticky properties, high viscosity and density. The viscosity of the mixture minimises penetration risk against WCO. Unfortunately, the study also found a tendency of SBE to cause spontaneous auto-ignition reactions due to the rapid oxidation of residue oil and autocatalysis action by clay minerals. This study shows that the SBE must first be treated to be free from residue oil and for safe use. According to Jong (2021), the minimum consideration for SBE as hazardous waste should be less than 3% of oil presence. The SBE also can be treated by adding (salt) to cut off the spontaneous auto-ignition reaction, as shown in Smallwood (2020). Using WCO as a base oil is a good idea because it is closely related to environmental protection quality and has a lower peroxide value. This waste source can be recycled to generate renewable energy. WCO should be filtered, heated, and stored in a tightly sealed container to reduce rancidity. Thus, the F.S. is recommended for use, but it must be properly managed, and continuous inhalation must be avoided during handling. MoS₂ is recommended to enhance grease performance as an antioxidant and heat-resistant agent. Wearing Personal Protective Equipment (PPE) is strongly advised to reduce the risk of exposure and silicosis disease.

ACKNOWLEDGMENT

The authors wish to acknowledge the financial support from the Ministry of Higher Education Malaysia through the grant RDU210147 (FRGS/1/2021/TK0/UMP/02/76) and from University Malaysia Pahang through the grants PGRS180396 and PGRS200356.

REFERENCES

- Abdulbari, H. A., Oluwasoga Akindoyo, E., & Mahmood, W. K. (2015). Renewable resource-based lubricating greases from natural and synthetic sources: Insights and future challenges. *ChemBioEng Reviews*, 2(6), 406-422. <https://doi.org/10.1002/cben.201500006>
- Abdulbari, H. A., Rosli, M. Y., Abdurrahman, H. N., & Nizam, M. K. (2011). Lubricating grease from spent bleaching earth and waste cooking oil: Tribology properties. *International Journal of the Physical Sciences*, 6(20), 4695-4699. <https://doi.org/10.5897/IJPS11.561>
- Abdulbari, H., Zuhan, N., & Mahmood, W. (2017). Biodegradable grease from palm oil industry wastes. *Journal of Advanced Research in Fluid Flow*, 1-10
- Adhikari, C., Proctor, A., & Blyholder, G. D. (1994). Diffuse-reflectance fourier-transform infrared spectroscopy of vegetable oil triglyceride adsorption on silicic acid. *Journal of the American Oil Chemists' Society* 71, 589-594. <https://doi.org/10.1007/BF02540584>
- Afzan, M., Ithnin, A. M., & Jazair, W. (2020). Combustion performance and exhaust emission analysis of Spent Bleaching Earth (SBE) oil as burner's fuel. In U. Sabino, F. Imaduddin & A. R. Prabowo (Eds.), *Proceedings of the 6th International Conference and Exhibition on Sustainable Energy and Advanced Materials* (pp. 713-721). Springer. https://doi.org/10.1007/978-981-15-4481-1_68
- Almeida, D. T., Viana, T. V., Costa, M. M., de Santana Silva, C., & Feitosa, S. (2019). Effects of different storage conditions on the oxidative stability of crude and refined palm oil, olein and stearin (*Elaeis guineensis*). *Food Science and Technology*, 39(1), 211-217. <https://doi.org/10.1590/fst.43317>
- Anderson, K. J. (1991). A history of lubricants. *MRS Bulletin*, 16(10), 69-69. <https://doi.org/10.1557/S0883769400055895>
- Antony, J., Mittal, B., Naithani, K., Misra, A., & Bhatnagar, A. (1994). Molybdenum disulphide combinations in lubricating greases. *Wear*, 174, 33-37
- Awogbemi, O., Onuh, E., & Inambao, F. L. (2019). Comparative study of properties and fatty acid composition of some neat vegetable oils and waste cooking oils. *International Journal of Low-Carbon Technologies*, 14(3), 417-425. <https://doi.org/10.1093/ijlct/ctz038>
- Barthel, H., Rösch, L., & Weis, J. (2005). Fumed silica - Production, properties, and applications. In N. Auner & J. Weis (Eds.), *Organosilicon Chemistry II* (pp.761-778). Wiley. <https://doi.org/10.1002/9783527619894.ch91>
- Bei, H., George, E., Kenik, E., & Pharr, G. (2003). Directional solidification and microstructures of near-eutectic Cr-Cr₃Si alloys. *Acta Materialia*, 51(20), 6241-6252. [https://doi.org/10.1016/S1359-6454\(03\)00447-6](https://doi.org/10.1016/S1359-6454(03)00447-6)
- Chanrai, N. G., & Burde, S. G. (2004). Recovery of oil from spent bleaching earth. *US Patent*, 6(780), 321.

- Cheong, K., Loh, S., & Salimon, J. (2013). Effect of spent bleaching earth based bio organic fertilizer on growth, yield and quality of eggplants under field condition. *AIP Conference Proceedings*, 1571, 744-748. <https://doi.org/10.1063/1.4858743>
- Cui, X., Chen, H., & Yang, T. (2016). Research progress on the preparation and application of nano-sized molybdenum disulfide. *Acta Chimica Sinica*, 74, 392-400. <https://doi.org/10.6023/A15110712>
- De Leonardis, A., Macciola, V., & Falice, M. (2000). Copper and iron determination in edible oil by graphite furnace atomic absorption spectrometry after extraction with dilute nitric acid. *International Journal of Food Science & Technology*, 35(4), 371-375. <https://doi.org/10.1046/j.1365-2621.2000.00389.x>
- Dees, S., Gasteuil, A., Kaufmann, R. K., & Man, M. (2008). *Assessing the factors behind oil price changes* (Working Paper No. 855). European Central Bank. https://www.researchgate.net/publication/4890967_Assessing_the_factors_behind_oil_price_changes
- Delaneau, J. (2021). *What is stearic acid for?* Oceanica Skincare. <https://oceanicaskin.care/blogs/news/what-is-stearic-acid-for>
- Dermawan, D., & Ashari, M. L. (2018). Studi pemanfaatan limbah padat industri pengolahan minyak kelapa sawit spent bleaching earth sebagai pengganti agregat pada campuran beton [Study on the utilization of palm oil processing industry solid waste spent bleaching earth as a substitute for aggregate in concrete mixtures]. *Jurnal Presipitasi Media Komunikasi dan Pengembangan Teknik Lingkungan*, 15(1), 7-10. <https://doi.org/10.14710/presipitasi.v15i1.7-10>
- Dye, J. L. (2021). *Lithium*. Encyclopedia Britannica. <https://www.britannica.com/science/lithium-chemical-element>
- Ephsteyn, Y., & Risdon, T. J. (2010, January 28-30). *Molybdenum disulfide in lubricant applications – A review*. [Paper presentation]. Proceedings of the 12 Lubricating Grease Conference, Goa, India. <http://www.nlgi-india.org/images/PDF/Yakov%20Ephsteyn.pdf>
- Farid, M. A., Roslan, A. M., Hassan, M. A., Hasan, M. Y., Othman, M. R., & Shirai, Y. (2020). Net energy and techno-economic assessment of biodiesel production from waste cooking oil using a semi-industrial plant: A Malaysia perspective. *Sustainable Energy Technologies and Assessments*, 39, Article 100700. <https://doi.org/10.1016/j.seta.2020.100700>
- Fattah, R. A., Mostafa, N. A., Mahmoud, M. S., & Abdelmoez1, W. (2014). Recovery of oil and free fatty acids from spent bleaching earth using sub-critical water technology supported with kinetic and thermodynamic study. *Advances in Bioscience and Biotechnology*, 5(3), 261-272. <https://doi.org/10.4236/abb.2014.53033>
- Feo, G. D., Domenico, A. D., Ferrara, C., Abate, S., & Osseo, L. S. (2020). Evolution of waste cooking oil collection in an area with long-standing waste management problems. *Sustainability*, 12(20), Article 8578. <http://dx.doi.org/10.3390/su12208578>
- Fink, J. (2021). *Petroleum Engineer's Guide to Oil Field Chemicals and Fluids* (3rd ed.). Gulf Professional Publishing. <https://doi.org/10.1016/C2020-0-02705-2>
- Garcia, D. D., Latorre, R. R., Sultan, N. M., Yerba, O. R., Palacios, E. A., & Cano, A. D. (2019). Silicosis: Origins and consequences. *American Journal of Medical Sciences and Medicine*, 7(3), 60-63. <https://doi.org/10.12691/ajmsm-7-3-2>

- Godson, T. E., & Vinoth, E. (2015). Biodiesel production from waste cooking oil. *International Journal of Students' Research In Technology & Management*, 3(8), 448-450. <https://doi.org/10.18510/ijstrtm.2015.383>
- Gordon, M. (2004). 7 - Factors affecting lipid oxidation. In R. Steele (Ed.), *Understanding and Measuring the Shelf-Life of Food* (pp. 128-141). Woodhead Publishing. <https://doi.org/10.1533/9781855739024.1.128>.
- Ha, S. W., Weitzmann, M. N., & Beck Jr, G. R. (2013). Chapter 4 - Dental and skeletal applications of silica-based nanomaterials. In K. Subramani, W. Ahmed, & J. K. Hartsfield (Eds.), *Nanobiomaterials in Clinical Dentistry* (pp. 69-91). William Andrew Publishing. <https://doi.org/10.1016/B978-1-4557-3127-5.00004-0>
- Handajani, U., Harsini, M., & Wicaksono, Z. (2014). Determine of copper metal in cooking oil by saponification method with atomic absorption spectrophotometer (AAS). *Malaysian Journal of Fundamental and Applied Sciences*, 10(4), 179-183. <https://doi.org/10.11113/mjfas.v10n4.270>
- Hernandez, E. M. (2016). 4 - Specialty oils: Functional and nutraceutical properties. In T. A. B. Sanders (Ed.), *Function Dietary Lipids* (pp. 69-101). Woodhead Publishing. <https://doi.org/10.1016/B978-1-78242-247-1.00004-1>.
- Israelachvili, J. N. (2011). *Intermolecular and Surface Forces*. Academic press. <https://doi.org/10.1016/C2009-0-21560-1>
- Jaarin, K., & Kamisah, Y. (2012). Repeatedly heated vegetable oils and lipid peroxidation. In A. Catala (Ed.), *Lipid Peroxidation* (pp. 211-228). InTech Open. <http://dx.doi.org/10.5772/46076>
- Japar, N. S. A., Aziz, M. A. A., & Razali, M. N. (2020). *Fundamental Study of Waste Oil Potential as Base Oil Alternative in Grease Formulation*. Core. <https://core.ac.uk/download/pdf/186358742.pdf>
- Johnson, O. A., & Affam, A. C. (2019). Petroleum sludge treatment and disposal: A review. *Environment Engineering Research*, 24(2), 191-201. <https://doi.org/10.4491/eer.2018.134>
- Jong, H. N. (2021). *Palm Oil Waste is Latest Item Declared Non-Hazardous by Indonesia*. Mongabay. <https://news.mongabay.com/2021/04/palm-oil-waste-spent-bleaching-earth-non-hazardous-indonesia/>
- Kamaruzaman, W. N., & Zin, N. S. M. (2019, June). *Recycle of used cooking oil*. [Paper presentation]. Conference: International Professional Learning Communities in Education 2019. Kuala Lumpur, Malaysia.
- Khalid, R. S., Helaluddin, A., Alaama, M., Abdulkader, M. A., Kasmuri, A., & Abbas, S. A. (2016). Reliability of graphite furnace atomic absorption spectrometry as alternative method for trace analysis of arsenic in natural medicinal products. *Tropical Journal of Pharmaceutical Research September*, 15(9), 1967-1972. <http://dx.doi.org/10.4314/tjpr.v15i9.22>
- Libert, M. A. (1987). Final report on the safety assessment of oleic acid, lauric acid, palmitic acid, myristic acid, and stearic acid. *International Journal of Toxicology*, 6(3), 321-401. <https://doi.org/10.3109/10915818709098563>
- Livent. (2018). *Handling Guide for Lithium Hydroxid*. Livent. <https://livent.com/wp-content/uploads/2018/10/Lithium-Hydroxide-Safe-Handling-Guide-v10.09.18.pdf>
- Lopes, M., Miranda, S. M., & Belo, I. (2020). Microbial valorization of waste cooking oils for valuable compounds production - A review. *Critical Reviews in Environmental Science and Technology*, 50(24), 2583-2616. <https://doi.org/10.1080/10643389.2019.1704602>

- Manarattanasuwan, S. (2011). *Toxic Trace Metals in Edible Oils by Graphite Furnace Atomic Absorption Spectrophotometry*. Semantic Scholar. <https://www.semanticscholar.org/paper/Toxic-Trace-Metals-in-Edible-Oils-by-Graphite/df2b51857be01662333351b98187a146c538a7c>
- Mannu, A., Garroni, S., Porras, J. I., & Mele, A. (2020). Available technologies and materials for waste. *Processes*, 8(3), Article 366. <https://doi.org/10.3390/pr8030366>
- Mohammed, M. A. (2013). Effect of additives on the properties of different types of greases. *Iraqi Journal of Chemical and Petroleum Engineering*, 14(3), 11-21.
- New Jersey Department of Health and Senior Services. (2014). *Lithium hydroxide monohydrate*. Hazardous Substance Fact Sheet. <https://nj.gov/health/eoh/rtkweb/documents/fs/1128.pdf>
- Nizam, N. A., & Misdan, N. (2022). Review of the production of biodiesel from waste cooking oil using acid/alkaline based catalysts. *Progress in Engineering Application and Technology*, 3(1), 954-966. <https://doi.org/10.30880/peat.2022.03.01.093>
- Noor, N. A. M., & Hua, A. K. (2016). Cooking oil management in cafeteria operator: A review. *International Research Journal of Humanities & Social Science*, 1(4), 29-39.
- Othman, N. (2009). *Production of grease from waste cooking oil* [Bachelor dissertation]. Universiti Malaysia Pahang, Malaysia. <https://www.semanticscholar.org/paper/PRODUCTION-OF-GREASE-FROM-WASTE-COOKING-OIL-BINTI-A-Othman/95a5a7edad68692a510a8918afc61369a47c3993>
- Panadare, D. C., & Rathod, V. K. (2015). Application of waste cooking oil than biodiesel: A review. *Iranian Journal of Chemical Engineering*, 12(3), 55-76.
- Piotrowska-Cyplik, A., Chrzanowski, L., Cyplik, P., Dach, J., Olejnik, A., Staninska, J., Czarny, J., Lewicki, A., Marecik, R., & Powierska-Czarny, J. (2013). Composting of oiled bleaching earth: Fatty acids degradation, phytotoxicity and mutagenicity changes. *International Biodeterioration & Biodegradation*, 78, 49-57. <https://doi.org/10.1016/j.ibiod.2012.12.007>
- Raghavan, S., Hou, J., Baker, G., & Khan, S. (2000). Colloidal interactions between particles with tethered nonpolar chains dispersed in polar media: Direct correlation between dynamic rheology and interaction parameters. *Langmuir*, 16(3), 1066-1077. <https://doi.org/10.1021/la9815953>
- Rahman, M. R., Hui, J. L. C., & Hamdan, S. (2018). 5 - Nanoclay dispersed phenol formaldehyde/fumed silica nanocomposites: Effect of diverse clays on physicomechanical and thermal properties. In M. R. Rahman (Ed.), *Silica and Clay Dispersed Polymer Nanocomposites (Preparation, Properties and Applications)* (pp. 59-70). Woodhead Publishing. <https://doi.org/10.1016/B978-0-08-102129-3.00005-1>
- Rahman, W., Aziz, M. A. A., Hamid, N., & Japar, N. S. A. (2020). Thermal stability study of grease formulated from industrial waste oil. *Platform: A Journal of Engineering*, 4(1), 20-28.
- Rajvanshi, A., & Pandey, P. K. (2016). Lubricating grease from waste cooking oil and waste motor sludge. *International Journal of Chemical and Molecular Engineering*, 10(9), 1220-1223. <https://doi.org/10.5281/zenodo.1126898>
- Rav, A. P., Sivasankar, S., Razali, N. K., Karmegam, K., Velu, P., Kulanthayan, S., & Naeini, H. S. (2020). A review of occupational safety and health problems among quarry plant workers. *Malaysian Journal of Medicine and Health Sciences*, 16(11), 194-200.

- Razali, M. N., Aziz, M. A. A., Hamdan, W. N. A. W. M., Salehan, N. A. M., & Rosli, M. Y. (2017). Synthesis of grease from waste oils and red gypsum. *Australian Journal of Basic and Applied Sciences*, *11*(113), 154-159.
- Rinaldi, L., Wu, Z., Giovando, S., Bracco, M., Crudo, D., Bosco, V., & Cravotto, G. (2017). Oxidative polymerization of waste cooking oil with air under hydrodynamic cavitation. *Journal Green Processing and Synthesis*, *6*(4), 425-432. <https://doi.org/10.1515/gps-2016-0142>
- Rokiah, O., Khairunisa, M., Youventharan, D., & Arif, S. M. (2019). Effect of processed spent bleaching earth content on the compressive strength of foamed concrete. *IOP Conference Series: Earth and Environmental Science*, *244*(1), Article 012013. <https://doi.org/10.1088/1755-1315/244/1/012013>
- Sani, G., & Florillo, A. (2020). The use of lithium in mixed states. *CNS Spectrums*, *25*(4), 449-451. <https://doi.org/10.1017/S1092852919001184>
- Savan, A., Pflüger, E., Voumard, P., Schröer, A., & Simmonds, M. (2006). Modern solid lubrication: Recent developments and applications of MoS₂. *Lubricant Science*, *12*(2), 185-203. <https://doi.org/10.1002/ls.3010120206>
- Sharma, U. C., & Singh, N. (2019). Biogrease for environment friendly lubrication. In B. R. Gurjar & S. Y. Rao (Eds.), *Environmental Science and Engineering Vol. 1 Sustainable Development* (pp. 305-317). Studium Press.
- Singh-Ackbarali, D., Maharaj, R., Mohamed, N., & Ramjattan-Harry, V. (2017). Potential of used frying oil in paving material: Solution to environmental pollution problem. *Environmental Science and Pollution Research*, *24*, 12220-12226. <https://doi.org/10.1007/s11356-017-8793-z>
- Sinitzyn, V. V., & Viktorova, Y. S. (1968). Graphite and molybdenum disulfide in plastic greases. *Chemistry and Technology of Fuels and Oils*, *4*(8), 585-588. <https://doi.org/10.1007/BF00717718>
- Smallwood, N. J. (2020). *Use of spent bleaching earth from edible oil processing in the formulation salt* (U.S. Patent No. 10,624,367). U.S. Patent and Trademark Office. <https://patentimages.storage.googleapis.com/48/75/77/682b1b67dce123/US10624367.pdf>
- Smith, W. N., McCloskey, J., & Atterbury, A. (2000). *Pouched ingredients for preparing greases* (U.S. Patent No. 6,153,563). U.S. Patent and Trademark Office. <https://patents.google.com/patent/US6153563A/en?q=US6153563A>
- Srinivas, V., Thakur, R. N. & Jain, A. K. (2017). Anti-wear, anti-friction and extreme pressure properties of motor bike engine oil dispersed with molybdenum disulphide nano-particles. *Tribology Transactions*, *60*(1), 12-19. <https://doi.org/10.1080/10402004.2016.1142034>.
- Sugino, Y., & Kawaguchi, M. (2017). Fumed and precipitated hydrophilic silica suspension gels in mineral oil: Stability and rheological properties. *Gels*, *3*(3), Article 32. <https://doi.org/10.3390/gels3030032>
- Sun, B., Wang, X., Liao, Y. P., Ji, Z., Chang, C. H., Pokhrel, S., Ku, J., Liu, X., Wang, M., Dunphy, D. R., Li, R., Meng, H., Madler, L., Brinker, C. J., Nel, A. E., & Xia, T. (2016). Repetitive dosing of fumed silica leads to profibrogenic effects through unique structure-activity relationships and biopersistence in the lung. *ACS Nano*, *10*(8), 8054-8066. <https://doi.org/10.1021/acsnano.6b04143>

- Susskind, L., Chun, J., Goldberg, S., Gordon, J., Smith, G., & Zaerpoor, Y. (2020). Breaking out of carbon lock-in: Malaysia's path to decarbonization. *Frontiers in Built Environment*, 6, Article 21. <https://doi.org/10.3389/fbuil.2020.00021>.
- Suzihaque, M., Alwi, H., Ibrahim, U. K., Abdullah, S., & Haron, N. (2022). Biodiesel production from waste cooking oil: A brief review. *Materials Today: Proceedings*, 63(1), S490-S495. <https://doi.org/10.1016/j.matpr.2022.04.527>
- Szelong, K., & Fan, K. (2020). *Chemistry of lithium (Z=3)*. Libretexts Chemistry. [https://chem.libretexts.org/Bookshelves/Inorganic_Chemistry/Supplemental_Modules_and_Websites_\(Inorganic_Chemistry\)/Descriptive_Chemistry/Elements_Organized_by_Block/1_s-Block_Elements/Group__1%3A_The_Alkali_Metals/Z003_Chemistry_of_Lithium_\(Z3\)](https://chem.libretexts.org/Bookshelves/Inorganic_Chemistry/Supplemental_Modules_and_Websites_(Inorganic_Chemistry)/Descriptive_Chemistry/Elements_Organized_by_Block/1_s-Block_Elements/Group__1%3A_The_Alkali_Metals/Z003_Chemistry_of_Lithium_(Z3))
- Tan, K. T., Lee, K. T., & Mohamed, A. R. (2011). Potential of waste palm cooking oil for catalyst-free biodiesel production. *Energy*, 36(4), 2085-2088. <https://doi.org/10.1016/j.energy.2010.05.003>
- Vansant, E. F., Van Der Voort, P., & Vrancken, K. C. (1995). *Characterization and Chemical Modification of the Silica Surface*. Elsevier.
- Vitz, E., Moore, J. W., Shorb, J., Prat-Resina, X., Wendorff, T., & Hahn, A. (2021). *Foods- vegetable oil hydrogenation, trans fats, and percent yield*. Chemistry LibreTexts. [https://chem.libretexts.org/Bookshelves/General_Chemistry/Book%3A_ChemPRIME_\(Moore_et_al.\)/03%3A_Using_Chemical_Equations_in_Calculations/3.04%3A_Percent_Yield/3.4.02%3A_Foods-_Vegetable_Oil_Hydrogenation_Trans_Fats_and_Percent_Yield](https://chem.libretexts.org/Bookshelves/General_Chemistry/Book%3A_ChemPRIME_(Moore_et_al.)/03%3A_Using_Chemical_Equations_in_Calculations/3.04%3A_Percent_Yield/3.4.02%3A_Foods-_Vegetable_Oil_Hydrogenation_Trans_Fats_and_Percent_Yield)
- Vollaard, B. (2017). Temporal displacement of environmental crime: Evidence from marine oil pollution. *Journal of Environmental Economics and Management*, 82, 168-180. <https://doi.org/10.1016/j.jeem.2016.11.001>
- Whitby, C. P. (2020). Structuring edible oils with fumed silica particles. *Frontiers in Sustainable Food Systems* 4, Article 585160. <https://doi.org/10.3389/fsufs.2020.585160>
- Yang, B., Kim, S., Choi, C. H., Jeoung, H. W., & Kim, H. (2017). Effects of scutellaria baicalensis extract on skin lesion of contact dermatitis induced by DNFB in mice. *Journal of Physiology & Pathology in Korean Medicine*, 31(1), 59-64. <https://doi.org/10.15188/kjopp.2017.02.31.1.59>
- Younes, M., Aggett, P., Aguilar, F., Crebelli, R., Dusemund, B., Filipic, M., Frutos, M. J., Galtier, P., Gott, D., Gundert-Remy, U., Kuhnle, G. G. Leblanc, J. C., Lillegaard, I. T., Moldeus, P., Mortensen, A., Oskarsson, A., Stankovic, I., Waalkens-Berendsen, U. Woutersen, R. A ... Lambre, C. (2018). Re-evaluation of silicon dioxide (E 551) as a food additive. *European Food Safety Authority Journal*, 16(1), Article e05088. <https://doi.org/10.2903/j.efsa.2018.5088>
- Zebox, A., Abutolib, S., & Vaxobjon, M. (2022). Ways to improve the lubricating properties of greases. *Texas Journal of Engineering and Technology*, 7, 1-4.



Review Article

The Unified Model of Electronic Government Adoption (UMEGA): A Systematic Literature Review with Meta-Analysis

Rakib Ahmed Saleh¹, Rozi Nor Haizan Nor^{1*}, Md. Tariqul Islam², Yusmadi Yah Jusoh¹ and Salfarina Abdullah¹

¹Department of Information System, Faculty of Computer Science and Information Technology, Universiti Putra Malaysia, 43400 UPM, Serdang, Selangor, Malaysia

²School of Business and Economics, Universiti Putra Malaysia, 43400 UPM, Serdang, Selangor, Malaysia

ABSTRACT

The unified Model of Electronic Government Adoption (UMEGA) was developed to bring novel insight into the context of citizen adoption of e-government services. As UMEGA is a recently evolved model, it demonstrates unequivocally the necessity for evaluating this model tailored to adopting e-government from the citizens' perspective. The current study aims to perform a systematic literature review on the empirical validation of the UMEGA accomplished in several countries since its inception in 2017 by following Preferred Reporting Items for Systematic Reviews and Meta-Analyses (PRISMA) guidelines. PRISMA is performed to synthesize the findings and analyze the performance of the constructs of the UMEGA. The systematic literature review encompassed the general characteristics, overall descriptive statistics, and synthesis of the constructs, analytical tools, and findings of the selected empirical articles. In the present study, the meta-analysis offered a strong confidence and prediction interval and significant combined effect size, suggesting that the constructs of the UMEGA, namely, performance expectancy, social

influence, perceived risk, and facilitating conditions, significantly influenced attitude and behavioral intention to use e-government services. The association between attitude and behavioral intention is also found to be significant. The heterogeneity of the true effect of behavioral intention among empirical studies was partially explained by subgrouping in terms of sampling techniques, and E-government Development

ARTICLE INFO

Article history:

Received: 23 July 2022

Accepted: 14 November 2022

Published: 27 July 2023

DOI: <https://doi.org/10.47836/pjst.31.5.26>

E-mail addresses:

rasaleh19@gmail.com (Rakib Ahmed Saleh)

rozinor@upm.edu.my (Rozi Nor Haizan Nor)

tariqul.tonmoy812@gmail.com (Md. Tariqul Islam)

yusmadi@upm.edu.my (Yusmadi Yah Jusoh)

salfarina@upm.edu.my (Salfarina Abdullah)

* Corresponding author

Index (EGDI) moderated the association between attitude and behavioral intention. The current study's findings can serve as a solid foundation for knowledge expansion, easing the way for theoretical development and helping the government understand what aspects need to be considered while establishing initiatives to enhance the utilization of e-government services.

Keywords: E-government adoption, meta-analysis, systematic literature review, UMEGA

INTRODUCTION

E-government ensures IT-based government operations. E-government, also known as electronic government, provides citizens with online government services and considerably impacts individual attitudes that lead to e-government services (Zahid & Din, 2019). E-governance has been crucial in developing and evolving how governments reach and serve their citizens. E-government aspires to increase government answerability and efficacy by offering quicker and more cost-effective services and empowering people via inclusive governance (Agangiba & Kabanda, 2016). The United Nations E-Governance Development Index (EGDI) is the most extensively used metric for monitoring e-governance advancement.

Scholars of information systems have used known technology adoption models in various empirical studies to evaluate the adoption of e-government over time. For example, Al-Hujran et al. (2015); Asmi et al. (2016); Demirdoven et al. (2020); Nofal et al. (2021); and Billanes and Enevoldsen (2021) employed the Technology Acceptance Model (TAM) model, Motohashi et al. (2012); Rokhman (2011); and Ismailova and Muhametjanova (2018) used the Diffusion of Innovations (DOI) model, Li et al. (2010) and Soufiane and Ibrahim (2018) used the Technology-Organization-Environment (TOE) model. In addition, Ibrahim and Zakaria (2016), Kurfalı et al. (2017), and Verkijika et al. (2018) used the Unified Theory of Acceptance and Use of Technology (UTAUT) model in the context of e-government adoption.

The existing previous IS/IT models indicated the insufficiency of providing a clear insight into the appropriate background due to the difficulties of e-government adoption. It was advocated that researchers develop a theory that fits into the e-government complications independently but is based on the core notions of IS/IT theories (Dwivedi et al., 2012). In this process, Dwivedi et al. (2017) designed the Unified Model of Electronic Government Adoption (UMEGA) in India as the most current e-government adoption model and a significantly plain model that achieves a compromise between model intricacy and predictive power. The validated UMEGA outperformed other models, including the UTAUT, because it used better-suited measurements for the UTAUT variables in e-government rather than relying on its original measures, which were based on technology adoption in the organizational context (Dwivedi et al., 2017).

UMEGA is a recently evolved model; hence, it demonstrates unequivocally the necessity for evaluating this model tailored to adopting e-government from the citizens' perspective. Literature is insufficient on the systematic literature review of the Unified Model of E-government Adoption since its development in 2017. In congruent with this effort, the current study presents a systematic literature review of the UMEGA following the PRISMA guidelines (Moher et al., 2009). This study will utilize a quantitative approach to perform a systematic literature review of the relevant previous studies by investigating the empirical validation of the Unified Model of E-government Adoption in several countries and exploring the factors influencing citizens' behavioral intention to utilize E-Government services. Thus, the main objectives of this study are to (1) conduct a systematic review of the empirical validation of UMEGA, (2) present the empirical evidence on the predictive validity of UMEGA in e-government contexts that have been collected thus far, and (3) incorporate and analyze the magnitude of the effect size using meta-analysis methods (King & He, 2006). More particularly, the study aims to utilize meta-analysis to identify and observe the overall magnitude of the relationship between behavioral intention to use e-government services while undertaking the Unified Model of E-Government Adoption and its antecedents.

UNIFIED MODEL OF ELECTRONIC GOVERNMENT ADOPTION

Dwivedi et al. (2017) established the UMEGA model, the most recent e-government acceptability model illustrated in Figure 1. Twenty-nine alternative constructs were discovered and tested, and nine renowned theoretical models of adopting information technology were analyzed, namely, the Theory of Reasoned Action (TRA) (Fishbein & Ajzen, 1975), the Technology Acceptance Model (TAM) (Davis, 1989), Social Cognitive Theory (SCT) (Compeau et al., 1999), Innovation Diffusion Theory (IDT) (Rogers, 2003), Diffusion Of Innovation (DOI) (Rogers, 2003), Decomposed Theory of Planned Behaviour (DTPB) (Taylor & Todd, 1995), Theory of Planned Behavior (TPB) (Ajzen, 1985, 1991), and Unified Theory of Acceptance and Use of Technology (UTAUT) by Venkatesh et al. (2003). Although the fundamental UTAUT has also been utilized in little research coupled with e-government-specific dimensions like trust and risk (Carter & Schaupp, 2009; Schaupp et al., 2010), the model has not performed as well as anticipated. It demonstrates unequivocally the necessity for a uniform methodology specifically tailored to study the adoption of e-government. Dwivedi et al. (2017) created and validated the unified electronic government adoption (UMEGA) model based on the UTAUT model's core idea to close this research gap.

Performance expectancy, effort expectancy, perceived risk, and social influence, according to the UMEGA, are likely to directly influence attitudes toward adopting e-government. In contrast, positive behavioral intention is expected to be influenced by

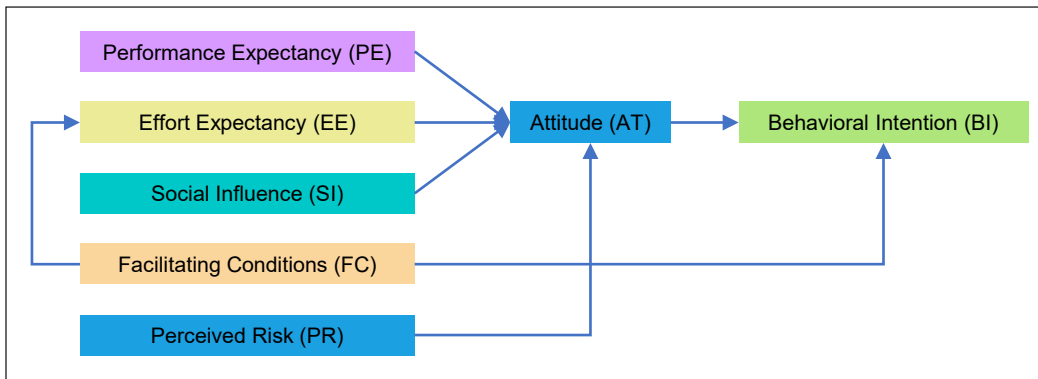


Figure 1. UMEGA research framework
Source: (Dwivedi et al., 2017)

attitude. Furthermore, the facilitating conditions are expected to impact behavioral intention and effort expectancy. According to its validation, UMEGA surpassed the rest of the models in describing behavioral intention to utilize e-government services (Dwivedi et al., 2017). The constructs of the UMEGA are described as follows:

Performance Expectancy

According to Venkatesh et al. (2003), performance expectation is the user’s conviction that adopting certain technology would help or enable them to accomplish a given task performance. It is one of the antecedents of the Unified Theory of UTAUT paradigm, which has attracted significant attention from multiple academics in various sectors of human effort (Bugembe, 2010; Khayati & Zouaoui, 2013; Venkatesh et al., 2003). According to their findings, performance expectation is a crucial element influencing information system adoption and eventual usage. This aspect is comparable to TAM’s perceived utility, relative benefit (from the DOI and IDT), and outcome expectancies (from the SCT). According to previous studies, performance expectancy significantly influences the propensity to use e-government services (AlAwadhi & Morris, 2008; Bhuasiri et al., 2016; Lu & Nguyen, 2016).

Social Influence

The term “social influence” relates to how much an individual’s opinions of others impact their choice to embrace a new system (Venkatesh et al., 2003). Social influence is one of the constructs of the UTAUT model and analogous to the encapsulation of other constructs, namely, subjective norms from the TRA and the TPB and social factors from MPCU (Venkatesh et al., 2003). In terms of e-government, social influence is how citizens assess the value of other people’s perceptions while determining whether to implement

e-Government (Venkatesh et al., 2003, 2012). Several previous studies explored the significant impact of social influence on e-government adoption (Bhuasiri et al., 2016; Dwivedi et al., 2017).

Perceived Risk

Perceived risk refers to the dismay or apprehension of using a certain information system due to projected results (Slade et al., 2015). Perceived risk is often used to describe a user's perception of the likelihood that their interests are at risk when using innovative technology, especially one that involves new technologies or methods. In e-government, perceived risk refers to citizens' belief that they will face some type of difficulties and loss while adopting e-government services, mainly since e-government services must be accessed via the internet system, which has its own set of risks and obstacles (Verkijika & Wet, 2018). This apprehension can constrain citizens' interactions with e-government services (Verkijika & Wet, 2018).

Facilitating Conditions

According to Davis (1989) and Venkatesh et al. (2003), facilitating conditions refer to a person's view of the technical resources and the organizational infrastructure required to operate the intended system. This definition encompasses perceived behavioral control, enabling conditions, and adaptation. It incorporates ideas from other root constructs, such as perceived behavioral control (from the TPB and the DTPB), enabling conditions (from the PC use model), and compatibility (from IDT). Several researchers have found that FC is the most critical factor influencing e-government adoption by individuals in various countries (Kurfalı et al., 2017; Lallmahomed et al., 2017; Rodrigues et al., 2016).

Effort Expectancy

Effort expectation defines the "degree of ease associated with customers' technology usage" (Komba & Ngulube, 2015; Venkatesh et al., 2012). It measures how individuals expect less mental or physical effort to perform specific tasks when using technology. In other words, effort expectancy refers to the effort people think they will have to use technology (Venkatesh et al., 2016). The idea of effort expectancy is summarized by the TAM's perceived ease of use, DOI's complexity, and IDT's ease of use (Venkatesh et al., 2003). It is a critical component of the UTAUT model and is widely used to examine people's intentions toward new technology (Venkatesh et al., 2012). Several studies suggested that effort expectancy is connected to behavioral intention by mediating the individual's beliefs about adopting a given technology (Alshare & Lane, 2011; Pynoo et al., 2011; Šumak & Šorgo, 2016).

Attitude And Behavioral Intention

Attitude relates to how a unit of adoption feels about the subject. According to Yang & Yoo (2004), attitude comprises affective and cognitive components. The affective component describes how much a person enjoys the object of thinking, whereas the cognitive part describes an individual's precise ideas about the thing of thought (Yang & Yoo, 2004).

Behavioral intention is critical when researching e-government adoption since it reflects citizens' attitudes toward utilizing the system. People who give a good rating or appraisal to a G2C system are more likely to embrace it, and vice versa. A previous study has found that attitudes influence behavioral intentions significantly to use e-government services (Alomari et al., 2012; Dwivedi et al., 2017; Susanto & Goodwin, 2013).

METHODOLOGY

A systematic literature review (SLR), as recommended by Kitchenham (2004), is used as the research methodology in this paper. The systematic literature review (SLR) explores, critically evaluates, and synthesizes all the literature on a certain issue using a set of thorough and rigorous criteria (Salahuddin & Ismail, 2015). The core purpose of the SLR approach is to minimize the risk of bias and maximize openness at every level of the review process by depending on clear, systematic processes to remove bias in research selection and inclusion, as well as to assess and summarize the quality of studies that are included objectively (Liberati et al., 2009; Petticrew, 2001). In addressing the knowledge gap and the numerous possible sources of bias in locating, selecting, synthesizing, and reporting primary studies, researchers advocated that the review process be treated as a scientific process in and of itself, which evolved into the SR process (Dixon-Woods, 2010). This study follows the PRISMA guidelines for systematic reviews and meta-analyses, containing four phases: identification, screening, eligibility, and inclusion (Figure 2).

Article Identification

A comprehensive literature search for citations was undertaken to utilize a range of well-known online scientific databases, including Scopus, ScienceDirect, Web of Science, and EBSCOhost (Academic Search Complete) Publications, following the PRISMA criteria. These databases were chosen because they contain the most significant and high-impact journals and general conference proceedings on information systems and explicitly respect e-government services. While searching for literature, the following keywords were used; UMEGA or "Unified Model of Electronic Government Adoption." The research papers were published between January 1, 2012, and December 31, 2021. The study titles and abstracts were evaluated to conduct the first extraction of all research. The search included peer-reviewed articles, conference proceedings, and book chapters. In the beginning, this search yielded 51 related papers.

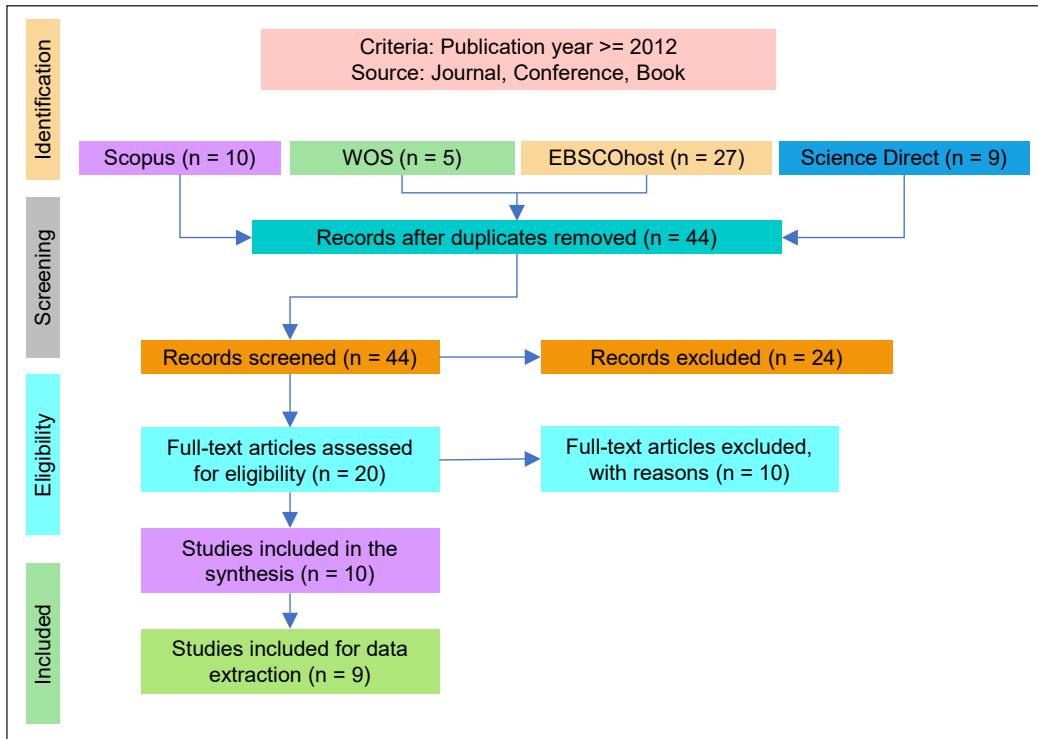


Figure 2. Flowchart diagram for SLR using PRISMA

Article Screening

Screening the selected documents is the second step of the PRISMA guidelines. As a result, the authors screened the retrieved documents based on each document’s title, abstract, and keywords (if needed). After removing the duplicates, a total of 44 documents were taken among 51 documents for the further screening process. Later, 24 documents were excluded, and 20 were retained for further exploration based on the title, abstract, and keywords.

Article Eligibility

According to the PRISMA checklist, several criteria for article eligibility were applied to assure the quality and consistency of the selected publications. The content of the selected literature was reviewed for relevance to the following inclusion criteria by looking at the title, abstract, and text; (1) it had investigated the validation of UMEGA in several countries, (2) it was penned in the English language, (3) presented in peer-reviewed journals, conference papers, and book chapters, and (4) the methodology, path coefficients, and confidence intervals were reported. After skimming through the title and abstract, 24 papers were excluded as not complying with the inclusion criteria. The full text of the remaining 20 papers was assessed and summarized. In this stage, nine more articles were excluded as

not fitting one or more of the inclusion criteria, and one paper (Syaifuddin et al., 2022) was excluded as the original UMEGA was distorted to a large extent by making the mediator attitude an independent variable, resulting in a total of 10 eligible papers, aligned with the objectives of the study. Finally, as structural model analysis or path co-efficient was not reported, one more paper (Alawadhi et al., 2021) was excluded, thus yielding nine papers (Table 1) being reviewed finally and analyzed in this systematic literature review.

Table 1
List of the selected articles obtained from SLR

No.	Title	Source
1	Adoption of Transactional Service in Electronic Government – A Case of Pak-Identity Service	(Khurshid et al., 2019)
2	Taxpayer Behavior in Using E-Vehicle in Indonesia	(Zubaidah et al., 2021)
3	E-Government Adoption in Uzbekistan: Empirical Validation of the Unified Model of Electronic Government Acceptance (UMEGA)	(Avazov & Lee, 2020)
4	E-government adoption in sub-Saharan Africa	(Verkijika & Wet, 2018)
5	Empirical validation of a unified model of electronic government adoption (UMEGA)	(Dwivedi et al., 2017)
6	Identifying Factors Affecting the Acceptance of Government-to-Government System in Developing Nations – Empirical Evidence from Nepal	(Rai et al., 2020)
7	E-Government Services Adoption: An Extension of the Unified Model of Electronic Government Adoption	(Mensah et al., 2020)
8	Adoption of Cloud-Based Accounting Practices in Turkey: An Empirical Study	(Altin & Yilmaz, 2021)
9	Determinants of citizen's intention to use online e-government services: A Validation of UMEGA Model	(Burhanuddin et al., 2019)

Data Extraction

From the previously selected nine review studies, each article was extracted by delving into the complete text, including article characteristics (paper title, publication year, name of the journal, reference domain, context, sampling technique, and sample size), synthesis of the model's constructs (research framework, dependent variables, independent variables, and mediating factor), and statistical insights (quantitative statistical analysis tools, methods for reliability and validity, statistical software, path co-efficient of the constructs, and significance level). The data was stored in Microsoft Office Excel 2016.

RESULTS AND DISCUSSION

The upcoming sections shed some light on the general characteristics, overall descriptive statistics, and synthesis of the constructs, analytical tools, and findings of the selected nine review papers. Finally, the meta-analysis, subgroup, moderator analysis, and publication

bias conforming to the PRISMA guideline will be presented to synthesize the insights and analyze the performance of the constructs of the UMEGA.

General Characteristics of Included Studies

First, an overview of the included studies' features is presented, including publication year, researched countries, and journals. The distribution of publications by year is depicted in Figure 3. The minimal number of articles could be due to the UMEGA being proposed by Dwivedi et al. (2017).

After 2017, one journal article was published in 2018, one journal paper and one conference paper were published in 2019, one conference and two journal papers were published in 2020, and finally, two journal articles were published in 2021. Journal publications comprised most of the papers in this systematic literature review, accounting for about 77.78% of the total. The conference proceedings are in the second position regarding contribution with 22.22%, and no book chapters are in the inclusion phase. Figure 4 represents the world distribution of the empirical validation of the UMEGA. As shown in Figure 4, most research studies were conducted in developing and least developing countries and confined to only two continents: Asia and Africa. Perhaps the UMEGA being first proposed in India inspired the researchers to choose the adjacent geographical regions and countries with similar e-government infrastructures and facilities.

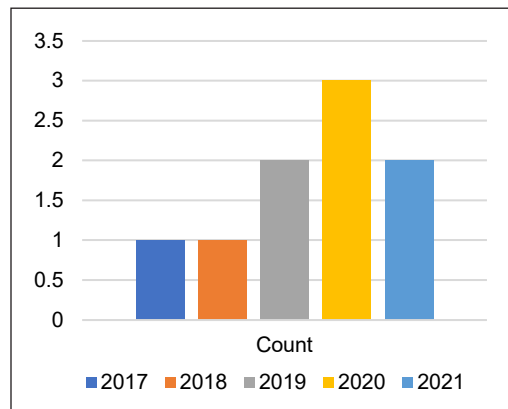


Figure 3. Publication trend

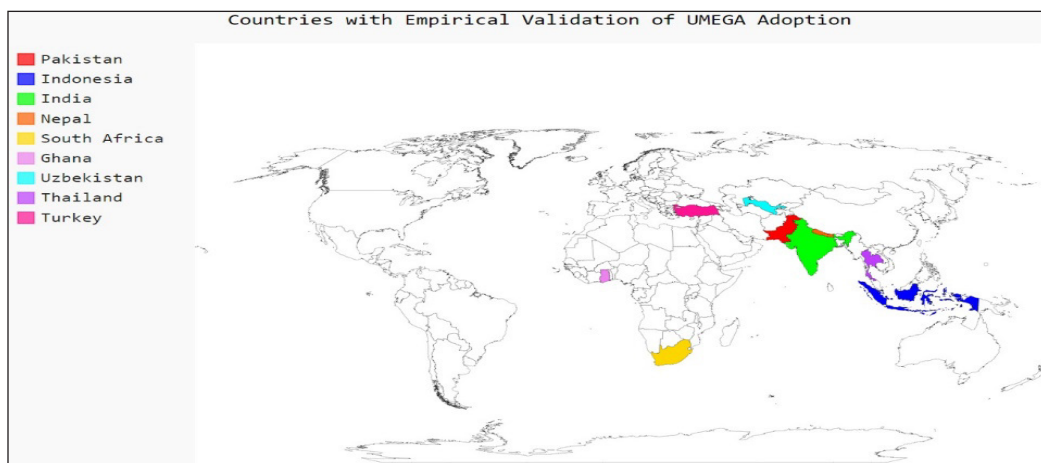


Figure 4. Countries with empirical validation of UMEGA adoption

Descriptive Statistics

There were 63 fundamental associations among dependent and independent constructs of the UMEGA discovered in these nine publications. Table 2 summarizes respondents, domains, contexts, sample size, and publication year, as mentioned in the nine publications in the current study, along with the corresponding EGDI of the respective countries. The descriptive statistics revealed that all the studies were conducted in the context of Asian and African countries, and citizens who are familiar with or are a part of e-government services were the respondents. Among all the studies, the highest number of participants were from India, and the maximum number of articles (03) with empirical validation of UMEGA was published in 2020.

Asia continent (Pakistan, Indonesia, Uzbekistan, India, Nepal, Turkey, and Thailand) accounts for 79.20% of responders, while Africa (Sub Sahara Africa and Ghana) accounts for 20.80% (Figure 5). The UNDP (2022) report suggests that UMEGA is empirically validated in the context of developing countries only.

Table 2
Descriptive statistics of the empirical validation of UMEGA adoption studies

Sources	Respondents	Domain	Context	Sample Size	EGDI	Year
(Khurshid et al., 2019)	Citizens	Pak-Identity, an e-government transactional service system	Pakistan	441	0.387	2019
(Zubaidah et al., 2021)	E-Samsat users	e-Samsat (e-vehicle tax) services	Indonesia	233	0.750	2021
(Avazov & Lee, 2020)	Students and Govt. Employees	Single Portal of Interactive Public Services	Uzbekistan	216	0.666	2020
(Verkijika & Wet, 2018)	E-government service users	e-government services	Africa	282	0.662	2018
(Dwivedi et al., 2017)	Citizens from different cities covering different demographics	Online Permanent Account Number (PAN) card registration system (OPCRS)	India	474	0.859	2017
(Rai et al., 2020)	Govt. Officials	G2G e-services	Nepal	234	0.369	2020
(Mensah et al., 2020)	Citizens within ministries and their environs	e-government services	Ghana	345	0.631	2020
(Altin & Yilmaz, 2021)	Employees of accounting departments of businesses	Cloud-based accounting applications	Turkey	391	0.893	2021
(Burhanuddin et al., 2019)	Taxpayer Citizens	Govt. Tax Portal	Thailand	396	0.713	2019

Overall Review of Selected Studies

Concerning UMEGA, most studies empirically validated the original model or its extended variation by tuning one or more independent variables. Nevertheless, only data about the original model has been emphasized in this review. Table 3 summarizes the evidence for behavioral intention to use e-government services while adopting UMEGA, as gathered from the reviewed empirical studies.

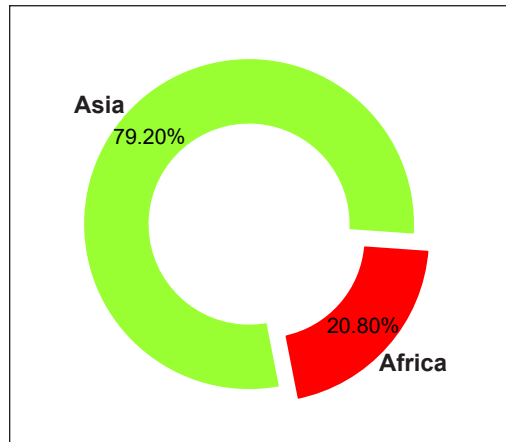


Figure 5. Distribution of respondents

Khurshid et al. (2019) used UMEGA to understand the adoption of Pak-Identity, a governmental transactional service system released by Pakistan’s national database and registration authority, by including four new constructs, namely, trust, herd behavior, price value, and grievance redressal. They investigated that facilitating conditions influenced effort expectancy directly, but effort expectancy, facilitating conditions, social influence, and perceived risk had no significant impact on e-government adoption.

Rai et al. (2020) empirically validated the Unified Model for E-Government Acceptance (UMEGA) by going through focus group meetings with government officials of the ministries of Nepal. They dropped two constructs of the UMEGA, namely, perceived risk and social influence, and added three new constructs: awareness among leadership, commitment from leadership, and transparency. They noticed that

Table 3
Synthesis of the constructs of the reviewed empirical studies

Source	Dependent Variable	Performance Expectancy	Effort Expectancy	Social Influence	Facilitating Conditions	Perceived Risk	Attitude
(Khurshid et al., 2019)	Behavioral Intention	√					√
(Zubaidah et al., 2021)	Taxpayer Behavior	√	√		√	√	√
(Avazov & Lee, 2020)	In Using E-Vehicle	√	√		√		√
(Verkijika & Wet, 2018)	Behavioral Intention	√	√	√	√	√	√
(Dwivedi et al., 2017)	Behavioral Intention	√	√	√	√	√	√
(Rai et al., 2020)	Behavioral Intention	√	√		√		√
(Mensah et al., 2020)	Behavioral Intention				√	√	√
(Altin & Yilmaz, 2021)	Behavioral Intention	√		√		√	√
(Burhanuddin et al., 2019)	Behavioral Intention						√

performance expectancy, effort expectancy, facilitating conditions, attitude, and the newly added constructs, strongly influenced the behavioral intention to use G2G E-government services. Avazov and Lee (2020) empirically validated the UMEGA by investigating the factors influencing citizens' behavioral intention to use e-government services named Single Portal of Interactive Public Services (SPIPS) in Uzbekistan. They discovered that all constructs' relationships were consistent with the original UMEGA study. Nonetheless, neither social influence nor perceived risk was a significant determinant of behavioral intention.

Mensah et al. (2020) tested an extended version of the UMEGA to identify the determinants that affected the intention of the citizens to use e-government services by incorporating two new constructs: perceived service quality and trust in government. They observed that facilitating conditions impacted effort expectancy significantly and behavioral intention to use e-government services. Nevertheless, surprisingly, performance expectancy, effort expectancy, and social influence failed to predict the attitude toward the behavioral intention. However, the newly added perceived service quality and trust in government had been found to have a significant impact on the behavioral intention by adding two new independent variables, namely, trust in technology and trust in government, and subsequently figured out that all the constructs of the original UMEGA, but social influence, and the newly added variables had a strong prediction toward intention to use e-Samsat services.

Altin and Yilmaz (2021) empirically validated the UMEGA to investigate the influencing factors that affected the behavioral intention of the employees of accounting departments of businesses in Turkey to use cloud-based accounting services. They dropped facilitating conditions and effort expectancy of the original UMEGA, incorporated computer self-efficacy, trust in government, and trust in the internet as independent variables, and slightly tuned the associated perceived risk with the mediator and dependent variable. They deduced that computer self-efficacy, social impact, and performance expectations had a positive and crucial effect, whereas perceived risk negatively impacted attitude.

Table 4 summarizes the selected empirical papers' sampling techniques, instruments, analysis methods, and tools. The outcome reveals that among all the studies, four studies employed random sampling, three studies utilized convenience sampling, and two adopted non-probabilistic sampling to collect data by online questionnaire through e-mail or paper-based. Most studies followed a quantitative research strategy along with a positivist research paradigm. Whereas few articles used structural equation modeling with SmartPLS, and a few employed AMOS to do statistical analysis and carried out reliability and validity analysis through Cronbach's alpha, Composite reliability, Factor loadings, Fornell-Larcker criterion, and the Heterotrait-Monotrait ratio (HTMT).

Table 4
The approaches used in the empirical studies of UMEGA

Study	Sampling Technique	Instrument	Reliability & Validity	Analysis Methods
(Khurshid et al., 2019)	Random	Online Questionnaire	Cronbach's Alpha, composite reliability, convergent validity, average variance extracted (AVE), and discriminant validity using the Fornell-Larcker criterion	Partial least squares Structure equation modeling using SmartPLS 3.0
Zubaidah et al., 2021)	Random	Questionnaires, Interviews	Cronbach's Alpha, composite reliability, convergent validity using outer loading, and average variance extracted (AVE)	Partial least squares Structure equation modeling using SmartPLS 3.0
(Avazov & Lee, 2020)	Convenience	Survey	Cronbach's Alpha, composite reliability, and average variance extracted (AVE)	Structure equation modeling
(Verkijika & Wet, 2018)	Random	Questionnaires	Cronbach's Alpha, composite reliability, convergent validity using factor loading, discriminant validity using the Fornell-Larcker criterion, and the heterotraitmonotrait ratio (HTMT)	Structure equation modeling using SmartPLS
(Dwivedi et al., 2017)	Convenience	Survey Questionnaires	Standardized factor loadings, Cronbach's Alpha, composite reliability, and average variance extracted (AVE)	Confirmatory factor analysis and Structure equation modeling using AMOS
(Rai et al., 2020)	Non-probabilistic	Paper-based Survey	Cronbach's Alpha, composite reliability, convergent validity using factor loading, and discriminant validity using the Fornell-Larcker criterion	Structure equation modeling
(Mensah et al., 2020)	Random	Research Questionnaire	Composite reliability, Average variance extracted (AVE), Cronbach's Alpha, factor loadings, and discriminant validity using the Fornell-Larcker criterion	Structure equation modeling using SmartPLS 3.0
(Altin & Yilmaz, 2021)	Non-probabilistic	Survey via E-mail	Cronbach's Alpha, composite reliability, convergent validity using factor loading, and discriminant validity using the Fornell-Larcker criterion	Structure equation modeling using SmartPLS
(Burhanudddin et al., 2019)	Convenience	Self-administrative	Cronbach's Alpha, composite reliability, Factor loading, Average variance	Structure equation modeling using SmartPLS

Meta-Analysis

Meta-analysis is the systematic strategy for combining quantitative data from various empirical research addressing the effect of an independent variable (or determinant, intervention, or treatment) on a specific outcome. As a result, a metric to measure their consequences is required (Bowman, 2012). The correlation and regression coefficients are examples of effect size measures utilized (Cooper et al., 2010). Because most papers suitable for meta-analysis indicated correlational effects, Pearson’s *r* was utilized as the primary effect size metric for the studies. *R* and its variance were obtained from correlation coefficients and sample sizes published in original publications whenever feasible. The statistical analyses and graphics were done using Meta-Essentials (Hak et al., 2016). The E-Governance Development Index (EGDI) was taken as a basis for meta-analysis because of its representative power on the ICT infrastructure and e-participation of the citizens of a country (UNDP, 2022).

Forest Plot

A forest plot depicts the meta-analysis in graphical form (Hak et al., 2016). The effect sizes and the forest plot of the meta-analysis of the cluster of the chosen reviewed papers are depicted in Table 6 and Figure 6, respectively.

The meta-analysis used the random-effects model to combine the retrieved effects, suitable for research with significant heterogeneity. The effect size is displayed on the

Table 6
R² of behavioral intention

Study	r	95 % CI		Weight
		Lower Limit	Upper Limit	
1	0.40	0.32	0.48	11.25%
2	0.63	0.55	0.70	10.95%
3	0.44	0.32	0.54	10.91%
4	0.65	0.57	0.71	11.06%
5	0.80	0.76	0.83	11.28%
6	0.50	0.40	0.59	10.96%
7	0.78	0.73	0.82	11.16%
8	0.56	0.49	0.62	11.21%
9	0.79	0.75	0.82	11.22%
Combined Effect Size				

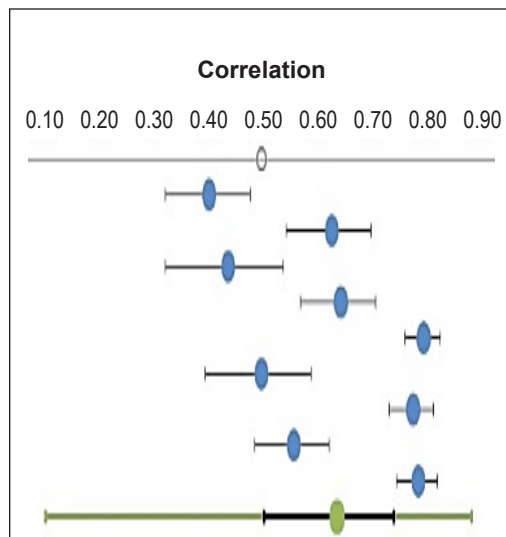


Figure 6. Forest Plot (*R² of behavioral intention*)

(Table 6 sources of study; 1: Khurshid et al., 2019; 2: Evi et al., 2021; 3: Avazov & Lee, 2020; 4: Verkijika & de Wet, 2018; 5: Dwivedi et al., 2017a; 6: Kirat Rai et al., 2020; 7: Mensah et al., 2020; 8: Altin & Yilmaz, 2021; 9: Burhanuddin et al., 2019)

X-axis. The blue circles of each row refer to the effect size for each association between behavioral intention to use e-government services and its constructs. While adopting UMEGA, the green circle on the bottom row represents the “combined effect size.” Table 5 enumerates the combined effect size (0.64), confidence, and prediction interval values.

Table 5
Combined effect size: Behavioral intention to use

Combined Effect Size (95% CI)	
Correlation	0.64
Confidence interval LL	0.51
Confidence interval UL	0.74
Prediction interval LL	0.10
Prediction interval UL	0.89

As shown in Figure 6, the confidence interval of the combined effect size lies on the right side of zero; hence the meta-analytic true effect between dependent and independent variables of the UMEGA in the empirical studies is statistically significant ($p = 0.000 < 0.05$; $Z = 8.67$). However, heterogeneity analysis ($Q = 200.76$, $I^2 = 96.02\%$, $T^2 (z) = 0.07$) for the selected studies revealed that the variability of the effect inconsistency was extremely substantial (Higgins et al., 2003), justifying the use of subgroup analysis and meta-regression for searching moderators.

The effect sizes and the forest plot of the mediator named attitude are presented in Table 7 and Figure 7, respectively. The combined effect size of attitude is 0.54, which is significant according to Cohen’s (1983) recommendation. The confidence interval of the combined effect size also lies on the right side of zero, i.e., the true effect between the mediator and independent variables of the UMEGA in the empirical studies is statistically

Table 7
R² of attitude

Study	r	Lower Limit	Upper Limit	Weight
1	0.65	0.59	0.70	11.29%
2	0.22	0.10	0.34	10.91%
3	0.60	0.51	0.68	10.85%
4	0.18	0.06	0.29	11.05%
5	0.49	0.42	0.56	11.32%
6	0.47	0.36	0.56	10.92%
7	0.63	0.56	0.69	11.17%
8	0.67	0.61	0.72	11.24%
9	0.72	0.67	0.77	11.24%
Combined Effect Size				

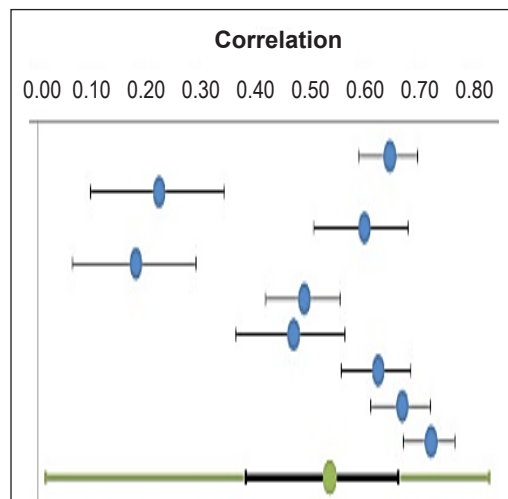


Figure 7. Forest Plot (R² of attitude)

(Table 7 sources of study; 1: Khurshid et al., 2019; 2: Evi et al., 2021; 3: Avazov & Lee, 2020; 4: Verkijika & de Wet, 2018; 5: Dwivedi et al., 2017a; 6: Kirat Rai et al., 2020; 7: Mensah et al., 2020; 8: Altin & Yilmaz, 2021; 9: Burhanuddin et al., 2019)

significant ($p = 0.000 < 0.05$; $Z = 7.03$) as well. The minimum and maximum limits of the confidence interval are 0.38 and 0.66, respectively. Furthermore, the prediction interval ranges from 0.01 to 0.83. Nevertheless, heterogeneity analysis ($Q = 158.47$, $I^2 = 94.95\%$, $T^2(z) = 0.06$) for the selected studies revealed that the observed inconsistency of the effects was large (Higgins et al., 2003).

Finally, the effect sizes and forest plots depicting the association between attitude and behavioral intention are illustrated in Table 8 and Figure 8, respectively. As the confidence interval of the combined effect size (0.49) lies on the right side of zero, the true effect between the mediator and dependent variables of the UMEGA is statistically significant ($p = 0.000 < 0.05$; $Z = 5.07$) (Burhanuddin et al., 2019). The confidence interval lies between 0.28 and 0.65, and the prediction interval ranges from -0.24 to 0.87. Like the previous two forest plots, its heterogeneity analysis ($Q = 277.32$, $I^2 = 97.12\%$, $T^2(z) = 0.10$) also revealed that the variability of the effect inconsistency was extremely substantial (Higgins et al., 2003).

Table 8
R² of association between attitude and behavioral intention

Study	r	95 % CI		Weight
		Lower Limit	Upper Limit	
1	0.33	0.25	0.41	11.21%
2	0.39	0.27	0.49	11.00%
3	0.27	0.14	0.39	10.96%
4	0.37	0.26	0.46	11.08%
5	0.77	0.73	0.80	11.23%
6	0.12	0.01	0.25	11.00%
7	0.65	0.59	0.71	11.15%
8	0.75	0.70	0.79	11.18%
9	0.46	0.38	0.54	11.19%
Combined Effect Size				

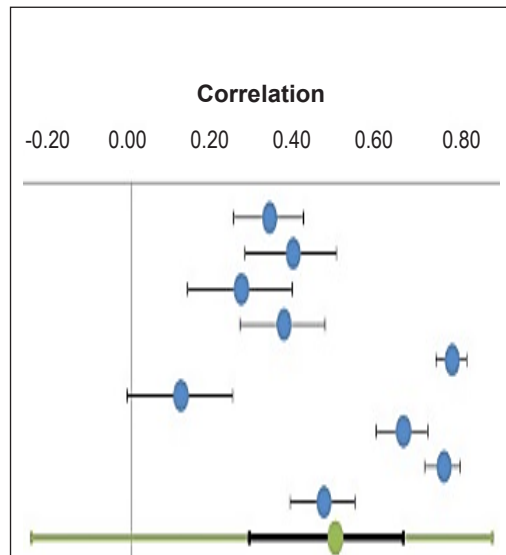


Figure 8. Forest Plot (association between attitude and behavioral intention)

(Table 8 sources of study; 1: Khurshid et al., 2019; 2: Evi et al., 2021; 3: Avazov & Lee, 2020; 4: Verkijika & de Wet, 2018; 5: Dwivedi et al., 2017a; 6: Kirat Rai et al., 2020; 7: Mensah et al., 2020; 8: Altin & Yilmaz, 2021; 9: Burhanuddin et al., 2019)

Subgroup Analysis

Following the dataset’s high level of heterogeneity (Figure 6), we did a subgroup analysis to see if the degree of heterogeneity diminished. The three groups were categorized based on sampling techniques, namely, random sampling, non-probabilistic sampling, and convenience sampling. The comparison of the effect sizes of the empirical reviewed

studies is presented in Table 9—each of the three studies employed these three sampling techniques. The corresponding forest plot is depicted in Figure 9.

The random-effect model was used to determine and compare the effect size for each subgroup. The result indicated that non-probabilistic ($Q = 0.57, I^2 = 00.00\%, T^2(z) = 0.00$) and random sampling subgroups ($Q = 2.21, I^2 = 9.51\%, T^2(z) = 0.00$) had produced an estimate of the same “true” effect size in a homogeneous population and the observed inconsistency of the effects belonging to the convenience sampling ($Q = 3.51, I^2 = 42.96\%, T^2(z) = 0.07$) was low (Higgins et al., 2003). Thus, subgrouping in terms of sampling techniques explained the heterogeneity of the combined effect size (behavioral intention) across the empirical studies.

Table 9
Subgroup Analysis (based on sampling techniques)

Study	95 % CI			Weight
	r	Lower Limit	Upper Limit	
1	0.63	0.55	0.70	28.84%
2	0.65	0.57	0.71	32.42%
3	0.56	0.49	0.62	38.74%
CS ¹	0.61	0.48	0.71	33.14%
4	0.80	0.76	0.83	39.05%
5	0.78	0.73	0.82	28.36%
6	0.79	0.75	0.82	32.59%
NPS ²	0.79	0.77	0.81	33.57%
7	0.40	0.32	0.48	47.84%
8	0.44	0.32	0.54	25.11%
9	0.50	0.40	0.59	27.06%
RS ³	0.44	0.31	0.55	33.30%
Combined	0.65	0.34	0.84	

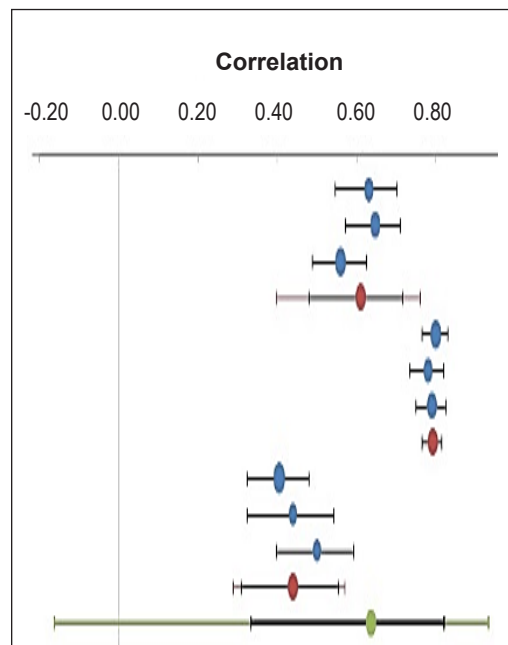


Figure 9. Forest Plot of subgroup analysis (based on sampling techniques)

Note. CS¹ = Convenience Sampling, NPS² = Non probabilistic Sampling, RS³ = Random Sampling, r = Correlation (Table 9 sources of study; 1: Evi et al., 2021; 2: Verkijika & De Wet, 2018; 3: Altin & Yilmaz, 2021; 4: Dwivedi et al., 2017a; 5: Mensah et al., 2020; 6: Burhanuddin et al., 2019; 7: Khurshid et al., 2019; 8: Avazov & Lee, 2020; 9: Kirat Rai et al., 2020)

Moderator Analysis

Apart from an endeavor to explain the dataset’s high level of heterogeneity (Figure 6) with subgroup analysis, moderator analysis was performed (random effect model) by testing meta-regression of the effect sizes (behavioral intention) based on EGDI (Table 1) of the respective researched countries in the publishing year (Figure 10). The combined effect

size (0.76) is significant (Cohen, 1983), but there was no evidence that EGDI moderated the effect sizes of the behavioral intention ($Q=2.32$, $p = 0.128 > 0.05$, $\beta = 0.51$, $df = 1$), accounting for 26.24% of the between-study variance.

However, while performing the same meta-regression of the correlation between the mediator named attitude and behavioral intention based on EGDI (Figure 11), it was found that EGDI moderated the association strongly ($Q=9.84$, $p = 0.002 < 0.05$, $\beta = 0.76$, $df = 1$), resulting in 57.45% of the between-study variance and significant combined effect size (0.54) (Cohen, 1983).

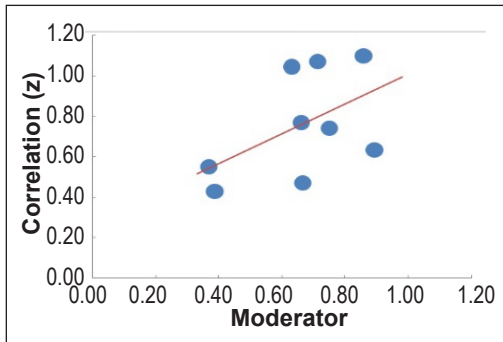


Figure 10. Meta-Regression of Behavioral Intention on EGDI

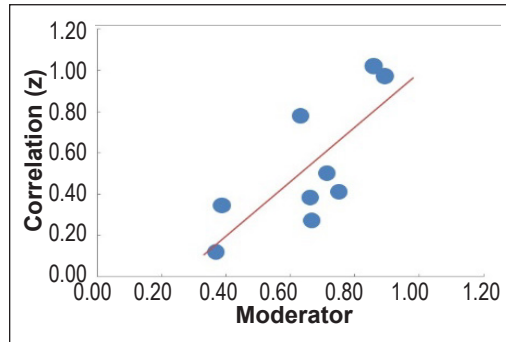


Figure 11. Meta-Regression of Attitude → BI association on EGDI

Publication Bias

Visual inspections of funnel plots and Egger’s test were conducted to determine whether there was any publication bias (Egger et al., 1997). We constructed a dataset from our list of selected papers for a publishing bias test. The dataset includes research that has produced r values for the association between behavioral intention and the remaining constructs of the UMEGA [independent-dependent variable association] (Figure 6). As shown in Figure 12, the pattern of findings reported in these analyses was unaffected by Duval and Tweedie’s (2000) trim and fill bias, implying that no studies were missing. Following this, Egger’s test also suggested no evidence of publication bias ($p = 0.22$) (Egger et al., 1997). However, according to Cochrane’s recommendation, as there were a small number of studies ($k < 10$), publication bias might be unreliable (Higgins et al., 2019). Over time, this bias can be rechecked with more studies published on the empirical validation of the Unified Model of Electronic Government Adoption.

DISCUSSION

The summary of the findings from the systematic literature review, including meta-analysis, the theoretical and practical implications, and the limitations of the study, are illustrated in the following sections.

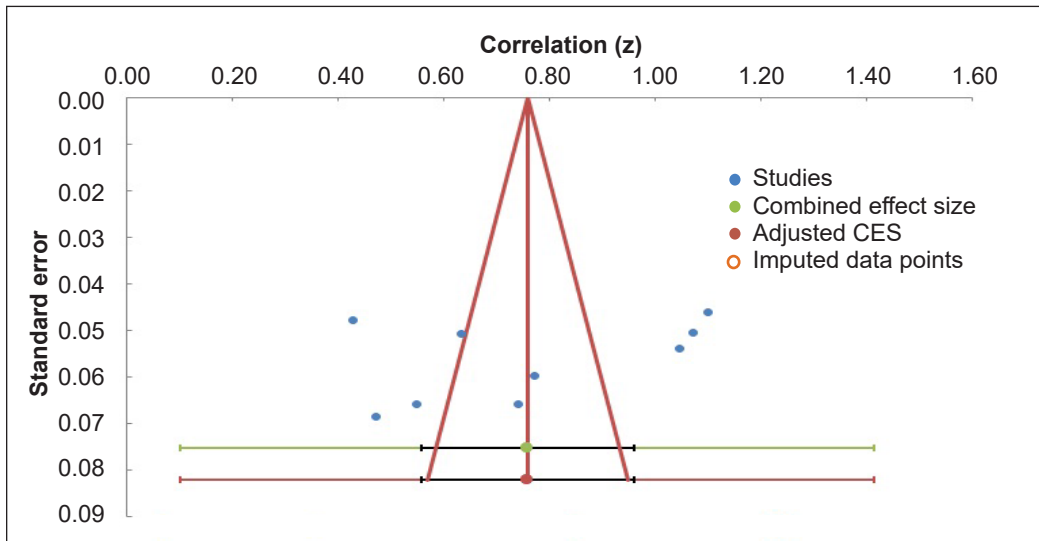


Figure 12. Funnel plot for behavioral intention effect sizes

Findings and Discussion

This study has the novelty to perform a systematic literature review, including meta-analysis, to analyze the empirical validation of the unified e-government adoption model, thus meeting the first objective. The nine publications in our work analyzed a wide range of respondents, domains, contexts, and constructs, offering a complete picture of the UMEGA components from which impact estimates on this connection could be extracted.

Since UMEGA was developed in 2017 in India, it has been validated in only two continents, Asia and Africa, where the former predominates. In all of the articles, the synthesis of the constructs revealed that the mediating role of attitude and the association between attitude and behavioral intention was positive and significant. The studies employed three types of sampling techniques, namely, random sampling, convenience sampling, and non-probabilistic sampling, to collect data by online questionnaire via e-mail or paper-based. Most studies followed a quantitative research strategy and a positivist research paradigm. They used structural equation modeling with SmartPLS, and a few employed AMOS to do statistical analysis and carried out reliability and validity analysis with the help of Cronbach's alpha, Composite reliability, Factor loadings, and Fornell-Larcker criterion, and the Heterotrait-Monotrait ratio (HTMT). Hence, a systematic literature review synthesizes findings presented in primary quantitative articles on the UMEGA model and puts an endeavor to conform to the second objective.

Along with SLR, the meta-analysis also provided the significance level, heterogeneity I^2 of the dataset, subgroup, and moderator analyses, and the biasedness among the publication utilizing the forest plot and funnel plot. The study included three meta-

analyses by emphasizing the true effect of (1) behavioral intention, (2) attitude, and (3) the association between attitude and behavioral intention. It was observed that the true combined effect size of behavioral intention was 0.64. The confidence interval was between 0.51 and 0.74, and the prediction interval ranged between 0.1 and 0.89. In terms of the mediator attitude, the true effect was 0.54. The confidence interval came up in the range of 0.38 to 0.66, and the prediction interval was between 0.01 and 0.83. Finally, the combined effect size of the association between the mediator and the independent variable was 0.49, whereas the confidence interval and prediction interval were between 0.28 and 0.65 and -0.24 and 0.87, respectively. All true effects were significant per Cohen's recommendation (Cohen, 1983).

Nevertheless, all three meta-analyses produced large heterogeneity, suggesting the necessity of a quest for sub-group and moderator analysis. The subgroup analysis of the true effect of behavioral intention was further carried out using the random effect model based on the sampling techniques. The result indicated that non-probabilistic ($Q = 0.57$, $I^2 = 00.00\%$, $T^2(z) = 0.00$) and random sampling subgroups ($Q = 2.21$, $I^2 = 9.51\%$, $T^2(z) = 0.00$) had lower I^2 , whereas that of convenience sampling was moderate (Higgins et al., 2003), thus explaining the heterogeneity of the meta-analysis of behavioral intention to some extent.

Subsequently, the moderator analysis following the random-effect model was performed in two phases: (1) meta-regression of the effect sizes (behavioral intention) based on EGDI, and (2) meta-regression of the effect sizes of the association between behavioral intention and attitude based on EGDI. It was found that EGDI did not moderate the effect sizes of the behavioral intention ($Q=2.32$, $p = 0.128 > 0.05$, $\beta = 0.51$, $df = 1$), yielding a combined effect size of 0.76 and 26.24% of the between-study variance, whereas EGDI moderated the association between behavioral intention and attitude strongly ($Q=9.84$, $p = 0.002 < 0.05$, $\beta = 0.76$, $df = 1$), resulting in 57.45% of the between-study variance and significant combined effect size (0.54).

Finally, the funnel plot suggests that the pattern of findings reported in these analyses was unaffected by Duval and Tweedie's trim and fill bias (Figure 12) (Duval & Tweedie, 2000), implying that no studies were missing. Following this, Egger's test has also indicated no evidence of publication bias (Duval & Tweedie, 2000). However, due to the high degree of heterogeneity ($I^2 = 0.962$) in the dataset (Hak et al., 2016), the funnel plot analysis did not prove publication bias precisely (Borenstein et al., 2009). Therefore, the meta-analysis analyses the performance of the constructs of the UMEGA obtained from the assessment of the empirical validation found in nine articles published since UMEGA was proposed in 2017. In particular, meta-analysis sheds some light on the combined effect size of the mediator and dependent variable and confirms the third objective of the study, which reveals the significant predictive power of attitude and behavioral intention while implementing UMEGA.

Implications

This article contributes theoretically and practically. From the theoretical perspective, a thorough systematic literature review can be served as a solid foundation for knowledge expansion, easing the way for theoretical development and highlighting areas that require more study. Second, we provide a clearer knowledge of the current trends and patterns in applying theoretical constructs and models, particularly for the most recent research model of e-government adoption, UMEGA. All the insights extracted from the SLR and meta-analysis of this study will pave the way for considering UMEGA or identifying the constructs of the desired model for e-government adoption, especially in the context of developing countries. The results of this study can be used by researchers as a strong base for a more precise and effective selection of constructs in an analysis of the adoption of e-participation, offering additional criteria for whether to include or not a variable in the research model. The study's findings significantly impact governments looking to establish e-participation platforms. It indicates that governments must pay close attention to measures that maintain citizens' good attitudes and perceptions of the platform's value.

Limitations

Limited sources were used to compile the results of this systematic literature review. Future research might look at other databases and journals. Most selected studies had a cross-sectional survey, indicating that this subject of study is currently in its early phases of development. As a result, no inferences can be drawn about the direction or cause of the associations among the latent constructs. Regarding exclusion criteria, research not written in any other language besides English was eliminated because of the lack of translation resources. The removal of unpublished research may have influenced the review's accuracy due to the 'file drawer' phenomenon. Irrespective of these methodical considerations, the meta-analyses having inconsequential selection bias show that any file drawer bias may not have notably influenced the outcomes found in the current study.

Due to the very recent development of the UMEGA and quality article screening following the PRISMA method, this study included only nine studies, failing to meet the minimum required dataset of studies for publication bias to be assessed (Sterne et al., 2011). Following suggestions to utilize this meta-analysis method while adding a few more studies to increase control over the likelihood of type I errors, Hedges' methodology was employed to adjust all effect sizes in the analyses (Field, 2003).

Additional sub-group and moderator analyses might have been conducted to look at systematic differences across methodological quality studies. However, these were deemed unacceptable due to the small number of studies and the consequently decreased range in quality of the study. In some articles, we could not delve deeper into the type of responses for various levels of e-participation due to a lack of clear descriptions. Moderator

factors (such as cultural aspects or demographics and second-order constructs) were rarely employed in the quantitative papers. As a result, this study did not consider subsequent moderator or second-order constructs analysis.

CONCLUSION

In summary, this is the first of its type in the Unified Model of E-government Adoption reviews, and it aims to summarize a wide variety of investigations. Because the research is still in its early phases, caution offers the findings. We reviewed numerous theoretical and methodological difficulties that might have been biased in the existing literature and the implications for future studies. Nonetheless, the data gathered for this research reveals a significant association of behavioral intention with the mediator named attitude and the independent latent constructs of the model. It is suggested that further study be conducted in this area to improve our understanding of this relationship. Furthermore, a country's policymakers may use the findings to build ICT infrastructure while attempting to implement the UMEGA as a framework.

ACKNOWLEDGEMENT

The researchers acknowledge financial support from the Information and Communication Technology Division (ICTD), Ministry of Posts, Telecommunication and Information Technology, Government of the People's Republic of Bangladesh (Memo no: 56.00.0000.052.33.001.22-66).

REFERENCES

- Agangiba, M., & Kabanda, S. (2016). E-government accessibility research trends in developing countries. In *10th Mediterranean Conference on Information Systems (MCIS) 2016 Proceedings*. AIS eLibrary.
- Ajzen, I. (1985). From intentions to actions: A theory of planned behavior. In J. Kuhl, & J. Beckmann, (Eds.), *Action Control: From Cognition to Behavior* (pp. 11-39). Springer. https://doi.org/10.1007/978-3-642-69746-3_2
- Ajzen, I. (1991). The theory of planned behavior. *Organizational Behavior and Human Decision Processes*, 50(2), 179-211. [https://doi.org/10.1016/0749-5978\(91\)90020-T](https://doi.org/10.1016/0749-5978(91)90020-T)
- Alawadhi, N., Al-Shaikhli, I., Alkandari, A., & Chab, S. K. (2021). Business owners' feedback toward adoption of open data: A case study in Kuwait. *Journal of Electrical and Computer Engineering, 2021*, Article 6692410. <https://doi.org/10.1155/2021/6692410>
- AlAwadhi, S., & Morris, A. (2008). The use of the UTAUT model in the adoption of E-government services in Kuwait. In *Proceedings of the 41st Annual Hawaii International Conference on System Sciences (HICSS 2008)* (pp. 219-219). IEEE Publishing. <https://doi.org/10.1109/HICSS.2008.452>
- Al-Hujran, O., Al-Debei, M. M., Chatfield, A., & Migdadi, M. (2015). The imperative of influencing citizen attitude toward e-government adoption and use. *Computers in Human Behavior*, 53, 189-203. <https://doi.org/10.1016/j.chb.2015.06.025>

- Alomari, M., Woods, P., & Sandhu, K. (2012). Predictors for e-government adoption in Jordan: Deployment of an empirical evaluation based on a citizen-centric approach. *Information Technology & People*, 25(2), 207-234. <https://doi.org/10.1108/09593841211232712>
- Alshare, K. A., & Lane, P. L. (2011). Predicting student-perceived learning outcomes and satisfaction in ERP courses: An empirical investigation. *Communications of the Association for Information Systems*, 28, 571-584. <https://doi.org/10.17705/1CAIS.02834>
- Altin, M., & Yilmaz, R. (2021). Adoption of cloud-based accounting practices in Turkey: An empirical study. *International Journal of Public Administration*, 45(11), 819-833. <https://doi.org/10.1080/01900692.2021.1894576>
- Asmi, F., Zhou, R., & Wu, M. (2016). Measuring e-readiness among non-users of internet banking in Pakistan: By TAM with CRM as external factor. *European Journal of Business and Management*, 8(29), 131-143.
- Avazov, S., & Lee, S. (2020). E-government adoption in Uzbekistan: Empirical validation of the unified model of electronic government acceptance (UMEGA). In *The 21st Annual International Conference on Digital Government Research* (pp. 338-339). ACM Publishing. <https://doi.org/10.1145/3396956.3397008>
- Bhuasiri, W., Zo, H., Lee, H., & Ciganek, A. P. (2016). User acceptance of e-government services: Examining an e-tax filing and payment system in Thailand. *Information Technology for Development*, 22(4), 672-695. <https://doi.org/10.1080/02681102.2016.1173001>
- Billanes, J., & Enevoldsen, P. (2021). A critical analysis of ten influential factors to energy technology acceptance and adoption. *Energy Reports*, 7, 6899-6907. <https://doi.org/10.1016/j.egy.2021.09.118>
- Borenstein, M. (2009). Effect sizes for continuous data. In H. Cooper, L. V. Hedges, & J. C. Valentine (Eds.), *The Handbook of Research Synthesis and Meta-Analysis* (2nd ed.) (pp. 221-235). Russell Sage Foundation.
- Bowman, N. A. (2012). Effect sizes and statistical methods for meta-analysis in higher education. *Research in Higher Education*, 53, 375-382. <https://doi.org/10.1007/s11162-011-9232-5>
- Bugembe, J. (2010). *Perceived usefulness, perceived ease of use, attitude and actual usage of a new financial management system: A case of Uganda National Examinations Board* [Masters' Thesis]. Makerere University, Uganda. <http://hdl.handle.net/10570/2806>
- Burhanuddin, B., Badruddin, S., & Yapid, B. M. (2019). Determinants of citizen's intention to use online e-government services: A validation of UMEGA model. *Polish Journal of Management Studies*, 20(1), 119-128. <http://dx.doi.org/10.17512/pjms.2019.20.1.10>
- Carter, L., & Schaupp, L. C. (1 C.E.). Relating acceptance and optimism to e-file adoption. *International Journal of Electronic Government Research*, 5(3), 62-74. <https://doi.org/10.4018/JEGR.2009070105>
- Cohen, A. (1983). Comparing regression coefficients across subsamples: A study of the statistical test. *Sociological Methods & Research*, 12(1), 77-94. <https://doi.org/10.1177/0049124183012001003>
- Compeau, D., Higgins, C. A., & Huff, S. (1999). Social cognitive theory and individual reactions to computing technology: A longitudinal study. *MIS Quarterly*, 23(2), 145-158. <https://doi.org/10.2307/249749>
- Cooper, R., Kuh, D., Hardy, R., & Group, M. R. (2010). Objectively measured physical capability levels and mortality: systematic review and meta-analysis. *BMJ*, 341, Article c4467. <https://doi.org/10.1136/bmj.c4467>

- Davis, F. D. (1989). Perceived usefulness, perceived ease of use, and user acceptance of information technology. *MIS Quarterly*, 13(3), 319-339. <https://doi.org/10.2307/249008>
- Demirdoven, B., Cubuk, E. B. S., & Karkin, N. (2020). Establishing relational trust in e-Participation: a systematic literature review to propose a model. In *Proceedings of the 13th International Conference on Theory and Practice of Electronic Governance (ICEGOV 2020)* (pp. 341-348). ACM Publishing. <http://dx.doi.org/10.1145/3428502.3428549>
- Dixon-Woods, M. (2010). Systematic reviews and qualitative methods. In D. Silverman (Ed.), *Qualitative Research: Theory, Method and Practice* (3rd ed.) (pp. 331-346). Sage.
- Duval, S., & Tweedie, R. (2000). A nonparametric “trim and fill” method of accounting for publication bias in meta-analysis. *Journal of the American Statistical Association*, 95(449), 89-98. <https://doi.org/10.1080/01621459.2000.10473905>
- Dwivedi, Y. K., Rana, N. P., Janssen, M., Lal, B., Williams, M. D., & Clement, M. (2017). An empirical validation of a unified model of electronic government adoption (UMEGA). *Government Information Quarterly*, 34(2), 211-230. <https://doi.org/10.1016/j.giq.2017.03.001>
- Dwivedi, Y. K., Weerakkody, V., & Janssen, M. (2012). Moving towards maturity. *ACM SIGMIS Database: The DATABASE for Advances in Information Systems*, 42(4), 11-22. <https://doi.org/10.1145/2096140.2096142>
- Egger, M., Smith, G. D., Schneider, M., & Minder, C. (1997). Bias in meta-analysis detected by a simple, graphical test. *BMJ*, 315(7109), 629-634. <https://doi.org/10.1136/bmj.315.7109.629>
- Field, A. P. (2003). Can meta-analysis be trusted? *The Psychologist*, 16(12), 642-645.
- Fishbein, M., & Ajzen, I. (1975). *Belief, Attitude, Intention, and Behavior: An Introduction to Theory and Research*. Addison-Wesley Reading.
- Hak, T., Van Rhee, H. J., & Suurmond, R. (2016). *How to Interpret Results of Meta-Analysis*. Erasmus Rotterdam Institute of Management. <http://dx.doi.org/10.2139/ssrn.3241367>
- Higgins, J. P. T., Thomas, J., Chandler, J., Cumpston, M., Li, T., Page, M. J., & Welch, V. A. (Eds.). (2019). *Cochrane Handbook for Systematic Reviews of Interventions* (2nd ed.). John Wiley & Sons. <https://doi.org/10.1002/9781119536604>
- Higgins, J. P. T., Thompson, S. G., Deeks, J. J., & Altman, D. G. (2003). Measuring inconsistency in meta-analyses. *BMJ*, 327(7414), 557-560. <https://doi.org/10.1136/bmj.327.7414.557>
- Ibrahim, O. A., & Zakaria, N. H. (2016). E-government services in developing countries: A success adoption model from employees perspective. *Journal of Theoretical & Applied Information Technology*, 94(2), 383-396. <http://www.jatit.org/volumes/Vol94No2/14Vol94No2.pdf>
- Ismailova, R., & Muhametjanova, G. (2018). Determinants of intention to use government web sites in Kyrgyz Republic. *International Journal of eBusiness and eGovernment Studies*, 10(2), 30-45. <https://dergipark.org.tr/en/pub/ijebe/issue/43700/536108>
- Khayati, S., & Zouaoui, S. K. (2013). Perceived usefulness and use of information technology: The moderating influences of the dependence of a subcontractor towards his contractor. *Journal of Knowledge Management, Economics and Information Technology*, 3(6), 1-28.

- Khurshid, M. M., Zakaria, N. H., Rashid, A., Ahmed, Y. A., & Shafique, M. N. (2019). Adoption of transactional service in electronic government - A case of pak-identity service. In I. O. Pappas, P. Mikalef, Y. K. Dwivedi, L. Jaccheri, J. Krogstie, & M. Mantymaki (Eds.), *Digital Transformation for a Sustainable Society in the 21st Century (13E 2019)* (pp. 439-450). Springer. https://doi.org/10.1007/978-3-030-29374-1_36
- King, W. R., & He, J. (2006). A meta-analysis of the technology acceptance model. *Information & Management*, 43(6), 740-755. <https://doi.org/10.1016/j.im.2006.05.003>
- Kitchenham, B. (2004). *Procedures for performing systematic reviews* (Technical Report 0400011T.1, pp. 1-28). Kitchenham. <https://citeseerx.ist.psu.edu/document?repid=rep1&type=pdf&doi=29890a936639862f45cb9a987dd599dce9759bf5>
- Komba, M. M., & Ngulube, P. (2015). An empirical application of the DeLone and McLean model to examine factors for e-government adoption in the selected districts of Tanzania. In I. S. Sodhi (Ed.), *Emerging Issues and Prospects in African E-Government* (pp. 118-129). IGI Global.
- Kurfali, M., Arifoğlu, A., Tokdemir, G., & Paçin, Y. (2017). Adoption of e-government services in Turkey. *Computers in Human Behavior*, 66, 168-178. <https://doi.org/10.1016/j.chb.2016.09.041>
- Lallmahomed, M. Z. I., Lallmahomed, N., & Lallmahomed, G. M. (2017). Factors influencing the adoption of e-Government services in Mauritius. *Telematics and Informatics*, 34(4), 57-72. <https://doi.org/10.1016/j.tele.2017.01.003>
- Liberati, A., Altman, D. G., Tetzlaff, J., Mulrow, C., Gøtzsche, P. C., Ioannidis, J. P. A., Clarke, M., Devereaux, P. J., Kleijnen, J., & Moher, D. (2009). The PRISMA statement for reporting systematic reviews and meta-analyses of studies that evaluate health care interventions: explanation and elaboration. *Annals of Internal Medicine*, 151(4), 65-94.
- Li, D., Lai, F., & Wang, J. (2010). E-business assimilation in China's international trade firms: the technology-organization-environment framework. *Journal of Global Information Management (JGIM)*, 18(1), 39-65.
- Lu, N. L., & Nguyen, V. T. (2016). Online tax filing - e-government service adoption case of Vietnam. *Modern Economy*, 7, 1498-1504. <http://dx.doi.org/10.4236/me.2016.712135>
- Mensah, I. K., Zeng, G., & Luo, C. (2020). E-government services adoption: An extension of the unified model of electronic government adoption. *SAGE Open*, 1-17. <https://doi.org/10.1177/2158244020933593>
- Moher, D., Liberati, A., Tetzlaff, J., & Altman, D. G. (2009). Preferred reporting items for systematic reviews and meta-analyses: the PRISMA statement. *Research Methods & Reporting*, 1-8. <https://doi.org/10.1136/bmj.b2535>
- Motohashi, K., Lee, D. R., Sawng, Y. W., & Kim, S. H. (2012). Innovative converged service and its adoption, use and diffusion: A holistic approach to diffusion of innovations, combining adoption-diffusion and use-diffusion paradigms. *Journal of Business Economics and Management*, 13(2), 308-333. <https://doi.org/10.3846/16111699.2011.620147>
- Nofal, M. I., Al-Adwan, A. S., Yaseen, H., & Alsheikh, G. A. A. (2021). Factors for extending e-government adoption in Jordan. *Periodicals of Engineering and Natural Sciences*, 9(2), 471-490. <http://dx.doi.org/10.21533/pen.v9i2.1824>
- Petticrew, M. (2001). Systematic reviews from astronomy to zoology: Myths and misconceptions. *BMJ*, 322, 98-101. <https://doi.org/10.1136/bmj.322.7278.98>

- Pynoo, B., Devolder, P., Tondeur, J., van Braak, J., Duyck, W., & Duyck, P. (2011). University students' acceptance of a web-based course management system. In T. Teo (Ed.), *Technology Acceptance in Education* (pp. 123-143). Sense Publishers. https://doi.org/10.1007/978-94-6091-487-4_7
- Rai, S. K., Ramamritham, K., & Jana, A. (2020). Identifying factors affecting the acceptance of government to government system in developing nations - empirical evidence from Nepal. *Transforming Government: People, Process and Policy*, 14(2), 283-303. <https://doi.org/10.1108/TG-05-2019-0035>
- Rodrigues, G., Sarabdeen, J., & Balasubramanian, S. (2016). Factors that influence consumer adoption of e-government services in the UAE: A UTAUT model perspective. *Journal of Internet Commerce*, 15(1), 18-39. <https://doi.org/10.1080/15332861.2015.1121460>
- Rogers, E. M. (2003). *Diffusion of Innovations*. Free Press.
- Rokhman, A. (2011). e-Government adoption in developing countries: The case of Indonesia. *Journal of Emerging Trends in Computing and Information Sciences*, 2(5), 228-236.
- Salahuddin, L., & Ismail, Z. (2015). Classification of antecedents towards safety use of health information technology: A systematic review. *International Journal of Medical Informatics*, 84(11), 877-891. <https://doi.org/10.1016/j.ijmedinf.2015.07.004>
- Schaupp, L. C., Carter, L., & McBride, M. E. (2010). E-file adoption: A study of U.S. taxpayers' intentions. *Computers in Human Behavior*, 26(4), 636-644. <https://doi.org/10.1016/J.CHB.2009.12.017>
- Slade, E. L., Dwivedi, Y. K., Piercy, N. C., & Williams, M. D. (2015). Modeling consumers' adoption intentions of remote mobile payments in the United Kingdom: extending UTAUT with innovativeness, risk, and trust. *Psychology & Marketing*, 32(8), 860-873. <https://doi.org/10.1002/mar.20823>
- Soufiane, B. M., & Ibrahim, M. (2018). Factors affecting the adoption of electronic government in Algeria: A proposed framework. *Journal of Advanced Research in Business and Management Studies*, 10(1), 52-64. <https://www.akademiabaru.com/submit/index.php/arbms/article/view/1286>
- Sterne, J. A. C., Sutton, A. J., Ioannidis, J. P. A., Terrin, N., Jones, D. R., Lau, J., Carpenter, J., Rücker, G., Harbord, R. M., Schmid, C. H., & others. (2011). Recommendations for examining and interpreting funnel plot asymmetry in meta-analyses of randomised controlled trials. *BMJ*, 343, Article d4002. <https://doi.org/10.1136/bmj.d4002>
- Šumak, B., & Šorgo, A. (2016). The acceptance and use of interactive whiteboards among teachers: Differences in UTAUT determinants between pre-and post-adopters. *Computers in Human Behavior*, 64, 602-620. <https://doi.org/10.1016/j.chb.2016.07.037>
- Susanto, T. D., & Goodwin, R. (2013). User acceptance of SMS-based e-government services: Differences between adopters and non-adopters. *Government Information Quarterly*, 30(4), 486-497. <https://doi.org/10.1016/j.giq.2013.05.010>
- Syaifuddin, M., Nurmandi, A., & Salahudin. (2022). The Behavior Patterns of the Yogyakarta Special Region Government Official in Reacting to e-Government Transformation. In X. S. Yang, S. Sherratt, N. Dey, & A. Joshi (Eds.), *Proceedings of Sixth International Congress on Information and Communication Technology* (pp. 249-259). Springer. https://doi.org/10.1007/978-981-16-2102-4_23

- Taylor, S., & Todd, P. (1995). Decomposition and crossover effects in the theory of planned behavior: A study of consumer adoption intentions. *International Journal of Research in Marketing*, 12(2), 137-155. [https://doi.org/10.1016/0167-8116\(94\)00019-K](https://doi.org/10.1016/0167-8116(94)00019-K)
- UNDP. (2022, September 20). *Country insights*. Human Development Reports. <https://hdr.undp.org/data-center/country-insights#/ranks>
- Venkatesh, V., Morris, M. G., Davis, G. B., & Davis, F. D. (2003). User acceptance of information technology: Toward a unified view. *MIS Quarterly* 27(3), 425-478. <https://doi.org/10.2307/30036540>
- Venkatesh, V., Thong, J. Y. L., & Xu, X. (2012). Consumer acceptance and use of information technology: extending the unified theory of acceptance and use of technology. *MIS Quarterly*, 36(1), 157-178.
- Venkatesh, V., Thong, J. Y. L., & Xu, X. (2016). Unified theory of acceptance and use of technology: A synthesis and the road ahead. *Journal of the Association for Information Systems*, 17(5), 328-376. <https://doi.org/10.17705/1jais.00428>
- Verkijika, S. F., & de Wet, L. (2018). E-government adoption in sub-Saharan Africa. *Electronic Commerce Research and Applications*, 30, 83-93. <https://doi.org/10.1016/j.elerap.2018.05.012>
- Yang, H. D., & Yoo, Y. (2004). It's all about attitude: Revisiting the technology acceptance model. *Decision Support Systems*, 38(1), 19-31. [https://doi.org/10.1016/S0167-9236\(03\)00062-9](https://doi.org/10.1016/S0167-9236(03)00062-9)
- Zahid, H., & Din, B. H. (2019). Determinants of intention to adopt e-government services in Pakistan: An imperative for sustainable development. *Resources*, 8(3), Article 128. <https://doi.org/10.3390/resources8030128>
- Zubaidah, E., Nurmandi, A., Pribadi, U., & Hidyati, M. (2021). Taxpayer behavior in using e-vehicle in Indonesia. *Asia Pacific Journal of Information Systems*, 31(3), 378-391. <https://doi.org/10.14329/apjis.2021.31.3.378>



Workload Characterization and Classification: A Step Towards Better Resource Utilization in a Cloud Data Center

Avita Katal^{1*}, Susheela Dahiya² and Tanupriya Choudhury^{1,2,3}

¹*School of Computer Science, University of Petroleum and Energy Studies, Dehradun, Uttarakhand, 248007, India*

²*Department of Computer Science and Engineering, Graphic Era Hill University, Dehradun, 248002, India*

³*Symbiosis Institute of Technology, Symbiosis International University, Pune, Maharashtra, 412115, India*

ABSTRACT

Advancements in virtualization technology have led to better utilization of existing infrastructure. It allows numerous virtual machines with different workloads to coexist on the same physical server, resulting in a pool of server resources. It is critical to understand enterprise workloads to correctly create and configure existing and future support in such pools. Managing resources in a cloud data center is one of the most difficult tasks. The dynamic nature of the cloud environment, as well as the high level of uncertainty, has created these challenges. These applications' diverse Quality of Service (QoS) requirements make data center management difficult. Accurate forecasting of future resource demand is required to meet QoS needs and ensure better resource utilization. Consequently, data center workload modeling and categorization are needed to meet software quality solutions cost-effectively. This paper uses traces of Bitbrain's data to characterize and categorize workload. Clustering (K Means and Gaussian mixture model) and Classification strategies (K Nearest Neighbors, Logistic Regression, Decision Trees, Random Forest, and Support Vector Machine) characterize and model the workload traces. K Means shows better results as compared to GMM when compared to the Calinski Harabasz index and Davies-Bouldin score. The results showed that the Decision Tree achieves the maximum accuracy

of 99.18%, followed by K Nearest Neighbor (KNN), Random Forest (RF), Support Vector Machine (SVM) Logistic Regression (LR), Multi-Layer Perceptron (MLP), and Back Propagation Neural Networks.

ARTICLE INFO

Article history:

Received: 16 August 2022

Accepted: 14 November 2022

Published: 27 July 2023

DOI: <https://doi.org/10.47836/pjst.31.5.27>

E-mail addresses:

avita207@gmail.com (Avita Katal)

susheela.iitr@gmail.com (Susheela Dahiya)

tanupriya1986@gmail.com (Tanupriya Choudhury)

* Corresponding author

Keywords: Classification, cloud data center, clustering, Gaussian mixture model, K Means, workload

INTRODUCTION

Data centers are undergoing rapid evolution in the age of virtualization, and new technologies like containerization are evolving rapidly. However, with the growth of cloud and serverless computing, the development of predictive analytics, edge computing, the arrival of 5G, and the COVID-19 pandemic has swept the entire globe, making almost everything online. People's online activities have increased, leading to data generation and resource utilization difficulties for data centers. The virtual machine (VM), as a key component of the cloud environment, is typically responsible for performing and maintaining the operating system's operation and storage and ensuring the operating system's normal operation (OS). The cloud platform is becoming more prominent and complex as it grows. Consequently, concerns regarding competitive segmentation of the platform's underlying hardware have arisen. Any VM behavior that is out of the ordinary can disrupt routine operations, resulting in a major loss for the organization, lowering computing capabilities, or even preventing the effective implementation and practice of cloud computing.

Cloud platforms are in high demand to host a variety of workloads, particularly web applications that require high Service Level Agreements (SLAs) agreed between the Cloud Service Provider (CSP) and the customer. In terms of accessibility, dependability, and efficiency, these services necessitate a diverse set of Quality of Service (QoS) requirements. Workloads that are typically transferred to cloud systems need resources such as memory, CPU, network bandwidth, and storage. Depending upon the resource these workloads use, more than others categorize them as specific resource-intensive workloads. The actual resource consumption of these workloads is often lower than the resources they have demanded. The service providers profit from this behavior by offering more resources at cheaper prices than the actual amount of resources they have, reliant on the fact that most customers' applications will not operate at maximum capacity. CSP exploits the dynamic provisioning characteristic of the cloud to provide on-demand performance. Recognizing workload behavior in a cloud data center is vital because it enables elastically scaling up and down provisioned services critical to its capabilities.

Workload characterization forecasts resource needs, making capacity management, allocation, and resource deployments more effective. The workload is typically characterized using one of two methodologies: trace-based (Abrahao & Zhang, 2004) or model-based (Delimitrou & Kozyrakis, 2011; Huang & Feng, 2009; Moro et al., 2009). The model-based technique is favored over the trace-based procedure since it is unconcerned about the operating platform upon which the trace was documented. Trace-based strategies have a limited number of production and quality traces which necessitates regular tinkering of workload characteristics to make them consistent with a new data center environment, making them less efficient than model-based strategies. Most workloads in cloud data centers are a combination of disparate applications (Mishra

et al., 2010). It is not easy to create a truly united approach to estimate the future usage of resources in these disparate application areas. These responsibilities show various behavior regarding periodicity, co-relation, and repeating trends. Workload classification requires a more thorough understanding of workload behavior and properties. However, few studies have been conducted on workload characterization due to the lack of open-source traces. Different scheduling models can be implemented by identifying workloads that heavily utilize shared resources.

The categorization and characterization of cloud workloads is an important research topic for better understanding workloads and managing cloud resources efficiently. There are many studies on workload characteristics. Google Cluster Trace (GCT) (Reiss et al., 2012), Bit Brains Trace (BBT) (Shen et al., 2015), Alibaba (<https://github.com/alibaba/clusterdata>) Yahoo trace (<https://webscope.sandbox.yahoo.com/catalog.php?datatype=i&did=67&guccounter=1>) and Wikipedia (http://www.wikibench.eu/?page_id=60) are four most common workload traces available in this domain. Workload qualities for data centers need to be statistically combined and evaluated to predict the future resource demand of the data center. Many researchers have employed statistical methods like Pearson Coefficient of Correlation (PCC), standard deviation, and mean techniques related to and existing methods (Birke et al., 2014)

Calzarossa et al. (2016) created a list of standard internet workloads, workloads from social networks, streaming platforms, mobile applications, and cloud computing infrastructure facilities. The workloads' characteristics were covered, and historical workload patterns like periodicity were considered an important distinguishing feature of cloud network workloads. With time-series analysis, Ali-Eldin et al. (2014) explored the time series of Wikipedia's workload and discovered that it is completely predictable and has strong seasonal variation. Self-similarity and burstiness are two of the main workload characteristics, according to Yin et al. (2015), so they developed a workload generator for cloud computing that is bursty and self-similar. Wang et al. (2015) examined workload process statistics. Combined optimization-based modeling of slow time-scale workload with stochastic modeling of fast time-scale workload is done to anticipate the value of dynamic resizing.

For proactive workload management, Zhang et al. (2014) created a service for workload factoring. It used a data item detection method to detach the application workload's two naturally distinct components, flash crowd, and base workload. In order to adapt to changing application data popularity, it evaluated incoming traffic based not just on quantity but also on data content. Recognizing and forecasting patterns in cloud workloads is a difficult problem that Patel et al. (2015) address. They presented a resource usage-based clustering approach to identify periodic tasks. Non-periodic tasks' resource consumption was depicted as a time series. Panneerselvam et al. (2014) classified cloud workloads in terms of workload patterns. They divided workloads into five categories: unpredictable,

static, continuously changing, periodic, and once-in-a-lifetime workloads, and used this classification to compare the performance of Markov modeling and Bayesian modeling.

Understanding workload characteristics is beneficial for enterprise data centers. Due to the scarcity of open-source workload traces, only a few attempts at characterizing cloud data center workloads have been made so far. The following are some of the most well-known research projects: The authors analyzed the BBT dataset representing business-critical workloads (Shen et al., 2015). Statistical methods such as standard deviation and mean, PCC, Autocorrelation Function, Peak Mean Ratio, and Coefficient of Variation were used to characterize the workload. The analysis was carried out using basic statistical and time pattern analysis. The findings from the study are as follows: (1) there is a strong correlation between demanded memory and CPU utilization, (2) Memory and CPU utilizations are easy to predict over short periods, and (3) disc and network utilization follow patterns, implying that prediction granularity is measured in days. The authors' proposed methodology has a major limitation in terms of trustworthiness. Errors in analysis are common in many fields of applied statistical data. The tools used for data gathering are another major disadvantage that puts the dataset's validity into question.

Zhang et al. (2011) presented a task usage shape classification that precisely reproduces the technical specifications of historical data on average job wait time and machine resource utilization. They utilized real-time data from Google and found that merely simulating the mean job usage can gain considerable precision in replicating resource utilization and task wait time. One major drawback is that the results are very complex and produce complex characterization of task shape classification. Rasheduzzaman et al. (2014) examined the production workload trace (version 2) by Google and utilized K-means clustering to group similar jobs together. They demonstrated a simple method for establishing workload attributes, knowledge, and insights for workload performance on cluster machines. The authors did not use the complete trace to perform the analysis, which led to the discrepancy in the results. The GCT dataset was used to classify workloads by Shekhawat et al. (2018). The authors used the K-means algorithm to generate task clusters after first identifying workload aspects such as low, high, and medium. To locate coordinate clusters, breakpoints within workload parameters were identified to find coordinate clusters.

Finally, utilizing coefficient of variation principles, the total number of clusters was minimized by merging nearby clusters. As per the key characteristics of the workload, the execution length of tasks was bimodal. Most tasks were short, and a few long-duration tasks had high demands of memory and CPU. Moro et al. (2009) introduced an innovative method to assess the execution workload performed by a computer precisely. Their proposed method directly utilized the memory reference sequence generated during program execution. The memory reference sequences were treated as sequences of floating-point numbers and subjected to analysis using signal-processing techniques. Spectral analysis

was employed during the feature extraction phase, while Ergodic Continuous Hidden Markov Models (ECHMMs) were used in the pattern matching phase. The effectiveness of the proposed algorithms was evaluated through trace-driven simulations utilizing the SPEC 2000 workloads. Ismaeel and Miri (2019) provide a real-time VM provisioning system that uses effective and unique clustering, time-series prediction, and placement algorithms to lower the energy consumed in a cloud data center.

It considers user behavior and previous VM utilization to anticipate the number of VMs required. It enhances the consolidation process while consuming the least amount of energy. On average, the results show an improvement of up to 80%. They have used only one day of data, which is a major drawback. Cheng et al. (2018) characterized the batch instance workloads based on: CPU utilization, memory utilization, and job timeframe into three different categories. The authors determined the arrival pattern for applications. The primary strength lies in the author's use of the traces of Alibaba's data center and workload categorization based on resource utilization. Mishra et al. (2010) proposed a multi-level task categorization technique and explained task categorization requests for capacity management and job scheduling. By monitoring resource usage by task class, task classification allows users to predict application expansion.

The authors use well-known statistical clustering techniques to implement proper research methods: (1) assess the workload aspects, (2) use an off-the-shelf method like k-means to construct task clusters, (3) evaluate the break marks of qualitative cartesian coordinates inside workload elements, and (4) combine adjoining task clusters to decrease the number of variables predictions. Their methodology yields eight workloads when applied to several Google compute clusters. They demonstrated that, for the same compute cluster, the features of each workload in relation to the number of tasks and resources consumed are coherent across days. In contrast, the medium-grain characterization detects discrepancies in workload features among clusters where such distinctions are predicted. They did not consider the job constraints, and they did not take the entire dataset for analysis which is the major drawback of their proposed approach. Ismaeel et al. (2019) introduced a new methodological process for selecting the appropriate task clustering approach in data centers based on validation indices and result correlation.

They developed an effective pre-processing strategy, reducing the big data challenge to a compact 2D matrix of independent jobs using CPU and memory requirements. Shekhawat et al. (2018) proposed a technique for classifying and characterizing data center workloads based on resource utilization. For workload classification, seven distinct machine-learning techniques have been used and compared. Workload distribution is approximated for GCT and BBT datasets using various application components. Finally, the authors have presented an approach for assessing the relevance of various categorization attributes. The authors have not considered and compared the results with any other clustering algorithm.

Due to the rapid advancement of hardware and resource management strategies, cloud data centers handle many application types. Recognizing the workload features and understanding the data centers is intrinsically critical for CSP to continue adopting cloud technology. In cloud data centers, proper resource management is crucial for predicting the future requirements of resources. The first step to better resource management is to characterize and classify the workload before placing it on the virtual machines. It also helps to meet the required or agreed QoS.

In this paper, the following research questions (RQs) are addressed:

RQ1: How workload categorization helps in better resource management in cloud data centers?

RQ2: How do K Means and the Gaussian Mixture Model aid in grouping various workloads?

RQ3: Which clustering algorithm performs better for the characterization of workload?

RQ4: How classification of workload helps in understanding the workload type, and which classification algorithm achieves maximum accuracy?

This paper uses K Means and Gaussian Mixture Model clustering algorithms to properly cluster the Bitbrains trace (Fast Storage) dataset to characterize the workload. Initially, the feature significance analysis is done to understand the important features. Feature selection becomes important in developing robust and efficient classification models while reducing training time (Onan & KorukoGlu, 2017). Both clustering algorithms are compared based on the Calinski-Harabasz index and Davies-Bouldin score coefficients. Following clustering, several ML methods are used to classify the data. The models built using these methods are also compared in terms of accuracy.

MATERIALS AND METHODS

Dataset Characteristics

Bitbrains' distributed data center is a managed hosting and business computing powerhouse. The dataset provides performance information for 1,750 virtual machines. Among the company's clients are numerous major banks, credit card companies, insurers, and others. Towers Watson and Algorithmics are two application manufacturers that host solvency applications on Bitbrains. These programs are typically used for accounting information completed after a fiscal quarter. Each file of the dataset includes the performance metrics for a single VM. These files are classified into two types: fastStorage and Rnd. FastStorage is the first trace, with 1,250 virtual machines (VMs) linked to Storage Area Network (SAN) storage devices. The second trace, Rnd, has 500 virtual machines (VMs) connected to either a fast SAN or a much slower Network Attached Storage (NAS) device. Because storage connected to the fastStorage devices is more effective, the fastStorage trace contains a greater fraction of server-side and computation units than the Rnd trace. In the Rnd trace,

on the other side, we notice a greater share of administration computers, which only require minimum storage and less frequent accesses. In the Rnd trace, on the other hand, we notice a greater share of management machines, which only require minimum storage and less frequent usage. The Fast Storage directory is divided into three sub-directories based on the month the data was collected. A row-based format is used in each file. Each row represents a performance metric observation.

Clustering Algorithms

Grouping data items using a similarity metric is known as clustering. Clustering can be hierarchical, partitional, complete, partial, overlapping, fuzzy, or exclusive. The partitional clustering technique, K-Means, divides data objects into non-overlapping groups (Onan, 2019). K-Means clusters are based on prototypes when the cluster is symbolized by a prototype and all nodes in the cluster are near it. Two common prototypes are centroid and medoid. Gaussian Mixture Models (GMM) clusters are based on density. A cluster based on density is a collection of high-density objects surrounded by low-density areas. Identifying and summarizing properties of interest is made easier by grouping data into clusters. Similar utilization trends of workload can help develop capacity strategies for meeting future resource requirements while preserving the SLA for operating services.

Classification Algorithms

The classification algorithm is a supervised learning approach that uses training data to determine the type of new observations. The software trains from a dataset or observations and then classifies additional observations. As a supervised learning approach, the classification algorithm employs labeled input data comprising input and output. The following classification algorithms have been used in this paper: Random Forest (RF), Logistic Regression (LR), K Nearest Neighbor (KNN), Support Vector Machine (SVM) and Decision Tree (DT), Multi-Layer Perceptron (MLP) and Back Propagation Neural Network.

Methodology

Figure 1 shows the methodology followed to characterize and categorize the workload. Generally, the workload in the data centers consists of different attributes. Some attributes are more important when it comes to characterizing the workload. Understanding the distribution of attributes in terms of significance is critical for determining the type of workload. It is important as, during the classification stage, the significance of the attribute determines how much weight has to be given to it or a group of attributes. The main purpose of performing a significance assessment is to order the attributes in terms of predictive power. The decision Tree Classifier algorithm has been used to perform the significance analysis. The top four attributes having the highest significance have been taken for further

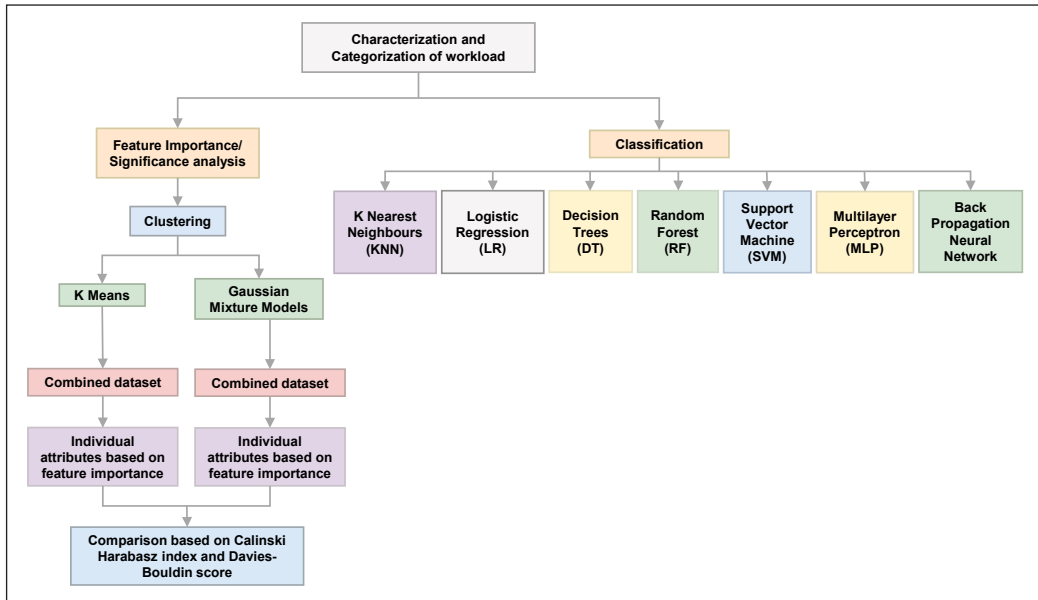


Figure 1. Methodology for categorization and characterization of workload

analysis. In the BBT dataset, memory usage [KB], disk read throughput, CPU usage [MHZ], network transmitted throughput, disk write throughput, and network received throughput have high percentages in attribute significance analysis. The disk writes throughput and disk read throughput are combined to form a single attribute named disk usage.

Similarly, network transmitted and received throughput are combined to form a single attribute named network usage. Normalization of the BBT dataset is done using min-max normalization. The K means technique was applied to the combined data set of highly significant attributes. The technique was further applied to each attribute to calculate K. The value of the number of clusters, K, is determined using the elbow criterion. If c represents the clusters obtained for CPU usage [MHZ], m for Memory usage [KB], d for Disk usage, and n represents clusters acquired for Network usage. The product of c, m, d, and n yields the number of possible workloads in the dataset. As a result, the frequency of various workloads is calculated. This analysis yielded the dataset's workload distribution.

GMM clustering is applied to all attributes first, followed by individual attributes. The outcomes of both algorithms are compared using parameters such as the Calinski-Harabasz index (CHI) and the Davies-Bouldin Index (DBI). CHI is also known as the Variance Ratio Criterion. A higher CHI score denotes a model with more defined clusters. The index is the ratio of all clusters' total between-cluster and within-cluster variance. The score is greater when clusters are large and well-spaced, which correlates to a classic cluster idea. The score is rapidly computed. When DBI is used to evaluate the model, a lower DBI indicates a model with greater cluster separation. This index represents clusters' average

similarity, which is defined as a criterion that relates cluster distance to several clusters. It distinguishes between clusters that are both remote and small. The Davies–Bouldin criterion is based on a weighted average of distances “within-cluster” and “between-cluster.” The lowest possible score is zero. Closer to zero indicates a better partition. Davies-Bouldin scores are easier to calculate because they only use point-wise distances, and the index is solely based on amounts and characteristics inherent in the dataset.

Following the characterization of the dataset, classification is done using different classification algorithms. The classification of workloads is an important step in workload analysis. The models’ accuracy is crucial for workload analysis, resource usage prediction, and provisioning. The classification accuracy analysis aids us in determining which algorithm is best for a given data center workload. The before-mentioned algorithms are applied to determine the accuracy.

RESULTS AND DISCUSSION

Firstly, the feature importance or attribute significance analysis uses a decision tree algorithm. The results are shown in Figure 2. The attributes are represented on the x-axis, while the value of coefficients is depicted on the y-axis. The importance of CPU usage [MHZ] is highest for the BBT dataset. Network and disk usage dominates the second and third position in terms of significance analysis. Memory usage has low significance among all the attributes.

The elbow method to determine the value of K is applied, and the graph is plotted between K and inertia, where the inertia value indicates how far apart the points in a cluster are. The graph is shown in Figure 3. The value of the x-axis depicts the K values, and the value of the Y-axis depicts the inertia value. At K = 4, it produces an elbow, indicating that the BBT fastStorage dataset has four types of workloads.

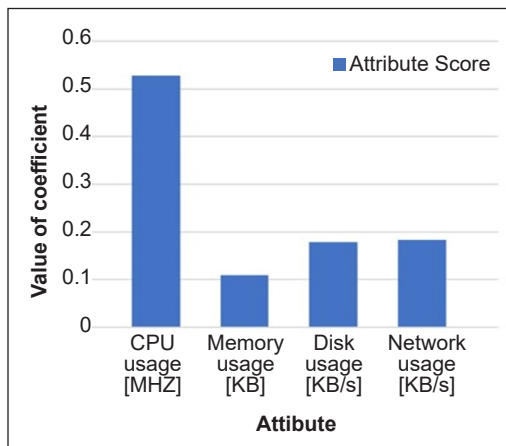


Figure 2. Attribute score of different attributes

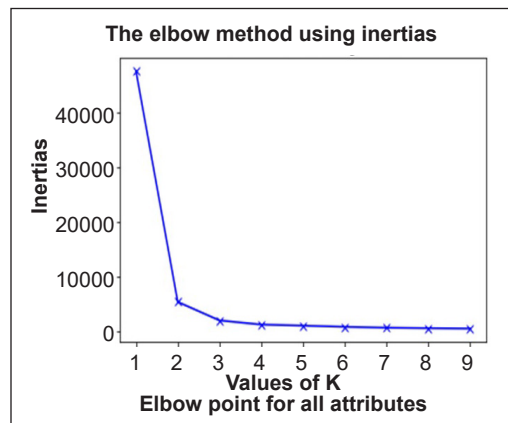


Figure 3. Value of K vs. inertias on highly significant attributes

The plots of the clustering results based on each attribute individually, such as CPU usage, memory usage, disk usage, and network usage, are depicted in Figures 4, 5, 6, and 7, respectively. It can be concluded from these graphs that for CPU usage, two different workloads have identified that is LOW (C_L) and HIGH (C_H); for memory, three different workloads have observed that is LOW(M_L), MEDIUM(M_M), and HIGH(M_H); two workloads have identified for LOW disk usage (D_L) and HIGH(D_H), and two workloads have identified for LOW network usage (N_L) and HIGH(N_H).

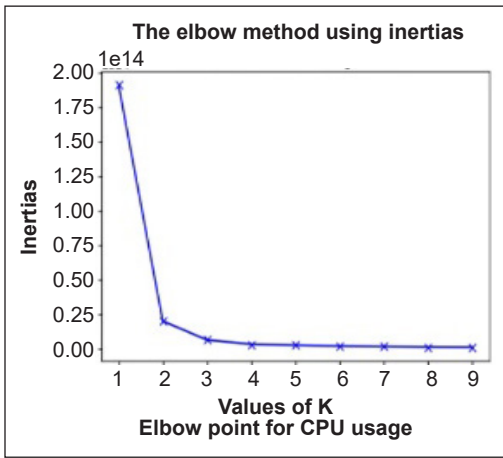


Figure 4. K vs. Inertia (CPU usage)

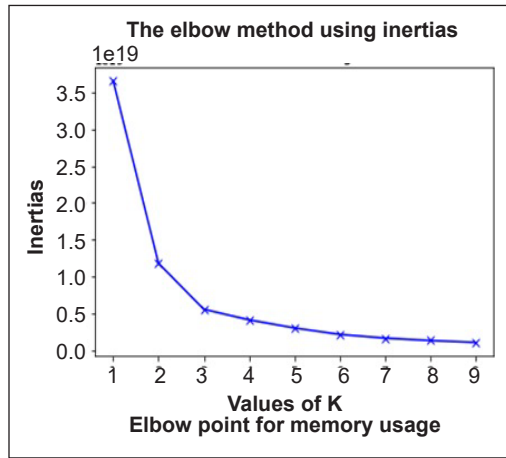


Figure 5. K vs. Inertia (Memory usage)

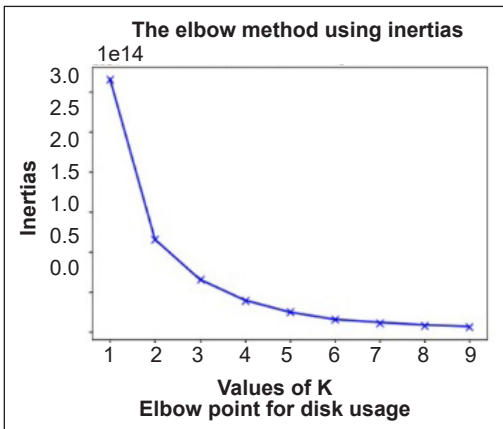


Figure 6. K vs. Inertia (Disk usage)

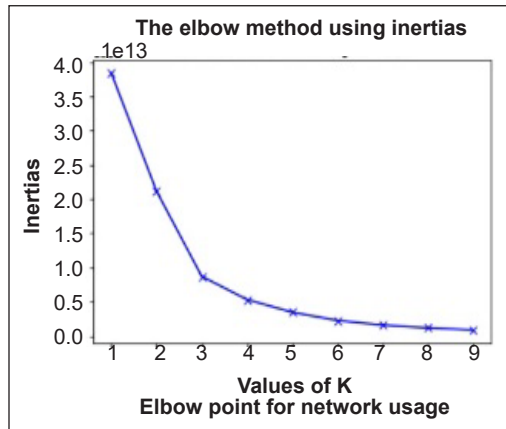


Figure 7. K vs. Inertia (Network usage)

The 24 distinct workload combinations are determined once the elbow point is calculated using K Means clustering. The percentage of tasks can be identified by calculating the number of tasks in each combination. Table 1 is formatted as [CPU usage][Memory usage][Disk usage][Network usage].

Table 1 shows that most tasks (93.38%) have modest resource utilization. These processes used less CPU, memory, storage space, and network bandwidth. These virtual machines are made up of short administrative chores and application inquiries. The workload then consists of 3.41% of jobs with high CPU, medium memory, and low disk and network use. Typically, these virtual machines are utilized to run CPU-intensive consumer applications.

Similarly, GMM clustering is applied to the BBT dataset. The Bayesian Information Criterion (BIC) and Akaike Information Criterion (AIC) graphs are plotted initially on the entire dataset. It can be concluded from the graph that there are seven types of workloads in the entire dataset. On the x-axis of Figure 8, the number of clusters or components is depicted, whereas, on Y-axis, the score of AIC and BIC is depicted. The value of AIC and BIC is the same for each analysis; therefore, both the lines overlap, which results in the depiction of one line in all graphs.

Once the clustering is done on the combined dataset, the GMM is applied to the individual attributes. Clustering based on individual attributes, CPU usage, memory usage, disk usage, and network usage yielded the results (Figures 9, 10, 11, and 12). It can be concluded that CPU and memory usage have five types of workloads, followed by disk and network usage having four types.

Once the number of components is identified for each attribute, 600 workload combinations are formed. There are some

Table 1
Percentage of tasks in each cluster (K Means)

Type of workload	Number of tasks	Percentage of tasks
[C _L][M _L][D _L][N _L]	10479078	93.380000
[C _L][M _L][D _L][N _H]	6242	0.050000
[C _L][M _L][D _H][N _L]	10823	0.090000
[C _L][M _L][D _H][N _H]	3150	0.020000
[C _L][M _M][D _L][N _L]	127939	1.140000
[C _L][M _M][D _L][N _H]	1492	0.01
[C _L][M _M][D _H][N _L]	1823	0.010000
[C _L][D _M][M _H][N _H]	401	0.000000
[C _L][M _H][D _L][N _L]	28650	0.250000
[C _L][M _H][D _L][N _H]	147	0.000000
[C _L][M _H][D _H][N _L]	3873	0.030000
[C _L][M _H][D _H][N _H]	9	0.000080
[C _H][M _L][D _L][N _L]	88450	0.780000
[C _H][M _L][D _L][N _H]	74	0.000600
[C _H][M _L][D _H][N _L]	4	0.000030
[C _H][M _L][D _H][N _H]	59	0.000500
[C _H][M _M][D _L][N _L]	382850	3.410000
[C _H][M _M][D _L][N _H]	50	0.000400
[C _H][M _M][D _H][N _L]	90	0.000800
[C _H][M _M][D _H][N _H]	6	0.000050
[C _H][M _H][D _L][N _L]	83166	0.740000
[C _H][M _H][D _L][N _H]	14	0.000100
[C _H][M _H][D _H][N _L]	3406	0.030000
[C _H][M _H][D _H][N _H]	3	0.000020

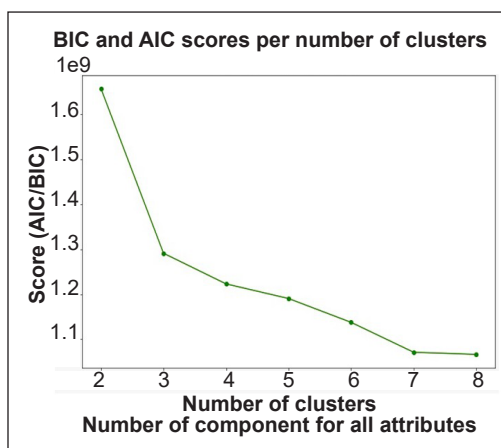


Figure 8. AIC and BIC plot for all attributes

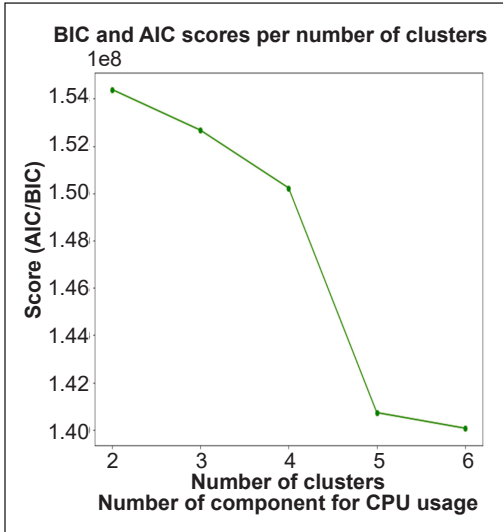


Figure 9. AIC and BIC plot (CPU usage)

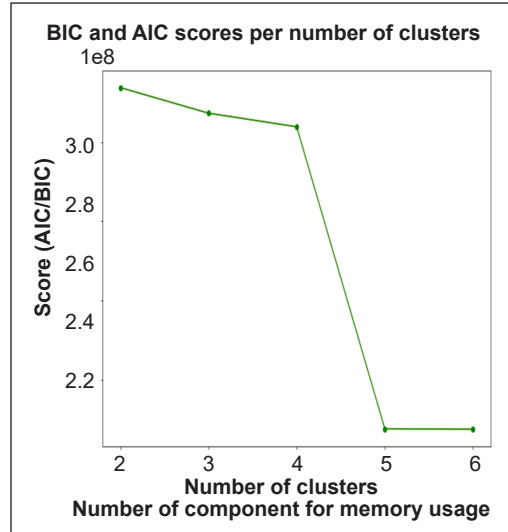


Figure 10. AIC and BIC plot (Memory usage)

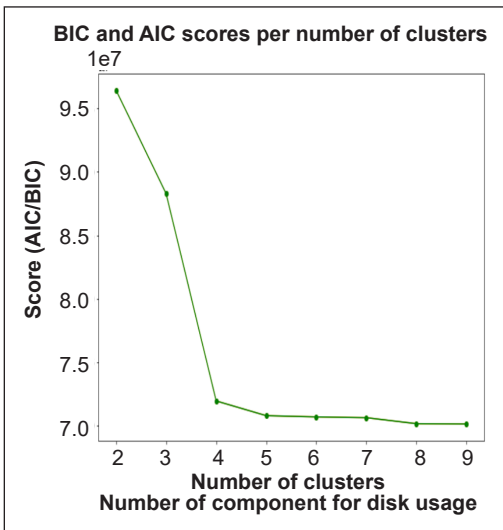


Figure 11. AIC and BIC plot (Disk usage)

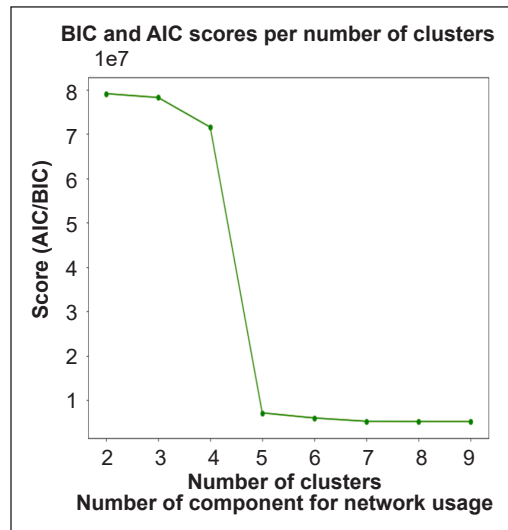


Figure 12. AIC and BIC plot (Network usage)

combinations in all clusters that are not identified. Therefore, 336 combinations are taken, which consist of workloads from all four attributes. Table 2 depicts the various clusters formed by the GMM.

K means, and GMM performance is evaluated based on the Calinski Harabasz index and Davies-Bouldin score. Table 3 shows the values of different parameters by applying K Means and GMM.

It can be concluded that K means it outperforms the GMM on all mentioned parameters (Table 3). The Davies-Bouldin score of K Means is 0.37, much better than that of

3.77 GMM. Closer the value to zero, the better the cluster separation. The Calinski Harabasz Index of K means 54500062.89, whereas, for GMM, it is 12027922.51. The greater the value of the Calinski Harabasz Index score better is the density and cluster separation.

An experimental assessment was done to approximate classification accuracy for various machine-learning algorithms to explore how workload distribution affects each model. The analysis was carried out using the BBT fastStorage dataset. The training and testing data ratio is kept at 70 and 30, respectively. Table 4 displays the accuracy results, AUC ROC score, and Precision for different algorithms.

Cloud computing guarantees high throughput, adaptability, and cost-effectiveness to address evolving processing

Table 2
Percentage of tasks in each cluster (GMM)

Types of workloads (CPU, DISK, NETWORK, MEMORY)				Percentage of tasks
C _{VL}	D _{VL}	N _{VL}	M _{VL}	15.10235435
C _{VL}	D _{VL}	N _{VL}	M _{VH}	16.61488353
C _{VL}	D _{VL}	N _L	M _{VH}	1.29211
C _{VL}	D _{VL}	N _H	M _{VL}	0.805227325
C _{VL}	D _{VL}	N _H	M _{VH}	6.928157693
C _{VL}	D _{VH}	N _{VL}	M _{VH}	2.761330624
C _{VL}	D _{VH}	N _H	M _M	0.545286852
C _{VL}	D _{VH}	N _H	M _{VH}	4.255609617
C _L	D _{VL}	N _H	M _H	1.256375982
C _M	D _L	N _L	M _M	0.614936998
C _M	D _L	N _L	M _H	0.627697874
C _M	D _{VH}	N _H	M _M	0.495963214
C _H	D _{VL}	N _{VL}	M _{VH}	1.344632768
C _H	D _{VL}	N _H	M _{VL}	1.736004919
C _H	D _{VL}	N _H	M _M	0.64278458
C _H	D _{VL}	N _H	M _{VH}	1.911226363
C _H	D _L	N _L	M _M	0.912589781
C _H	D _L	N _H	M _M	1.64271329
C _H	D _L	N _H	M _{VH}	0.655527634
C _H	D _{VH}	N _{VL}	M _{VL}	0.598780944
C _H	D _{VH}	N _{VL}	M _M	1.03473596
C _H	D _{VH}	N _{VL}	M _{VH}	3.523222656
C _H	D _{VH}	N _L	M _M	0.821481402
C _H	D _{VH}	N _H	M _{VL}	1.349453742
C _H	D _{VH}	N _H	M _M	5.648532321
C _H	D _{VH}	N _H	M _{VH}	9.933228181
C _{VH}	D _{VL}	N _H	M _H	0.637268531

Table 3
Scores for performance evaluation parameters

Parameter	K Means	Gaussian Mixture Models
Calinski Harabasz Index	54500062.89	12027922.51
Davies-Bouldin score	0.37	3.77

Table 4
Accuracy percentage of classification algorithms

Algorithms	Accuracy in %	AUC ROC Score	Precision
K Nearest Neighbors (KNN)	98.79	0.963	0.96
Logistic Regression (LR)	79.19	0.941	0.93
Decision Trees (DT)	99.18	0.976	0.97
Random Forest (RF)	97.80	0.958	0.95
Support Vector Machine (SVM)	84.34	0.922	0.91
Multi-Layer Perceptron	79.72	0.825	0.82
Back Propagation Neural Network	80.00	0.847	0.84

necessities. As the quantity of data continues to grow at an appalling rate, many firms are turning to data centers to make effective choices and achieve a competitive edge. The cloud-computing model is used for a multitude of applications. These applications differ in their characteristics and have varying demands on the Physical Machines' resources (PMs). The requirements of database applications (which perform intensive read and write operations on discs, for example) differ from those of a scientific computing application (which demands significant computing power from the CPU). To effectively configure cloud resources, network managers must be able to characterize and predict the workload on VMs. Clustering the tasks into groups or clusters is feasible based on the different demands of dissimilar tasks of cloud applications.

The clustering process can identify characterizations that can improve the efficiency of historical workload traces over a wide range of critical performance parameters, such as increasing the utilization of PMs hosted in cloud data centers. Any workload classification should consider the usage of resources, job progression, and other issues that necessitate adherence to service-level agreements (SLAs). Analytical models (Bennani & Menascé, 2005; Bodnarchuk & Bunt, 1991) and performance metrics (Bienia et al., 2008), (Jackson et al., 2010) are used in workload characterization. Analytical models are the models of mathematics having a closed-form solution, which indicates that the solution to the equations used to explain system changes may be expressed mathematically as an analytic function.

A performance model is used to characterize the fundamental elements of how a planned or existing system performs in terms of usage of resources, demand for resources, and delays induced by processing or physical restrictions. To maximize earnings, cloud providers aim to get as many new requests as feasible; conversely, they must encounter QoS constraints in line with the appropriate SLA with end-users. One needs efficient resource provisioning mechanisms to achieve this goal. Users typically have sporadic access to cloud resources, and workloads will fluctuate. Workload fluctuation causes under-provisioning and over-provisioning issues, wasting resources and time. One solution is forecasting workload based on past consumption behaviors and the present state of cloud resources. The trends equate user requests with cloud resources depending on the type of requirement.

CONCLUSION

The utilization and prominence of cloud computing as among the most well-known internet-based inventions for supplying computational power and infrastructural facilities to IT organizations for executing/hosting cloud workloads is expanding every day and is anticipated to expand even further. Consumers upload heterogeneous cloud workloads to the cloud through internet services, banking applications, online payment processing assistance, portable computing assistance, and graphics-based services, with varying QoS parameters

in the form of SLA. The significance of workload characterization and classification in cloud data centers is discussed in this paper. The workload of types is clustered using two different clustering techniques. Workload distribution is accomplished by combining distinct workload pairings in both clustering modes. After clustering is completed, the performance is examined to determine which clustering works best.

Most tasks, according to the K Means algorithm (93.38%), have low resource utilization (CPU, memory, storage space, and network bandwidth). Short administrative tasks and application inquiries make up these virtual machines. GMM shows a maximum of 16.61% of the tasks consume CPU (Very Low), Disk (Very Low), Network (Very Low), and Memory (Very High) resources. However, the results demonstrate that K means beats in Calinski Harabasz and the Davies-Bouldin Index. After clustering, classification is carried through by utilizing several classification techniques. The decision tree shows a maximum accuracy of 99.18%. Compared to the existing study, this work explains different clustering and classification strategies for cloud data center workloads.

ACKNOWLEDGEMENT

The authors would like to express their sincere gratitude and appreciation to the University of Petroleum and Energy Studies, India, for providing invaluable resources and opportunity to conduct the research. This work has been undertaken as part of first author's doctoral studies.

REFERENCES

- Abraham, B., & Zhang, A. (2004) *Characterizing application workloads on CPU utilization for utility computing* (HPL-2004-157). Hewlett-Packard Company. <https://www.hpl.hp.com/techreports/2004/HPL-2004-157.html>
- Ali-Eldin, A., Rezaie, A., Mehta, A., Razroev, S., Luna, S. S. de, Seleznev, O., Tordsson, J., & Elmroth, E. (2014, March 11-14). *How will your workload look like in 6 years? Analyzing Wikimedia's workload*. [Paper presentation]. 2014 IEEE International Conference on Cloud Engineering, Boston, USA. <https://doi.org/10.1109/IC2E.2014.50>
- Bennani, M. N., & Menascé, D. A. (2005, June 13-16). *Resource allocation for autonomic data centers using analytic performance models*. [Paper presentation]. Second International Conference on Autonomic Computing, ICAC'05. Seattle, USA. <https://doi.org/10.1109/ICAC.2005.50>
- Bienia, C., Kumar, S., Singh, J. P., & Li, K. (2008, October 25-29). *The PARSEC benchmark suite: Characterization and architectural implications*. [Paper presentation]. Proceedings of the 17th International Conference on Parallel Architectures and Compilation Techniques. Toronto, Canada. <https://doi.org/10.1145/1454115.1454128>
- Birke, R., Chen, L. Y., & Smirni, E. (2014, May 5-9). *Multi-resource characterization and their (in) dependencies in production datacenters*. [Paper presentation]. IEEE/IFIP Network Operations and Management Symposium (NOMS), Krakow, Poland. <https://doi.org/10.1109/NOMS.2014.6838300>

- Bodnarchuk, R., & Bunt, R. (1991, May 21-24). *A synthetic workload model for a distributed system file server*. [Paper presentation]. Proceedings of the 1991 ACM SIGMETRICS Conference on Measurement and Modeling of Computer Systems, California, USA. <https://doi.org/10.1145/107971.107978>
- Calzarossa, M. C., Massari, L., & Tessera, D. (2016). Workload characterization. *ACM Computing Surveys (CSUR)*, 48(3), 1-43. <https://doi.org/10.1145/2856127>
- Cheng, Y., Chai, Z., & Anwar, A. (2018, August 27-28). *Characterizing co-located datacenter workloads: An Alibaba case study*. [Paper presentation]. Proceedings of the 9th Asia-Pacific Workshop on Systems, Jeju, Korea. <https://doi.org/10.1145/3265723.3265742>
- Delimitrou, C., & Kozyrakis, C. (2011, June 20-24). *Cross-examination of datacenter workload modeling techniques*. [Paper presentation]. International Conference on Distributed Computing Systems Workshops, Minneapolis, USA. <https://doi.org/10.1109/ICDCSW.2011.45>
- Huang, S., & Feng, W. (2009, May 18-21). *Energy-efficient cluster computing via accurate workload characterization*. [Paper presentation]. 9th IEEE/ACM International Symposium on Cluster Computing and the Grid, Shanghai, China. <https://doi.org/10.1109/CCGRID.2009.88>
- Ismaeel, S., Al-Khazraji, A., & Miri, A. (2019, April 15-17). *An efficient workload clustering framework for large-scale data centers*. [Paper presentation]. 8th International Conference on Modeling Simulation and Applied Optimization, Manama, Bahrain. <https://doi.org/10.1109/ICMSAO.2019.8880305>
- Ismaeel, S., & Miri, A. (2019, January 7-9). *Real-time energy-conserving VM-provisioning framework for cloud-data centers*. [Paper presentation]. IEEE 9th Annual Computing and Communication Workshop and Conference, Las Vegas, USA. <https://doi.org/10.1109/CCWC.2019.8666614>
- Jackson, K. R., Ramakrishnan, L., Muriki, K., Canon, S., Cholia, S., Shalf, J., Wasserman, H. J., & Wright, N. J. (2010, November 30 – December 3). *Performance analysis of high performance computing applications on the Amazon Web Services cloud*. [Paper presentation]. IEEE Second International Conference on Cloud Computing Technology and Science, Indianapolis, USA. <https://doi.org/10.1109/CLOUDCOM.2010.69>
- Mishra, A. K., Hellerstein, J. L., Cirne, W., & Das, C. R. (2010). Towards characterizing cloud backend workloads. *ACM SIGMETRICS Performance Evaluation Review*, 37(4), 34-41. <https://doi.org/10.1145/1773394.1773400>
- Moro, A., Mumolo, E., & Nolich, M. (2009, September 16-18). *Ergodic continuous hidden markov models for workload characterization*. [Paper presentation]. Proceedings of the 6th International Symposium on Image and Signal Processing and Analysis, Salzburg, Austria. <https://doi.org/10.1109/ISPA.2009.5297771>
- Onan, A. (2019). Consensus Clustering-based undersampling approach to imbalanced learning. *Scientific Programming*, 2019, 1-14. <https://doi.org/10.1155/2019/5901087>
- Onan, A., & KorukoGlu, S. (2017). A feature selection model based on genetic rank aggregation for text sentiment classification. *Journal of Information Science*, 43(1), 25-38. <https://doi.org/10.1177/0165551515613226>
- Panneerselvam, J., Liu, L., Antonopoulos, N., & Bo, Y. (2014, December 8-11). *Workload analysis for the scope of user demand prediction model evaluations in cloud environments*. [Paper presentation]. IEEE/ACM 7th International Conference on Utility and Cloud Computing, London, United Kingdom. <https://doi.org/10.1109/UCC.2014.144>

- Patel, J., Jindal, V., Yen, I. L., Bastani, F., Xu, J., & Garraghan, P. (2015, March 25-27). *Workload estimation for improving resource management decisions in the cloud*. [Paper presentation]. IEEE 12th International Symposium on Autonomous Decentralized Systems, Taichung, Taiwan. <https://doi.org/10.1109/ISADS.2015.17>
- Rasheduzzaman, M., Islam, M. A., Islam, T., Hossain, T., & Rahman, R. M. (2014, February 21-22). *Task shape classification and workload characterization of google cluster trace*. [Paper presentation]. IEEE International Advance Computing Conference, Gurgaon, India. <https://doi.org/10.1109/IADCC.2014.6779441>
- Reiss, C., Tumanov, A., Tumanov, A., Ganger G. R., & Katz, R. (2012). *Towards understanding heterogeneous clouds at scale: Google trace analysis*. ResearchGate. https://www.researchgate.net/publication/265531801_Towards_Understanding_Heterogeneous_Clouds_at_Scale_Google_Trace_Analysis
- Shekhawat, V. S., Gautam, A., & Thakrar, A. (2018, December 1-2). *Datacenter workload classification and characterization: An empirical approach*. [Paper presentation]. IEEE 13th International Conference on Industrial and Information Systems, Rupnagar, India. <https://doi.org/10.1109/ICIINFS.2018.8721402>
- Shen, S., van Beek, V., & Iosup, A. (2015, May 4-7). *Statistical characterization of business-critical workloads hosted in cloud datacenters*. [Paper presentation]. IEEE/ACM 15th International Symposium on Cluster, Cloud, and Grid Computing, Shenzhen, China. <https://doi.org/10.1109/CCGRID.2015.60>
- Wang, K., Lin, M., Ciucu, F., Wierman, A., & Lin, C. (2015). Characterizing the impact of the workload on the value of dynamic resizing in data centers. *Performance Evaluation*, 85-86, 1-18. <https://doi.org/10.1016/J.PEVA.2014.12.001>
- Yin, J., Lu, X., Zhao, X., Chen, H., & Liu, X. (2015). BURSE: A bursty and self-similar workload generator for cloud computing. *IEEE Transactions on Parallel and Distributed Systems*, 26(3), 668-680. <https://doi.org/10.1109/TPDS.2014.2315204>
- Zhang, H., Jiang, G., Yoshihira, K., & Chen, H. (2014). Proactive workload management in hybrid cloud computing. *IEEE Transactions on Network and Service Management*, 11(1), 90-100. <https://doi.org/10.1109/TNSM.2013.122313.130448>
- Zhang, Q., Hellerstein, J., & Boutaba, R. (2011) *Characterizing task usage shapes in Google compute clusters*. Google Research. <https://research.google/pubs/pub37201/>



Reactivity Enhancement of Lignin Extracted from Preconditioning Refiner Chemical-Recycle Bleached Mechanized Pulp (PRC-RBMP) Black Liquor by Phenolation

Lim Kah Yen^{1,2}, Tengku Arisyah Tengku Yasim-Anuar¹, Farhana Aziz Ujang¹, Hazwani Husin¹, Hidayah Ariffin^{3,4}, Paridah Md Tahir^{4,5}, Li Xin Ping⁶ and Mohd Termizi Yusof^{2*}

¹Research and Development Department, Nextgreen Pulp & Paper Sdn Bhd, Taman Tun Dr. Ismail, 60000 Kuala Lumpur, Malaysia

²Department of Microbiology, Faculty of Biotechnology and Biomolecular Sciences, Universiti Putra Malaysia, 43400 UPM, Serdang, Selangor, Malaysia

³Department of Bioprocess Technology, Faculty of Biotechnology and Biomolecular Sciences, Universiti Putra Malaysia, 43400 UPM, Serdang, Selangor, Malaysia

⁴Institute of Tropical Forestry and Forest Products, Universiti Putra Malaysia, 43400 UPM, Serdang, Selangor, Malaysia

⁵Department Forest Production, Faculty of Forestry, Universiti Putra Malaysia, 43400 UPM, Serdang, Selangor, Malaysia

⁶College of Bioresources Chemical and Materials Engineering, Shaanxi University of Science and Technology, Wei Yang District, 710021 Xi'an, Shaanxi Province, China

ABSTRACT

Despite black liquor's (BL) renown as a difficult-to-manage contaminant in the pulp and paper industry, BL has been found as a viable alternative material for adhesive formulation due to its high lignin content. Nevertheless, modification is required to enhance lignin's reactivity, and there is currently a lack of study focusing on this aspect for BL-lignin. This study aims to increase the phenolic hydroxyl content of BL-lignin by phenolation.

After being phenolated at lignin to phenol ratio of 1:1, at a temperature of 100°C for 110 minutes, and with the addition of 8% sulfuric acid (H₂SO₄) as a catalyst, the phenolic hydroxyl content improved by 51.5%. The results of Fourier transform infrared spectroscopy (FTIR), UV/Vis spectrophotometry, proton nuclear magnetic resonance (¹H-NMR), thermogravimetry-differential scanning calorimetry (TG-DSC), and its differential curve showed that the structural change in phenolated lignin

ARTICLE INFO

Article history:

Received: 23 August 2022

Accepted: 14 November 2022

Published: 27 July 2023

DOI: <https://doi.org/10.47836/pjst.31.5.28>

E-mail addresses:

kellylim@nextgreenglobal.com (Lim Kah Yen)

tengkuarisyah@nextgreenpnp.com (Tengku Arisyah Tengku Yasim-Anuar)

farhana.azizujang@nextgreenpnp.com (Farhana Aziz Ujang)

hazwani.husin@nextgreen.pnp.com (Hazwani Husin)

hidayah@upm.edu.my (Hidayah Ariffin)

paridah@upm.edu.my (Paridah Md Tahir)

lixp@sust.edu.cn (Li Xin Ping)

mohdtermizi@upm.edu.my (Mohd Termizi Yusof)

* Corresponding author

opened up more active sites, implying that this lignin could be a good substitute for phenol in phenol-formaldehyde resin manufacturing.

Keywords: Adhesive, black liquor, lignin, modification, phenolation, phenol-formaldehyde resin, pulp and paper, sustainability

INTRODUCTION

Other than solely focusing on pulp and paper products, many pulp and paper companies are driven to diversify their products to contribute to sustainability. With modern technology, most pulp and paper mills could improve the utilization of available renewable resources, such as black liquor (BL). Conventionally, BL was discharged to waterways as a disposal method or directed to a recovery boiler to recover chemicals and generate bioenergy (Lora & Glasser, 2002). Nevertheless, lignin, the major constituent of BL, can be utilized for various bioproducts development due to its variable functional groups (Ibrahim et al., 2011). Numerous researchers agreed that the abundant industrial lignin produced from pulp and paper mills could be an alternative material to replace some petrochemical feedstocks in the future (Kazzaz et al., 2019; Luo et al., 2020; Podschun, Saake, et al., 2015; Yang & Fang, 2014).

Nonetheless, studies have found that the pulping or processing conditions used to make paper, primarily sulfite, and kraft, can cause the lignin fraction in BL to have large impurities, limiting its use (Sammons et al., 2013). There are numerous different types of pulping and extraction procedures, and each one produces lignin with different purity and chemical properties depending on the feedstock. The structural variations in lignin caused by processing conditions are obstacles that must be overcome for lignin to be employed in a wide range of applications (Hidayati et al., 2020). Depending on the feedstock and pretreatment employed in the pulping process, a variety of lignin preparations with varied chemical structures and physical properties can be created and used in new applications, such as in the phenol-formaldehyde formulation, which was often used for wood adhesive, owing to its high phenolic content (Hussin et al., 2019; Ibrahim et al., 2013).

Nevertheless, lignin has complex and random cross-linked structures, and it is made up of three units of a phenolic core or also known as monolignols, which are p-hydroxyphenyl (H), guaiacyl (G), and syringyl (S) (Hussin et al., 2019). The existence of these monolignols in the structure of lignin enables it to undergo many modifications. However, due to lignin structural complexity and poor chemical reactivity, there are broad chemical differences depending on the source, processability, and depolymerization reaction, which remains a challenge (Gan & Pan, 2019; Chung & Washburn, 2012). Numerous researches have been carried out to enhance lignin reactivity, and one of them is through chemical modification to overcome this challenge (Hu et al., 2011; Kazzaz et al., 2019; Mansouri & Salvadó, 2006; Wang et al., 2017; Zhang et al., 2019).

Lignin modification through phenolation is one of the effective modification methods that can reduce the relative molecular mass and methoxy content of lignin and increase the phenolic hydroxyl group on the lignin structural unit with the application of catalyst and heating (Podschun, Saake, et al., 2015; Taleb et al., 2020; Thébault et al., 2020). The reaction process is simple, and the number of lignin active points can be increased to an extent that gives a positive performance (Hu et al., 2011; Yang et al., 2014). In terms of the positive performance of reactivity, Ghaffar and Fan (2013) discovered that the phenolic hydroxyl group is significantly affecting the physical and chemical properties of lignin, which is influenced by the modification process of lignin that plays a significant role in the lignin-formaldehyde reaction for adhesive production.

It was also supported by Laurichesse & Avérous (2014), who discovered that through phenolation, the resulting material could react rapidly with formaldehyde due to phenolation with free ortho and para units. Besides that, to support the results of modification, brominable substance content is also an auxiliary factor that could reflect the effectiveness of phenolation and reactivity of lignin (Jin et al., 2010; Qiao et al., 2016). According to China National Standard GB/T 14074, it can be determined by the percentage of the mass of phenol converted from the mass of brominable active groups to the total mass of the sample during the reaction. Phenolation reaction has triggered phenol to increase the reactive sites of lignin maximally. It explains that the lower the amount of brominable substance, which indicates the lesser the free phenol in the reaction, the higher the effectiveness of phenolation (Qiao et al., 2016).

Regarding this matter, phenolation can be considered a promising and practical method to modify lignin. Unlike primary sources of biomass such as fiber, wood logs, woodchips, bark, and sawdust, there is still a lack of reports on the phenolation of lignin extracted from a secondary source of biomass such as an empty fruit bunch-black liquor (EFB-BL). Due to the differences in the composition, structure, and functional group content of EFB-Lignin and other lignins, the reaction conditions of phenolation are also different. Verification tests are needed to set reasonable reaction conditions. Much research literature showed that it is known that the conditions affecting the phenolation effect of lignin are: the ratio of lignin/phenol, reaction temperature, reaction time, and catalyst dosage (Hu et al., 2011; Jiang et al., 2018; Yang et al., 2014; Zhang et al., 2019).

Preconditioning Refiner Chemical-Recycle Bleached Mechanized Pulp (PRC-RBMP) is a hybrid process that involves using steam for a short time, low concentration of the alkaline solution, and extrusion to produce EFB pulps. The processing eliminates oil and light contaminants, and the thermally treated fiber was further stretched and torn to the desired condition. Black liquor was collected and used in this study, henceforward referred to as EFB-BL. Unlike kraft and soda pulping, which relies on chemical treatment, the PRC-RBMP applies mechanical, thermal, and chemical treatments to disintegrate lignin,

hemicelluloses, and cellulose to enhance the pulp's quality sustainably. The process does not create any hazardous chemicals, and it is cost-, energy- and time-efficient as well as practical to be applied on an industrial scale.

This study hence attempts to modify the lignin extracted from EFB-BL, which has undergone an integrated pulping and extraction method which, are PRC-RBMP and LignoBoost, by exploring the effect of four modification parameters on the phenolic hydroxyl content and brominable substances, which are the ratio of lignin to phenol (L/P ratio), reaction temperature, reaction time, and dosage of catalyst acid. The phenolated EFB-Lignin was subjected to UV/Vis spectrometry, Fourier transforms infrared (FTIR) spectroscopy, ^1H NMR, and thermogravimetric (TG) analyses to determine its properties and its potential for partial incorporation into phenolic resins such as phenol-formaldehyde resin.

MATERIALS AND METHODS

Lignin Extraction

Lignin was extracted from the black liquor (BL) of oil palm empty fruit bunch (EFB), and the pulping residues were collected from Nextgreen Pulp & Paper Sdn. Bhd. (Pekan, Pahang, Malaysia). Chemicals: H_2SO_4 (98% v/v,) which acts as a catalyst, phenol reagent, KBrO_3 (99.99% w/v), and KBr (99% w/v) were purchased from Tianjin Damao Chemical Reagent Factory (Tianjin, China) and used as received. Black liquor (BL), which has undergone a Preconditioning Refiner Chemical-Recycle Bleached Mechanised Pulp (PRC-RBMP) treatment, a patented technology developed by Nextgreen Global Berhad (Grant no.: MY172437A, MY144559A), was then subjected to "LignoBoost" treatment to solely extract lignin (modified from Ma et al., 2007; Zhang & Lei, 2010; Zhu, 2013). Lignin was precipitated from 10 mL of EFB-BL through the acidification process, performed at pH 3, for 1 h, and at 60°C . Sulphuric acid (80 wt%) was slowly added into the sample until the desired pH was achieved, and the mixture was then left to allow lignin precipitation to occur. The sample was then vacuum-filtered prior to phenolation.

Lignin Modification by Phenolation

The optimum condition of lignin phenolation was identified by phenolate of the extracted lignin at certain conditions of lignin/phenol (L/P) ratio, reaction temperature, reaction time, and catalyst dosage (H_2SO_4), as shown in Table 1. These four evaluation factors were selected based on a few studies which affect the phenolation (Hidayati et al., 2020; Jiang et al., 2018; Podschun, Saake et al., 2015). Each range of the independent variables was selected based on a few studies which gave positive outcomes (Podschun, Stucker et al., 2015; Thébault et al., 2020; Yang et al., 2014). Approximately 2 g of lignin, a prescribed amount of phenol, and 98% concentrated H_2SO_4 were mixed in a flask equipped

with a condenser and a mechanical stirrer. The mixture was then heated to a set reaction temperature and time in a temperature-controlled water bath. The effect of variables' conditions on the content of brominable substances and phenolic hydroxyl group were then determined.

Table 1

Prescribed composition of L/P ratio, reaction temperature, reaction time, and catalyst dosage for phenolation

Experiment	A	B	C	D
Evaluation factor	L/P ratio	Reaction temperature	Reaction time	Catalyst dosage
L/P ratio	1:2, 1:1.5, 1:1, 1.5:1, 2:1	1:2	1:2	1:2
Reaction temperature (°C)	100	80, 90, 100, 110, 120	100	100
Reaction time (min)	90	90	30, 50, 70, 90, 110	90
Catalyst dosage (%)	4	4	4	2, 4, 6, 8, 10

Determination of Phenolated Hydroxyl Content of Lignin Sample

The phenolic hydroxyl content of lignin was determined, referring to a method by Lai et al. (2007). Approximately 10 mL of dried lignin was dissolved in 100 mL distilled water. The solution was stirred, and NaOH was slowly dropped until the dried lignin was completely dissolved. Approximately 1 mL of dissolved lignin was transferred to a 50 mL volumetric flask. Then, 3 mL Folinol reagent and 30 mL distilled water were added into the dissolved lignin, followed by 10 mL of 20% Na₂CO₃ after 5–8 min. Distilled water was added until it reached 50 mL. The mixture was stirred for 2 h at room temperature prior to UV/Vis spectrometry analysis. The absorbance at 760 nm was measured with a sample having a phenol concentration of 0 as a blank. The measured absorbance was compared with the concentration-absorbance value standard curve to obtain the content of phenolic hydroxyl groups in the lignin sample.

Determination of Content of Brominable Substance of Lignin Sample

The content of the brominable substance was determined according to China National Standard GB/T 14074/2017. A solution was prepared by mixing 2.8 g potassium bromate with 10 g potassium bromide and 1000 ml distilled water. Separately, 0.5 g of lignin was diluted with 500 mL distilled water, then 50 mL of this diluted lignin was added with 25 mL potassium bromate-potassium bromide solution and 5mL hydrochloric acid (analytical reagent). The solution was then quickly stirred until it was homogeneously mixed and placed in the dark for 15 min. After 15 min, 1.8 g potassium iodide was added to the solution and kept in the dark for another 5 min.

Titration was then conducted using 0.1 mol/L $\text{Na}_2\text{S}_2\text{O}_3$ solution as a standard. It was slowly added until the color of the solution turns to pale yellow. Titration was continued by adding 3 mL starch indication until the blue color disappeared. A blank test was performed by substituting samples with 50 mL of distilled water. The calculation to determine the brominable substance content is as in Equation 1:

$$B = \frac{(V1 - V2) \times C \times 0.01568 \times 500}{(m \times 50) \times 100\%} \quad (1)$$

Where,

$V1$: the volume of the $\text{Na}_2\text{S}_2\text{O}_3$ standard solution consumed by the blank test, in units of mL;

$V2$: the volume of the $\text{Na}_2\text{S}_2\text{O}_3$ standard solution consumed by the titration sample, in units of mL;

C : $\text{Na}_2\text{S}_2\text{O}_3$ standard solution concentration, the unit is mL;

0.01568 - the concentration of C ($\text{Na}_2\text{S}_2\text{O}_3$) = 0.167 mol / L sodium thiosulfate standard solution corresponding to the molar mass of phenol, the unit is g / mmol;

m : The mass of the sample, the unit, is g.

UV/Vis Spectrometry Analysis

UV/Vis spectrophotometry (Lambda 25 UV/VIS, Perkin Elmer, Waltham USA) was used to determine the lignin content on the phenolated EFB-Lignin. Absorbance within a 200 to 400 nm spectral range was measured at 1 nm spectral resolution at a scan speed of 250 nm/min. The non-phenolated EFB-Lignin was used to reference the phenolated EFB-Lignin (Skulcova et al., 2017).

Fourier-Transform Infrared Spectroscopy

The functional group of both phenolated and non-phenolated EFB-Lignin was analyzed by Fourier-transform infrared spectroscopy (FTIR) using KBr pellets containing 1% finely ground samples. Each spectrum was recorded at a range of 500 – 4000 cm^{-1} using an infrared spectrometer (Vertex70, Bruker, Massachusetts, USA) (Y. Zhang et al., 2020).

^1H NMR Analysis

The chemical structure of phenolated and non-phenolated EFB-Lignin was determined by ^1H NMR spectroscopy (German Bruker 400MHz nuclear magnetic resonance (NMR) spectrometer, specification model: ADVANCEIII 400MHz.) About 1 mg of samples were dissolved in 0.5 mL of deuterated chloroform (CDCl_3). The NMR spectrum was recorded at 400 MHz, at a probe temperature of 25°C, and chemical shifts are given in ppm.

Thermogravimetric Analysis

Thermal stability of phenolated and non-phenolated EFB-Lignin was determined by subjecting approximately 10 mg of samples to the thermogravimetry-differential scanning calorimetry (TG-DSC) thermal analyzer (STA449F3-1053-M, Netzsch, Selb Germany). The samples were heated from 30 to 800°C at 10°C min⁻¹ under constant nitrogen (H. Zhang et al., 2020).

Statistical Analysis

The brominable substances and phenolic hydroxyl content of different tested conditions were statistically analyzed using a one-way analysis of variance (ANOVA) in a general linear model using Statistical Analysis Software (SAS) Ver. 9.5. The mean for each measured parameter was separated statistically using Duncan Multiple Range Test (DMRT) at $p < 0.05$.

RESULTS AND DISCUSSION

Effects of Lignin/Phenol Ratio on the Content of Phenolic Hydroxyl and Brominable Substance

The effectiveness of phenolation was measured by determining the phenolic hydroxyl content and brominable substances of the phenolated EFB-Lignin. In order to determine the optimum L/P ratio that can produce the highest content of phenolic hydroxyl, several variables were set constantly, which were reaction temperature (100°C), reaction time (90 min), and catalyst dosage (4%). The objectives are to achieve maximum phenol incorporation and lignin fragmentation with the optimum L/P ratio (Podschn, Saake et al., 2015). It can be observed from Figure 1 that there is a significant difference in phenolic hydroxyl content produced from different L/P ratios. Nevertheless, among all L/P ratios, the L/P = 1:1 yielded the highest phenolic hydroxyl content at 8.12 mol.g⁻¹.

It shows that an equal ratio of phenol to lignin allows better phenolation than those with a higher ratio of phenol to lignin, allowing maximum production of phenolic hydroxyl content. It was also proven by Gan & Pan (2019), where the yield of phenolic hydroxyl content decreased significantly with the increase of phenol to lignin ratio. The same author also reported that applying a low mass ratio of L/P (1:1) has reduced the molecular weight from 14,400 to 6,000 g/mol, which indicates that lignin has been depolymerized during phenolation. Despite a similar L-to-P ratio, it revealed enough acid to hydrolyze and phenolate the lignin (Jiang et al., 2018).

Besides the content of phenolic hydroxyl, an efficient phenolation process is also reflected by the content of brominable substances. Qiao et al. (2016) agreed that the lesser the content of brominable substances in a sample, the more complete the phenolation

process, as it contains a lesser amount of free phenol in the reaction. This study shows that an L/P ratio 1:1 can produce a relatively low amount of brominable substances compared to the second high L/P ratio (indicated L/P ratio of 2:1 in Figure 1). It could also support the idea that using more lignin in the L/P ratio to produce high phenolic hydroxyl content was unnecessary since it could obstruct phenolation and alter other parameters as lignin may polymerize. In this study, a higher phenol (1:2) in the L:P ratio does not result in a higher phenolic hydroxyl content, as excessive phenol may accelerate lignin re-polymerization (Gan & Pan, 2019).

In comparison to other studies stated in Table 2, which used a higher phenol-to-lignin ratio to produce high phenolic hydroxyl content, this study discovered that a 1:1 L/P ratio is sufficient, as it produces the maximum phenolic hydroxyl content when compared to other L/P ratio compositions. It was also revealed that at similar L/P ratios, different feedstocks and pulping procedures yielded varied phenolic hydroxyl content yields. It is supported by Sammons et al. (2013) theory that the phenolation process was influenced directly by the feedstock and pulping process.

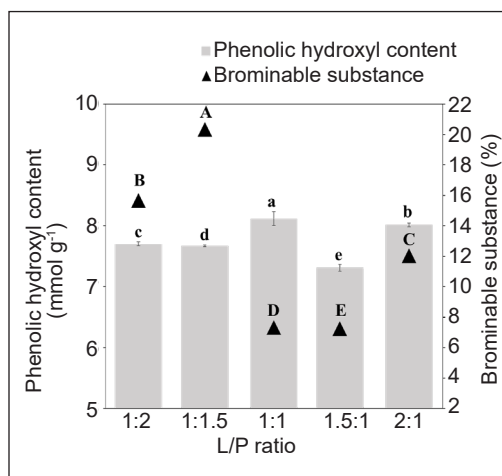


Figure 1. The effect of the L/P ratio on the content of phenolic hydroxyl and brominable substances. All data are means of 3 replicates \pm SD. Capital letters indicate a significant difference ($p < 0.05$) of brominable substance, while small letters indicate a significant difference ($p < 0.05$) in phenolic hydroxyl content among different L/P ratio samples

Effects of Reaction Temperature on the Content of Phenolic Hydroxyl and Brominable Substance

Further analysis was then carried out to determine the effect of phenolation temperature on the phenolic hydroxyl content, with 3 different temperatures ranging from 80 to 120°C. This study's constant variables were the L/P ratio, set at 1:2, the reaction time at 90 minutes, and the catalyst dosage at 4%. Figure 2 shows that the phenolic hydroxyl content increased by increasing the reaction temperature from 80 to 100°C by 14.7%. It indicates that the phenolation reaction progresses completely at 100°C after gradually increasing the phenolic hydroxyl content. Jiang et al. (2018) found a similar pattern of results, concluding that increasing the reaction temperature can produce more phenolic hydroxyl content. Alonso et al. (2005) also discovered that phenol conversion is greater at high temperatures. Meanwhile, a rapid drop in phenolic hydroxyl content at 120°C may be attributed to re-condensation, which occurs when the phenolation temperature exceeds 100°C, lowering the phenolic hydroxyl content. According to Podschun, Saake et al. (2015), and Jiang et

al. (2018), such conditions could be due to extreme degradation caused by the reaction conditions, or they could be related to the solubility of lignin in phenol.

As the reaction temperature rises, so does the amount of brominable substance. The amount of brominable substances increased dramatically from 2.62 % (at 80°C) to 11.52 % (at 90°C), reaching a maximum increment at 100°C. It indicates that increasing the temperature impacts the concentration of brominable substances. Nonetheless, when the temperature increased to 120°C, a drop in brominable substances was observed. Although the phenolation reaction increases as the temperature rises, the release of free phenol also increases, weakening the overall reaction effect. It is also supported by Qiao

et al. (2016). Theoretically, the amount of derived brominable substance indicates the free phenol in the reaction, reflecting the phenolation process's efficiency. Phenolation is assumed to occur efficiently if the amount of brominable substance is low, as the reaction reduces free phenols from the sample. A similar graph pattern can also be observed on the phenolic hydroxyl content, as when the temperature is set to 100°C, the phenolic hydroxyl content reaches its maximum. For this study, a reaction temperature of 100°C was chosen for phenolation by considering a thorough reaction, experimental goal, energy consumption, and applicability on a commercial scale.

Effects of Reaction Time on the Content of Phenolic Hydroxyl and Brominable Substance

The reaction time, in addition to the L/P ratio and reaction temperature, may impact the phenolic hydroxyl content. As a result, the samples were subjected to 5 different reaction times ranging from 30 to 110 minutes at 100°C, with a constant L/P ratio of 1:2 and a catalyst dosage of 4 %. When the reaction time was increased from 30 to 110 min, the phenolic hydroxyl content increased (Figure 3). It could be due to the irreversible polymerization of degraded lignin during long-term high-temperature reactions. It then explains that sufficient reaction time was necessary for the desired depolymerization to enhance the phenolation process. However, re-polymerization of lignin may occur if the reaction is extended, supported by Gan and Pan (2019). Compared to the L/P ratio, reaction temperature, and

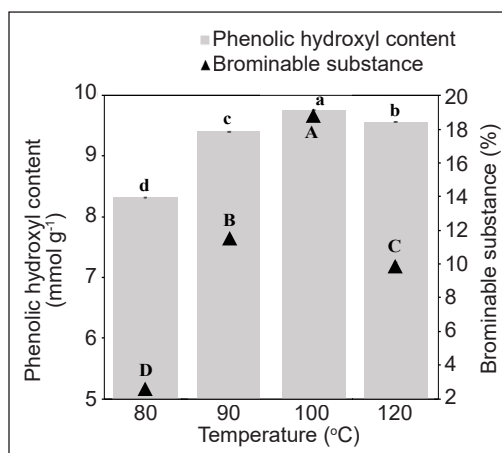


Figure 2. The effect of reaction temperature on the content of phenolic hydroxyl and brominable substances. All data are means of 3 replicates \pm SD. Capital letters indicate a significant difference ($p < 0.05$) in brominable substance, while small letters indicate a significant difference ($p < 0.05$) in phenolic hydroxyl content among different temperature samples

acid concentration, Podschun, Saake, et al. (2015) also found that reaction duration has little effect on the degree of phenolation. Meanwhile, the content of brominable substances fluctuated throughout short and long durations, eventually reaching a minimum after 110 min of treatment. As a result, 110 min is the best duration for a complete phenolation reaction when both phenolic hydroxyl contents and brominable substances are considered.

Effects of Catalyst Dosage on the Content of Phenolic Hydroxyl and Brominable Substance

In this study, a catalyst (H_2SO_4) was also added to speed up the phenolation reaction to the samples. In order to determine the optimum dosage of catalyst needed to produce a high amount of phenolic hydroxyl content, a different dosage of catalyst in a range of 2%–10% was added. The L/P ratio, reaction temperature, and reaction time were fixed at 1:2 = L/P, 100°C, and 90 min. Meanwhile, several catalyst dosages were tested, which were 2%, 4%, 6%, 8%, and 10%. The analysis was conducted at 100°C for 90 min and at a constant L/P ratio=1:2. Figure 4 shows an increase in phenolic hydroxyl content by increasing the catalyst dosage from 2% to 8%. The phenolic hydroxyl dosage notably achieved a maximum increment after 8% catalyst was added into the sample, which was 8.7 mmol g⁻¹. It shows that a high catalyst dosage may help complete the phenolation reaction and indirectly influence the production of phenolic hydroxyl.

A similar result was also reported by Zhang et al. (2019), where a significant increment of phenolic hydroxyl content was seen in samples added with a high percentage of H_2SO_4 which acts as a catalyst. It shows that a high percentage of catalysts may facilitate the phenol incorporation, lignin fragmentation, and hydrolysis of the polysaccharides. The author also agreed that the catalyst (H_2SO_4) might be diluted when more phenol is added, as phenol can act as a reactant and solvent. Meanwhile, the H_2SO_4 charge was based on the weight of lignin alone. However, a reduction in phenolic hydroxyl content was observed after adding 10% catalyst. It was due to the re-condensation of phenolated lignin, which affected the reaction's production of phenolic hydroxyl and free phenol. It is also possible that over a period at a specified temperature, this EFB-Lignin is still not phenolated in acid conditions. This factor may also explain the pattern of reaction temperature results

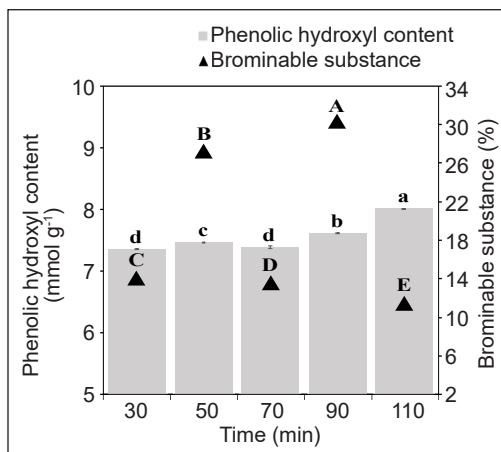


Figure 3. The effect of reaction time on the content of phenolic hydroxyl and brominable substances. All data are means of 3 replicates \pm SD. Capital letters indicate a significant difference ($p < 0.05$) of brominable substance, while small letters indicate a significant difference ($p < 0.05$) in phenolic hydroxyl content among different time samples

(Figure 2). It is speculated that concentrated sulfuric acid might not be the most suitable acid catalyst for EFB-Lignin from PRC-RBMP pulping. However, this study also proves the ability of H_2SO_4 to catalyze the phenolation reaction at a moderate temperature, as reported by other studies as tabulated in Table 2.

Meanwhile, results also revealed that the content of brominable substances reduced tremendously after 6%–10% catalysts were added, with a minimum amount (11.52%) recorded when 8% catalyst was added. Similar to other variables, the catalyst dosage also created a direct relationship between brominable substances and the amount of phenolic hydroxyl. In this study, adding an 8% catalyst was the most effective in producing the highest phenolic hydroxyl contents and the lowest amount of brominable substances. The dosage of the catalyst was in a similar range to other studies. Podschun, Saake et al. (2015) discovered that phenolic hydroxyl content was noticeably increased in samples with a 6.7%–7.5% catalyst. Similarly, Jiang et al. (2018) also reported that samples containing 4%–8% catalysts produced higher phenolic hydroxyl content compared to samples with the addition of 10%–15% catalyst.

Hence, considering the experimental objectives, energy-saving, cost-effectiveness as well as practicability to be applied on a commercial scale, the overall findings discovered that the optimum phenolation greatly occurred at a condition of L/P ratio = 1:1 at a temperature of 100°C for 100 min, and with the addition of 8% catalyst. In addition, the phenolic hydroxyl content of phenolated EFB-Lignin was improved by 51.5% after phenolation, which is 7.896 mmol g⁻¹.

Table 2 compares the phenolic hydroxyl content and the best phenolation conditions for various raw materials. Despite using a secondary biomass source in the form of EFB-BL, this study was able to yield the highest phenolic hydroxyl content when compared to other types of biomasses, including those primary sources of biomass such as poplar wood, corn cob, bamboo, wheat straw, and many more. It could be owing to PRC-RBMP and LignoBoost's efficient integrated process during pulping and lignin extraction. It demonstrates that EFB-BL has a similar and comparable potential to be used as the primary feedstock for lignin extraction and, ultimately, adhesive production.

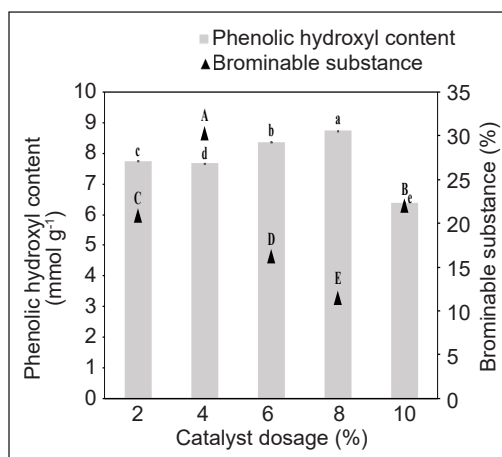


Figure 4. The effect of catalyst dosage on the content of phenolic hydroxyl and brominable substances. All data are means of 3 replicates \pm SD. Capital letters indicate a significant difference ($p < 0.05$) in brominable substance, while small letters indicate a significant difference ($p < 0.05$) in phenolic hydroxyl content among different catalyst dosage samples

Table 2
Comparison of phenolation conditions between different raw materials

Raw Materials	Lignin extraction	Phenolation (Acid/Alkali)	The ratio of lignin to phenol	Temperature (°C)	Time (minute)	Catalyst	Catalyst concentration (%)	Phenolic hydroxyl content (mmol g ⁻¹)	Reference
Lignin									
EFB Lignin from black liquor	PRC-RBMP and LignoBoost	Acid	1:1	100	110	H ₂ SO ₄	8	7.9	This Study
Pine kraft lignin	LignoBoost	Acid	3:5	90	120	H ₂ SO ₄	5	4.47	Jiang et al., (2018)
Spruce industrial kraft lignin	-	Acid	1:10	25	60	H ₂ SO ₄	40	5.81	Zhang et al., (2021)
Alkali Lignin	-	Acid	1:4	110	120	H ₂ SO ₄	5	5.66	Zhen et al., (2021)
Kraft lignin	-	Alkali	1:3	160	120	NaOH	50	4.52	Gan & Pan, (2019)
Sugarcane bagasse kraft lignin	Precipitated	Alkali	1:4	110	150	NaOH	30	6.63	Luo et al., (2020)
Black Liquor									
Kraft black liquor	Precipitated (acidifying)	Alkali	1:1	80	240	NaOH	10	-	Abdelwahab & Nassar (2011)
Kraft black liquor	-	Alkali	1:1	95	60	NaOH	30	2.20	Yang et al., (2014)
Fibers									
Air-dried wood	Ethanol-benzene	Acid	-	100	60	H ₂ SO ₄	3	1.5	Funaoka et al., (1995)
Beech wood	Ethanol water pulping	Acid	1:2	110	20	H ₂ SO ₄	19.8	4.1	Podschun, Stucker et al. (2015)
Poplar wood	Hydrothermal	Alkali	1:1	95	60	NaOH	30	2.23	Yang et al., (2014)
Poplar wood	Ethanol water pulping	Acid	1:2	110	20	H ₂ SO ₄	19.8	3.5	Podschun, Stucker et al. (2015)

Table 2 (continue)

Raw Materials	Lignin extraction	Phenolation (Acid/Alkali)	The ratio of Lignin to phenol	Temperature (°C)	Time (minute)	Catalyst	Catalyst concentration (%)	Phenolic hydroxyl content (mmol g ⁻¹)	Reference
Pinewood	Ethanol water pulping	Acid	1:2	110	20	H ₂ SO ₄	19.8	2	Podschun, Stuecker et al., (2015)
Beechwood chips	Ethanol water pulping	Acid	1-2:0.3-2	110	20	H ₂ SO ₄	6.7	6.2	Podschun, Saake et al., (2015)
Corn cob	Hydrothermal and chemical	Alkali	1:1	95	60	NaOH	30	3.14	Yang et al., (2014)
Bamboo	Precipitated (acidifying)	Alkali	1:1	90	60	NaOH	30	2.15	Pang et al., (2017)
Bamboo	Organosolv pulping a process with acetic acid	Alkali	1:1	90	60	NaOH	30	1.75	Pang et al., (2017)
Wheat straw	Ethanol water pulping	Acid	1:2	110	20	H ₂ SO ₄	19.8	1.9	Podschun, Stuecker et al., (2015)
Wheat straw	Autohydrolysis followed by mechanical refining and enzymatic hydrolysis	Acid	1:3	120	120	H ₂ SO ₄	10	2.67	Zhang et al (2019)
Wheat straw	Hydrothermal and chemical	Alkali	1:1	95	60	NaOH	30	3.17	Yang et al (2014)
EFB	Hydrothermal and chemical	Acid	1:3	130	60	H ₂ SO ₄	5	6.5	Ahmadzadeh et al., (2009)

Unlike most of the other studies listed in Table 2 that rely on the catalyst with an average of 22%, this study only uses 8% H₂SO₄ to speed up the phenolation reaction and at a low L/P ratio (1:1). It demonstrates that a higher phenolic hydroxyl content can be produced by adjusting low catalyst dosage with L/P ratio, temperature, and phenolation time. It is beneficial as the usage of phenol and catalyst can be minimized. It can also be assumed that phenolation occurs effectively under mild phenolation conditions for lignin extracted from EFB-BL, compared to those extracted lignins from a primary source of biomass. The low L/P ratio, reaction temperature, reaction time, and catalyst quantity used in this modification are all examples of mild phenolation conditions.

Properties of Phenolated and Non-Phenolated EFB-Lignin

The properties of the optimized phenolated EFB-Lignin were compared to those of the non-phenolated EFB-Lignin. The UV/Vis analysis determines any changes in conjugated phenolics of the phenolated EFB-Lignin. Maximum absorption peaks of lignin at 250, 300, and 350 to 360 nm can be observed, as shown in Figure 5. The two absorption peaks at 250 nm and 300 nm are caused by the chromophoric shift of the benzene ring absorption band in the lignin structure, and the third absorption peak is composed of the α -carbonyl group-containing phenol structure. It was also observed that the phenolated EFB-Lignin has a stronger absorption band near 205 to 220 nm than the non-phenolated EFB-Lignin, which might be due to the ionization of the phenolic hydroxyl group during phenolation. It indicates that selective and effective phenolation at reactive sites in the side chains leads to the disappearance of conjugated systems (Funaoka et al., 1995).

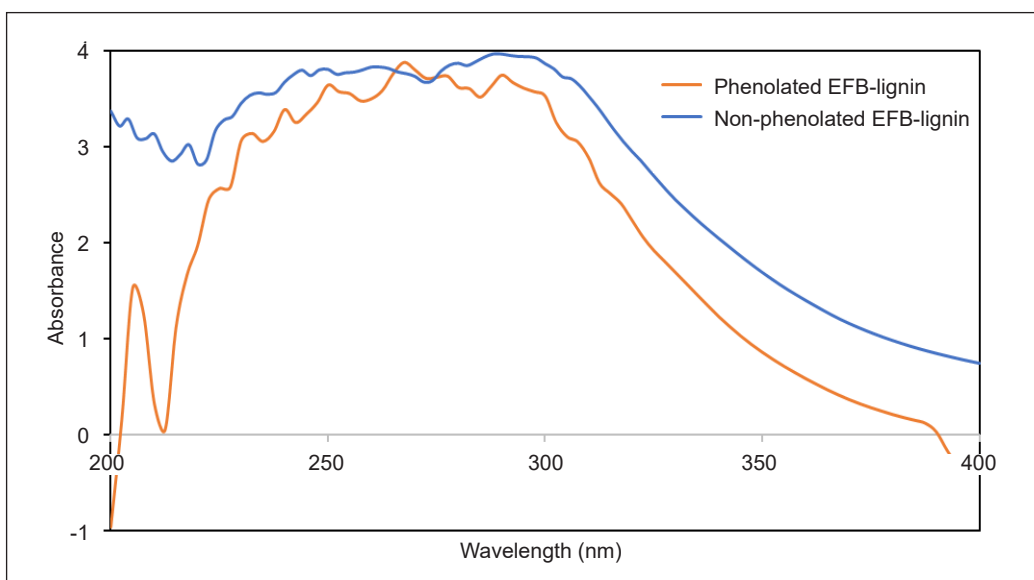


Figure 5. UV spectra of non-phenolated and phenolated EFB-lignin

Similar to the UV/Vis spectra, spectral differences in the FTIR peaks were observed between the non-phenolated and phenolated EFB-Lignins (Figure 6). The absorption peaks of the infrared spectrum of EFB-Lignin before and after phenolation are similar, and the intensity has somehow changed. A similar trend was also observed on peaks around $3000 - 3500 \text{ cm}^{-1}$, which denotes the hydroxyl group (O-H). It was observed that the non-phenolated EFB-Lignin has intense peaks at around $640-1820 \text{ cm}^{-1}$ and $2800-3800 \text{ cm}^{-1}$, and it indicates the complex crosslinking in the lignin structure (Inwood, 2014). Figure 6 shows a new band at the peak of 755 cm^{-1} for the phenolated EFB-Lignin. This band arises from the reaction between phenol in ortho or para-position and a-hydroxyl groups in the side chain of lignin (Alonso et al., 2005). It was also noticeable that peaks around $1043-1200 \text{ cm}^{-1}$ which indicate the presence of $-\text{CH}_2$ and syringyl and guaiacyl units, have disappeared after phenolation. It shows that phenolation has caused CH deformation from the CH_2 group (Inwood et al., 2018). Meanwhile, 1120 cm^{-1} is the stretching vibration peak of the methoxy group (O-C), and it can be observed here that the absorption peak of the phenolated EFB-Lignin is weakening, indicating that part of the methoxy group of the phenolated EFB-Lignin is shed due to groups cleavage (Alonso et al., 2005). It is also to note that there is an enhanced absorption peak at 1230 cm^{-1} , which belongs to the phenolic hydroxyl group on the spectrum of phenolated EFB-Lignin, and this indicates a successful phenolation for the phenolated EFB-Lignin (Inwood, 2014; Luo et al., 2020).

Meanwhile, a peak at 1394 cm^{-1} , which belongs to the C-H stretch in methyl groups, significantly reduced in the phenolated lignin. It is also mirrored by the peak of 837 cm^{-1} , which was attributed to the aromatic C-H bending (Rashid et al., 2016). The aromatic skeletal or benzene ring skeleton vibrations, which can be observed around $1400-1600 \text{ cm}^{-1}$ on the non-phenolated EFB-Lignin, were seen to be reduced after phenolation, as shown by the spectra of phenolated EFB-Lignin.

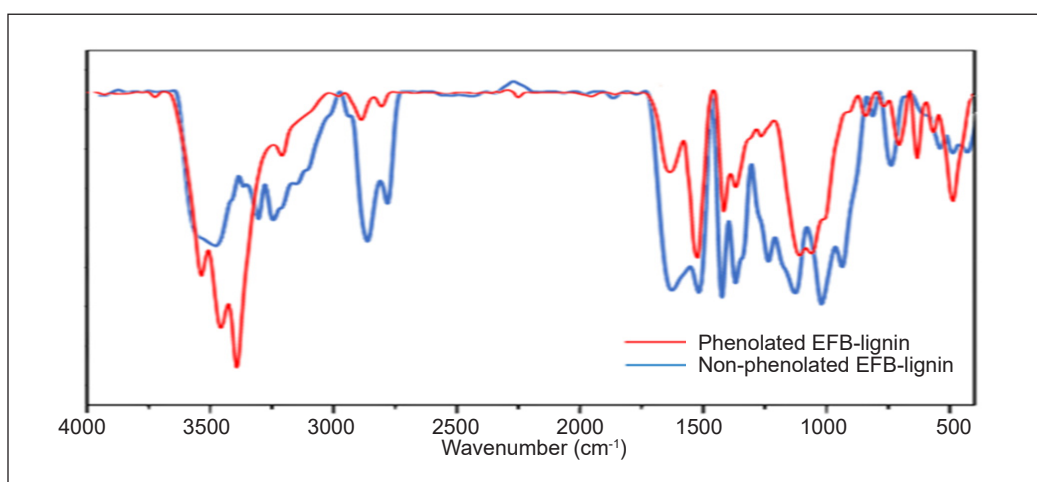


Figure 6. FTIR spectrum of non-phenolated and phenolated EFB-lignin

The $^1\text{H-NMR}$ spectrum was integrated to evaluate the change in the content of the compound (Gao et al., 2021). In this study, $^1\text{H NMR}$ was used to evaluate the change of the compound in lignin after phenolation. $^1\text{H NMR}$ spectrum of phenolated and non-phenolated EFB-Lignin is shown in Figure 7. For this study, tetramethylsilane (TMS) was used as an internal standard, and for further quantitative analysis, deuterated chloroform (d -chloroform) was used as an internal standard. D -chloroform is a good solvent for many resins as it produces only small proton impurity peaks compared to other deuterated solvents (Garrigues, 2019). Meanwhile, TMS was used as it is good as the internal reference standard of $^1\text{H NMR}$ (Makulski & Jackowski, 2020).

A peak at 7.29 ppm in Figure 7 refers to the internal standard of d -chloroform (Pretsch et al., 2020). Compared to the non-phenolated EFB-Lignin, the phenolated EFB-Lignin shows an intense peak from 6.84 to 7.26 ppm. This range of points represents the aromatic

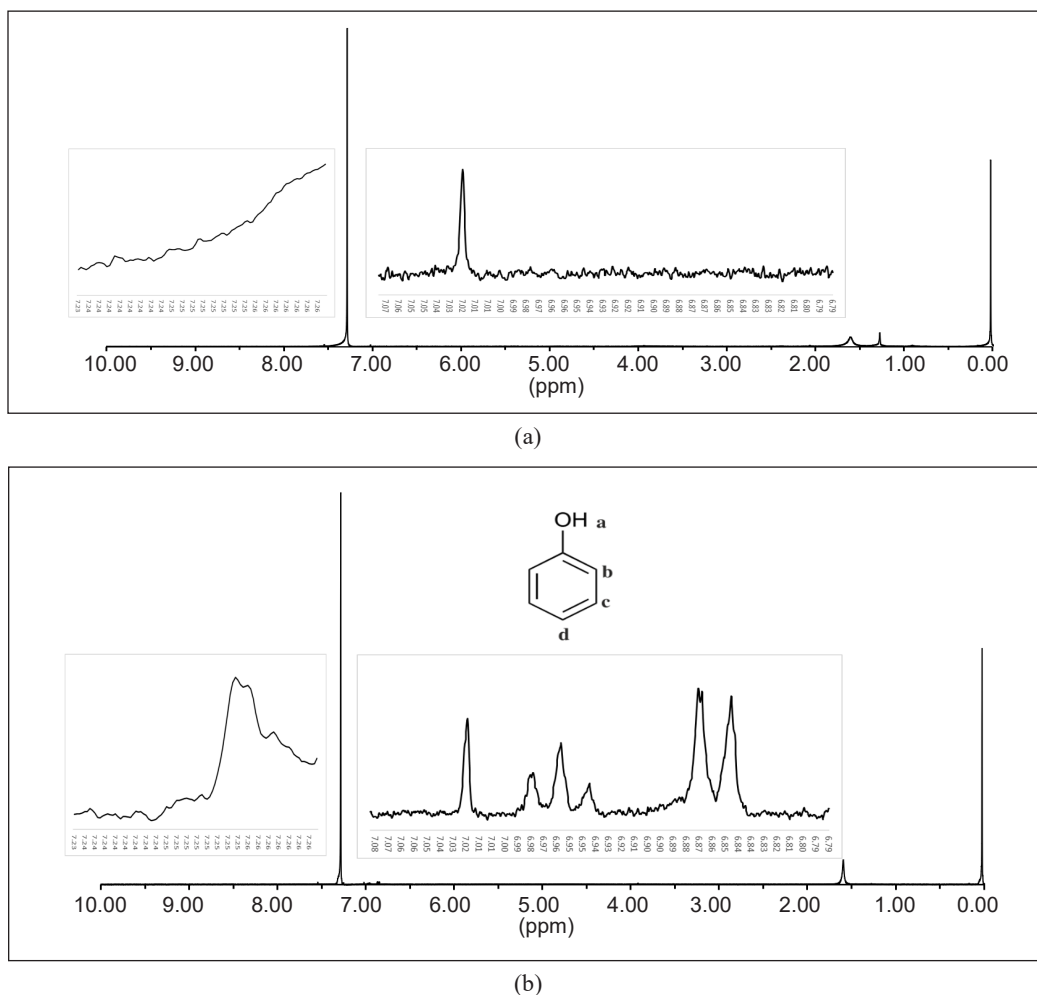


Figure 7. $^1\text{H NMR}$ of non-phenolated (a) and phenolated EFB-lignin (b)

compound. According to Pretsch et al. (2020), by using d-chloroform as an internal standard, the appearance of peaks that represent an aromatic structure can be observed, and it was depicted in Figure 7(b) as peaks at 6.84–6.87 ppm, 6.94–6.98 ppm and 7.24–7.26 ppm that represent the aromatic structure of b, d, and c, were respectively observed. Meanwhile, Figure 7(a) shows no peak from 6.84 to 7.26 ppm. It shows that the aromatic structure was not there prior to phenolation.

The non-phenolated EFB-Lignin sample exhibits no peak at point 4.69 ppm. However, the phenolated EFB-Lignin sample shows an intense peak at this point. According to the literature, this point represents the OH component (a) in the aromatic structure observed in peak 6.84 to 7.26 ppm. As seen in Figure 7(b), this peak demonstrates that the phenolation of EFB-Lignin has a phenolic structure. It then proves that the phenolation of lignin was successful. According to Ibrahim et al. (2011), the phenolic compound in the phenolated EFB-Lignin is contributed by the cleaving of alkyl–aryl ether linkages during lignin modification, which led to the formation of new phenolic groups in the phenolated EFB-Lignin. It also leads to the higher existence of reactive sites, allowing the phenolated EFB-Lignin to be more reactive to combine with other materials, such as formaldehyde.

The thermal stability of non-phenolated and phenolated EFB-Lignin was evaluated based on the decomposition temperature at 5% weight loss ($T_{d5\%}$), 10% weight loss ($T_{d10\%}$), and 30% weight loss ($T_{d30\%}$) of the samples. The TG thermogram, as shown in Figure 8, indicates the weight loss percentage, while the first DTG curves indicate the corresponding rate of weight loss (Hussin et al., 2018). It can be observed from the TG graph of phenolated and non-phenolated EFB-Lignin, that the pyrolysis of lignin occurred in phases. First, as the temperature reaches 25°C–160°C, a little amount of water in the lignin begins to evaporate. The quality of lignin will deteriorate to some level at this time, but not rapidly. It primarily disintegrates glycan chains, some low molecular weight, and easily decomposable lignin groups. In the temperature range of 180°C–300°C, the C-chain of lignin begins to break, and the lignin macromolecules begin to degrade in the temperature range of 300°C–600°C (Gerassimidou et al., 2020). After phenolation, the lignin is mainly p-hydroxyphenyl lignin, as shown in the ^1H NMR, and the pyrolysis product produces a large amount of phenol, which also proves that the phenolation reaction can condense both phenol and lignin.

Nevertheless, the phenolated EFB-Lignin degraded earlier at $T_{d10\%}$, at 165°C, than the non-phenolated EFB-Lignin, which degraded at 192°C. A similar trend was also recorded for $T_{d30\%}$, as phenolated EFB-Lignin started to degrade earlier at 243°C, compared to non-phenolated EFB-Lignin, which started to degrade at 324°C. It was implied that the main lignin degradation starts at this stage. This stage of degradation implies the breakdown of weak chemical bonds in phenolated EFB-Lignin, such as hydroxyl bond, carbon bond in the alkyl side chain, and alkyl ether bond (Taleb et al., 2020). In addition, the breakage of methylene and methine bridges in the molecular chain of phenolated EFB-Lignin and

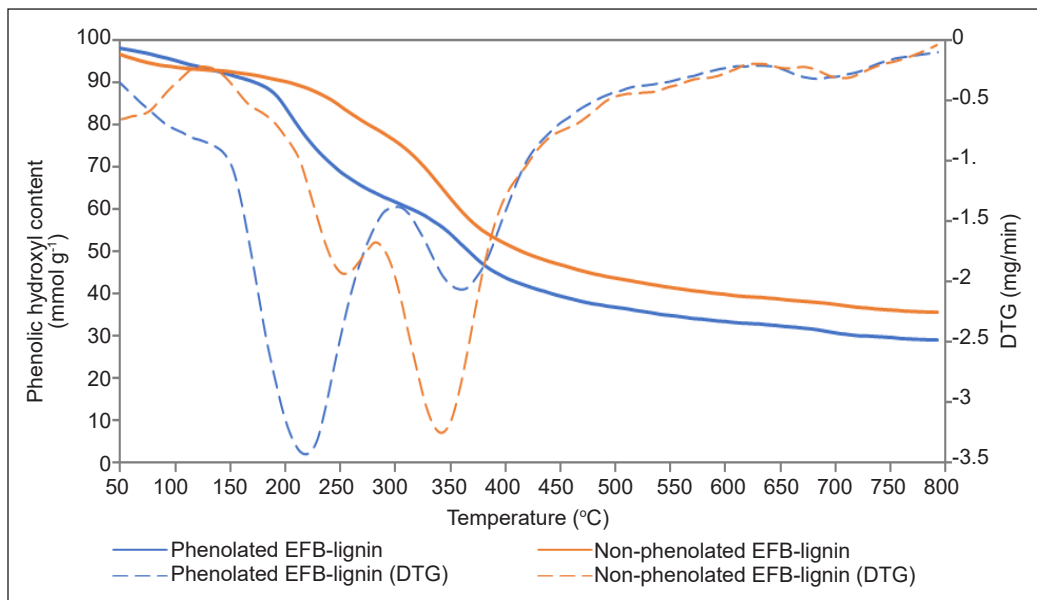


Figure 8. TG and DTG thermograms of non-phenolated and phenolated EFB-lignin

the pyrolysis of aromatic rings led to rapid degradation (H. Zhang et al., 2020). It also confirms the findings of ¹H NMR, as it indicates the presence of aromatic rings following the phenolation process.

Observation on phenolated and non-phenolated lignins also discovered a high rate of weight loss in the temperature range of 350°C to 600°C, but the trend is gradually slowing down. It is mainly due to combining lignin macromolecules with air and oxidative degradation into volatile small molecules (Gerassimidou et al., 2020). After 600°C, the inorganic matter in the lignin is decomposed. When the temperature reaches 800°C, the weight loss tends to balance, and the residual rate is higher, indicating that the ash impurity content in the EFB lignin is relatively small.

Ház et al. (2019) reported that lignin with a higher proportion of guaiacyl units has higher activation energy and thermal stability, which is reflected in this study. From the FTIR spectrum (Figure 6), peaks related to guaiacyl units have disappeared in the phenolated EFB-Lignin, which explains its low thermal stability. The lower thermal stability also may be due to the higher hydroxyl content in phenolated EFB-Lignin, which volatilizes at a relatively low temperature at 202.9°C and 366.0°C (Jiang et al., 2018). The non-phenolated lignin did not undergo additional modification. Therefore, the aromatic structure of lignin was largely retained, which attributed to the higher thermal stability. It was also supported by Wang et al. (2019), that discovered in their study that the non-phenolated EFB-Lignin has stronger chemical linkages and carbohydrates in the lignin fractions, which helps to delay the thermal degradation.

At the final stage of degradation, both phenolated and non-phenolated EFB-Lignin did not record a remarkable difference in the percentage of char residues, as phenolated EFB-Lignin had 30% char residues and non-phenolated EFB-Lignin had 34% char residues. It can be inferred that the thermal stability of EFB-Lignin was affected much by phenolation (difference <5%), which has changed its structure. Hence, a deep understanding of the changes in EFB-Lignin structure from different modification conditions can reflect its functionality in its subsequent application. The low thermal stability of phenolated EFB-Lignin might also indicate its ability to react with other ingredients to produce adhesive.

CONCLUSION

This study explored the possibility of EFB-Lignin, derived from EFB-BL subjected to the PRC-RBMP and Lignoboost processes, to be used in a resin. It was phenolated to increase its phenolic hydroxyl content, and this study found that the best conditions for extracting lignin from the EFB-BL were at a 1:1 L/P ratio, a temperature of 100°C for 110 min, and the addition of 8% H₂SO₄ as a catalyst. This phenolation provided a high phenolic hydroxyl content of 7.9 mmol g⁻¹ despite mild phenolation conditions. The parameters found in this study increased reactivity, as shown from the data of UV/vis, FTIR, ¹H NMR, and TG/DTG, indicating that more active sites in lignin are available to react with formaldehyde in a resin. Characterization of phenolated EFB-Lignin determined in this study could provide useful information for its future use in resin adhesives.

ACKNOWLEDGEMENTS

The authors want to express their special gratitude for the support from Nextgreen Pulp & Paper Sdn. Bhd., Universiti Putra Malaysia, Malaysia, and Shaanxi University of Science and Technology, China.

REFERENCES

- Abdelwahab, N. A., & Nassar, M. A. (2011). Preparation , optimisation and characterisation of lignin phenol formaldehyde resin as wood adhesive. *Pigment & Resin Technology*, 40(3), 169-174. <https://doi.org/10.1108/03699421111130432>
- Ahmadzadeh, A., Zakaria, S., & Rashid, R. (2009). Liquefaction of oil palm empty fruit bunch (EFB) into phenol and characterization of phenolated EFB resin. *Industrial Crops and Products*, 30(1), 54-58. <https://doi.org/10.1016/j.indcrop.2009.01.005>
- Alonso, M. V., Oliet, M., Rodriguez, F., Gilarranz, M. A., & Rodriguez, J. J. (2005). Modification of ammonium liginosulfonate by phenolation for use in phenolic resins. *Bioresource Technology*, 96(9), 1013-1018. <https://doi.org/10.1016/j.biortech.2004.09.009>
- Chung, H., & Washburn, N. R. (2012). Improved lignin polyurethane properties with lewis acid treatment. *American Chemical Society Applied Materials & Interfaces*, 4, 2840-2846. <https://doi.org/10.1021/am300425x>

- Funaoka, M., Matsubara, M., Seki, N., & Fukatsu, S. (1995). Conversion of native lignin to a highly phenolic functional polymer and its separation from lignocellulosics. *Biotechnology and Bioengineering*, *46*, 545-552. <https://doi.org/10.1002/bit.260460607>
- Gan, L., & Pan, X. (2019). Phenol-Enhanced Depolymerization and Activation of Kraft Lignin in Alkaline Medium. *Industrial & Engineering Chemistry Research*, *58*(19), 7794-7800. <https://doi.org/10.1021/acs.iecr.9b01147>
- Gao, C., Li, M., Zhu, C., Hu, Y., Shen, T., Li, M., Ji, X., Lyu, G., & Zhuang, W. (2021). One-pot depolymerization, demethylation and phenolation of lignin catalyzed by HBr under microwave irradiation for phenolic foam preparation. *Composites Part B: Engineering*, *205*, Article 108530. <https://doi.org/10.1016/j.compositesb.2020.108530>
- Garrigues, S. (2019). Paints | organic solvent-based. In P. Worsfold, C. Poole, A. Townshend, & M. Miró (Eds.), *Encyclopedia of Analytical Science* (3rd ed.) (pp. 110-120). Elsevier. <https://doi.org/10.1016/B978-0-12-409547-2.14227-1>
- Gerassimidou, S., Velis, C. A., Williams, P. T., & Komilis, D. (2020). Characterisation and composition identification of waste-derived fuels obtained from municipal solid waste using thermogravimetry: A review. *Waste Management and Research*, *38*(9), 942-965. <https://doi.org/10.1177/0734242X20941085>
- Ghaffar, S. H., & Fan, M. (2013). Structural analysis for lignin characteristics in biomass straw. *Biomass and Bioenergy*, *57*, 264-279. <https://doi.org/10.1016/j.biombioe.2013.07.015>
- Ház, A., Jablonský, M., Šurina, I., Kačík, F., Bubeníková, T., & Ďurkovič, J. (2019). Chemical composition and thermal behavior of kraft lignins. *Forests*, *10*(6), Article 483. <https://doi.org/10.3390/F10060483>
- Hidayati, S., Satyajaya, W., & Fudholi, A. (2020). Lignin isolation from black liquor from oil palm empty fruit bunch using acid. *Journal of Materials Research and Technology*, *9*(5), 11382-11391. <https://doi.org/10.1016/j.jmrt.2020.08.023>
- Hu, L., Pan, H., Zhou, Y., & Zhang, M. (2011). Methods to improve lignin's reactivity as a phenol substitute and as replacement for other phenolic compounds: A brief review. *BioResources*, *6*(3), 3515-3525. <https://doi.org/10.15376/biores.6.3.3515-3525>
- Hussin, M. H., Aziz, A. A., Iqbal, A., Ibrahim, M. N. M., & Latif, N. H. A. (2019). Development and characterization novel bio-adhesive for wood using kenaf core (*Hibiscus cannabinus*) lignin and glyoxal. *International Journal of Biological Macromolecules*, *122*, 713-722. <https://doi.org/10.1016/j.ijbiomac.2018.11.009>
- Hussin, M. H., Samad, N. A., Latif, N. H. A., Rozuli, N. A., Yusoff, S. B., Gambier, F., & Brosse, N. (2018). Production of oil palm (*Elaeis guineensis*) fronds lignin-derived non-toxic aldehyde for eco-friendly wood adhesive. *International Journal of Biological Macromolecules*, *113*, 1266-1272. <https://doi.org/10.1016/j.ijbiomac.2018.03.048>
- Ibrahim, M. N. M., Zakaria, N., Sipaut, C. S., Sulaiman, O., & Hashim, R. (2011). Chemical and thermal properties of lignins from oil palm biomass as a substitute for phenol in a phenol formaldehyde resin production. *Carbohydrate Polymers*, *86*(1), 112-119. <https://doi.org/10.1016/j.carbpol.2011.04.018>
- Ibrahim, V., Mamo, G., Gustafsson, P. J., & Hatti-Kaul, R. (2013). Production and properties of adhesives formulated from laccase modified Kraft lignin. *Industrial Crops and Products*, *45*, 343-348. <https://doi.org/10.1016/j.indcrop.2012.12.051>

- Inwood, J. P.W., Pakzad, L., & Fatehi, P. (2018). Production of sulfur containing kraft lignin products. *BioResources*, 13(1), 53-70. <https://doi.org/10.15376/biores.13.1.53-70>
- Inwood, J. P. W. (2014). *Sulfonation of kraft lignin to water soluble value added products* [Doctoral thesis, Lakehead University]. Lakehead University. <https://knowledgecommons.lakeheadu.ca/bitstream/2453/573/1/InwoodJ2014m-1a.pdf>
- Jiang, X., Liu, J., Du, X., Hu, Z., Chang, H.-M., & Jameel, H. (2018). Phenolation to improve lignin reactivity toward thermosets application. *ACS Sustainable Chemistry & Engineering*, 6(4), 5504-5512. <https://doi.org/10.1021/acssuschemeng.8b00369>
- Jin, Y., Cheng, X., & Zheng, Z. (2010). Preparation and characterization of phenol - formaldehyde adhesives modified with enzymatic hydrolysis lignin. *Bioresource Technology*, 101(6), 2046-2048. <https://doi.org/10.1016/j.biortech.2009.09.085>
- Kazzaz, A. E., Feizi, Z. H., & Fatehi, P. (2019). Grafting strategies for hydroxy groups of lignin for producing materials. *Green Chemistry*, 21, 5714-5752. <https://doi.org/10.1039/c9gc02598g>
- Lai, Y., Zhang, Z., Huang, G., & Chi, C. (2007). Determination of the content of phenolic hydroxyl groups in lignin and pulp with fe-method. *Transactions of China Pulp and Paper*, 22(1), 54-58. <https://doi.org/10.3321/j.issn:1000-6842.2007.01.014>
- Laurichesse, S., & Avérous, L. (2014). Chemical modification of lignins: Towards biobased polymers. *Progress in Polymer Science*, 39(7), 1266-1290. <https://doi.org/10.1016/j.progpolymsci.2013.11.004>
- Lora, J. H., & Glasser, W. G. (2002). Recent industrial applications of lignin: A sustainable alternative to nonrenewable materials. *Journal of Polymers and the Environment*, 10, 39-48. <https://doi.org/10.1023/A:1021070006895>
- Luo, B., Jia, Z., Jiang, H., Wang, S., & Min, D. (2020). Improving the reactivity of sugarcane bagasse kraft lignin by a combination of fractionation and phenolation for phenol - formaldehyde adhesive applications. *Polymer*, 12(8), Article 1825. <https://doi.org/10.3390/polym12081825>
- Ma, X., Dai, B., & Yang, X. H. (2007). Recovery of lignin from reed black liquor of paper-making by acidulation method. *Technology and Development of Chemical Industry*, 36(8), 44-46.
- Makulski, W., & Jackowski, K. (2020). ¹H, ¹³C and ²⁹Si magnetic shielding in gaseous and liquid tetramethylsilane. *Journal of Magnetic Resonance*, 313, Article 106716. <https://doi.org/10.1016/j.jmr.2020.106716>
- Mansouri, N.-E. E., & Salvadó, J. (2006). Structural characterization of technical lignins for the production of adhesives: Application to lignosulfonate, kraft, soda-anthraquinone, organosolv and ethanol process lignins. *Industrial Crops and Products*, 24(1), 8-16. <https://doi.org/10.1016/j.indcrop.2005.10.002>
- Pang, B., Yang, S., Fang, W., Yuan, T.-Q., Argyropoulos, D. S., & Sun, R.-C. (2017). Structure-property relationships for technical lignins for the production of lignin-phenol-formaldehyde resins. *Industrial Crops & Products*, 108, 316-326. <https://doi.org/10.1016/j.indcrop.2017.07.009>
- Podschun, J., Saake, B., & Lehnen, R. (2015). Reactivity enhancement of organosolv lignin by phenolation for improved bio-based thermosets. *European Polymer Journal*, 67, 1-11. <https://doi.org/10.1016/j.eurpolymj.2015.03.029>

- Podschun, J., Stucker, A., Saake, B., & Lehnen, R. (2015). Structure – Function relationships in the phenolation of lignins from different sources. *ACS Sustainable Chemistry & Engineering*, 3(10), 2526-2532. <https://doi.org/10.1021/acssuschemeng.5b00705>
- Pretsch, E., Bühlmann, P., & Badertscher, M. (2020). *Structure Determination of Organic Compounds*. Springer. <https://doi.org/10.1007/978-3-662-62439-5>
- Qiao, W., Li, S., & Xu, F. (2016). Preparation and characterization of a phenol-formaldehyde resin adhesive obtained from bio-ethanol production residue. *Polymers and Polymer Composites*, 24(2), 99-105. <https://doi.org/10.1177/096739111602400203>
- Rashid, T., Kait, C. F., & Murugesan, T. (2016). A “Fourier Transformed Infrared” compound study of lignin recovered from a formic acid process. *Procedia Engineering*, 148, 1312-1319. <https://doi.org/10.1016/j.proeng.2016.06.547>
- Sammons, R. J., Harper, D. P., Labbé, N., Bozell, J. J., Elder, T., & Rials, T. G. (2013). Characterization of organosolv lignins using thermal and FT-IR spectroscopic analysis. *BioResources*, 8(2), 2752-2767.
- Skulcova, A., Majova, V., Kohutova, M., Grosik, M., Sima, J., & Jablonsky, M. (2017). UV/Vis Spectrometry as a quantification tool for lignin solubilized in deep eutectic solvents. *BioResources*, 12(3), 6713-6722. <https://doi.org/10.15376/biores.12.3.6713-6722>
- Taleb, F., Ammar, M., Mosbah, M. B., Salem, R. B., & Moussaoui, Y. (2020). Chemical modification of lignin derived from spent coffee grounds for methylene blue adsorption. *Scientific Reports*, 10, Article 11048. <https://doi.org/10.1038/s41598-020-68047-6>
- Thébault, M., Kutuzova, L., Jury, S., Eicher, I., Zikulnig-Rusch, E. M., & Kandelbauer, A. (2020). Effect of phenolation, lignin-type and degree of substitution on the properties of lignin-modified phenol-formaldehyde impregnation resins: Molecular weight distribution, wetting behavior, rheological properties and thermal curing profiles. *Journal of Renewable Materials*, 8(6), 603-630. <https://doi.org/10.32604/jrm.2020.09616>
- Wang, M., Sjöholm, E., & Li, J. (2017). Fast and reliable quantification of lignin reactivity via reaction with dimethylamine and formaldehyde (Mannich reaction). *Holzforschung*, 71(1), 27-34. <https://doi.org/10.1515/hf-2016-0054>
- Wang, Y., Liu, W., Zhang, L., & Hou, Q. (2019). Characterization and comparison of lignin derived from corncob residues to better understand its potential applications. *International Journal of Biological Macromolecules*, 134, 20-27. <https://doi.org/10.1016/j.ijbiomac.2019.05.013>
- Yang, C. Y., & Fang, T. J. (2014). Combination of ultrasonic irradiation with ionic liquid pretreatment for enzymatic hydrolysis of rice straw. *Bioresource Technology*, 164, 198-202. <https://doi.org/10.1016/j.biortech.2014.05.004>
- Yang, S., Wen, J. L., Yuan, T. Q., & Sun, R. C. (2014). Characterization and phenolation of biorefinery technical lignins for lignin-phenol-formaldehyde resin adhesive synthesis. *RSC Advances*, 4(101), 57996-58004. <https://doi.org/10.1039/c4ra09595b>
- Zhang, F., Jiang, X., Lin, J., Zhao, G., Chang, H.-M., & Jameel, H. (2019). Reactivity improvement by phenolation of wheat straw lignin isolated from a biorefinery process. *New Journal of Chemistry*, 43, 2238-2246. <https://doi.org/10.1039/c8nj05016c>

- Zhang, H.-N., Ren, H., & Zhai, H.-M. (2021). Analysis of phenolation potential of spruce kraft lignin and construction of its molecular structure model. *Industrial Crops & Products*, *167*, Article 113506. <https://doi.org/10.1016/j.indcrop.2021.113506>
- Zhang, H., Chen, T., Li, Y., Han, Y., Sun, Y., & Sun, G. (2020). Novel lignin-containing high-performance adhesive for extreme environment. *International Journal of Biological Macromolecules*, *164*, 1832-1839. <https://doi.org/10.1016/j.ijbiomac.2020.07.307>
- Zhang, Y., Li, N., Chen, Z., Ding, C., Zheng, Q., Xu, J., & Meng, Q. (2020). Synthesis of high-water-resistance lignin-phenol resin adhesive with furfural as a crosslinking agent. *Polymers*, *12*(12), Article 2805. <https://doi.org/10.3390/polym12122805>
- Zhang, Y., & Lei, Z.-F. (2010). Study on antioxidant activity of lignin from pulping black liquor. *Journal of Fudan University (Natural Science)*, *49*(1), 60-65.
- Zhen, X., Li, H., Xu, Z., Wang, Q., Zhu, S., Wang, Z., & Yuan, Z. (2021). Facile synthesis of lignin-based epoxy resins with excellent thermal-mechanical performance. *International Journal of Biological Macromolecules*, *182*, 276-285. <https://doi.org/10.1016/j.ijbiomac.2021.03.203>
- Zhu, W. (2013). *Equilibrium of Lignin Precipitation: The Effects of pH, Temperature, Ion Strength and Wood Origins* [Licentiate Thesis]. Chalmers University of Technology, Sweden. <https://publications.lib.chalmers.se/records/fulltext/186940/186940.pdf>



***Fusarium solani* Species Complex (FSSC) in Nests of Hawksbill Turtles (*Eretmochelys imbricata*) with High Hatching Success in Melaka, Malaysia**

Khai Wei See* and Nurul Salmi Abdul Latip

School of Biological Sciences, Universiti Sains Malaysia, 11800 USM, Penang, Malaysia

ABSTRACT

Hatching failure is one of the threats to the declining sea turtle population. Sea turtle egg fusariosis, an emerging fungal disease, has been linked to lower hatching success in sea turtle nests. The disease is associated with the presence of members of the *Fusarium solani* species complex (FSSC). Samples of cloacal mucus, nest sand, eggshells, and eggs were collected from seven hawksbill turtles and their corresponding nests at Melaka's nesting beaches and hatchery site. FSSC was prevalent in the unhatched eggs ($n = 32$) from the seven study nests, colonising 96.9%. The remaining eggs from the study nests were found to have high hatching success, with a mean of $85.8 \pm 10.5\%$ ($n = 7$). It is unknown if the presence of FSSC contributed directly to embryonic mortality in this study. There are two possible roles of FSSC in sea turtle eggs: as a saprophyte or a primary pathogen. The presence of FSSC in the nest did not always compromise the hatching success of the entire egg clutch. FSSC was not detected in the sand samples of all nests, even though all nests contained *Fusarium*-colonised eggs. The concentration of FSSC in the sand might influence the infection rate of sea turtle eggs and their hatching success. Best practices for hatchery must be in place to achieve high hatching success for sea turtle conservation.

Keywords: Fungal infection, *Fusarium solani* species complex (FSSC), hatchery management, hatching success, hawksbill turtle

ARTICLE INFO

Article history:

Received: 10 September 2022

Accepted: 25 January 2023

Published: 27 July 2023

DOI: <https://doi.org/10.47836/pjst.31.5.29>

E-mail addresses:

seekhaiwei@gmail.com (Khai Wei See)

salmi@usm.my (Nurul Salmi Abdul Latip)

* Corresponding author

INTRODUCTION

Of the seven extant sea turtle species worldwide, six are categorised as Vulnerable, Endangered, or Critically Endangered on the International Union for Conservation of Nature (IUCN) Red List of Threatened Species (IUCN, 2021). Sea turtles face

various threats throughout their life cycle, and the failure of their eggs to hatch is one of the threats to the population decline of sea turtles. The reported sea turtle hatching success in different nesting sites in Malaysia has been ranging from around 60% to 80% (Chan, 2013; Mutalib & Fadzly, 2015; Salleh & Sah, 2014), with the study site, Melaka, having a hatching success of around 55% (DoF Melaka, unpublished data), which is at the lower end of the range. The variability in hatching success reflects various factors influencing hatchling production (Lindborg et al., 2016).

Sea turtle eggs are vulnerable to multiple human and natural threats, such as climate change (Howard et al., 2014); poaching activities (Chan, 2006); sea water inundation (Pike et al., 2015); nest destruction by beach erosion (García et al., 2003); predation (Heithaus, 2013); and microbial infection (Sarmiento-Ramírez et al., 2010). There are concerns that high fungal density in nests could cause infections of sea turtle eggs and deplete respiratory gases, resulting in reduced hatching success (Bézy et al., 2015; Sarmiento-Ramírez et al., 2010). Sea turtle egg fusariosis is an emerging fungal disease that causes egg failure and mortality, making it a high priority for a study. This disease has been associated with *Fusarium keratoplasticum* and *F. falciforme*, members of the *F. solani* species complex (FSSC) (Smyth et al., 2019). FSSC is a diverse complex comprising at least 60 phylogenetically distinct species with overlapping morphological and cultural characteristics. Infections caused by the members of the FSSC are generally referred to as *F. solani* infections (Short et al., 2013; Zhang et al., 2006).

The genus *Fusarium* has a widespread impact on causing diseases in humans and animals, and it is also known to contain many plant-pathogenic fungi (Leslie & Summerell, 2006). It causes many plant diseases, such as root rots, stalk rots, and vascular wilt diseases. *Fusarium* species have been recovered as the pathogens of several economically important host plants, including bananas, legumes, maize, peas, and sweet potatoes (Summerell et al., 2003; Zhang et al., 2006). FSSC has been implicated as the causative agent of human mycoses, causing fatal infections, particularly in immunocompromised patients (Zhang et al., 2006). *Fusarium* species has also been found to act as an opportunistic pathogen colonising the eggs of the Iberian rock lizard, which died during incubation and spread to infect adjacent live eggs (Moreira & Barata, 2005). In addition, FSSC was commonly found to occur in sea turtles' lesions. Many captive baby loggerhead turtles in the Bahamas were infected with FSSC on their shells and skins (Rebell, 1981). FSSC was also isolated from the lesions of loggerhead turtles in the rescue centres in Italy (Cafarchia et al., 2020). FSSC had also been reported as the agent of a cutaneous infection in an immunosuppressed loggerhead sea turtle, with the source of infection being the sand of the tank where the sea turtle was kept (Cabañes et al., 1997).

FSSC was found to be widely distributed, and many studies have isolated FSSC from sea turtle eggs in nesting sites around the world (e.g., Bailey et al., 2018; Neves et al., 2015; Phillott, 2004; Sarmiento-Ramírez et al., 2014). Sarmiento-Ramírez et al. (2010)

implied that FSSC poses an extremely high risk to the survival of sea turtles, following large numbers of failed loggerhead turtle eggs found having symptoms of fungal infection by FSSC. Despite Melaka being an important hawksbill turtle nesting rookery in Malaysia, in addition to the hawksbill turtle's status as a Critically Endangered species, there is a paucity of published research on hawksbill turtles in Malaysia. In Melaka, a previous study found FSSC on the surface of unhatched eggs and in the hatchery nest sand (Sidique et al., 2017). Nonetheless, many gaps remain because no study has taken samples from the nesting turtles nor the *in-situ* nest sand of beaches in Melaka, which could be the potential source of infection in sea turtle eggs (Keene et al., 2014). *Fusarium* species had been isolated from the cloaca of sea turtles in Pacific Costa Rica and Australia (Keene et al., 2014; Phillott et al., 2002).

Additionally, the fact that the same hatchery site and nest substrates are used across multiple nesting seasons in Melaka's hatchery could be a reason for concern, as pathogens might be able to accumulate in the sand (Patino-Martinez et al., 2012). Pathogens could be introduced by rangers and hatchery personnel when handling the eggs for relocation. Studies on FSSC and sea turtle eggs rarely mention the type of nests or the management strategies used (i.e., *in-situ* or *ex-situ* aspects of the nests). It is difficult to compare between studies because the solution to the problem will differ depending on the type of nest. The present study will address this gap, particularly in the contexts of hatchery management and relocation practices.

This study aims to determine the presence of FSSC in nesting sea turtles, nest sand, and eggs of hawksbill turtles in Melaka, as well as the hatching success of the study nests. The trend for the presence of FSSC across nesting site and hatchery site samples, along with egg mortality stages, can be used to assess the role of FSSC in unhatched eggs and whether it constitutes a threat to sea turtle eggs and therefore hatching success. The findings from this study will be used to propose several recommendations for the best practices for hatchery management.

MATERIALS AND METHODS

Study Site

The study was conducted at the hatchery and sea turtle nesting beaches in Melaka, which contain the highest number of hawksbill turtle nests in Peninsular Malaysia. Hawksbill turtles lay their eggs in various locations on the beaches, including the woody vegetation areas, open sand areas, grassy areas, and the beach's backshore. Among these locations, hawksbill turtles mostly prefer to nest in woody vegetation, especially within an area of sea lettuce (*Scaevola taccada*) (Salleh et al., 2018). Padang Kemunting hatchery, established in 1990, is an *ex-situ* site for incubating and hatching sea turtle eggs. Padang Kemunting is the prime nesting beach in Melaka. The hatchery is a permanent structure on the beach, and the substrate is replaced

every two years with sand from nearby beaches. The conservation of hawksbill turtles in Melaka is managed in collaboration with the Department of Fisheries Melaka (DoF Melaka) and the Worldwide Fund for Nature Malaysia (WWF-Malaysia). DoF rangers patrol sea turtle nesting beaches in Melaka every night during the nesting season, relocating any nests found to the Padang Kemunting hatchery for incubation. For this study, three beaches in Melaka, namely Padang Kemunting ($2^{\circ}18'28.9''\text{N}$, $102^{\circ}04'28.8''\text{E}$), Kem Terendak ($2^{\circ}16'47.4''\text{N}$, $102^{\circ}05'49.9''\text{E}$), and Tanjung Dahan ($2^{\circ}22'06.3''\text{N}$, $101^{\circ}59'24.3''\text{E}$) (Figure 1), were patrolled with DoF rangers to conduct *in-situ* sample collection during August 2018. Study nests were relocated to Padang Kemunting hatchery for incubation, and *ex-situ* sample collection was carried out at the hatchery before and after the egg incubation.



Figure 1. Locations for sample collection in Melaka, Malaysia

Sample Collection

Before Egg Incubation. At the nesting site, all eggs deposited by each nesting sea turtle were collected while wearing gloves and were arranged in a bucket along with the sand from the nest for relocation to the hatchery. All gloves and buckets were sterilised with 70% ethanol prior to usage. Three oviposited eggs were randomly collected straight from the turtle's cloaca and kept in separate sterile bags to prevent fungal contamination from contact with the sand (Sarmiento-Ramírez et al., 2010). Cloacal mucus secreted from the turtle during oviposition was aseptically collected on three replicates per turtle after around 20 eggs were deposited so

that potential contaminants introduced during the nesting process could be flushed off (Keene et al., 2014). An *in-situ* nest sand sample was aseptically taken after collecting all the eggs for relocation by scraping a sterile 50 ml centrifuge tube from the bottom to the top of the egg chamber (Keene et al., 2014). The eggs were then promptly transported to the hatchery site.

At the hatchery site, an egg chamber was dug to a depth of 45 to 50 cm while wearing sterile gloves. A hatchery nest sand sample was collected by a sterile 50 ml centrifuge tube from the bottom to the top of the egg chamber. After that, the eggs were reburied in the egg chamber for incubation.

After Egg Incubation. The nests were excavated after the hatchlings emerged from the nest (50 to 70 days). Sterile gloves were worn to excavate each nest (Bézy et al., 2015). Hatchery nest sand samples from the bottom to the top of the egg chamber were again collected. Five unhatched eggs were sampled from each clutch (except for one clutch in which there were only two unhatched eggs). Eggshell fragments from five hatched eggs were also sampled from each clutch.

Each sampling procedure before and after egg incubation was conducted aseptically to ensure that the samples collected were free from the human introduction of contaminants. The aseptic technique includes cleaning and disinfecting surfaces before use and sterilising equipment that comes into contact with samples (Bykowski & Stevenson, 2008). A total of seven clutches were sampled and labelled as nests A-G.

Hatching Success and Egg Mortality

During post-emergence nest excavation at the hatchery site, the remains of each nest were removed and placed next to the nest. The excavated materials were sorted into empty eggshells and unhatched eggs. The hatching success for each clutch was calculated as the percentage of successfully hatched eggs represented by the number of empty eggshells relative to the total number of eggs incubated in a clutch (Miller, 1999).

To avoid contamination, the unhatched eggs collected as samples at the hatchery site were opened in the laboratory under aseptic conditions during fungal isolation. Unhatched eggs were opened and examined for embryonic development signs and were categorised into the undeveloped stage, the early embryonic stage, the mid-embryonic stage, the late embryonic stage, and the advanced decomposition stage. Categories of early, mid, and late embryonic stages were identified based on Miller et al. (2017) and Rings et al. (2015).

Isolation and Identification of *Fusarium* Species

Each sand sample was diluted by serial dilution before plating onto Peptone Pentachloronitrobenzene Agar (PPA) plates to process the sand samples (including *in-situ* and hatchery nest sand). Cloacal mucus samples were also inoculated on PPA. Egg samples

(including eggs at oviposition and unhatched eggs) were surface-sterilised with sodium hypochlorite, 70% ethanol and sterile distilled water to remove the surface contaminants. After drying the egg with sterile filter paper, the egg's surface was swabbed with a sterile cotton swab to inoculate the PPA. The egg was then opened with a sterile scalpel blade (Wyneken et al., 1988). A sterile cotton swab was swiped through the egg's contents to inoculate PPA (Keene et al., 2014). Five eggshell fragments were randomly cut from each egg sample and cultured on a PPA plate. On the other hand, the eggshell samples of hatched eggs were also surface-sterilised before being cultured on PPA.

All PPA plates were incubated under standard conditions (alternating 12-hour periods of light and darkness) (Leslie & Summerell, 2006). Each fungus grown in PPA was subcultured onto Potato Dextrose Agar (PDA) to obtain axenic cultures and observe the fungi's macroscopic characteristics. Fungi were then subcultured onto Carnation Leaf-Piece Agar (CLA). For identification, the microscopic characteristics of the fungi growing on the leaf pieces in the CLA were observed and identified under a light microscope with reference to Leslie and Summerell (2006) and Nelson et al. (1983). The three types of culture media used in this study, PPA, PDA, and CLA, were prepared according to the standard recipes and procedures from Leslie and Summerell (2006).

RESULTS

Isolation and Identification of *Fusarium* Species

Fusarium was found in 64 of the 130 samples collected from seven nests. All cultures were identified as members of FSSC. Only FSSC was found in the samples in which it was identified based on its morphological characteristics.

By observing the microscopic characteristics of the CLA cultures, FSSC produced wide, straight and stout macroconidia. The macroconidial apical cells were rounded and blunt, while the basal cells had a notched end. The microconidia produced were oval, ellipsoid or fusiform. The monophialides were long and bearing microconidia. Chlamydoconidia were globose and formed singly or in short chains (Figure 2). Macroscopic characteristics were

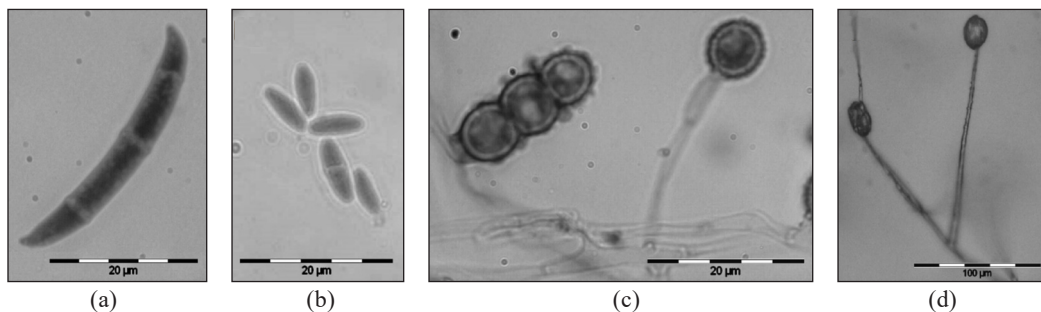


Figure 2. Microscopic characteristics of FSSC: (a) macroconidia, (b) microconidia, (c) chlamydoconidia in a short chain on the left and singly on the right, and (d) monophialides bearing microconidia

observed on PDA. Cultures of FSSC were white with sparse to abundant mycelium. Many cultures did not produce pigments, while some produced light brown pigments (Figure 3).

Determination of FSSC Presence in Samples

The sample types which contained FSSC included the eggshells of unhatched eggs, the contents of unhatched eggs, *in-situ* nest sand, the eggshells of hatched eggs, and hatchery nest sand after egg incubation. From all the sample types, the percentage of recovering FSSC was the highest in unhatched eggs, 96.9% of the eggshells ($n = 32$) and 84.4% of the content ($n = 32$). In contrast, FSSC only recovered from 5.7% of the eggshells of hatched eggs ($n = 35$). FSSC had a low occurrence in the sand samples as well, with only 28.6% of the *in-situ* nest sand ($n = 7$), 28.6% of the hatchery nest sand after egg incubation ($n = 7$), and none in the hatchery nest sand before egg incubation ($n = 7$) (Table 1).

None of the samples from eggs at oviposition and cloacal mucus were found to have FSSC. Additionally, all samples of the surface of the eggs swabbed did not contain FSSC due to surface-sterilisation, which showed that the method of surface-sterilisation used was reliable and confirmed that the FSSC isolated from the unhatched eggs were indeed from the eggshells and the egg content instead of the surface (Table 1).

Hatching Success and Egg Mortality

In this study, the nests had a high mean hatching success, at $85.8 \pm 10.5\%$ ($n = 7$). A trend was observed between the hatching success and FSSC presence in sand samples. When FSSC was detected in *in-situ* nest sand or hatchery nest sand after egg incubation, nests C, D, and E had lower hatching success than the other nests (Table 2).

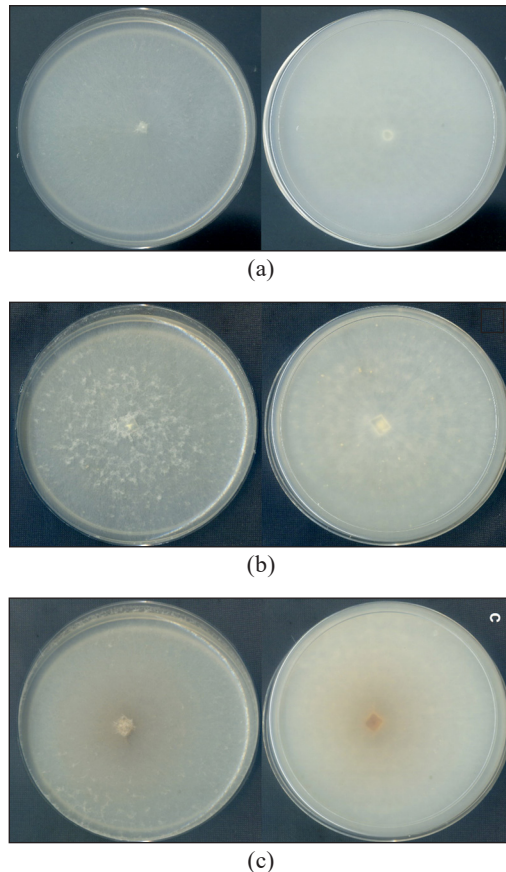


Figure 3. Macroscopic characteristics of FSSC on PDA. In each pair from (a) to (c), the left plate is the upper surface, and the right plate is the under the surface: (a) sparse mycelium; no pigmentation, (b) abundant mycelium; no pigmentation, and (c) sparse mycelium; light brown pigmentation

Table 1
The number and type of samples collected with FSSC presence in samples

Sample types	Number of samples collected	Percentage of recovering FSSC from each sample type (%)
Eggs at oviposition	21	0
Cloacal mucus	21	0
<i>In-situ</i> nest sand	7	28.6
Hatchery nest sand before egg	7	0
Hatchery nest sand after egg incubation	7	28.6
Eggshells of hatched eggs	35	5.7
Unhatched eggs:	32	
Surface		0
Eggshells		96.9
Content		84.4
Total	130	

Table 2
Hatching success of study nests and FSSC presence in different sample types for each nest

Nests	A	B	C	D	E	F	G
Nesting beaches	KT	PK	PK	PK	KT	KT	TD
Clutch size	117	101	103	157	112	177	150
Hatching success (%)	86.3	93.1	76.7	70.7	79.5	95.5	98.7
Eggs at oviposition	-	-	-	-	-	-	-
Cloacal mucus	-	-	-	-	-	-	-
<i>In-situ</i> nest sand	-	-	-	+	+	-	-
Hatchery nest sand before egg incubation	-	-	-	-	-	-	-
Hatchery nest sand after egg incubation	-	-	+	+	-	-	-
Eggshells of hatched eggs	+	-	-	-	+	-	-
Unhatched eggs (eggshells)	+	+	+	+	+	+	+
Unhatched eggs (content)	+	+	+	+	+	+	+

Abbreviations used: KT for Kem Terendak, PK for Padang Kemunting, TD for Tanjung Dahan
 Symbols used: “+” for FSSC isolated from the samples, “-” for FSSC not isolated from the samples

For unhatched eggs containing FSSC, the highest percentage of egg mortality occurred during the undeveloped stage (51.6%), followed by the early embryonic stage (25.8%), which means that most eggs sampled died early in the incubation period. Less dead eggs were found at the late embryonic stage (16.1%) and advanced decomposition stage (6.5%). No mortality was observed in the mid-embryonic stage (Table 3).

Table 3
The proportion of unhatched eggs with FSSC in each egg mortality stage

Stages of unhatched eggs	Number of eggs	Percentage (%)
Undeveloped stage	16	51.6
Early embryonic stage	8	25.8
Mid embryonic stage	0	0
Late embryonic stage	5	16.1
Advanced decomposition stage	2	6.5
Total	31	100

DISCUSSION

The Source of *Fusarium* Species

From the analysis of FSSC presence in the samples collected, the results showed that nest sand samples in the hatchery did not contain FSSC initially, but the condition changed after the egg incubation to around one-third of the nests being infested with FSSC. When a nest is established for egg incubation, the nest environment will differ from that before incubation, becoming warmer and moister than the sand alone (Gammon et al., 2020; Wyneken et al., 1988). It is caused by sea turtles releasing a substantial amount of cloacal mucus and eggs to the nests during nesting (Wyneken et al., 1988). Furthermore, embryos generate heat during the metabolic process of development (Gammon et al., 2020). The changes in the nest environment during incubation might encourage the growth of fungi (Keene et al., 2014; Wyneken et al., 1988). However, nest conditions like temperature and humidity might not be the sole factor determining disease development. Other factors like embryo physiology and physical environments, such as natural immunosuppression and sand composition, might also play a role (Phillott & Parmenter, 2001; Sarmiento-Ramírez et al., 2010). For instance, sea turtle nests with clay/silt content were more susceptible to *Fusarium* invasion (Sarmiento-Ramírez et al., 2014).

In this study, *Fusarium* species were not detected in sand samples of all nests, even though they contained *Fusarium*-colonised eggs, which is also consistent with a previous study in Melaka by Sidique et al. (2017). Elshafie et al. (2007) and Neves et al. (2015) also isolated fungi from the sea turtle eggs but not from the corresponding sand samples. Some studies implicated that the source of *Fusarium* infection was the nesting sand because only eggs in contact with the sand were infected, while *Fusarium* species is also common as a soil saprophyte (Phillott et al., 2002; Sarmiento-Ramírez et al., 2014). FSSC was not isolated from some of the sand samples in this study, possibly because FSSC was not present at a detectable level in the sand. Wyneken et al. (1988) indicated that fungi might be present in the sand at very low levels and thus could be missed when the samples are collected. When FSSC was at detectable levels and isolated from the sand samples in this

study, the nests from which they were sampled were found to have lower hatching success (Table 2). It may indicate that the concentration of FSSC in the sand might influence the infection rate of sea turtle eggs and their hatching success. Thus, it is important to include the measurement of FSSC concentration in future studies.

The study by Bézy et al. (2015) found that high fungal abundance in the nesting sand had negatively affected hatching success by which fungal decomposition of the organic matter diminished the oxygen supply in the nests. Nest sand in the study site by Bézy et al. (2015) was found to have high organic matter content. The organic matter content in nest sand could be an important factor in determining the level of microbial activity in the nests (Trullas & Paladino, 2007). Since FSSC was not detected in some of the nest sand samples in the present study, the organic matter content in the sand might be low in this case. Future studies should determine the organic matter content in the sand at this study site and the relationship between the concentration of FSSC and hatching success.

A study by Sarmiento-Ramírez et al. (2014) revealed the presence of the members of the FSSC, namely *F. falciforme* and *F. keratoplasticum*, in the eggs of six sea turtle species (i.e., green, loggerhead, hawksbill, olive ridley, leatherback, and flatback) in various nesting locations across the Atlantic Ocean, Indian Ocean, Pacific Ocean, and Caribbean Sea, implying that FSSC is globally distributed. In a different study by Sidique et al. (2017) in Melaka, *F. falciforme* and *F. keratoplasticum* had also been isolated from the sand of egg chambers in Padang Kemunting hatchery, confirming the presence of FSSC in Melaka, but like in the present study, they also did not manage to isolate FSSC from all corresponding sand samples. Thus, another potential circumstance for *Fusarium* species to come into contact with sea turtle eggs is via the oviduct of nesting turtles (Phillott et al., 2002). Although FSSC was not isolated from the cloacal mucus sampled from the nesting turtles in this study, microbial transfer from the nesting turtles to the eggs may still occur in the oviduct before oviposition. Microbes may not have been detected in the cloacal mucus sampled during oviposition because the phase of microbial shedding may have ended (Wyneken et al., 1988).

The ovipositor of sea turtles is often exposed to beach sand during the nesting process. Soil microbiota can accumulate on the ovipositor and enter the reproductive tract when the ovipositor retracts into the cloaca. When fungal spores are lodged in the sperm storage tubules, they could be transported along with spermatozoa and be enclosed in the egg (Phillott et al., 2002). In Australia, FSSC has been isolated from both the cloaca of nesting sea turtles and the exterior of unhatched eggs, suggesting that intra-oviductal contamination of eggs is possible (Phillott et al., 2002). *Fusarium* species have also been isolated from the cloacal mucus of olive ridley turtles in Pacific Costa Rica, though it was not isolated from the eggs (Keene et al., 2014).

FSSC was not isolated from the eggs at oviposition in this study. Although we did not find evidence of eggs being contaminated in the oviduct, FSSC could still be included in

eggs at a very low level or prevalence (A. D. Phillott, personal communication). Personnel handling nest relocation were also unlikely to introduce *Fusarium* species, as all contacts were properly sterilised. In short, FSSC could only be traced from the sand in this study but not all samples contained FSSC. As only seven clutches were sampled in this study, to increase the reliability, more samples and a longer study period are required to confirm the source of FSSC in Padang Kemunting hatchery, as well as the conditions that will lead to high FSSC concentrations in sand samples.

The presence of FSSC in sea turtle nests has been implicated in causing mass mortalities and low hatching success in sea turtle eggs (Sarmiento-Ramírez et al., 2010). However, even though FSSC was present and prevalent in the sampled unhatched eggs in this study, the nests from which they were sampled were found to have high hatching success. From this study, it was impossible to determine if FSSC contributed directly to egg mortality because *Fusarium* species recovered from diseased materials could be primary pathogens or saprophytes (Leslie & Summerell, 2006; Phillott, 2002). As a primary pathogen, *Fusarium* could cause diseases and mortalities in live sea turtle eggs (Sarmiento-Ramírez et al., 2010), whereas as a saprophyte, *Fusarium* may only colonise eggs after they have died (Phillott & Parmenter, 2001). Thus, the following sections will discuss the different mechanisms in which how these two roles of *Fusarium* might play out in this study.

***Fusarium* Species as a Primary Pathogen**

This study discovered that FSSC was much more prevalent in the unhatched eggs than in the hatched eggs. FSSC strains might have penetrated the eggshells of unhatched eggs into the contents of the eggs. Mechanisms that FSSC might use as primary pathogens to cause the death of live eggs include producing enzymes to degrade the eggshells (Phillott, 2004). FSSC can also extract and reduce calcium content in the eggshell, impairing its functions as a barrier and thus allowing fungi to penetrate the egg. The loss of calcium in the eggshell could also lead to a calcium deficiency in the embryos, as embryos would be unable to obtain calcium from the eggshell for embryonic development, potentially resulting in embryonic mortality (Phillott et al., 2006). Once FSSC is inside a sea turtle egg, it might invade the embryonic tissues, such as the liver, heart, and gut (Phillott, 2004). In the study by Sarmiento-Ramírez et al. (2010), when sea turtle eggs were infected with FSSC, the size of the infected areas was observed to grow over time and developed into large necrotic lesions, causing embryonic mortality.

Another mechanism that fungi might also use to affect embryonic development and egg hatching by secreting toxic compounds called mycotoxins. FSSC is known to secrete harmful mycotoxins, though it should be noted that not all FSSC strains produce mycotoxins (Azliza et al., 2014). No study has been done yet on whether FSSC produces mycotoxins on sea turtle eggs and its impact. Nevertheless, the mycotoxins of another fungal species

called *Aspergillus flavus* are extracted from the eggshells and eggs of dead sea turtles eggs. The level of mycotoxins was believed to be able to cause embryonic mortality (Elshafie et al., 2007).

Sarmiento-Ramírez et al. (2010) conducted pathogenicity tests on loggerhead turtle eggs with isolates from the member of the FSSC called *F. keratoplasticum* through inoculation challenge experiments. As a result of the experiments, *F. keratoplasticum* was reported as pathogenic to loggerhead turtle eggs because they fulfilled Koch's postulates. *F. keratoplasticum* and *F. falciforme* are the members of FSSC found to have high virulence in sea turtle eggs. They are also highly adapted to the host environment because their optimal growth temperature coincides with the optimal incubation temperature for sea turtle eggs (Sarmiento-Ramírez et al., 2014). An environment conducive to turtle egg incubation is also ideal for the growth and colonisation of these pathogens, thus presenting a significant threat to sea turtle eggs (Keene et al., 2014; Sarmiento-Ramírez et al., 2014; Wyneken et al., 1988). Since FSSC is pathogenic to sea turtle eggs, FSSC isolates recovered in this study may be likewise pathogenic.

***Fusarium* Species as a Saprophyte**

Fusarium is soil-borne and can act as an opportunistic fungus that feeds on dead eggs (Moreira & Barata, 2005; Phillott & Parmenter, 2001). It is commonly recovered from diseased plant parts as a saprophyte (Leslie & Summerell, 2006). Unhatched eggs in this study were sampled after 50 to 70 days of incubation during post-emergence nest excavation. Most sampled unhatched eggs were in the undeveloped stage, and some were in the early embryonic stage (Table 3). It means that the eggs had ceased development since the beginning of incubation, which could range from day 1 to day 10 of the incubation period (Miller et al., 2017). Saprophytes and secondary pathogens are more likely to be recovered from samples that have been dead for a long time compared to newly colonised samples because the longer the period between mortality and analysis, the more likely it is for other fungal species that are not the primary coloniser to infiltrate the samples (Leslie & Summerell, 2006).

Opportunistic pathogens could use dead eggs to gain nutrient resources and then spread to kill other live eggs (Moreira & Barata, 2005). In the laboratory incubation of green and loggerhead turtle eggs in eastern Australia by Phillott and Parmenter (2001), the first appearance of FSSC was always on a dead egg, indicating a saprophytic role of the FSSC. The dead egg then acted as a nutrient source and a focus for spreading FSSC to other live eggs in the clutch (Phillott & Parmenter, 2001). In extreme cases, eggs were colonised, and none hatched (Phillott & Parmenter, 2001; Sarmiento-Ramírez et al., 2010). Similar observations were also seen in a laboratory experiment conducted by Moreira and Barata (2005) on the eggs of another reptile species, the Iberian rock lizard. *Fusarium*

was found colonising eggs that failed during incubation and spread to colonise adjacent eggs (Moreira & Barata, 2005). In these experiments, the eggs with healthy appearances did not show signs of fungal presence until they were colonised from the adjacent eggs. The spread of FSSC was suggested as an opportunistic invasion (Moreira & Barata, 2005; Phillott & Parmenter, 2001).

Since most of the unhatched eggs in this study had been dead from the early days of incubation, they could have also been the source of the colonisation of adjacent eggs. However, all nests containing FSSC in this study had a mean hatching success of around 86%, suggesting that FSSC in the unhatched eggs did not spread widely to kill other eggs. In the field experiment by Moreira and Barata (2005), fungi colonised dead eggs of the Iberian rock lizard but did not spread and affect other live eggs. As a result, it is feasible that *Fusarium* species present in the nest and acts as a saprophyte colonising dead eggs without compromising the hatching success of the entire egg clutch, which could be the case in the present study.

Nevertheless, both roles of *Fusarium* species as a primary pathogen or as a saprophyte have pointed to mass mortalities and low hatching success of sea turtle eggs in other studies, while the results of the present study indicated otherwise. A recent study by Bailey et al. (2018) discovered FSSC in sea turtle nests with high and low hatching success, but the reason for this discrepancy is unknown. Perhaps the nest's physical environment and conditions, as discussed above, such as organic matter content and composition, temperature, and humidity, could be important in determining whether FSSC would proliferate in sea turtle nests. Further studies are needed to determine the nest conditions in which FSSC would spread and infect sea turtle eggs.

Implications for Hatchery Management

Even though FSSC was present in the hatchery nests in the current study, the mean hatching success was around 86% ($n = 7$), as contrasted with the hatchery's consistently low hatching success, which ranged from 38.0% to 61.4% in the recent years from 2014 to 2018, with a mean of 55.5% ($n = 2410$) (DoF Melaka, unpublished data). Sea turtle egg relocation to hatcheries has been implied to cause low hatching success (Mortimer, 1999), but the results of this study show that relocation does not always have a negative impact on hatching success. Hatching success did not appear to be greatly affected by the reuse of the hatchery site and nest substrate across several nesting seasons at the current study site, which is also consistent with a study by Patino-Martinez et al. (2012). Thus, the high hatching success in this study might be attributed to the researcher's good handling practices for nest relocation as opposed to usual hatchery practices. High hatching success can be achieved in a hatchery when all precautions are taken and all protocols are followed closely while also being subjected to variations like environmental conditions that differ from site

to site. Eggs in this study were collected directly from the ovipositors during nesting by hands while wearing sterilised gloves. The eggs were gently placed in a sterile bucket and carefully transported to the hatchery without any shocking movement or delay. It would require frequent patrolling to relocate the eggs on time. Eggs were reburied gently in the hatchery in which the nest parameters approximate the natural nest of hawksbill turtles.

Rangers and hatchery personnel should avoid direct skin contact with sea turtle eggs by wearing gloves and cleaning the tools when handling eggs for a relocation because fungi or even other microbes may be transferred from nest to nest or from beach to beach through personnel handling different nests. Relocation practice is important and could contribute to the contamination of eggs if done incorrectly, yet it is rarely highlighted in studies. A comparison of hatchery manuals and guidelines from different locations shows inconsistencies in the relocation practices (Table 4). Using gloves and clean tools is often not documented or emphasised as precautionary measures during relocation. Although the use of gloves is documented in Malaysia’s manual (Sukarno et al., 2007), it commonly does not happen in practice (personal observation and consultations). Hatchery manuals and guidelines should be revised and made compulsory for the use of gloves during the collection and reburial of eggs and change with new ones each time when handling different clutches.

Clean buckets or containers should also be used to transport the eggs to prevent cross-contamination. Retraining of personnel must be conducted regularly to ensure consistency and reliability. It is even more important at sites where personnel often change with each nesting season. As an additional mitigation, it is also important to ensure that hatchery sands are regularly refreshed by replacing them at every nesting season, if possible, to reduce fungal or other microbial contamination, especially at permanently placed hatcheries. While the present study only included seven clutches, good handling practices can result in high hatching success. Furthermore, maintaining hygiene practices could

Table 4
Summary of the relocation practices listed in hatchery manuals and guidelines

Practice	Reference
“Catch eggs by hand as they drop from the cloaca and place them gently in a bag or bucket.”	Mortimer (1999)
“Hand should be clean and dry before handling the eggs.”	Ahmad et al. (2004)
“Excavate the eggs by hand and place them in a rigid container.”	North Carolina Wildlife Resources Commission (2006)
“Whilst wearing gloves the eggs are carefully placed in a plastic bag.”	Couchman et al. (2009)
“Translocation of eggs from the original nest into a rigid container must be done carefully. Prepare equipment such as buckets or rigid containers and rubber gloves.” ^a	Sukarno et al. (2007)
“Catch eggs as they are being laid by hand or into a clean plastic bag.”	Phillott and Shanker (2018)

^aTranslated into English from original content in Bahasa Malaysia

protect staff from microbial infections and diseases such as *Fusarium* keratitis, which can affect immunocompetent individuals (Chang et al., 2006). It is best to leave sea turtle eggs undisturbed in their original location (*in-situ*), but since relocation (*ex-situ*) is highly necessary for sea turtle conservation in many of the nesting sites due to immense human and natural threats, strict practices must be in place.

CONCLUSION

In this study, FSSC is prevalent in the unhatched eggs but not in the hatched eggs. Sources of FSSC were traced to the sand samples, but not all samples contained FSSC, indicating that further studies are needed to confirm the source of FSSC and the conditions that will result in the spread of FSSC in sea turtle nests. This study also revealed that FSSC, recognised as the causal factor of an emerging fungal disease at other nesting sites, does not necessarily compromise the hatching success of sea turtle nests. Good hatchery management, stringent handling practices, and well-trained staff are the key to high hatching success. As this is one of the earliest studies in Malaysia to associate FSSC, hatching success, and egg mortality, more research is required in this regard in Malaysia.

ACKNOWLEDGEMENT

We thank the Department of Fisheries (DoF) Malaysia for permitting us to conduct this study in Melaka. We are thankful to Worldwide Fund for Nature Malaysia (WWF-Malaysia) for providing logistical and accommodation support and assistance in the field. Special thanks to the dedicated team of DoF rangers for guiding us in beach patrolling and locating the sea turtles. Thank you to the School of Biological Sciences, Universiti Sains Malaysia (USM), for providing the laboratory facilities and supplies needed for this study. We also thank Dr Rosnida Tajuddin and Dr Nik Izham for guiding techniques in isolating and identifying *Fusarium* species.

REFERENCES

- Ahmad, A., Zulkifli, T., Mahyam, M. I., Solahuddin, A. R., & Azman, Z. N. (2004). *A guide to set-up and manage sea turtles hatcheries in the Southeast Asian Region*. SEAFDEC/MFRDMD.
- Azliza, I. N., Hafizi, R., Nurhazrati, M., & Salleh, B. (2014). Production of major mycotoxins by *Fusarium* species isolated from wild grasses in Peninsular Malaysia. *Sains Malaysiana*, 43(1), 89-94.
- Bailey, J. B., Lamb, M., Walker, M., Weed, C., & Craven, K. S. (2018). Detection of potential fungal pathogens *Fusarium falciforme* and *F. keratoplasticum* in unhatched loggerhead turtle eggs using a molecular approach. *Endangered Species Research*, 36, 111-119. <https://doi.org/10.3354/esr00895>
- Bézy, V. S., Valverde, R. A., & Plante, C. J. (2015). Olive ridley sea turtle hatching success as a function of the microbial abundance in nest sand at Ostional, Costa Rica. *PLOS ONE*, 10(2), Article e0118579. <https://doi.org/10.1371/journal.pone.0118579>

- Bykowski, T., & Stevenson, B. (2008). Aseptic technique. *Current Protocols in Microbiology*, 11, A.4D.1-A.4D.11. <https://doi.org/10.1002/9780471729259.mca04ds11>
- Cabañes, F. J., Alonso, J. M., Castellá, G., Alegre, F., Domingo, M., & Pont, S. (1997). Cutaneous hyalohyphomycosis caused by *Fusarium solani* in a loggerhead sea turtle (*Caretta caretta* L.). *Journal of Clinical Microbiology*, 35(12), 3343-3345. <https://doi.org/10.1128/jcm.35.12.3343-3345.1997>
- Cafarchia, C., Paradies, R., Figueredo, L. A., Iatta, R., Desantis, S., Di Bello, A. V. F., Zizzo, N., & van Diepeningen, A. D. (2020). *Fusarium* spp. in loggerhead sea turtles (*Caretta caretta*): From colonization to infection. *Veterinary Pathology*, 57(1), 139-146. <https://doi.org/10.1177/0300985819880347>
- Chan, E. H. (2006). Marine turtles in Malaysia: On the verge of extinction? *Aquatic Ecosystem Health & Management*, 9(2), 175-184. <https://doi.org/10.1080/14634980600701559>
- Chan, E. H. (2013). A report on the first 16 years of a long-term marine turtle conservation project in Malaysia. *Asian Journal of Conservation Biology*, 2(2), 129-135.
- Chang, D. C., Grant, G. B., O'Donnell, K., Wannemuehler, K. A., Noble-Wang, J., Rao, C. Y., Jacobson, L. M., Crowell, C. S., Sneed, R. S., Lewis, F. M. T., Schaffzin, J. K., Kainer, M. A., Genese, C. A., Alfonso, E. C., Jones, D. B., Srinivasan, A., Fridkin, S. K., & Park, B. J. (2006). Multistate outbreak of *Fusarium* keratitis associated with use of a contact lens solution. *Journal of the American Medical Association*, 296(8), 953-963. <https://doi.org/10.1001/jama.296.8.953>
- Couchman, O., Wulfeld, E., Muurmans, M., Steer, M., & Fanning, E. (Eds.). (2009). *Sea turtle monitoring: Methods manual* (Report no. 4). Society for Environmental Exploration UK, UNANLeón and LIDER Foundation. https://www.researchgate.net/publication/341368602_Sea_Turtle_Monitoring_Methods_Manual
- Elshafie, A., Al-Bahry, S. N., AlKindi, A. Y., Ba-Omar, T., & Mahmoud, I. (2007). Mycoflora and aflatoxins in soil, eggshells, and failed eggs of *Chelonia mydas* at Ras Al-Jinz, Oman. *Chelonian Conservation and Biology*, 6(2), 267-270. [https://doi.org/10.2744/1071-8443\(2007\)6\[267:MAAISE\]2.0.CO;2](https://doi.org/10.2744/1071-8443(2007)6[267:MAAISE]2.0.CO;2)
- Gammon, M., Fossette, S., McGrath, G., & Mitchell, N. (2020). A systematic review of metabolic heat in sea turtle nests and methods to model its impact on hatching success. *Frontiers in Ecology and Evolution*, 8, Article 556379. <https://doi.org/10.3389/fevo.2020.556379>
- García, A., Ceballos, G., & Adaya, R. (2003). Intensive beach management as an improved sea turtle conservation strategy in Mexico. *Biological Conservation*, 111(2), 253-261. [https://doi.org/10.1016/S0006-3207\(02\)00300-2](https://doi.org/10.1016/S0006-3207(02)00300-2)
- Heithaus, M. R. (2013). Predators, prey, and the ecological roles of sea turtles. In J. Wyneken, K. J. Lohmann, & J. A. Musick (Eds.), *The Biology of Sea Turtles, Volume III* (pp. 249-284). CRC Press. <https://doi.org/10.1201/b13895>
- Howard, R., Bell, I., & Pike, D. A. (2014). Thermal tolerances of sea turtle embryos: Current understanding and future directions. *Endangered Species Research*, 26, 75-86. <https://doi.org/10.3354/esr00636>
- IUCN. (2021). *The IUCN red list of threatened species. Version 2021-1*. International Union for Conservation of Nature's. <https://www.iucnredlist.org>

- Keene, E., Soule, T., & Paladino, F. (2014). Microbial isolations from Olive Ridley (*Lepidochelys olivacea*) and East Pacific Green (*Chelonia mydas agassizii*) sea turtle nests in Pacific Costa Rica, and testing of cloacal fluid antimicrobial properties. *Chelonian Conservation and Biology*, 13(1), 49-55. <https://doi.org/10.2744/CCB-1051.1>
- Leslie, J. F., & Summerell, B. A. (2006). *The Fusarium laboratory manual*. Blackwell Publishing. <https://doi.org/10.1002/9780470278376>
- Lindborg, R., Neidhardt, E., Witherington, B., Smith, J. R., & Savage, A. (2016). Factors influencing loggerhead (*Caretta caretta*) and green turtle (*Chelonia mydas*) reproductive success on a mixed use beach in Florida. *Chelonian Conservation and Biology*, 15(2), 238-248. <https://doi.org/10.2744/CCB-1206.1>
- Miller, J. D. (1999). Determining clutch size and hatching success. In K. L. Eckert, K. A. Bjorndal, F.A. Abreu-Grobois, & M. Donnelly (Eds.), *Research and Management Techniques for the Conservation of Sea Turtles* (pp. 124-129). IUCN/SSC Marine Turtle Specialist Group.
- Miller, J. D., Mortimer, J. A., & Limpus, C. J. (2017). A field key to the developmental stages of marine turtles (*Cheloniidae*) with notes on the development of *Dermochelys*. *Chelonian Conservation and Biology*, 16(2), 111-122. <https://doi.org/10.2744/CCB-1261.1>
- Moreira, P. L., & Barata, M. (2005). Egg mortality and early embryo hatching caused by fungal infection of Iberian rock lizard (*Lacerta monticola*) clutches. *The Herpetological Journal*, 15(4), 265-272.
- Mortimer, J. A. (1999). Reducing threats to eggs and hatchlings: Hatcheries. In K. L. Eckert, K. A. Bjorndal, F.A. Abreu-Grobois, & M. Donnelly (Eds.), *Research and Management Techniques for the Conservation of Sea Turtles* (pp. 175-178). IUCN/SSC Marine Turtle Specialist Group.
- Mutalib, A. H. A., & Fadzly, N. (2015). Assessing hatchery management as a conservation tool for sea turtles: A case study in Setiu, Terengganu. *Ocean & Coastal Management*, 113, 47-53. <https://doi.org/10.1016/j.ocecoaman.2015.05.010>
- Nelson, P. E., Toussoun, T. A., & Marasas, W. F. O. (1983). *Fusarium species: An Illustrated Manual for Identification*. The Pennsylvania State University Press.
- Neves, M. S. C., Moura, C. C. D. M., & Oliveira, L. G. D. (2015). Mycobiota from the eggs, nests and stillbirths of *Eretmochelys imbricata* Linneus 1766 (*Testudines: Cheloniidae*) in Pernambuco State, Brazil. *African Journal of Microbiology Research*, 9(17), 1195-1199. <https://doi.org/10.5897/AJMR2015.7389>
- North Carolina Wildlife Resources Commission. (2006). *Handbook for sea turtle volunteers in North Carolina*. North Carolina Wildlife Resources Commission. http://www.seaturtle.org/PDF/NCWRCNorthCarolinaWildlifeResourcesCommission_2006_HandbookforseaturtlevolunteersinNor.pdf
- Patino-Martinez, J., Marco, A., Quiñones, L., Abella, E., Abad, R. M., & Diéguez-Urbeondo, J. (2012). How do hatcheries influence embryonic development of sea turtle eggs? Experimental analysis and isolation of microorganisms in leatherback turtle eggs. *Journal of Experimental Zoology Part A: Ecological Genetics and Physiology*, 317A(1), 47-54. <https://doi.org/10.1002/jez.719>
- Phillott, A. D. (2002). *Fungal colonisation of sea turtle nests in Eastern Australia* [Doctoral dissertation, Central Queensland University]. Central Queensland University's Institutional Repository, ACQUIRE. https://acquire.cqu.edu.au/articles/thesis/Fungal_colonisation_of_sea_turtle_nests_in_eastern_Australia/13426184/1

- Phillott, A. D. (2004). Penetration of the eggshell and invasion of embryonic tissue by fungi colonising sea turtle eggs. *Herpetofauna*, 34(1), 44-47.
- Phillott, A. D., & Parmenter, C. J. (2001). The distribution of failed eggs and the appearance of fungi in artificial nests of green (*Chelonia mydas*) and loggerhead (*Caretta caretta*) sea turtles. *Australian Journal of Zoology*, 49(6), 713-718. <https://doi.org/10.1071/ZO00051>
- Phillott, A. D., & Shanker, K. (2018). Best practices in sea turtle hatchery management for South Asia. *Indian Ocean Turtle Newsletter*, 27, 31-34.
- Phillott, A. D., Parmenter, C. J., & McKillup, S. C. (2006). Calcium depletion of eggshell after fungal invasion of sea turtle eggs. *Chelonian Conservation and Biology*, 5(1), 146-149. [https://doi.org/10.2744/1071-8443\(2006\)5\[146:CDOEAF\]2.0.CO;2](https://doi.org/10.2744/1071-8443(2006)5[146:CDOEAF]2.0.CO;2)
- Phillott, A. D., Parmenter, C. J., Limpus, C. J., & Harrower, K. M. (2002). Mycobiota as acute and chronic cloacal contaminants of female sea turtles. *Australian Journal of Zoology*, 50(6), 687-695. <https://doi.org/10.1071/ZO01057>
- Pike, D. A., Roznik, E. A., & Bell, I. (2015). Nest inundation from sea-level rise threatens sea turtle population viability. *Royal Society Open Science*, 2(7), Article 150127. <https://doi.org/10.1098/rsos.150127>
- Rebell, G. (1981). *Fusarium* infections in human and veterinary medicine. In P. E. Nelson, T. A. Toussoun, & R. J. Cook (Eds.), *Fusarium: Diseases, Biology and Taxonomy* (pp. 210-220). The Pennsylvania State University Press.
- Rings, C. C., Rafferty, A. R., Guinea, M. L., & Reina, R. D. (2015). The impact of extended preovipositional arrest on embryonic development and hatchling fitness in the flatback sea turtle. *Physiological and Biochemical Zoology*, 88(2), 116-127. <https://doi.org/10.1086/677951>
- Salleh, S. M., & Sah, S. A. M. (2014). Hatching success and nesting depth of *Chelonia mydas* (family: *Cheloniidae*) in eggs relocation programme at Penang Island, Peninsular Malaysia. *Malaysian Applied Biology*, 43(2), 59-70.
- Salleh, S. M., Nishizawa, H., Sah, S. A. M., & Safri, M. F. (2018). Spatiotemporal preferences in nesting of the hawksbill turtle (*Eretmochelys imbricata*) in Melaka, Malaysia. *Journal of the Marine Biological Association of the United Kingdom*, 98(8), 2145-2152. <https://doi.org/10.1017/S0025315417001734>
- Sarmiento-Ramírez, J. M., Abella, E., Martín, M. P., Tellería, M. T., López-Jurado, L. F., Marco, A., & Diéguez-Uribeondo, J. (2010). *Fusarium solani* is responsible for mass mortalities in nests of loggerhead sea turtle, *Caretta caretta*, in Boavista, Cape Verde. *FEMS Microbiology Letters*, 312(2), 192-200. <https://doi.org/10.1111/j.1574-6968.2010.02116.x>
- Sarmiento-Ramírez, J. M., Abella-Pérez, E., Phillott, A. D., Sim, J., van West, P., Martín, M. P., Marco, A., & Diéguez-Uribeondo, J. (2014). Global distribution of two fungal pathogens threatening endangered sea turtles. *PLOS ONE*, 9(1), Article e85853. <https://doi.org/10.1371/journal.pone.0085853>
- Short, D. P. G., O'Donnell, K., Thrane, U., Nielsen, K. F., Zhang, N., Juba, J. H., & Geiser, D. M. (2013). Phylogenetic relationships among members of the *Fusarium solani* species complex in human infections and the descriptions of *F. keratoplasticum* sp. nov. and *F. petroliphilum* stat. nov. *Fungal Genetics and Biology*, 53, 59-70. <https://doi.org/10.1016/j.fgb.2013.01.004>

- Sidique, S. N. M., Azuddin, N. F., & Joseph, J. (2017). First report of *Fusarium* species at nesting sites of endangered sea turtles in Terengganu and Melaka, Malaysia. *Malaysian Applied Biology*, *46*(3), 195-205.
- Smyth, C. W., Sarmiento-Ramírez, J. M., Short, D. P. G., Diéguez-Uribeondo, J., O'Donnell, K., & Geiser, D. M. (2019). Unraveling the ecology and epidemiology of an emerging fungal disease, sea turtle egg fusariosis (STEF). *PLOS Pathogens*, *15*(5), Article e1007682. <https://doi.org/10.1371/journal.ppat.1007682>
- Sukarno, W., Ridzuan, M. A. M., Zabawi, S. M., Najib, R. M., Aziim, M. Y. A., Mansor, Y., Azwa, A. H., Farizan, S., Khasah, M. M. K., Robert, L. H. F., Karim, S. A., Zakaria, S., Abdullah, S. A. K. S., Zulkifli, T., Wahidah, M. A., Wahab, A. A., & Fahiezah, S. N. (2007). *Prosedur piawaian pengurusan penyu Semenanjung Malaysia* [Standard operating procedure of sea turtle management in Peninsular Malaysia]. Jabatan Perikanan Malaysia.
- Summerell, B. A., Salleh, B., & Leslie, J. F. (2003). A utilitarian approach to *Fusarium* identification. *Plant Disease*, *87*(2), 117-128. <https://doi.org/10.1094/PDIS.2003.87.2.117>
- Trullas, S. C., & Paladino, F. V. (2007). Micro-environment of olive ridley turtle nests deposited during an aggregated nesting event. *Journal of Zoology*, *272*(4), 367-376. <https://doi.org/10.1111/j.1469-7998.2006.00277.x>
- Wyneken, J., Burke, T. J., Salmon, M., & Pedersen, D. K. (1988). Egg failure in natural and relocated sea turtle nests. *Journal of Herpetology*, *22*(1), 88-96. <https://doi.org/10.2307/1564360>
- Zhang, N., O'Donnell, K., Sutton, D. A., Nalim, F. A., Summerbell, R. C., Padhye, A. A., & Geiser, D. M. (2006). Members of the *Fusarium solani* species complex that cause infections in both humans and plants are common in the environment. *Journal of Clinical Microbiology*, *44*(6), 2186-2190. <https://doi.org/10.1128/JCM.00120-06>



Review Article

Progress, Trends and Development of Drying Studies on Coconut Kernel Products: A Review

Yahya Sahari^{1,2}, Mohd Shamsul Anuar^{2*}, Mohd Zuhair Mohd Nor², Nur Hamizah Abdul Ghani² and Suraya Mohd Tahir³

¹Postharvest and Food Processing Mechanization Program, Engineering Research Centre, Malaysian Agricultural Research and Development Institute (MARDI), 43400 Serdang, Selangor, Malaysia

²Department of Process and Food Engineering, Faculty of Engineering, Universiti Putra Malaysia, 43400 UPM, Serdang, Selangor, Malaysia

³Department of Mechanical and Manufacturing Engineering, Faculty of Engineering, Universiti Putra Malaysia, 43400 UPM, Serdang, Selangor, Malaysia

ABSTRACT

There are several different forms of coconut kernel products, such as copra, desiccated coconut, coconut chips, strips, and flakes, each with its identity, industrial standard, and use in the food sector. In view of this, many studies concentrate on drying kinetics and the quality of the final dried product and extend from laboratory-scale research to industrial operations. This article discusses the application of various drying processes for various types of coconut kernel products, the pre-treatment involved prior to drying and some qualitative aspects associated with the final product. The use of mathematical modelling in various drying techniques was also examined and compared in this article. The effects of drying parameters such as air temperature, velocity, and pre-treatment on drying rate, time, colour quality, energy consumption, and yield are particularly interesting. Future suggestions and directions are emphasised and featured to fill the research gap in this product and sector.

Keywords: Coconut kernel, dried quality product, drying kinetics, drying methods, drying model

ARTICLE INFO

Article history:

Received: 24 September 2022

Accepted: 25 January 2023

Published: 27 July 2023

DOI: <https://doi.org/10.47836/pjst.31.5.30>

E-mail addresses:

gs62219@student.upm.edu.my (Yahya Sahari)

mshamsul@upm.edu.my (Mohd Shamsul Anuar)

zuhair@upm.edu.my (Mohd Zuhair Mohd Nor)

nurhamizah@upm.edu.my (Nur Hamizah Abdul Ghani)

su_mtahir@upm.edu.my (Suraya Mohd Tahir)

* Corresponding author

INTRODUCTION

In post-harvesting processes, drying or dehydration is crucial to preserve food materials before further processing. Due to the high moisture and nutritional content in most agricultural products, they are

susceptible to spoilage, which could end up lowering the shelf life and quality of the product (These, 2016). The degradation of product quality is mainly due to microbial, chemical, and physical actions that occur within the product and its surroundings (Lamidi et al., 2019). Therefore, food materials must be dried or dehydrated to retain their quality for longer periods. In principle, drying depends on two fundamental factors (heat and mass transfer). When heat is applied to the product, water vapour is eliminated from its surface and released into the surrounding environment, resulting in a dried material with a longer shelf life and reduced water activity in food products (Erkmen & Bozoglu, 2016).

In drying food products, heat can be applied via conduction, convection, radiation, or a combination of these methods. In principle, sun drying and solar drying are considered natural drying, whereas convective drying, fluidised bed drying, microwave drying, infrared drying, heat pump drying, and freeze drying are categorised as artificial drying. Recently, there have been remarkable developments in the use of novel drying techniques such as microwave, infrared, pulsed electric field, ultraviolet, and ohmic, which improve drying efficiency and product quality (Guiné, 2018). Apart from that, most agricultural products also undergo pre-treatment prior to drying to retain the nutrients better and enhance the appearance of the dried product (Hii & Ogugo, 2014).

It is also true for coconut kernel-based products such as desiccated coconut, copra, coconut chips and flakes, and coconut strips and slices (Figure 1), whereby drying is needed in the production of each product. At complete development and full maturity, the coconut comprises an average of 33% husk, 16% shell, 33% kernel, and 18% coconut water (Konan et al., 2009). Generally, the coconut fruit is spherical to oval with a rough outer husk, and the size varies depending on the source and breed (Arulandoo et al., 2017). The kernel of a mature coconut is rich in oil and, in fact, the most valuable part of the fruit, as it provides an important ingredient in the food. The details of fresh coconut kernel composition can be referred to in Table 1. Coconuts play a significant part in human eating because of the presence of physiologically vital components such as fatty acids. Natural coconut fat in the diet helps improve the immune system's anti-inflammatory response (Joshi et al., 2020).

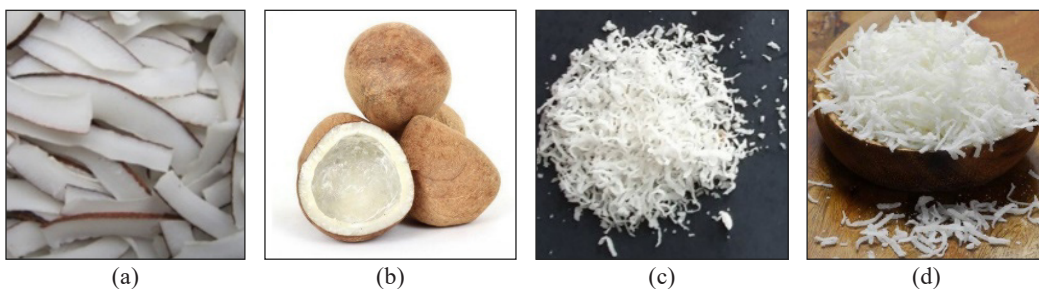


Figure 1. Common coconut kernel products: (a) coconut slices; (b) copra; (c) desiccated/grated coconut; (d) sweetened coconut flakes

Fresh coconut meat is high in protein, lipids, and carbohydrates, making it an excellent supplement for the growth of microorganisms (Gupta et al., 2010). Subsequently, they have a very short shelf life, and during processing and storage, coconut meats go through physico-chemical and biological changes like browning, drying out or hardening, changes in texture, mould growth, and others (Gupta et al., 2010). In the coconut industry, the drying process is vital in downstream unit operations. While there are numerous post-harvest losses, the efficacy of the drying process is the most critical stage since it can determine subsequent losses in product quality and market prices (Mithra et al., 2013). It is true, as Nor et al. (2021) mentioned, that traditional and conventional drying of coconut kernels could potentially degrade the quality of final and subsequent products with oxidative rancidity, aflatoxin contamination, unpleasant colour, and aroma.

Therefore, by determining through experiments what proper drying methods and strategies are, they can contribute to the quality of the coconut kernel-based products being produced. A harmful loss can occur during post-harvest processing if there is a lack of knowledge about correct drying techniques. As with many other agricultural products, a thorough understanding of the physical and chemical changes during drying is essential. The physico-chemical properties and related parameters of air as a medium (temperature, thermal conductivity, specific heat capacity, air velocity, relative humidity, and density) are required to analyse the drying mechanism. Size, shape, dimension, structure, porosity, and specific types of product interest are also highlighted in terms of the product's physical properties. These factors play a significant role in drying kinetics and mechanisms (Mühlbauer & Müller, 2020a). Furthermore, adequate drying kinetics models must be introduced and established to describe the quantitative monitoring of physico-chemical changes during the process. On top of that, the mathematical considerations related to proper assumptions and parametric considerations in the design of the dryers would lead to an optimum process design, less energy consumption, and increased profitability (Inyang et al., 2018).

Therefore, this paper aims to let the reader understand the effect and impact of drying methods and strategies on the quality of coconut kernel-based products. This paper will also focus on the selected types of coconut kernel-based products, pre-treatment, drying strategies, energy requirements, drying kinetics and modelling, and final product quality.

Table 1
Fresh coconut kernel composition per 100 g (Lal et al., 2003)

Water	36.3 ml
Protein	4.5 g
Fat	41.6 g
Carbohydrates	13 g
Fibre	3.6 g
Minerals	1.0 g
Among the minerals present:	
Ca	10 mg
P	24 mg
Fe	1.7 mg

COCONUT KERNEL PRODUCTS

Copra

Copra is the main traditional product processed from coconut and is always perceived as a low-value product. As such, more than half of the world's coconut production is converted into copra. Copra is a dried endosperm and a source of coconut oil. It is an intermediate product and can be classified into edible copra and milling copra (Mithra et al., 2013). Sun drying, solar drying, conventional smoke kiln drying, indirect drying, and cabinet drying are some methods used to make copra. Copra is always referred to as an inferior-quality product, where the oil extracted from it is of poor quality and further refinement is expected to fulfil global standards.

The important factors in copra processing are to quickly reduce the moisture level of the coconut to 6% w.b. after splitting the coconut to avoid microbiological deterioration and to preserve the oil composition and quality (Thanaraj et al., 2007). Indonesia boasts the world's largest coconut plantation and produces most world's copra. Nevertheless, the quality of copra produced in rural regions is somewhat low and is complained about by the international market as it contains aflatoxin (Santosa et al., 2019). Small farmers and smallholders in India also face problems related to copra quality. Coconut products are mostly traded internationally because of their major processing product, copra. These days, as significant coconut-creating nations are capable and outfitted with modern crushing units that allow them to export crude oil, almost no more traded copra is traded on the international market (Prades et al., 2016).

Desiccated Coconut

Desiccated coconut is a significant commercial product with global demand and is used in various food industries, particularly confectionery and bakery (Mithra et al., 2013). In another study reported by (Nelsonkanem et al., 2020), dried shredded coconut or desiccated coconut could also be used to produce coconut oil by extracting the oil using a mechanical press. Generally, desiccated coconut is produced from fully developed and matured coconut kernels under strict hygienic conditions. According to Marikkar & Madurapperuma (2012), a fresh mature coconut kernel's granulated or shredded white meat is dried to make desiccated coconut. It should contain less than 3% moisture content and no less than 60% oil. Oil contents of less than 60% can be considered low-fat desiccated coconut. After the coconut milk is removed from the coconut meat, low-fat desiccated coconut is sometimes called "coconut residue." Desiccated coconut is considered a contemporary, non-traditional coconut product traded in the world market. The Philippines and Indonesia, as members of the Asian and Pacific Coconut Community (APCC), are the leading exporters of desiccated coconut, accounting for 44% of total exports (Jayasekhar et al., 2017).

Coconut Flakes/Chips

In principle, coconut flakes are made from coconut residue, a by-product of coconut milk production. Like any other snack item, coconut chips or flakes are available in salted or sweetened varieties. It also has distinct characteristics such as no preservatives, no frying in oil, no loss of flavour in the kernel, and is sometimes treated with osmotic dehydration or agents prior to drying (Pravitha et al., 2022). Manikantan et al. (2015) suggested that coconut kernels must be parred, blanched, osmotically dehydrated, and dried before being made into ready-to-eat coconut chips.

PRE-TREATMENT EFFECTS ON DRYING RATE AND QUALITY OF COCONUT KERNEL PRODUCT

In most situations, fresh agricultural products are perishable, decaying quickly due to their high moisture content and physical tender texture. While drying is one of the most frequent preservation procedures, pre-treatment prior to drying is equally essential for producing a high-quality end product. According to Yu et al. (2017), prior to drying, physical and chemical pre-treatments can be given to fruits and vegetables to reduce drying time, reduce energy consumption and protect product quality.

Pre-treatment is a substantial operation that aims to increase the drying rate, maintain quality, and decrease the microbial load of products (Deng et al., 2019). It is also true when pre-treatments are applied to coconut kernel products to achieve certain product qualities and optimum processing parameters. The coconut meat was immersed in a 50-ppm chlorine solution for 5 minutes to inactivate microorganisms, according to (Madhiyanon et al., 2009; Niamnuay & Devahastin, 2005). In another attempt, Chantaro et al. (2016) compared three different pre-treatments ($K_2S_2O_5$, $CaCl_2$, and hot water blanching) on coconut kernel cubes. The coconut cubes were then subjected to a sucrose solution for 24 hours prior to drying. The authors discovered that hot water blanching at 95°C for 5 minutes increased the total sugar and lightness (L^*) of dried osmotic dehydrated coconut cubes, improving the colour and making the product more consumer-acceptable. Furthermore, Waisundara et al. (2007) revealed that the pre-treatment used (blanching and freezing) had suppressed the chemical and enzymatic deterioration of coconut kernels, whereas the untreated coconut kernels are likely to result in the loss of quality of the coconut milk when extracted.

Meanwhile, after blanching in hot water at 90–95°C for 2 minutes, coconut slices are dipped in an osmotic medium known as a syrup for one hour to create coconut chips (Manikantan et al., 2015). Kamalanathan & Meyyappan (2014) also reported a similar method, as the authors applied to blanching and immersing the coconut in a citric solution followed by osmotic dehydration. According to Manikantan et al. (2015), the osmotic medium differs based on the type of coconut chips. The rule of thumb is that the coconut slices after osmotic dehydration need to be dried immediately. Sarkar et al. (2020)

discovered that osmotic dehydration reduces the drying time of coconut samples since the initial water content is lost. In contrast, no special pre-treatment has been reported with regard to copra production. As such, using chemical dip can only add to the cost of processing, and health authorities also raise the concern about chemical residues. Very often, coconut kernel products such as dried grated coconut or desiccated coconut must go through some kind of pre-treatment prior to drying, as this will ensure that the colour and quality of the product meet industrial standards. However, several laboratory studies that focused primarily on drying kinetics did not apply pre-treatment prior to hot air drying (Wutthigarn et al., 2018; Yahya et al., 2020). Kurniawan et al. (2021) revealed the necessity of having a steam-blanching process during the production of desiccated coconut. Devi and Ghatani (2022) also recommended a similar approach to reduce the microbial load of coconut flakes before the drying process.

Hot water blanching, which involves immersing fresh products at a steady temperature of 70–100°C for several minutes before drying, is still a popular pre-treatment (Guida et al., 2013). On the other hand, oxidase inactivation is also linked to the significant decline in food quality during the hot water blanching process, particularly with the emergence of cooked-off tastes, colour changes, and the loss of thermosensitive components (Deng et al., 2019). Since hot water blanching produces much wastewater, which raises the pollution level, steam blanching, high humidity hot air impingement blanching, ohmic blanching, ultrasound, infrared and microwave blanching are all alternate thermal blanching methods that are quite appealing for the food sector to adopt them.

EFFECTS OF DRYING METHODS AND STRATEGIES ON THE QUALITY OF COCONUT KERNEL PRODUCTS

Sun Drying and Kiln Drying

Copra is typically dried using one of two methods: kiln drying or sun drying. Sun drying copra takes roughly 5 to 6 days during the dry season, as illustrated in Figure 2. Due to unpredictable weather, copra becomes dark, rancid, and mouldy as the drying rate is interrupted during sun drying. A similar finding by Mohanraj & Chandrasekar (2008a) reported that sun drying was very slow compared to solar drying due to lower heat and mass transfer coefficients. The authors also revealed that the moisture content of copra was increased by 0.11.0% due to desorption during cloudy hours; hence, nearly 25% of the copra was affected



Figure 2. Sun drying of copra (Arun et al., 2014)

by bacterial infection due to the extended drying period. Consequently, poor quality copra would not only reduce the market prices but, to some extent, increase health hazards due to contamination of polycyclic aromatic hydrocarbons (PAH) and also aflatoxin. The quality of extracted coconut oil from low-quality copra could also be affected; hence, additional extraction oil refinement is required to meet international requirements.

Direct kiln drying, on the other hand, uses smoke as a media and directly contacts the copra, and this method is likely to form PAH in copra. It is supported by Thanaraj et al. (2007), who revealed that the thermal efficiency of the kiln dryer was better than the solar dryer. Nonetheless, direct contact with smoke and kiln dryer burnt gases may result in the formation of carcinogenic substances. There was no chance to make white copra with a direct kiln drier. A semi-direct kiln dryer was also available, which appeared adaptable and economical for small farmers. Indirect kiln dryers of a different type, in which smoke does not contact the coconut kernel, were studied by Dippon and Villaruep (1996). The authors also noted that the indirect kiln dryer outperformed the direct kin dryer in terms of copra quality. However, maintenance and repair costs must be considered because the dryer component is exposed to high temperatures and strong gases, which would cause corrosion. There is also a concern about considerable heat loss unless the heat exchanger is designed efficiently.

Convective/Cabinet Drying

Unlike a kiln or a smoke dryer, a convective dryer or so-called cabinet dryer is used to dry coconut kernels by passing uncontaminated hot air through the product. In this case, the product can be guaranteed to be clean and white. Figure 3 shows the laboratory scale of a cabinet dryer for drying coconut kernels. Samson (1971) study's suggested that fresh coconut meat may withstand temperatures up to 100°C without considerable protein solubility loss. It also indicated that protein solubility would be low when the coconut meat turned brown and had a toasted odour. There was an attempt by Deepa et al. (2015) to use cabinet drying to dry copra at different air temperatures (60, 70, 80, and 90 °C). It was found that the drying temperature of 90 °C had the least drying time and took only 12 hours to reach the desired moisture content, whereas 60 °C had the longest drying period of 42 hours. On top of that, Deepa et al. (2015) also noticed that the mouldy cups of the kernel were higher (5%) at 60 °C compared to 90 °C with only 2%. Other than that, the higher temperature also contributed to the higher percentage of chips due to the case hardening of copra, hence the small broken pieces.



Figure 3. Hot air drying of copra (Pestaño & Jose, 2016)

Interestingly, the recovery of oil extracted from samples dried at 60, 70, 80, and 90 °C was 65.27%, 67.10%, 42.70%, and 40.1%, respectively.

Another attempt was made by Guarte et al. (1996), where the study focused on the single layer of halved nuts, consisting of the meat and the shell. The divided nuts were dried at temperatures ranging from 40 to 100 °C and oriented upwards and downwards with respect to the direction of the air stream, and drying times decreased exponentially as the drying temperature increased. For producing high-quality copra and coconut oil in the shortest amount of time, a drying temperature of 90 °C is recommended. Guarte et al. (1996) also concluded that there was no significant influence on the position of halved nuts during drying. The findings from Deepa et al. (2015) and Guarte et al. (1996) are consistent with the research done by Satter (2001), where moisture removal from wet copra increases with temperature. Nevertheless, the study also mentioned a limitation to the temperature used without compromising copra quality. Moreover, prolonged exposure of copra to temperatures beyond 90 °C may cause the copra surface to become hard and scorched as a result of further moisture and oil removal.

A recent attempt also declared that a handy electrical heat dryer, designed, fabricated, and tested by Thiyagarajan et al. (2020), can considerably reduce the drying period of copra. The results also revealed that the copra could reach its final moisture content of 6% in just 11 hours with better quality in colour and aroma. In a different approach to drying desiccated coconut, Yahya et al. (2020) reported that a specially designed cabinet dryer using the tumbling effect had proven that temperature, air velocity, and rotational speed of the tumbler played a significant role in the drying time of desiccated coconut. Unlike desiccated coconut, coconut residue, also called low-fat desiccated coconut, is a by-product of coconut milk extraction. At a 50–110 °C drying temperature, the drying time and drying rate (DR) were 540–100 minutes and 0.0048–0.0182 g water/g minutes, respectively (Wutthigarn et al., 2018). A research study by Jongyingcharoen et al. (2019) also likewise tracked down those drying temperatures (50–80 °C) and layer thickness (5–10 mm), which contributed altogether to the drying time, whiteness, and oil content of coconut residue.

On the other hand, there was a study done by Prieto et al. (2011) with regard to drying green coconut pulp. It was reported that drying in a cabinet dryer at 70 °C led to a better and more snack-like product after 8 hours of drying. However, it largely depends on the degree of maturity and fat content of the coconut. In an attempt to use a laboratory cabinet dryer, many authors (Abidin et al., 2014; Pestano & Jose, 2016; Sarkar et al., 2020) have discovered interesting findings with regard to coconut slices, copra, coconut cut, and desiccated coconut, respectively.

Fluidised Bed Drying

Fluidised bed drying is one of the most successful due to its extensive mixing behaviour, which speeds up heat and mass product transfer. Due to the amount of free water on the

product surface, the moisture content reduced significantly in the early drying stage, as expected, before it became more difficult to expel water. The chopped coconut was dried at drying temperatures of 60–120°C at a constant velocity of 2.5 m/s to dry from around 105% d.b. to roughly 3% d.b., according to Madhiyanon et al. (2009). In another study, Niamnuy and Devahastin (2005) discovered that air velocity and temperature influence the drying kinetics and qualitative features of dried coconut, such as colour and surface oil content.

Interestingly, air velocity has played a more important role in determining the quantity of oil on the surface of dried coconut than the inlet temperature. For green coconut pulp, drying at 70°C using a pulsed fluidised bed dryer was reported to be advantageous due to its high productivity and ability to produce a snack-like product (Prieto et al., 2011). A schematic diagram of a fluidised bed dryer can be seen in Figure 4.

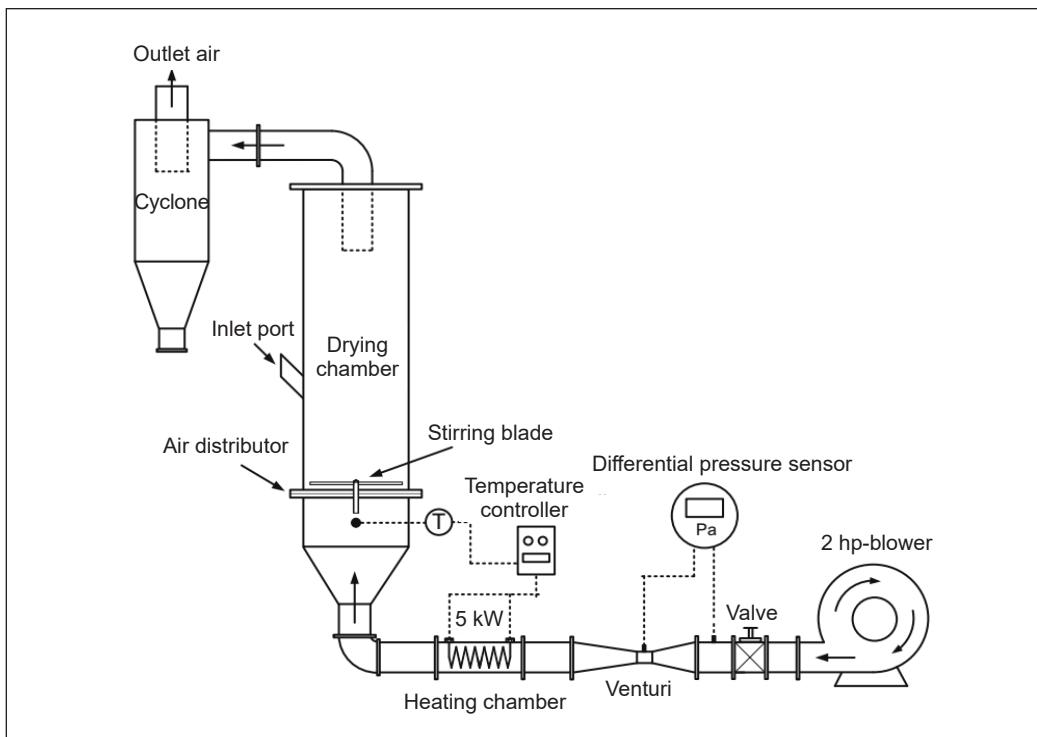


Figure 4. Schematic diagram of fluidised bed dryer for drying coconut kernel product (Madhiyanon et al., 2009)

Solar Drying

Solar dryers are becoming more popular as a drying method because they are cost-effective and energy-efficient. Nevertheless, the efficiency of solar dryers depends on the type, design, and material used. Figure 5 shows the schematic diagram of a solar dryer used to dry copra. A solar dryer with an evacuated tube collector achieved 70°C of drying air

and could dry 20 kg of copra in 28 hours from an initial moisture content of 52.5% to a final moisture content of 7%, according to Krishna and Mathew (2018). Apart from that, the efficiency of the evacuated solar collector, which is incorporated with 30 tubes, was claimed to reach 44%, producing a better quality of copra with a minimum drying time. In another approach by Mohanraj and Chandrasekar (2008b), it was suggested that applying forced air convection in a solar dryer could produce more than 75% of high-quality milling copra grade 1 (MCG1) with 24% thermal efficiency. The authors also mentioned that the copra obtained was free of smoke, dust, and rodent damage.

Research findings by Thanaraj et al. (2007) also point to the advantages of solar dryers. It was found that the solar dryer was superior to the kiln dryer when it came to the high quality and yield of the white copra. Similarly, Arun et al. (2014) discovered that combining a solar tunnel greenhouse dryer with a biomass backup heater shortened the drying time of copra by allowing the biomass heater to deliver heat to the dryer during periods of low sunlight intensity. As a result, copra dried in a solar tunnel greenhouse dryer will be of higher quality than copra dried in the open sun.

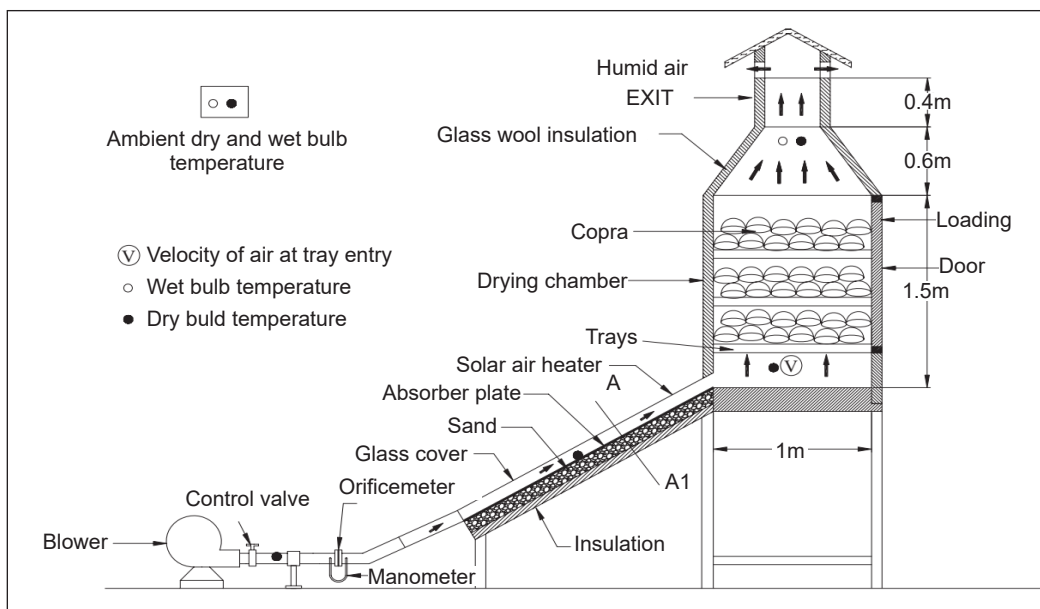


Figure 5. Schematic diagram of the solar dryer for drying copra (Mohanraj & Chandrasekar, 2008b)

Heat Pump Drying

A heat pump dryer is a promising technology for preserving product quality while reducing drying energy usage, especially for high-value products such as fruits and vegetables. To preserve the quality of the product, Mohanraj et al. (2008) found a potential method to dry copra using a heat pump. The experiments were conducted at a significantly lower

temperature (40 °C) with a 1.5 m/s air velocity. According to the findings, the moisture content of the copra was reduced from 52.6% (wet basis) to 8.5% in 48 hours. Because 92.7% of the dried copra was classified as milling copra grade 1 (MCG1), heat pump drying is better suited for large-scale copra processing and generating high-quality oil (MCG1). Even though the drying period is longer than fluidised bed drying, heat pump drying retains colour, has better physical properties, and is suitable for heat-sensitive products (Salehi, 2021).

Furthermore, with the ability to recover latent and sensible heat, energy efficiency in heat pump drying can be significantly improved, which would otherwise be wasted in the environment in conventional dryers (Fayose & Huan, 2016). A schematic diagram of heat pump drying is shown in Figure 6.

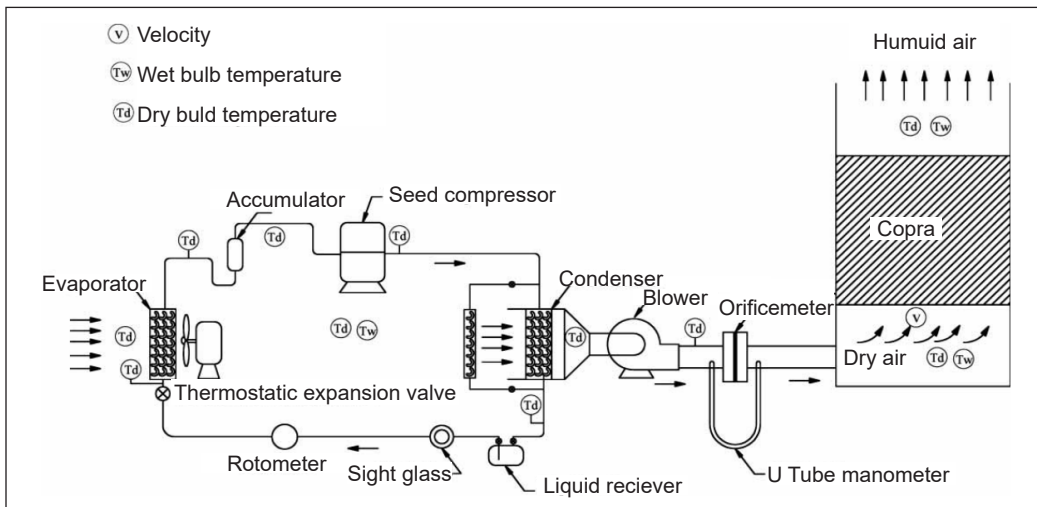


Figure 6. Schematic diagram of heat pump drying (Mohanraj et al., 2008)

Microwave Drying

One modern technique is microwave drying, which employs radiation as a heat source to dry food products. Microwave drying is a potential food dehydration method since it frequently results in a significant decrease in drying time and improved product quality (Feng et al., 2012). Using microwave energy to dry food products is a good solution to some of the problems with traditional drying. Domestic microwave ovens expose food to microwave radiation, typically at 2450 MHz (Sutar & Prasad, 2008).

Various food products have been investigated using microwave dryings, such as corn (Liu et al., 2021), radish (Lee et al., 2018), and bamboo shoots (Bal et al., 2010). With regard to coconut, there was also a study done by Moses et al. (2013). The study found that microwave drying at 180 and 360 W improved the desiccated coconut's colour, indicating that the microwave technique could potentially be used to produce a better-quality product.

However, desiccated coconut had a higher rehydration capacity at much higher microwave powers (720 and 900 W) as a result of the structural damage caused by overheating and rapid drying (Moses et al., 2013). Similar findings were also reported by Tepe and Tepe (2020), whereby the rehydration ratio of dried apple slices using the microwave was greater than hot air drying. The details of the drying parameters and the effect of drying methods on coconut kernel products for the past ten years are summarised in Table 2.

Table 2
Summary of drying methods, parameters, and significant findings of coconut kernel products for the past ten years

Drying method	Coconut kernel product	Drying parameters	Significant finding(s)	References
Solar dryer	Copra	The drying chamber was at 70°C. The collector efficiency was 44%.	Required 28 hours to complete drying of copra.	(Krishna & Mathew, 2018)
		Solar tunnel greenhouse dryer type. Combine polyethene film with biomass backup heater.	It required about 44 hours to complete the drying of the copra. Biomass heater provides backup heating. Copra produced was better than sun drying.	(Arun et al., 2014)
Fluidised bed dryer	Chopped coconut	Comparing parameters: First part: inlet air temperature of 65°C and air velocity of 3.82 m/s. Second part: stepwise change in inlet air temperature of 65, 80, and 120°C, and air velocity of 5.94, 4.98, and 3.82 m/s.	Drying from 60% d.b to 2% d.b. The colour of the dried product was most affected by inlet air temperature, while the quantity of surface oil was more affected by air velocity	(Deng et al., 2019)
	Coconut residue	Drying air temperature of 70–100°C and air velocity of 1.07 m/s	The drying behaviour of coconut residue was significantly affected by the air temperatures	(Kalayanamitra & Assawarachan, 2022)
Microwave dryer	Desiccated coconut	Samples with uniform size (~ 1 cm) were dried at power levels ranging from 180–900 W.	Colour changes were minimum at 180 and 360 W compared to conventional drying. Higher power levels caused higher rehydration capacity	(Moses et al., 2013)
Convective and cabinet dryer	Copra	Cabinet dryer with different drying air temperatures (60, 70, 80, and 90°C).	Required 24 hours of drying copra from 52% (w.b) to 6.1% (w.b) at 70°C. The fastest drying period (12 hours) was at 90°C. Based on the BIS standard, the best quality copra was obtained at a drying temperature of 70°C.	(Deepa et al., 2015)

Table 2 (continue)

Drying method	Coconut kernel product	Drying parameters	Significant finding(s)	References
		The handy electrical convective heat dryer with SMER was about 0.12 kg/kWh. It has a drying rate of 0.0001 kg/s with 0.2265 m ³ /s of mass air flow rate.	Managed to dry copra in 11 hours, with 92.7% of the copra graded as MCG1.	(Thiyagarajan et al., 2020)
	Desiccated coconut	Three factors of drying parameters (air temperature, air velocity, and rotational speed of the tumbler) were studied using a convective dryer with a tumbler.	A combination of 60°C, 6 RPM, and 4.31 ms ⁻¹ had the shortest drying time and the highest drying rate. The drying rate rose as the air temperature, rotating speed, and air velocity increased.	(Yahya et al., 2020)
	Coconut residue/low-fat desiccated coconut	Air drying temperatures of 50–80°C and 5–15 mm layer thickness.	Air drying temperatures and layer thickness essentially impacted drying time, whiteness, and oil content buildup. In the shortest drying period, the highest temperature and thinnest layer were achieved (70 minutes).	(Jongying-charoen et al., 2019)
		A thickness of 1 cm of coconut residue and drying at 50, 60, 70, 90, and 110°C. The air velocity was fixed at 1 m/s. The targeted final moisture content was 0.03 g water/g dry matter.	An increase in drying temperature by 20°C reduced drying time by 50 minutes or higher.	(Wutthigarn et al., 2018)
	Coconut chips	Immediately after osmotic dehydration, the samples were dried using a forced hot air electric tray dryer at 70–80°C.	The drying time was about (5–6 hours)	(Manikantan et al., 2015)
	Coconut slices	Hot air batch dryer with about 30–40% relative humidity. Drying air temperatures (60–80°C) and a constant air velocity of 0.80 ms ⁻¹ were used.	At 80°C, it produced the shortest drying time of 181.05 minutes.	(Pestaño, 2015)
		Hot air batch dryer with a single layer of thinly sliced coconut meat.	Produced white copra with high-quality coconut oil and clean white pressed cake. High-quality copra with aflatoxin and PAH-free.	(Pestaño & Jose, 2016)

Table 2 (continue)

Drying method	Coconut kernel product	Drying parameters	Significant finding(s)	References
	Coconut strips	The pre-treated coconut strips (three different sucrose solution concentrations and immersed in three different water bath temperatures) were dried in an oven at a drying temperature of 60 °C.	As the pre-treatment temperature increased, the initial drying rates were reduced.	(Agarry & Aworanti, 2012)
	Coconut cuts	Pre-treated with different concentrations of sugar solutions (40, 50, and 60° Brix), and the temperature of the solution was maintained at 35, 45, and 55°C. The drying process was then done at 60°C and 60% relative humidity.	Osmotic dehydration reduces the drying time considerably. It also had a considerable impact on coconut thermal air drying.	(Sarkar et al., 2020)

MATHEMATICAL MODELLING OF COCONUT KERNEL PRODUCT

A proper understanding and research of physical phenomena during the drying process are crucial to identify the behaviour of the product being dried. For this reason, drying kinetics or mathematical modelling of drying is a necessary tool for quantitatively describing the physico-chemical changes of a product. Thin layer drying equations are one of the most frequently used by researchers and can be categorised into three different types of models, such as theoretical, semi-empirical, and empirical (Mühlbauer & Müller, 2020).

These models have been used in identifying and verifying appropriate drying methods and parameters by obtaining the best-fit kinetic model for certain drying conditions and products. There are many types of products whose drying behaviour can be explained through drying kinetic models. Table 3 shows the drying kinetics models, effective moisture diffusivity and activation energy for coconut kernel products using different drying methods. Theoretical models are based on Fick’s second law of diffusion, where D represents the diffusion coefficient as shown in Equation 1:

$$\partial MC/\partial t = \nabla^2 . D . MC \tag{1}$$

where MC is the moisture content on a dry basis (d.b), t is the time (s), and D is the moisture diffusivity (m^2/s). Like many agricultural and food products, they can be prepared and

processed into several types of geometries to suit the final product requirement and the unit operation involved. However, to solve the equation, geometry has to be idealised as a sphere, cylindrical or cuboid with assumptions such as homogeneity, uniform temperature distribution, neglect of volume shrinkage or constant moisture diffusivity, which can lead to substantial differences between experimental data and calculated drying curves. On the other hand, Semi-empirical models are based on diffusion theory and are thus valid within the experimental range of temperature, relative humidity, air velocity and moisture content. It can also be described by Newton's Law of Cooling (Equation 2):

$$MR = \frac{MC(t) - MC_{eq}}{MC_1 - MC_{eq}} = \exp(-k_o \cdot t) \quad (2)$$

where MR is the moisture ratio, $MC(t)$ is the moisture content of a product measured or determined during drying, MC_1 is the moisture content of a product prior to the start of drying, MC_{eq} is the moisture content of a product in equilibrium with mean dry bulb temperature and relative humidity of the drying air, t is the time (s) and k_o represents the drying coefficient. Therefore, semi-empirical models provide some understanding of the transport processes during the drying operation. Nevertheless, due to some simplifications required, accuracy is still lacking. Researchers have used and applied many semi-empirical models, such as Lewis/Newton, Page, Henderson/Pabis and Two-term, Logarithmic.

Unlike the semi-empirical model, the empirical model strongly relies upon experimental conditions without thought of the transport processes and fundamentals of drying. Some empirical models observed that the Page model adequately captured the drying characteristics of sliced coconut meat at 80°C in their kinetic modelling of coconut kernel products Kalayanamitra and Assawarachan (2022). Research findings by Madamba (2003) and Pestaño (2015) also point towards drying kinetic modelling on osmotic coconut strips and found that the Page model better fit the experimental data. Interestingly, the Page model successfully fits the coconut kernel product and other commodities, such as tubers (Vera et al., 2021). The success of Page's equation is connected to incorporating the term n in the equation and to a phenomenological justification for its consideration tracked down through the solution of diffusion phenomena (Simpson et al., 2017).

In another experiment with grated coconut, Abidin et al. (2014) reported that the Logarithmic model at 60°C is the most accurate prediction for the drying kinetics of grated coconut via oven drying. Nonetheless, the author only compared a few models in the trials. Wutthigarn et al. (2018) also examined a similar drying method, whereby a Linear plus-exponential model provided the best fit for drying coconut residue or so-called low-fat desiccated coconut. The only thing lacking in the studies made by Abidin et al. (2014), Pestaño (2015) and Wutthigarn et al. (2018) was no further investigation

on the effective moisture diffusivity and activation energy. In a different study using the fluidised bed drying method, Madhiyanon et al. (2009) found that the Modified Henderson and Pabis model was the most precise model to describe the drying behaviour of chopped coconut, as reflected by the highest value of R^2 and the lowest value of root mean square error (RMSE). In contrast, Kalayanamitra and Assawarachan (2022) reported that the Midilli model had satisfactorily predicted the drying behaviour of coconut residue under the same fluidised bed drying method. It could be due to the different types of coconut kernel products, which behave differently when it comes to drying.

Interestingly, some researchers that worked on coconut residue products had suggested different drying models: linear plus exponential and Midilli using hot air and fluidised bed drying, respectively (Kalayanamitra & Assawarachan, 2022; Wutthigarn et al., 2018). Another attempt by Moses et al. (2013) claimed that the Midilli model better predicted desiccated coconut's drying behaviour during microwave drying.

According to Mohanraj and Chandrasekar (2008b), effective moisture diffusivity is determined using Fick's diffusion equation for objects having spherical geometry, such as chopped coconut and using Equation 3 as follows:

$$MR = \frac{6}{\pi^2} \sum_{n=1}^{\infty} \frac{1}{n^2} \left(-\frac{n^2 \pi^2 D_{eff} t}{r^2} \right) \tag{3}$$

where D_{eff} is the effective diffusivity (m^2/s), r is the radius of the sphere (m), and n is the positive integer. Taking into consideration the first term in the series Equation 4 and the natural logarithmic form as follows:

$$\ln MR = \ln \left(\frac{6}{\pi^2} \right) - \left(\frac{\pi^2 D_{eff} t}{r^2} \right) \tag{4}$$

Other than the assumption of sphere geometry, there was also a study done by (Agarry & Aworanti, 2012), where the assumption of the slab was used for coconut strips. Equation 5 is as follows:

$$\ln MR = \ln \left(\frac{8}{\pi^2} \right) - \left(\frac{\pi^2 D_{eff} t}{4l^2} \right) \tag{5}$$

where l is the thickness (m) to determine the effective diffusivity coefficient (D_{eff}). First, the slope of the relationships between $\ln MR$ and time (Equation 4) is computed, and D_{eff} is then calculated by the following Equation 6:

$$Slope = \frac{\pi^2 D_{eff}}{r^2} \tag{6}$$

In the case of the effective moisture diffusivity value of coconut kernel product, it can be seen that Madhiyanon et al. (2009) reported that the value was higher than

the one produced by Agarry and Aworanti (2012). The different drying methods and parameters predominantly cause the difference in value. Compared to a fixed bed or tray dryer, fluidised bed drying produces a more consistent temperature, which speeds up the moisture removal of the product. It is proven as the moisture diffusivity of chopped coconut using a fluidised bed dryer (Madhiyanon et al., 2009) was much higher as compared to coconut strips using hot air drying (Agarry & Aworanti, 2012; Madamba, 2003). Similar findings were published by Motevali et al. (2016) and Sharabiani et al. (2021), who found that increasing hot air temperature and air velocity improved moisture diffusivity for certain agricultural products (leaves and apples, respectively). As far as pre-treatment is concerned, osmotic pre-treatment increases the effective moisture diffusivity of the coconut kernel product. Similar trends were also noticed by Ramaswamy and Nsonzi (2007) and Revaskar et al. (2014) on the effect of pre-treatment on moisture diffusivity.

For further analysis, activation energy could also be obtained from the Arrhenius correlation, which demonstrates the effective diffusivity's reliance on temperature as shown in the following Equation 7:

$$D_{eff} = D_o \exp\left(\frac{E_a}{RT_{abs}}\right) \quad (7)$$

where D_o is the pre-exponential factor of the Arrhenius equation (m^2/s), E_a is the activation energy (kJ/mol), R is the universal gas constant (kJ/mol K), and T_{abs} is the absolute temperature (K). By taking the natural logarithm of both sides, the above exponential form of Arrhenius can be transformed into a linear, logarithmic form, and the E_a can be computed from the slope of Equation 8:

$$\ln D_{eff} = \ln D_o - \frac{E_a}{RT_{abs}} \quad (8)$$

While many research findings investigated the activation energy of rice products using various drying methods (Ahou et al., 2014; Anuththara et al., 2019; Khanali et al., 2016) and apples (Cruz et al., 2015; Meisami-asl et al., 2010; Sharabiani et al., 2021), very few studies have been done on coconut kernel products except the one that was reported by Kalayanamitra and Assawarachan (2022) and Madhiyanon et al. (2009). Table 3 shows that the result of the activation energy of chopped coconut was 25.92 kJ/mol, which was close to the other findings of coconut residue at 26.09 kJ/mol using the same fluidised bed drying method. Only two drying methods, fluidised bed drying and hot air drying, were used in the previous studies on drying kinetics. It demonstrates that work on coconut kernel products, particularly in drying kinetics, is still lacking. Research in finding the activation energy of coconut kernel products with different drying methods is necessary for designing alternative and better drying systems.

Table 3
List of drying kinetic models, moisture diffusivity and activation energy for coconut kernel product

Coconut kernel product	Best fit model	Moisture diffusivity (D_{eff}) and Activation energy (E_a)	Drying method	References
Chopped coconut	Modified Henderson and Pabis	$D_{eff} = 5.9902 \times 10^{-8}$ to $2.6616 \times 10^{-7} \text{ m}^2/\text{s}$ $E_a = 25.92 \text{ kJ/mol}$	Fluidised bed drying	(Madhiyanon et al., 2009)
Osmotic Coconut strips	Page	D_{eff} (osmosised) = 5.74 to $7.88 \times 10^{-10} \text{ m}^2/\text{s}$ D_{eff} (non-osmosised) = 5.44 $\times 10^{-10} \text{ m}^2/\text{s}$	Hot air drying	(Agarry & Aworanti, 2012)
Osmotic pre-dried young coconut strips	Page	$D_{eff} = 1.71$ to $5.51 \times 10^{10} \text{ m}^2/\text{s}$	Oven drying	(Madamba, 2003)
Grated coconut	Logarithmic	-	Convective oven	(Abidin et al., 2014)
Coconut residue	Linear plus-exponential	-	Hot air drying	(Wutthigarn et al., 2018)
	Midilli	$E_a = 26.09 \text{ kJ/mol}$	Fluidised bed drying	(Kalayanamitra & Assawarachan, 2022)
Coconut slices	Page	-	Hot air drying	(Pestaño, 2015)

CONCLUSION

The drying methods, parameters, and types of final products predominantly influence the drying behaviour and characteristics of coconut kernel products. For drying parameters, it is deliberately mentioned that air temperature, velocity, and pre-treatments contributed to the increment of the drying rate and the quality of the final coconut kernel product. Apart from that, it is well understood that certain traditional products, such as copra, do not need pre-treatment prior to drying, while some recent developments in new products, such as desiccated coconut and osmosised coconut strips, do need pre-treatment beforehand to retain some quality standards set by the industry. However, there has been no research into optimising coconut kernel products' drying process. In terms of the drying method, it is clearly stated that physico-chemical properties and the coconut kernel product market determine the drying method being applied. It is true as most copra products go through the traditional way of drying and serve as second-grade products, whereas products like desiccated coconut and coconut flakes use a more advanced drying technique, such as fluidised bed drying. Convective drying, such as cabinet drying, remains the most popular method for coconut kernel products. Nevertheless, as technology advances, there is still room for research in drying coconut kernel products, particularly using other recent drying techniques such as hybrid and non-thermal pre-treatments. Also, very few studies have been carried out on the drying kinetics model of coconut kernel products, and among the models presented, it was found that most of the well-suited models were semi-empirical

type models. The Page model performed the best in fitting the drying of coconut kernel products. Also, very few studies were reported on the effective moisture diffusivity and activation energy of coconut kernel products compared to other agricultural products.

Finally, more comprehensive studies regarding drying parameters, pre-treatment methods, appropriate kinetic models, and optimisation of drying could provide a better understanding of the drying of coconut kernel products, thereby contributing to an efficient drying method and high quality of the final product. In the future, other recent drying methods, such as radiation-type and hybrid drying, could also be considered with more systematic design protocols. Moreover, attempts should also be made to scale up certain laboratory drying methods to an industrial scale.

ACKNOWLEDGEMENT

The authors gratefully acknowledge the Universiti Putra Malaysia (UPM) and the Malaysian Agricultural Research and Development Institute (MARDI) for their PhD scholarships, technical support, and guidance towards the success of this research work. On top of that, the authors also express gratitude for the financial support for this research provided by the Universiti Putra Malaysia under the *Inisiatif Putra Siswazah* Research Grant (GP-IPS/2022/9722300) with VOT number: 972230.

REFERENCES

- Abidin, M. H. Z., Sabudin, S., Zakaria, J. H., & Batcha, M. F. M. (2014). Thin layer modeling of grated coconut drying. *Applied Mechanics and Materials*, 660, 367-372. <https://doi.org/10.4028/www.scientific.net/AMM.660.367>
- Agarry, S. E., & Aworanti, O. A. (2012). Modelling the drying characteristics of *osmosised* coconut strips at constant air temperature. *Journal of Food Processing & Technology*, 3(4), Article 1000151. <https://doi.org/10.4172/2157-7110.1000151>
- Ahou, K., Emmanuel, A. N., Patrice, K., & Benjamin, Y. (2014). Modelling of rough rice solar drying under natural convection. *European Scientific Journal*, 10(3), 141-156.
- Arulandoo, X., Sritharan, K., & Subramaniam, M. (2017). The coconut palm. In B. Thomas, B. G. Murray & D. J. Murphy (Eds.) *Encyclopedia of applied plant sciences* (2nd ed.: pp. 426-430). Elsevier. <https://doi.org/10.1016/B978-0-12-394807-6.00237-9>
- Anuththara, J. G. M., Edirisinghe, E. A. V. U., Amarasinghe, B. M. W. P. K., & Jayatunga, G. K. (2019, July 03-05). *Kinetics and mathematical modeling of drying of parboiled paddy in a packed bed dryer*. [Paper presentation]. Moratuwa Engineering Research Conference (MERCCon), Moratuwa, Sri Lanka. <https://doi.org/10.1109/MERCCon.2019.8818766>
- Arun, S., Balaji, S. S., & Selvan, P. (2014). Experimental Studies on drying characteristics of coconuts in a solar tunnel greenhouse dryer coupled with biomass backup heater. *International Journal of Innovative Technology and Exploring Engineering*, 4(5), 56-60.

- Bal, L. M., Kar, A., Satya, S., & Naik, S. N. (2010). Drying kinetics and effective moisture diffusivity of bamboo shoot slices undergoing microwave drying. *International Journal of Food Science and Technology*, 45(11), 2321–2328. <https://doi.org/10.1111/j.1365-2621.2010.02402.x>
- Erkmen, O., & Bozoglu, T. F. (2016). Food preservation by reducing water activity. In *Food microbiology: Principles into practice* (pp. 44–58). Wiley. <https://doi.org/10.1002/9781119237860.ch30>
- Chantaro, P., Sriuathong, S., Charoen, R., & Chalermchaiwat, P. (2016). Pre-treatment conditions affect quality and sensory acceptability of dried osmotic dehydrated coconut. *International Food Research Journal*, 23(4), 1453-1458.
- Cruz, A. C., Guiné, R. P. F., & Gonçalves, J. C. (2015). Drying kinetics and product quality for convective drying of apples (cvs. golden delicious and granny smith). *International Journal of Fruit Science*, 15(1), 54-78. <https://doi.org/10.1080/15538362.2014.931166>
- Deepa, J., Rajkumar, P., & Arumuganathan, T. (2015). Quality analysis of copra dried at different drying air temperatures. *International Journal of Agricultural Science and Research (IJASR)*, 5(4), 1-5.
- Deng, L. Z., Mujumdar, A. S., Zhang, Q., Yang, X. H., Wang, J., Zheng, Z. A., Gao, Z. J., & Xiao, H. W. (2019). Chemical and physical pretreatments of fruits and vegetables: Effects on drying characteristics and quality attributes - A comprehensive review. *Critical Reviews in Food Science and Nutrition*, 59(9), 1408-1432. <https://doi.org/10.1080/10408398.2017.1409192>
- Devi, M., & Ghatani, K. (2022). The use of coconut in rituals and food preparations in India: A review. *Journal of Ethnic Foods*, 9(1), 1-13. <https://doi.org/10.1186/s42779-022-00150-7>
- Dippon, K., & Villarup, E. R. (1996, July 15-19). *Copra dryers and copra drying technologies*. [Paper presentation]. Proceedings of the XXXIII Cocotech Meeting, Kuala Lumpur Malaysia.
- Fayose, F., & Huan, Z. (2016). Heat pump drying of fruits and vegetables: Principles and potentials for Sub-Saharan Africa. *International Journal of Food Science 2016*, 9673029. <https://doi.org/10.1155/2016/9673029>
- Feng, H., Yin, Y., & Tang, J. (2012). Microwave Drying of food and agricultural materials: Basics and heat and mass transfer modeling. *Food Engineering Reviews*, 4(2), 89–106. <https://doi.org/10.1007/s12393-012-9048-x>
- Guarte, R. C., Mühlbauer, W., & Kellert, M. (1996). Drying characteristics of copra and quality of copra and coconut oil. *Postharvest Biology and Technology*, 9(3), 361–372. [https://doi.org/10.1016/S0925-5214\(96\)00032-4](https://doi.org/10.1016/S0925-5214(96)00032-4)
- Guida, V., Ferrari, G., Pataro, G., Chambery, A., Di Maro, A., & Parente, A. (2013). The effects of ohmic and conventional blanching on the nutritional, bioactive compounds and quality parameters of artichoke heads. *LWT - Food Science and Technology*, 53(2), 569-579. <https://doi.org/10.1016/j.lwt.2013.04.006>
- Guiné, R. (2018). The drying of foods and its effect on the physical-chemical, sensorial and nutritional properties. *ETP International Journal of Food Engineering*, 4(2), 93–100. <https://doi.org/10.18178/ijfe.4.2.93-100>
- Gupta, V., Vijayalakshmi, N. S., Ashwini, B., Anbarasu, K., Vijayalakshmi, G., Prakash, M., Indiramma, A. R., Rangarao, G. C. P., & Ramesh, B. S. (2010). Shelf life enhancement of coconut burfi - an Indian traditional sweet. *Journal of Food Quality*, 33(3), 329–349. <https://doi.org/10.1111/j.1745-4557.2010.00312.x>

- Hii, C. L., & Ogugo, J. F. (2014). Effect of pre-treatment on the drying kinetics and product quality of star fruit slices. *Journal of Engineering Science and Technology*, 9(1), 122–134.
- Inyang, U. E., Oboh, I. O., & Etuk, B. R. (2018). Kinetic models for drying techniques—Food materials. *Advances in Chemical Engineering and Science*, 8(2), 27–48. <https://doi.org/10.4236/aces.2018.82003>
- Jayasekhar, S., Chandran, K. P., Thamban, C., Jaganathan, D., & Muralidharan, K. (2017). Analyzing the trade competitiveness of Indian coconut sector in the liberalization regime. *Journal of Plantation Crops*, 44(3), 147. <https://doi.org/10.19071/jpc.2016.v44.i3.3163>
- Jongyingcharoen, J. S., Wuttigarn, P., & Assawarachan, R. (2019). Hot air drying of coconut residue: Shelf life, drying characteristics, and product quality. *IOP Conference Series: Earth and Environmental Science*, 301(1), Article 012033. <https://doi.org/10.1088/1755-1315/301/1/012033>
- Joshi, S., Kaushik, V., Gode, V., & Mhaskar, S. (2020). Coconut oil and immunity: What do we really know about it so far? *The Journal of the Association of Physicians of India*, 68(7), 67–72.
- Kalayanamitra, K., & Assawarachan, R. (2022). Modeling the drying of coconut residue in fluidized bed dryer. *Journal of Culinary Science & Technology*, 1-15. <https://doi.org/10.1080/15428052.2022.2036662>
- Kamalanathan, G., & Meyyappan, R. M. (2014). Osmotic drying out of coconut slices in salt solution: Optimization of process parameters using response surface methodology. *International Journal of ChemTech Research*, 7(6), 2773-2785.
- Khanali, M., Banisharif, A., & Rafiee, S. (2016). Modeling of moisture diffusivity, activation energy and energy consumption in fluidized bed drying of rough rice. *Heat and Mass Transfer*, 52, 2541-2549. <https://doi.org/10.1007/s00231-016-1763-z>
- Konan, B. R., Konan, J. L., Assa, R. R., Oule, M., & Amanai, G. (2009). The physicochemical characteristics of coconut (*Cocos nucifera L.*) kernels in germination. *Seed Science and Technology*, 3(1), 1–7.
- Krishna, S., & Mathew, G. (2018). Development of a solar copra dryer incorporated with evacuated tubes. *International Journal of Current Microbiology and Applied Sciences*, 7(6), 2457-2465. <https://doi.org/10.20546/ijcmas.2018.706.292>
- Kurniawan, H., Sukmawaty, S., Ansar, A., Yuniarto, K., Sabani, R., & Murad, M. (2021). Introduksi teknologi pengolahan kelapa menjadi coconut chips di UKM maju bersama Desa Kekait, Gunung Sari, Lombok Barat [Introduction of coconut processing technology of coconut chips in UKM with Kekait Village, Gunung Sari, Lombok Barat]. *Jurnal Ilmiah Abdi Mas TPB Unram*, 3(1), 8-14. <https://doi.org/10.29303/amtpb.v3i1.55>
- Lal, J. J., Sreeranjit Kumar, C. V., & Indira, M. (2003). Coconut palm. In L. Trugo & R. M. Finglas (Eds.), *Encyclopedia of Food Sciences and Nutrition* (2nd ed., pp.1464-1475). Academic Press. <https://doi.org/10.1016/B0-12-227055-X/00263-7>
- Lamidi, R. O., Jiang, L., Pathare, P. B., Wang, Y. D., & Roskilly, A. P. (2019). Recent advances in sustainable drying of agricultural produce: A review. *Applied Energy*, 233–234, 367–385. <https://doi.org/10.1016/j.apenergy.2018.10.044>
- Lee, D., So, J. D., Jung, H. M., Mo, C., & Lee, S. H. (2018). Investigation of drying kinetics and color characteristics of white radish strips under microwave drying. *Journal of Biosystems Engineering*, 43(3), 237–246.

- Liu, H., Liu, H., Liu, H., Zhang, X., Hong, Q., Chen, W., & Zeng, X. (2021). Microwave drying characteristics and drying quality analysis of corn in China. *Processes*, 9(9), 1511. <https://doi.org/10.3390/pr9091511>
- Madamba, P. S. (2003). Thin layer drying models for osmotically pre-dried young coconut. *Drying Technology*, 21(9), 1759-1780. <https://doi.org/10.1081/DRT-120025507>
- Madhiyanon, T., Phila, A., & Soponronnarit, S. (2009). Models of fluidized bed drying for thin-layer chopped coconut. *Applied Thermal Engineering*, 29(14-15), 2849-2854. <https://doi.org/10.1016/j.applthermaleng.2009.02.003>
- Manikantan, M. R. R., Arumuganathan, T., Arivalagan, M., Matthew, A. C., & Hebbar, K. B. (2015). Coconut chips: A healthy non-fried snack food. *Indian Coconut Journal*, 34-36.
- Marikkar, J. M. N., & Madurapperuma, W. S. (2012). Coconut. In M. Siddiq (Ed.) *Tropical and subtropical fruits: Postharvest physiology, processing and packaging* (pp. 159-177). Wiley. <https://doi.org/10.1002/9781118324097.ch9>
- Meisami-asl, E., Rafiee, S., Keyhani, A., & Tabatabaefar, A. (2010). Drying of apple slices (var. Golab) and effect on moisture diffusivity and activation energy. *Plant Omics*, 3(3), 97-102.
- Mithra, A., Swamy, G. J., Rajendran, S. P., Chandrasekar, V., Shanmgam, S., & Hasker, E. (2013). Coconut-value added products coconut : An extensive review on value added products. *Indian Food Industry Magazine*, 32(6), 1-9.
- Mohanraj, M., & Chandrasekar, P. (2008a). Comparison of drying characteristics and quality of copra obtained in a forced convection solar drier and sun drying. *Journal of Scientific and Industrial Research*, 67(5), 381-385.
- Mohanraj, M., & Chandrasekar, P. (2008b). Drying of copra in a forced convection solar drier. *Biosystems Engineering*, 99(4), 604-607. <https://doi.org/10.1016/j.biosystemseng.2007.12.004>
- Mohanraj, M., Chandrasekar, P., & Sreenarayanan, V. V. (2008). Performance of a heat pump drier for copra drying. *Proceedings of the Institution of Mechanical Engineers, Part A: Journal of Power and Energy*, 222(3), 283-287. <https://doi.org/10.1243/09576509JPE548>
- Moses, J. A. A., Paramasivan, K., Sinija, V. R. R., Alagusundaram, K., Brijesh kumar, T., Alugusundaram, K., & Kumar, B. (2013). Effect of microwave treatment on drying characteristics and quality parameters of thin layer drying of coconut Jeyan. *Asian Journal of Food and Agro-Industry*, 6(02), 72-85.
- Motevali, A., Chayjan, R. A., Salari, K., & Taghizadeh, A. (2016). Studying the effect of different drying bed on drying characteristic of mint leaves. *Chemical Product and Process Modeling*, 11(3), 231-239. <https://doi.org/10.1515/cppm-2015-0045>
- Mühlbauer, W., & Müller, J. (2020). Quality kinetics. In *Drying atlas* (pp.63-66). Woodhead Publishing. <https://doi.org/10.1016/b978-0-12-818162-1.00007-9>
- Nelsonkanem, E., Alonge, A., George, E., & Ossom, I. (2020). Optimization of mechanically expressed coconut (*Cocos Nucifera* L.) oil using response surface methodology. *The International Journal of Engineering and Science*, 9(6),1-9. <https://doi.org/10.9790/1813-0906010109www.theijes.com>
- Niamnuy, C., & Devahastin, S. (2005). Drying kinetics and quality of coconut dried in a fluidized bed dryer. *Journal of Food Engineering*, 66(2), 267-271. <https://doi.org/10.1016/j.jfoodeng.2004.03.017>

- Nor, N. F. A., Ya'akob, H., Idris, A., Ngadiran, S., Anuar, N. S., & Sarmidi, M. R. (2021). Evolutions in virgin coconut oil: Liquid to powder. *Jurnal Teknologi*, 83(3), 119–132. <https://doi.org/10.11113/jurnalteknologi.v83.16265>
- Pestaño, L. D. B. (2015, April 11-12). *Mathematical modeling of the drying process*. [Paper presentation]. Third International Conference on Advances in Applied Science and Environmental Engineering (ASEE), Kuala Lumpur, Malaysia. <https://doi.org/10.15224/978-1-63248-055-2-80>
- Pestaño, L. D. B., & Jose, W. I. (2016). Engineering an improved coconut processing system in the Philippines at the farm-level. *Journal of Advanced Agricultural Technologies*, 3(1), 58-62. <https://doi.org/10.18178/joaat.3.1.58-62>
- Prades, A., Salum, U. N., & Pioch, D. (2016). New era for the coconut sector. What prospects for research? *Oilseeds & Fats, Crops and Lipids*, 23(6), 4–7. <https://doi.org/10.1051/ocl/2016048>
- Pravitha, M., Manikantan, M. R., Ajesh Kumar, V., Shameena Beegum, P. P., & Pandiselvam, R. (2022). Comparison of drying behavior and product quality of coconut chips treated with different osmotic agents. *Lwt*, 162, 113432. <https://doi.org/10.1016/j.lwt.2022.113432>
- Prieto, W. H., Iguti, A. M., & Nitz, M. (2011). Drying evaluation of green coconut pulp for obtaining a snack-like product. *Procedia Food Science*, 1, 1618–1627. <https://doi.org/10.1016/j.profoo.2011.09.239>
- Ramaswamy, H. S., & Nsonzi, F. (2007). Convective-air drying kinetics of osmotically pre-treated blueberries. *Drying Technology*, 16(235), 743-759. <https://doi.org/http://dx.doi.org/10.1080/07373939808917433>
- Revaskar, V. A., Pisalkar, P. S., Pathare, P. B., & Sharma, G. P. (2014). Dehydration kinetics of onion slices in osmotic and air convective drying process. *Research in Agricultural Engineering*, 60(3), 92-99.
- Salehi, F. (2021). Recent applications of heat pump dryer for drying of fruit crops: A review. *International Journal of Fruit Science*, 21(1), 546–555. <https://doi.org/10.1080/15538362.2021.1911746>
- Samson, A. S. (1971). Heat treatment of coconut meats and coconut meal. *Journal of the Science of Food and Agriculture*, 22(6), 312–316. <https://doi.org/10.1002/jsfa.2740220612>
- Santosa, I., Sulistiawati, E., & Aktawan, A. (2019). Mathematical modeling of drying behavior of coconut grate in a modified screw mixed dryer. *IOP Conference Series: Materials Science and Engineering*, 674(1), 1–6. <https://doi.org/10.1088/1757-899X/674/1/012009>
- Sarkar, A., Ahmed, T., Alam, M., Rahman, S., & Pramanik, S. K. (2020). Influences of osmotic dehydration on drying behavior and product quality of coconut (*Cocos nucifera*). *Asian Food Science Journal*, 15(3), 21-30. <https://doi.org/10.9734/afs/j/2020/v15i330153>
- Satter, M. A. (2001, December 26-28). *Optimization of copra drying factors by taguchi method*. [Paper presentation]. 4th International Conference on Mechanical Engineering, Dhaka, Bangladesh.
- Sharabiani, V. R., Kaveh, M., Abdi, R., Szymanek, M., & Tanaś, W. (2021). Estimation of moisture ratio for apple drying by convective and microwave methods using artificial neural network modeling. *Scientific Reports*, 11(1), 1-12. <https://doi.org/10.1038/s41598-021-88270-z>
- Simpson, R., Ramírez, C., Nuñez, H., Jaques, A., & Almonacid, S. (2017). Understanding the success of Page's model and related empirical equations in fitting experimental data of diffusion phenomena in food matrices. *Trends in Food Science and Technology*, 62, 194-201. <https://doi.org/10.1016/j.tifs.2017.01.003>

- Sutar, P., & Prasad, S. (2008, February 1-3). *Microwave drying technology-recent developments and R&D needs in India*. [Paper presentation]. 42nd ISAE Annual Convention, Bhopal, India.
- Tepe, T. K., & Tepe, B. (2020). The comparison of drying and rehydration characteristics of intermittent-microwave and hot-air dried-apple slices. *Heat and Mass Transfer*, 56(11), 3047–3057. <https://doi.org/10.1007/s00231-020-02907-9>
- Thanaraj, T., Dharmasena, N. D. A., & Samarajeewa, U. (2007). Comparison of drying behaviour, quality and yield of copra processed in either a solar hybrid dryer or in an improved copra kiln. *International Journal of Food Science and Technology*, 42(2), 125-132. <https://doi.org/10.1111/j.1365-2621.2006.01087.x>
- Thiyagarajan, R., Srinivasan, P., Aneesh, T., & Mayilvakanan, S. (2020). Design and fabrication of semi automatic coconut copra electric dryer. *International Journal of Innovative Technology and Exploring Engineering*, 9(6), 637-641. <https://doi.org/10.35940/ijitee.f3323.049620>
- These, H. (2016). Spoilage of vegetables and fruits. In O. Erkmen & T. F. Bozoglu (Eds.) *Food microbiology: Principles into practice* (pp.337–363). Wiley <https://doi.org/10.1002/9781119237860.ch20>
- Thiyagarajan, R., Srinivasan, P., Aneesh, T., & Mayilvakanan, S. (2020). Design and fabrication of semi automatic coconut copra electric dryer. *International Journal of Innovative Technology and Exploring Engineering*, 9(6), 637–641. <https://doi.org/10.35940/ijitee.f3323.049620>
- Vera, F. H. C., Soriano, A. N., & Dugos, N. P. (2021). A Comprehensive review on the drying kinetics of common tubers. *Applied Science and Engineering Progress*, 14(2), 146-155. <https://doi.org/10.14416/j.asep.2021.03.003>
- Waisundara, V. Y., Perera, C. O., & Barlow, P. J. (2007). Effect of different pre-treatments of fresh coconut kernels on some of the quality attributes of the coconut milk extracted. *Food Chemistry*, 101(2), 771-777. <https://doi.org/10.1016/j.foodchem.2006.02.032>
- Wutthigarn, P., Hongwiangjan, J., & Sripinyowanich Jongyingcharoen, J. (2018). Modeling of hot air drying of coconut residue. *MATEC Web of Conferences*, 192, 1-4. <https://doi.org/10.1051/mateconf/201819203061>
- Yahya, S., Shahrir, A. M., Syarifuddin, M. A. A. A., Shafie, A., Shukri, J. M., Zaimi, Z. A. A. M., & Redzuan, S. A. (2020). A study of drying parameters on drying time and colour quality of grated coconut using tumbling mechanism in convective dryer. *Food Research*, 4(Suppl. 6), 64-69. [https://doi.org/10.26656/fr.2017.4\(S6\).023](https://doi.org/10.26656/fr.2017.4(S6).023)
- Yu, Y., Jin, T. Z., & Xiao, G. (2017). Effects of pulsed electric fields pretreatment and drying method on drying characteristics and nutritive quality of blueberries. *Journal of Food Processing and Preservation*, 41(6), Article e13303. <https://doi.org/10.1111/jfpp.13303>

REFEREES FOR THE PERTANIKA JOURNAL OF SCIENCE & TECHNOLOGY

Vol. 31 (5) Aug. 2023

The Editorial Board of the Pertanika Journal of Science and Technology wishes to thank the following:

Abdelkader Baghdad Bey
(UNIV-MASCARA, Algeria)

Galuh Yuliani
(UPI, Indonesia)

Marina Mohd Top
(UPM, Malaysia)

Aloysius Akaangee Pam
(FUL, Nigeria)

Geetha Annavi
(UPM, Malaysia)

Mohamad Hasnul Bolhassan
(UNIMAS, Malaysia)

Aminu Rabiu
(UDUS, Nigeria)

Giovani L. Zabot
(UFSM, Brazil)

Mohd Azan Mohammed Sapardi
(IIUM, Malaysia)

Amir Izzwan Zamri
(UMT, Malaysia)

Gupta Surbhi
(Amity University, India)

Mohd Fareed Mohd Sairi
(UKM, Malaysia)

Ana Sakura Zainal Abidin
(UNIMAS, Malaysia)

Helena Sovová
(ICPF, Czech Republic)

Mohd Hanafi Idris
(UTM, Malaysia)

Andrew Alek Tuen
(UNIMAS, Malaysia)

Hossein Barani
(University of Birjand, Iran)

Mohd Khairul Nizam Mohd
Zuhan
(UTHM, Malaysia)

Arpah Abu
(UM, Malaysia)

Husnul Azan Tajarudin
(USM, Malaysia)

Mohd Shahrime Mohd Asaari
(USM, Malaysia)

Aytuğ Onan
(IKCU, Turkey)

Imran Memon
(Zhejiang University, China)

Mohd Shamsul Anuar
(UPM, Malaysia)

Che Mohd Imran Che Taib
(UMT, Malaysia)

Joseph Babalola Agboola
(University of Lagos, Nigeria)

Muhammad Azril Hezmi
(UTM, Malaysia)

Ch'ng Huck Ywih
(UMK, Malaysia)

Kek Sie Long
(UTHM, Malaysia)

Muhammad Najib Razali
(UTM, Malaysia)

Claudia Maria Simonescu
(UPB, Romania)

Leo Choe Peng
(USM, Malaysia)

Najah Ghazali
(UNIMAP, Malaysia)

Earl of Cranbrook
(UWSP, UK)

Liangli Zhen
(A*STAR, Singapore)

Nazeha Khalil
(Menoufia University, Egypt)

Fam Soo Fen
(UTeM, Malaysia)

M Tanveer Hossain Parash
(UMS, Malaysia)

Noor Hisyam Noor Mohamed
(UNIMAS, Malaysia)

Fariza Hanis Abdul Razak
(UiTM, Malaysia)

Mahadimenakbar Mohd.
Dawood
(UMS, Malaysia)

Nor Afiqah Aleng
(UMT, Malaysia)

Farshid Keynia
(GUAT, Iran)

Maisarah Mohamed Bazin
(UniKL, Malaysia)

Norasiha Hamid
(UCYP, Malaysia)

Filippo Pierini
(Polish Academy of Sciences, Poland)

Marife Leonardo Pesino
(CBSUA, Philippines)

Norshita Mat Nayan
(UKM, Malaysia)

Nurfatimah Mohd Thani
(UKM, Malaysia)

Rizwan Nasir
(University of Jeddah, Saudi Arabia)

Wan Mohd Rauhan Wan Hussin
(UMT, Malaysia)

Nurhuda Faujan
(USIM, Malaysia)

Sadia Chowdhury Shimmi
(UMS, Malaysia)

Yusuf Chong Yu Lok
(UiTM, Malaysia)

Nurul Hawa Ahmad
(UPM, Malaysia)

Sharifah Adzila Syed Abu Bakar
(UTHM, Malaysia)

Zarani Mat Taher
(UTM, Malaysia)

Ooi Boon Yaik
(UTAR, Malaysia)

Shervan Fekri-Ershad
(Islamic Azad University, Iran)

Zeinab Abbas Jawad
(Curtin University, Malaysia)

Pavol Bozek
(STU, Slovakia)

Suzita Ramli
(UPSI, Malaysia)

Zhongqiang Luo
(SUSE, China)

Rabiatul Adawiah Zainal Abidin
(MARDI, Malaysia)

Vivien How
(UPM, Malaysia)

A*STAR – Agency for Science, Technology and Research
CBSUA – Central Bicol State University of Agriculture
FUL – Federal University Lokoja
GUAT – Graduate University of Advanced Technology
ICPF – Institute of Chemical Process Fundamentals
IUM – International Islamic University Malaysia
IKCU – Izmir Katip Çelebi University
STU – Slovak University of Technology
SUSE – Sichuan University of Science and Engineering
UCYP – University College of Yayasan Pahang
UDUS – Usmanu Danfodiyo University Sokoto
UFSM – Universidade Federal de Santa Maria
UiTM – Universiti Teknologi MARA
UKM – Universiti Kebangsaan Malaysia
UM – Universiti Malaya
UMK – Universiti Malaysia Kelantan
UMS – Universiti Malaysia Sabah

UMT – Universiti Malaysia Terengganu
UniKL – University Kuala Lumpur
UNIMAP – Universiti Malaysia Perlis
UNIMAS – Universiti Malaysia Sarawak
UNIV-MASCARA – University of Mustapha Stambouli Mascara
UPB – Politehnica University of Bucharest
UPI – Universitas Pendidikan Indonesia
UPM – Universiti Putra Malaysia
UPSI – University Pendidikan Sultan Idris
USIM – Universiti Sains Islam Malaysia
USM – Universiti Sains Malaysia
UTAR – Universiti Tunku Abdul Rahman
UTeM – Universiti Teknikal Malaysia Melaka
UTHM – Universiti Tun Hussein Onn Malaysia
UTM – Universiti Teknologi Malaysia
UWSP – University of Warwick Science Park

While every effort has been made to include a complete list of referees for the period stated above, however if any name(s) have been omitted unintentionally or spelt incorrectly, please notify the Chief Executive Editor, *Pertanika* Journals at executive_editor.pertanika@upm.edu.my

Any inclusion or exclusion of name(s) on this page does not commit the *Pertanika* Editorial Office, nor the UPM Press or the university to provide any liability for whatsoever reason.

<i>Review Article</i>	
The Unified Model of Electronic Government Adoption (UMEGA): A Systematic Literature Review with Meta-Analysis <i>Rakib Ahmed Saleh, Rozi Nor Haizan Nor, Md. Tariqul Islam, Yusmadi Yah Jusoh and Salfarina Abdullah</i>	2531
Workload Characterization and Classification: A Step Towards Better Resource Utilization in a Cloud Data Center <i>Avita Katal, Susheela Dahiya and Tanupriya Choudhury</i>	2559
Reactivity Enhancement of Lignin Extracted from Preconditioning Refiner Chemical-Recycle Bleached Mechanized Pulp (PRC-RBMP) Black Liquor by Phenolation <i>Lim Kah Yen, Tengku Arisyah Tengku Yasim-Anuar, Farhana Aziz Ujang, Hazwani Husin, Hidayah Ariffin, Paridah Md Tahir, Li Xin Ping and Mohd Termizi Yusof</i>	2577
<i>Fusarium solani</i> Species Complex (FSSC) in Nests of Hawksbill Turtles (<i>Eretmochelys imbricata</i>) with High Hatching Success in Melaka, Malaysia <i>Khai Wei See and Nurul Salmi Abdul Latip</i>	2601
<i>Review Article</i>	
Progress, Trends and Development of Drying Studies on Coconut Kernel Products: A Review <i>Yahya Sahari, Mohd Shamsul Anuar, Mohd Zuhair Mohd Nor, Nur Hamizah Abdul Ghani and Suraya Mohd Tahir</i>	2621

A Study on Bio-Stabilisation of Sub-Standard Soil by Indigenous Soil Urease-Producing Bacteria <i>Abdulaziz Dardau Aliyu, Muskhazli Mustafa, Nor Azwady Abd Aziz and Najaatu Shehu Hadi</i>	2389
Occupational Formaldehyde Exposure and the Health Symptoms Among Histopathology Laboratory Workers in North Borneo <i>Alif Ramli, Shamsul Bahari Shamsudin, Jac Fang Lim and Mei Ching Lim</i>	2413
Estimating Disability-Free Life Expectancy of Malaysian Population Using the Sullivan's Approach <i>Khairunnisa Mokhtar, Syazreen Niza Shair and Norazliani Md Lazam</i>	2427
Effects of UV Irradation on Electrospun PLLA and PAN in the Production of Short Electrospun Fibres Using Ultrasonication Method <i>Marini Sawawi, Cheryl Rinnai Raja, Shirley Jonathan Tanjung, Sinin Hamdan, Siti Kudnie Sahari, Rohana Sapawi, Ervina Junaidi, Mahshuri Yusof and Noor Hisyam Noor Mohamed</i>	2441
A Comparison of the Performance of MAPbI ₃ and MASnI ₃ as an Inverted Perovskite Structure Using NiO as HTL Through Numerical GPVDM Simulation <i>Subathra Muniandy, Muhammad Idzdihar Idris, Zul Atfyi Fauzan Mohammed Napiah, Zarina Baharudin Zamani, Marzaini Rashid and Luke Bradley</i>	2453
Fabrication of PES MMMs with Improved Separation Performances Using Two-Dimensional rGO/ZIF-8 and MoS ₂ / ZIF-8 Nanofillers <i>Noor Fauziyah Ishak, Nur Hidayati Othman, Najihah Jamil, Nur Hashimah Alias, Fauziah Marpani, Munawar Zaman Shahrudin, Lau Woei Jye and Ahmad Fauzi Ismail</i>	2473
The Influence of Abiotic Factors on the Occurrence of Jackfruit Dieback Disease <i>Nurul Hawani Idris, Erneeza Mohd Hata, Norliza Adnan, Sazlieya Saupi Teri, Mohamad Jahidi Osman, Ami Hassan Md Din and Mohamad Hafis Izran Ishak</i>	2487
<i>Review Article</i>	
The Grease Formulation Using Waste Substances from Palm Oil Refinery and Other Industrial Wastes: A Review <i>Muhammad Auni Hairunnaja, Mohd Aizudin Abd Aziz, Nur Amira Fatihah Bashari, Mohd Azmir Arifin, Navinash Nedumaran, Khairuddin Md Isa and Umi Fazara Md Ali</i>	2505

Correlation Studies and Kinetic Modelling of Electrocoagulation Treatment of Pepper Wastewater <i>Puteri Nurain Megat Ahmad Azman, Rosnah Shamsudin, Hasfalina Che Man and Mohammad Effendy Ya'acob</i>	2273
<i>Short Communication</i>	
The Digestibility and Bacterial Growth Rates of Microwave Treated Sago (<i>Metroxylon sagu</i>) Starch <i>Mohd Alhafizh Zailani, Hanisah Kamilah, Ahmad Husaini, Awang Zulfikar Rizal Awang Seruji and Shahrul Razid Sarbini</i>	2283
Effects of Microwave Power and Carrier Materials on Anthocyanins, Antioxidants, and Total Phenolic Content of Encapsulated <i>Clitoria ternatea</i> Flower Extract <i>Nurul Asyikin Md Zaki, Junaidah Jai, Mohd Hakim Syuwari Hasan, Nur Qistina Mohamad Kamarul Azman, Syafiza Abd Hashib, Nozieana Khairuddin, Norashikin Mat Zain and Nurul Hidayah Samsulrizal</i>	2291
Utilization of Water Hyacinth and Spent Coffee Ground as Raw Materials to Produce Bio-Compost <i>Thanakorn Saengsanga and Napat Noinumsai</i>	2303
Effect of Pre-Treatment Methods on the Extractability of <i>Christia vespertilionis</i> by Supercritical Carbon Dioxide <i>Izni Atikah Abd Hamid, Najla Laazizi, Ana Najwa Mustapa and Norazah Abd Rahman</i>	2311
Spatial Distribution of Malaysian Storks Determined Based on Citizen Science (eBird) Data <i>Ain Afifah Tolohah, Fatimah Najihah Arazmi, Shukor Md. Nor and Mohammad Saiful Mansor</i>	2329
<i>Review Article</i>	
Analysis of Environmental Stresses on the Mechanical Properties of Laminated Glass Composites: A Review of Experimental Results and Outlook <i>Ufuoma Joseph Udi, Mustafasanie M. Yussof Felix Nkapheeyan Isa and Luqman Chuah Abdullah</i>	2339
Thermal Properties of Kenaf Fiber Reinforced Polyamide 6 Composites by Melt Processing <i>Norihan Abdullah, Khalina Abdan, Mohd Huzaifah Mohd Roslim, Mohd Nazren Radzuan, Lee Ching Hao and Ayu Rafiqah Shafi</i>	2361
Innovative Formulation and Characterisation of Grease Made from Waste Engine Oil <i>Muhammad Auni Hairunnaja, Mohd Aizudin Abd Aziz, Nurul Waheeda Abdu Rahman, Mohd Azmir Arifin, Khairuddin Md Isa and Umi Fazara Md Ali</i>	2375

Pertanika Journal of Science & Technology
Vol. 31 (5) Aug. 2023

Content

Foreword <i>Mohd Sapuan Salit</i>	i
<i>In Silico</i> Screening of Breadfruit (<i>Artocarpus altilis</i>) Prenylated Flavonoids Identify Potential SARS-CoV Inhibitors <i>Nisha Govender, Siti Nur Athirah Mohd Kaspi, Thennavan Krishnan and Zeti-Azura Mohamed-Hussein</i>	2145
Super-Resolution Approach to Enhance Bone Marrow Trephine Image in the Classification of Classical Myeloproliferative Neoplasms <i>Umi Kalsom Mohamad Yusof, Syamsiah Mashohor, Marsyita Hanafi, Sabariah Md Noor and Norsafina Zainal</i>	2161
Weight Development of Captive Malayan Sun Bears (<i>Helarctos malayanus</i>) in the Malaysian Wildlife Rehabilitation Centre <i>Muhammad Izzat-Husna, Noor Nabilah Nazri, Kamaruddin Zainul Abidin, Mohammad Saiful Mansor, Zubaidah Kamarudin, Rahmat Topani and Shukor Md Nor</i>	2177
<i>Review Article</i> <i>Salmonella</i> Biofilm on Food Contact Surfaces and the Efficacy of Chemical Disinfectants: A Systematic Review <i>Xue Wei Tee and Noor Azira Abdul-Mutalib</i>	2187
Chest Computed Tomography (CT) and Clinical Findings Among COVID-19 Patients of Tertiary Hospital in Bangladesh <i>Tarek Shams, Jamil Haider Chowdhury, Hasna Hena Chowdhury, Qumrul Ahsan, Hrionmoy Dutta, Mohammad Ali Tareq, Lubna Shirin, Sanjida Akhter and Tania Islam</i>	2203
Image Retrieval Using Fusion of Sauvola and Thepade's Sorted Block Truncation Coding-Based Color Features <i>Jaya H. Dewan and Sudeep D. Thepade</i>	2217
On Estimating the Parameters of the Generalised Gamma Distribution based on the Modified Internal Rate of Return for Long-Term Investment Strategy <i>Amani Idris Ahmed Sayed and Shamsul Rijal Muhammad Sabri</i>	2241
Underdetermined Blind Source Separation of Bioacoustic Signals <i>Norsalina Hassan and Dzati Athiar Ramli</i>	2257



Pertanika Editorial Office, Journal Division,
Putra Science Park,
1st Floor, IDEA Tower II,
UPM-MTDC Center,
Universiti Putra Malaysia,
43400 UPM Serdang,
Selangor Darul Ehsan
Malaysia

<http://www.pertanika.upm.edu.my>
Email: executive_editor@upm.edu.my
Tel. No.: +603- 9769 1622

PENERBIT
UPM
UNIVERSITI PUTRA MALAYSIA
PRESS

<http://www.penerbit.upm.edu.my>
Email: penerbit@upm.edu.my
Tel. No.: +603- 9769 8851

